SCALED GEOTECHNICAL CENTRIFUGE MODELLING OF GELIFLUCTION

James Seymour Smith

School of Earth, Ocean and Planetary Sciences
University of Wales, Cardiff

2004

ProQuest LLC
789 East Eisenhower Parkway
P.O. Box 1346
Ann Arbor, MI 48106-1346

RESEARCH SUMMARY

This thesis describes the laboratory modelling of gelifluction processes using the geotechnical centrifuge technique. Thirteen 1/10 scale planar slope models were frozen from the surface downwards on the laboratory floor and thawed, also from the surface downwards, under gravitational acceleration of 10 gravities (approximately 98.1 ms^{-2}). A natural sandy silt soil from Quaternary periglacial slope deposits collected in SW England formed the base test material and slope models at gradients 4°, 8°, 12° and 16° were constructed using this soil. 10% and 20% by weight increments of glaciolacustrine silt and Kaolinite clay were added to the natural soil and a series of slope models were constructed at gradients of 4°, 8°, and 12° using these soils. Each slope model was subjected to four cycles of freezing and thawing except for the four slope models that underwent rapid slope failure. During thaw, soil temperatures and pore water pressures were recorded continuously, together with soil thaw settlement and surface displacement. Following each experiment, models were sectioned to observe displacement columns that showed the profiles of soil movement and allowed volumetric displacements to be calculated. It was shown that thaw settlement and slope gradient strongly affected the rate of surface movement and the subsurface profile of movement. Increasing slope gradient generated greater amounts of subsurface and surface movement as a function of increased gravitational shear stress. Thawing ice lenses inclined parallel to the slope gradient provided localised zones of microshearing in response to localised low frictional resistance. Rates of movement increased between the 4° and 8° models, but a greater increase occurred between the 8° and 12° models. A slope failure was initiated within the 16° slope model. Rates of gelifluction were dominantly influenced by increasing silt content impacting upon the distribution of segregated ice and the reduction of frictional shear strength. Increasing silt content generated high positive porewater pressures commonly in excess of hydrostatic and consequently greater amounts of pre-failure strain. A clear behavioural threshold was identified between the 10% and 20% silt soils, with far greater gelifluction in the latter than the former. Increasing clay content had a less pronounced impact upon rates of gelifluction when compared to increasing silt due to cohesion. Rates of movement increased between the 10% and 20% clay in response to lower shear strength. A sawtooth style of pore pressure response caused by water escape events within the 20% clay prevented maximum potential pressures being achieved and possibly impacted upon the overall rate of gelifluction. A successful simulation of both landsliding and slow mass wasting processes was undertaken and future applications for the technique have been outlined.

ACKNOWLEDGEMENTS

I would like to acknowledge the following people for their patience and technical support during the completion of this research project:

- Professor Charles Harris
- Mr Harry Lane
- Mr Len Czekaj
- Mr Lawrence Badham
- Mr Derek John
- Mr Duncan Montgomery
- Mr Neil Ross
- Mr Andrew George
- Mr Andy Robinson
- Dr Julian Murton
- Dr John McKinley

I would like to give extra special thanks to the following people for the revitalising unconditional love and support given to me during the many difficult years spent completing this research:

- **Phoebe Smith**
- **Katerina Kolotourou**
- **Amy Smith**

"Education is what remains after one has forgotten everything he learned in school"

(Albert Einstein)

Financial support is acknowledged from the Natural Environment Research Council (NERC)

TABLE OF CONTENTS

LIST OF FIGURES

LIST OF TABLES

CHAPTER ONE : Introduction

1.1. Aims and Objectives

The purpose of this project is to understand the effect of soil properties and slope geometry on thaw-related mass movement processes, primarily through a series of simulation experiments undertaken in the laboratory. The research reported here has created a comprehensive dataset that enables analysis of the key parameters controlling gelifluction in the field. A key aim has been to demonstrate the variety and effectiveness of scaled centrifuge modelling of cryogenic mass movement processes, particularly gelifluction.

1.2. Research Questions

The proposed systematic investigation of periglacial mass wasting processes will answer the following specific research questions:

- What is the effect of soil geotechnical properties on the rate and style of gelifluction?
- What is the impact of slope geometry on the rate and style of gelifluction?
- Is it possible to accurately simulate prototype periglacial conditions using geotechnical centrifuge modelling?
- Is it possible to validate laboratory data through comparative analyses of analogue field information?

1.3. Global Context of this Research

The significance of the current research project can be outlined through a brief examination of current issues concerning the potential engineering problems associated with thawing ice-rich slopes, and of global climactic amelioration affecting permafrost in high latitudes and altitudes (Harris *et al.*, 2003b).

It has been estimated that some 25% of the Earth's land surface falls within the periglacial zone (French, 1996); this importantly includes some 5 million km^2 of middle and low latitude mountains underlain by permafrost (Gorbunov, 1988). Slope mass movements present a potential engineering hazard, and create risk for infrastructure, settlements and communications (Harris & Haeberli, 2003; Williams, 1979). These globally active processes include slow soil movements and rapid failures such as shallow landslides, mudflows, debris flows and rock falls (Davies, 1972; Ballantyne & Harris, 1994). However, the periglacial environment creates a distinctive suite of mass movement processes; these are characteristically associated with the release of meltwater during the thaw of frozen ground (Harris, 1987; Lewkowicz, 1988). Therefore, both mountainous permafrost areas and arctic lowlands are likely to experience widespread changes to slope hydrology and geomorphic activity as a consequence of predicted atmospheric warming (Ohmura & Beniston, 1996).

Estimates of Northern Hemispheric temperature over the last 1000 years have suggested that the 1990s were the warmest decade within the millennium, leading to the global-mean surface air temperature record being broken four times during the 1990s (Hulme, 1999). There are many projects currently researching the influence of anthropogenic activity upon the observed upward trend in global temperature, most involving numerical modelling but some are compiling palaeoclimatic records from lake sediments, trees, glaciers and marine sediments (Overpeck *et al.*, 1997). Importantly for the purpose of this project, global warming at the current rate, will lead to significant changes within the rate of environmental evolution. Any level of accelerated environmental change will give a wide-ranging impact upon related ecosystems, human activities and consequently the scale of any geotechnical engineering problems.

Permafrost is sensitive to changes in atmospheric temperature; and has been identified as one of six cryospheric indicators of global climate change within the monitoring framework of the WMO Global Climate Observing System (GCOS) (Harris *et al.*, 2003b). However, global warming will not be uniformly distributed across permafrost regions. Most General Circulation Models (GCMs) have suggested that atmospheric warming will be greater in Polar Regions than at lower

latitudes and more pronounced at high altitudes than in lowlands (Overpeck *et al.*, 1997; Kemp, 1994). Recent thermal measurements in the European Union PACE mountain permafrost monitoring network (Harris *et al.*, 2001a) has demonstrated pronounced near-surface warming over the 20th Century and into the 21st, from the Alps through the Scandinavian Mountains to the arctic island of Svalbard, with the greatest changes recorded in Svalbard. The evolution of higher temperature conditions will lead to enhanced levels of near surface permafrost degradation in mountainous regions (Haeberli & Burn, 2002). The physical stability of mountain permafrost terrain is highly sensitive to atmospheric temperature, in that a rise in air temperature will lead directly to an increase in the rates and depths of slow soil movements and an acceleration of the scale and frequency of slope failures (Harris *et al.*, 2001b). There are other implications for climate warming in ice-rich permafrost, such as increased thaw settlement, the inundation of low-lying coastal areas, and a decrease in the strength of frozen rock joints through increased unfrozen water contents coupled with a decrease in ice-bonded cementation (Nelson *et al.*, 2001; Davies *et al.*, 2001; Williams & Smith, 1989).

As global warming creates a deeper permafrost active layer it becomes critical to improve both process understanding and hazard assessment, especially with regards to how the changing ground ice conditions will impact upon the rate and frequency of disruptive mass movement (Matsuoka & Humlum, 2003). Researchers have noted the increase in potential hazard; this has led to the creation of permafrost monitoring networks (i.e. the EU PACE project) and also propagated interest from mainstream UK media sources (e.g. The Guardian, 2001; The Telegraph, 2001; BBC News, 2000). It is this new interest in cryogenic slope research that provides an important scientific backdrop for the investigation that forms the subject of this thesis (Thorn, 2003).

An increase in slope instability associated with permafrost degradation will change the scale and frequency of mass movements. It is relatively easy to identify and assess the risks associated with rapid flow and slide processes, especially as mountain settlements often lie below steep slopes. However it becomes more difficult to perceive the hazard associated with slow mass movements, such as gelifluction. In reality, slow mass movements can pose significant geotechnical

problems to foundations and other infrastructure, for example pipelines, roads, etc (Harris *et al.*, 2001a; Tart, 2003). It may soon become necessary for engineering projects within mountainous areas to carefully investigate the impact of any potential gelifluction upon the stability of any proposed design (see figs. 1.3.1 and 1.3.2).

An understanding of the main parameters controlling the rate and style of gelifluction has increased rapidly during the last two decades. Laboratory studies of the phenomena have lead to greater understanding of the principal processes (e.g. Harris *et al.*, 2003a) whilst field studies have comprehensively outlined real-time rates of movement (e.g. Matsuoka, 2001). Many researchers are now focussing upon the quantitative determination of processes and materials across different spatio-temporal scales (Haeberli, 2000). An important part of this objective is to numerically monitor and model past evolutions and future developments of phenomena and resultant landforms (Chorley, 1978; Harris, 1996). The use of modern innovative experimental techniques is providing high-quality quantitative data that is constraining and developing earlier geomorphological speculation (Haeberli, 2000).

Figure 1.3.1. The impact of gelifluction on the concrete foundations of a small mountain building, Finse, Southern Norway (Photograph: Ivar Berthling).

Figure 1.3.2. Active-layer solifluction around vertical pile supports for the Trans Alaska Pipeline System (TAPS), Alaska, USA. The vertical support members are embedded in permafrost, and near-surface solifluction has caused significant distortion of the pile. (Photograph: R. G. Tart).

1.4. Field Measurements of Geocryological Processes

The use of advanced field, laboratory and computing techniques has lead to a more interdisciplinary approach to cryogenic science (Pissart, 1990). It is of key scientific importance to separate and monitor the individual influences of the disparate variables involved in periglacial mass movements (Barsch, 1993) and the interdisciplinary approach has lead to fundamental breakthroughs in process understanding; see for example Harris *et al.* (2003a) (Thorn, 2003).

However, it should be noted that the current research climate has also highlighted the critical importance of high quality field studies (Harris, 1996). Without such field data it is impossible to validate the results of experimental modelling. Field validation is a key aspect of any physical or numerical modelling; in particular it provides information on the spatial and temporal variability inherent in the modelled geomorphological system or process (Schumm, 1979; Thornes, 1983).

Although field studies must always form the basis for process understanding of any periglacial mass movement, such field studies are inevitably site specific. Therefore, if the quantifiable effect of particular variables such as slope gradient, soil properties, ice content, etc. are to be heuristically analysed on the basis of field studies, it becomes necessary to monitor large numbers of sites over long time periods (e.g. Washburn, 1999; Matsuoka *et al.*, 1997). Most field studies of solifluction are complicated by the natural variability of field conditions, in that key mass movement parameters, such as soil moisture, soil geotechnical properties, slope gradient, slope aspect, ground cover, and ground thermal regime, may vary considerably across relatively small areas (e.g. Smith, 1975; Gold, 1967). It can be difficult to identify the influence of site-specific field conditions on a dominant transport process, especially when variations in micro-scale conditions can give equifinality of frequency, rate and form across the long time scales necessary to identify gelifluction processes (e.g. Smith, 1992). Therefore in order to arrive at a detailed quantitative overview of gelifluction, a series of field studies must cover different settings with respect to both climate and soil conditions.

Furthermore, there is a difficulty attached to predicting exactly where and when conditions will be suitable for the transition from slow gelifluction to rapid active-layer detachment landsliding. This presents an obstacle when attempting to install equipment in advance of such spatially discontinuous and potentially random events (Lewkowicz, 1988). In addition, field studies are frequently hampered by problems of installing and maintaining instrumentation within remote and climatically hostile environments. These instrumentation difficulties are again compounded by seasonal variations, in that it may be difficult to monitor the degree to which short-term conditions influence the style of the long-term phenomena. For example, buried Rudberg columns cannot fully represent the impact yearly variations will have upon the overall rate of downslope movement (e.g. Carver *et al.*, 2002), and due to the relatively short time scale of most field studies, movement rates measured over a few years may not be representative of longer-term trends (Rudberg, 1964).

1.5. Scaled Centrifuge Modelling

A new, highly effective experimental technique has been pioneered within cryogenic process studies through scaled modelling under enhanced gravity fields (see Ketcham and Black, 1995; Yang & Goodings, 1998; Harris *et al.*, 2000; Harris *et al.*, 2001b).

Centrifuge modelling has increasingly been recognised as a powerful tool in many fields of geotechnical engineering (Schofield, 1980) because it allows rapid and repeatable modelling with controllable and defined boundary conditions. A prerequisite of accurate physical modelling is to accurately reproduce the in-situ stresses that exist at prototype scale in the laboratory model. This means that on the laboratory floor, under the earth's gravitational field, simulations must be carried out at full-scale. However, this can be also be achieved if scaled physical models are tested within an elevated gravity field, produced through the rotation of a centrifuge platform. In a 1/N scale model tested at one gravity (g), self-weight stress at any depth below the surface is 1/N that at the equivalent depth in the prototype, and prototype soil stress-strain behaviour cannot be accurately modelled. However, placing a scaled model in a geotechnical centrifuge of radius r and angular velocity ω, generates a centrifugal acceleration of $r\omega^2$ on the model. If the centrifugal acceleration is equivalent to Ng, stress similitude between model and prototype may be readily demonstrated:

for prototype $\sigma_p = h \rho g$

for model $\sigma_m = \frac{h \rho (N g)}{N} = h \rho g$ and $\sigma_p = \sigma_m$ *(1.1)*

where σ_p and σ_m are self-weight stress in the prototype and model respectively, h is depth below the surface and g the gravitational field. Thus, by accurately reproducing full-scale prototype self-weight stress within the scaled model, stress/strain responses may be accurately modelled. Use of the prototype soil in the model ensures similitude in soil properties. A full discussion of centrifuge scaling factors is given in Chapter two.

The centrifuge modelling technique also allows precision instrumentation to be installed accurately, and facilitates continuous monitoring. The approach therefore

should enable us to measure the influence of individual variables on gelifluction, for example thermal gradient, pore water pressure, frost heave and thaw settlement, etc. The experimental technique will also give greater control over boundary conditions, for example slope model soil properties can be consistently manufactured to meet exact scenarios. The use of physical modelling is also time efficient since time scaling is proportional to the square of the gravitational field (e.g. at 10g, prototype time scales to 100 x model time) and the annual freeze/thaw cycle can be reproduced in days. It therefore becomes possible to undertake multiple modelling procedures within a single research project, thus ultimately increasing the potential to develop new ideas and predictive models (Platt, 1964).

1.6. Research Strategy

1.6.1. Laboratory Simulation Experiments

The aim of this thesis is to explore the potential of customised physical modelling to undertake an analysis of the geo-environmental variables that affect gelifluction processes on thawing periglacial slopes. The project will engage in primary data collection through: (a) the systematic centrifuge modelling of planar slopes created with varying slope geometries/soil grainsize composition, (b) a dedicated field monitoring site in Dovrefjell (Norway), and (c) a full suite of geotechnical soil mechanical experiments. It is hoped the body of experimental data will provide a theoretical framework to facilitate experimental design for future field studies, have a direct application for periglacial geomorphology, slope stability and hazard assessment, and assist in the interpretation of relict Quaternary periglacial deposits in both cohesive and non-cohesive soils.

The bulk of the primary data were created via a comprehensive centrifuge-modelling program based on a series of geometrically simple planar slope models. The models were instrumented and subjected to a series of freeze/thaw cycles: they were first frozen on the laboratory floor and then thawed in the geotechnical centrifuge under enhanced gravity. This approach to primary data collection capitalised upon the time and cost advantages inherent within scaled centrifuge modelling and also allowed precision instrumentation, high quality data logging, replicate testing, and

most importantly a high level of control over critical environmental and geotechnical conditions. The physical modelling element of the project provided information on the general relationships between thermal regime, pore water pressure, subsurface volumetric transport, surface movement, thaw consolidation, and frost susceptibility. It also created a dataset that highlighted governing thresholds for slope failure and indicated potential triggers for particular failure mechanisms.

The centrifuge-modelling program has been divided into two principal components (see table 1.6.1). The primary element provides base data on the effect of slope geometry, specifically the role of slope gradient in the gelifluction process for an active layer consisting of a natural silty soil. This element created a set of behavioural parameters that provide perspective within the second phase of the program. The second element of the modelling program involved varying the soil composition between models with identical slope angle. It investigated the response of active-layer processes to progressively increasing clay and silt contents. It is envisaged that the collation of both sets of information will provide new insights into the role of soil properties in controlling rates and style of periglacial mass movement.

Table 1.6.1. The centrifuge-modelling program.

SERIES NUMBER	SLOPE (°)	HOST MATERIAL	TEST ELEMENT	F/T CYCLES	SERIES REFERENCE	SERIES DATE
1	12	Lacustrine Silt	Proof Test	1	*PROOF*	Sep-00
2	12	Natural	Primary	4	*12D/NS*	Dec-00
3	16	Natural	Primary	1	*16D/NS*	Mar-01
4	8	Natural	Primary	4	*FAULT*	Jun-01
5	4	Natural	Primary	4	*4D/NS*	Sep-01
6	8	10% Silt	Secondary	2	*8D/10S*	Dec-01
7	12	10% Clay	Secondary	1	*12D/10C*	Feb-02
8	4	10% Silt	Secondary	4	*4D/10S*	May-02
9	8	Natural	Primary	4	*8D/NS*	Jun-02
10	8	10% Clay	Secondary	1	*8D/10C*	Jul-02
11	4	20% Silt	Secondary	4	*4D/20S*	Aug-02
12	4	10% Clay	Secondary	4	*4D/10C*	Nov-02
13	4	20% Clay	Secondary	4	*4D/20C*	Dec-02

1.6.2. Field Monitoring

A field monitoring station was established in order to validate the experimental procedures used during the centrifuge-modelling program. The field station in Dovrefjell, Norway is located on an active solifluction slope to monitor soil movement, frost heave, thermal regime, and pore water pressures via a remote logging system. The field station data will be augmented with previously published field studies, in an effort to parameterise any derived experimental results (Harris, 1996). It is necessary to add secondary sources of field information due to the short-term time scale of the current field-monitoring site constructed for the project (Matsuoka & Humlum, 2003). It is felt that a single field season of primary data will not provide enough validating information to create an accurate frame of reference for the experimental program.

1.7. Geotechnical Characterisation of Test Soils

A complete suite of geotechnical experiments was carried out on all the test soils used within the centrifuge program. Laboratory testing included direct drained shear box testing, Atterberg limit tests, Oedometer testing, X-ray diffraction analysis, grainsize determination, and undisturbed resin impregnated thin sections interpreted through optical microscopy. This element of the project is of key importance considering the non-linear nature of stress/strain behaviour within granular soils of differing compositions.

1.8. Thesis Structure

The introductory chapter outlines the main issues addressed by the project including an appraisal of the general scientific context, the principal research objectives and an outline of the approach taken to best investigate the chosen research questions.

Chapter two discusses the controls on mass wasting processes within the periglacial zone, paying special attention to the processes and limiting factors involved in the development of solifluction landforms. Chapter two will also address the different modelling and monitoring techniques used by geomorphologists to better understand solifluction activity - this will be through a brief synopsis of previous field and laboratory studies. Included within this chapter will be a discussion around the

historical development of periglacial physical modelling (large scale) and the governing principles involved within scaled centrifuge modelling (small scale).

Chapter three outlines the experimental procedures developed and adopted during the scaled geotechnical centrifuge-modelling program, it will also discuss limitations imposed by the technique, for example the resolution of instrumentation and scaling issues.

Chapter four presents the test soils used within the project – including their main geotechnical properties and resultant classifications.

Chapter five presents results from seven series of experimental gelifluction modelling and outlines information gathered on thermal regime, frost heave, thaw consolidation, pore water pressure, and downslope surface and subsurface movement. Experimental data will be analysed and discussed but only with respect to the general mechanisms of periglacial activity, namely all the relationships that are not exclusive to active gelifluction lobes.

Chapter six focuses specifically upon the analyses of relationships fundamentally controlling the rates of downslope surface and volumetric transport. The chapter will examine the interaction between variables involved in gelifluction. Special attention is paid to the impact of fluctuating pore water pressure, the rate of thaw consolidation, and the influence of frost heave upon the scale and style of mass movement. The chapter will confine interpretation to the relationships commonly associated with cryogenic solifluction processes.

Chapter seven will investigate the thresholds and mechanisms for slope failure on thawing ice-rich slopes. The chapter will present movement and thermal data from four series within the experimental program. It will also synthesise excess pore water pressure results for back analyses of slope stability.

Chapter eight outlines the techniques used to collect short and long-term field data from Dovrefjell, Norway. The resultant dataset will be analysed in an attempt to validate both conjoined experiments through comparing the field and laboratory

information collected within the project. This chapter also examines the collected soil, thermal and gelifluction movement data and discusses its implications upon process understanding with a special focus upon the style of movement relating to the specific impact of field conditions, for example microclimate and ground cover, upon frost heave and the dissipation of pore water pressures.

Finally, chapter nine summarises the test program and draws conclusions concerning the significance of specific environmental variables and individual soil constituent properties on the nature and rate of periglacial mass movement. The value of the physical modelling approach is reviewed, and recommendations for future applications are made.

CHAPTER TWO : A Review of the Literature on Periglacial Slope Processes

This chapter will provide a background to the research presented within this investigation. The review will introduce the general characteristics of the periglacial region, and explore the fundamental mass wasting processes that characterise many periglacial slopes. It will detail results from previous field studies of solifluction, to provide a frame of reference regarding early geomorphic investigation of the phenomena. The chapter will introduce the historical development of experimental methodologies developed to examine gelifluction, focusing on full-scale laboratory techniques developed before the application of enhanced gravity field research techniques to this problem. The chapter will then outline the basic chronological expansion of centrifugal studies, in particular outlining the fundamental scaling principles and the initial application of these enhanced gravity studies within civil engineering. Finally the chapter will present recent applications of centrifuge testing within cryogenic geomorphology and Quaternary reconstruction.

2.1. Characteristics of the Periglacial Environment

Lozinski first introduced the concept of a unique 'periglacial' climatic zone in 1909, it was proposed to describe the cold climate surrounding high glaciers whilst mapping summit blockfields in the mountains of central Europe (French, 2000). Lozinski classified the periglacial zone as being exclusively peripheral to Pleistocene ice sheets and emphasised the mechanical weathering of rocks through intense freezing (French, 1996). After further research this early definition was deemed spatially and temporally limited, as it was restricted to relict forms and did not acknowledge that active frost dominated environments were not always constrained to the peripheries of ice sheets, for example the periglacial regions of Central Alaska (Dylik, 1964). An updated definition of the concept was developed whereby a periglacial region was one experiencing 'conditions, processes, and landforms associated with cold, non-glacial environments' (ACGR, 1988, p.63). As a unifying refinement Washburn (1979) had suggested that these areas were characterised by intense frost action regardless of age and spatial proximity to glaciers, where frost action was defined as 'any process stemming directly from the freezing and/or

thawing of ground ice' and referred to frost cracking, ice wedging, frost sorting, frost heave, etc. (Thorn, 1992, p.25). The modern concept of the periglacial zone includes any region where freeze thaw processes occur in the presence of moisture, where snow cover exists for only part of the year, and where permanently frozen ground may exist (Ballantyne & Harris, 1994; French, 1996).

2.1.1. Spatial Limits of the Periglacial Zone

The periglacial zone encompasses great variability in terms of climate, geology, and Quaternary history; as a result many researchers have attempted to subdivide the zone based on climate, vegetation, and surface micro relief criterion (e.g. Jahn, 1975, p.14-17). For example, several researchers have attempted to define the spatial limits of the periglacial zone using mean annual air temperature (e.g. Peltier 1950, Tricart 1967, Wilson 1968, Karte 1979, etc), but despite several attempts the periglacial concept has remained too imprecise to allow spatial delineation (Washburn, 1979; French, 2003). These rough classifications were useful for broad generalisation, but the distribution and climatic significance of most periglacial features was poorly known and this restricted any direct quantification of the periglacial concept. The lack of quantified climatic limits made it impossible to formulate an accurate palaeoclimatic interpretation of relict periglacial assemblages, especially as the dating of such features, for example ice-wedge casts, presented significant problems (e.g. Burbidge *et al.*, 1988; Black, 1976; Karte, 1987). Even within the modern research community many climatic threshold values remain to be precisely validated in terms of an overall indication of the potential air temperature needed for landform inception (see table 2.1.1) (Murton & Kolstrup, 2003; Kasse, 1999). In addition, there still remains a need to establish a clear visual rationale for the identification of many relict features (Mackay, 1986).

It has been estimated that the periglacial zone covers approximately 25% of the earth surface, with its distribution being controlled by an integration of regional climate (e.g. high latitudes), topography (e.g. high altitudes) and local modifying factors (e.g. aspect, etc) (French, 1996).

2.1.2. The Periglacial Climate

The periglacial climate is broadly controlled by latitude, altitude and continentality. Latitude influences the overall radiation balance for an area. The annual equilibrium heat budget for an area consists of a complex balance of different radiation types, with the exact specifications of the heat flux being influenced by both atmospheric and ground cover conditions (see Rouse, 1993, p.68, fig. 3.2). The annual radiation balance can be described through calculating the net all-wave radiation at the surface (Q^*) via the energy balance equation:

$$Q_{LE} + Q_G + Q_H = Q^* = K\Downarrow(1-\alpha) + L\Downarrow - L\Uparrow \qquad (2.1)$$

where $K\Downarrow$ (W m^{-2}) is a climatic factor which represents incoming direct short wave solar radiation depending upon latitude and time of year/day, α (%) is a site specific property and symbolises the surface albedo characteristics of the ground cover (see Williams & Smith, 1989, p.68, table 3.1), $L\Downarrow$ (W m^{-2}) characterises incoming long wave terrestrial radiation reflected back from the troposphere and is mainly a climatic factor depending on cloud cover and atmospheric humidity, and $L\Uparrow$ (W m^{-2}) represents the amount of outgoing long wave terrestrial radiation that has escaped from the atmosphere after reflection from the ground surface, Q_{LE} is a function of evaporation rates as determined by net radiation and availability of water, Q_G highlights net heat flux into the ground via direct conduction, Q_H symbolises the transfer of energy away from the ground via the convection of sensible heat with an upward flux during day and downward flux at night. To summarise:

$$Q^* = K^* + L^* \qquad (2.2)$$

where K^* is net solar radiation and L^* is net long wave radiation. A value for Q^* will therefore be unique to any area of land or sea as it will vary with each individual ground cover characteristic. For example, at higher latitudes there is normally a decrease in Q^* because more short wave radiation is reflected back into the atmosphere via the high albedo of permanent snow cover. The influence of latitude on surface radiative characteristics and heat flux within different latitudinal climatic zones has been numerically documented by Rouse (1993, p.67, table 3.1). It should be noted that these numerical models are limited by an inability to predict

disequilibrium periglacial condition, i.e. where permafrost temperatures are related to past climatic conditions (see section 2.1.5).

Altitude defines climatic temperature through the environmental lapse rate, as altitude increases then temperature decreases at approximately 6.5°C km^{-1}, this effect can be illustrated by the upland high altitude periglacial areas that exist even at mid to low latitudes. For example, the Fengou Shan, Qinghai-Xizang Plateau, Tibet, maintains a periglacial climate as far south as 34°N (Wang & French, 1994). Continentality impacts upon seasonal variations in temperature, and is a measure of how a land area is affected by its remoteness from oceanic (moisture laden) air. An increase in continentality will give rise to an increase in seasonal temperature variation as maritime influences normally mitigate temperature extremes and therefore decrease the amplitude of the seasonal temperature cycle. The continentality of an area is often expressed in terms of the difference between average air temperatures in January and July, for example, Yakutsk in central Siberia has high continentality with a 62°C annual range, whereas Jan Mayen Island in the northern Atlantic exhibits a predominantly maritime climate with low continentality and consequently displays a lower annual temperature range of just 8°C.

2.1.3. Geomorphological Periglacial Processes

No single geomorphic process characterises the periglacial setting, instead there is a varying mixture of processes dependent upon the local conditions of moisture, temperature, sediment grain size, bedrock, and snow cover. However, the most important set of processes are all related to frost action. The intense frost action that characterises the periglacial domain can occur on many temporal scales; diurnal cycles (e.g. mountain environments), short-term cycles (e.g. cold flux), seasonal cycles (e.g. freeze-thaw of annually frozen ground), or long-term cycles (e.g. glacial and interglacial periods) (Matsuoka *et al.*, 1998). Frost action dominates the periglacial environment but operates alongside other processes such as mass wasting (e.g. needle ice creep), fluvial/lacustrine/marine processes, seasonal snowpack activity (nivation), and wind action. These geomorphic processes can be subdivided into (a) *zonal periglacial processes* which are unique to the cryotic zone, (b) *polyzonal* that operate at a higher intensity and efficacy under periglacial conditions,

and (c) *azonal* which function throughout the world (French, 1996). Zonal processes include the formation of permafrost, thermal contraction cracking, thermokarst activity, and the formation of wedge and intrusive ice (Washburn, 1979). Polyzonal processes include ice segregation, seasonal frost action, mass movement, and frost weathering. Azonal processes reflect the impact of ubiquitous processes such as running water and wind action that may be highly effective in the periglacial realm due to the sparse vegetation and dry sediments. Recently, however, the palaeoclimatic significance of a number of periglacial features was reviewed by Huijzer and Vendenberghe (1998) as part of their palaeoenvironmental reconstruction of Late Glacial Europe. Their suggested thermal limits (in terms of mean annual temperatures and in some cases, mean temperature of the coldest month associated with particular landforms and processes) are summarized in Table 2.1.1.

Table 2.1.1. Assumed thermal criteria for relict periglacial features based on modern analogues. (Source: Huijzer & Vendenberghe, 1998).

Periglacial Structure	**Mean Annual Air Temperature (MAAT) (°C)**	**Mean Temperature Coldest Month (°C)**
Ice-wedge Casts	Fine substrate < -4 Coarse substrate < -8	< -20
Sand-wedge	< -8	
Seasonal Soil-wedges	< -1 to 0	<-8
Large scale Involutions > 0.6 m (Type 2)	Fine substrate < -4 Coarse substrate < -8	
Small-scale Involutions < 0.6 m (Type 3)	< -1	
Solitary forms in drops or diapers (Type 4)	< -1	
Open-system Pingos	< -3 to < -1	
Closed-system Pingos	< -6 to < -4	
Palsas	Organic < -1 Mineral <-6 to <-4	
Soil microfabrics	<-1 to <0	

Essentially, ice-wedge and sand-wedge formation is restricted to areas of continuous permafrost, open system pingos and related palsa-type features, develop in discontinuous permafrost, while all other features may form in both permafrost

conditions, or as a result of deep seasonal ground freezing. It is notable that solifluction deposits and landforms are not included in Table 2.1.1. This reflects the fact that the palaeoclimatic signal is not diagnostic of any particular periglacial climate type, with solifluction processes occurring from the high arctic continuous permafrost zones to alpine areas of seasonal ground freezing (Jaesche *et al.*, 2003).

2.1.4. Periglacial Ground Thermal Regime

The periglacial climate creates a unique ground thermal regime that triggers multiple geo-environmental consequences for geomorphic processes. Frozen periglacial ground can be divided into two basic categories; that which thaws annually, often called seasonally frozen, and that which does not thaw and is called permafrost (Williams & Smith, 1989). The depth of frost penetration during winter will depend upon the intensity and duration of the cold ambient temperature (degree days below zero) coupled with the thermal and physical properties of the regolith and its ground cover (Williams & Nickling, 1971). The thermal properties of the ground material and the geothermal heat flux from the Earth's core will both modify the effect of surface temperature upon permafrost and seasonally frozen ground (see fig. 2.1.1).

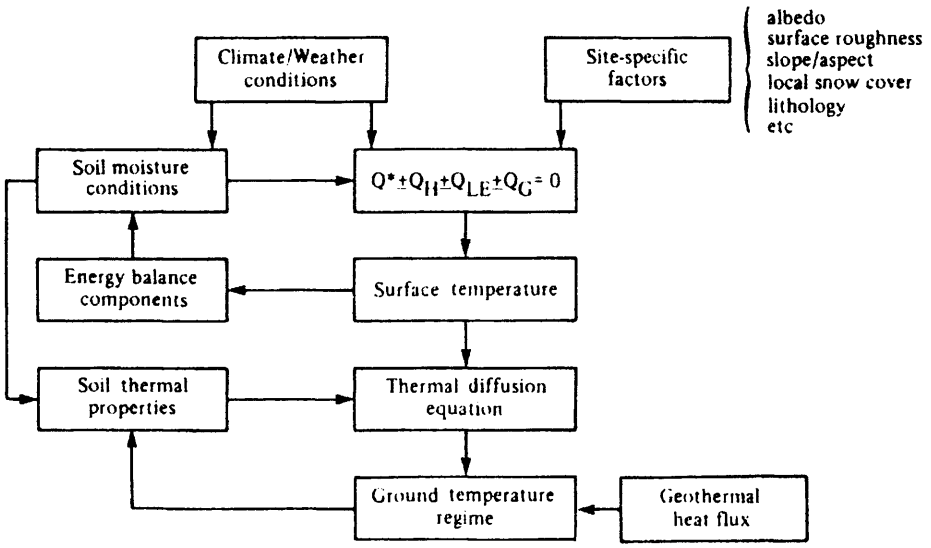

Figure 2.1.1. Schematic flow diagram of climate-ground thermal interaction. (Source: Williams & Smith, 1989, p.66).

There are many site-specific aerodynamic, radiative, hydrologic and conductive factors that can influence the ground thermal regime for a particular site (fig. 2.1.1). The interplay of these factors within the near surface boundary layer will affect overall ground temperature, but ultimately soil thermal properties will determine specific ground conditions (Thornthwaite, 1961). Important thermal properties include thermal conductivity, specific heat capacity, thermal diffusivity, and the latent heat of fusion (Williams & Smith, 1989). However it may be impossible to specify which unique thermal properties influence the efficacy of each elemental thermal process, since an individual soil profile contains variations in moisture, temperature, grain size, soil density, etc (Williams, 1991).

Thermal conduction is the major heat transfer process within a periglacial soil matrix (Williams, 1991). Heat is transferred from places of higher to lower temperature within a substance by the interaction of atoms or molecules possessing greater kinetic energy with those atoms/molecules possessing a lower kinetic energy (Harlan & Nixon, 1978). The conduction effect is most important in solids (e.g. soil and rock) but heat transfers in the ground may also be affected by moving water, water vapour, and air, causing heat advection (Grober *et al.*, 1961). Many researchers use a steady state heat conduction equation to analyse ground temperature profiles:

$$Qg = -K\,(dT/dz) \qquad (2.3)$$

where Q_g equals the ground heat flux (W m^{-2}), K represents thermal conductivity as a constant of proportionality (W m^{-1} $°C^{-1}$), and dT/dz represents the temperature gradient ($°C\ m^{-1}$). This steady state approach to quantifying ground thermal regime assumes a homogenous medium (ground) within which heat only flows by conduction in a vertical direction. It also specifies that steady conditions exist with constant temperature and invariable thermal properties. However, localised ground conditions are infinitely complex and this may limit the applicability of such a simple conduction model. For example variations in ice and water content can lead to variations in thermal conductivity and diffusivity (see below), and surface temperature gradients rarely achieve a steady state due to diurnal and microclimatic influences continually creating disequilibria of free energy states.

It is known that soil moisture and soil mineralogy are key controls on the thermal properties found within frozen soil or rock. A change in ground temperature will lead to a change in the proportions of ice and unfrozen water and this will in turn modify the thermal properties within the soil profile. A lowering of soil temperature will cause an increase in ice content and a decrease in unfrozen water content. This effect creates a positive feedback cycle as a decrease in ground temperature in the presence of adequate moisture levels will lead to ground ice growth which promotes higher thermal conductivity and further ground ice nucleation (Shen & Ladanyi, 1987). The relative proportions of ice and water in any soil profile will modify its internal thermal properties because ice has a thermal conductivity four times that of water. The actual volume of ice and water will itself be temperature dependent, especially between 0°C and –3°C as water freezes across a range of negative temperatures due to the effects of capillarity and adsorption (Williams, 1991).

Frost penetration into unfrozen ground and thaw penetration into frozen ground is strongly influenced by the quantity of water stored within the soil or rock, so that wet areas experience less seasonal frost penetration than adjacent dry areas. The reduction of frost or thaw penetration in wetter areas is caused by the much higher value of latent heat of fusion of water (333 kJ kg^{-1}) compared to its specific heat capacity (4.19 kJ kg^{-1}). During phase change at the freezing front or thawing front, ground temperature remains constant and this period is referred to as the zero curtain. The zero curtain is most pronounced during freezing or thawing of saturated fine grained soils with high void ratios and therefore high saturation moisture contents. In addition, the process of ice segregation leads to water migration towards the freezing front, increasing moisture/ice contents and the amount of latent heat (see fig. 2.1.6) (Williams & Smith, 1989).

There is no simple direct relationship between atmospheric climate and ground thermal regime (Brown, 1978). There are many interrelated microclimatic controls which condition local variations within the annual net radiation balance, for example, topography, wind, aspect, residual water bodies, vegetation, bedrock, snow cover, etc (Gold, 1967; Hugenholtz & Lewkowicz, 2002). No single factor can explain a local ground thermal condition as the impact of individual factors cannot be isolated.

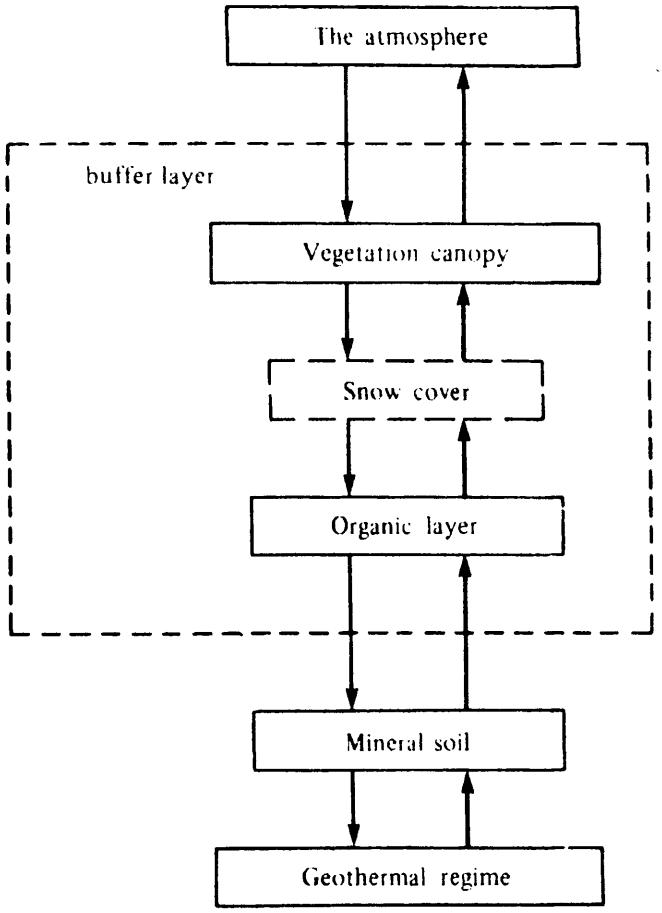

Figure 2.1.2. Schematic diagram showing a conceptual model of the climate-ground thermal regime relationship. (Source: Williams & Smith, 1989, p.71).

In an attempt to simplify the near surface relationship a buffer model has been suggested to describe the interaction between net surface radiation balance and the actual thermal properties of the ground (see fig. 2.1.3). The buffer model does not manage to entirely describe the complex interrelated nature of the system; but serves to highlight the site-specific factors that constrain climatic signals from completely determining ground thermal regime (see section 2.1.2). There are many microclimatic factors within the buffer layer that influence ground thermal regime, these modify the overall climatic signal of the region and create the specific temperature profile found within an area (see figs. 2.1.3 & 2.1.1). For example, an organic layer (i.e. peat) will seasonally influence the thermal diffusivity of the soil profile; because within a well drained site (e.g. palsa) the organic layer will be dry in summer and contain air filled pores that have low thermal conductivity, but during winter it will be wet, with a much higher thermal conductivity (Zuidoff, 2003). This seasonal change in thermal conductivity found within the upper organic layers of a

soil profile can create a distinct near surface temperature offset within an equilibrium thermal profile (see fig. 2.1.3) (Burn & Smith, 1988). A vegetation layer also influences thermal conditions because evapotranspiration cools the ground and greater surface roughness leads to higher rates of evaporation (Rouse, 1984; Smith, 1975). The thickness and longevity of any layer of snow cover will influence thermal regime by controlling the insulation of the ground and by its high albedo reflecting radiation back into atmosphere (Jaesche *et al.*, 2003). It has been demonstrated that within areas of discontinuous or sporadic permafrost, snow cover may be the most critical factor for determining the presence of permanently frozen ground (see fig. 2.1.5) (Sollid *et al.*, 2003).

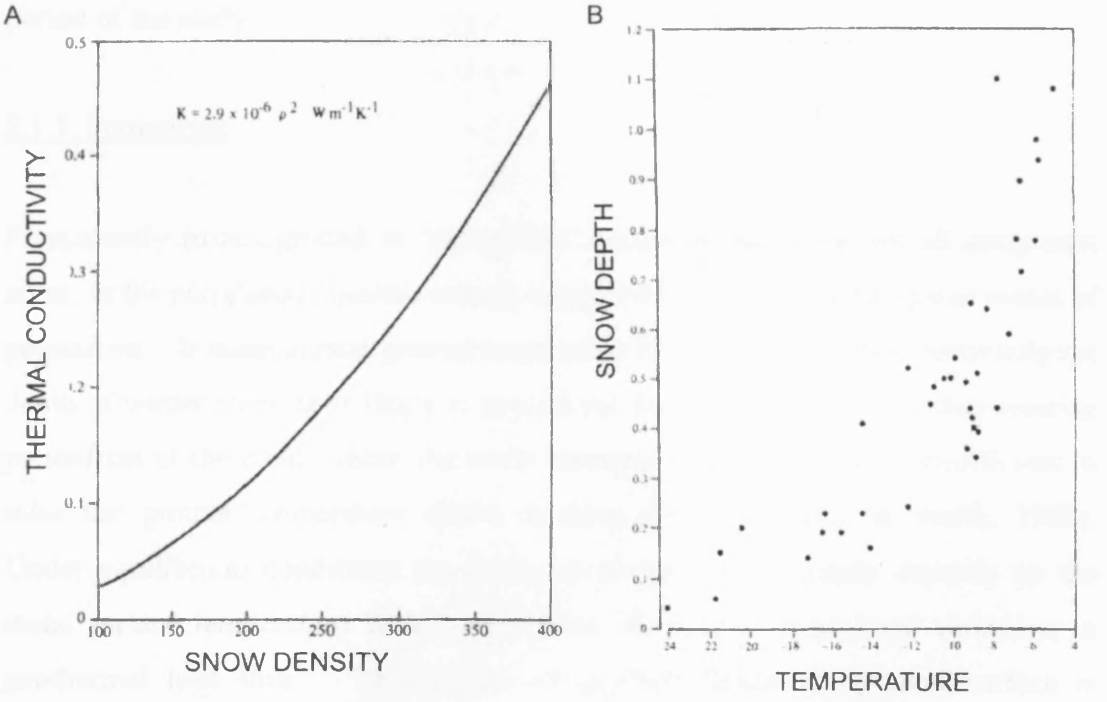

Figure 2.1.3. Graphs showing the microclimatic impact of snow cover upon ground thermal regime: (A) the relationship between ground thermal conductivity and density of snow, (B) the effect of snow depth on ground surface temperature. (Source: Williams & Smith, 1989, p.110 & Smith, 1975, p.1427).

It should also be noted that site specific disruption to near surface conditions can lead to complex disruptions within ground thermal regime, as the interrelated nature of the near surface boundary system creates cascading feedback loops that may dampen or exacerbate existing climatic fluctuations (see fig. 2.1.1). For example, it is well documented that degradation or formation of permafrost can be linked to both anthropomorphic disturbances to the natural environment (i.e. deforestation related to gas or oil exploration, Mackay, 1970), or via natural occurrences which modify

existing ecosystems (i.e. fire, snow storms, etc, Mackay, 1977; Viereck, 1982; Rouse, 1984). Any removal, damage or compaction of the ground surface materials (vegetation, peat, soil, snow) within the buffer layer will alter the delicate balance of surface energy transfers which will generally lead to an imbalance within the surface energy exchange. Mackay (1997) monitored an artificially drained lake in the continuous permafrost of the Mackenzie Delta, Canada in order to determine the environmental response to an induced modification of the buffer layer. The disruption to surface conditions (i.e. the removal of insulating water) modified active layer depths and encouraged consequential permafrost growth in the underlying exposed ground where equilibrium conditions were not achieved during the 25-year period of the study.

2.1.5. Permafrost

Permanently frozen ground or 'permafrost' occurs in many but not all periglacial areas; as the periglacial climatic zone is considerably bigger than the spatial extent of permafrost. If mean annual ground temperature falls below 0°C, then potentially the depth of winter freezing is likely to exceed the depth of summer thaw thus creating permafrost at the depth where the warm seasonal variation becomes insufficient to raise the ground temperature above freezing point (Williams & Smith, 1989). Under equilibrium conditions the thickness of permafrost mainly depends on the mean surface temperature with a significant contribution from local variations in geothermal heat flux. The geothermal gradient below the ground surface is controlled by ground thermal conductivity and local crustal conditions. The increase in temperature down through the soil profile defines the permafrost depth, and Williams and Smith (1989) have shown that the geothermal gradient normally averages around 30°C km^{-1} (see fig. 2.1.4). Deep permafrost will exist where low surface temperatures are combined with high ground thermal conductivity and low geothermal heat flux.

Permafrost is a purely thermal condition that bears no relation to the presence of ground ice because ground ice forms within a range of subzero temperature conditions (Ballantyne & Harris, 1994). In North America, three gradational spatial zones have been defined: the zone of sporadic permafrost, where mean annual air

temperature is close to 0°C and permafrost survives only in favoured spots; the zone of discontinuous permafrost, where mean annual air temperatures range from around -1°C to around -8°C; and the zone of continuous permafrost, where temperatures are generally lower than -8°C (fig. 2.1.5). In Siberia, however, the correlation between permafrost distribution and air temperatures is poor because of the presence of large areas with relict permafrost, surviving from the last Cold Stage of the Pleistocene, and is out of equilibrium with present day temperatures (Osterkamp, 1983).

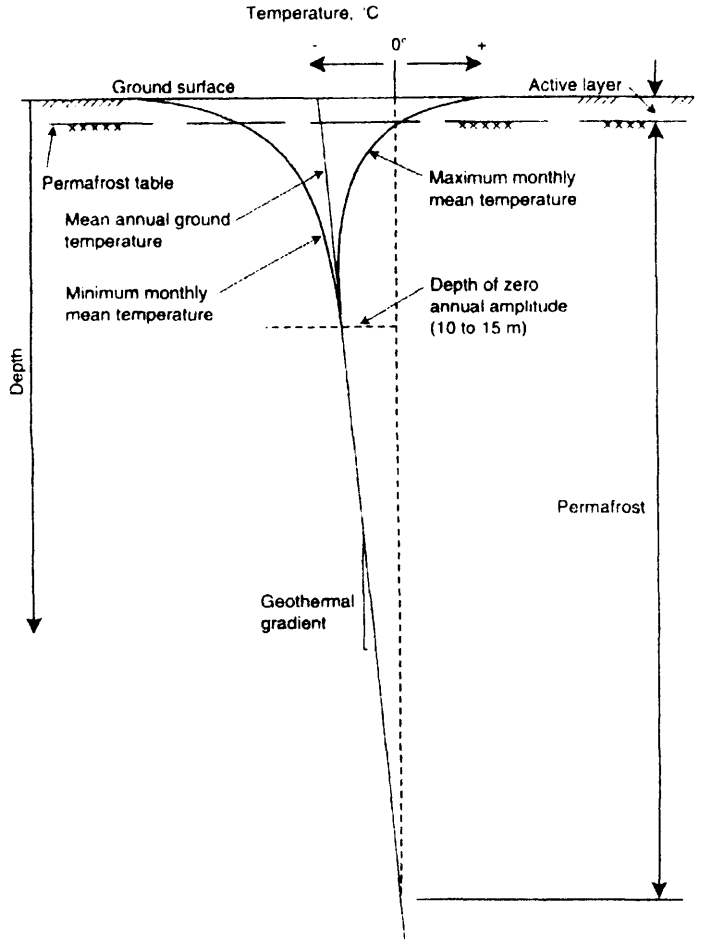

Figure 2.1.4. A schematic diagram of the equilibrium thermal regime within permafrost. (Source: Brown, 1970).

Permafrost often has a profound effect on geomorphological processes. For instance, slow permafrost creep has been recognised as a potentially important denudational process on steep permafrost slopes (Lewkowicz, 1988). The slow continuous deformation of the frozen substrate is of prime importance to geotechnical engineers involved in the design and performance of structures built on permafrost, as it occurs at stresses below those normally required to cause flowing, sliding or rupture (Williams, 1979). Permafrost creep results from gravitational forces imparting

stress on the plastic ice and soil mixture and rates of movement have been shown to increase as temperatures rise. This is because ice stiffness decreases as the ice warms and the proportion of unfrozen water in the soil increases (Irving, 2000). Movement rates of around 2.5-3.0 mm yr^{-1} have been recorded on a 15-24° slope of ice-rich clay in Mackenzie Valley, Canada (Morgenstern, 1985). Measurements taken within a discontinuous permafrost zone revealed volumetric movement rates of around 800-1000 cm^3 cm^{-1} yr^{-1} whilst average creep rates of 1.1 mm yr^{-1} at 0.35m depth to 0.4 mm yr^{-1} at 0.65m have been noted upon Melville Island, Canada (Bennett & French, 1988; Lewkowicz, 1988).

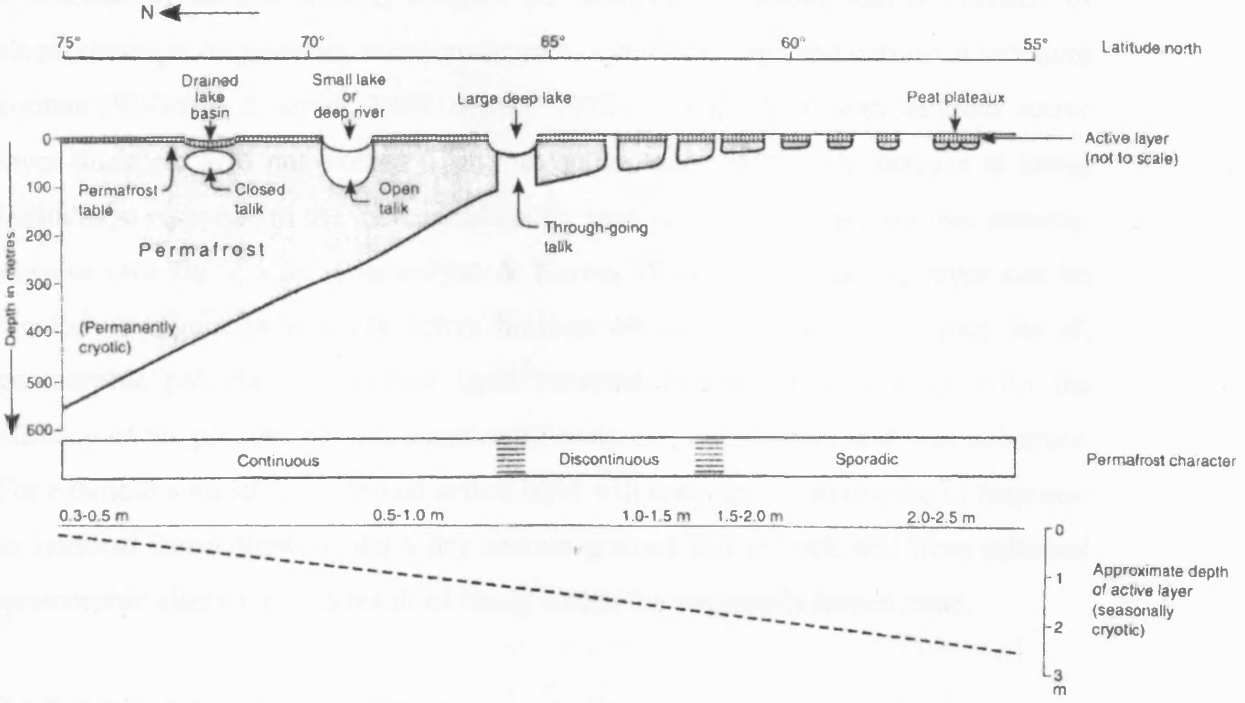

Figure 2.1.5. Periglacial ground characteristics along a typical North-South transect. (Modified from source: Brown, 1970 & Lewkowicz, 1989).

The depth of winter freezing within seasonally frozen ground is a function of the previous summer's above-freezing air temperatures (degree days above zero), since all stored sensible heat must be removed in order to allow ground freezing to commence. Frost penetration may be limited in areas with highly continental climates as they may exhibit large annual temperature ranges, where despite low winter temperatures, the ground will have stored a relatively large amount of summer heat that will need to dissipate before the instigation of soil freezing.

2.1.6. The Active Layer

Overlying permafrost is a layer of ground that will thaw and refreeze annually due to the seasonal above- and below-zero thermal cycle, commonly known as 'the active layer' (French, 1996). Generally the active layer will thicken in response to higher ground temperatures. The base of the active layer normally reaches the permafrost table in areas of continuous permafrost, however in areas of discontinuous permafrost a residual thaw layer may exist immediately above the permafrost table due to the incomplete freezing of the active layer during a mild or snow-laden winter (see fig. 2.1.4). The annual thickness of the active layer can vary according to the interaction of factors such as ambient air temperature, degree and orientation of slope, drainage, vegetation, snow cover, rock and/or soil type and entrained moisture content (Williams & Smith, 1989; Brown, 1978). Generally at high latitudes active layer thickness will not exceed 0.5m, but active layer depth will increase at lower latitudes in response to the increased heating associated with longer warmer summer seasons (see fig. 2.1.5) (Ballantyne & Harris, 1994). The active layer can be viewed as a geocryologically active horizon which has great significance for all geomorphic processes dependent upon seasonal freezing and thawing, with the efficacy of the process being a function of moisture, temperature and host substrate. For example a moist fine grained active layer will undergo cryoturbation in response to seasonal freeze/thaw whilst a dry coarser grained soil or rock will have minimal geomorphic alteration as a result of being within the seasonally frozen zone.

2.1.7. Active Layer Characteristics

The necessity to plan, design and construct engineering structures in areas underlain by permafrost has led to significant research into understanding the geomorphology and hydrology of the active layer (Williams & Smith, 1989). This research has improved scientific awareness of the importance of active-layer thermal regime, that may be influenced by two-sided freezing where permafrost is "cold" and by the presence of unfrozen water in freezing and frozen active layer soils (French, 1988). The unique thermal and physico-mechanical properties of the active layer leads to thermal and moisture driven processes such as ice segregation, frost heave, cryoturbation and the upfreezing of buried objects (e.g. Mackay, 1984). In finer-grained soils, temperature gradients close to the freezing front create hydraulic

gradients, causing the migration of unfrozen water in the direction of greatest heat flow (Beskow, 1935).

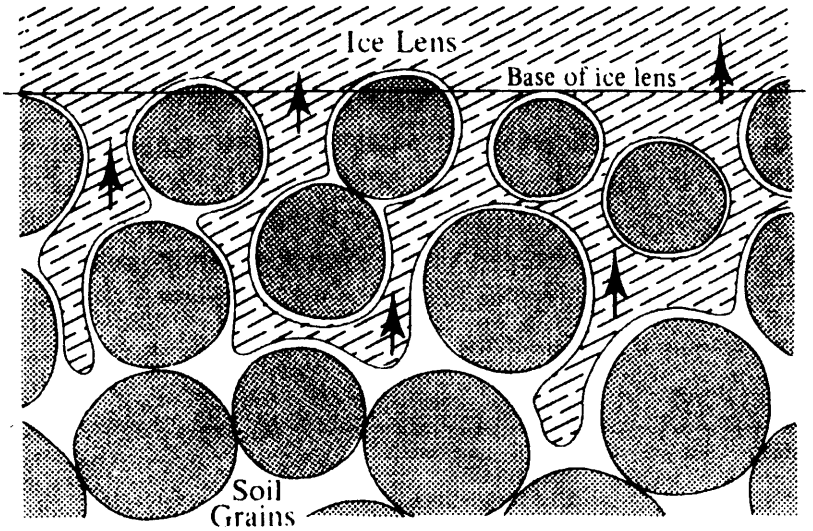

Figure 2.1.6. Schematic diagram of the frozen fringe highlighting unfrozen water migration towards the freezing front. (Source: O'Neill & Miller, 1985).

Upward migration of unfrozen water will occur during winter active-layer freezing when soil temperatures increase with depth, e.g. Cheng (1983) who recorded an increase in water content at the top of seasonally frozen ground between January and April at Reshui, Qilian Shan, China. During summer, warming of the ground from above causes a negative temperature gradient and this creates downward migration of unfrozen water from the active-layer into the underlying permafrost table. Mackay (1983) has observed that this migration increases moisture content within the lower part of the active layer and the upper part of the permafrost below. The migration of unfrozen water is often seasonally unequal as more water migrates downwards towards the permafrost table during annual thaw cycles than migrates upwards during the annual freezing cycle (Woo & Steer, 1983). This inequality occurs because summer downward migration takes place during a time of high-unfrozen water content, increased hydraulic conductivity, and within an open system water supply created by thawing ice lenses, snowmelt, rain, and groundwater flow. In contrast, winter upward migration occurs during a time of low unfrozen water content, reduced hydraulic conductivity, and within a closed hydraulic system where water movement is restricted to the redistribution of hygroscopic unfrozen water moving via mineral grains within the soil matrix (see fig. 2.1.6) (Smith, 1985). The inequality of water distribution within the active layer creates a net accumulation of

segregated ice at the top of the permafrost table, this ice rich layer has wide ranging geomorphic consequences, particularly wasting processes, by promoting late summer frost heave (see Mackay, 1984; section 2.2.4) and causing high basal porewater pressures when the upper permafrost table melts in response to extreme summer warmth (Harris & Lewkowicz, 2000).

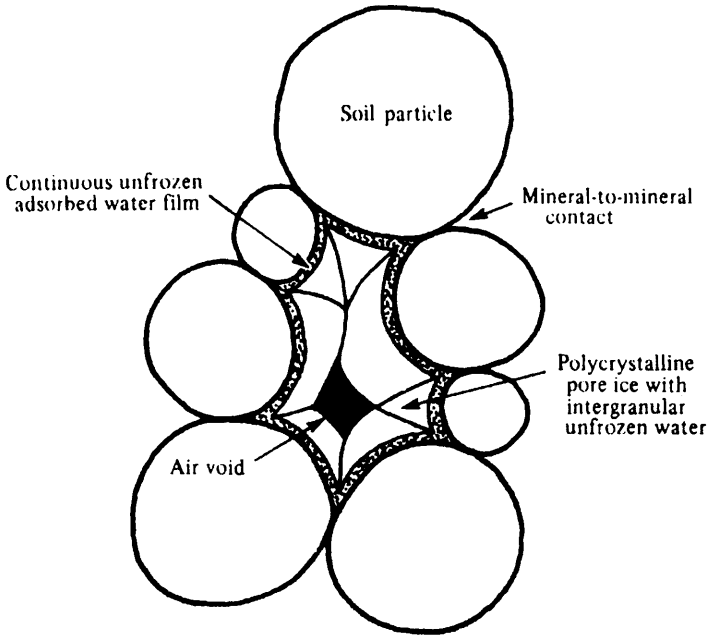

Figure 2.1.7. Schematic diagram showing the structural element of a freezing granular soil matrix. (Source: Williams & Smith, 1989, p.235).

The partially frozen soil found behind the advancing freezing front in winter, and immediately below the thawing front in summer is a multiphase system consisting of mineral particles, ice, water and air (fig. 2.1.7). A film of unfrozen water exists around soil mineral particles attached by intermolecular Van der Waal forces; this adsorbed film prevents inter-pore ice from being in direct physical contact with the soil mineral grains (see fig. 2.1.7) (Beskow, 1935; Moore & Mitchell, 1974). This effect is especially pronounced within fine-grained soils as the large surface area of clay minerals allows a high volume of mobile unfrozen water to be adsorbed within the ice/soil matrix. The air-water interfaces in unfrozen soil behave similarly to the ice-water interfaces in a frozen soil, in that capillarity acting across a water pressure gradient will drive moisture movement via interfacial tension within the boundary meniscus. Adsorbed water within fine soils plays a critical role in ice segregation processes that are often responsible for high active-layer ice contents, and these are discussed below.

2.1.8. Active Layer: The Seasonal Freezing Cycle (Winter)

Intra-pore ground ice forms within the soil matrix and creates upward movement of soil grains through the 9% volumetric expansion that occurs during water phase change from a liquid to a solid state (Taber, 1929; 1930). As the surface temperature falls below freezing point a planar 0°C isotherm descends through the ground, this isotherm is termed the freezing front. Ice crystals begin to nucleate within the soil matrix at and immediately behind the freezing front (see fig. 2.1.8). Hygroscopic water adjacent to the newly forming ice also begins to freeze due to the lowering of the free energy of water. The free energy imbalance establishes a water potential gradient that causes moisture migration towards the freezing front in order to maintain thermal equilibrium. The hydraulic gradients leading to this water migration are termed cryosuction and are responsible for frost heaving of frost susceptible soils (Williams, 1972; Chamberlain, 1981).

A frost susceptible soil such as a clay or silt creates high-pressure gradients more easily due to its smaller pore spaces (Beskow, 1935). These smaller pore spaces also provide a greater number of water transport pathways within the soil matrix. This is the key property because ground ice requires a constant supply of water in order to maintain growth, in coarser grained materials such as sand and gravels, lower pressures are generated and in-situ pore water freezing is more common (see fig. 2.1.9) (Palmer, 1967). Such soils are classified as non-frost susceptible.

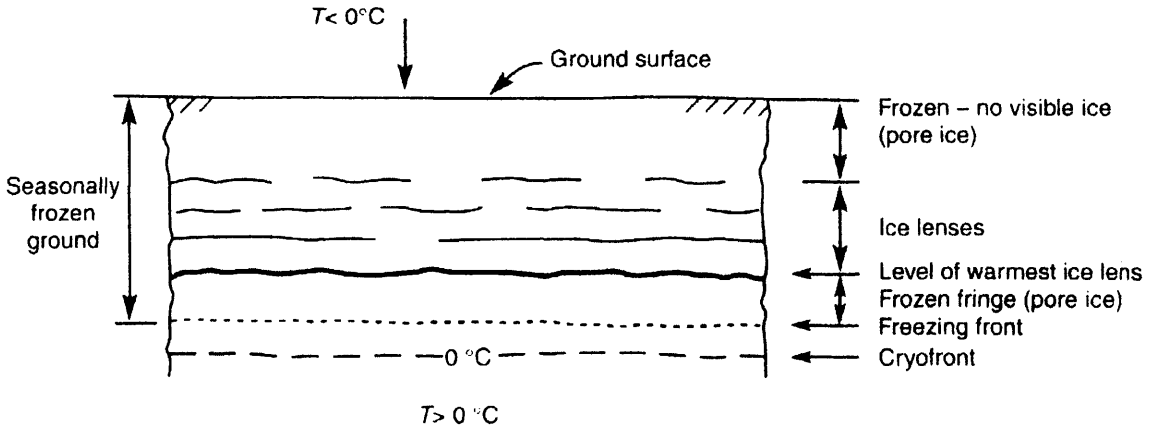

Figure 2.1.8. Schematic diagram showing the relative position of the different freezing fronts during the progressive one-sided downward freezing of a fine-grained, frost-susceptible soil. (Source: French, 1996, p.133, fig. 8.5)

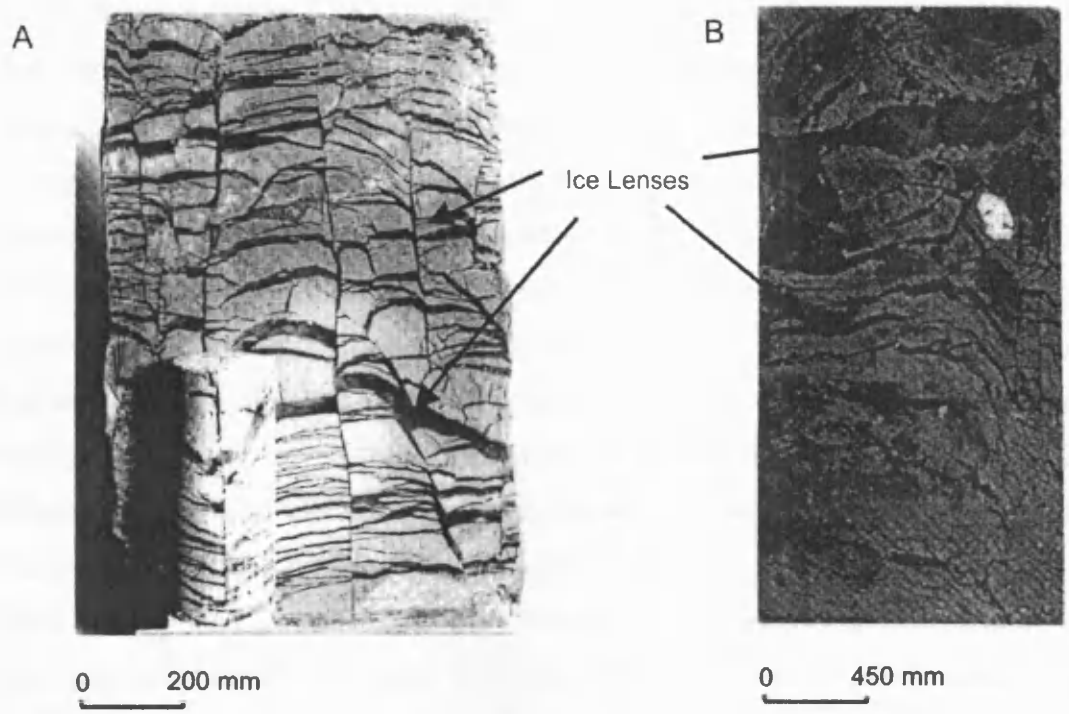

Figure 2.1.9. Images showing the presence of segregated ice nucleated within a laboratory environment. Note (A): Frozen clay showing typical ice layers or lenses. The ice was mainly formed by water being drawn into the freezing zone and is the cause of the expansion constituting frost heave. Note (B): Frozen soil shows ice lenses deformed by differential heave as the soil to the left had a higher silt content than the sandy material to the right. Hence the silty soil was able to feed the ice lens and continue growth. (Adapted from source: Williams & Smith, 1989).

Segregated ice provides an important source of upward physical motion of the soil mass during freezing and a key supply of intra-soil moisture during thawing. Segregated ice lenses can grow indefinitely when the potential water supply equals or exceeds the freezing rate (Mackay, 1984). Discrete lenses enlarge through the addition of ice formed via upwardly migrating soil moisture (see fig. 2.1.7); and as such they form parallel to the soil surface along the downward isothermal freezing plane meaning volumetric expansion and heaving pressures exist in the direction of heat flow (see fig. 2.1.9). The lateral extent of any ice lens will depend upon the homogeneity of the surrounding material, uniformity of the water supply, and any existing temperature gradients (White *et al.*, 1992).

2.1.9. Active Layer – Seasonal Thaw Cycle (Summer)

Summer thawing of the active layer leads to the release of excess soil moisture as segregation ice melts, and is associated with the annual occurrence of thaw consolidation. Thaw consolidation is the time-dependent consolidation of the soil body resulting from the thawing of segregation ice and subsequent drainage of pore

water (Nixon & Ladanyi, 1978). Thaw consolidation is a key active layer process that impacts upon the style and rate of mass wasting processes within periglacial areas. Thaw consolidation normally leads to increased levels of porewater pressure during thaw, depending mainly on the ratio between rate of thaw (meltwater release) and rate of consolidation (rate of meltwater expulsion) (McRoberts & Morgenstern, 1974). The downward thaw of ice-rich ground leads to the release of more meltwater than can be accommodated by the capacity of normal pore space within the soil matrix (see fig. 2.1.7). The intergranular voids left by the melting of segregated ice can only be closed if excess meltwater is expelled from the soil. However, the rate of expulsion is limited by the permeability of the thawed soil. The permeability is a function of grain size, so that coarse-grained soils will allow rapid drainage and as such allow the rapid diffusion of any localised elevation of porewater pressure (Morgenstern & Nixon, 1971). However, fine-grained soils restrict the movement of unfrozen water between pore spaces within the matrix and as such allow porewater pressures to reach elevated levels during thaw cycles. Fine grained soils are commonly associated with higher amounts of segregation ice and this creates a positive feedback cycle during thaw phases (see section 2.2). This relationship can be described via the thaw consolidation ratio calculated by Morgernstern & Nixon (1971):

$$R = \frac{1}{2}\left[\frac{\alpha}{\sqrt{C_v}}\right] \qquad (2.4)$$

where

$$\alpha = \frac{X_t}{\sqrt{t}} \qquad (2.5)$$

X_t is the depth of thaw in time t and C_V is the coefficient of consolidation, which is a function of the permeability of the material. High values of R lead to high porewater pressures being generated during thaw. Where values of R are greater than one there is an increased likelihood of slope failure, as sustained high porewater pressures will be generated at the thaw front. If the rate of thaw is sufficiently fast and the C_V parameter sufficiently small, meltwater is produced at a faster rate than it can drain, porewater pressures may exceed hydrostatic, and even approach geostatic. Under these circumstances, part or all of the overburden pressure becomes supported by pore water rather than mineral grains (see fig. 2.1.7), reducing intergranular

friction and the shear strength so that the soil can mobilise. This may lead to slope failure, and certainly contributes to the slow downslope mass movements that form the subject of this research.

2.2. Periglacial Slope Processes

The following section will focus on geomorphic processes that specifically operate on periglacial slopes. These processes can be divided into slopewash, rapid mass movements and slow mass movements. Slopewash processes include surface wash and subsurface wash. Rapid mass movements comprise retrogressive thaw slumping, active layer detachment failures, slush flows, debris flows, avalanches, and rockfalls (French, 1996). Slow mass movements consist of annual frost creep and gelifluction, needle ice creep, diurnal frost creep, permafrost creep and plug-like solifluction. Slope failure reflects reduction in shear strength of the recently thawed soil until the stability threshold is reached (see chapter 7). The main body of this investigation will focus on gelifluction that occurs within the active layer upon low angle slopes through a combination of seasonal ground freezing and thaw consolidation. Even though solifluction operates very slowly, generally at rate of at most 0.1 m $year^{-1}$, its widespread distribution makes it a key contributing process within the evolution and history of most upland periglacial landscapes (Matsuoka, 2001) and the process was widely important in the UK during Pleistocene cold stages (Ballantyne & Harris, 1994).

2.2.1. Definition of Solifluction

The term 'solifluction' has an ambiguous definition and currently serves as an umbrella term for a composite of several geomorphic slope processes. The definition was originally proposed by Andersson (1906, p.95-96) to describe the 'slow flowing from higher to lower ground of masses of waste saturated by water' and thereby included any downslope movement occurring within a saturated soil. Andersson's definition was indistinct, as it did not specify the range or rate of processes nor the prevalent climatic conditions required for the presence or initiation of solifluction. Dylik (1951) adapted the definition to explain soil movement during active layer thawing above permafrost; he created the term 'congelifluction' as being

'earth flow occurring under conditions of frozen ground'. Congelifluction was further refined by Baulig (1957) who outlined the phrase 'gelifluction' to describe soil flow generated by the melting of ice rich soils associated with both permafrost and seasonally frozen ground. Washburn (1979) adopted the term gelifluction to refer to the downslope saturated flow of soil within the active layer during seasonal thaw as it was recognised that earlier definitions of solifluction and congelifluction did not acknowledge the role of seasonal frost heave within the mass wasting process. The process of frost creep associated with downslope sediment transfer by frost heave had been previously well documented by quantitative field studies after having been first identified in 1889 by Davison (Williams, 1959; 1962). Washburn (1979, p.78) was able to distinguish the role of frost creep in solifluction and defined it as the 'rachet-like movement of particles as a result of frost heaving of the ground and subsequent settlement upon thawing, the heaving being predominantly normal to the slope and the settling nearly vertical'. In this sense Washburn pioneered the view that frost heave was the precursor to all forms of solifluction movement, with the main contributor to frost heave being the formation of segregated ice. Ice segregation (the process whereby discrete lenses of ice nucleate within the soil matrix and cause an increase in soil volume, see section 2.1.5) is largely responsible for winter frost heaving and subsequent summer thaw consolidation, widely considered to be the key mechanisms in both frost creep and gelifluction (Williams & Smith, 1989). Harris (1981) stressed the need to regard mass wasting by solifluction as a composite process involving both frost creep and gelifluction, whereby both processes result from the thawing of frozen soil containing excess ice.

These early definitions have been modified by later research studies which revealed that slow mass movements in cold regions are multi-faceted, site specific, and do not always require complete regolith saturation to operate efficiently (ACGR, 1988; Harris *et al.*, 1997). Whilst the term solifluction has never been unequivocally defined, a modern explanation is that solifluction represents a collective term for a suite of processes that involve the slow mass wasting of a slope associated with freeze-thaw action (Ballantyne & Harris, 1994; French, 1996; Matsuoka, 2001). Solifluction can be subdivided into needle ice creep, frost creep, gelifluction, and plug-like flow. This classification uses the criteria of the position of the particles during movement and the vertical extent of the movement (see fig. 2.2.1). The depth

of concentrated ice lens development, i.e. depth of developed frost heave, controls the vertical extent or velocity profile of the movement, although some solifluction deposits may exhibit some degree of equifinality of form (Benedict, 1970; Harris, 1972).

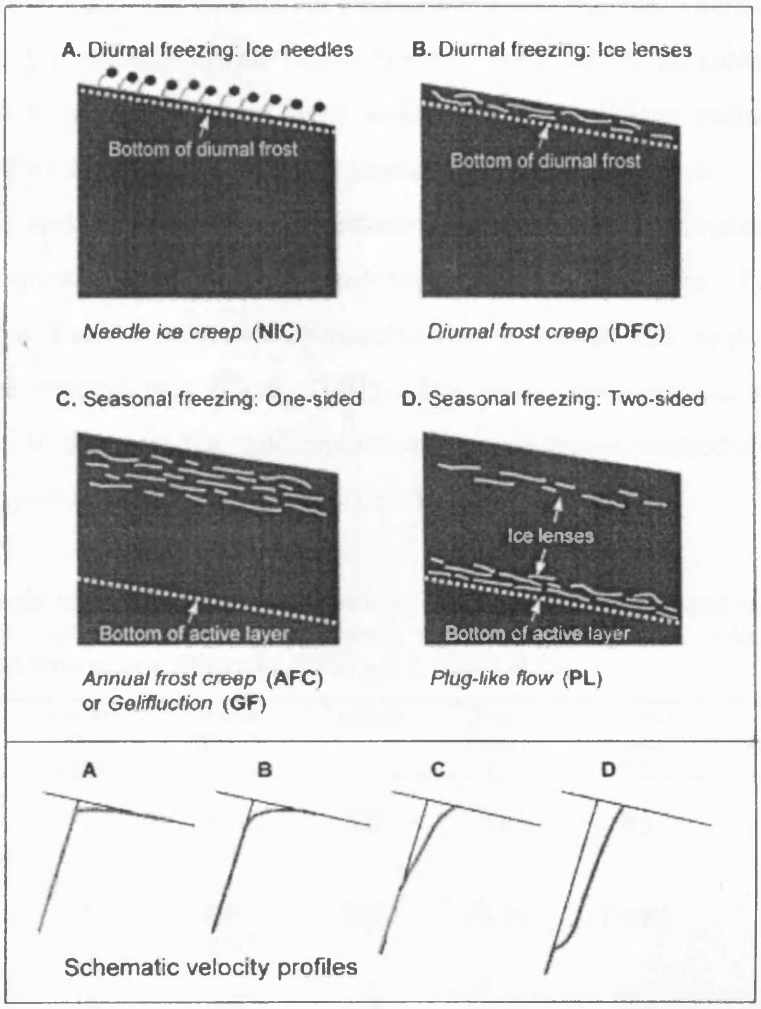

Figure 2.2.1. Schematic diagram showing types of frost heave and classic velocity profiles for the different classified types of solifluction movement. (Source: Matsuoka, 2001, p.109).

2.2.2. Needle Ice Creep

Needle ice creep is a near surface diurnal frost creep. It occurs when surface debris becomes entrained and lifted by ice needles and then falls back to the surface upon thawing. Needle ice being defined as the 'accumulation of slender, bristle-like crystals (needles) practically at, or immediately beneath, the surface of the ground' (Washburn, 1979, p.92). The growth of needle ice reflects a shallow nocturnal surface cooling where the frost plane stays within the uppermost centimetres of the soil profile where clusters of long thin crystals usually grow to between 5-30mm

long (Lewkowicz, 1988). Needle ice normally forms at night as a result of strong radiative cooling creating ice segregation in the surface of the soil. Ground material must be sufficiently permeable to allow rapid migration of water to the freezing plane, this is necessary to keep the freezing plane stationary within the near surface zone and allow a high nightly freezing duration and cooling rate. Thermal conditions for needle ice growth will mainly occur in early winter when the subsurface soil is warm enough to allow nocturnal frost penetration and morning radiation remains strong enough to sufficiently raise air temperature to thaw needle ice. Needle ice is common in alpine areas with maritime or temperate climates and high tropical/subtropical mountain ranges as they create a high number of freeze thaw-cycles per year, have a restricted longevity of snow cover, and frequently contain moist silty or organic soil (Grab, 2001). However, there remains a paucity of definitive data to describe the rigid environmental conditions controlling the growth and ablation cycles of needle ice (Grab, 2001).

Table 2.2.1. Needle ice creep data from field studies conducted within periglacial zones defined by both altitude, i.e. mid-latitude to tropical mountain regions, and latitude, i.e. polar and sub-polar regions. (Adapted from source: Matsuoka, 2001, p.112, table 1 & 2).

Location	Monitoring Period (year)	Major Processes	Landform	Slope Gradient (°)	Maximum Heave (cm)	Surface Velocity (cm year^{-1})	Research Study
S. Georgia. Sub Antarctic	1	AFC, NIC	SSP	21	9.5	47	Smith (1960)
S. Japanese Alps	3	DFC, NIC	SBL	14-30	1.4-2.9	16.9	Matsuoka (1998)
Coast Mts, Canada	10	NIC	SSP	10-15	Nd	25	Mackay & Matthews (1974)
Bolivian Andes	3-5	NIC	SBL	19-28	Nd	100	Francou & Bertran (1997)
Venezuelan Andes	4	NIC	SBT	18-25	Nd	16.3	Perez (1987)
Venezuelan Andes	4	NIC	SSP	19-25	Nd	6.0	Perez (1992)
Nagano, C. Japan	0.5	NIC	GS	27	2.5	0.3	Nakaya (1995)

Throughout the table 'Nd' indicates no data available.
AFC = Annual Frost Creep, DFC = Diurnal Frost Creep, NIC = Needle Ice Creep.
SBL = Stone-banked Lobes, TBT = Turf-banked Terraces, SSP = Sorted Stripes, GS = Grazing Steps.

Downslope movement occurs due to the mechanical weakness of the ice needles allowing a rotational downward movement of the soil grain (e.g. Higashi & Corte, 1971, p.482, fig. 3). This means that there is a rapid decrease in soil movement with depth, for example Mackay and Matthews (1974) reported that movement rates became zero at depth of 7cm. The average superficial layer that undergoes diurnal frost creep is 5-10cm thick (Matsuoka, 2001). The repetition of the diurnal freeze-thaw cycle can lead to rapid downslope movement, for example Mackay and Matthews (1974) reported up to 15cm of downslope movement in 33 days whilst Czudek and Demek have mentioned a comparable value of 14-18cm within surface stones across a 36-day period upon a slope in eastern Siberia (Lewkowicz, 1988). A key parameter affecting rates of movement is particle size, for example within an overall downslope transport rate of approximately $13cm^3\ cm^{-1}\ yr^{-1}$, fine material can be moving downslope on average $33cm\ yr^{-1}$ compared to coarser (i.e. heavier) material travelling at only $15cm\ yr^{-1}$ (Mackay & Matthews, 1974). High transport rates can be achieved because needle ice has been observed to lift surface particles and stones of up to 3mm in diameter by 50mm or more (Lewkowicz, 1988). For a detailed summary of field rates of needle ice creep refer to Table 2.2.1. However, despite the numerous studies it remains unclear as to the actual geomorphologic significance of needle-ice creep within hillslope denudation.

2.2.3. Frost Creep

Frost creep can be described as the net downslope displacement of a soil mass that occurs when a soil, during freezing, expands normal to the surface and, during thaw, settles in a near vertical direction (Washburn, 1979; Benedict, 1970). This displacement has often been described as a rachet-like movement, where the maximum potential frost creep (AC) can be calculated by:

$$AC = h \tan \alpha \qquad (2.6)$$

where h indicates the amount of frost heave (mm) and α represents the angle of the slope (see fig. 2.2.2). There are several problems with calculating the maximum potential movement (AC) via $h \tan \alpha$. The maximum potential frost creep calculation assumes that no soil cohesion exists during thaw, but laboratory studies

have shown that cohesion between grains prevents completely vertical settlement and can create retrograde (upslope) movement during thaw (see Harris *et al.*, 1997, p.858). This retrograde movement will reduce actual rates of frost creep in relation to any calculated maximum potential frost creep, to account for this upslope motion Jahn (1975) proposed an equation for frost creep that includes a coefficient of cohesion:

$$l = k\, h \tan \beta \qquad (2.7)$$

Where l equals movement parallel to the slope, k is a coefficient of soil cohesion, h represents the amount of frost heave and β is the angle of the slope.

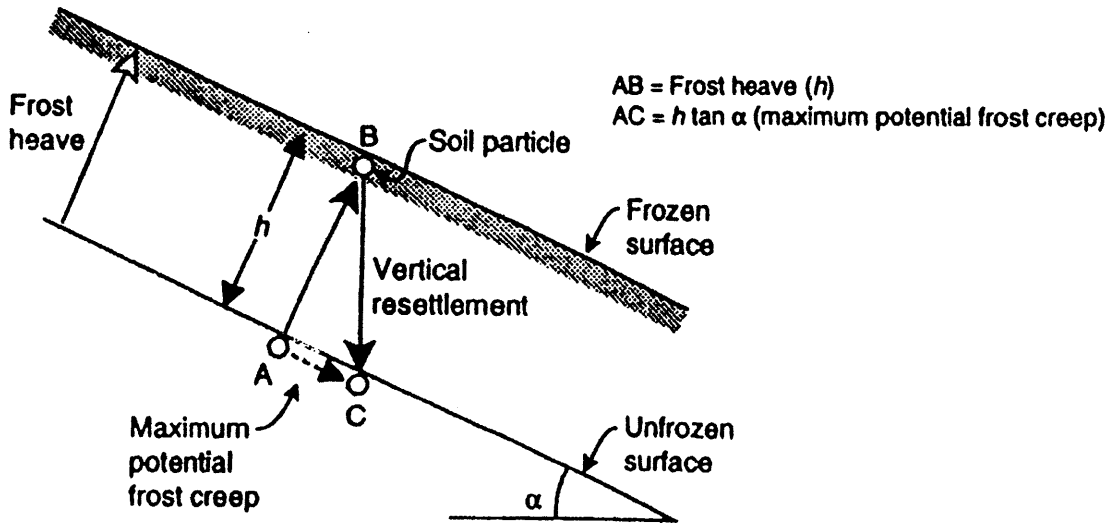

Figure 2.2.2. The mechanism of frost creep. (Source: Ballantyne & Harris, 1994, p.114, fig. 7.2).

Mackay (1981) has suggested that further displacements beyond the calculated maximum may occur on steep slopes as a result of ice lens geometry, where greater creep occurs over the centre of the lens but continuity of mass forces additional transitional movement upon soil grains residing on the downslope periphery of the ice body. The continuity of mass implies that observed rates of net soil movement are not independent of the size and shape of segregated ice lenses creating the discontinuous upward and downward motion of the soil surface. In addition, inclined or vertical ice veins may also be present within the soil matrix, whilst these would have a minor effect upon amounts of frost heave they would present a significant surface across which soil creep could occur (Lewkowicz, 1988; Van

Vliet-Lanoë *et al.*, 1984). It is therefore felt by many researchers that actual rates of frost creep may considerably exceed any rates of frost creep (*AC*) predicted by via $h \tan \alpha$ or $k\, h \tan \beta$.

Frost creep creates a concave downslope vertical displacement profile as ice lenses become fewer with depth in areas of discontinuous permafrost experiencing single sided downward freezing. Ice-lens growth is hindered with increasing depth through desiccation created by segregated ice formation within the upper soil restricting the availability of unfrozen water necessary for ice lens nucleation. This desiccation will occur independently of frost plane penetration depths within the soil profile, and because frost heave is a function of ice lens growth, a decrease in the volume of segregated ice will lead to a decrease in volumetric frost creep with depth (see fig. 2.2.1). Frost creep can be divided into diurnal frost creep and annual frost creep dependent upon the relative period of completion for the freeze-thaw cycle, the difference in this duration controls the depth of soil movement by impacting upon frost depth penetration (see fig. 2.2.1). Annual frost creep will undergo deeper frost penetration and therefore experience a deeper depth of segregated ice leading to greater frost heave; in comparison diurnal frost creep will mainly dislocate the uppermost centimetres of soil (e.g. Matsuoka, 1998).

Frost creep will occur with greatest efficacy upon steep slopes that experience conditions suitable for the growth of intra-pore segregated ground ice, namely frost susceptible soils within a periglacial climatic regime (see section 2.1.7). Benedict (1970) during a long-term field study measured rates of frost creep movement of 7.2mm yr^{-1} in seasonally frozen ground within the Colorado Front Range, USA. He found rates of frost creep exceeded rates of gelifluction in some areas, but later researchers have felt he did not account for the impact of ice lens geometry upon observed rates (Mackay, 1981). Washburn (1967) has recorded surface frost creep rates of between 4.4mm yr^{-1} and 26.2mm yr^{-1} on silty diamicton slopes of 2.5-14° (gradient), although all sites were underlain by continuous permafrost he observed that at drier sites frost creep exceeded gelifluction by as much as 5:3:1. As such both Benedict and Washburn found frost creep rates exceeded gelifluction in areas where mass wasting was originally slow, i.e. moisture poor field sites where azonal denudational slope processes were inhibited by the lack of mobile moisture.

It should be noted that some authors have included frost creep as part of the gelifluction process (e.g. Jahn, 1975; McRoberts & Morgernstern, 1974) whilst other have discussed frost creep as an entirely independent process (e.g. Washburn, 1979; Mackay, 1981). For the purposes of the current investigation it is concluded that frost creep is an integral part of gelifluction because differentiation is only appropriate for specific areas, e.g. zones of seasonally frozen ground where there is no summer frost heave. Gelifluction is therefore taken to be defined as being the amalgam of frost creep during freezing cycles (section 2.2.3) and classic gelifluction during thaw cycles, because both processes occur simultaneously. The experimental procedures described in this thesis can monitor the movement of surface markers allowing calculation of potential maximum frost creep, but as noted above, due to soil cohesion the differentiation between amounts of actual and potential frost creep are likely to be much less than the theoretical maximum (see fig. 2.2.3) (Washburn, 1999; Smith, 1992).

2.2.4. Gelifluction

Gelifluction has been defined as the slow downslope flow of unfrozen earth materials on a frozen substrate (Harris, 1981). Gelifluction occurs when seasonal thawing causes a plastic soil layer to deform downslope, this deformation results largely from frictional flow or creep (see fig. 2.2.3) (Harris *et al.*, 1995). The thaw consolidation of seasonally frozen ground and/or the inflow of additional water from snowmelt or rainfall cause raised subsurface pore pressure conditions that reduce soil shear strengths and encourage the slow downslope displacement of the soil mass (Harris *et al.*, 1997; Harris & Davies, 2000). Gelifluction is promoted by a decrease in the effective strength of the soil unit due to ice segregation creating a physical separation of soil particles during freezing and by high thaw-consolidation ratios that cause excess porewater pressures. These excess porewater pressures reduce the effective stress (i.e. the frictional shear strength) allowing elasto-plastic soil deformation (Harris *et al.*, 2003a). Therefore a key control on volumetric transport via gelifluction is the distribution of segregated ice within the soil profile.

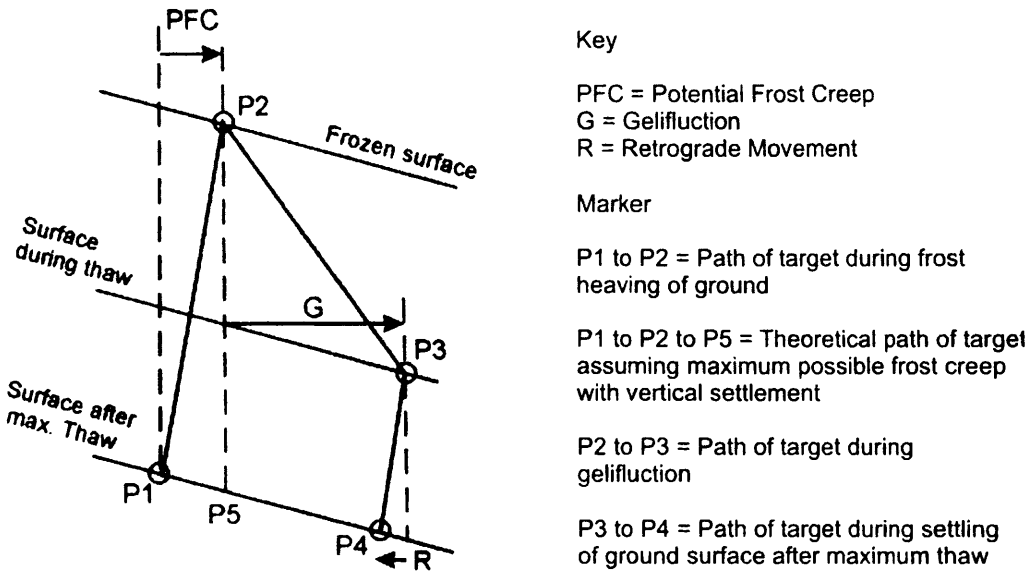

Figure 2.2.3. Schematic diagram showing the individual components of horizontal gelifluction movement. (Adapted from source: Harris & Davies, 2000, p.205).

Gelifluction is virtually ubiquitous in periglacial regions, having been observed on slopes as gentle as 1°, and occurs mainly in the near surface region of the soil profile within seasonally frozen ground (Washburn, 1979). Many field investigations have described gelifluction movement as being laminar, with a linear decrease in movement occurring with increasing depth (see fig. 2.2.1) (Gamper, 1983; Harris, 1977). The concentration of movement in the upper soil layers is because self-weight stresses are low so thawing leads to significant shear strain in the wet soft sediment. It has been shown that the thawing of deeper zones within the active layer does still cause thaw consolidation but creates little downslope movement. Within deeper zones of the active layer a progressive decrease in void ratio and moisture content leads to an increase in undrained shear strength within the more continuous soil matrix. The greater self-weight stress creates higher frictional strength within the unit through a progressive decline in segregated ice volume occurring with depth. Conditions are suitable for gelifluction in areas where the downward percolation of water through the soil becomes limited by underlying frozen ground and by the melting of segregated ice lenses creating excess water to reduce internal cohesion between mineral grains (Hallet & Waddington, 1992). As such gelifluction is therefore a thaw phase process that becomes particularly efficient upon slopes below late-lying or perennial snowbanks (French, 1996). However, within areas of continuous permafrost where moisture migration is seasonally complex, a

phenomenon known as 'plug-like flow' occurs due to a concentration of ice segregation within the base of the active layer, this occurrence is discussed within section 2.2.5.

Table 2.2.2. Gelifluction data from field studies conducted within periglacial zones defined by altitude, i.e. mid-latitude to tropical mountain regions. (Source: Matsuoka, 2001, p.112, table 2).

Location	Monitoring Period (year)	Major Processes	Landform	Slope Gradient (°)	Maximum Heave (cm)	Surface Velocity (cm year^{-1})	Research Study
N. Tibetian Plateau	5	GF	SBL	15-25	Nd	0.3-3	Harris et al. (1998)
W. Tianshan, Kazakhstan	20	AFC, GF	TBL	5-25	Nd	6.5	Gorbunov & Seversky (1999)
Daietsu Mts, N. Japan	8	DFC, GF	SBL	12-27	Nd	3.0	Sone et al. (1998)
Colorado Front Range, USA	5	AFC, GF	TBL	13	Nd	1.7	Benedict (1970)
Colorado Front Range, USA	3	GF	SSP	12.5	Nd	2.2	Benedict (1970)
Colorado Front Range, USA	4	AFC, GF	TBL	6-7	21	1.0	Benedict (1970)
E. Tianshan, Kazakhstan	2	GF	TBL	20	Nd	11.2	Gengnian et al. (1995)
Swiss Alps, Switzerland	4	GF	SBL	7	5.1	3.4	Matsuoka (2001)
Hohe Tauern, Austria	2	GF	TBL	10-20	7	21	Jaesche et al. (1997)
N. Japanese Alps, Japan	2	NIC, GF	SBL & TBL	11-30	Nd	26	Sohma et al. (1979)
Swiss Alps, Switzerland	4	AFC, GF	TBL	25	Nd	4.1	Gamper (1983)
Kitakami Mts, N. Japan	2	NIC, GF	TBL	10	5.8	5.8	Sawaguchi & Koaze (1998)
Nagano, C. Japan	0.5	AFC, GF	TBL	22	6.3	6.3	Nakaya (1995)

Throughout the table 'Nd' indicates no data available.
GF = Gelifluction, AFC = Annual Frost Creep, DFC = Diurnal Frost Creep, NIC = Needle Ice Creep.
SBL = Stone-banked Lobes, TBL = Turf-banked Lobes, SSP = Sorted Stripes.

Field measurements have indicated that rates of gelifluction are highly variable but that gelifluction generally causes surface rates of movement of a few centimetres per year (e.g. Matthews & Berrisford, 1993). The type of dominating process can be defined by whether periglacial conditions exist as a function of altitude or latitude as these determine the relative influence of near surface conditions (see 2.1.3). Rates are likely to vary according to climatic and topographic parameters that define such factors as soil moisture, vegetation cover, slope gradient, and soil grain size distribution (see tables 2.2.2 & 2.2.3). Gelifluction can occur on slopes underlain by either warm or cold permafrost. In order to operate with complete efficacy it requires a thick zone of fine material as this allows ice segregation at depth by promoting the cryosuction of unfrozen water into the regolith during freezing. Gelifluction can operate under either a diurnal or annual prevailing freeze thaw action, and creates distinct surface expressions of movement as medium sized lobes, sheets or stripes (see section 2.3.2) (Matsuoka, 2001). The data within tables 2.2.2 and 2.2.3 outline gelifluction rates recorded from 27 sites; 13 from high altitude periglacial zones and 14 from high latitude zones. The compilation has excluded data from field studies that did not explicitly state that gelifluction was an observed movement type. The inclination of studied slopes ranged from 5° to 25°, with the mean average of 13.5° slope. The process parameters recorded in the table describe soil movement through components normal to the slope (frost heave) and horizontal to the slope (gelifluction surface velocity). Different monitoring methods were used by individual research workers to measure each component and a discussion of accuracy will be outlined in section 2.3.1. Tables 2.2.2 and 2.2.3 show the great variation that exists within recorded surface velocity rates, these directly reflect subsurface volumetric rates because gelifluction normally dislocates a soil layer that is shallower than 60cm in thickness (Matsuoka, 2001). Profiles of volumetric movement are normally concave downslope in response to the distribution of segregated ice and the presence of surface vegetation (Harris, 1981). Gelifluction occurs as a response to prevailing seasonal frost heaving dominating over the conditions necessary for diurnal frost action. Gelifluction therefore occurs at greater depths towards the poles with velocity profiles becoming increasingly convex in response to the decline in surface diurnal frost creep. However, the presence of a vegetation mat will also reduce near surface rates of movement by roots binding the soil and creating thermal insulation to hinder surface radiation in directly controlling

ground thermal regime. The presence of vegetation and clasts can create convex downslope velocity profiles that mimic higher latitude gelifluction profiles, for example the mid-latitude mountains described by Smith (1992).

Table 2.2.3. Gelifluction data from field studies conducted within periglacial zones defined by latitude, i.e. polar and sub-polar regions. (Source: Matsuoka, 2001, p.112, table 1).

Location	Monitoring Period (year)	Major Processes	Landform	Slope Gradient (°)	Maximum Heave (cm)	Surface Velocity (cm year^{-1})	Research Study
Melville Island, Canadian Arctic	2-3	AFC, GF, PFC	NSP	4.5	18.5	1.6	Bennett & French (1991)
Cornwallis Island, Canada	8	AFC, GF	SSP	7	Nd	3.0	Washburn (1999)
Banks Island, Canadian Arctic	11	AFC, GF, PLF	NSP	2-8	Nd	0.6	Eggington & French (1985)
Svalbard	6	GF, AFC	SBL	6-31	3	3.0	Sawaguchi (1995)
Svalbard	2	GF, PL	NSP	7-15	5	2.2	Matsuoka & Hirakawa (2000)
SW Yukon, Canadian Arctic	16-21	GF, ALG	TBL	14-18	Nd	1.3	Price (1991)
Svalbard	2	GF	SBL	10	8.8	3-4	Jahn (1985)
Svalbard	Nd	GF	TBL	10	Nd	5.1	Repelewska-Pekalowa & Pekala (1993)
Svalbard	2	GF	TBL	20	Nd	2.5	Matsuoka & Hirakawa (2000)
Svalbard	23	Nd	SBL	2-10	Nd	4.4	Akerman (1996)
Svalbard	23	Nd	SBL	4-12	Nd	3.5	Akerman (1996)
Kebnekaise, N. Sweden	8	AFC, GF	TBL	7-25	1	1.9	Jahn (1991)
Abisko, N. Sweden	4	GF	TBL	20	Nd	5.2	Nyberg (1993)
Okistindan, N. Norway	1	AFC, GF	TBL	5-17	2-6	2.1	Harris (1972)
Iceland	2	GF	TBT	7-10	Nd	0.9	Douglas & Harrison (1996)

Throughout the table 'Nd' indicates no data available.
GF = Gelifluction, AFC = Annual Frost Creep, DFC = Diurnal Frost Creep, PL = Plug-like Flow, NIC = Needle Ice Creep, AFG = Active-layer Glide.
SBL = Stone-banked Lobes, TBL = Turf-banked Lobes, SS = Smooth Slope, NSP = Non-sorted Stripes, SSP = Sorted Stripes, TBT = Turf-banked Terrace.

2.2.5. Plug-like Flow

Plug-like flow is a solifluction process that takes place exclusively within regions underlain by continuous permafrost. Plug-like flow occurs as a result of year-round frost heave creating a zone of ice-rich soil at the base of the active layer, during summer this zone undergoes thaw settlement that allows flow of the basal soil layer as the overlying active-layer is displaced downslope in a single continuous body of soil (see fig. 2.2.4). The vertical velocity profile for volumetric movement is convex downslope because plug-like movement is associated with positive pore water pressures along basal shearing zones causing localised loss of strength (Eggington & French, 1985). Plug-like flow can induce movement within a soil mass that is 60cm or thicker (Matsuoka, 2001). The basal zones may episodically flow for some distance downslope before losing moisture and reconsolidating into a state below the liquid limit.

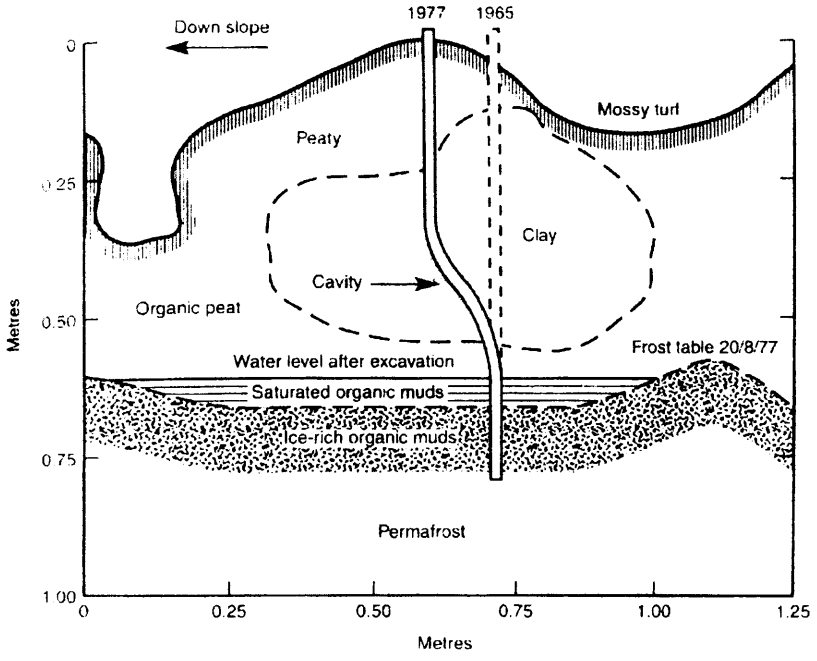

Figure 2.2.4. Field diagram illustrating a vertical velocity profile experiencing plug-like flow on Garry Island, NWT, Canada. (Source: Mackay, 1981, p.1672, fig. 7).

The process is intimately related to the movement of soil moisture during the year. Frost heaving occurs during autumn freezeback but also during summer thaw when near surface moisture percolates downwards into the soil profile via a thermal gradient created by the underlying permafrost table. The augmentation of basal ice

content via the simultaneous effect of a second freezing plane advancing upwards from the base of the active layer is termed two-sided freezing (see section 2.1.8 for description). The creation of two zones of ice-rich soil creates a desiccated layer in the centre of the active layer within which negative heave can be created via consolidation of pore spaces within the soil matrix. The formation of the desiccated zone also aids the downward movement of unfrozen water vapour towards the upward freezing plane which is especially important within the closed system created by continuous underlying permafrost. Mackay (1981) was able to report that most ice-lenses formed at the secondary upward freezing front and caused approximately 5-10mm of heave each year with rates of hummock movement between 0.2 and 10mm per year recorded over a 10-13 year period. These rates of movement indicated a volumetric transport rate of between 7 and 52 cm^{-3} cm^{-1} yr^{-1} that would appear to validate the efficacy of plug-like flow as significant denudational process within perennially frozen ground (see table 2.2.4). In order for plug-like flow to operate the soil must contain a clay fraction of around 25-30 per cent, as this will increase the probability of moisture conditions pushing the soil above its liquid limit and initiating basal liquefaction (Mackay, 1981; Lewkowicz & Clark, 1998).

Table 2.2.4. Plug-like flow data from field studies conducted within periglacial zones defined by latitude, i.e. polar and sub-polar regions. (Adapted from source: Matsuoka, 2001, p.112, table 1).

Location	Monitoring Period (year)	Major Processes	Landform	Slope Gradient (°)	Maximum Heave (cm)	Surface Velocity (cm $year^{-1}$)	Research Study
Ellesmere Island, Canadian Arctic	5	PL, AFC	SS	5-9	Nd	1.7-3.1	Lewkowicz & Clark (1998)
Garry Island, Canadian Arctic	13	PL	HK	3-7	14.4	0.7	Mackay (1981)
Garry Island, Canadian Arctic	11-12	PL	TBL	3-7	Nd	0.5	Mackay (1981)

Throughout the table 'Nd' indicates no data available.
GF = Gelifluction, AFC = Annual Frost Creep, PL = Plug-like Flow
TBL = Turf-banked Lobes, SS = Smooth Slope, HK = Hummock

2.3. Field Studies of Solifluction Processes

The following section will outline recently conducted field studies, and attempt to synthesise results into a general synopsis that identifies the main solifluction

processes alongside the rate and form of any recorded movement. The ubiquitous activity of solifluction and the distinctive nature of the landforms it creates (see fig. 2.3.5) have led to researchers publishing several hundred field-based papers on solifluction form and process (Hugenholtz & Lewkowicz, 2002, p.301).

The lack of standardisation of methodology, monitoring apparatus, and analytical techniques has made it difficult to directly compare results from individual studies (Matsuoka & Humlum, 2003). Many field studies reflect the site-specific nature of the solifluction process, in that recorded results may only be applicable to that particular regional set of climatic, geologic, geomorphic, hydrologic and vegetative parameters (Lewkowicz, 1988; Pissart, 1993). This has made it difficult to place spatially disparate studies into a coherent regional perspective, especially when specific regions have been heavily studied and reported in response to industrial pressures (for example studies related to gas/oil exploration infrastructure within the Mackenzie Valley in Canada). Therefore the measured rates and conceptual ideas concerning solifluction processes may have been overly influenced by the data collection techniques and specific locations in which the majority of studies have been undertaken (Thorn, 2003).

Field descriptions of slope processes in periglacial areas have been published from as early as the nineteenth century (e.g. Tarr in 1897). Improved logistical accessibility to remote periglacial areas alongside the increasing sophistication of recording techniques have created a more concentrated interest in field slope process studies within the last 40 to 50 years (e.g. Matsuoka, 1994; Lewkowicz, 1992). The following review will highlight particular long-term field studies as quality indicators of the most significant prototype conditions impacting upon solifluction and its incumbent processes (for full review see tables 2.2.2. & 2.2.3). It should be noted that these field studies have only been able to undertake inter-annual monitoring of volumetric soil movement. The term 'gelifluction' will refer to the combined effects of each individual geomorphic process outlined in section 2.2 as intra-annual field monitoring would be necessary to distinguish the different component processes of summer and winter frost creep and summer gelifluction in areas of continuous cold permafrost (Mackay, 1984; Lewkowicz & Clark, 1998).

A number of detailed long-term studies of gelifluction have been carried out within both permafrost and non-permafrost environments. In the last twenty years field research has concentrated upon the collection of baseline data in order to improve estimates of long term rates that can be used for validating numerical and physical laboratory modelling (e.g. Akerman, 1993). A small number of contemporary studies have used instrumentation to monitor the timing and explicit mechanism of soil displacement during gelifluction in the field (e.g. Matsuoka *et al.*, 1997). However, the large quantity of parameter-based field studies has made it possible to collate data and contextually relate the impact of specific environmental factors upon the rate and form of gelifluction (e.g. see fig. 2.3.4a). For example, researchers have attempted to assess the influence of soil texture (i.e. grain size distribution; Harris, 1981) or surface energy balance (i.e. mean annual air temperature; Matsuoka, 2001) upon periglacial slope movements. Detailed year round measurement of gelifluction via electronic data collection and/or long-term observation has allowed recent major theoretical advances to influence the broad conceptual framework explaining the development of different gelifluction landforms (i.e. Washburn, 1999; Smith, 1988; Matsuoka, 1998; Mackay, 1981). Several researchers have also used tephrostratigraphic or organic radiocarbon dating techniques upon buried soil horizons in an attempt to detail rates of past movement within formerly periglacial areas (see table 2.3.1) (for example Matthews *et al.*, 1986; Alexander & Price, 1980; Hirakawa, 1989). The collation of field measurements across different time scales provides a large frame of reference that creates the future possibility of developing more robust hypotheses regarding the spatial and geographic variation that exists within modern global gelifluction processes. Researchers have found it difficult to generate testable hypotheses concerning process-form interactions within gelifluction (see for example Kirkby, 1995), however the rate and specific process have been found to generally define the type and dimension of a landscape feature (Matthews & Berrisford, 1993; Hugenholtz & Lewkowicz, 2002).

2.3.1. Field Parameters influencing Gelifluction Movement

The large number of published field studies makes it a complex task to collate and understand general relationships between such disparate datasets. It can be difficult to distil data into appropriate groupings in order to better understand the influence of

a particular variable, especially when data collection and statistical techniques have developed through the duration of many long-term field studies (e.g. Washburn, 1999). The following section will use syntheses carried out by Harris (1981) and Matsuoka (2001) as key reference literature, as they provide an excellent broad framework for understanding the relative influence of different field parameters. Both authors collated large datasets in order to describe the rates and style of different gelifluction processes in relation to geo-environmental parameters. In doing so they highlighted the inherent variability of micro-climatic conditions; which made it impossible for single field studies to accurately classify or identify the influence of specific variables at a field scale (Lewkowicz, 1988).

Field studies have used a variety of methods to measure gelifluction phenomenon, these have either attempted to record velocity distribution with depth, amounts of frost heave and/or surface rates of movement. Many researchers have measured the upfreezing of a buried stake to record cumulative frost heave at a locality; this technique is of low accuracy because partial subsidence of the stake can occur during temporary thawing (e.g. Washburn, 1967). The upfreezing stake technique may cause a significant underestimation of annual frost heave ratios, especially in areas dominated by diurnal heave cycles, such as mid-latitude mountains (Francou & Bertran, 1997). Another approach was to provide differential measurements between the ground surface and a fixed datum at depth; medium accuracy data resulted from such bedstead measurements (e.g. Benedict, 1970). For manual measurement techniques to provide cumulative movement data they must be resurveyed at regular intervals (e.g. Washburn, 1999; Carver *et al.*, 2002). For this reason the highest accuracy occurs when recording is automated and combined with bedstead measurement techniques, as these allow the detection of multiple heave events within a yearly cycle (e.g. Jaesche *et al.*, 1997; Smith, 1988). Bedstead survey methods have included theodolite measurements from bedrock benchmarks or deeply inserted stakes (e.g. Washburn, 1967), and steel tape measurements from large boulders or deeply inserted datum posts (Harris, 1981). Surface velocity displacements have been determined through an amalgam of marked stones, tilting rods, painted lines and pegs. The type of technique used by a field study may determine the amount of recorded velocity, for example painted lines and marked stones will indicate the movement of the uppermost soil particles whilst tilting rods

and pegs will reflect movement in the uppermost soil layer because they are partially buried during installation (Matsuoka, 2001, p.116). Surface velocity measurements can therefore be skewed when compared to buried markers since only the surface markers will be able to move downslope in response to the relatively rapid process of needle ice creep (e.g. Matsuoka, 1998a).

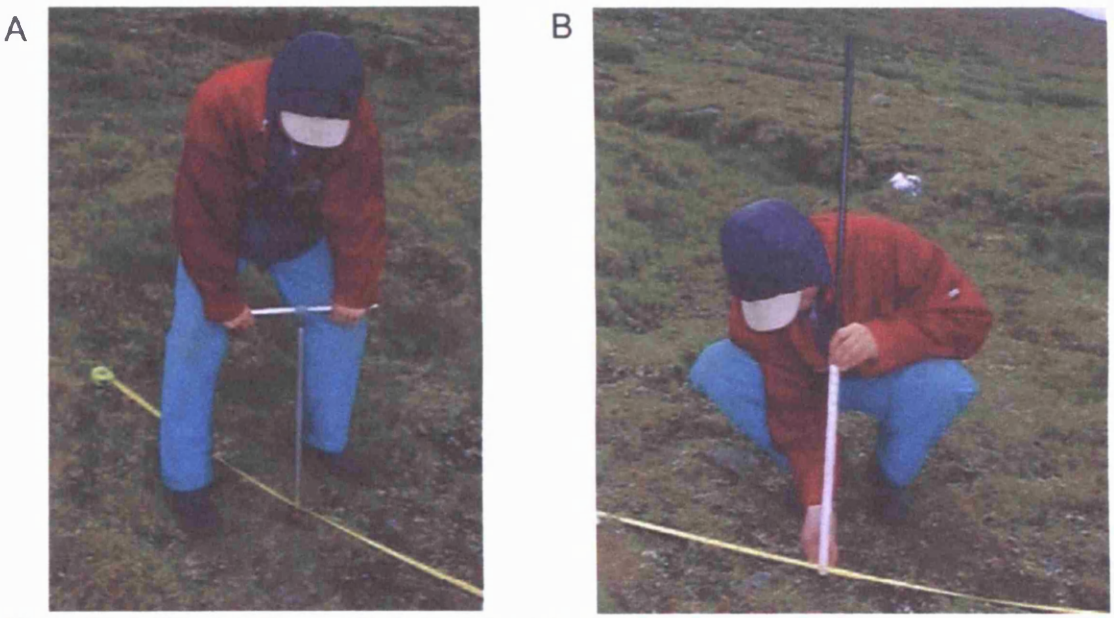

Figure 2.3.1. The installation of plastic tube columns to measure depth of volumetric movement within a turf-banked solifluction lobe upon slopes of Folldal in Dovrefjell, southern Norway. (Photograph: James Smith).

The subsurface velocity profile can be evaluated by the deformation of a buried sensor installed into the ground, with the length and repetition of a specific monitoring program determining whether the sensor needs to be electric or non-electric. The subsurface sensors are assumed to move with the soil mass, so their deformation provides definitive information on the distribution and depth of soil movement (Harris, 1981). Sensors are installed by either direct placement into the ground or by being placed into an excavated vertical hole (see fig. 2.3.1). Non-electric sensors such as buried wooden columns, flexible plastic tubing or aluminium foil strips require re-excavation of the ground in order to obtain velocity results (e.g. Rudberg, 1964; Benedict, 1970; Harris, 1977). The major disadvantage with non-electric sensors is that the field experiment will terminate through any attempt to collect subsurface velocity data from the buried columns. In contrast electric sensors allow non-invasive data collection via inclinometers, strain probes, and solifluction meters, as these can indicate subsurface movement profiles without the

need for excavation (e.g. Williams, 1962; Auzet & Ambroise, 1996; Yamada *et al.*, 2000). Non-invasive electrical meters therefore allow longer monitoring programs. Year-round, accurate, and continuous intra-annual monitoring can be undertaken when electric sensors are combined with data logging equipment (e.g. Matsuoka, 1994; Lewkowicz, 1992); intra-annual velocity rates can be correlated with intra-annual climatic or hydrological variations within the monitoring site (Matsuoka *et al.*, 1997). The accuracy of any measurements being taken within the field will depend upon the adopted methodology alongside the length of the envisaged monitoring period. Longer periods can account for inter-annual variations in movement rates created by specific climate fluctuations (e.g. Akerman, 1996), and minimise the impact of sensor installation, i.e. local soil disturbance, upon derived results (e.g. Smith, 1988). Most field studies have ranged from one winter to more than 30 years, with the mode period of study ranging from between 2 and 5 years (for a selection see table 2.2.2 & 2.2.3) (Matsuoka, 2001, p.117).

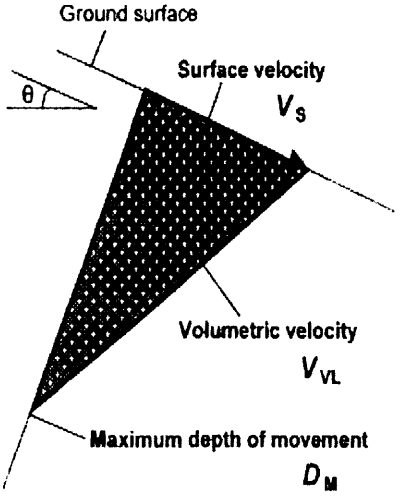

Figure 2.3.2. Common soil movement parameters measured by most field studies of gelifluction. (Source: Matsuoka, 2001, p.117, fig. 3).

The three most important components of movement recorded within most monitoring studies are: surface velocity, volumetric velocity and maximum depth of movement (see fig. 2.3.2). Research programs have found these three parameters can be analysed and compared to give an indication of the spatial variability of solifluction. The three movement parameters show individual variations with respect to the influence of various regional climatic trends alongside local variability in slope topography and soil properties.

Field studies have shown that ground freezing conditions, prevailing freeze-thaw action and the thickness of a fine soil layer will directly influence solifluction typology and downslope movement rates since these factors control the depth and thickness of ice segregation lenses, subsurface moisture status, and the frequency of freeze-thaw cycles. For example, thin stone banked lobes will be created by rapid shallow movement associated with diurnal frost creep in areas of warm discontinuous permafrost, whereas gelifluction processes will dislocate a deeper soil layer within soil climates undergoing seasonal frost, whilst plug-like flow will occur in High-Arctic areas of cold permafrost (see table 2.3.1).

Table 2.3.1. The influence of ground freezing conditions, prevailing freeze-thaw action, and thickness of active layer upon solifluction typology and associated landforms. Note: CPF (DT): cold permafrost with diurnal thaw, CPF (ST): cold permafrost with seasonal thaw, WPF: warm permafrost, SF: seasonal frost, DF: diurnal frost. (Source: Matsuoka, 2001, p.127, fig. 14).

	Ground freezing condition	Prevailing freeze-thaw action	Thin ← Fine soil layer → Thick	
Permafrost	CPF (DT)	Diurnal	**Diurnal frost creep** in the superficial layer ↓ Thin lobes and small-scale stripes (?)	
Permafrost	CPF (ST)	Annual	Freeze-thaw action very weak	**Plug-like flow** in the basal active layer ↓ Thick lobes and large-scale stripes (?)
Permafrost	WPF	Diurnal + Annual	**Diurnal frost creep** in the superficial layer ↓ Thin lobes and small-scale stripes	**Annual frost creep and gelifluction** in the upper active (or seasonal frost) layer ↓ Medium-sized lobes and stripes
Non-permafrost	SF	Diurnal + Annual		
Non-permafrost	DF	Diurnal	**Diurnal frost creep** in the superficial layer ↓ Thin lobes and small-scale stripes	

Soils undergoing solifluction in arctic and alpine areas mainly consist of sand and silt with a clay content of less than 20 percent (Harris, 1981). The lack of high clay contents within periglacial soil is because the cold periglacial regime minimises chemical reactivity and therefore impedes clay mineral production via secondary

weathering. The preponderance of hard rocks mainly undergo primary mechanical weathering, i.e. frost shatter weathering, to create diamictons of large angular clasts entrained within a sand/silt matrix. Washburn (1967) and Benedict (1970) have attempted to show the significance of textural variation upon rates of solifluction, they managed to show that silt content was a critical variable in determining the susceptibility of a soil to solifluction. Washburn reported that clay soils were too impermeable, and restricted adequate porewater movement during soil freezing which impeded the moisture necessary to support long-term ice lens growth whilst coarse sand and gravel soils were observed to allow rapid drainage and therefore alleviate the pore-water pressure conditions required for saturated gelifluction movement (Harris, 1981). The fine sand and silt soils that experience the highest field rates of solifluction movement have low liquid limits, low plasticity indices, and are largely bound by frictional strength due to the lack of clay minerals. The relative lack of cohesion has been highlighted as an important parameter that aids the generation of flow displacement in response to high porewater pressures (Harris, 1977). The shear strength parameters within solifluction deposits have been reported by Williams (1966), Harris (1972), and Washburn (1967).

Ice segregation during freezing and water seepage pressures during initial thaw reduces the unit weight of the soil, and increases its void ratio. Thaw consolidation, with attendant raised pore pressures, causes spring and early summer solifluction before thaw settlement and compaction increased shear strengths towards the end of summer. Field studies have been able to record variations in soil density across single solifluction features within a single annual season (e.g. Washburn, 1967). The spatial variability of soil texture and density can lead to variable velocity distribution, especially because needle ice creep is directly dependent upon the grain size of the uppermost layer (Mackay & Matthews, 1974). The significance of the influence of soil granulometry and soil index properties has been emphasised by specific laboratory studies examined in section 2.4 (e.g. Rein & Burrous, 1980; Harris *et al.*, 1993).

The main topographic control upon rates of observed solifluction would appear to be slope inclination. The influence of slope inclination upon soil movement has been described through several mathematical and physical models (e.g. Harris *et al.*,

2003). The simplest model was suggested by Williams and Smith (1989) and is outlined in section 2.2.3. An increase in solifluction rates with increasing slope gradient has been widely reported from field studies in polar mountains, for example Washburn (1967) in the Canadian Arctic and Akerman (1996) in Svalbard (see table 2.2.3 for a full synopsis). In lower latitude areas the influence of slope inclination can be masked by other slope conditions, i.e. spatial variation within other factors such as soil surface texture can mediate movement rates (Harris, 1981). The spatial variability of field conditions and the influence of site-specific topographic parameters can be shown to influence rates of movement within Figure 2.3.3. A clear delineation can be observed between sites governed by diurnal freeze-thaw (needle ice) action and those experiencing deeper solifluction processes such as gelifluction. These processes respond differently to slope gradient, where needle ice creep is explicitly more efficient on steep slopes due to the impact of higher gravity upon the toppling or rolling of entrained particles. Slope gradient has therefore been observed to impart direct control upon landform development (see section 2.3.2). Slope inclination and micro-slope form (e.g. convex, concave or irregular) will also impact upon micro-climatic conditions within the near surface layer by affecting snow distribution, drainage conditions, and regolith thickness that will determine the efficacy of any solifluction (Matsuoka, 2001).

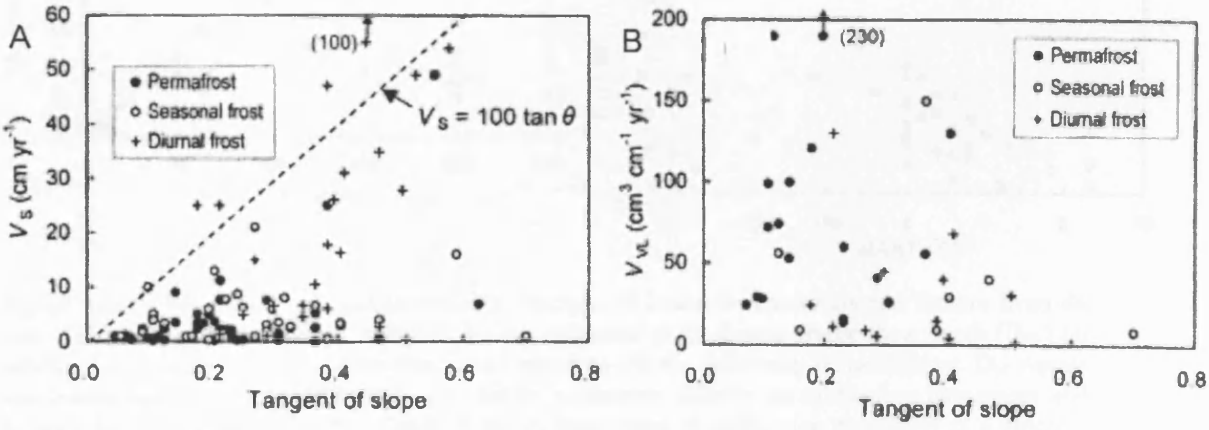

Figure 2.3.3. Solifluction rates as a function of slope gradient. Note: Solifluction movement is described via the following nomenclature: V_{VL} indicates volumetric velocity of solifluction movement and V_S specifies the surface velocity. (Source: Matsuoka, 2001, p.123, fig. 10).

The major environmental factors influencing solifluction have been identified by field studies as: (a) mean annual air temperature, (b) frost type (i.e. permafrost, seasonal frost, etc) and (c) the depth of freeze-thaw action. These three variables

have a direct influence upon the mean annual ground temperature, freeze-thaw frequency, and soil moisture content that determine the style and rate of observed solifluction movements. Variation in mean annual air temperature (MAAT) can create large variations in movement parameters (see fig. 2.3.4a), where surface velocity (V_S) has been shown to be low on slopes with MAAT below –6°C because the underlying permafrost is cold and continuous and does not promote the diurnal freeze-thaw cycles that lead to high rates of needle ice creep.

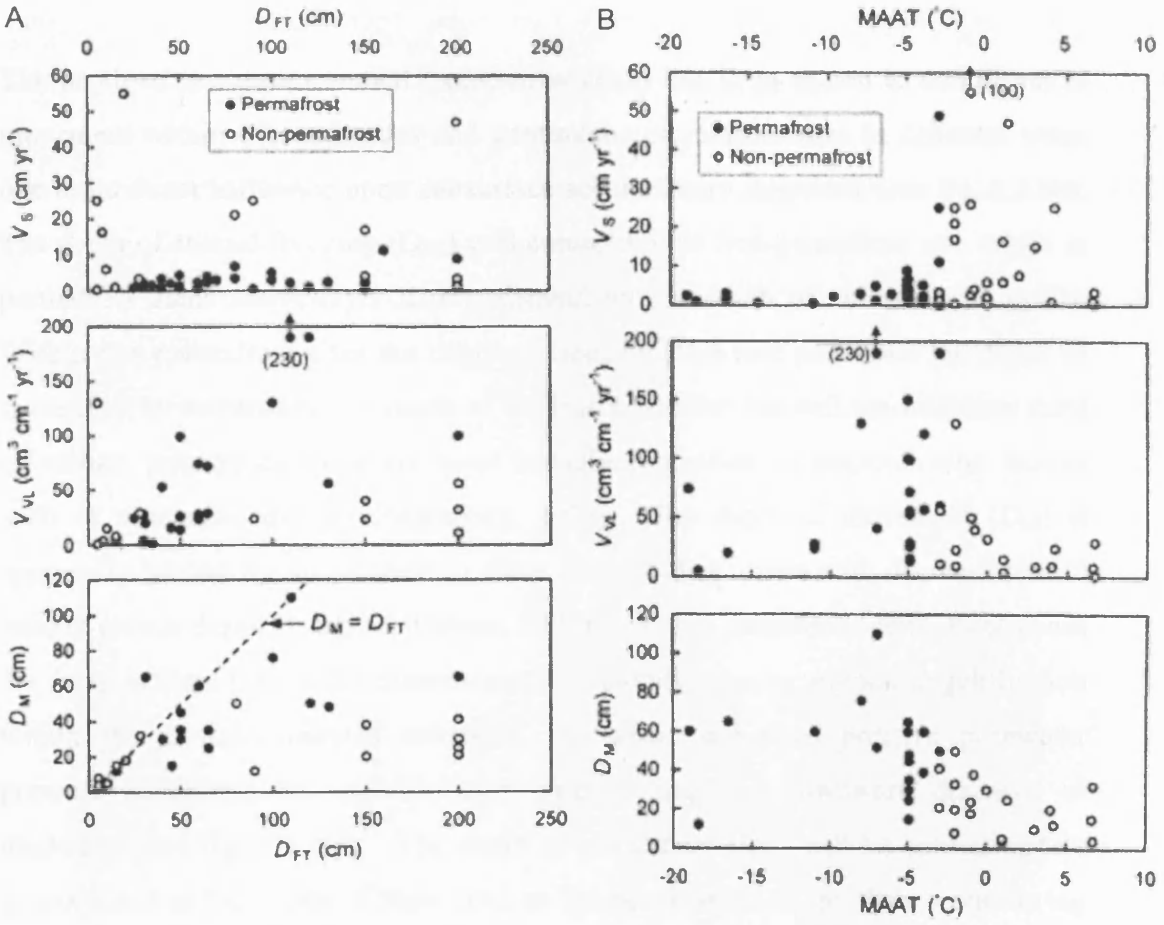

Figure 2.3.4. Periglacial soil movement as a function of measured environmental factors from 46 individual field studies. Graph A highlights the influence of the annual freeze-thaw depth (D_{FT}) on solifluction. Note: Solifluction movement is described via the following nomenclature: D_M equals maximum depth of soil movement, V_{VL} indicates volumetric velocity of solifluction movement and V_S specifies the surface velocity. Graph B shows mean rates of solifluction movement as a function of mean annual air temperature (MAAT). (Source: Matsuoka, 2001, p.117 & p.118, figs. 4 & 5).

Fieldwork has shown an optimum zone of surface velocity (V_S) occurs where MAAT reaches between –3°C and –5°C, as this zone includes slopes underlain by discontinuous (warm) permafrost and those with deep seasonal freezing and thawing that commonly occur on low-latitude high mountains. The highest rates of surface

movement tend to be associated with needle ice creep that can dominate within the thin superficial layer by frequent diurnal freezing, e.g. such as the tropical high mountain slopes monitored by Francou & Bertran (1997) (see table 2.2.4). An opposite pattern emerges with respect to the depth of solifluction movement (D_M), field studies have shown that cold permafrost areas have the deepest displacements, in excess of 60cm, commonly as a result of plug-like flow along basal shear planes (see fig. 2.3.4a). The depth of movement within discontinuous permafrost has been measured to range from a few centimetres up to 50cm (Matsuoka, 2001).

The depth of maximum annual freeze-thaw (D_{FT}) has been shown to contribute to movement within discontinuous and continuous permafrost sites in different ways due to its direct influence upon subsurface soil moisture migration (see fig. 2.3.4b). The depth of annual freezing (D_{FT}) will control this in non-permafrost site, while in permafrost areas active-layer depths depend on the depth of annual thawing D_T. Within non-permafrost sites the depth of freezing (D_F) will determine the depth of movement by controlling the depth of ice lens formation but will not influence rates of surface velocity as these are more broadly controlled by microclimatic factors such as vegetation density (Matsuoka, 2001). The depth of movement (D_M) is apparently limited by an increase in shear strength that occurs with decreasing void ratio at greater depth (Harris & Davies, 2000). Within continuous permafrost zones the depth of thaw (D_T) will influence surface velocity rates by promoting gelifluction within the partially thawed substrate, i.e. where enhanced positive porewater pressure conditions become dominant through impeded downward drainage of meltwater (see fig. 2.3.4b). The depth of movement (D_M) will be approximately proportional to the depth of thaw (D_T) as the progression of the thaw front during summer will determine whether plug-like flow will actually occur within the ice-rich basal substrate of the active layer (Mackay, 1981). Overall, field observations have suggested that the nature of soil freezing and thawing, largely determined by ground thermal regime and soil geotechnical characteristics, influences the overall depth and concentration of ground ice and therefore the nature of gelifluction (see section 2.2 and table 2.2.4). The relative efficacy of solifluction will directly impact upon landform creation if movement remains consistent over a long-term period (see section 2.3.2).

In terms of global thermal regime, field studies have shown that the dominant solifluction environment can be separated along both warm and cold margins, with mixed processes existing in several sub-domains (Matsuoka, 2001). The warm margin ranges from mid-latitude lowlands to tropical uplands and is characterised by seasonal needle ice creep occurring during winter periods of freezing. These winter processes cause a shallow dislocation of the uppermost soil layer commonly around 5-10cm thick but less than 20cm depth, the surface movement creates thin lobes and stripes, especially in areas of vegetation removal (see table 2.3.1) (Mackay & Matthews, 1974). The diurnal frost environment can by identified upon tropical high mountains, such as the Andes, central Africa, and Hawaii alongside low-latitude discontinuous permafrost zones (Matsuoka, 2001).

Figure 2.3.5. Successive stepped solifluction sheets upon the slopes of Folldal in Dovrefjell, southern Norway. Note: the presence of vegetation has created turf-banked terraces that reflect the retardation of the creeping debris by the bands of insulating vegetation and binding through the accompanying root network. (Photograph: James Smith).

Seasonal frost penetration becomes increasingly influential at higher latitudes and altitudes; this allows slopes to undergo both annual and diurnal freeze-thaw action. The mixed frost environment has been observed to occur mainly above the treeline on mid-latitude mountains (Matsuoka *et al.*, 1997). Frost creep dominates within this mid-latitude and sub-polar mountain environment, with the frequency of

movement being dependent upon the thickness of fine soil layers, snow distribution, and drainage conditions (see fig. 2.3.5). For example, towards the crest of mid-latitude high alpine slopes the frost susceptible soil layer is shallow and allows diurnal freeze-thaw action to dominate, creating small lobes and patterned ground. However, towards the foot of slopes there can be an accumulation of material, the thickening of frost susceptible sediment allows an intensification of annual freeze-thaw processes such as gelifluction through poor drainage allied with more distinct seasonal climatic patterns at lower altitudes. The annual freeze-thaw processes can lead to well-defined forms that are larger than diurnally derived features (see fig. 2.3.5 & section 2.3.2). The individual balance of diurnal frost processes against annual frost processes is extremely site-specific, with movement indices and rates being highly dependent upon intra-annual fluctuations within the near surface buffer zone.

Within the higher latitudes of the solifluction domain, the more continuous permafrost region allows annual freeze-thaw processes to dominate through the lowering of ground temperatures and a thinning of the active layer (see fig. 2.1.5). Diurnal processes are inhibited within the cold permafrost environment because the short autumn and spring period and high levels of prolonged snow cover dampen daily climatic variations. The active layer normally consists of fine soil, and has a complex closed system moisture supply that revolves around the annual balance between surface and basal freezing to determine the direction of high levels of seasonal moisture migration. The continuous permafrost creates poor drainage which keeps the base of the active layer saturated during both freezing and thawing; this leads to plug-like flow and the formation of large lobes and hummocks upon the slope surface. Finally, at the hyper-arid cold margins of the solifluction zone, diurnal freeze-thaw action can operate in summer when sufficient moisture is made available via site-specific snowmelt. Downslope movement therefore occurs only as a result of diurnal ice creep, but not as needle ice creep, because the very cold permafrost promotes high levels of nocturnal freezeback that create intra-pore ground ice before ice needles can begin to nucleate at the surface (Matsuoka, 2001).

2.3.2. Geomorphic Landforms

The main geomorphic features created by frost creep and solifluction include units of locally derived material that can appear as either uniform sheets or tongue-shaped lobes (see fig. 2.3.5). Landforms can be generally grouped into lobes (or sheets), terraces (or steps), stripes, and hummocks (see fig. 2.3.6). The definition of these features broadly follows a field classification by Benedict (1970), although Harris (1981) has further commented that there is no sharp delineation between lobes and terraces on most gelifluction slopes. Lobes are common on slopes where the surface environment (e.g. vegetation, material and topography) is variable whereas terraces are associated with more homogeneous surface conditions (Matsuoka, 2001). Lobes can be further subdivided into turf-banked and stone-banked dependent upon the presence of vegetation upon the lobe. Turf-banked forms can include those having complete vegetation cover and those having vegetation only on the riser. The stripe group of features consist of sorted and non-sorted stripes; occasionally a complex form can be created by the presence of stripes and hummocks being superimposed upon a larger lobe or sheet. Sites showing no specific form can be described as smooth slopes.

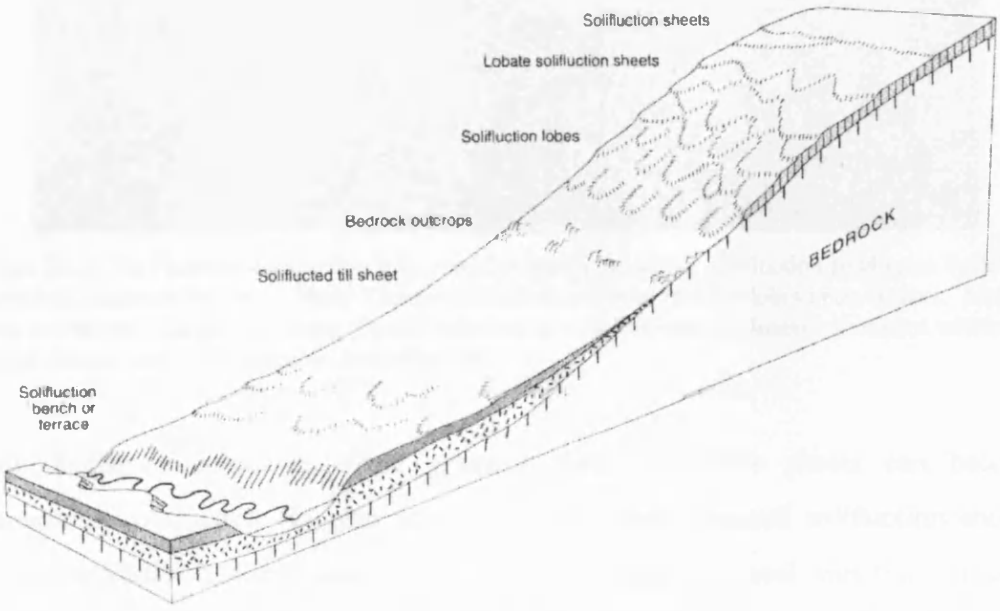

Figure 2.3.6. Schematic catena of typical solifluction phenomena such as those found upon the slopes of British mountains. (Source: Ballantyne & Harris, 1994, p.206, fig. 11.1).

Solifluction sheets occur as a result of extensive frost creep and gelifluction and produce uniform expanses of modified terrain (French, 1996). The evolution of

solifluction sheets occurs where gelifluction becomes more dominant in the wetter, axial portions of a feature and frost creep more significant in the drier, peripheral parts of the sheet. These sheets occur on gentle high altitude slopes and are normally composed of frost-weathered regolith creating a continuous debris mantle that buries underlying bedrock (see fig. 2.3.6). Where slope gradient increases the smooth solifluction sheets can terminate downslope and form regular steps or risers, if successive sheets descend downslope onto a steeper gradient a 'staircase' effect can be created upon the upper parts of some mountain slopes (see fig. 2.3.5).

Figure 2.3.7. Turf banked solifluction lobe complex within an active gelifluction field upon Folldal in Dovrefjell, southern Norway. Note: The central lobe has several smaller lobes upon surface. Smaller lobes are moving across the slower frontal lobe due to a lack of concise linear movement within the central frontal lobe. (Photograph: James Smith).

With further increases in slope gradient these successive sheets can become increasingly crenulated (in plan form) to form lobate terraced solifluction sheets. Lobate solifluction sheets can also form in response to local variations in near surface conditions, i.e. vegetation, availability of debris, etc where reduced velocity causes the overturning of superficial soil (Ballantyne & Harris, 1994, p.205). Solifluction lobes are therefore common where a limiting factor reduces velocity in the toe of a feature, for example if a fine soil layer overrides coarse sediment or where gradient decreases dramatically downslope then soil layers will thicken at the

front (see fig. 2.3.7). Solifluction sheets and lobes are capable of movement on low angled slopes but in order for gelifluction lobes and terraces to fully develop to maximum dimensions, rates of deep gelifluction must exceed diurnal frost creep and be concentrated into well-defined linear paths. Given sufficient time, larger gelifluction lobes will eventually advance downslope and bury superficial or relict solifluction lobes developed at lower elevations (see fig. 2.3.9) (French, 1996). This type of movement has been described as a 'caterpillar-like advance of soil mass' caused by the deceleration of movement at lower elevations (Matsuoka, 2001, p.126; Benedict, 1970). When solifluction sheets extend downslope to the valley floor they may accumulate large amounts of soil material, and where a fluvial feature intersects a deposited accretion it may create a solifluction terrace (see fig. 2.3.6).

Lobes often contain a concentration of large frost shattered clasts or boulders at their downslope (toe) edge with these features being termed stone-banked lobes. If vegetation is present upon the lobe surface then these are termed either mixed or turf banked lobes dependent upon the density of plant and/or clast coverage within the near surface soil layer. The presence of vegetation will further prevent diurnal frost creep and needle ice creep and therefore aid further lobe development through the deeper processes of annual frost creep or gelifluction. Solifluction lobes have also been observed to entrain large boulders from frost weathered bedrock (see fig. 2.3.7), these large boulders are rafted upon the sheet surface and move at a rate exceeding the surrounding soil mass with their undersides resting at or near the permafrost table. Occasionally the moving blocks will leave a shallow upslope trough that indicates their path of downslope movement (Ballantyne, 2001; Berthling *et al.*, 2001). The phenomena of rafting boulder movements are often referred to as 'ploughing boulders'.

Solifluction lobes typically consist of a riser around 0.2 m-2 m in height and a tread with a dimension of around 2m-50m in width and length (e.g. Harris, 1981). The type of dominant process will determine the dimensions of the lobe, for example on turf-free stone banked lobes the predominance of diurnal freeze thaw action results in shallow fast movement by needle ice creep. In order for larger features to develop a depressed diurnal cycle and enhanced annual cycle can cause slower but deeper movement via gelifluction (Matsuoka, 2001, p.125). In this sense large

solifluction lobes are associated with a thick organic mat, a thin active layer, and a high content of fine material. After lobe initiation the individual micro-site conditions will specify the lobe developmental cycle and eventually define the maximum dimension of the lobe complex (Hugenholtz & Lewkowicz, 2002, p.312). This means broad patterns can be estimated via downslope trends in controlling climatic/topographic conditions, i.e. the observed distribution of different forms will be related to the altitudinal position of the vegetation line, tree line, and snow line (Stromquist, 1983).

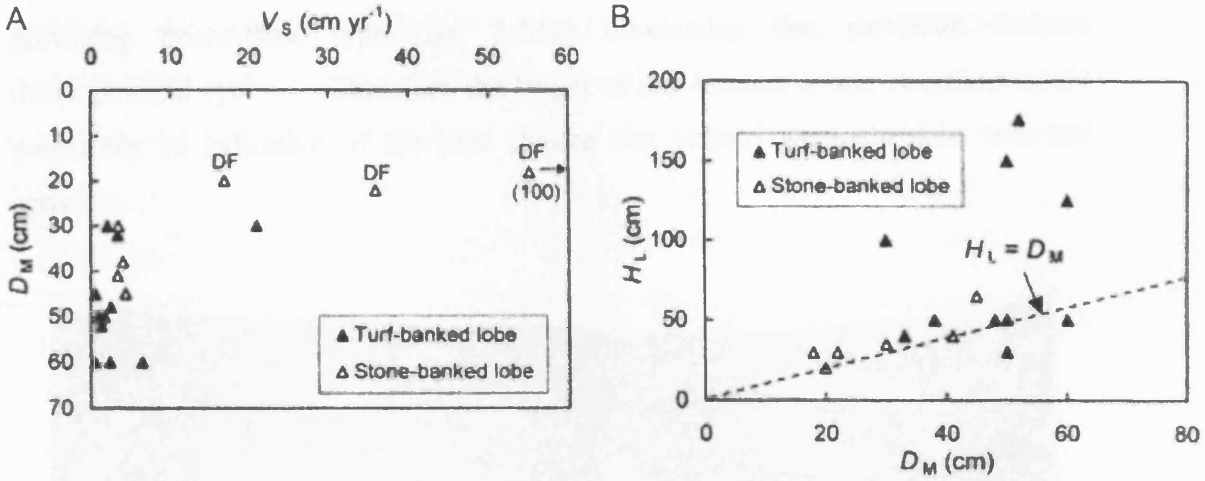

Figure 2.3.8. Soil movement and resulting landforms. Note: Solifluction movement is described via the following nomenclature: D_M equals maximum depth of soil movement and V_S specifies the surface velocity. DF shows lobes where diurnal frost was dominant and H_L represents the frontal height of a lobe. (Source: Matsuoka, 2001, p.126, fig. 13).

The dimension and internal sedimentary structure of a feature will relate directly to a process parameter, this means that analyses of feature form can indicate the nature of any movement within an active landform (e.g. Benedict, 1976) (see table 2.3.1). For example, thin stone banked lobes will suggest the predominance of shallow diurnal freeze-thaw cycles or reflect a suppression of frost depth by a thin active layer overlying bedrock. A high proportion of thick lobes may reflect continuous moisture development during seasonal freezing or an occurrence of two-sided freezing and potential plug-like flow (although plug-like flow often occurs on slopes lacking lobate features – see table 2.2.4) (Matsuoka & Hirahawa, 2000).

Some researchers have also interpreted of the orientation of clasts entrained within a solifluction lobe to indicate the relative amounts of contemporary surface and

subsurface movement within the landform (Price, 1991). It has been suggested that some features may indicate surface movement to be greater than subsurface movement, for example where entrained clasts are horizontal or submerged to exhibit a downslope inclination (see fig. 2.3.2) (Douglas & Harrison, 1996). In contrast, where subsurface movement is greater the majority of entrained clasts will be tilted upwards and appear to be emerging from the terrace or lobe. The correlation between process and landform has been noted by Matsuoka (2001) to indicate that the frontal height of a lobe (i.e. its crenulated toe) could be representative of both the maximum depth of movement (fig. 2.3.8b) and the prevailing freeze-thaw type (fig. 2.3.8a) dominating that particular features developmental cycle. Therefore the height of any inactive lobate structures could potentially be indicative of the past climate that existed when the lobe was last active.

Figure 2.3.9. Mixed solifluction lobe within an active gelifluction field upon Folldal in Dovrefjell, southern Norway. Note: the upward orientation of the emerging entrained stones within the soil matrix. Scale provided by 12cm circular disk in centre of photograph. (Photograph: James Smith).

Many studies have used back-analyses of relict field structures to undertake palaeoclimatic reconstruction in order to calculate previous rates of movement or to indicate the previous presence of periglacial conditions (see table 2.3.2) (Hutchinson,

1991, p.287, fig. 3; Nesje *et al.*, 1989; Gamper, 1983). It should be noted that the presence of landforms of particular dimensions are not always unequivocally indicative of prevalent climatic or pedological conditions, as equifinality of form can lead to different climactic factors producing the same field result (Matthews & Berrisford, 1993, p.376).

Table 2.3.2. Long-term advance rates of solifluction lobe movement as estimated from tephrostratigraphic or buried organic layer analysis (Source: Matsuoka, 2001, p.126, table 3).

Location	Duration (year)	Peak Rate (cm year^{-1})	Mean Rate (cm year^{-1})	Research Study
Iceland	7000	0.1-0.2	0.3	Hirakawa (1989)
Okstindan, Norway	5500	0.2	Nd	Worsley (1993)
Jostedalsbreen, Norway	4000	Nd	0.2-0.7	Nesje et al. (1989)
Jotunheimen, Norway	1000	0.8	Nd	Matthews et al. (1986)
Swiss Alps, Switzerland	5000	Nd	3	Gamper (1983)
Brooks Range, AK, USA	7000	0.3	Nd	Reanier & Ugolini (1983)
Ruby Range, Yukon, USA	2500	0.6-1.0	Nd	Alexander & Price (1980)
Canadian Rockies, Canada	2000	0.5	1.5	Smith (1987)
Colorado Rockies, USA	2500	0.2	2.3	Benedict (1970)

Throughout the table 'Nd' indicates no data available.

2.4. Full-scale Physical Modelling of Gelifluction Processes

The following section describes the developmental processes undertaken by successive research programs undertaking laboratory modelling of periglacial phenomena. These full-scale simulation studies should be viewed as precursors to the currently adopted enhanced gravity approach to investigating gelifluction. The current methodology can be seen as a direct result of the chronological improvements undertaken by these research programs that progressively refined the physical modelling techniques used within cryogenic investigation (e.g. Jumikis, 1956; Palmer, 1967; Higashi & Corte, 1971; Coutard & Mucher, 1985; Harris *et al.*, 1995). The experimental approach of these research programs will be outlined alongside the general relationships discovered by the reported results.

Physical modelling within cryogenic slope studies initially built upon process knowledge gained through rigorous qualitative field observation by earlier workers (see section 2.3). Increasingly sophisticated technology was utilised in experimental procedures (e.g. Rein & Burrous, 1980; Harris, 1996), and the use of equipment from other fields of science have enabled most dimensions of a physical slope model to be accurately and continuously monitored (e.g. subsurface pore water pressure conditions in Harris & Davies, 1998). Continuous monitoring via electronic data logging has allowed the quantitative influence of exact and specified boundary conditions to be examined at a micro-scale within the laboratory (e.g. Coutard *et al.*, 1988). This has meant the affect of individual environmental parameters (e.g. temperature, soil type, moisture content) has been separately analysed enabling the desegregation of the physical systems involved within gelifluction (see Harris *et al.*, 2003a). It is felt that the full-scale cryogenic soil studies examined below have created a secure conceptual framework for the current investigation.

The first laboratory experiment to successfully simulate solifluction was conducted by Higashi and Corte (1971) who examined the influence of slope angle upon both gelifluction and frost creep. Slope models were constructed in an insulated container (67cm x 42cm) to a thickness of 100mm, and frozen within a chest freezer under open system hydraulic conditions. The models used a highly frost susceptible silty clay. Soil temperature was measured via embedded thermocouples throughout the model and measurements of surface and subsurface markers gave movement rates and depths. They reported approximately 30mm of downslope surface movement on a 15° slope after three freeze-thaw cycles which reduced to 2-4mm of subsurface movement at 20mm depth. The movement within this model was attributed to the growth and thawing of surficial needle ice (see fig. 2.4.1). However, on a 3° slope, downslope surface movement rates reduced to approximately 10-15mm with no sharp decrease in movement with increasing depth, this movement was attributed to gelifluction where excess water was retained for longer within the thawed soil. The low inclination of the soil model restricted rates of drainage and promoted gelifluction rather than frost creep.

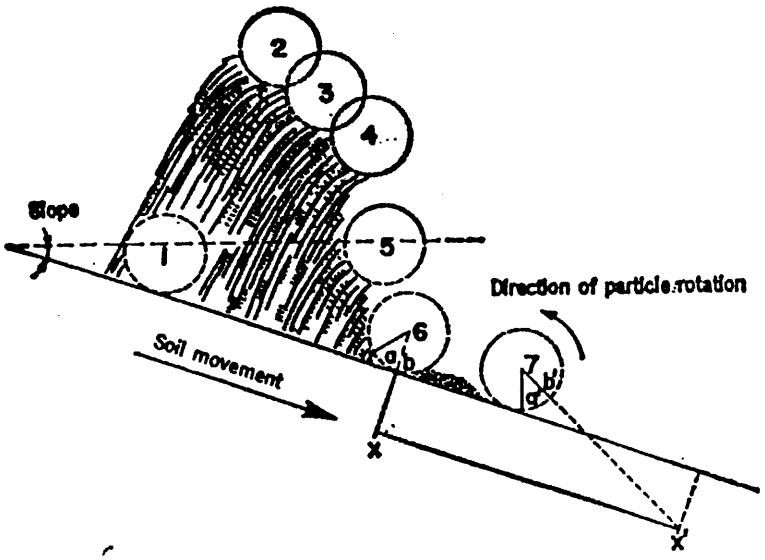

Figure 2.4.1. Schematic diagram showing the path of movement of a particle at the surface of the slope undergoing needle ice creep. (Source: Higashi & Corte, 1971, p.482, fig. 3).

Rein and Burrous (1980) examined the influence of soil ice distribution on subsurface displacements within 5° slope models. The experiments were conducted within a large-scale insulated chamber (2.5m x 3.5m) that could be tilted to achieve different slope gradients. Thermal conditions were controlled via cooling elements within the base of the chamber; resulting in freezing from the base upwards under open hydraulic conditions. The slope models consisted of a field derived frost susceptible silt loam; a 25cm thick soil layer was placed upon a sand base with model drainage being achieved via a sand baffle along the downslope edge of the chamber. The model was instrumented with thermocouples and paste columns embedded to record volumetric transport profiles. Results indicated that most of the measured subsurface displacement could be associated with basal shearing zones created by distinct soil layers rich in segregated ice (more than 150% ice content) (see fig. 2.4.2). The basal sediment had excess ice content due to the optimum conditions created for segregated ice nucleation through upward freezing. They concluded that the distribution of excess ice determines the depths at which thaw consolidation strains are the highest and therefore determines the depth of soil shear strain. The resultant loss of soil strength was given as a key factor in promoting solifluction, and indicated that the formation of a narrow displacement zone is the consequence of abrupt variations in soil ice content (see fig. 2.4.2).

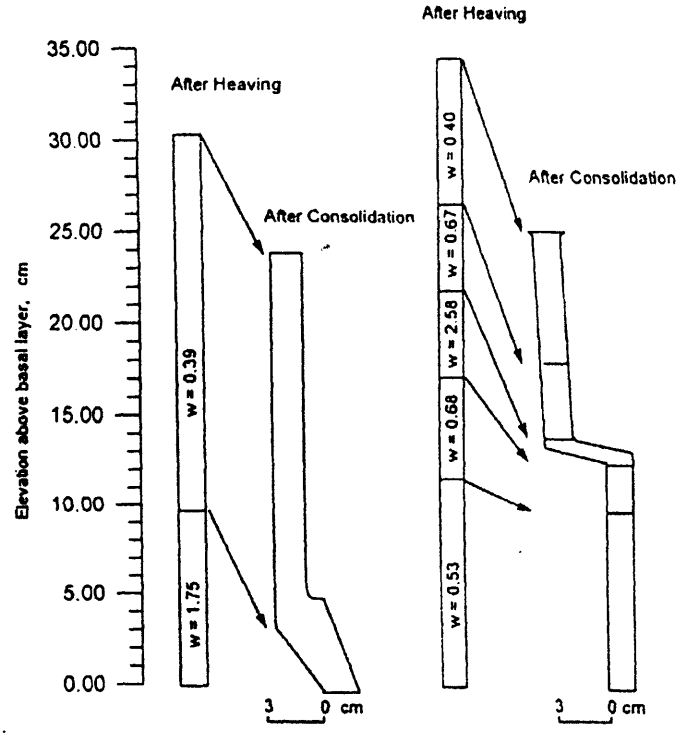

Figure 2.4.2. Comparison of positions of separation between layers of constant ice content and each displacement profile; indicative of the thaw consolidation and downslope displacement observed during both experiments. (Source: Rein & Burrous, 1980, p.357, figs. 11 & 12).

Van Vliet-Lanoë *et al.* (1984) took a different approach and examined the micromorphology of laboratory samples that had undergone repeated freeze/thaw cycles. They identified the development of distinct micromorphologies in laboratory mixed loam soils undergoing induced frost creep or gelifluction and reported vesicles throughout the soils but found microstructures were especially prevalent within the upper 5cm of the profile, which suggested the mode of formation for these features came through air expulsion during thaw consolidation. A key conclusion from the study was the identification of micromorphological shear planes and prismatic structures due to frost creep processes. Similar experiments were conducted by Coutard and Mucher (1985) to examine deformation within laboratory mixed silt loam. Laminated soil models were created and subjected to 18 freeze/thaw cycles within a large (5m x 1m) insulated chamber. Underlying the silt loam was a compacted sand base that remained unfrozen throughout the experimental cycles. Freezing was from the surface downwards and conducted under open hydraulic conditions via an artificial water table. They concluded that downslope movement was entirely due to frost creep, and that this ice segregation process created new structures and microfabrics in the form of vesicles, platy

structures, shear planes and micro-undulations due to the mechanical stresses of thawing excess ice. Van Vliet-Lanoë (1985) utilised further micromorphological evidence to stress that slow frost creep is not associated with the rotation of sand grains but that gelifluction (i.e. saturated flow) does cause grain rotation which leads to the rounding of individual peds and the development of matrix silt coatings (or 'cutans') on sand grain surfaces (Ballantyne & Harris, 1994). In contrast, Betran (1993) postulated that flat disc shaped clasts do not undergo any rotation during solifluction, and concluded that there is no simple relationship between soil microstructure and type of gelifluction or frost creep movement.

Coutard *et al.* (1988) undertook a major addition to laboratory slope process research when they attempted to define variations in the magnitude of frost creep with respect to variations in granulometry and water supply. A large-scale experimental procedure was developed to examine rates of downslope movement resulting from one-sided downward freezing of laboratory mixed loam, silty sandy gravel, and sandy loam upon a 12° slope. An insulated tank (5m x 5m) was filled with a basal sand zone and three experimental soils were constructed into an experimental layer of adjacent 30cm thick zones. The experimental layer was then subjected to 22 freeze/thaw cycles with each cycle being of three weeks duration. Several measurements were recorded including atmospheric and soil thermal conditions, surface frost heave, surface movement and subsurface vertical displacement. Measured surface frost creep was greatest in the loam and least in the heterogeneous material, this disparity was attributed to freezing rates because the loam was the slowest to both freeze and thaw. The rate of thaw within the loam was inversely proportional to the amount of ice in the soil profile. The maximum downslope displacement occurred at the model surface where average surface displacement was directly related to average frost heave (see fig. 2.4.3). However, actual downslope displacement exceeded the calculated maximum potential frost creep and most recorded field values (see section 2.2). This was explained by the experimental slope not being limited by bedrock geometry and vegetation cover. An important observation was also the presence of microshear surfaces within the soil; these were attributed to localised soil sliding over the upper surfaces of thawing ice lenses and reinforced the micromorphological conclusions of Van Vliet-Lanoë *et al.* (1984).

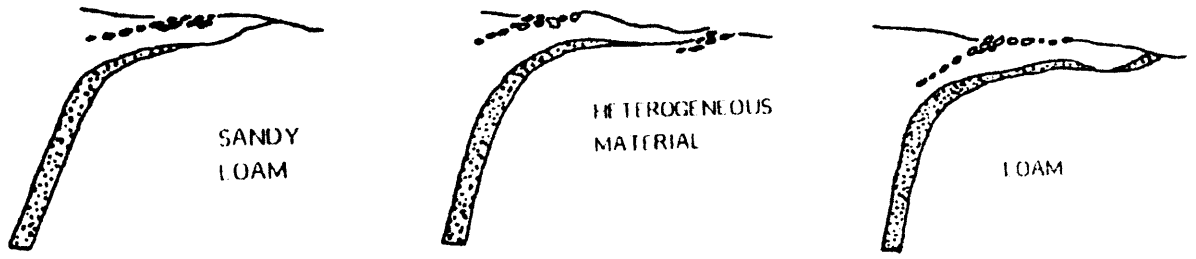

Figure 2.4.3. Schematic representation of the deformation of embedded coloured bands by frost creep after 22 freezing and thawing cycles. Note: the convex downslope pattern of displacement indicative of typical one-sided freezing segregated ice patterns. (Adapted from source: Coutard *et al.*, 1988, p.18, fig. 3).

Harris *et al.* (1993) used the same 5m x 5m environmental facility as Coutard *et al.* (1988) and created 12° slope models of differing soil types in adjacent strips. All were natural non-cohesive soils derived from the weathering of different bedrocks – granite, limestone, mudstone, and slate (Harris, 1993). These soils were frozen from the surface downwards with water being supplied via a basal supply under open hydraulic conditions. Frost heaving and downslope movement was measured after each cycle, with the slope models undergoing 15 complete cycles. Several measurements were recorded by both manual and electronic methods, including atmospheric and soil thermal conditions, surface frost heave, surface movement and subsurface vertical displacement via Rudberg tile columns. Results indicated that average surface solifluction rates increased with decreasing soil grain size, for example 19mm per cycle for the sandy granite-derived soil versus 93mm per cycle for silty slate-derived soil. Soil grainsize was also reported to determine the relative contribution of frost heave and gelifluction, where frost creep accounted for 80% of surface movement in granite-derived soil against only 15% in the silty-slate soil. The gelifluction component was calculated through determining potential frost creep after each freezing phase and removing this value from the total movement measured after the thaw phase. An overall conclusion was that frost creep accounted for most movement in the sandy granite and limestone soils because the high permeability created near-surface needle ice leading to significant downslope creep but no high pore water pressures during thaw. In comparison, thaw induced gelifluction accounted for movement in the silty mudstone and slate soils because the lower permeability created cryosuction forces that formed greater ice segregation at depth. The amount of frost heave was noted as a key variable

influencing rates of downslope movement with the melting of excess ice creating high porewater pressures and a subsequent decrease in frictional strength during thaw. Water contents immediately above the thaw plane generally exceeded the liquid limit and created viscous flow that allowed more consistent downslope movement throughout the soil profile. The amount of segregated ice was therefore highlighted as the key factor determining potential downslope movement rates within both frost creep and gelifluction (see fig. 2.4.4).

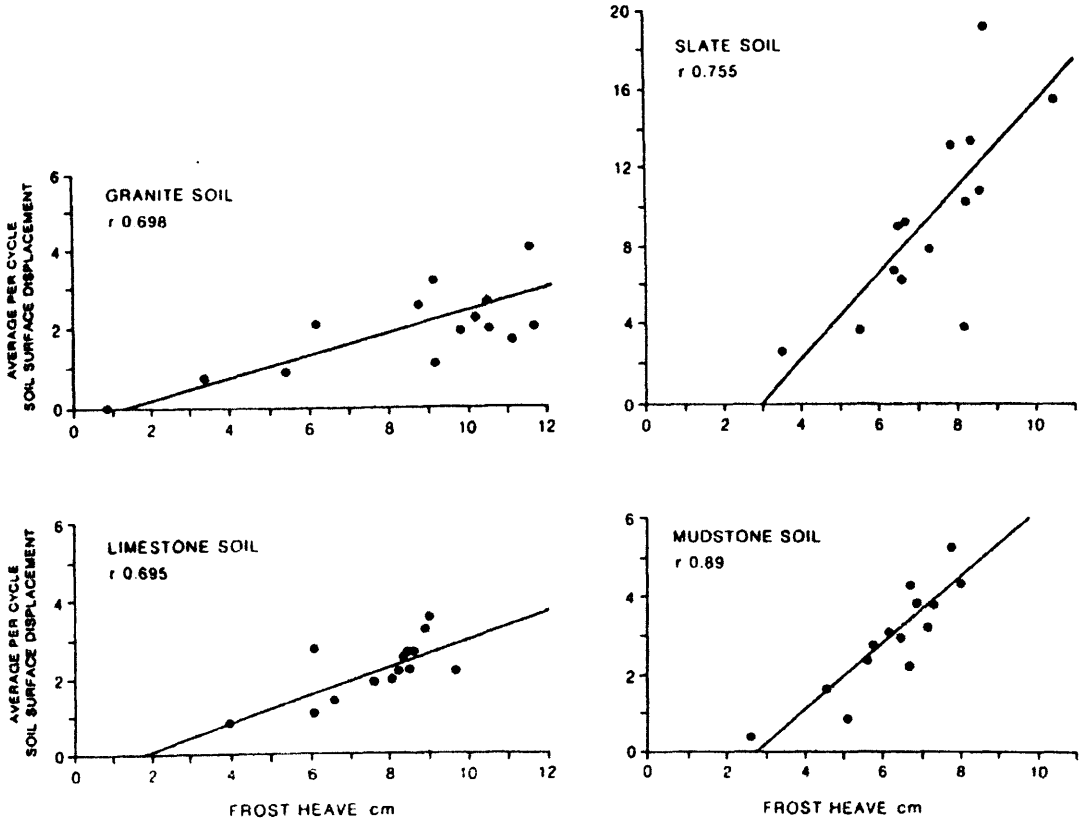

Figure 2.4.4. Relationship between average per cycle frost heave and average per cycle surface displacement for different soil types. (Source: Harris *et al.*, 1993, p.395, fig. 10).

A new phase in the physical modelling of experimental slopes was introduced by Harris *et al.* (1995) through the pioneering use of electronic instrumentation to continuously monitor model conditions. They constructed a 12° slope model formed in slate (gravelly silt) and mudstone (sandy silt) derived soils and logged data on temperature, frost heave, thaw consolidation, surface movement rates and internal porewater pressures (Harris, 1996; Harris *et al.*, 1997; Harris & Davies, 1996, 1998, & 2000). Slope models were constructed within the same refrigerated 5m x 5m container used by Coutard *et al.* (1988) and Harris *et al.* (1993), the two soils were placed in adjacent strips upon a sand basal drainage layer and subjected to one-sided

downward freezing and thawing under open hydraulic conditions. The slopes were instrumented with semiconductor temperature sensors, miniature pore pressure transducers, and a pair of linear voltage displacement transducers to measure surface movement; for a full description of experimental design refer to Harris *et al.* (1996) (see fig. 2.4.5). Thawing was from the surface downwards with a complete freeze/thaw cycle taking approximately 4-6 weeks.

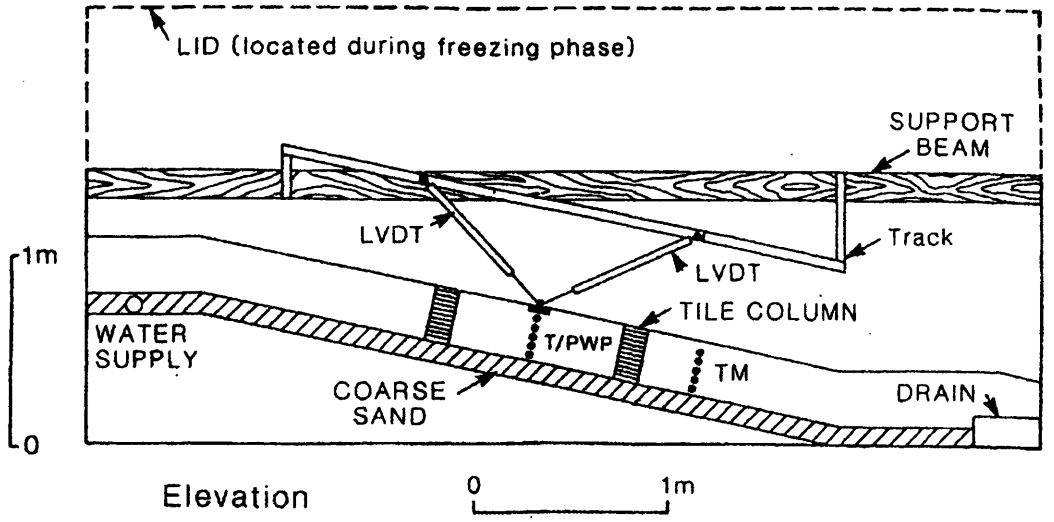

Figure 2.4.5. Experimental design used by Harris *et al.* (1995-2000). Note: TM = thermistors; T = semiconductor temperature sensors; PWP = pore pressure transducers. (Source: Harris & Davies, 1998, p.434, fig. 1).

Slope models underwent seven cycles of successive downward freezing and thawing with the experimental slope responding consistently to each phase. Harris *et al.* (1995; 1997) described the internal thermal and pore pressure conditions within slope models alongside surface movement trajectories during solifluction (see fig. 2.4.6). The results supported previous relationships observed by Harris (1993) and consistently showed that the greatest amounts of frost heave occurred in the fine grained soil due to slower frost penetration and higher frost susceptibility, with resulting downslope displacement being a function of ice content within the soil profile (Harris & Davies, 1996). It was felt the consistency of recorded results highlighted the reproducible nature of the experimental procedure used to simulate gelifluction (Harris *et al.*, 1997, p.857). Downslope displacement profiles were concave-upslope indicating a shear strain which increased towards the model surface, these profiles were similar to those observed upon unvegetated field sites within discontinuous permafrost regions. Surface vectors of movement resembled those measured in field studies, with each freeze-thaw cycle representing an annual

field cycle of downslope movement, such as those observed by Washburn at Mesters Vig, Greenland (Washburn, 1967). The two-dimensional vectors of surface displacement revealed a consistent style of movement between freeze-thaw cycles with all observed movement trends corresponding to the conceptual frameworks for frost creep, gelifluction and retrograde upslope movement (see fig. 2.4.6 and section 2.2.4). It was also concluded that simulated rates of movement were similar to those reported in field studies (Harris *et al.*, 1997, p.864).

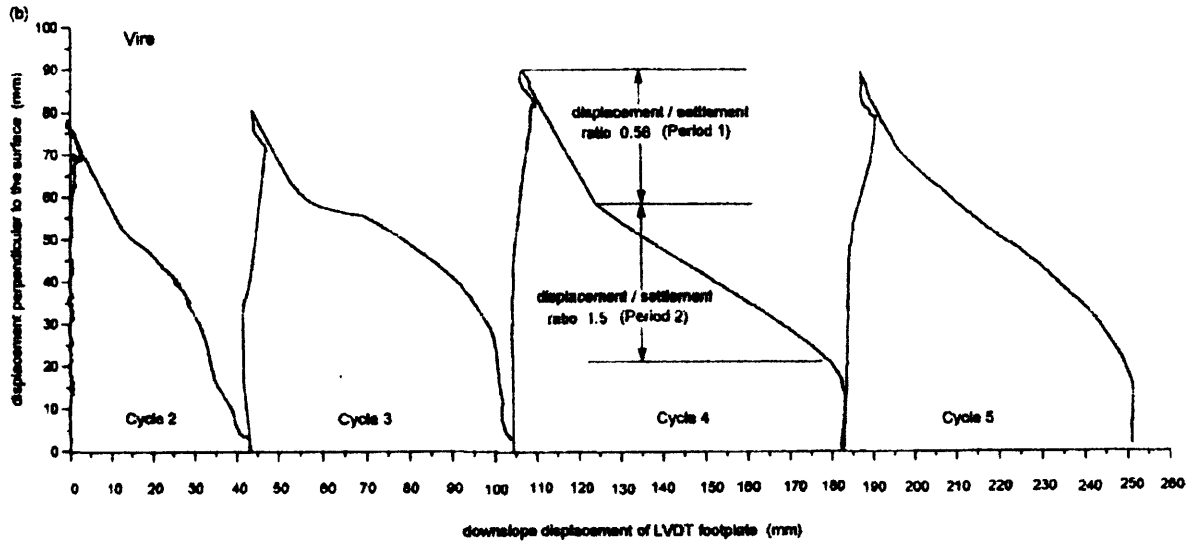

Figure 2.4.6. Vectors of surface downslope solifluction movement measured via LVDT for successive freeze/thaw cycles in the Vire soil. (Source: Harris *et al.*, 1997, p.858, fig. 7).

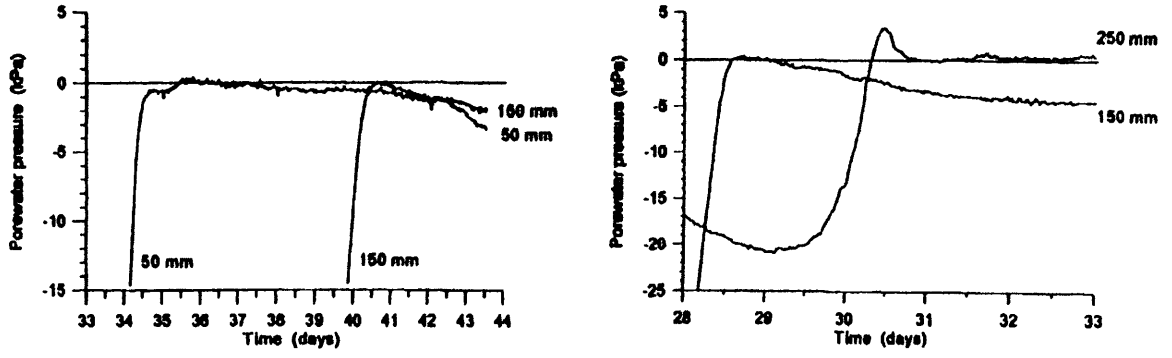

Figure 2.4.7. Porewater pressure data recorded during thaw phase. Note: Data reveals an upward hydraulic gradient between 50mm and 150mm on days 40 to 44 on left graph, and between 150mm and 250mm on days 33 to 33 on right graph. (Source: Harris & Davies, 1996, p.1167, fig. 51.9).

Measurement of porewater pressure indicated that negative pressures (i.e. suction) occurred at each depth prior to the arrival of the thaw front, with values ranging from –5 kPa and –15 kPa (Harris & Davies, 1998). Porewater pressures were observed to rapidly rise through the period of the thermal zero curtain when progressive phase

changes were occurring due to segregated ice melt at that depth (fig. 2.4.7). Positive porewater pressures were recorded immediately above the thaw plane, with values rising to between 15 kPa and 40 kPa to indicate fully saturated conditions. The observed porewater pressures were shown to often exceed hydrostatic, and reduced intergranular friction and shear strength, leading to downslope soil displacement (Harris & Davies, 2000). Standard slope stability analyses showed that recorded positive porewater pressures were insufficient to cause landsliding within the experimental slope as factors of safety remained above unity (Harris *et al.*, 1995, 1997). As the thaw front progressed though zones of excess ice a slow fall in positive porewater pressure was monitored as meltwater subsequently drained through the base of the model, this led to the slope regaining shear strength through intergranular friction towards the end of each thaw cycle. It was suggested that a hydraulic gradient in excess of hydrostatic would result in upward water seepage that would promote superior conditions for gelifluction movement via maintaining high water contents in upper soil horizons and create seepage pressures to further reduce intergranular friction.

2.5. Geotechnical Centrifuge Modelling

Centrifuge modelling is a well-established technique in soil mechanics that uses small-scale tests of geotechnical phenomena to predict full-scale conditions. The centrifugal acceleration induced at the end of a rotating beam models the earth's gravitational acceleration, but can be increased to several hundred times earth's gravity. The principal advantages of using a centrifuge are that correct prototype soil stress conditions may be established within a small-scale model and that long-term behaviour can be simulated at smaller time scales (Schofield, 1980). A centrifuge is a rotating apparatus that, in simple terms, separates substances of different densities by centrifugal force. Centrifugal force is defined as a force that impels a rotating body or objects on it, away from the centre of rotation. In general, a centrifuge consists of a central rotational axis, an arm that swings around this axis and a motor that controls the centrifuge's intended acceleration (see fig. 3.1.1). Centrifuge modelling has become a widespread technique within the fields of civil engineering, environmental engineering, soil dynamics, and cold region research (Craig, 1988).

2.5.1. The Historical Development of Centrifuge Modelling

The principles of centrifuge modelling date back to the nineteenth century where Phillips in 1869 suggested that experiments could be undertaken on small-scale models within the centrifuge (Craig, 1989). Phillip's research into elastic solids required the use of an experimental method that duplicated the behaviour of gravity, for this he proposed the use of inertia forces and, in particular, the centrifugal force to enable force congruity and behavioural similitude between a prototype and the small-scale model (Craig, 1989). Phillips stated general principles for the design of beam centrifuges but his approach was not fully adopted by academia and industry until the 1930's where progress was made within the field of geotechnical engineering. The rediscovery of the centrifuge as an experimental approach led to Bucky, of Columbia University, USA applying the technique to rock mechanics research, and also to Pokravski studying the stability of earth structures at the soil mechanics laboratory of the Gidro-Texgeo Institute of Hydrogeology and Hydraulics, Moscow. Geotechnical centrifuge modelling subsequently remained restricted to military and mining applications until Schofield pioneered further research at Cambridge University in the 1970's. Schofield's research program led to the establishment of an International Technical Committee on Centrifuge Testing in 1981 to provide official recognition for the wide-ranging value of the geotechnical centrifuge methodology within physical modelling (Taylor, 1995). The wider recognition of centrifuge modelling has lead to the development of rigorous methodologies and more diverse institutions investing in the design and implementation of centrifuge research – this has lead to the development of modern drum centrifuges which are increasingly replacing the basic rotating beam design pioneered by Phillips (Taylor, 1995). Developments within other fields of technology have aided centrifuge research – for example the evolution of sophisticated miniaturised instrumentation, data logging and image processing has allowed the centrifuge field to expand and embrace a wider range of quantitative civil, mechanical and geotechnical engineering applications such as critical state rock/soil mechanics (e.g. Davies *et al.*, 2001; Ko, 1988).

The geotechnical centrifuge approach has specific benefits within experimental geotechnics because confining pressure determines a number of soil properties, i.e.

the frictional strength of a soil depends upon effective stress. The deformation characteristics of a soil element under shear stress also depends upon the confining stress acting upon all sides of the unit, where the stress-strain relationship is both non-linear and stress history dependent. In-situ body forces, induced through the acceleration of gravity, act upon the soil element to determine prototype soil stresses. These 'self-weight' forces are dominant in determining the confining pressures that govern the behaviour of a soil mass. Within a small-scale laboratory model the dimensions are small compared to prototype dimensions, so self weight soil stresses are explicitly smaller as a result, i.e. if both model and prototype exist at 1g then model results cannot be representative of the prototype situation because the Earth's gravitational field is uniform at the scale at which surface processes operate (Irving, 2000). A geotechnical centrifuge can solve the scaling problem of inappropriate distribution of self-weight stresses within the small-scale model, by creating an enhanced gravity field through centrifugal acceleration (Taylor, 1995). The model is mounted within a centrifuge and subjected to centripetal force that applies a radial stress from the axis of rotation that acts normal to the base of the model (Schofield, 1978). The centrifuge technique therefore allows a process to be modelled using a scaled physical replica of a larger system but only as long as the corresponding processes can be compared using predefined numerical scaling laws (see table 2.5.1).

2.5.2. The Principles of Centrifuge Modelling

Centrifuge modelling provides a stable apparatus that allows the modelling of complex natural systems in a controlled laboratory environment. The primary objectives of any modelling are simulation and prediction, prediction requires theoretical models to explain the process under examination via simulation through a set of governing equations resolved by analytical or numerical methods. It is difficult to obtain accurate quantitative field data on natural phenomena so it becomes imperative to gain experimental data under well-defined conditions. The data are fundamental for assessing the predictive capabilities of existing theoretical models and guides the formulation, and parameterisation of improved predictive models (Taylor, 1995; Phillips, 1995).

Geotechnical centrifuge modelling consists of experimental methods used by researchers to obtain soil stress conditions that are homologous between laboratory model and field prototype, this is achieved by subjecting a scaled model to centrifugal acceleration (see fig. 2.5.1) (Taylor, 1995). In order to replicate the gravity-induced stresses of a prototype in a $1/n$ reduced scale model, it becomes necessary to test the model in a gravitational field n times larger than that of the prototype.

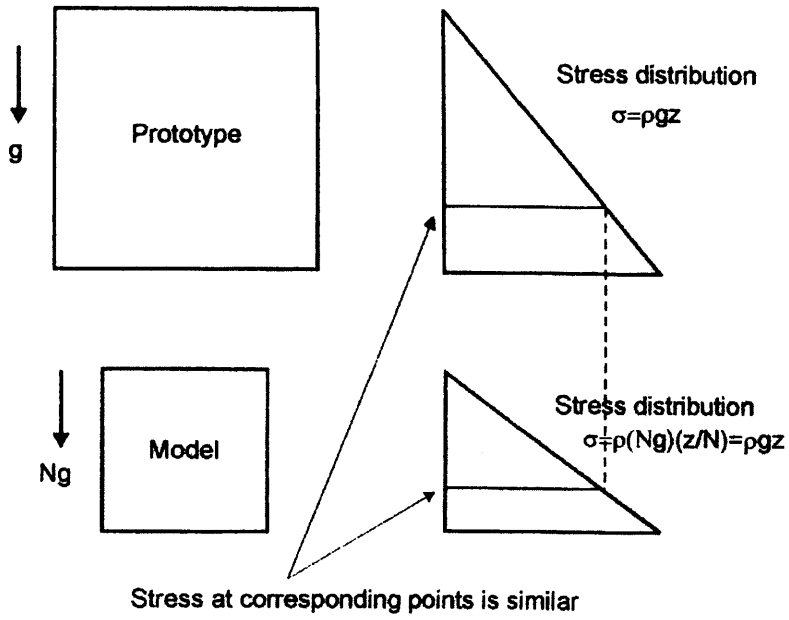

Figure 2.5.1. Stress distribution in a centrifuge model compared to prototype situation. (Source: Depountis, 2000, p.49, fig. 4.1).

To ensure the model can be studied as a valid substitute for the original prototype it is necessary that lengths, time, forces, and stresses must be scaled correctly. The correct scaling permits the prediction of corresponding quantities of deformation, forces, stresses, and acceleration between scaled model and unscaled prototype. In general the main advantages of the centrifuge technique are that complex problems may be studied in a controlled environment where analytical solutions can be verified, behaviour that is difficult to isolate or measure in a prototype can be replicated multiple times, experimental time is reduced due to the use of small scale models, it can provide an environment where stress-strain response are similar to prototype conditions, and instrumentation can be installed and monitored with relative ease (Schofield, 1978). There are limitations involved in geotechnical centrifuge modelling; these involve radial errors within the continuity of a

centrifugal acceleration field, scaling problems involving increasing grain size influencing mechanical properties and cohesive Van der Waal's force, difficulties in creating an appropriate stress history or correct subsoil condition when modelling a prototype situation, and an inconsistency of certain scaling factors involving time-dependent processes (Goodings & Gillette, 1991).

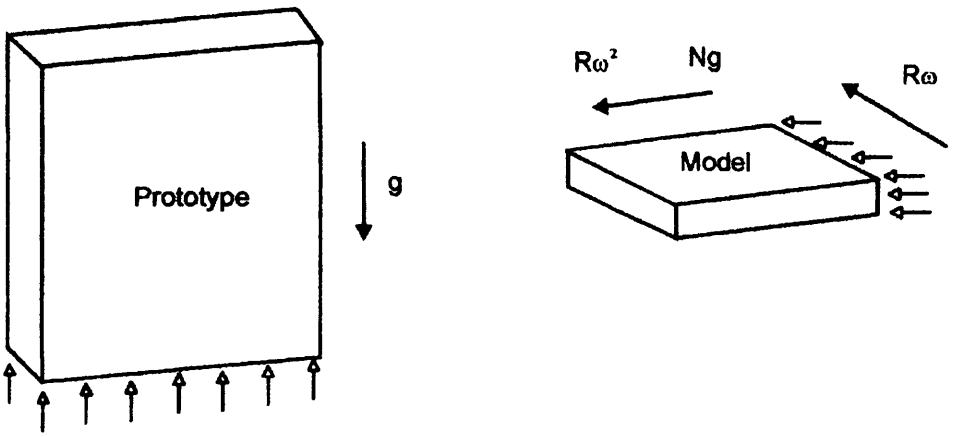

Figure 2.5.2. Gravity effects between a model and prototype (after Schofield, 1980). (Source: Depountis, 2000, 50, fig. 4.2).

The primary principle when designing a physical model is to ensure that each dimensional element in the model is accurately scaled. This ensures that the model contains the same relative ratio with respect to proportion, dimension, values and structure. The most fundamental scaling law requires stress similarity between the model and the prototype which means actual similitude between model and prototype can only be achieved when dimension analysis concludes that the same principle dimensionless numbers and scaling laws are governing both the model and prototype (Schofield, 1988). It is important that once the appropriate scaling laws have been determined that these are verified with physical tests known as 'modelling of models', where results from two different scales are considered similar and therefore that the process relationship remains valid in any model or prototype scale (see section 3.6) (Phillips, 1995, p.39). If a 1/n scaled model is constructed with a prototype soil and placed under the appropriate acceleration level then the stresses in the small-scale model can be considered similar to the stresses existing within the prototype (see fig. 2.5.1). In general, the scaling factor should be as small as possible to maximise the physical size of the model as small models are difficult to

instrument and more sensitive to disruption via construction and sensor installation procedures.

A prototype body will experience the same pressures across its volume due to the Earths gravitational field as a small-scale model within a centrifuge exposed to centripetal acceleration. Schofield (1980) postulated that the centrifugal force acts within the centre of mass of each atom that determine material self-weight properties, but does not significantly alter the orbit of electron shells that determine all other material properties. The upper surface of the body remains unstressed, whether in a centrifuge or Earths force field, whilst pressure increases with further depth into the body. This means that the stress-strain relationship promotes behaviour of a point in the model to be homologous to the point in the prototype (see fig. 2.5.2). In a centrifuge, a model will be subjected to a constant acceleration ($R\omega$), where the direction of acceleration creates enhanced gravity Ng proportional to $R\omega^2$, (see figure 2.5.2 in which a scaled soil model is shown where all linear dimensions are reduced by a factor of n and the model is accelerated by n gravities). This is the basic scaling law where longitudinal dimensions are reduced by n times then the gravity is increased by n times in order to preserve identical stresses in model compared to prototype (Yang & Goodings, 1996). The centrifuge has been identified as the most appropriate apparatus to provide the increased gravitational field required to simulate prototype stress in small-scale models. Schofield (1980) showed that the appropriate centrifuge acceleration level should be selected at one-third the depth of interest in the soil model, assuming the acceleration level is constant with depth and overall soil depth does not exceed 10% of the effective centrifuge radius.

The specific scaling laws required for centrifuge modelling within the current investigation have been derived from the requirement for geometric and kinematic similarity, and specific soil mechanical relationships (Croce *et al.*, 1985; Savidou, 1988). These are summarised below in Table 2.5.1 and assume that soil properties are the same in the prototype and the model.

Table 2.5.1. Geotechnical centrifuge scaling laws relevant to the current investigative study. (Source: Croce *et al.*, 1985; Savidou, 1988).

Quantity	Prototype	Model
Linear dimensions and displacement	1	1/N
Mass density	1	1
Stress	1	1
Force	1	$1/N^2$
Strain	1	1
Time for viscous flow similarity	1	1
Time for seepage similarity	1	$1/N^2$
Time for conductive and advective heat transfer	1	$1/N^2$

The thaw consolidation theory (Morgenstern and Nixon, 1971; McRoberts & Morgernstern, 1974), provides a framework for the analysis of effective stress within thawing ice-rich soils, the governing factors being the rate of thaw penetration (controlling rate of release of melt-water) and the coefficient of consolidation (controlling rate of dissipation of excess pore water pressure).

It is critically important that no scaling conflicts arise in the thaw consolidation ratio during centrifuge modelling. This was demonstrated to be the case by Harris *et al.* (2001b) as follows:

$$\alpha_p = \frac{X_m.N}{\sqrt{t_m.N^2}} = \frac{X_m}{\sqrt{t_m}} = \alpha_m \qquad (2.8)$$

$$C_{vp} = T_v \frac{(d_m.N)^2}{t_m.N^2} = T_v \frac{d_m^{\,2}}{t_m} = C_{vm} \qquad (2.9)$$

where subscript p indicates prototype scale and subscript m model scale. Thus the thaw factor α scales 1/1 between prototype and model. Similarly, considering the Coefficient of Consolidation:

$$C_{vp} = T_v \frac{(d_m.N)^2}{t_m.N^2} = T_v \frac{d_m^{\,2}}{t_m} = C_{vm} \qquad (2.10)$$

where subscript p indicates prototype scale and subscript m model scale. The coefficient of consolidation C_V therefore scales 1/1 between prototype and model, and the thaw consolidation ratio scales similarly. Centrifuge modelling of the thaw consolidation process therefore involves no scaling conflicts.

It is important to note, however, that the time scaling factor for viscous force similarity in centrifuge modelling is 1/1, while that for thaw and consolidation is $1/N^2$, so potential temporal scaling conflicts may arise where the dynamic response of the thawing soil is a function of its viscosity (Harris *et al.*, 2000). However, Harris *et al.* (2003a) have demonstrated that soil shearing during solifluction can be accurately replicated at different scales and gravitational accelerations, from full-scale 1g experiments to 1/30 scale 30g experiments. They conclude therefore that the process reflects deformation of very soft plastic frictional soil rather than flow of a viscous fluid. Thus, no scaling conflicts arise in the application of centrifuge modelling to simulation of periglacial solifluction.

2.6. Previous Geotechnical Centrifuge Modelling of Cryogenic Processes

The use of geotechnical centrifuge techniques has been a recent advance within geocryology physical modelling. Spatially disparate research groups have adopted the centrifuge modelling technique to examine engineering problems associated with cold regions because of the centrifuges ability to compress time scales and model large forces. The use of laboratory physical modelling techniques is especially useful for cold region research because engineering and testing within such regions is impractical, hazardous and expensive. This has lead to the development of refined experimental procedures that encompass the simulation of many aspects of the periglacial environment; where technological developments have allowed better simulation of cold climatic extremes (see Smith, 1995). The following section will briefly outline some broad areas of particular experimental progress such as; the in-flight freezing of soil, investigation of processes of cryoturbation, ice-wedge casting, and active-layer mass movement.

2.6.1. Soil Freezing & Frost Heave

There has been a paucity of experiments which report in-flight freezing of small-scale models. Chen *et al.* (1993) have described a single closed system cycle of frost heave and thaw settlement induced within a small soil model being placed within a refrigerated small centrifuge. They described the basic methodology and indicated the potential for further research within the modelling of pipeline frost heave. Ketcham and Black (1995) further utilised a centrifuge to model a freezing soil profile. They reported time savings could be obtained compared to full-scale field experiments, and calculated the relevant scaling principles that allow enhanced gravity model similarity within the soil freezing process when compared to prototype conditions. They managed to freeze a small soil sample within a refrigerated small centrifuge and concluded that scaling laws remain valid when modelling the formation of segregation ice.

Yang and Gooding (1996; 1998) further developed an experimental methodology for in-flight freezing and reported detailed results for different soils. They demonstrated that the centrifuge technique could produce scaled segregated ice lenses and noted that small-scale models can 'simulate in hours a full scale freezing response which may develop in the field over one or more winters' (Yang & Goodings, 1998, p.1186). They investigated the influence of temperature regime on frost heave characteristics and showed consistent results which were considered to validate the experimental approach for modelling frost heave.

Ketcham *et al.* (1997) reported detailed results from the frost heave of a constrained footing within a saturated silt substrate, a modelling of models was undertaken to investigate the validity of scale factors being used to predict small-scale frost heave modelling. Results supported a homologous scaling similarity and provided an indication that centrifuge-modelling techniques are applicable to the modelling of frost heave loading of rigid embedded structures. Clark and Phillips (2003) further developed the technique by simulating a prototype frost heave scenario within the centrifuge and they concluded that the rate of heave of pipelines modelled in the centrifuge is similar to the rate of heave of the prototype for the same soil and provided validation of the centrifuge technique by demonstrating behavioural similarity between 1g and 30g experiments.

2.6.2. Involutions, Ice-wedge casting and Ice-filled Rock Joints

In order to correctly model the past distribution of periglacial climatic and permafrost conditions it is necessary to quantify and model the process-landform relationship within relict structures (e.g. Huijzer & Isarin, 1997; Murton & French, 1993). Laboratory techniques can be used to simulate the former ground conditions thought responsible for the formation of now relict structures, and to examine their climatic significance (Isarin, 1997). Harris *et al.* (2000) simulated soft sediment deformation during the thawing of ice-rich soils to examine the development of involutions and soil injection features. They recorded fluctuations in temperature and porewater pressure caused by water escape events during the development of small-scale structures. They reported a theoretical mechanism for involution development and postulated that these features mark phases of distinct permafrost degradation. Murton and Harris (2003) have simulated the creation of ice-wedge casts within a range of thawing soils in an attempt to determine the effect of host granulometry and ice content on the mechanisms of ice-wedge casting and the size or structure of the resultant features. It has been postulated that the spatial extent of ice-wedge casts can be used to define the former distribution of permafrost (Black, 1976). Some researchers have also suggested that basic palaeotemperature and aridity conditions can also be inferred from the form of an ice-wedge cast (Harry & Gozdzik, 1988). In a methodological breakthrough Murton and Harris successfully simulated the formation of ice-wedge casts within six different host sediments. Temperature, soil deformation, ice-wedge infilling and porewater pressure measurements were recorded. Cast geometry indicated that the centrifuge approach can has good potential to enable further controlled simulation of ice-wedge casting by downward thaw.

The centrifuge can also be used to investigate the impact predicted climate change will have upon geomorphic processes within the periglacial domain (Harris *et al.*, 2001a). Davies *et al.* (2001) utilised enhanced gravity modelling to examine the impact of temperature on the stability of ice-cemented jointed rock slopes. They reported that the factor of safety against slope failure fell as temperatures approached zero, and was lowest at temperatures of between -1° and - 0.5°C, that is before the joints thawed.

2.6.3. Gelifluction

A research team within the Cardiff Geotechnical Centrifuge Centre have assessed the validity of using the centrifuge technique for cryogenic slope process investigations (Harris *et al.*, 2000). The enhanced gravity investigations followed a future strategy outlined as the next feasible stage after the completion of full-scale physical modelling experiments carried out by Harris and co-workers during the mid 1990's (e.g. Harris *et al.*, 1997; Harris, 1996). A series of solifluction experiments were outlined within the auspices of the EU PACE program investigating the influence of climatic change upon permafrost degradation and related geomorphic processes (see Harris *et al.*, 2001c). These small-scale slope experiments reported an experiment designed to validate the scaling laws involved in centrifuge modelling of solifluction movement (Harris *et al.*, 2001b, 2003a). A "modelling of models" approach was adopted in which identical slope models at 1/10 and 1/30 scale were subjected to a sequence of thawing phased within the centrifuge at gravitational accelerations of 10g and 30g respectively. Rates of shear strain during gelifluction were shown to be virtually identical at these different scales, and to be comparable with that observed during the earlier full-scale gelifluction modelling. The soil stress-strain relationship was shown to correspond to an elasto-plastic deformation of a very soft frictional soil, and a first approximation 'flow law' was proposed based on the 'Cam Clay' constitutive model for soils (Harris *et al.*, 2003a).

The experimental program investigated the transition from slow annual gelifluction to rapid thaw-induced mudflows by using progressively steeper slope gradients within 1/10 scale models tested at 10 gravities (Harris, 2000). The methodological approach was vindicated as high quality results were reported, including data on surface velocity, subsurface volumetric displacement, soil temperature, and porewater pressure (Harris *et al.*, 2001b). Initial analyses of the derived data indicated that contrasting patterns of porewater pressure exist within different host sediments during thaw consolidation (Harris *et al.*, 2002). This research has demonstrated the effectiveness of the centrifuge modelling approach, and provide the foundations for the research programme reported in this thesis.

2.7. Conclusions

The extensive field-based investigations discussed in this chapter demonstrate primarily that slow periglacial mass wasting (solifluction) is virtually ubiquitous within the periglacial realm. It has been observed from high alpine regions of deep seasonal frost to the high arctic polar desert regions where permafrost is cold and active-layers are thin. The spatial variability in rates and styles of movement has made generalisations concerning process variables extremely difficult, but sufficient data is now available for statistical treatments (e.g. Matsuoka, 2001). The spatial and temporal variability of the natural world makes detailed quantification of the significance of process variables challenging. Thus, laboratory simulation experiments, in which material properties and model boundary conditions can be accurately controlled, and monitoring is facilitated, provide a potentially effective alternative to field-based process studies. Such an approach forms the subject of the present thesis. Experimental procedures have been designed to quantify the significance of slope geometry and the properties of the frozen soils. Methodology and results are presented and outcomes discussed in the context the existing knowledge-base, as outlined in this chapter.

CHAPTER THREE : Centrifuge Modelling – Experimental Procedure

The following chapter will outline the experimental procedures developed and adopted during the scaled centrifuge-modelling program. Each stage in a complete cryogenic slope modelling cycle will be described. The chapter includes a summary of the technical specifications within the Cardiff Geotechnical Centrifuge Centre (see fig. 3.0.1), a complete methodology for slope model construction and instrumentation, a description of the equipment used during model freezing and thawing, and finally a synopsis of the manual and electronic data collection techniques. The chapter will also highlight inherent limitations that existed within the adopted experimental procedure and how these limitations were minimised.

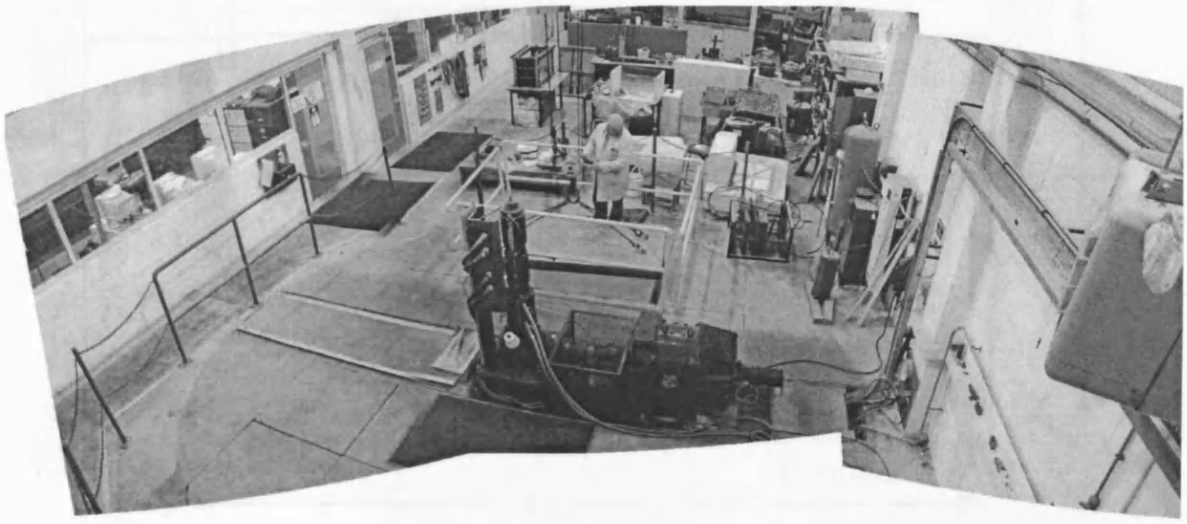

Figure 3.0.1. The Cardiff Geotechnical Centrifuge Centre. The centrifuge motor and axle protrude vertically in the foreground, the circular floor structure is the cover for the centrifuge pit, and the control room is located through the windows on the left of the picture. (Photograph: Peter Brabham).

3.1 Description of the Centrifuge Facility

The Cardiff Geotechnical Centrifuge is a balanced beam centrifuge with a single swinging gondola platform; the platform has a payload capacity of 700kg. The platform can accommodate a test unit of up to 0.9m in each direction and can accelerate this unit through an operating range of 1·5–100 gravities. The radius to the centrifuge pivot is 1·6m, the distance from the pivot to the platform surface is 0·985m (see fig. 3.1.1). The test unit is positioned with its centre of mass a set distance above the platform surface. The angle of inclination of the platform and

the radius to the centre of mass of the test unit depends on the imposed net centrifugal acceleration level. Standard documented procedures were used during test bed flight acceleration – these procedures account for the effect of gondola angular velocity on platform inclination (see section 3.5). The centrifuge has a swinging platform that maintains a net acceleration directly perpendicular to the platform surface when at steady centrifuge velocities.

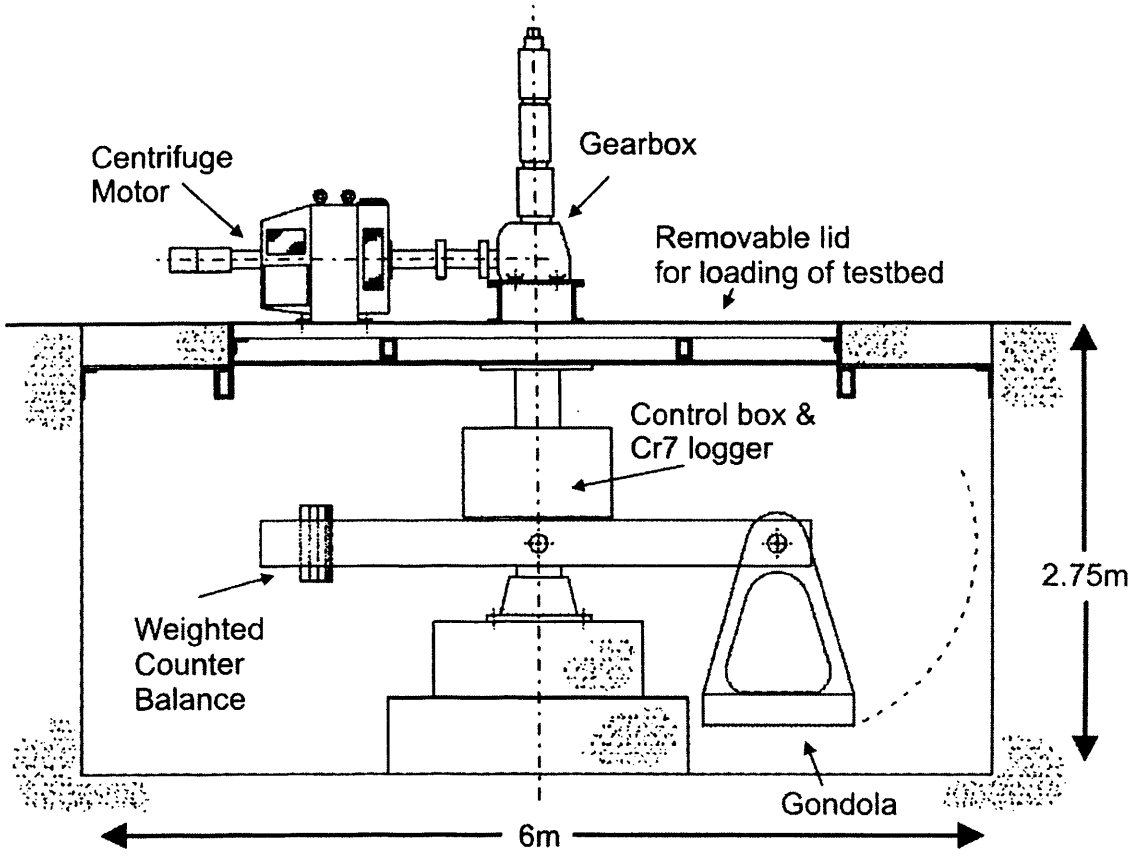

Figure 3.1.1. Schematic technical diagram for the Cardiff Geotechnical Centrifuge.

The centrifuge has several power slip rings which provide 240V 50HZ 13A ac mains power to the central instrument housing that supplies the on-board data acquisition system, video and still cameras, lights, sensors and actuators. Shielded signal slip rings allow the monitoring of output signals from the test unit. The signal rings are also used to carry signals from two platform mounted industrial CCD micro-cameras, these signals are boosted back to video recorders in the centrifuge control room.

An integral part of the centrifuge is the strongbox that contains the model during centrifuge flight. The strongbox provided a secure environmental chamber used

during each thaw phase and comprised of two units: a steel strong box and an inner aluminium liner. The strong box had internal dimensions of 900mm long, 500mm wide and 500 mm high. It was built from three 20mm steel plates, a base and two reinforced end members. The side of the box comprised of two translucent 50mm Perspex plates, these were bolted in place by a load-bearing frame around each edge. The strong box was insulated to aid downward thaw and contained a drainage outlet for the escape of meltwater. An aluminium liner was built from 20mm plate, it comprised of two end pieces and a base. Within each end was a conduit running along the length of the plate to aid the displacement of meltwater from the foot of the thawing slope. The aluminium liner sat between the steel/Perspex strongbox and polypropylene liner holding the slope model (see fig. 3.5.1).

3.2 Slope Model Construction

A base test soil of natural sandy-silt was sourced from Prawle Point, south Devon. Before model construction this material was disaggregated by hand using a 10kg drop hammer, the soil was also passed through a 3mm sieve to remove large clasts and organic matter. Specific soil compositions were required for slope models within the secondary phase of the test program, i.e. ten/twenty percent-added clay/silt. These artificial soils were pre-mixed in an industrial mixer. The required percentages of specific dry weight increments of Speswhite kaolin clay or lacustrine silt (Park Slip quarry, South Wales) were blended into the base test soil material. Details of all test soil properties are outlined within Chapter 4. These manufactured soils were mechanically mixed twice, in an attempt to create a consistently uniform soil fabric. This standard disaggregating and mixing procedure was carried out upon all soils prior to use in any of the experimental systems, this prevented any previous soil stress-history from unduly influencing behaviour within a new constructed slope or geotechnical test.

Slope models were entirely constructed within a transparent polypropylene test box with the internal dimensions of 750mm long by 450mm wide by 500mm deep. The planar slope models were constructed through the placement of a uniform 70mm layer of test substrate upon a layer of coarse sand inclined at the required slope angle (see fig. 3.2.2). The sand basal layer allowed free entry of water into the test soil

during freezing, and since it was non-compressible, provided a stable reference surface for measuring frost heave and thaw settlement within the test soil. The test box was tilted so that the soil surface was horizontal, this aided confirmation that the test substrate was constructed at the correct slope angle.

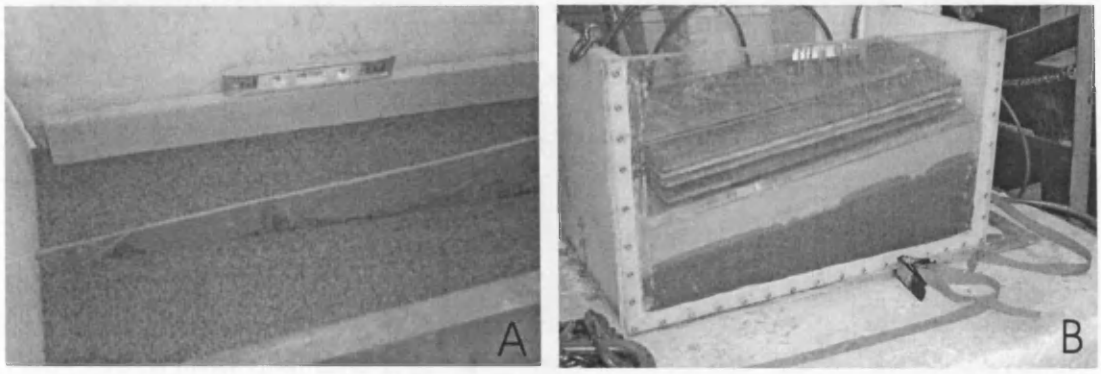

Figure 3.2.1. Slope model during preparation. (A) The slope former and slope depth indicator are placed on the sand basal layer to create a model with consistent specifications and (B) slope model following construction. Note the water table moving through the basal sand layer to saturate the slope prior to consolidation.

After the test substrate had been manually levelled to the required angle through the use of a wooden slope former and steel trowel (see fig. 3.2.1a), water was supplied into the basal sand layer via a header tank (see fig. 3.2.1b). The water table was set parallel to the model surface and the model substrate became saturated via an external cooled constant head water supply. The water supply was cooled through the addition of ice-filled containers to the header tank, these were replaced daily during the model saturation and model freezing phases of each slope model preparation. Prior to slope instrumentation, a vertical drainage channel was created in the end wall at the foot of the model (see fig. 3.2.2). This channel was in the centre of the wall and consisted of a gauze screen and fine nylon mesh that protected a zone of coarse sand set in front of three drainage holes. The coarse sand was reshaped after every thaw cycle to maintain a zone of free drainage at the foot of the slope. Finally the slope model was consolidated for 24 hours under a load of 3.8 kN/m^2 to allow ease of instrumentation (see fig. 3.2.1b).

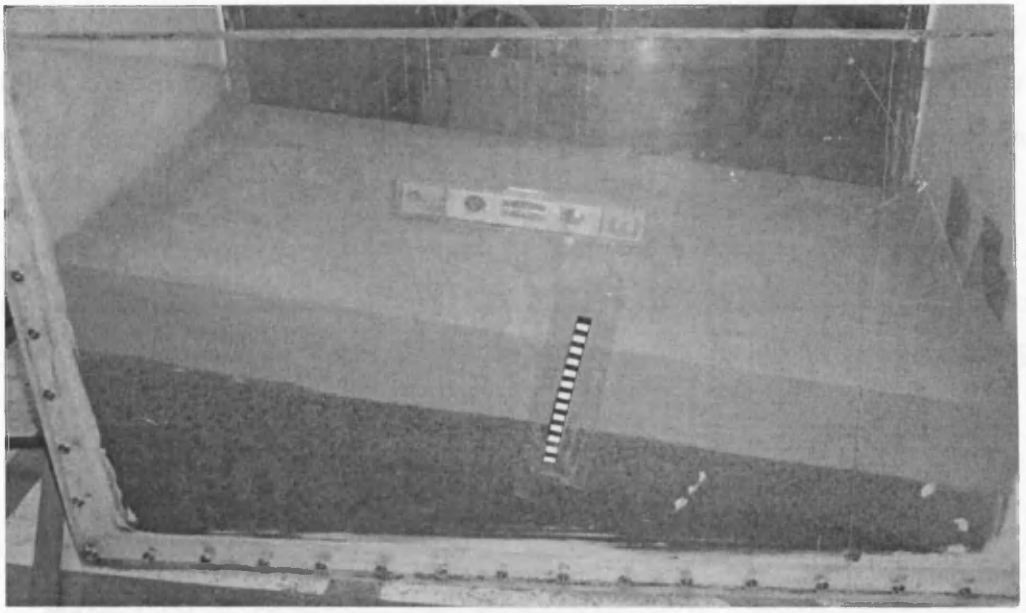

Figure 3.2.2. A newly constructed slope model before saturation, consolidation, and instrumentation. Note: Scale bar placed upon polypropylene side used for visual analysis of thaw settlement rates via video link into control room. The vertical drainage channel can be seen at the foot of the slope model (right of photograph).

3.3 Slope Model Instrumentation

Within any experimental procedure the presence of instrumentation should not modify the behaviour of the phenomena being modelled. Within cryogenic centrifuge studies, any chosen instrumentation should be physically light so as to impart no extraneous stress upon the slope model at high gravity levels, it should not affect the internal thermal conditions of the slope model, and it must be robust enough to function reliably under enhanced stress fields and subzero temperature conditions. The final choice of instrumentation and the method of installation were directly influenced by the need to overcome those perceived limitations. The instrumentation used within the slope can be divided into manual or visual methods and electronic measurements; the apparatus reflected the need for either periodic or continuous assessment of model behaviour.

The slope model was instrumented with manual data collection indicators that gave a visual datum both at the end of every freeze/thaw cycle and after excavation of the final model condition (see figs. 3.3.2 & 3.6.1). Fifteen 10mm diameter plastic markers were placed along three transects upon the slope model surface in order to monitor and measure surface movement (see fig. 3.3.2b). Two rows of columns of

plastic cylinders were inserted through the soil to record subsurface displacement profiles. Each column contained fourteen cylinders that were 5mm in length and 5mm in external diameter. These were installed perpendicular to the model surface in order to replicate the Rudberg columns used in long-term field studies such as Washburn (1999). A rod was used to push the cylinders into the soil via a previously formed cavity; the rod was then withdrawn, leaving a column of markers free to move downslope with the soil during subsequent phases of the test (fig. 3.3.2b).

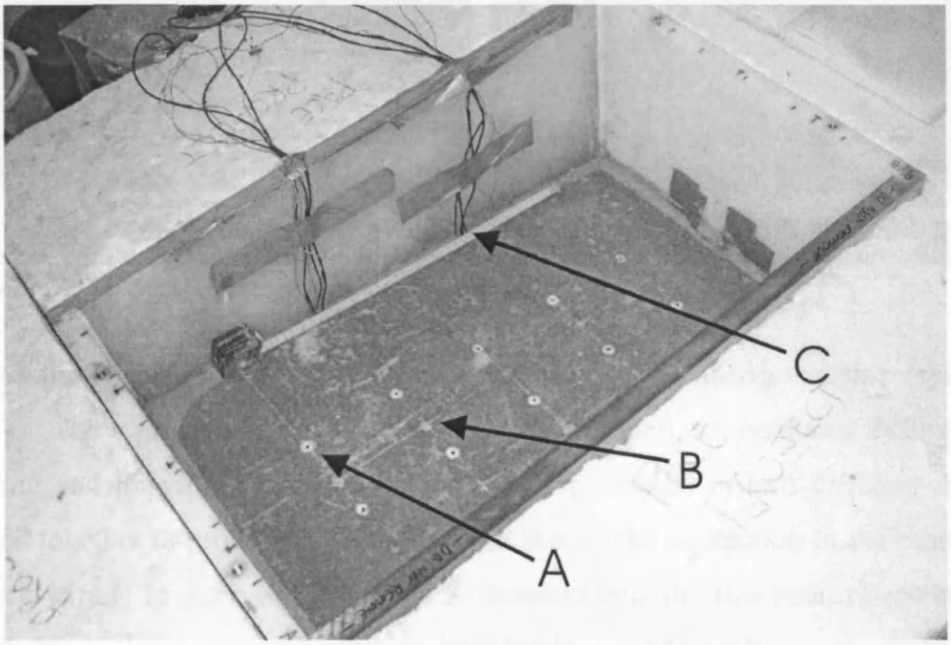

Figure 3.3.1. Fully instrumented slope model after a freezing phase. Note: the presence of surface slope markers (a) and subsurface profile markers (b), and the cables for two strings of thermocouples and pore water pressure transducers (c).

The slope model was instrumented with two vertical strings of electronic sensors, these allowed continuous precision monitoring of internal model conditions. The vertical strings were installed in the upper and lower slopes through the careful excavation, burial and insertion of sensors at different depths (see fig. 3.3.3). Each string consisted of five thermocouples and three miniature pore pressure transducers, each string was placed approximately 200mm from one side of the model to minimise disruption to the planar surface contour of the model. The placement of sensors away from the model boundary prevented any edge effects from influencing output data (see fig. 3.3.1). Thermocouples were installed at the model surface, model base, and at 10, 30 and 50mm depth, whilst pore water pressure transducers

were installed at 10, 30 and 50mm depth (see fig. 3.3.3). The pore water pressure transducers and thermocouples were directly combined at 10, 30 and 50mm to gauge the influence of the zone of partially frozen soil upon pore water pressure conditions at successive depths from the surface downwards.

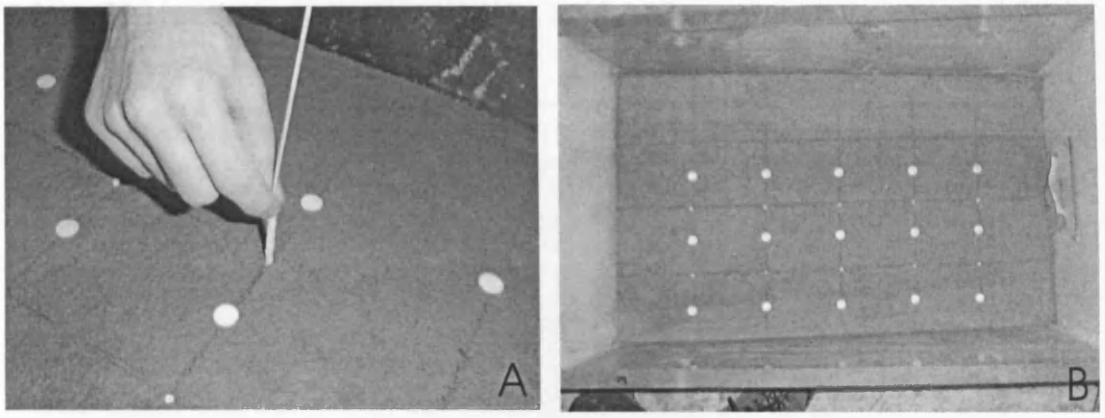

Figure 3.3.2. A model during(a) and after(b) the instrumentation phase. Note(a): the installation of a subsurface profile marker. Note(b): the final form of a slope model before the installation of thermocouple and pore water pressure transducer strings.

Temperature conditions were measured via ten K-type thermocouples (see fig. 3.3.3). These provided information on the internal thermal conditions during both freezing and thawing phases. A thermocouple consists of two different metals welded together to produce a probe junction that works in reaction to the other end of each wire. In the case of a Type K thermocouple the two reactive metals are nickel-chromium (Chromel) and nickel-aluminium (Alumel). A voltage is generated when the junction between the two dissimilar metals becomes excited by temperature. Data acquisition software receives the voltage signal and converts it into useable temperature data. Because a similar reaction would occur between any two dissimilar metals being heated or cooled, special care was taken during installation to ensure no other circuit junctions were created. This would introduce additional outside voltages and thereby skew derived voltage/temperature readings.

A variety of traditional devices have been used for measuring pore water pressure in soil (see for examples Fredlund & Rahardjo, 1993). The current experimental technique utilised Druck PDCR81 miniature pore pressure probes to measure pore water pressures within the thawing slope models. The PCDR81 consists of a 0.09-mm-thick, single-crystal, silicon diaphragm with a fully active strain gauge

bridge diffused into the surface. A high air entry porous stone is placed at the tip of the transducer, so that one side of the diaphragm is exposed to the atmosphere while the other side is exposed to the pore water via the porous stone (see fig. 3.3.4). Deformation of the diaphragm causes a change in the voltage measured across the strain gauge that is equated to a change in pressure, with a nominal sensitivity of +/- 0.2% of the maximum value within a zero to 73.5 kPa range.

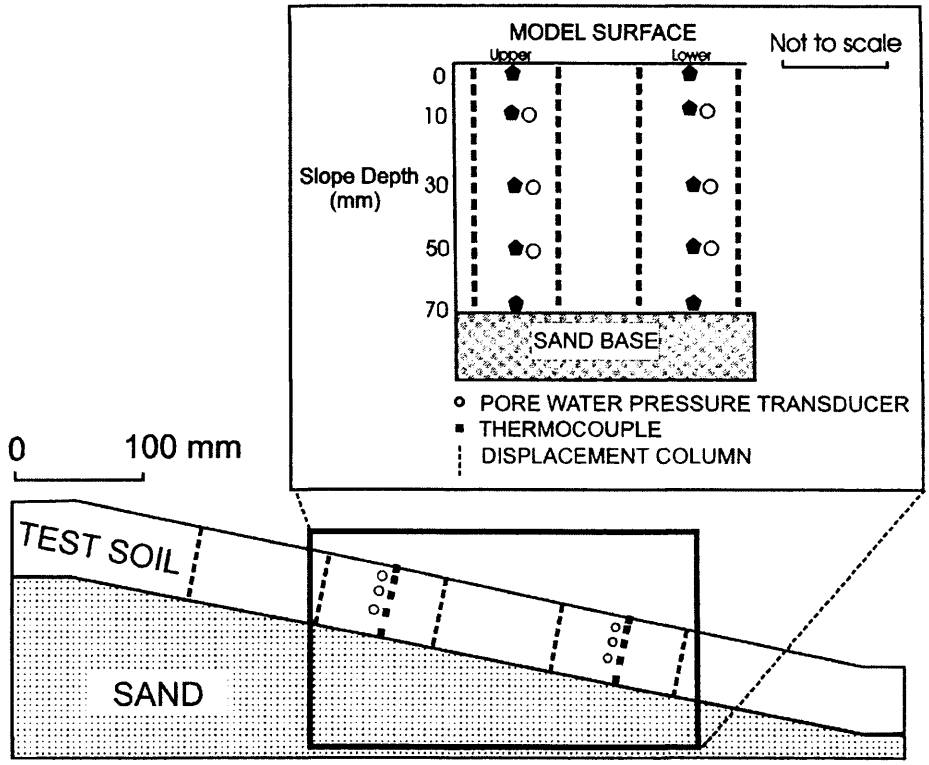

Figure 3.3.3. Diagram illustrating the depth of all subsurface instrumentation installed prior to first freezing phase.

The PDCR81 overcame a majority of the problems commonly associated with more traditional devices (Muraleetharan & Granger, 1999). The PCDR81's small size minimised disruption during installation and therefore reduced the influence of the device upon overall soil behaviour, it also gave the instrument a quick response time as a small amount of fluid was required to highlight changes in pressure (Druck, 1999). The PCDR81's electrical output also allowed for continuous dynamic measurement of pore water pressure conditions even under enhanced gravity fields. The PDCR81 also exhibited a low sensitivity to change in temperature; this was key importance as the probes were placed under high stress when frozen within the soil matrix.

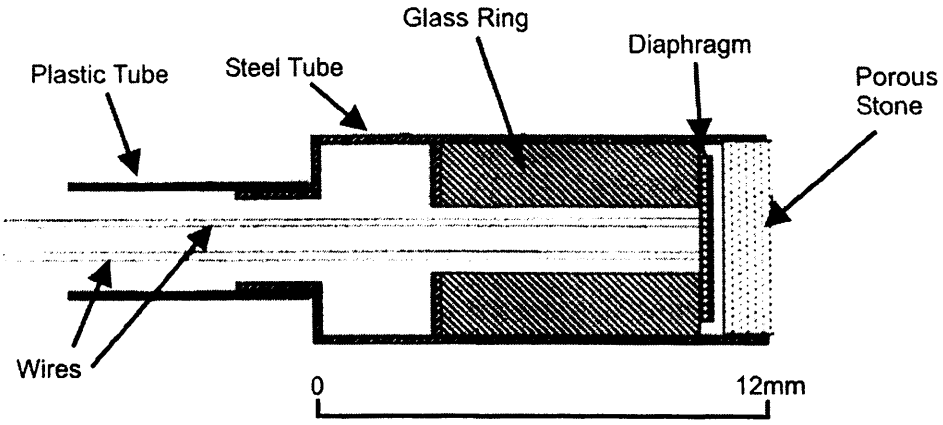

Figure 3.3.4. Schematic diagram for the miniature pore pressure transducer Druck PDCR81 (Adapted from: Muraleetharan & Granger (1999), p.226, fig. 1).

Prior to installation the pore water pressure transducers were de-aired in an ethylene glycol (antifreeze) solution. The transducers were placed in a 1:1 water/antifreeze solution within a vacuum desiccator set to 20in/Hg for approximately 120 minutes. Fluid saturation of the gap between the stone and diaphragm meant a change in diaphragm deformation would be directly equated to a change in water pressure rather than the compression of any residual air packets. The anti-freeze solution also impregnated the porous stone to prevent segregation ice from forming within the stone during the freezing phase. It was important to prevent ice lens growth within that region of the probe, as bodies of ice would create erroneous pressure readings and puncture the silicon diaphragm. The transducers were then calibrated to different depths within the centrifuge gondola – this allowed a voltage output to be converted into a relevant pressure reading and importantly allowed the replacement of poorly responding (damaged) transducers before undertaking long multiple phases of freezing and thawing for each slope model (see appendix D.1).

3.4 Freeze Phase for Slope Model

Within the current project it was deemed appropriate to use a freezing system comprising of vortex coolers. Smith (1995) provides a review of other cooling methods used within centrifuge studies. The cooling system comprised two main groups of components. Firstly, the air treatment units that provided clean dry air

for the set of vortex coolers feeding the cooling plate. Secondly, the vortex coolers that converted the clean air supply into two streams of hot and cold air.

The air supply for model refrigeration was sourced from a 7.5 bar, 30 litres per minute compressor. The supply was firstly routed into a 220-litre storage reservoir; this reservoir would maintain constant pressure for up to 15 minutes in the absence or reduction of airflow from the upstream houseline compressor. The compressed air was then filtered through a DEMCO-Miller compressed air dryer to remove moisture from the air. Further air sterilisation was conducted via two five micron desiccated filters within a Flair EuroDry 2080, these last two filters were mounted to remove additional grease and any remaining condensed water vapour and droplets. The air cleaning process was vitally important because it lowered the dew point of the compressed air. Without a lowering of the dew point ice growth would occur within the orifices of the vortex generator inside the vortex chamber when temperatures within the vortex tube reached 0°C (see fig. 3.4.1).

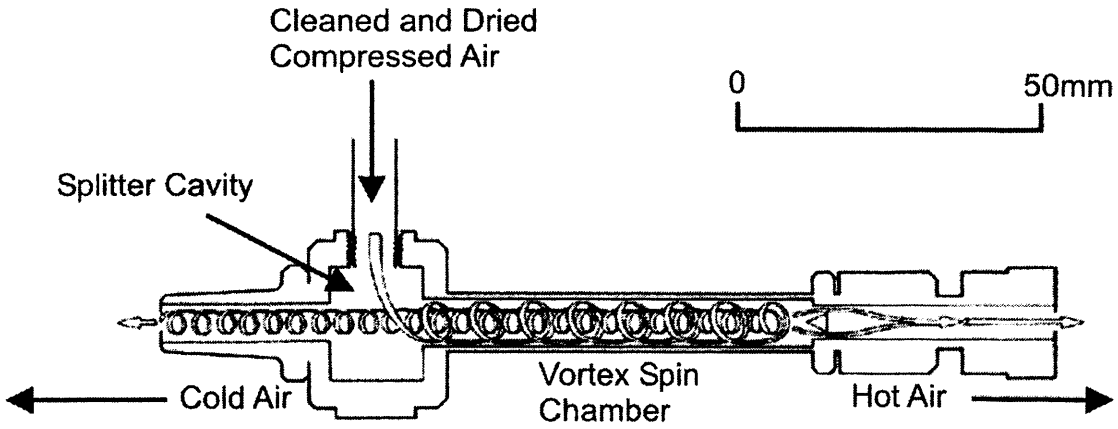

Figure 3.4.1. Schematic diagram illustrating the internal mechanism of the Meech Vortex Tubes used to supply freezing plate.

Once the air had been fully prepared it was moved into three identically configured MEECH-ARTEX vortex coolers. In summary, vortex coolers produce two streams of air from 150mm long, hollow, cylindrical units. An air stream initially passes through a splitter cavity upon entry into the vortex unit. The splitter cavity contains a short plastic splitter unit that is mounted axially with an upstream array of 2mm high arcing fins. These fins disrupt the air supply and eject it tangentially into the vortex spin chamber, the air stream revolves at up to 1,000,000 RPM causing it to

expand and reduce pressure. Some air escapes from the warm end of the vortex cooler via a control valve, the remaining air, still spinning, is forced back through the centre of the outer vortex. The inner stream gives off kinetic energy in the form of heat to the outer stream and exits the vortex tube as cold air (see fig. 3.4.1).

The percentage of air directed to the cold outlet of the vortex tube is called the 'cold fraction', low cold fractions (less than 50%) produce the lowest temperatures but cold airflow rate is sacrificed in order to achieve the lower temperature. Basically, higher cold fractions give greater airflow but will not give the lowest temperatures so it became necessary to define a threshold for maximum refrigeration. Cold airflow and temperature was easily controlled via an adjustment to either the plastic splitter unit that controls the diameter of the initial vortex, or to the slotted aperture valve which defines the amount of warm air which can leave the initial upward vortex (see fig. 3.4.1).

The splitter unit and aperture valve of the narrow warm air exit were configured to allow optimum energy removal by the complete refrigeration unit. The optimum energy removal rate was found to be at a flow rate of 150 l/min and a cold exit temperature of -17°C (or 256 K) (Irving, 2000, p.142). Each vortex tube was set to this rating and mounted into a vertical position in order to feed the cooling plate with the appropriate level of refrigerated airflow (see fig. 3.4.3).

Slope models were completely encased in polystyrene insulation and placed under a confining load and consolidated under a stress of 3.8 kN/m^2, this surcharge stress is equivalent to the self-weight stress at the centre of the soil profile during thaw at elevated gravity within the centrifuge. It is equivalent to the self-weight of the soil at a model-scale depth of approximately 35mm (350mm depth at prototype scale). Freezing of the model under an induced stress field attempts to overcome a scaling problem regarding the stress field during freezing in relation to the stress field during thaw (see section 3.6). Prior to freezing the constant head water supply was reset so that the phreatic surface resided just above the base of the soil model and the end wall central drainage channel was closed. The slope model was frozen under open hydrological conditions in order to best replicate the natural growth of segregation

ice seen within the active layer of most permafrost field systems (Williams & Smith, 1989). Slope models were then frozen on the laboratory floor (see fig. 3.4.2).

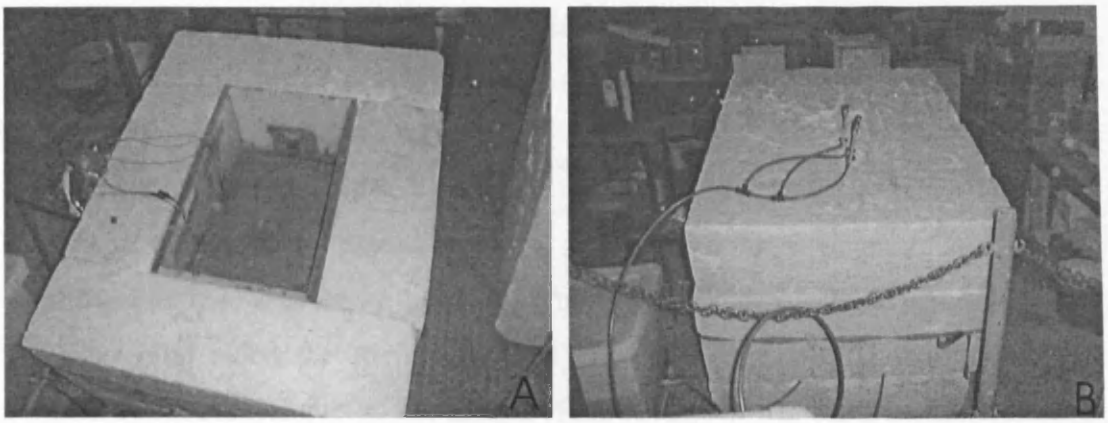

Figure 3.4.2. (A) Slope model being prepared and (B) during the freezing phase. Note (A): Confining load has not been placed onto freezing plate to aid visual inspection of plate position prior to freezing. Note (B): The header tank used to maintain consistent open system conditions can be seen bottom-left of photograph.

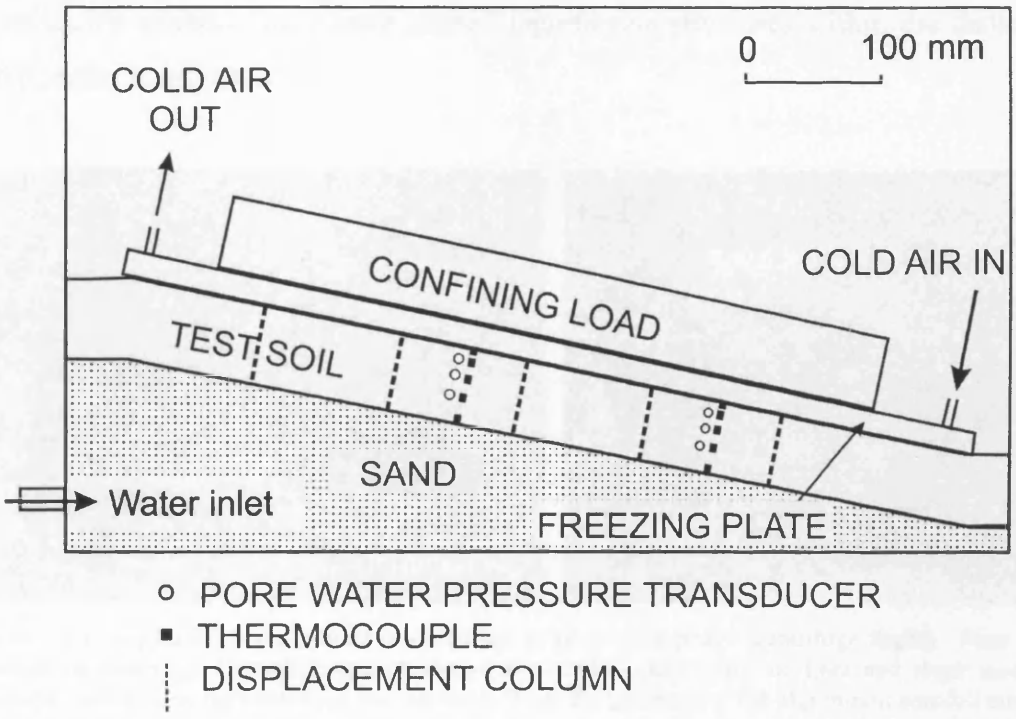

Figure 3.4.3. Diagram showing the experimental design used during freezing phase.

Before commencement of freezing, the model surface was covered in protective plastic to prevent excessive cryogenic sublimation (dehydration) of the slope surface. The cooling plate was then placed onto the model surface. The cooling plate comprised of a hollow steel plate containing copper radiator pipes through which the cold compressed air refrigerates the plate and therefore cools the model from the

surface downwards (see fig. 3.4.3) (Nixon *et al.*, 1982). The freezing phase for most slope model's lasted approximately 48-54 hours. The cooling plate achieved a steady temperature of $-10^{o}C$ after 1.5 hours of operating amid sustained compressed air pressure. Freezing occurred from the surface downwards (see fig. 3.4.3).

3.5 Thaw Phase for Slope Model

The slope models were placed inside a secure environmental strongbox for the centrifugal thaw phases (see fig. 3.5.1). The strongbox gave a stable positioning for the slope, and aided the maintenance of an appropriate thermal regime for the duration of each test flight. The design of the strongbox was fixed by the geometry of the centrifuge gondola and by safety considerations involving weight stability at high rotational speeds. It created a means of securely bolting the slope model to the centrifuge gondola, thereby preventing additional vibration during centrifuge flight, as excessive vibration may have created liquefaction structures within the thawing soil (Coelho *et al.*, 2003).

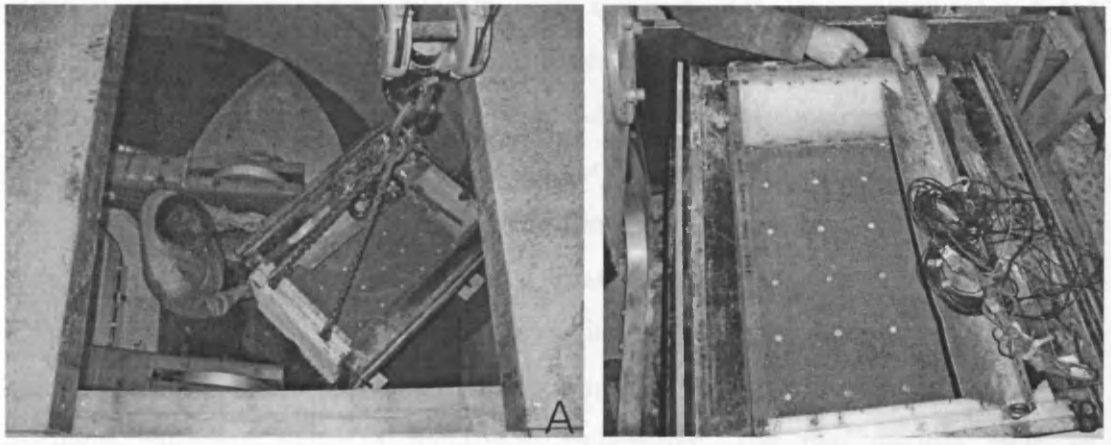

Figure 3.5.1. (A) Model being placed in centrifuge prior to thaw phase (centrifuge flight). Note the presence of centrifuge strongbox and insulation surrounding polypropylene liner and slope model. (B) Model secured on the centrifuge test platform. Note the presence of the aluminium aerofoil above model surface to maintain airflow across the model and the three liners (strong box, aluminium liner and polypropylene inner liner).

Each slope model was weighed prior to entering the centrifuge chamber. This determined the correct counter-balance required to keep the centrifuge stable during flight (see fig. 3.1.1 & appendix B). This was an important safety precaution as the exact weight of each slope model varied with each freezing phase, in that variations in segregated ice content directly influenced a models corresponding weight. It was

of prime importance to keep the centrifuge stable during flight as the complete model package (ice filled slope model, polypropylene liner, aluminium liner, and steel strongbox) commonly weighed in the region of 500kg.

After the slope model was securely placed into the centrifuge gondola and all connected instrumentation became fully operational, the centrifuge was rotated to produce the required net acceleration of 10g at the centre of the slope model. This acceleration was made up of two orthogonal components: the radial centripetal acceleration due to the rotation; and the downward gravitational acceleration. The speed of rotation, ω, in RPM, for a required centripetal acceleration, a, in gravities, was calculated using the relationship:

$$\omega = \frac{60}{2\pi}\sqrt{\frac{9.81a}{r}} \qquad (3.1)$$

where r is the effective radius of the centre of mass of the unit. The net acceleration in gravities applied to the unit under test is $\sqrt{a^2+1}$. The use of the swinging platform ensured that the principal axes of the unit under test maintained a fixed orientation with respect to the direction of the net acceleration. As the rotational speed of the centrifuge changed, the principal direction of acceleration was the line perpendicular to the axis of the platform pivot bearings and therefore passed through the centre of gravity of the swinging platform. The centrifuge achieved the set speed of 64.4 RPM in three stepped 3.3g phases. It took approximately ten minutes for the centrifuge to achieve a steady gravitational force set to the desired level. The speed of rotation of the centrifuge was constantly measured using its tachometer and regularly validated using a hand-held tachometer. The two devices were in agreement for all of the tests.

Slope models were subjected to downward thaw via warm convective airflow across the model surface (see fig. 3.5.2). An aluminium aerofoil was used to encourage a uniform air current across the model, without the aerofoil the vacuum wake created by the spinning gondola would have minimised the airflow reaching the model surface. The aerofoil decreased the duration of the thaw phase flight time. For a

full description of test conditions during thaw, such as centrifuge pit temperature and test duration, please refer to section 5.1.

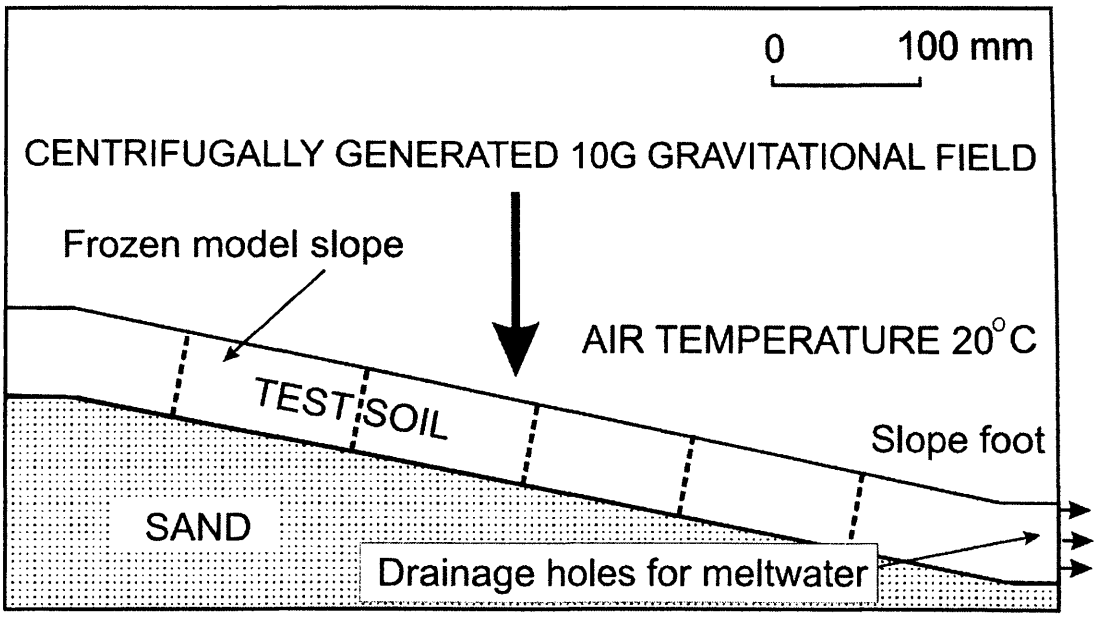

Figure 3.5.2. Diagram showing experimental design used during centrifuge thaw phase.

3.6 Data Collection

The experimental design was to subject all slope models to four individual freezing and thaw phases. This occurred for all models except the slopes that underwent rapid transitional slope failures. Data was recorded before, during and after every freeze and thaw phase. The data collection techniques can be divided into electronic, manual and visual components. The synthesis of all these individual components has given rise to a complex and consistently high quality dataset that comprehensively describes all slope behaviours created within the centrifuge-modelling program.

Due to logistics, electronic data capture could only be conducted during the thaw phase. The centrifuge onboard data acquisition system could monitor 32 low frequency signals and was based around a commercial data logger, a Campbell Scientific CR7 data logger. The system was configured with analogue-to-digital converters for signal voltage measurement of ±5V, and a thermocouple interface board for temperature measurement. For the purpose of this investigation this

allowed the collection of output from six pore water pressure and ten temperature sensors using dedicated data acquisition software within the centrifuge control room. Data was called from the on board CR7 logger every second and collated every ten seconds (see appendix C).

Manual data collection techniques were carried out before and after each freezing and thawing phase. The slope profile was measured against a fixed datum along eight equally spaced transects. Profiles of the model surface were measured along x (up-slope), y (across slope), and z (height) axes. This gave an evenly distributed grid of 72 individual slope spot heights. The spot height grid produced a general surface contour for further Digital Terrain Model (DTM) analyses such as mapping areas of differential heave or settlement, i.e. areas of disparate segregation ice growth. The position of the fifteen surface displacement discs was also recorded using the same co-ordinate system. The surface discs provided information on the rate of slope movement before and after both freezing and thawing, this data was extremely valuable as it was directly linked to heave/settlement information by the presence of the marker.

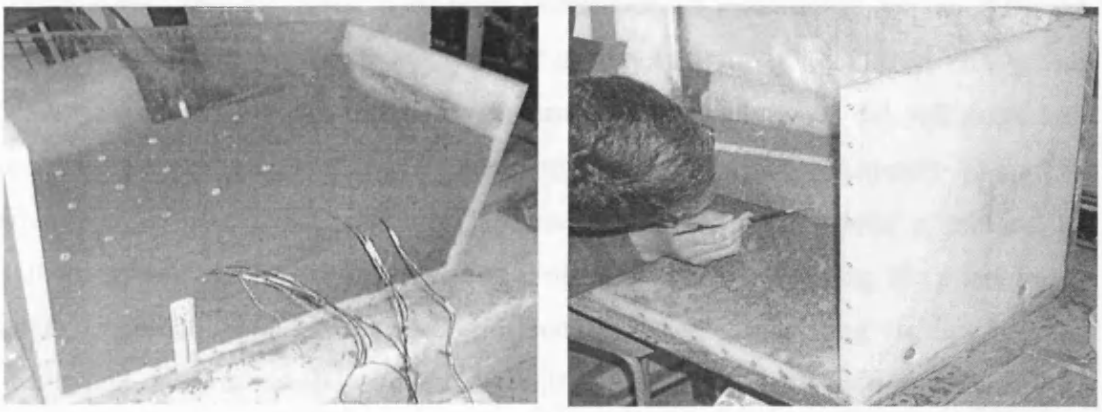

Figure 3.6.1. Post-thaw excavation of a slope model after final thaw phase. (A) Model partially dried, prior to excavation. (b) Cleaning columns using a fine paintbrush.

The cylinder columns buried during model instrumentation were precisely excavated after the final thaw phase in order to determine the rate and style of volumetric subsurface movement (see 3.14). The soil was allowed to dry sufficiently in order to support a vertical section, each subsurface profile section was then excavated using trowels and palette knifes. Columns were finally cleaned for photographing using a fine artists paintbrush and water (fig. 3.6.1). During the excavation of the strain

profiles two undisturbed soil samples were taken to allow the creation of resin-impregnated thin sections in order to investigate micro-scale soil structure under optical microscopy (for thin section preparation procedure see section 5.7).

Video monitoring and time-lapse still photography were used to monitor surface movement and progressive thaw consolidation. A digital camera was attached to the central housing to give a plan view of the slope model surface. A micro-CCD camera relayed live pictures of the plan and side view of the slope model into the control room. The live visual link was used to monitor the slope model for any inappropriate complications that may have developed during centrifuge flight. The video record of every centrifuge test was used to review slope models that contained rapid detachment failures during thaw.

3.7 Experimental Limitations

It is standard practice for centrifuge studies to investigate scaling issues by undertaking 'modelling of models' (Ko, 1988) experiments. During a modelling of models program a hypothetical full scale phenomenon is simulated using the same soil material and boundary conditions (similitude of conditions) but at different scales with a corresponding adjustment of gravity levels, e.g. 1/10 scale at 10g and 1/30 scale at 30g. Both model results are then extrapolated to the full scale and predictions from the different models are compared for consistency (Yang & Goodings, 1996). The modelling of models technique provides a method of validating whether any of the typical scaling effects are influencing the phenomena under examination. Typical scaling effects that can be identified via this process are: a non-uniform acceleration field (Phillips, 1995), various particle size effects (Goodings & Gillette, 1991), the presence of Coriolis acceleration (Ko, 1988), or any boundary effects caused by a model operating at a too small scale (Coelho *et al.*, 2003). Under ideal circumstances a model of models would have provided primary data to directly validate the scaling of the current research program. However, due to time constraints the current experimental program could not contain a series of modelling of models. It is felt that this does not present a serious limitation as previous research by Harris *et al.* (2003a) has reported consistency of scaling

between 1/10 and 1/30 scale slope models in which solifluction processes were simulated.

The radial direction of the centrifugal acceleration field does create a small additional anomaly, in that the direction of the acceleration is actually only normal to the base of the gondola at the centre of the strongbox (see Irving, 2000, p.137; Taylor, 1995). To combat this inherent limitation, key areas of instrumentation and measurement were placed in central positions where the acceleration error was small (Phillips, 1995).

It would have been advantageous to conduct the freezing phase within an enhanced gravity field. This would have created consistent stress conditions between the freezing and thaw phases by manufacturing appropriately scaled segregated ice lenses. This is a significant but irresolvable limitation to the existing methodology. It is acknowledged that other researchers have managed to freeze small soil models within a centrifuge (e.g. Yang & Goodings, 1998; Ketcham & Black, 1995). But to freeze a slope model with the current experimental design would have been unworkable due to the energy demands required to refrigerate such a large soil mass. Any attempt to freeze the slope model would have been further complicated by the relatively high pit temperatures (around 20°C) created by the small beam radius centrifuge functioning within a subsurface chamber (see fig. 3.1.1). The overall centrifuge time and energy consumption demand needed for in flight freezing made it an impractical proposition.

The aluminium centrifuge gondola would become heated by air friction during flight. Its temperature would rise to a constant 25°C within the first hour of a test and hence may have provided a source of energy that may have been transferred into the sample via the steel strongbox and aluminium liner. It is felt that over longer duration flights heat may have been conducted into the base of the slope model, meaning that thawing may not have been exclusively from the surface downwards. Previous researchers have noted an approximate 0.5°C per hour rise in temperature at the base of the steel strong box (Irving, 2000). A lack of physical space within the centrifuge gondola made it impossible to rectify this problem. However it is felt that the impact of gondola warming was negligible because the basal sand layer

created a cold buffer zone between the model and the warming strongbox base. Thermocouple data suggested that in all tests thawing of the model soil was accomplished solely from the upper soil/air boundary downwards.

There was no possibility to monitor the progression of frost heave during the freezing phase. A continuous monitoring of frost heave rates would have allowed a better control over the ice distribution within the slope model. Logistical problems and limitations on physical space dictated that no data could be electronically or manually logged during the freezing phases. These restrictions occurred due to the arrangement of the freezing plate, overburden weights and vortex tubes (see fig. 3.4.2). A dataset containing thermal data alongside rates of frost heave would give an exact indication of the timing and therefore the depth of greatest segregation ice development. This would have provided useful information with regard to the influence of ice lens distribution upon the rate and form of gelifluction processes. Field studies have identified the influence of subsurface ice distribution on the style of active-layer gelifluction within both continuous and discontinuous permafrost areas (e.g. Matsuoka, 2001; Lewkowicz & Clark, 1998; Mackay, 1981).

The miniature pore water pressure transducers created a small scaling issue. During the thaw phase the transducer had a scaled diameter of 65mm – thus creating a problem of precision with respect to identifying an exact position for the interfaces between frozen soil, the zone of partially frozen soil and the unfrozen soil. A thermocouple was attached to each pore pressure transducer, and this could have been indicating that the thaw front had passed through the zone adjacent to the transducer. However, the transducer may have exhibited a delayed response whilst the 65 mm thick adjacent soil layer became entirely unfrozen and influenced by free melt water (see fig. 3.3.4). Unless smaller pore water pressure transducers were used it would be impossible to prevent this delay, however, smaller transducers would not necessarily survive the harsh environmental conditions created by cyclical freezing and thawing.

CHAPTER FOUR : Test Substrate – Soil Classification

Test soils used in the centrifuge-modelling program are described in this chapter. Soil granulometry, soil mineralogy, Atterberg Limits, permeability, compressibility, and shear strength parameters are presented since these parameters have been identified as key controls on the stability of thawing periglacial slopes (Harris, 1977). The sequence of slope simulations discussed in this thesis began with a natural soil obtained from slope deposits at Prawle Point, south Devon, and this is referred to as the 'natural soil'. This base soil material was modified, firstly by the addition of pure silt collected from glaciolacustrine deposits at the Park Slip opencast site near Bridgend, and referred to as 'silt'. Secondly, the base soil was modified by the addition of commercially available Kaolinite clay, and this material is referred to here as 'clay'.

Engineering soils are particulate materials consisting of assemblages of mineral grains with pore spaces residing between the discrete grains (see fig. 3.3.2). These pore spaces contain variable amounts of water and air (and sometimes other gases) (BS1377: Part 1). The physical behaviour of a soil will be determined by its intrinsic material properties and the magnitude of externally applied stresses (Azizi, 1999). Soils are classified for engineering purposes according to their state and nature; with the nature of a soil being described by the distribution of grain sizes and grain mineralogy and soil state by its specific volume at the current effective stress (Atkinson, 1981). Mathematical models of soil behaviour are required to calculate soil behaviour and classify the material according to essential stress-strain relationships (Powrie, 1997).

The analysis of periglacial mass movement processes through the determination of geotechnical and mechanical properties of the sediment has been undertaken in several studies. Knowledge of soil parameters allows back analysis of slope and soil conditions necessary to initiate mass movement (e.g. Morgernstern & Nixon, 1971; McRoberts & Morgernstern, 1974; Harris, 1972; Skempton and Weeks, 1976; Skempton, 1988; Skempton *et al.*, 1991; Hutchinson, 1991).

4.1. Test Soils – Source Site Description

4.1.1 Prawle Point Substrate

The base soil for the centrifuge-modelling program was sampled from a gelifluction ('head') deposit near Prawle Point, south Devon (National Grid Reference: SX 773 350). Prawle Point lies on the southern end of Lannacombe Bay, to the southeast of Salcombe, on the South Hams coastline (see fig. 4.1.1). The region contains a Site of Special Scientific Interest (SSSI) for its geology and wildlife that consists of 10km of foreshore, cliff section and raised beaches. The Prawle Point coastline provides an outstanding example of periglacial head deposits, and includes an assemblage of periglacial features (i.e. shear fabrics, relict involutions, etc; Gallop, 1991).

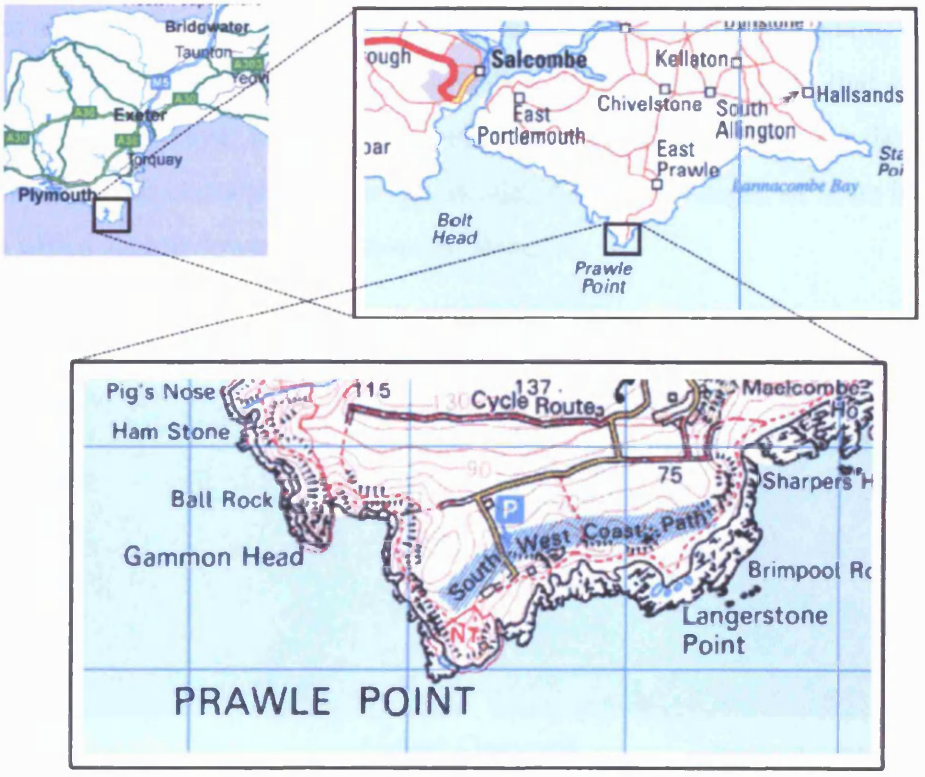

Figure 4.1.1. Source area for the base natural soil used within the centrifuge-modelling program. (Source: HMSO Crown Copyright).

The Quaternary history of this region of Southwest England has been outlined in several publications, e.g. Campbell *et al.*, 1998. Periods of intense periglacial activity occurred during cold stadials in the Devensian. The solid geology of the region mainly consists of greenschist members of the Start schist complex. The sample site contains aprons of Devensian head deposit that formed in front of a relict

Ipswichian cliff-line during intermittent periods of periglacial activity occurring approximately 15-10,000 years BP (see fig. 4.1.2) (Ballantyne & Harris, 1994; Mottershead, 1976). The 3m thick exposures of head rests uncomformably on a discontinuous raised beach and a rock platform cut into Devonian schist (Gallop, 1991, p.79). The Pleistocene gelifluction deposits have been described as highly variable diamicts containing identifiable flow structures as a result of the solifluction activity (Keen, 1998). The fine head also contains pronounced horizons of clast rich sediment, with apparent crude bedding dipping away from the pre-Quaternary cliff-line (Mottershead, 1977). Interbedding of the raised beach and lower members of the head deposits would suggest that solifluction lobes transported material into the littoral zone and that these lobes then became buried by marine sediment (Mottershead, 1977; Kalaugher & Grainger, 1991). In close proximity to the relict cliff-line are boulder accumulations forming relict talus deposits (talluvium) (Gallop; 1991, p.79). Mottershead (1971) and Gallop (1991) have shown that the head contains a strong clast fabric, with preferred orientation parallel to the line of greatest slope, and clasts tending to dip parallel to the slope angle, or in an imbricate fashion with a slightly lower angle than the slope.

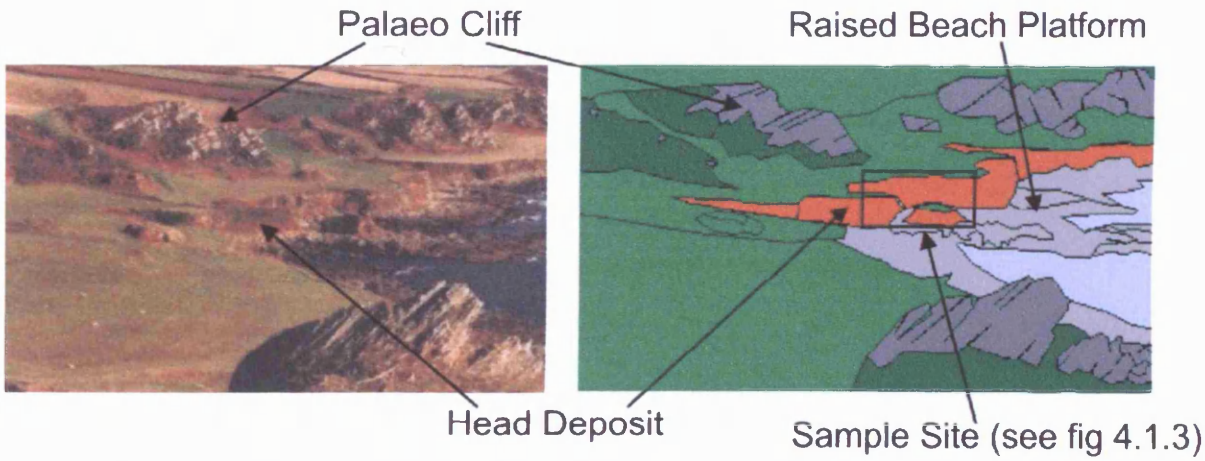

Figure 4.1.2. Photograph and Schematic diagram showing the head apron overlying the wave-cut platform upon the raised beach at Prawle Point, South Devon (Source: Prawle Point SSSI).

Samples were manually excavated from a single source of fallen debris (see fig. 4.1.2). Samples were collected on three separate occasions. The head deposit rested upon a raised wave-smoothed surface at the foot of the cliff, this allowed easy access for samples to be manually removed from the single source, approximately one metre above the exhumed inter-tidal wave cut platform (see fig. 4.1.3).

In the field the soil sample was poorly sorted, and composed of clayey, sandy silt matrix containing clasts ranging from granule to cobble size. To facilitate transportation to the laboratory, the material was dry sieved in the field to remove clasts larger than 100mm. Clast lithology reflected the nature of the exposed bedrock upslope, i.e. a combination of quartz-mica and green (chlorite/hornblende) schist, this bedrock apparently being highly susceptible to frost weathering (Keen, 1998; Gallop, 1991; Mottershead, 1976, 1982).

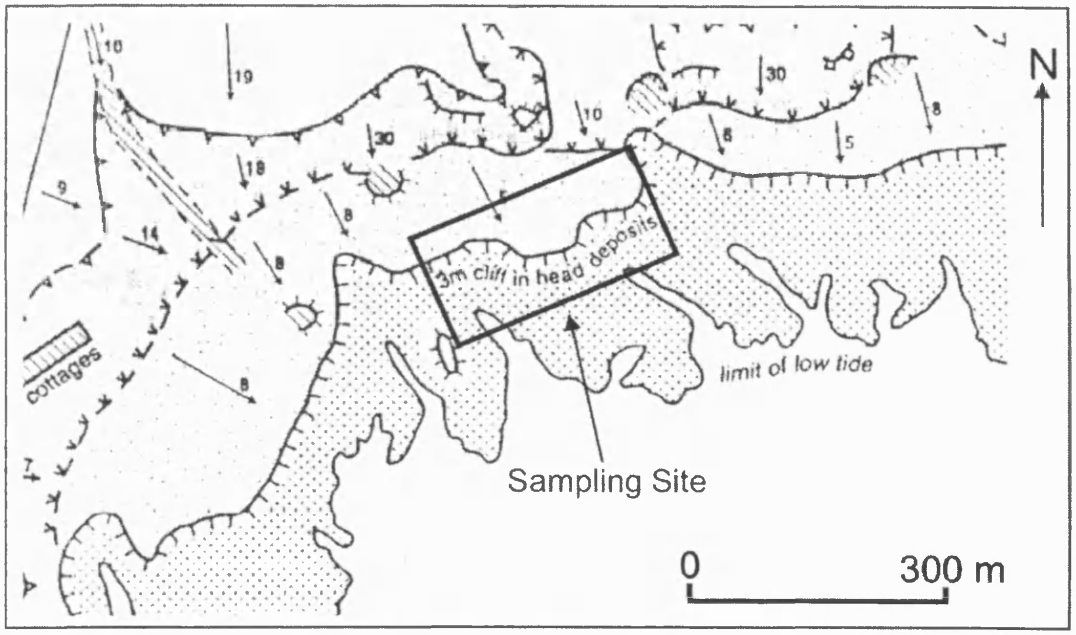

Figure 4.1.3. The location of the soil-sampling site at Prawle Point, South Devon. (Adapted from source: Gardiner & Dackombe, 1987).

4.1.2 Park Slip Silt

The glaciolacustrine silt was removed from the Celtic Energy, Park Slip West opencast mine site at Kenfig Hill near Bridgend, South Wales (National Grid Reference: SS 837 829). Samples were manually excavated from a 5m high section comprising a basal till overlain by horizontally laminated silt containing occasional dropstones. These were removed by dry sieving the mass sample through a 2mm sieve.

4.1.3 Kaolinite Clay

The Speswhite kaolin clay test soil was commercially acquired from ECC International. No pre-laboratory soil preparation was required.

4.2. Test Soil Description – Granulometry

The mass behaviour of soils is to a large degree governed by the size of the grains making up the soil mass (e.g. Folk & Ward, 1957). The grain size determination testing was carried out following the exact experimental procedures outlined in BS1377: Part 2 (1990) and BS5930: Part 2 (1981) (Head, 1992). Particle size distribution for the sand to coarse silt classification was determined through a series of dry sieving procedures (BS1377: 1990). The analysis of sediments passing the 63μm used a Micromeritics Sedigraph 5100 after first washing through the 63μm sieve and oven-drying (BS5930: 1981).

The sedigraph therefore measured the grain size distribution of sediments within the clay and silt size range between ~1 and 63 microns. The instrument uses the settlement of soil particles in water, measuring the attenuation of an X-ray beam passed through the settling suspended sediment. The instrument assumed Stoke's Law whereby a drag coefficient can be calculated for a spherical particle (with a low Reynolds number) to give an estimation of particle mass and physical size. Stoke's Law states that the rate of settlement of a particle in a fluid is a function of the density of the particle, density of the fluid, viscosity of the fluid, temperature of the fluid, and the square of the radius of the particle (Azizi, 1999). Stokes Law enables the sedigraph to determine the diameter of a particle by measuring the rate of settlement within a fluid of specific physical properties. It should be noted that preparation of the test soils prior to use within the experimental program involved pre-test dry sieving to 2mm (200 micron) diameter. This defines the upper limit of the sand fraction by BS1377 (1990). Repeat procedures were undertaken for each test soil to account for sample variability. A total of nine tests were performed and all results were recorded and are summarised below:

Table 4.2.1. Sand/Silt/Clay content for the test substrates as defined by BS5930 (1981).

Test Substrate	Sand (%)	Silt (%)	Clay (%)
Natural Soil (NS)	69.35	20.33	5.23
Clay (CL)	0	24.2	75.8
Silt (SI)	0	63.93	36.07
NS + 10% CL	62.42	25.55	12.03
NS + 20% CL	55.48	20.34	24.18
NS + 30% CL	48.55	17.83	33.62
NS + 10% SI	62.42	28.55	9.03
NS + 20% SI	55.48	29.82	14.7
NS + 30% SI	48.55	36.41	15.04

Grain size distributions for the natural soil and the clay and silt additives are shown in Figures 4.2.1 – 4.2.4, and for the manufactured test soils in Figures 4.2.5 and 4.2.6. Finally the percent clay silt and sand in each test soil is illustrated graphically in Figure 4.2.7.

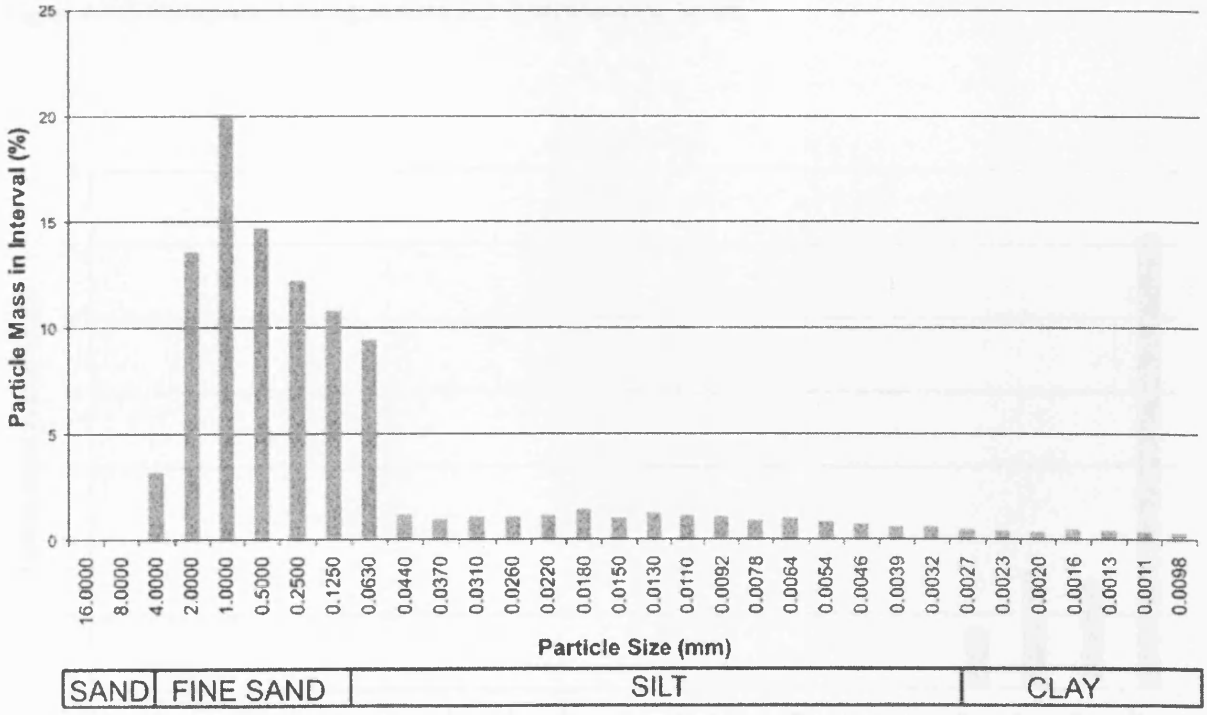

Figure 4.2.1. Histogram showing particle size distribution for the natural soil.

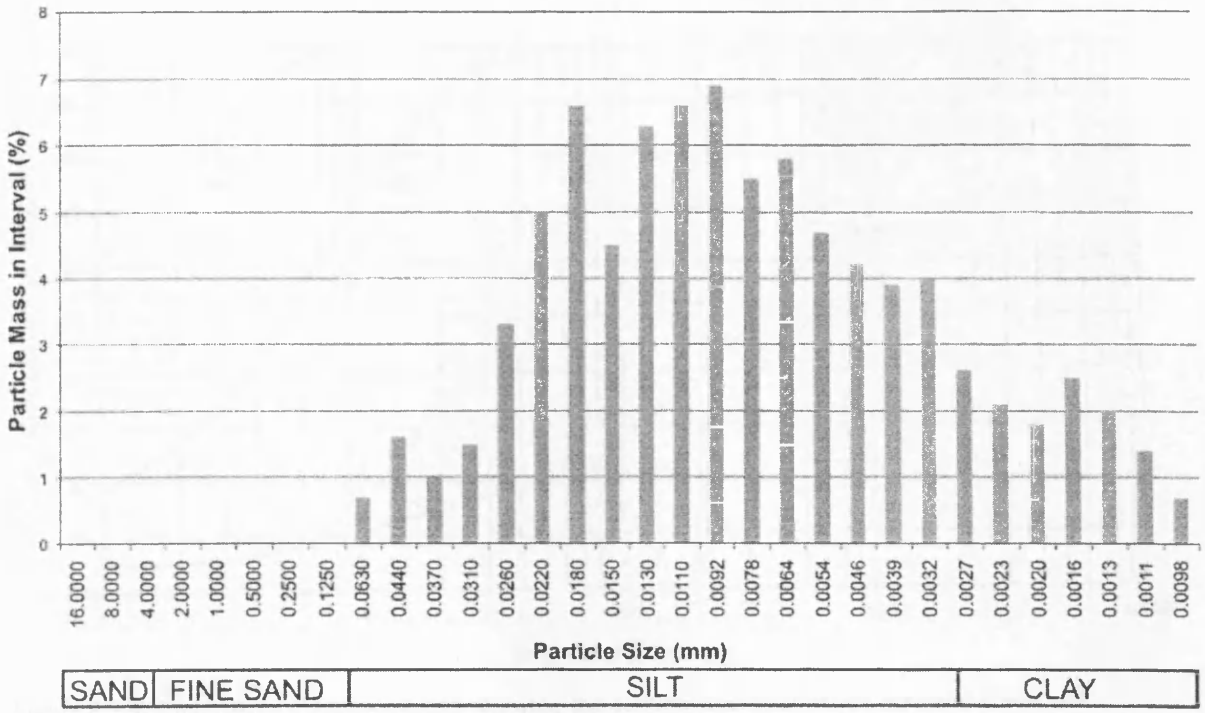

Figure 4.2.2. Histogram showing particle size distribution for the silt.

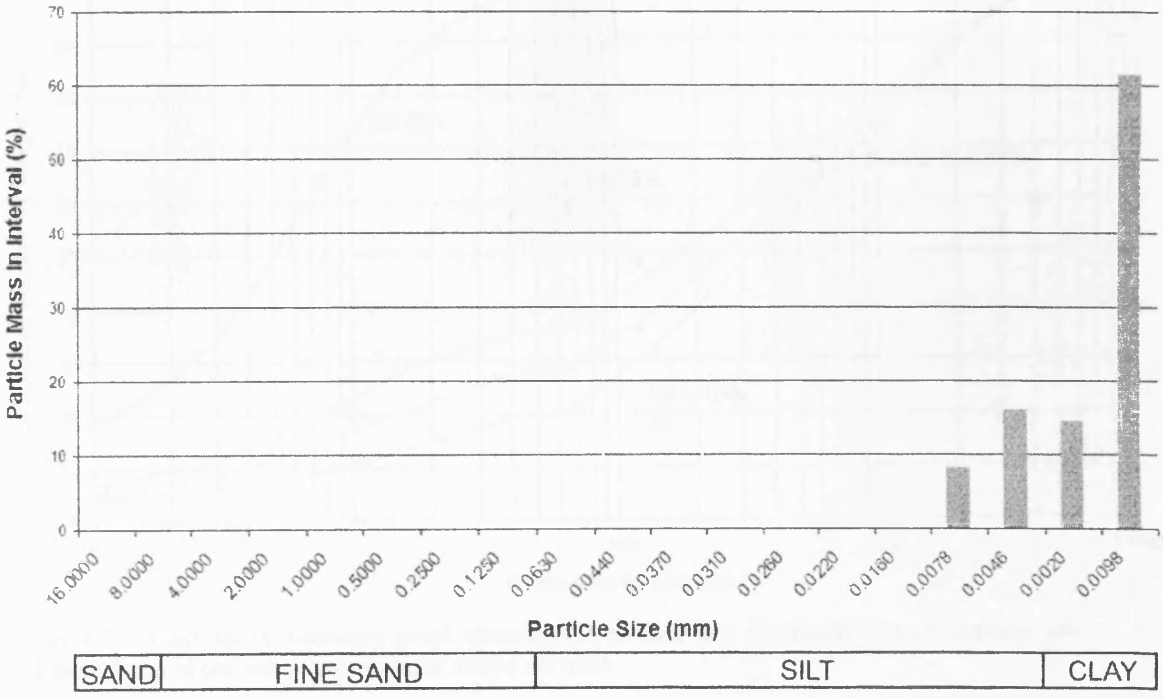

Figure 4.2.3. Histogram showing particle size distribution for the clay.

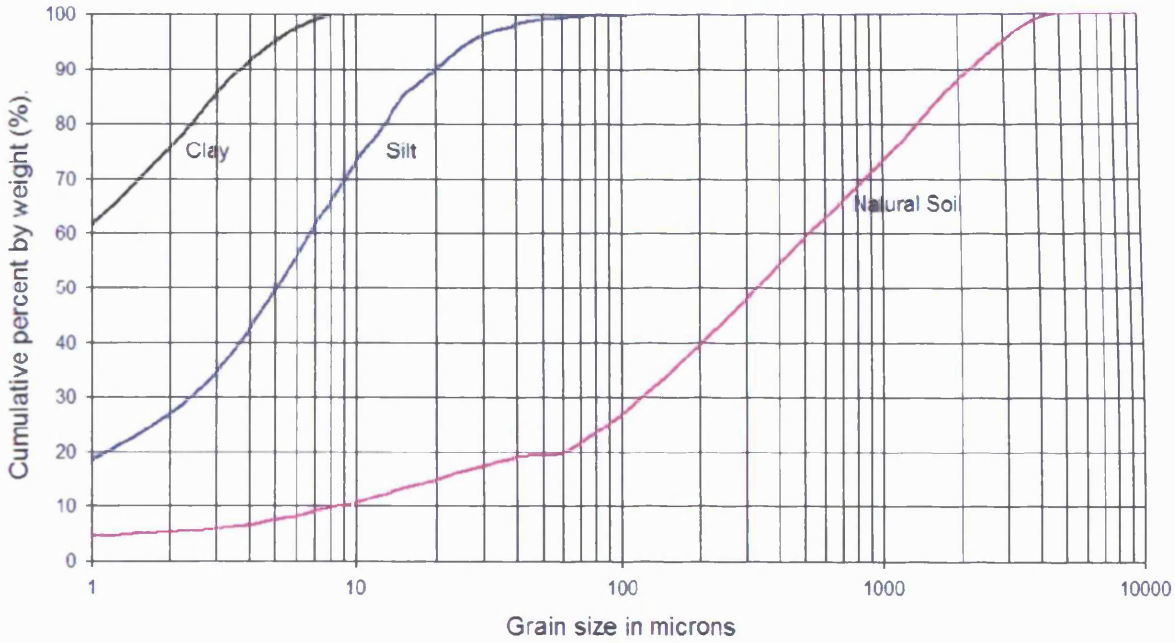

Figure 4.2.4. Cumulative frequency graph showing the particle size distribution for natural soil, silt and clay soils.

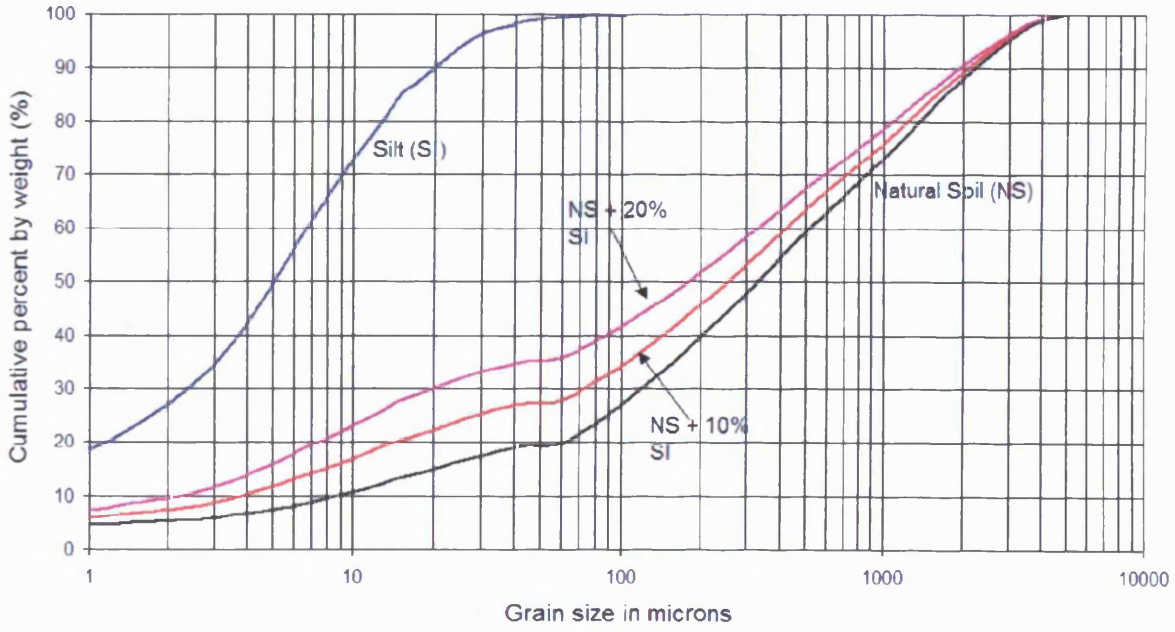

Figure 4.2.5. Cumulative frequency graph showing the particle size distribution for silt, natural soil and manufactured ten and twenty percent added silt soils.

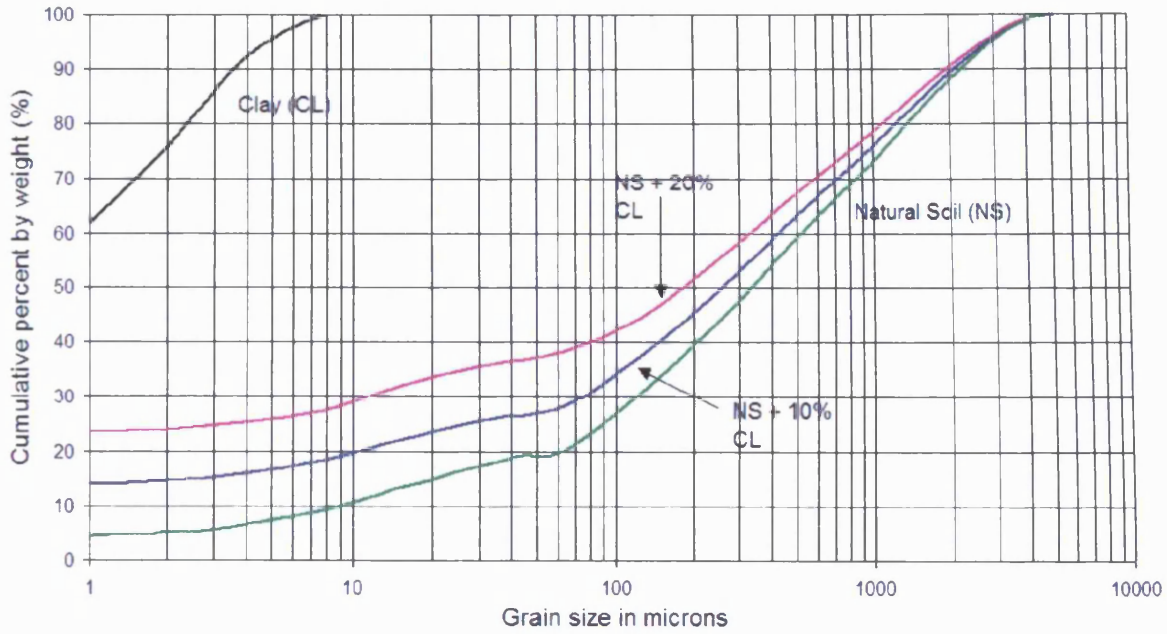

Figure 4.2.6. Cumulative frequency graph showing the particle size distribution for clay, natural soil and manufactured ten and twenty percent added clay soils.

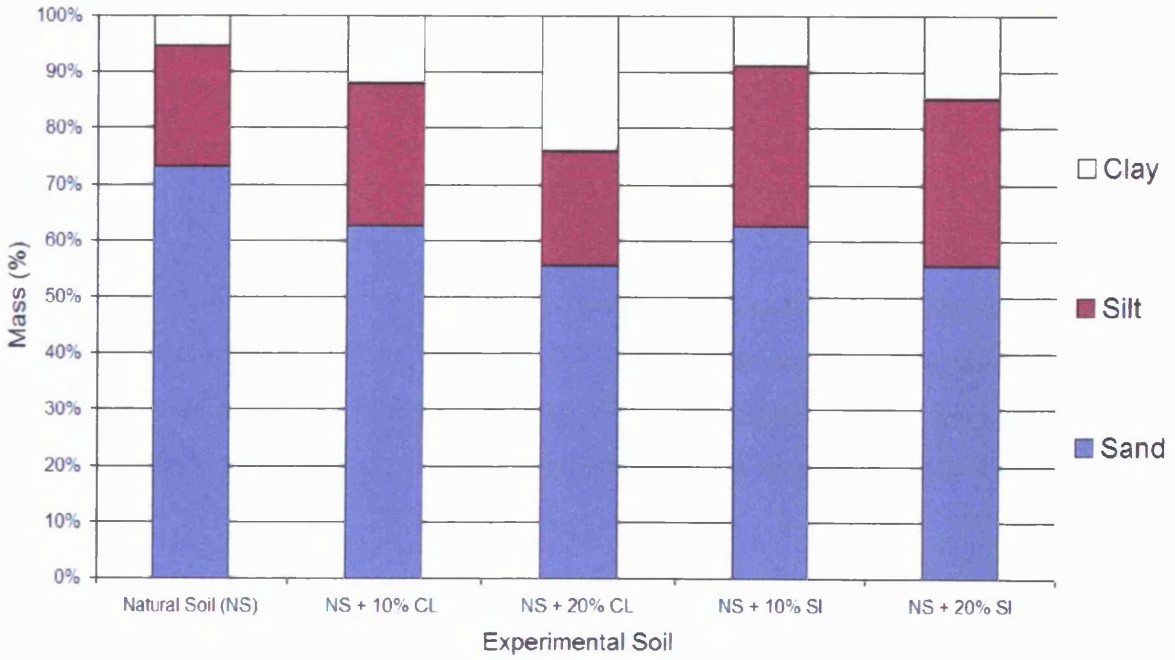

Figure 4.2.7. Percentage distribution of particle size class boundaries within each of the manufactured experimental soils.

4.3. Test Soil Description – Atterberg Limits

The consistency of a soil mass refers to the response of the soil to remoulding. The consistency of soil changes as moisture content increases, passing through the plastic and liquid thresholds defined by the Atterberg Limits. Atterberg Limit testing was

carried out following the exact experimental procedures outlined in BS1377: Part 2 (1990) (Head, 1992). Liquid Limits were calculated via repeated testing using a cone penetrometer, and Plastic Limits determined through repetition of the hand rolling method using a glass sheet. The Plastic Limit (W_P) is defined as the moisture content at which the soil ceases to behave as a brittle solid and becomes a ductile plastic. The Liquid Limit (W_L) is the moisture content at which disturbance of the soil transforms it into a viscous fluid or slurry. The moisture content (w) was calculated for each soil specimen as a percentage of dry mass to the nearest 0.1% using:

$$w = (m_2 - m_3 / m_3 - m_1)\ 100\ \% \qquad (4.1)$$

where m_1 is the mass of the container (g), m_2 is the mass of container and wet soil (g), and m_3 is the mass of the container and dry soil (g) (BS812-109, 1990).

The Plasticity Index (I_P) is the difference between W_L and W_P and describes the range of moisture content over which soil behaves as a ductile plastic solid:

$$I_P = W_L - W_P \qquad (4.2)$$

Plasticity is attributed to the deformation of the adsorbed water around clay mineral particles, therefore the degree of plasticity is related to the amount and type of clay minerals present within the soil unit (Powrie, 1997). Skempton (1953) expressed the relationship between I_p and clay content, and termed the Activity Index of a clay soil (A).

$$A = I_P / \textit{Percentage of clay in soil unit} \qquad (4.3)$$

where the percent of clay was taken as the percentage by mass finer than 0.002 mm.

When analysing the test soils a number of repeated tests were undertaken to account for individual soil sample variability. A total of 27 tests were performed and results are summarised in Table 4.3.1 and Figure 4.3.1.

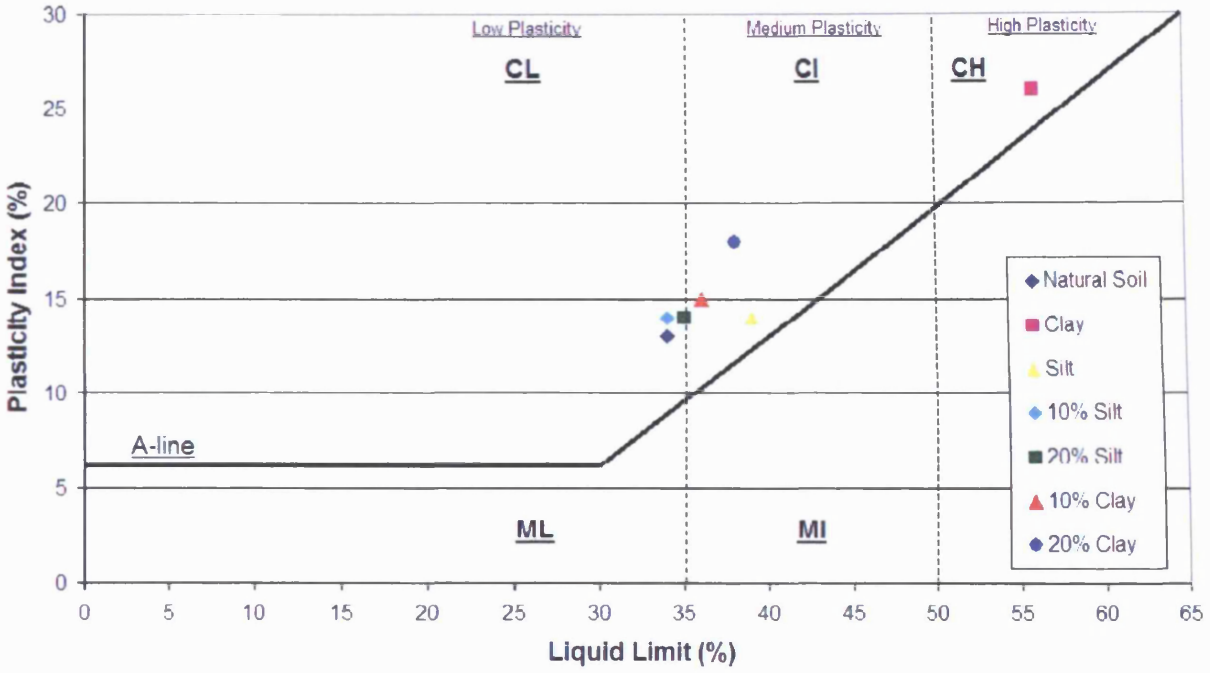

Figure 4.3.1. Casagrande plasticity chart for the experimental test soils. Note: M = Silt soil, C = Clay soil. (Source: Casagrande, 1932; BS 5930: 1981).

Table 4.3.1. Atterberg limits for the experimental soils.

Test Soil Type	Liquid Limit W_L (%)	Plastic Limit W_P (%)	Plasticity Index I_P (%)
Natural Soil (NS)	34	21	13
Clay (CL)	56	30	26
Silt (SI)	39	25	14
NS + 10% SI	34	20	14
NS + 20% SI	35	21	14
NS + 30% SI	37	24	13
NS + 10% CL	36	21	15
NS + 20% CL	38	20	18
NS + 30% CL	41	20	21

The natural soil and silt had similar Plasticity Indices with the silt having a higher Liquid Limit due to its finer texture. As expected, the clay shows higher plasticity than the natural soil and silt. The addition of silt to the natural soil did not significantly affect the Atterberg Limits of the soil (see fig. 4.3.1). The addition of silt raised both the Liquid Limit and Plastic Limit by approximately equal amounts. As a consequence, the Plasticity Index remained roughly constant. The progressive addition of clay to the natural soil raised the Liquid Limit but had less effect on the Plastic Limit. The addition of 10% and 20% clay lead to a respective 99% and

233% rise in the Activity Index. A 30% increase in the clay content caused a 28% increase the plasticity index. The classification of slope sediments in terms of their Atterberg Limits can be used to indicate the sensitivity of the soil to changes in moisture content. Field studies have reported Liquid Limits of around 25% in active granular periglacial soils, but also noted that actual field moisture contents can be greater (Washburn, 1967). Liquid Limit values in excess of 80% have been reported within clay rich periglacial slope sediments, with the high values being a function of high clay contents (Skempton & Weeks, 1976). In his classification of Pleistocene periglacial soils in the UK, Hutchinson (1991, p.289, fig. 7) showed that soils with clay contents less than 30% and Plasticity Index below 28% have fabrics consistent with shear distributed throughout the moving mass. Soils with higher clay contents and Plasticity Index were more liable to fail by shearing along a distinct slip surface, generating imprinted shears within the soil mass. Harris (1981) showed that in most modern periglacial areas where solifluction is active, soils have low plasticity, with Plasticity Index less than 16%. Thus, the test soils analysed above are likely to be susceptible to solifluction and are not expected to develop imprinted shears during mass movement.

4.4. Test Soil Description – Consolidation and Permeability Parameters

Determination of soil consolidation and permeability parameters is necessary in order to analyse the thaw consolidation ratio of the thawing soils during centrifuge modelling (see chapter six). Soil consolidation is the reduction in volume caused by an increase in overburden pressure, and results from a decrease in void ratio. Consolidation testing was undertaken using an oedometer, which maintains the cross-sectional area of the specimen so that the volume strain may be quantified though measurement of change in thickness. During testing three distinct elements contribute to observed reduction in sample thickness following loading, (a) immediate settlement caused by the bedding in of mechanical components of the oedometer, (b) primary consolidation, when the increase in confining stress causes expulsion of pore water and reduction in void volume, and (c) secondary consolidation (creep), then change in soil fabric allows continued slight reduction in thickness (see fig. 4.4.3). The Terzaghi theory of one-dimensional consolidation (Terzaghi & Peck, 1967) applies to the primary consolidation phase only, and this is

determined in the oedometer test procedure. The total settlement of consolidation (S_T) can be represented by:

$$S_T = S_I + S_C + S_S \qquad (4.4)$$

where S_I represents immediate settlement, S_C is the primary consolidation phase, and S_S indicates secondary settlement. The process of soil consolidation leads to an increase in stiffness of the soil. Soils consolidate in response to increases in effective pressure ($\Delta\sigma'$) where:

$$\Delta\sigma' = \Delta\sigma - u \qquad (4.5)$$

where $\Delta\sigma$ is increase in total stress and u indicating porewater pressure. So when u = zero, then $\Delta\sigma' = \Delta\sigma$ (Azizi, 1999). A reduction in void ratio (e) will occur with an increase in the effective pressure (σ'). The void ratio is the ratio of total volume of voids (V_v) against the total volume of solids (V_S):

$$e = V_v / V_s \qquad (4.6)$$

The volume change due to a unit increase in effective stress depends upon the compressibility of the host material. The coefficient of volume compressibility of the soil unit (M_V) is a measure of the amount by which the soil will compress when loaded and allowed to consolidate.

$$M_v = (\frac{\Delta h}{h}) / \Delta\sigma_v' \qquad (4.7)$$

The rate at which consolidation can occur is dependent on the rate at which water can escape from the void space; this is therefore related to the permeability (k) of the soil. This time related consolidation factor is expressed as the coefficient of consolidation (C_V) and indicates the time period over which consolidation settlement will take place.

$$C_v = k / (M_v / \gamma_W) \qquad (4.8)$$

where γ_W is the unit weight of water.

Steady state water seepage conditions will develop within a soil profile if hydraulic boundary conditions remain constant. The permeability (k) of the experimental sediment can therefore be calculated since:

$$k = C_V \; M_V \; \gamma_W \qquad (4.9)$$

The one-dimensional consolidation testing was carried out using a Wykeham Farrance oedometer following the exact experimental procedures outlined in BS1377: Part 5 (1990) (Head, 1994). Example output from consolidation testing is shown in Figure 4.4.1.

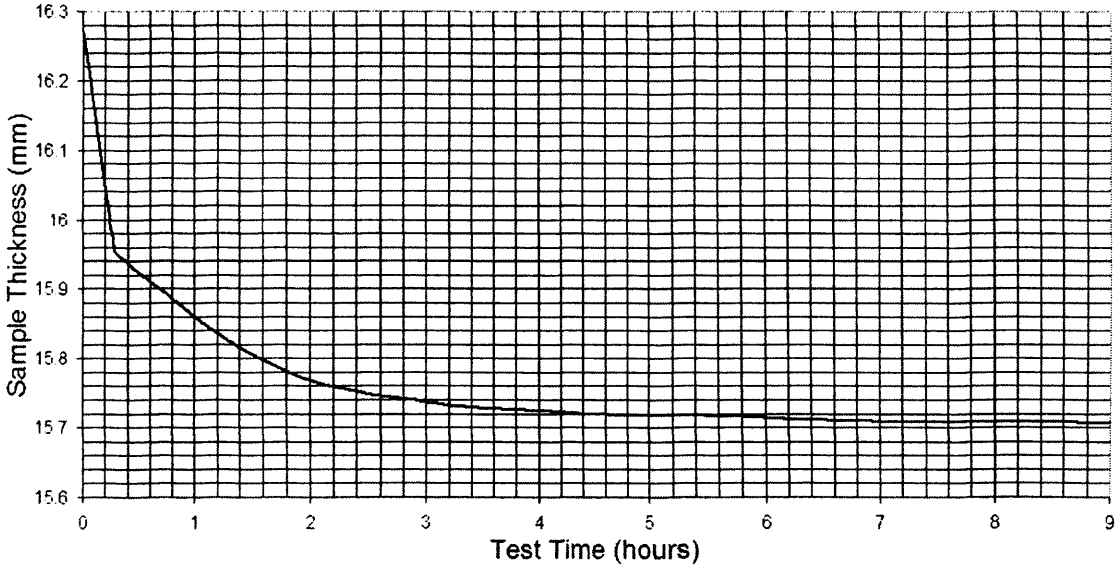

Figure 4.4.1. An example set of continuously recorded oedometer data taken during a stage of consolidation for the 10% clay experimental soil under 7.3kN overburden load. Note: presence of both initial compression and primary consolidation phases.

Consolidation properties were determined for the primary consolidation phase (see fig. 4.4.1) for saturated soil specimens. Soil samples were subjected to vertical axial pressure and allowed to drain freely from the top and bottom surfaces. Vertical axial pressure was exerted in increments of applied stress but no lateral deformation of the sample was allowed. Each vertical compression increment was observed for 24 hours to allow primary consolidation to fully complete. Height measurements were taken at suitable intervals during primary consolidation by a dedicated

computer logging system (see fig. 4.4.1). A Fourier series solution to the consolidation differential equation derived by Taylor (1948) was applied to the height measurement data in order to determine the degree of consolidation (U_V) that was plotted against square root of time factor (T_V). It should be noted that the determination of T_V assumed an instantaneous application of the stress increment:

$$U_V = \textit{consolidation after time (t) / total consolidation} \qquad (4.10)$$

$$T_V = C_v\, t / d^2 \qquad (4.11)$$

where d is the drainage path length, which within the current experimental procedure equalled half the average sample thickness, and t is a unit of time measured in years (Taylor, 1948). The calculation of U_V using Taylor's square root of time fitting method also allowed the determination of both the coefficient of volume compressibility (M_V) and the coefficient of consolidation rate (C_V) via the equation:

$$T_{V\,90} = C_v\, t_{90} / d^2 \qquad (4.12)$$

A series of Oedometer tests were carried out under successive 7.3, 14.6, and 21.8 kN/m^2 load increments (see fig. 4.4.2). Since the modelling experiments were undertaken under relatively low confining stresses, data from load increment 2 (14.6 kN/m^2) are used in the analysis of experimental results.

Table 4.4.1. Summarised results for M_V, C_V, and k values for all experimental soils used within the centrifuge-modelling program. Soil calculations using compressive vertical load of 14.6kN/m^2.

Test Soil Type	M_V (m^2/kN)	C_V (m^2/year)	k (m/year)	k (m/sec)
Natural Soil (NS)	0.0007133	12.737712	0.1695796	5.37733^{-09}
NS + 10% SI	0.0007417	14.953057	0.2069873	6.56352^{-09}
NS + 20% SI	0.0010335	10.740608	0.2071895	6.56993^{-09}
NS + 30% SI	0.0010395	14.994015	0.2909046	9.22453^{-09}
NS + 10% CL	0.0010632	6.6284947	0.1315295	4.17077^{-09}
NS + 20% CL	0.0011865	5.5984634	0.1239777	3.93131^{-09}
NS + 30% CL	0.0012732	4.7263085	0.1123112	3.56136^{-09}

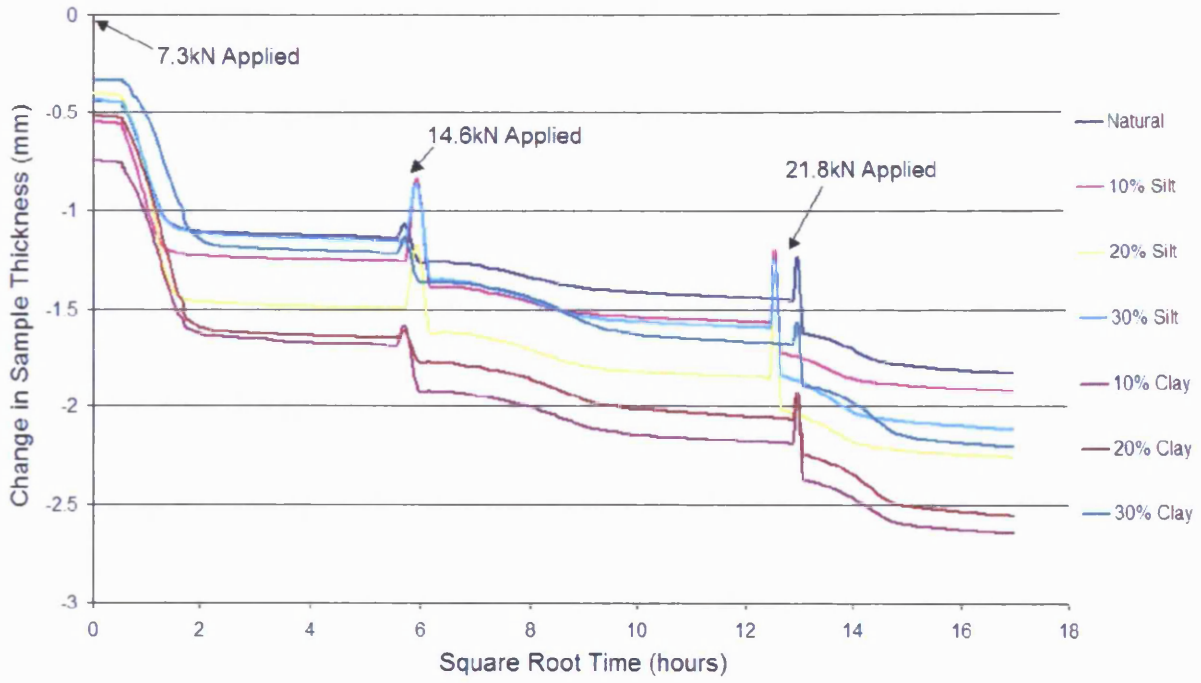

Figure 4.4.2. Changes to oedometer sample thickness under successive increments of increasing vertical overburden pressure. The one-dimensional compression data were continuously recorded via dedicated electronic data acquisition software.

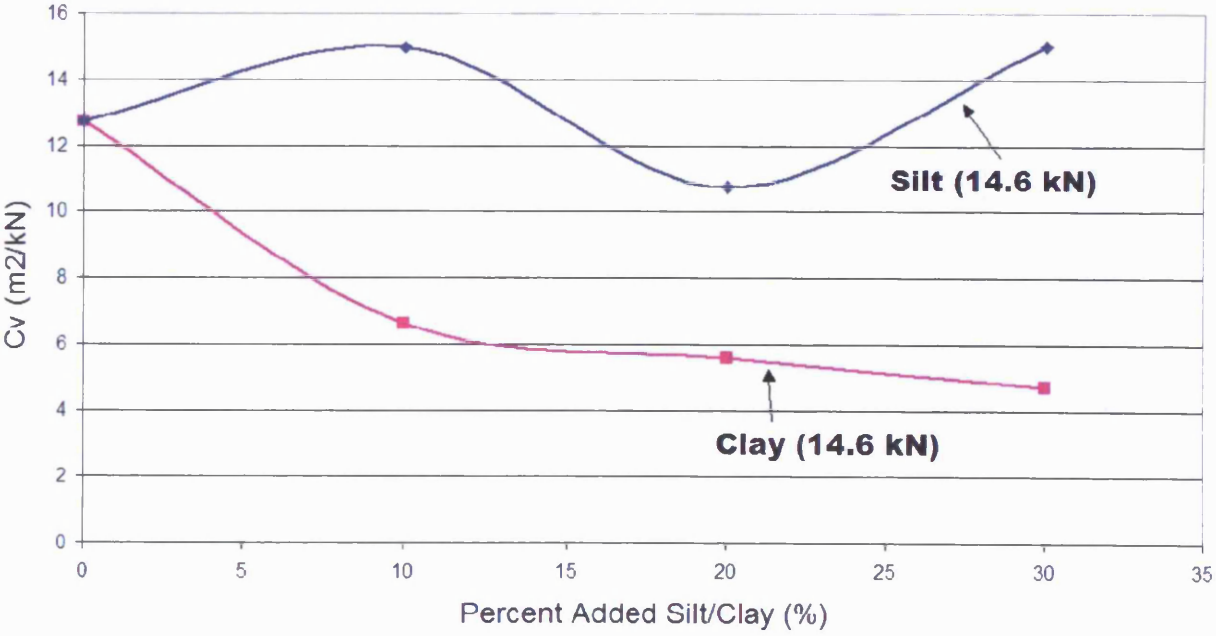

Figure 4.4.3. Coefficient of consolidation (C_V) for each experimental and manufactured soil.

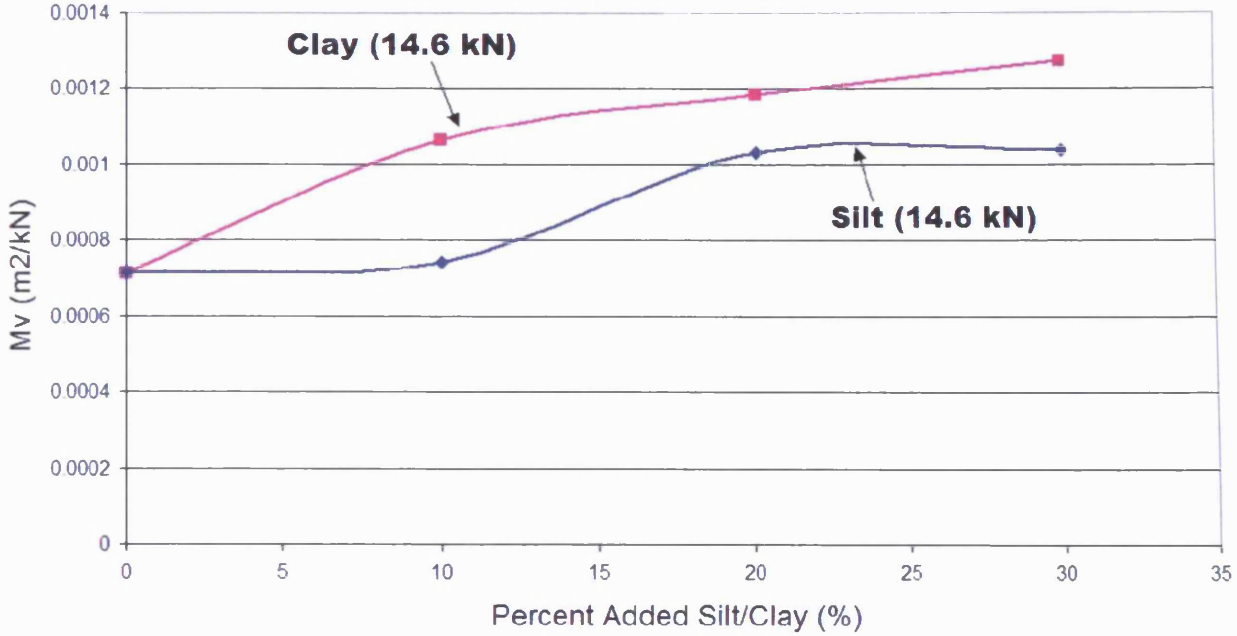

Figure 4.4.4. Coefficient of volume compressibility (M_V) for each experimental and manufactured soil.

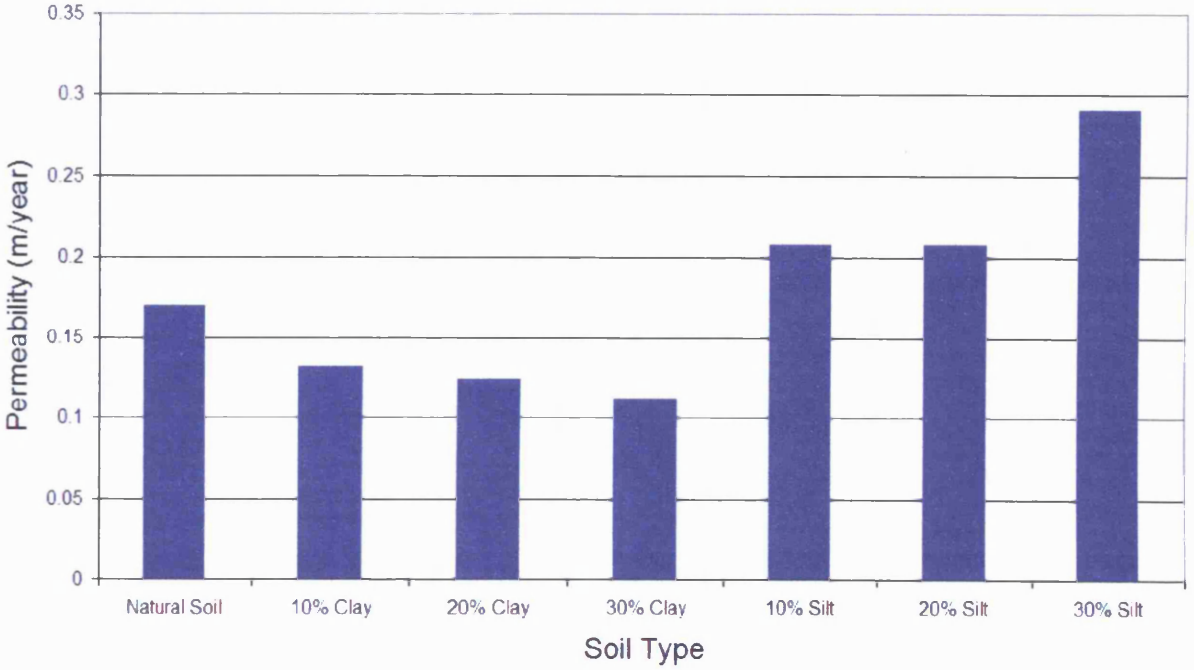

Figure 4.4.5. Permeability parameter (k) for each experimental soil.

Soil permeability decreased significantly by 28% with the addition of 10% clay to the natural soil, and for successive 10% increments, continued to fall. Overall, there was an observed 66% decrease between the natural soil and 30% clay soil (see fig. 4.4.5). The addition of 10% silt caused an initial 18% rise although little change in

permeability occurred with the successive 20% increment. The k value rose markedly for the 30% silt soil when compared with the raw natural soil. The coefficient of volume compressibility (M_V) increased with the addition of both silt and clay (see fig. 4.4.4). The addition of 10% silt had no influence upon M_V although a 30% rise was observed for the successive 20% silt soil. The manufactured clay soils showed a different pattern with an initial 32% rise for the 10% clay material but little additional increase for the 20% clay soil. The coefficient of consolidation (C_V) showed no consistent change as silt content was progressively increased. The value ranged between 10.7 and 14.9 m^2/kN. The incremental addition of clay reduced C_V progressively, giving a 92% reduction in the 10% clay soil and 127% decrease in the 20% clay sediment (see fig. 4.4.3). These soil parameters play a key role during thaw consolidation and the associated elevation of pore water pressures, since M_V provides an indication of the potential change in void ratio during thaw settlement and C_V determines the rate at which excess pore water released during thaw can be dissipated.

4.5. Test Soil Description – Shear Strength Parameters

The strength of a soil depends upon its resistance to shearing stresses. In that the shear strength of a soil defines the maximum available resistance of a soil to movements being induced by a shearing stress (Anderson *et al.*, 1978). Shear strength is a function of frictional grain-to-grain contacts, the effective pressure placed upon the soil unit, and the amount of soil cohesion as determined by the colloidal properties of the sediment clay fraction. Grain-to-grain interlocking increases with particle size and particle angularity, and the density of the soil grain packing (i.e. the soil consolidation). The resistance to shear is provided by friction between solid mineral particles and is therefore proportional to the normal force acting within the soil matrix. The frictional resistance to movement along individual grain-to-grain contacts is measured by the angle of internal friction (ϕ). Shearing resistance due to friction is given by:

$$\tau_f = \sigma' \tan \phi' \qquad (4.13)$$

where σ' is the effective normal stress and ϕ' indicates the effective angle of friction or the angle of shearing resistance (Terzaghi & Peck, 1967). The friction coefficient is a function of the roughness of the slip surface. In clay soils a second element that may contribute to shearing resistance is the cohesion, defined as the shearing resistance when the normal stress on the slip surface is zero. Thus, the Coulomb equation may be written as:

$$\tau_f = c' + \sigma' \tan \phi' \qquad (4.14)$$

The shear strength testing was carried out following the exact experimental procedures outlined in BS1377: Part 7 (1990) (Head, 1992). Determination of soil shear strength was conducted via direct shear within Wykeham Farrance small shear box apparatus. Direct shear tests measured the shearing force causing failure. A square unit of soil was laterally restrained and sheared along a mechanically induced horizontal plane whilst being subjected to pressure being applied normal to the plane (BS1377-1990). Drained tests were conducted where the rate of horizontal movement was sufficiently slow to allow the dissipation of porewater pressures during peak shearing.

The test specimen was consolidated under a vertical normal load until the primary consolidation phase was complete (for example see fig. 4.5.2), it was then sheared at a rate of displacement (0.024mm min^{-1}) that was slow enough to prevent the development of excess pore pressures. Regular displacement measurements were made of the shearing resistance being offered by one portion of the soil unit sliding across the basal unit. The horizontal shearing force was measured by means of a calibrated proving ring (see appendix D). Unit failure occurred when the shearing resistance reached the maximum value that the soil could sustain, i.e. when the particles began to move relative to one another.

Measurements were electronically recorded via a portable Campbell CR7 datalogger attached to a set of Linear Voltage Displacement Transducers (LVDTs) that consisted of a sprung piston with a magnetic head within a cylinder that contained an induction coil (see fig. 4.5.1). The position of the magnet within the coil determined the degree to which the base voltage is increased or decreased as the piston and

magnetic head passed along the coil. The LVDTs were regularly calibrated to measure accuracy and working range, and the amount by which voltage output varied was linear for 95% of the 50mm measuring range (see appendix D).

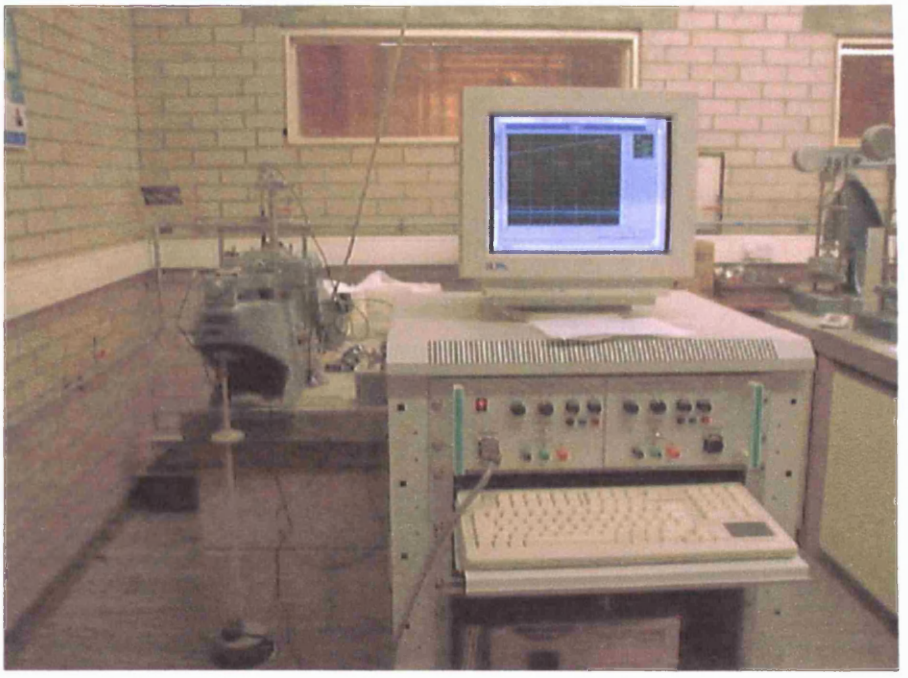

Figure 4.5.1. The portable Campbell CR7 data logger attached to the direct shear box prior to testing. (Photograph: James Smith).

Shear strength testing was conducted upon a set of four similar specimens for each soil type. Each specimen was subjected to different normal pressure with testing being carried out with an overburden pressure of 8, 16, 32, and 64kN/m^2 (see fig. 4.5.3). The repeated procedure at different vertical loads allowed a relationship between measured shear stress at failure and normal applied stress to be obtained (see figs. 4.5.6 & 4.5.7).

Data from the five individual series (20 tests) enabled the effective peak (ϕ') and residual (ϕ_r') shear strength parameters to be derived through converting force into stress by dividing values of applied force by the area of the shear box. Residual strength was defined as the constant shearing resistance after large shear displacements had been applied, and occurred after the peak strength had been mobilised (see fig. 4.5.5) (BS1377 – 1990). The recorded results are fully summarised below:

Table 4.5.1. Summarised results for peak shear strength (kPa) (ø') for the experimental soils used within the centrifuge-modelling program.

Normal Pressure (kPa)	Natural Soil (NS)	NS + 10% Clay	NS + 20% Clay	NS + 10% Silt	NS + 20% Silt
8	5.708	4.788	1.9	4.648	3.3
16	11.224	10.024	No Data	11.06	6.4
32	No Data	20.188	9.3	21	12.7
64	45.412	39.592	17.1	41.86	No Data

Table 4.5.2. Summarised results for residual shear strength (kPa) ($ø_r$') for the experimental soils used within the centrifuge-modelling program.

Normal Pressure (kN)	Natural Soil (NS)	NS + 10% Clay	NS + 20% Clay	NS + 10% Silt	NS + 20% Silt
8	5.064	3.414	1.2	3.92	2.4
16	10.832	9.406	No Data	9.856	4.6
32	No Data	18.87	8.7	19.824	10.2
64	37.74	33.878	15.9	37.492	No Data

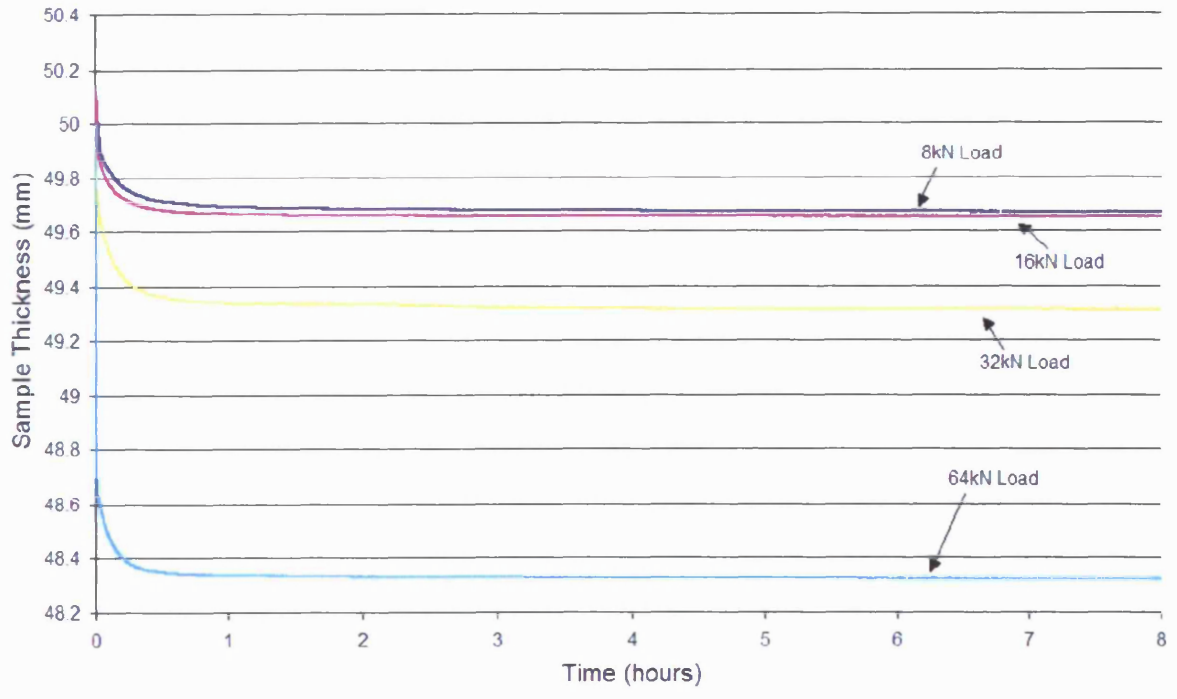

Figure 4.5.2. Continuously recorded shear box data showing changes to sample thickness for natural soil samples under normal effective stress; i.e. showing the vertical settlement of samples during primary consolidation.

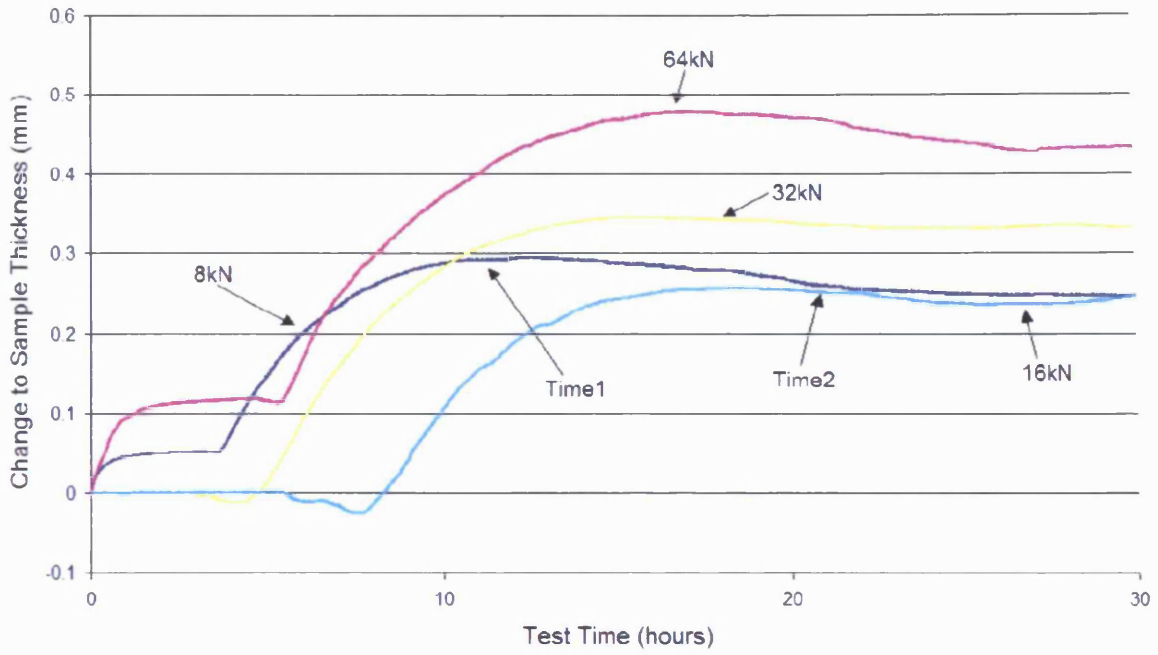

Figure 4.5.3. Sample thickness (Δh) during shear for the for the 10% silt experimental soil being placed under differing effective stress. Note: changes to thickness of sample during shear are related to soil dilation. Resistance to shearing builds up to a peak (time1) as a small amount of deformation occurs, after which dilation occurs and sample density falls (time2) which leads to less resistance to shearing force, i.e. a looser soil fabric along the formation of slip surface.

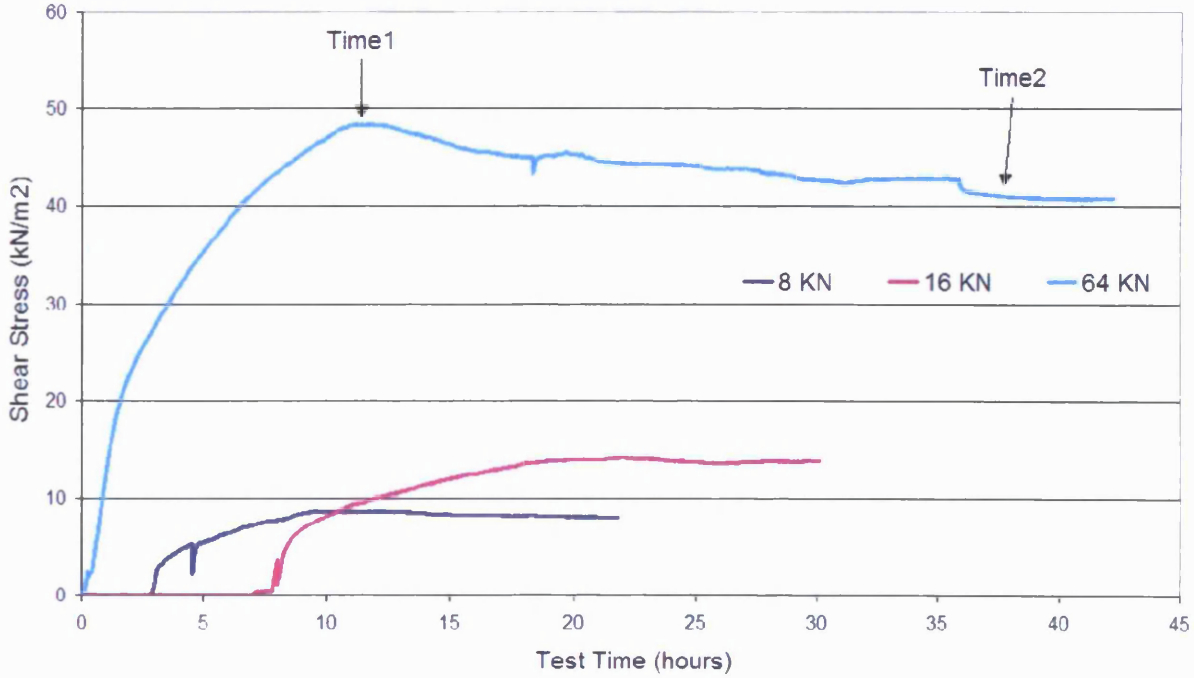

Figure 4.5.4. Shear stress (kN/m^2) over experimental time under imposed conditions of different normal stress for the Natural experimental soil. Note: Time1 = peak strength, Time2 = residual strength.

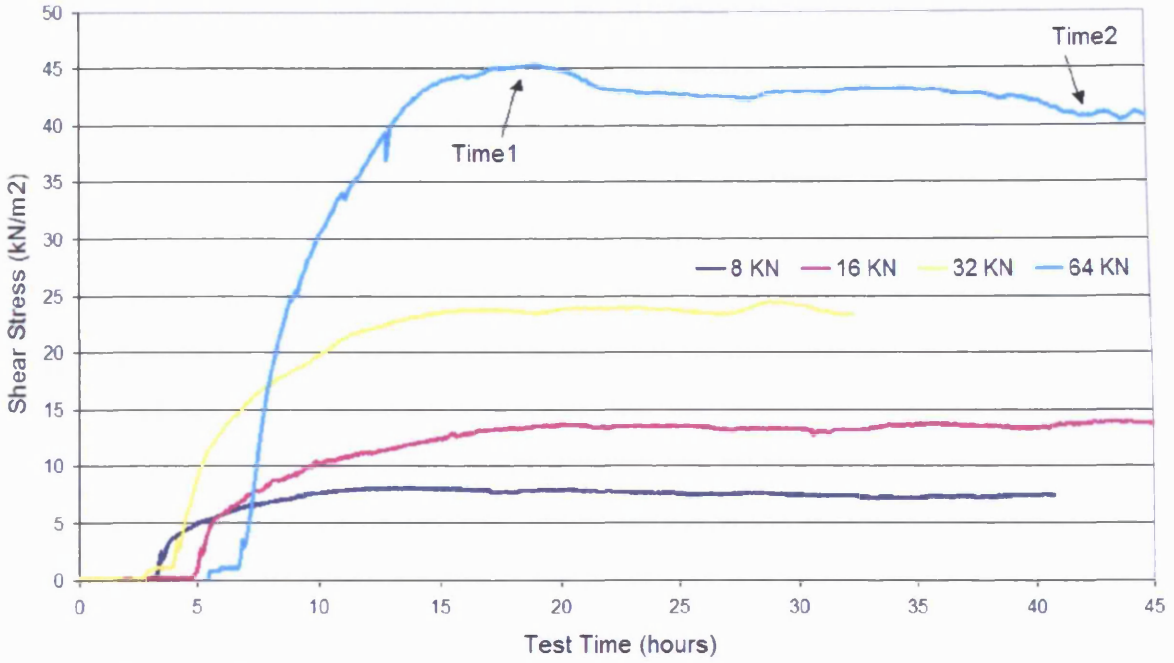

Figure 4.5.5. Shear stress (kN/m^2) over experimental time under imposed conditions of different normal stress for the 10% Silt experimental soil. Note: Time1 = peak strength, Time2 = residual strength.

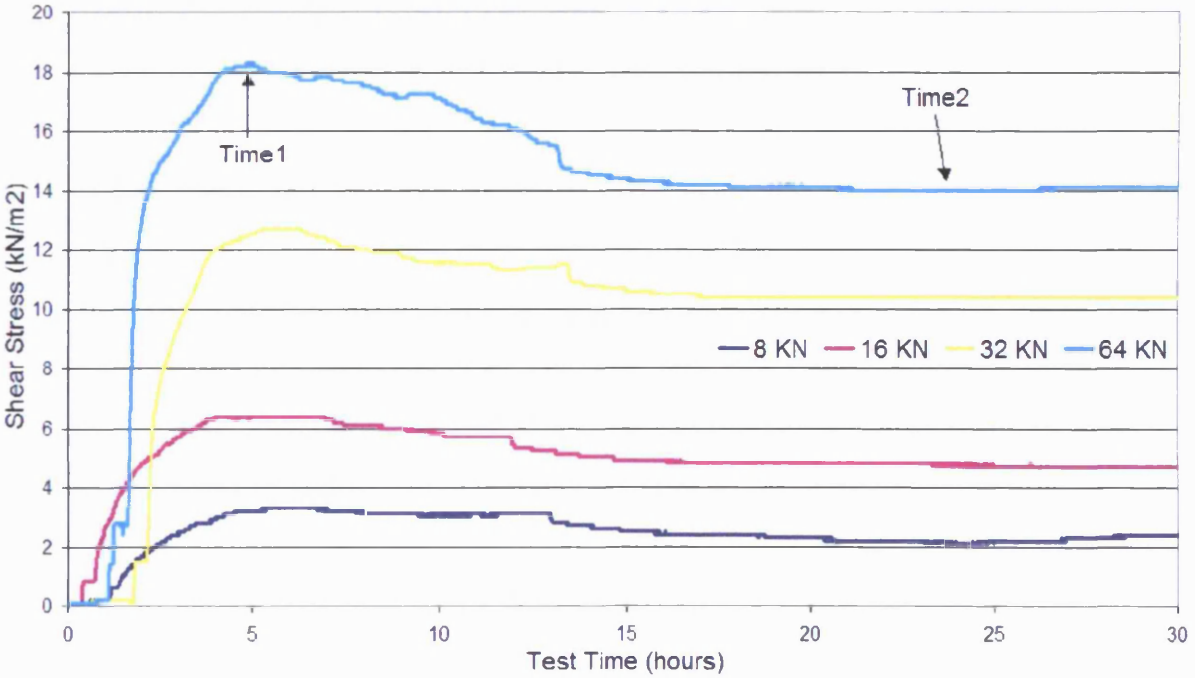

Figure 4.5.6. Shear stress (kN/m^2) over experimental time under imposed conditions of different normal stress for the 20% Silt experimental soil. Note: Time1 = peak strength, Time2 = residual strength.

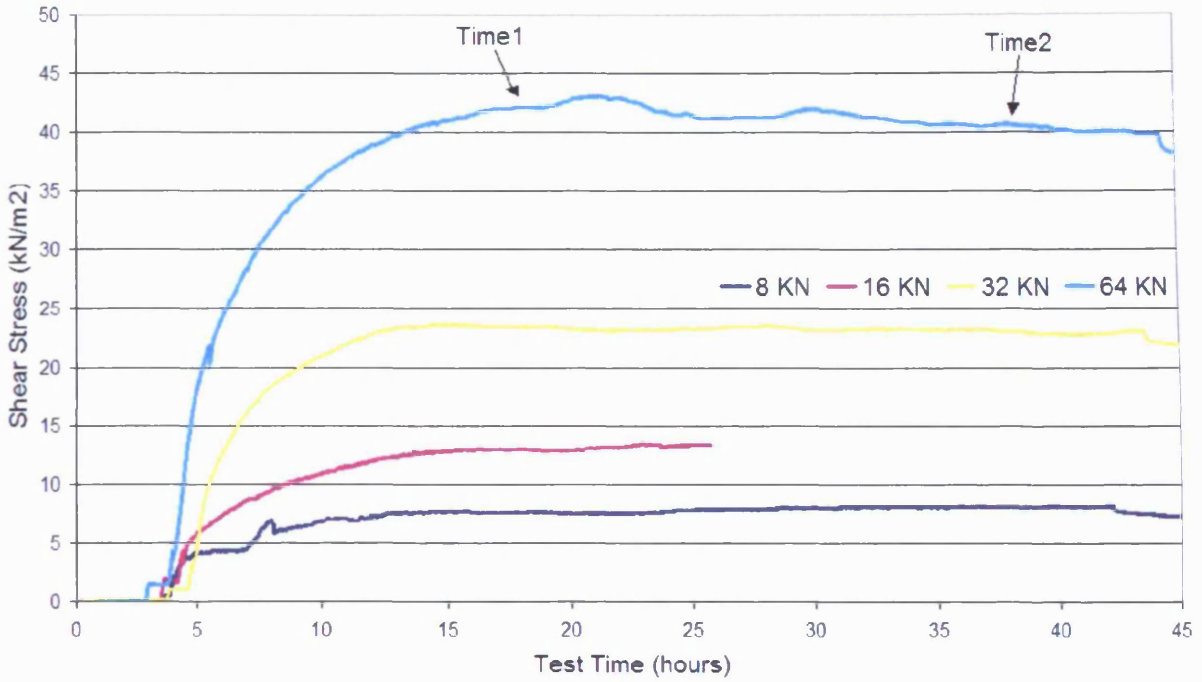

Figure 4.5.7. Shear stress (kN/m^2) over experimental time under imposed conditions of different normal stress for the 10% Clay experimental soil. Note: Time1 = peak strength, Time2 = residual strength.

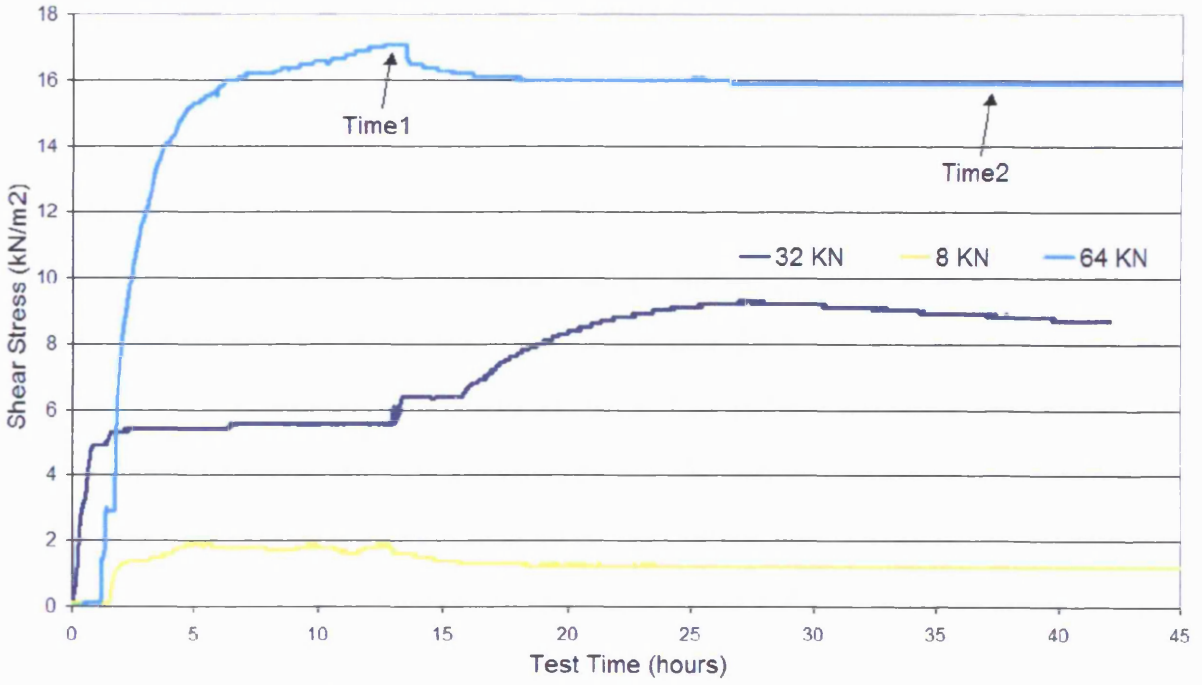

Figure 4.5.8. Shear stress (kN/m^2) over experimental time under imposed conditions of different normal stress for the 20% Clay experimental soil. Note: Time1 = peak strength, Time2 = residual strength.

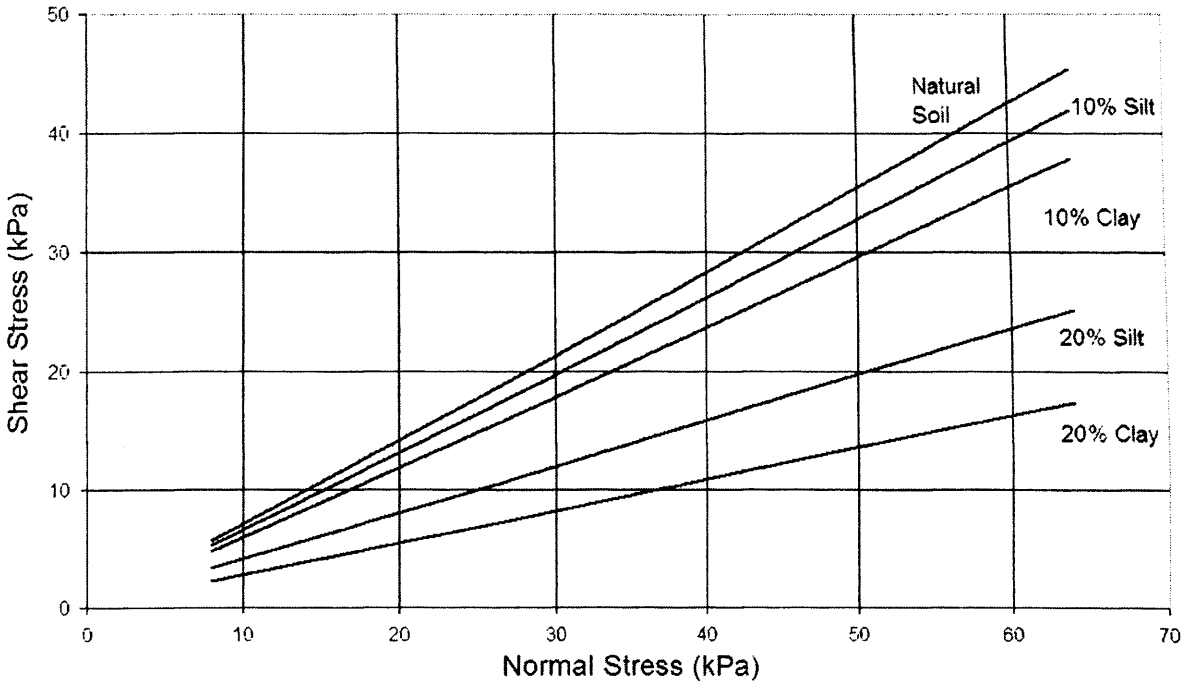

Figure 4.5.9. Maximum peak shear stress (τ) against normal stress (σ) for the various experimental soils used within the centrifuge program.

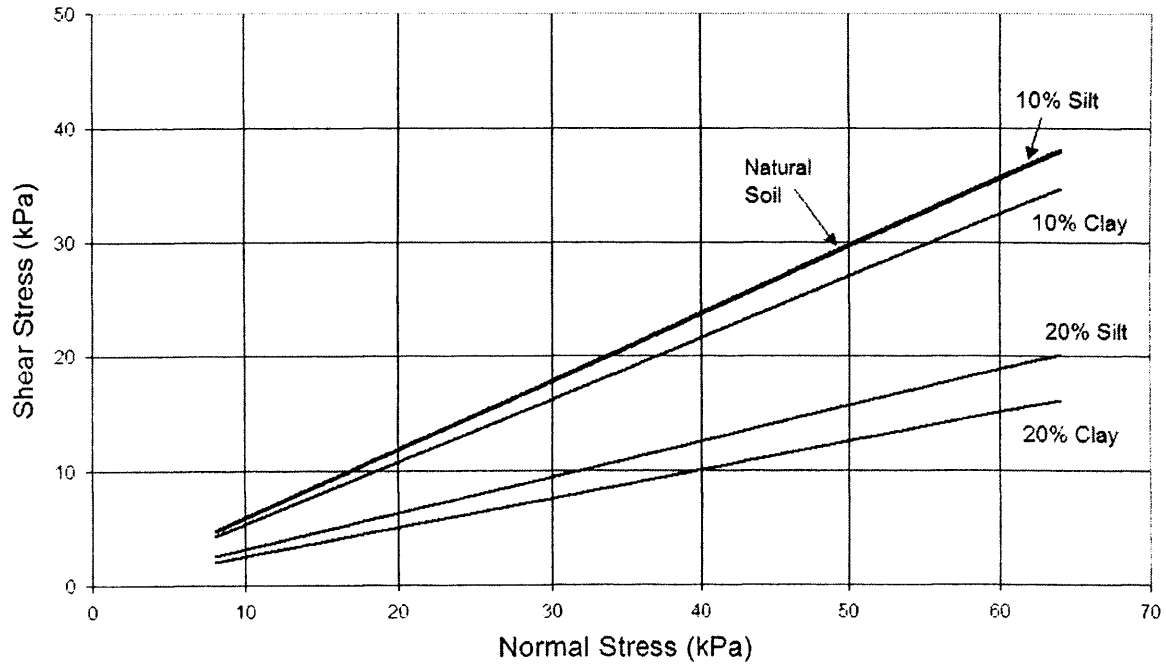

Figure 4.5.10. Residual shear stress (τ) against normal stress (σ) for the various experimental soils used within the centrifuge program.

Table 4.5.3. Summarised shear strength results for the experimental soils used within the centrifuge-modelling program.

Internal Angle of Friction (°)	Natural Soil (NS)	NS + 10% Clay	NS + 20% Clay	NS + 10% Silt	NS + 20% Silt
Ø'	35.3	31.8	15.1	33.2	21.4
$Ø_r$'	30.7	28.4	14.1	30.6	17.4

The addition of silt to the natural soil caused a 6% and 64% reduction in ø' for the 10% and 20% soils – the residual strength also declined in response to increased silt content. The incremental supplement of clay into the natural soil created a 11% and 133% reduction in ø' for both soils (see table 4.5.3). A positive relationship also exists for increasing silt/clay content and decreasing $ø_r$' where the addition of 20% silt and clay caused a respective decrease of 76% and 117% in residual strength. Recorded values from other research projects have observed the same general relationship that residual soil strength becomes reduced with increasing fine material content. For example, Harris (1977) has recorded $ø_r$' values of around 29° and 33° within a silty soil in Okstindan, Norway, whereas McRoberts and Morgernstern (1974) have reported $ø_r$' values of 23° within an illite clay in the Mackenzie Valley, Canada, whilst Skempton & Weeks (1976) also noted lower $ø_r$' values of 14° to 16° in a clayey periglacial soil from Kent.

4.6. Test Soil Description – Mineralogy

The mineralogical composition of the test soils was identified using a widely used research tool, X-Ray Diffraction (XRD). The data presented here was created using a Philips Automated Powder Diffractometer (models PW1710 and PW1840). The soil samples were sieved to the silt particle size range (below 63 microns) and packed into an aluminium holder. The holder was then placed into the central chamber of the Goniometer and bombarded with X-rays generated via a copper/cobalt tube. The diffracted rays were collected by a detector and, using the Bragg equation, converted into a set of d-values for specific intensities. The Bragg equation relates the angles at which X-rays are scattered with forced separation. The derived information from each angled electron deflection was then shown graphically in the form of a diffraction pattern for the soil sample. Specialist software then cross-referenced the diffractogram pattern against a database of 70,000

pre-recorded phases. The XRD can specifically identify every pure mineral or compound because each unit has a unique identifying X-ray diffraction pattern. The XRD 'fingerprinting' process can therefore identify and quantify individual minerals rather than just supply a list of composite elements present within the sediment sample. A number of repeated tests were undertaken for each test soil to account for individual soil sample variability. All results were recorded and are summarised below:

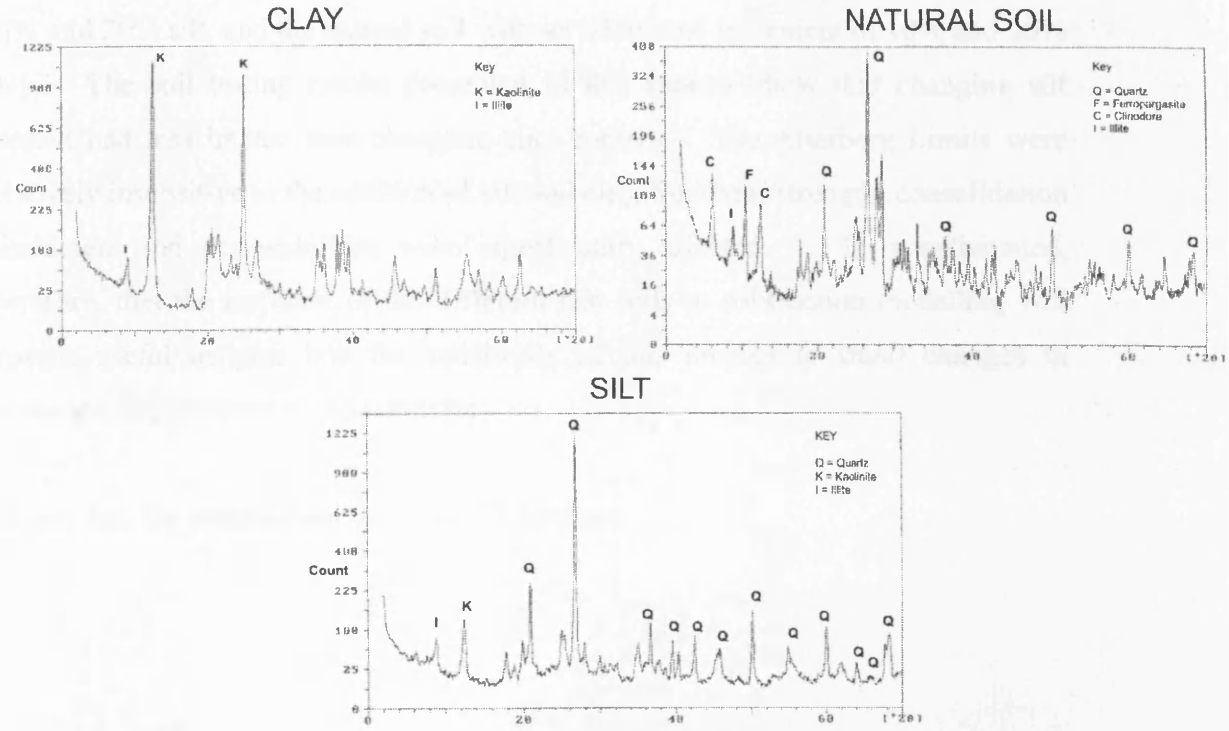

Figure 4.6.1. Diffractograms showing the reflective d-value 'fingerprint' plots for the three base test soils.

Table 4.6.1. Mineral compositions for the three main experimental soils.

Natural Soil (NS)	Silt (SI)	Clay (CL)
Quartz	Quartz	Kaolinite
Ferropargasite	Kaolinite	Illite
Clinodore	Illite	
Illite		

The silt is dominated by quartz with a small additional presence of inactive clay minerals in the form of illite and kaolinite. The natural soil is predominantly quartz-based; the mineralogy reflects the original bedrock source (as described in section

4.1) where the schist consists of a limited range of mineral types (Mottershead, 1977).

4.7. Overall Test Soil Categorisation

The modelling experiments described in this thesis investigate the significance of changing soil properties to the rate and style of mass movement. Therefore, slope models were formed in five different soil types; the natural soil, the natural soil plus 10% and 20% silt, and the natural soil with an additional increment of 10% and 20% clay. The soil testing results presented in this chapter show that changing silt content had less impact than changing clay content. The Atterberg Limits were relatively insensitive to the addition of silt and clay, but shear strength, consolidation parameters and permeabilities were significantly affected. It is anticipated, therefore, that the response of the different test soils to solifluction modelling will provide useful insights into the sensitivity of this process to small changes in geotechnical properties of the substrate.

All test data are summarised in Table 4.7.1 below:

Table 4.7.1. A summary of the main geotechnical parameters influencing the behaviour of the five different test soils used within the centrifuge-modelling program.

Parameter	Natural Soil (NS)	Silt (SI)	Clay (CL)	NS + 10% CL	NS + 20% CL	NS + 10% SI	NS + 20% SI
LL	21	25	30	21	20	20	21
PL	34	39	56	36	38	34	35
PI	13	14	26	15	18	14	14
AI	2.48	0.38	0.34	1.24	0.74	1.55	0.95
Sand (%)	69.35	0.4	0	62.42	55.48	62.42	55.48
Silt (%)	20.33	63.93	24.2	25.55	20.34	28.55	29.82
Clay (%)	5.23	36.07	75.8	12.03	24.18	9.03	14.7
M_V (m^2/kN)	0.00071	Nd	Nd	0.00106	0.00119	0.00074	0.00103
C_V (m^2/kN)	12.7377	Nd	Nd	6.62849	5.59846	14.9531	10.7406
k (m/year)	0.16958	Nd	Nd	0.13153	0.12398	0.20699	0.20719
Ø'	35.3	Nd	Nd	31.8	15.1	33.2	21.4
$Ø_r$'	30.7	Nd	Nd	28.4	14.1	30.6	17.4

Nd = No Data

CHAPTER FIVE : Centrifuge Modelling Program – Experimental Results

This chapter reports experimental results derived from thirty-two centrifuge flights that were undertaken over a period of two years. These flights were used to model nine separate slope models through a number of distinct freeze-thaw cycles (see table 5.0.1). The chapter outlines data recorded during each freeze-thaw phase for each model; this includes information on thermal regime, frost heave, thaw settlement, pore water pressure, surface movement, subsurface volumetric movement, and soil microstructure.

Table 5.0.1. Centrifuge modelling program.

SERIES NUMBER	SLOPE (°)	HOST MATERIAL	TEST ELEMENT	F/T CYCLES	SERIES REF	SERIES DATE
1	12	Lacustrine Silt	Proof Test	1	PROOF	Sep-00
2	12	Natural	Primary	4	12D/NS	Dec-00
3	16	Natural	Primary	1	16D/NS	Mar-01
4	8	Natural	Primary	4	FAULT	Jun-01
5	4	Natural	Primary	4	4D/NS	Sep-01
6	8	10% Silt	Secondary	2	8D/10S	Dec-01
7	12	10% Clay	Secondary	1	12D/10C	Feb-02
8	4	10% Silt	Secondary	4	4D/10S	May-02
9	8	Natural	Primary	4	8D/NS	Jun-02
10	8	10% Clay	Secondary	1	8D/10C	Jul-02
11	4	20% Silt	Secondary	4	4D/20S	Aug-02
12	4	10% Clay	Secondary	4	4D/10C	Nov-02
13	4	20% Clay	Secondary	4	4D/20C	Dec-02

Results will not be presented for test series one (PROOF) as this slope model sequence used lacustrine silt as its base material (see section 4.1.2) and was only used to resolve electronic data capture issues and scrutinise the overall robustness of the centrifuge-modelling methodology previously described in Chapter 3. It should also be noted that a replica test series was undertaken for Series 8D/NS because external water supply problems compromised the integrity of the last freezing phase during the original test sequence (see table 5.0.1). For this reason, Series 8D/NS will be regarded as the tangible slope model. The previously acquired dataset from series FAULT has been presented within Appendix A.1.

5.1. Ambient Laboratory Conditions

Thermal conditions within the centrifuge chamber or pit were recorded for every thaw phase to ensure that model conditions were not being adversely affected by extraneous seasonal climatic factors. Tables 5.1.1, 5.1.2 and 5.1.3 present the ambient laboratory conditions alongside the duration of each test flight.

Table 5.1.1. Test details for natural soil test series.

	12D/NS				8D/NS				4D/NS			
Thaw Cycle	*1*	*2*	*3*	*4*	*1*	*2*	*3*	*4*	*1*	*2*	*3*	*4*
Minimum Pit Temperature (°C)	16.4	16.2	15.1	15.4	20.4	18.9	18.8	19.1	17.8	19.6	18.6	19.4
Maximum Pit Temperature (°C)	22	22.4	21.8	20.6	24.1	23.8	24.2	23.8	22.1	23.7	22.7	23.2
Rise in Ambient Air Temperature (°C)	5.6	6.2	6.7	5.2	3.7	4.9	5.4	4.7	4.3	4.1	4.1	3.8
Prototype Test Duration (days)	23.8	33.1	29.5	32.3	23.0	26.6	27.8	29.1	20.7	24.0	24.3	22.8

Prior to testing the centrifuge chamber conditions were controlled by existing ambient conditions. For example, Series 8D/NS had the highest temperature (20.4°C) and warmest pre-test average (19.3°C) as the test occurred in June. In comparison, the majority of testing for Series 12D/NS took place in December when the lowest starting pit temperature (15.1°C) and the coldest pre-test average (15.7°C) were recorded.

Table 5.1.2. Test details for series involving incremental additions of silt.

	4D/10S				4D/20S			
Thaw Cycle	*1*	*2*	*3*	*4*	*1*	*2*	*3*	*4*
Minimum Pit Temperature (°C)	18.8	19.4	19.2	20.1	21.8	20.7	21	20
Maximum Pit Temperature (°C)	24.1	24.2	24.4	24.9	25.1	23.2	25.6	24.8
Rise in Ambient Air Temperature (°C)	5.3	4.8	5.2	4.8	3.3	2.5	4.6	4.8
Prototype Test Duration (days)	20.3	22.5	22.8	19.5	15	20.8	18.8	20.4

However, after the commencement of a test flight the maximum pit temperature was unrelated to the pre-existing seasonal ambient conditions. Variation in the maximum temperatures measured in the pit during tests was negligible throughout the year, for example in August the maximum temperature average was 22.9°C

(Series 4D/NS) compares very favourably to the December maximum temperature average of 21.7°C (Series 12D/NS).

Table 5.1.3. Test details for series involving incremental additions of clay.

	4D/10C				4D/20C			
Thaw Cycle	*1*	*2*	*3*	*4*	*1*	*2*	*3*	*4*
Minimum Pit Temperature (°C)	18.8	18.1	18.5	19.3	17.6	17	15.3	16.5
Maximum Pit Temperature (°C)	23	22.5	23.2	22.6	20.3	22.3	20.8	21.5
Rise in Ambient Air Temperature (°C)	4.2	4.4	4.7	3.3	2.7	5.3	5.5	5
Prototype Test Duration (days)	20.3	19.3	24.4	16.8	26.4	28.4	30.8	26.7

The centrifuge chamber temperature was broadly controlled by the speed of gondola rotation (RPM) and the temperature quickly reached a maximum plateau because the test platform generated a large amount of frictional resistance via airflow passing across the centrifuge gondola (see fig. 3.1.2).

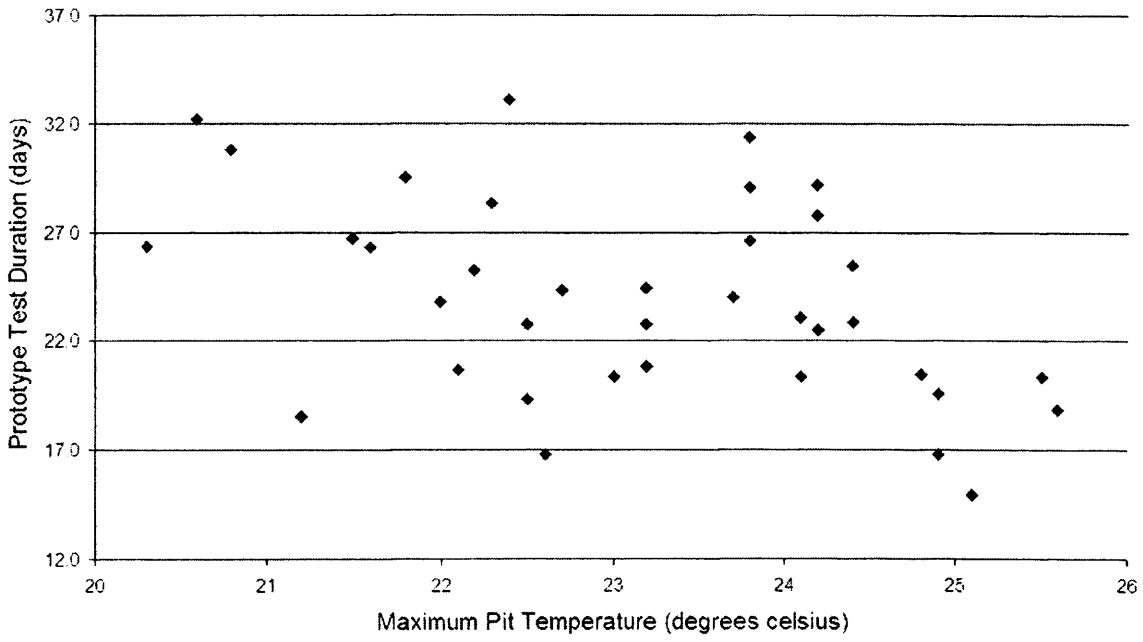

Figure 5.1.1. Relationship between maximum centrifuge chamber temperature and the duration of a slope model thaw phase (test flight).

The rotation of the test platform remained consistent for every thaw phase and thereby a constant thermal environment was generated within the centrifuge chamber for each test (see table 5.0.1). As in-flight ambient conditions remained consistent

within the laboratory chamber, the duration of a test flight was not related to either the maximum chamber temperature (see fig. 5.1.1) or the total rise in chamber temperature (see fig. 5.1.2). It is therefore concluded that the two variables manipulated within the experimental methodology – soil ice content and slope geometry – were principally responsible for influencing the duration of each thaw phase (test flight).

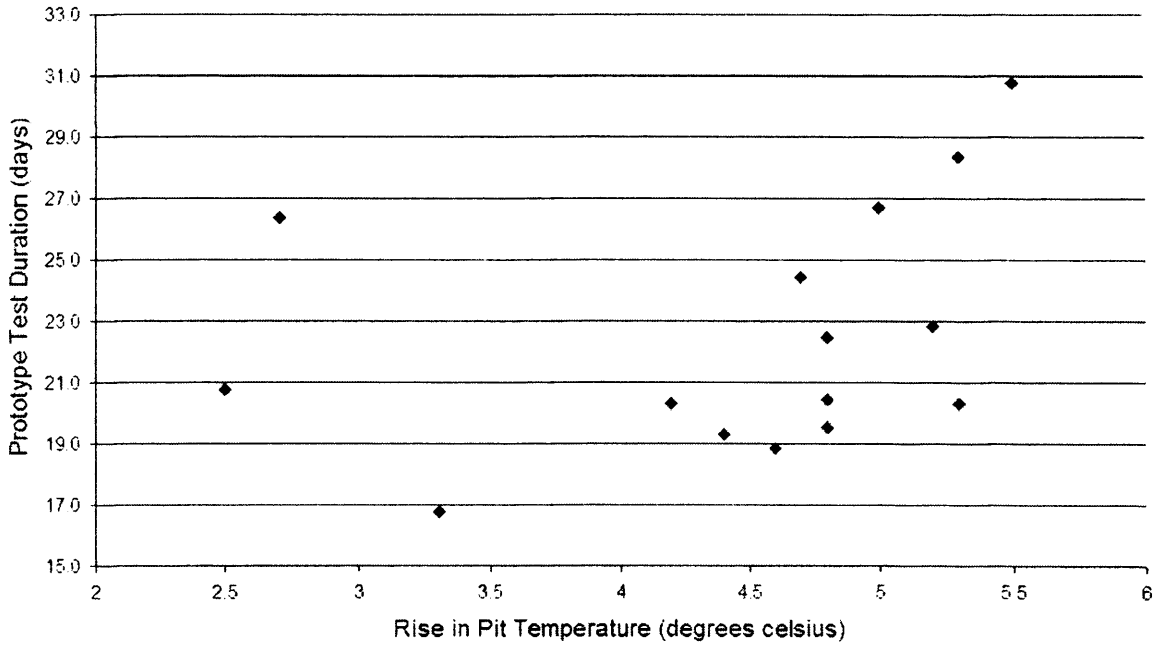

Figure 5.1.2. Relationship between the rise in centrifuge chamber temperature and the duration of a slope model thaw phase (test flight).

5.1.1. Summary

- Ambient laboratory conditions were not adversely affected by seasonal temperature conditions and remained steady within all test series thaw cycles.
- Maximum pit temperatures were defined by the rotational speed of the centrifuge gondola at 10g which remained constant for all test series.

5.2. Thermal Regime

Slope models were subjected to four cycles of freezing and thawing – each cycle was monitored via ten embedded thermocouples (see fig. 3.3.3). During the thaw phase the zero degree Celsius isotherm was regarded as the discrete boundary between

frozen and thawed soil. It was decided to define 'thawed material' as existing above the zero degree isotherm, and frozen below it because (a) freezing point depression in the test soils could not be determined under the testing regime, and (b) progressive decrease in the proportion of unfrozen soil water below 0°C makes precise definition of phase transition difficult, especially in the models with additional finer fractions (either silt or clay) (for discussion see Williams & Smith, 1989, p.175). The use of the zero degree isotherm to define phase change therefore enabled the correlation of thermal and pore-water pressure information between different test series.

Prior to testing, the frozen slope models consistently demonstrated an internal temperature profile of between –2°C (model surface) to –8°C (model base). However, as warm air was passed across the model surface in the centrifuge, two distinctive patterns of thaw penetration were observed. The thaw phase illustrated in Figure 5.2.1 (8° slope, natural soil) shows a consistent progression of the thaw front through the upper layers of the soil model: see for example the steady linear rise in soil temperature at 30mm depth. The rate of penetration is then observed to decrease at greater depth.

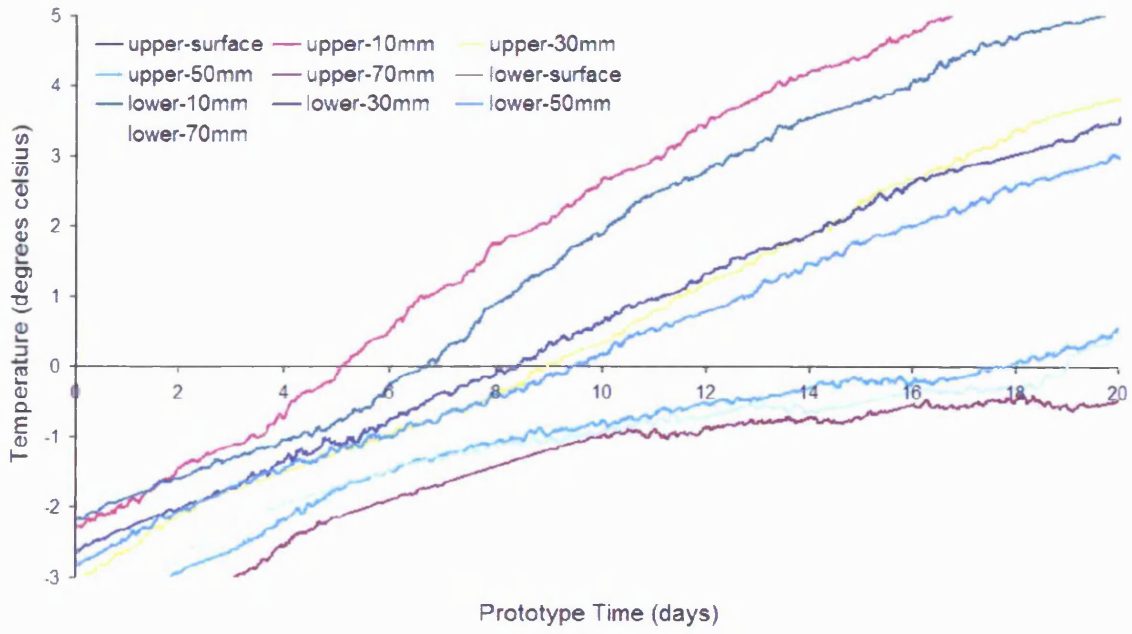

Figure 5.2.1. Slope model thaw phase for series 8D/NS (thaw cycle one).

The consistent increase in soil temperature shown in Figure 5.2.1 can be contrasted with the attenuated pattern observed within Figure 5.2.2 where a prolonged delay occurred during the progression of the zero degree isotherm through slope model. This period when soil temperatures remained in the approximate range of –1°C to 0°C for several hours at model time and several days at prototype time, corresponds with the release of latent heat during soil ice melting, and is termed the "zero curtain" (section 2.1.4; Williams & Smith, 1989, p.105).

Clearly, once all ice has melted and all latent heat released, the soil temperatures rise once again in response to the downward heat flux through the soil. The duration of the zero curtain can therefore give an indication of the distribution of segregated soil ice within a particular slope model (Penner & Goodrich, 1980). Figure 5.2.1 suggests that the slope model had a roughly uniformly distributed, relatively low ice content, whereas Figure 5.2.2 suggests that ice content was concentrated within the middle to lower portion (30mm-50mm) of the slope model profile. The style of thaw penetration was used to visually assess all the model thaw phases in order to infer the distribution of segregated ice within the initial frozen slope model (see table 5.2.1). The full thermal dataset is presented in Appendix A.1.

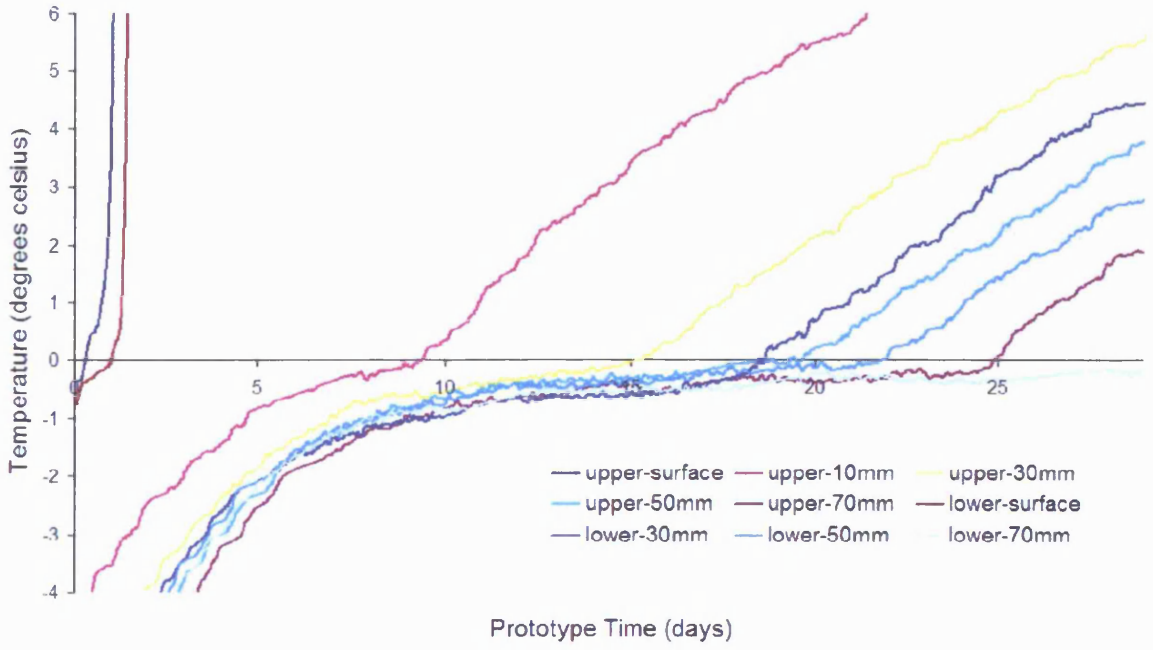

Figure 5.2.2. Slope model thaw phase for series 4D/NS (thaw cycle four).

Table 5.2.1. Inferred presence of segregated ice within slope model profile.

Series	Thaw Cycle	Model Depth (mm)			
		0-15	*15-35*	*35-55*	*55-70*
12D/NS	1		X	X	X
	2	X		X	X
	3		X	X	
	4	X	X	X	X
8D/NS	1				X
	2			X	X
	3		X	X	X
	4		X	X	X
4D/NS	1			X	
	2		X	X	X
	3			X	X
	4		X	X	X
4D/10S	1				X
	2			X	X
	3			X	X
	4		X	X	X
4D/20S	1			X	
	2		X	X	X
	3		X	X	X
	4				X
4D/10C	1				X
	2			X	X
	3				X
	4			X	X
4D/20C	1			X	X
	2			X	X
	3			X	X
	4			X	X

Table 5.2.1 suggests that the majority of slope models contained a concentration of segregated ice towards the model base (between 35mm-70mm depth). This may have been due to the model freezing conditions, (i.e. the basal water supply and single-sided downward freezing), or through greater levels of near-surface heat conduction generating a higher thermal gradient and therefore more rapid freezing in the upper layers (Qiang, 1988). However, the zero curtain effect may also have been shortened in near-surface regions of the soil profile because the surface temperatures imposed a steeper thermal gradient near the surface than was the case at depth, leading to more rapid conduction of latent heat. Additionally, seepage away of meltwater as thawing took place was more rapid near the surface than at depth, again facilitating warming (Loch & Kay, 1978).

Each soil model contained two instrumentation strings of five thermocouples placed within the upper and lower portions of the slope. It was occasionally observed that the model thaw phases contained a lag period in the rate of thaw penetration between upper and lower strings (see fig. 5.2.3). Models appeared to show considerable variability in behaviour across a complete four thaw phase series (e.g. fig. 5.2.4). Thawing took longer in the lower slope of the 4° model than the upper slope, with thaw penetration being significantly faster in the upper slope towards the end of the test (see fig. 5.2.3). In contrast, the 12° model showed a fairly consistent thaw rate. This may have reflected differences in soil ice contents, but it is noteworthy that during thaw of the lower gradient model, cold melt water was observed to pond around the central drain, thereby insulating the underlying material from higher air temperatures and slowing thaw penetration later in the thaw periods.

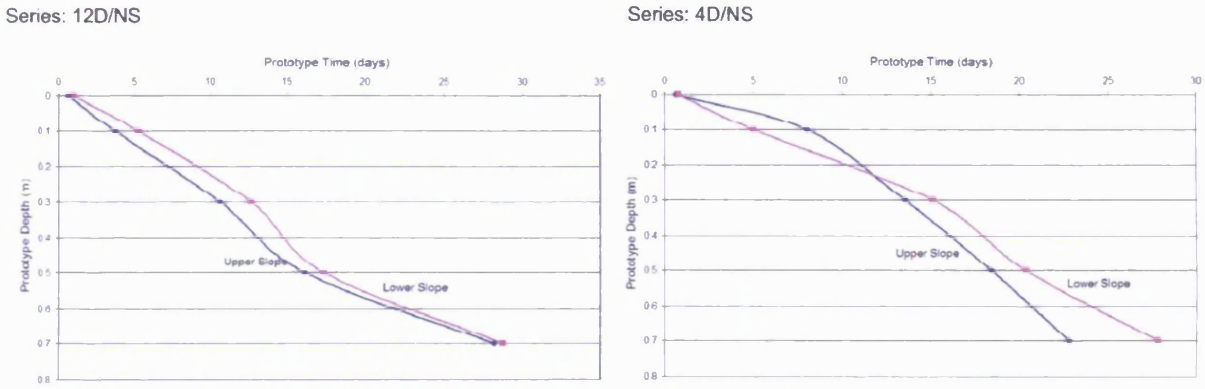

Figure 5.2.3. Average penetration of the zero degree isotherm across the upper and lower slope model thermocouple strings through four thaw phases within the 4° and 12° natural soil models.

Figure 5.2.4 serves to highlight the inherent variability in thaw rates between successive freeze thaw cycles during individual tests. This intra-test variability was probably a function of the amount of ice segregation during successive freezing cycles (see section 5.8). Although water supply and the temperature of the surface freezing plate were not varied greatly between cycles, the experimental design aimed to investigate the significance of small variations in frost heave upon gelifluction movement, so that freezing conditions, particularly water supply, were changed slightly to achieve this aim prior to each freezing phase.

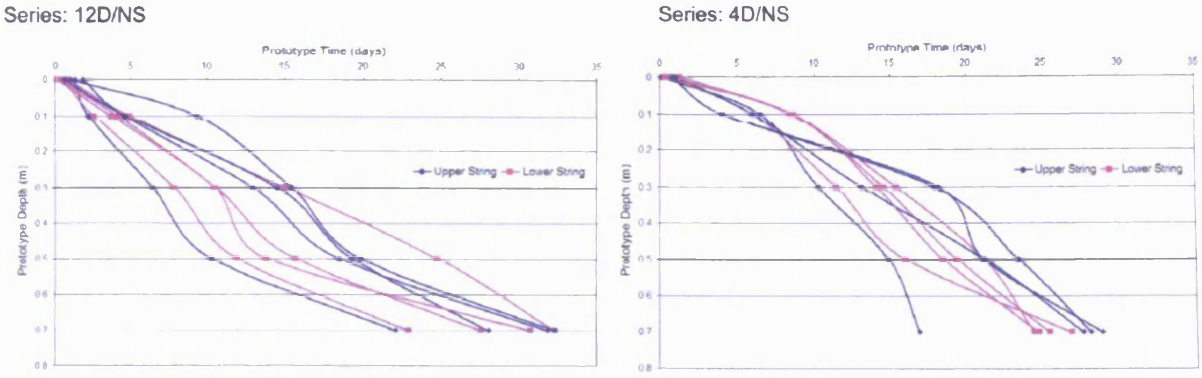

Figure 5.2.4. Average penetration of zero degree isotherm through the upper and lower slope model thermocouple strings for each individual thaw phase within the 4° and 12° natural soil models.

In general, many tests showed a slight reduction in thaw rate in the lower slope towards the end of a given thaw phase. This effect is thought to be associated with drainage of meltwater from the upper slope, reducing the thermal capacity of the upper slope thawed soil, and promoting more rapid heat flux to the thawing lower layers (Williams, 1991). In contrast, drainage of cold meltwater from upslope through the lower slope thawed layer tended to reduce its temperature, raise its moisture content and heat capacity, and hence slowed the thawing of the deeper layers.

Table 5.2.2. Average lag period between thaw penetration at different depths between upper and lower thermocouple strings across all four thaw phases. Note: A negative lag period indicates lower string passed zero degree isotherm before upper string.

Series	Average Lag Period (prototype days)		
	at 30mm	*at 50mm*	*at 70mm*
12D/NS	-2.05	-1.23	-0.58
8D/NS	+2.05	+4.67	+2.84
4D/NS	-1.57	-1.97	-5.03
4D/10S	-1.11	+3	+0.47
4D/20S	-0.36	+1.58	+4.78
4D/10C	-1.81	+0.57	Nd
4D/20C	-3.55	-1.27	+2.81

Nd = 'Thermocouple Failure'

5.2.1. Rate of Thaw Penetration

Table 5.2.3 shows that the overall rate of thaw penetration was modified by incremental changes to soil type and slope geometry in successive test series. The overall effect of slope angle upon the rate of thaw penetration appeared negligible

beyond influencing localised hydraulic conditions. The rate of thaw penetration into the slope model would therefore appear to be dependent on the latent heat, thermal conductivity and specific heat capacity of the individual soil mixture rather than the slope gradient (e.g. Penner, 1970).

Table 5.2.3. Average rate of thaw penetration for each thaw phase.

	Prototype Scale	
Series	mm/day	m/day
12D/NS	24.58	0.025
8D/NS	33.11	0.033
4D/NS	27.69	0.028
4D/10S	34.22	0.034
4D/20S	43.96	0.044
4D/10C	31.95	0.032
4D/20C	25.15	0.025

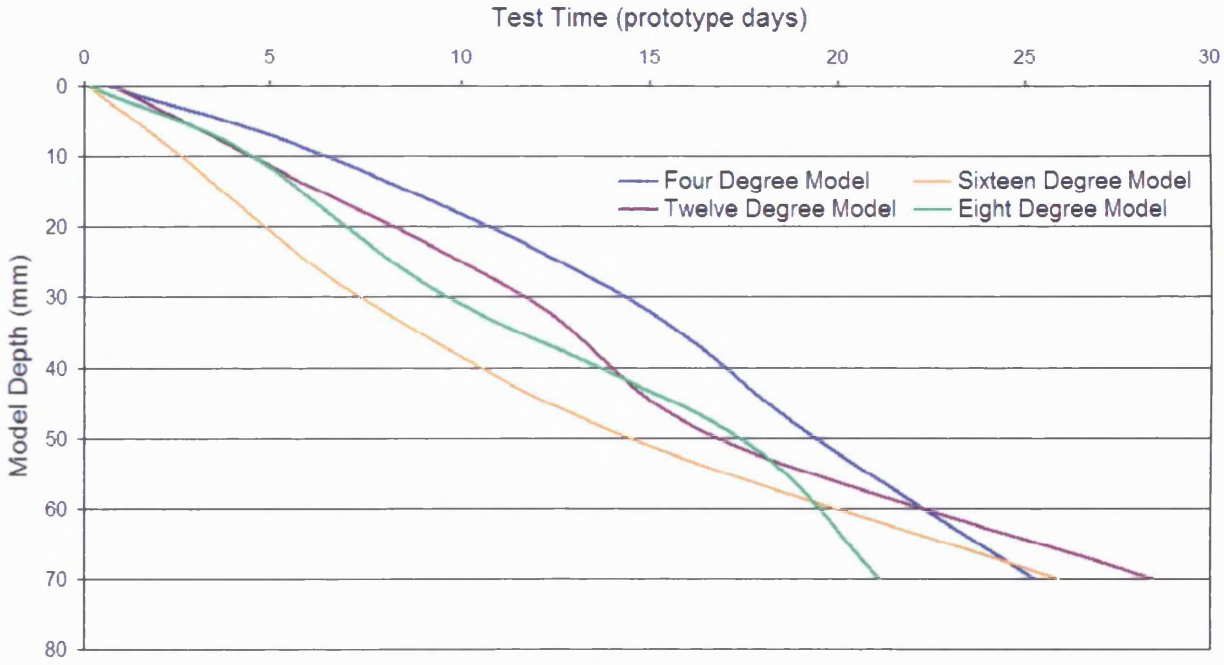

Figure 5.2.5. Average per thaw cycle progression of zero degree isotherm through the natural soil (NS) slope models.

Figure 5.2.6 suggests that there was a clear relationship between the amount of additional silt and clay within the model soils and the rate of thaw penetration. Figure 5.2.7 illustrates the effect of additional silt content upon the progression of the zero degree isotherm through the soil model. In the 4° model, the addition of ten and twenty percent silt when compared to the natural soil was associated with an average thaw rate acceleration of 19% (4D/10S) and 37% (4D/20S). Figure 5.2.9

indicates that the progression of the zero degree isotherm was on average 13% faster in the natural soil plus 10% clay, compared to the equivalent 4° natural soil model, but was 10% slower when the increment of clay was increased to 20% (4D/20C) (see table 5.2.3).

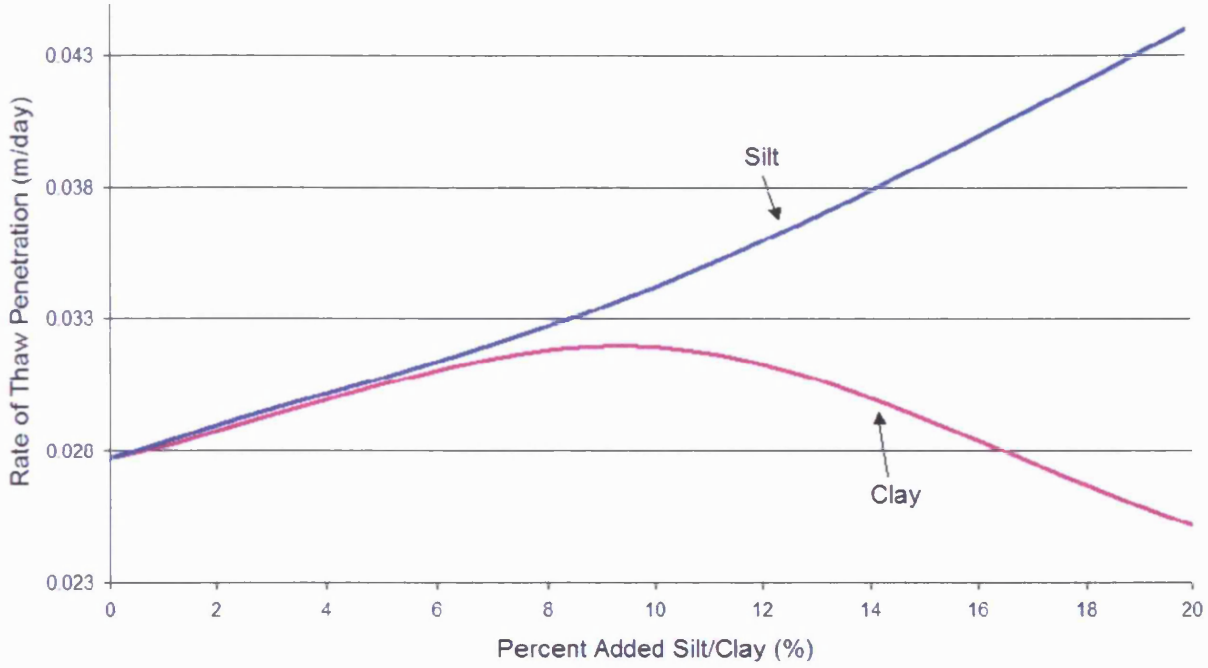

Figure 5.2.6. The effect of added fine material upon the rate of thaw penetration.

The observed relationship between soil granulometry and rate of thaw appears counter-intuitive with respect to the incremental silt series (4D/10S & 4D/20S) (fig. 5.2.7). It would be expected that under constant thermal and hydraulic conditions the rate of thaw penetration would be consistently lower with increased percentages of silt, as additional silt content would normally increase the frost susceptibility of the material leading to increased segregation ice content (Konrad & Morgenstern, 1980). The anticipated increase in ice segregation may not have occurred as a result of (a) the increments of silt were insufficient to significantly alter frost susceptibility, or, more likely, (b) problems with freezing of the input water pipes during preparation of the two silt enhanced slope models restricted water flux to the freezing soil, and prevented the full frost heave potential of these models being achieved. The influence of the overall amount of soil ice within the model on the rate of thaw penetration can be clearly identified within Figure 5.2.8.

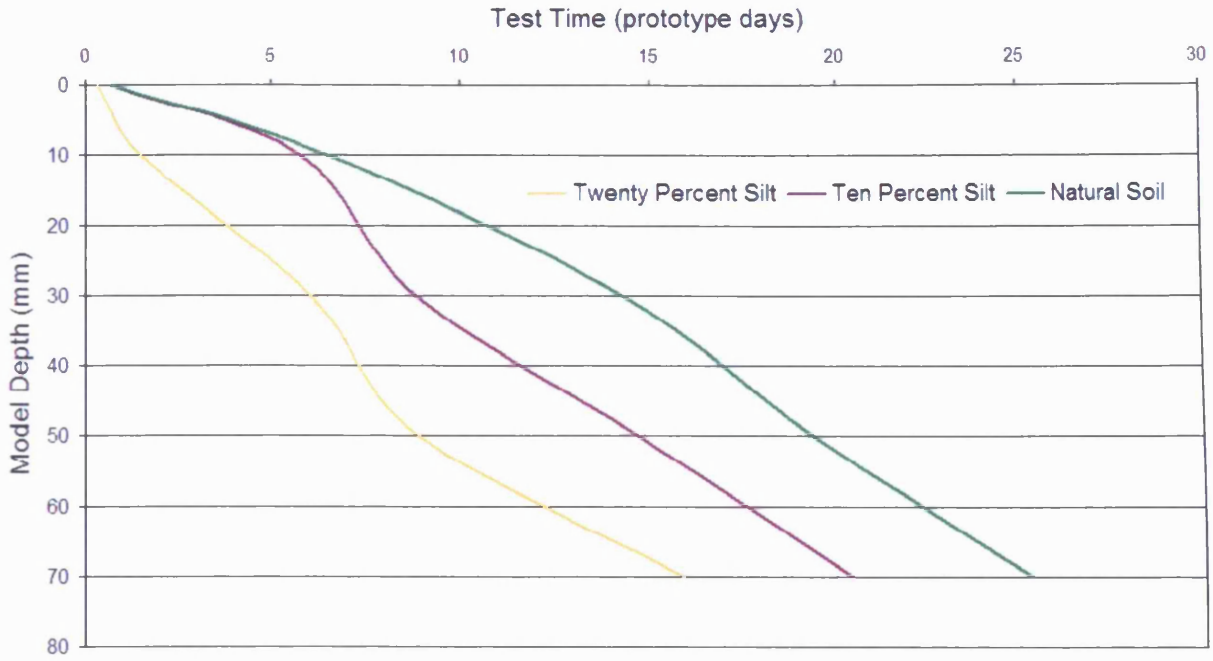

Figure 5.2.7. Average per thaw cycle progression of zero degree isotherm through the additional silt (10S & 20S) slope models.

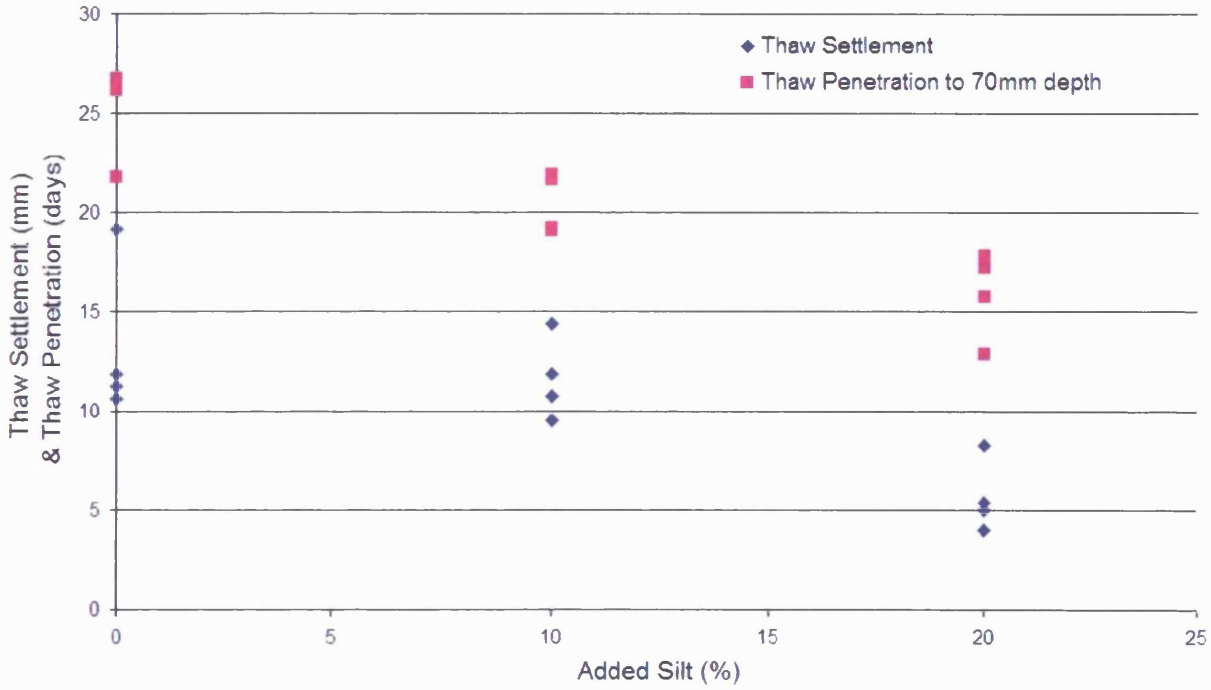

Figure 5.2.8. Average per thaw cycle progression of zero degree isotherm through the additional silt (10S & 20S) slope models.

Figure 5.2.9 outlines the relationship observed between incremental additions of clay within series 4D/10C and 4D/20C and the rate of thaw penetration. The influence of the addition of clay to the soil may either (a) increase frost susceptibility and

cryosuction, by reducing average pore size (Taber, 1930; Williams, 1972), or (b) reduce permeability sufficiently to restrict water migration to the freezing front, thereby reducing frost heave (Beskow, 1935; Palmer, 1967).

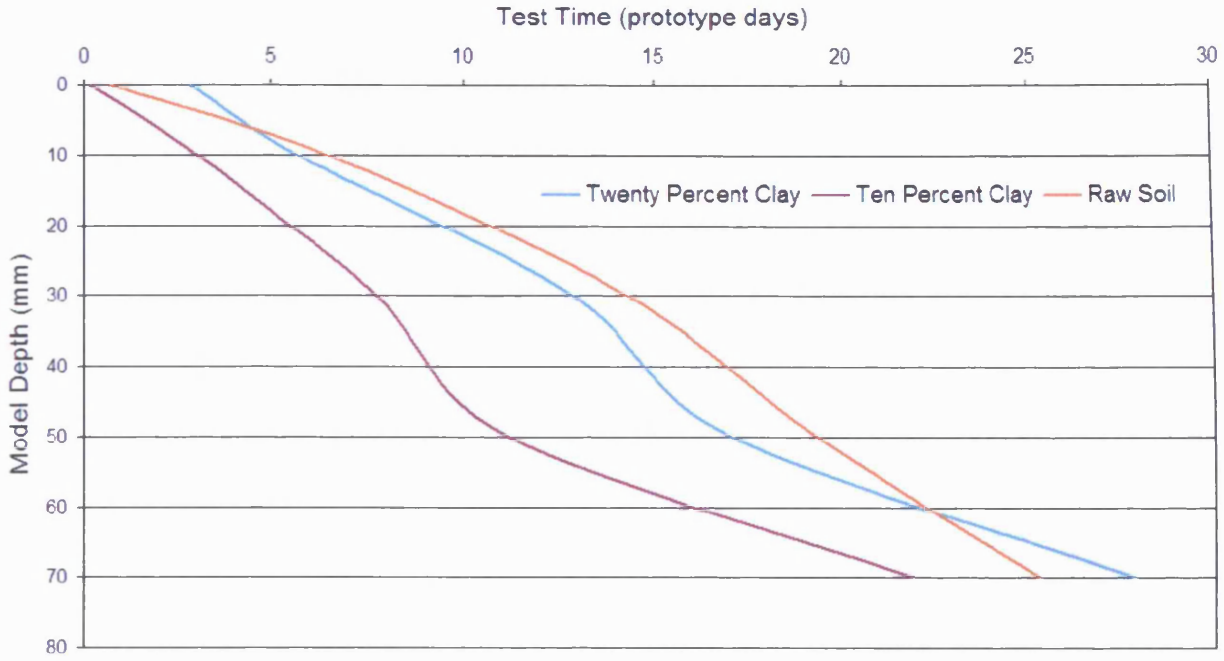

Figure 5.2.9. Average per thaw cycle progression of zero degree isotherm through the natural clay (10C & 20C) slope models.

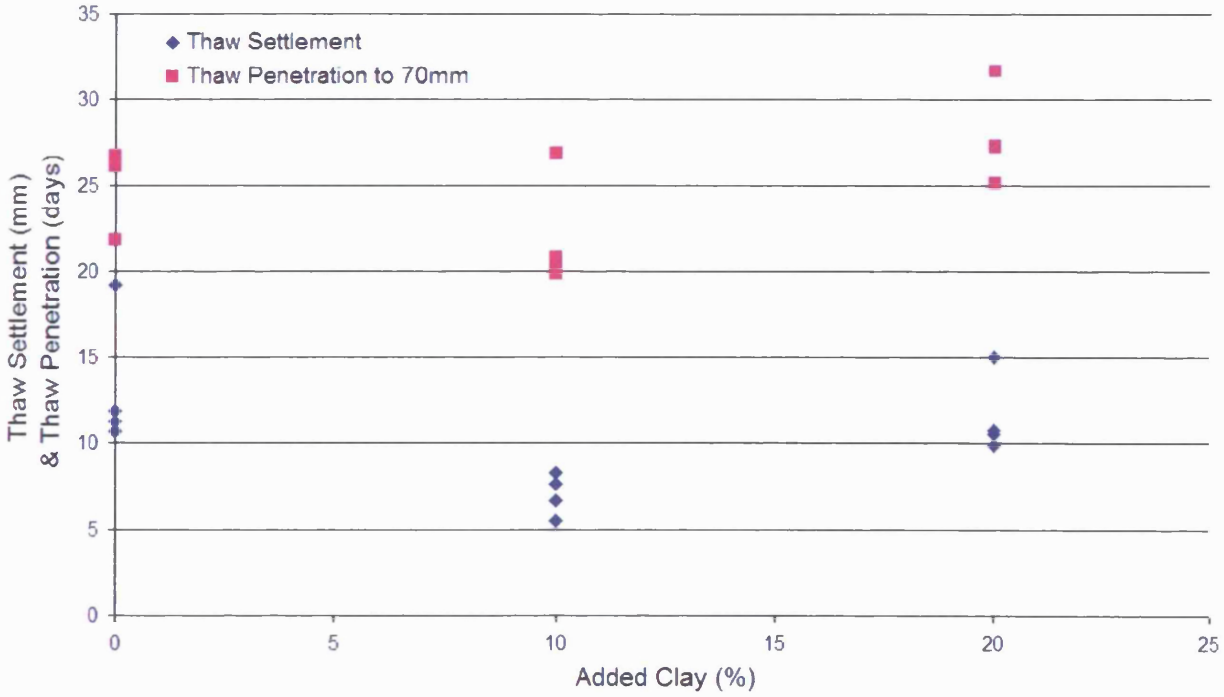

Figure 5.2.10. Average per thaw cycle progression of zero degree isotherm through the additional silt (10S & 20S) slope models.

Figure 5.2.10 indicates the relationship between the amount of thaw settlement and the duration of the thaw period within series 4D/10C and 4D/20C. The addition of ten percent clay to the natural soil was associated with a slight increase in thaw penetration rate and corresponding decrease in thaw subsidence, but the addition of twenty percent clay caused an overall decrease in the rate of thaw and higher thaw settlement. The variations were, however, relatively small, and it is considered that as with the silt models, slight variation in external water supply to the model during freezing were probably controlling frozen ice content rather than the intrinsic soil properties.

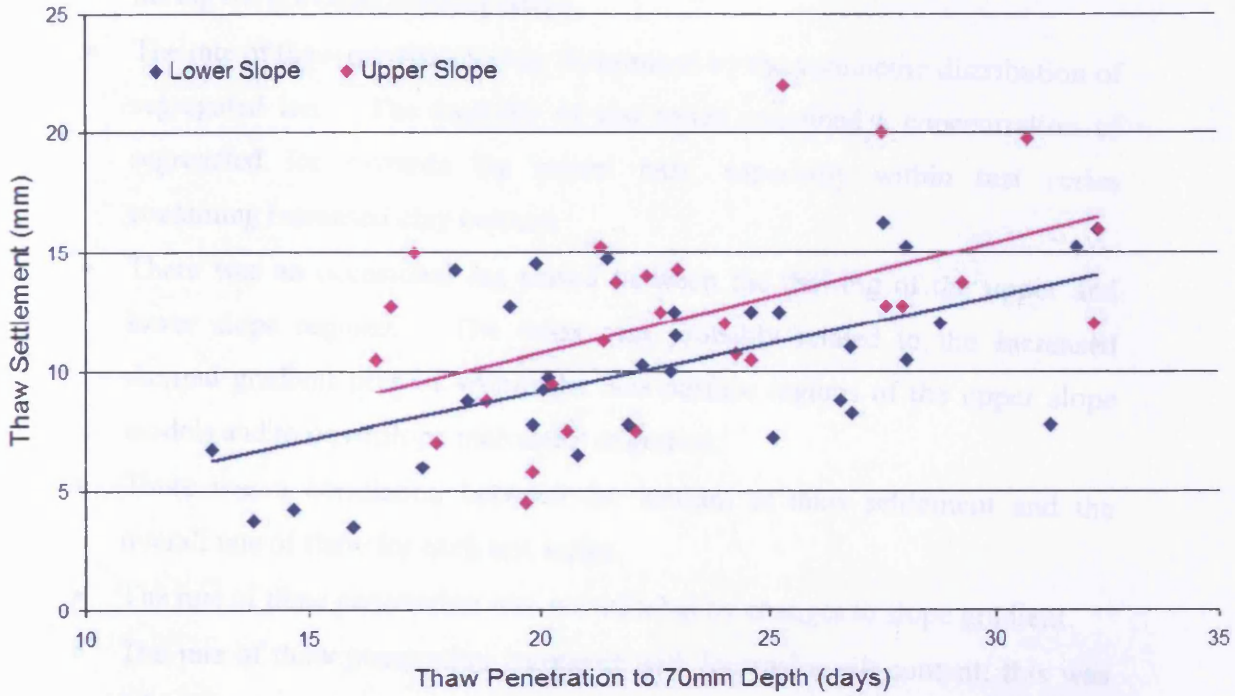

Figure 5.2.11. Time for progression of zero degree isotherm to the model base related to the overall amount of thaw settlement for the localised area around both instrumentation strings for all test series.

The overall distribution of soil ice has been shown to determine the relative rate of thaw progression through a particular depth, whilst the overall ice content of the whole slope controlled the overall time taken to complete each thaw phase. The thaw settlement within the soil model is the best indicator of the amount of segregated ice melted during each thaw phase. Figure 5.2.11 therefore reiterates the overall relationship by illustrating that greater amounts of thaw settlement lead to slower the progression of the zero degree isotherm. Overall, it can therefore be concluded that the thermodynamic behaviour of the warming soil slope models was an ice-content related process. The regression lines suggest that for a given rate of

thaw, the thaw settlement was slightly greater in the upper than in the lower slope sections. It should be borne in mind however, that downslope solifluction progressively lowered the slope gradient, with net soil loss on the upper slopes exceeding soil loss on the lower slopes. Hence this contrast may in part be reflected in this secondary control on the geometry of the thawed slope models.

5.2.2. Summary

- A zero degree curtain effect was noted within most test series. The presence of a zero curtain was used to infer the depth of segregated ice formation during the previous freezing phase.
- The rate of thaw penetration was determined by the volumetric distribution of segregated ice. The majority of test series contained a concentration of segregated ice towards the model base, especially within test series containing increased clay content.
- There was an occasional lag period between the thawing of the upper and lower slope regions. The delay was probably related to the increased thermal gradient present within the near-surface regions of the upper slope models and to downslope meltwater migration.
- There was a correlation between the amount of thaw settlement and the overall rate of thaw for each test series.
- The rate of thaw penetration was not affected by changes to slope gradient.
- The rate of thaw penetration increased with increasing silt content; this was felt to be as a function of decreasing segregated ice content arising from some limitation to water supplies during freezing.
- The rate of thaw penetration decreased with increasing clay content.

5.3. Frost Heave / Thaw Settlement

Frost heave and thaw subsidence was measured via 72 individual spot-height measurements that were evenly distributed across the slope model surface (fig. 5.3.1). Measurements from this matrix were undertaken before and after each individual freezing and thawing phase to give an accurate assessment of the changes in surface level occurring between the four test cycles within each series.

Unless explicitly stated, all measurements presented within this section are derived from a defined 'key area' on the model surface (see fig. 5.3.1). This area was identified in order to remove the influence of the model boundary on for example, thermal conditions and drainage conditions during thaw and water supply during freezing.

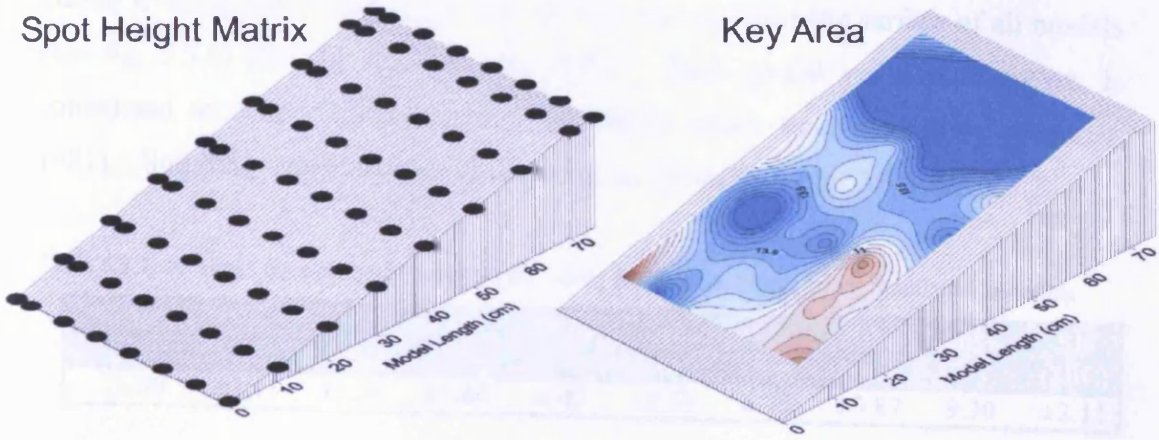

Figure 5.3.1. The defined 'key area' on the model surface as measured by the spot height matrix prior to every freeze and thaw phase.

5.3.1. Frost Heave

The development of segregated ice parallel to the upper surface caused the model surface to heave during each freezing phase. The upward motion of the slope surface occurred as a result of ice segregation processes within the freezing soil (section 2.1.8). The distribution of this frost heave action was therefore directly determined by the distribution of ice lenses within the soil profile. There are many complex thermal and hydraulic relationships involved in ice lens inception and development, for example segregated ice growth requires specific conditions such as the continual migration of interstitial water towards the freezing plane (see fig. 2.1.9) (Williams, 1991; Konrad & Morgenstern, 1981). A large number of previous research studies have examined one-dimensional frost heave through detailed experimental, mathematical and field analyses (e.g. Feldman, 1988; Chamberlain, 1987; Williams, 1988; Mikkola & Hartikainen, 2001; Smith & Williams, 1990). Laboratory studies have consistently utilised specialist equipment to enable robust monitoring of conditions and accurately control the experimental procedure during

freezing. For example, many studies have utilised variations on an enclosed temperature controlled columnar cell design for both enhanced gravity and full-scale laboratory research into one-sided primary frost heave (e.g. Yang & Goodings, 1996; Ketcham *et al.*, 1997; Kumai, 1988). In the experiments described in this thesis the laboratory model was relatively large and therefore underwent a less precisely controlled freezing phase. The size of the model allowed slight variation of test soil properties, basal water supply and thermal conditions to exist, these dissimilarities during freezing led to spatial variation in frost heave across the surface of all models (see fig. 5.3.6) (Penner & Goodrich, 1980). Such spatial variation, however, is considered to reflect similar natural variability under field conditions (Mackay, 1981). Summary statistics on frost heaving are given in Tables 5.3.1 and 5.3.2.

Table 5.3.1. Average frost heave at model scale (mm) for each soil type. SD = Standard Deviation.

Natural Soil	SD (NS)	10% Silt	SD (10S)	20% Silt	SD (20S)	10% Clay	SD (10C)	20% Clay	SD (20C)
11.39	±3.11	11.74	±3.44	6.02	±2.32	6.75	±0.87	9.30	±2.11

The natural soil underwent the greatest average amount of overall frost heave during freezing. The series involving additions of silt to the natural soil soils showed 11% less volumetric expansion whilst the modified clay soils generated 33% less surface frost heave during freezing. The silt soils showed the greatest variation in average frost heave whilst the clay soils had the most consistent reaction to each freezing cycle (see table 5.3.1). The 4° and 8° natural soil slope models underwent an average of 36% and 25% less frost heave respectively when compared to the 12° slope models. However, as discussed in the previous section, it is considered that the prime control on frost heaving in these experiments was the water supply during freezing rather than the inherent frost susceptibility of the soils.

Table 5.3.2. Average frost heave at model scale (mm) for each slope gradient. SD = Standard Deviation.

12°	SD (12°)	8°	SD (8°)	4°	SD (4°)
11.26	±1.64	8.22	±0.40	8.96	±2.53

Figures 5.3.2, 5.3.3 and 5.3.4 illustrate in plan view the average amount of frost heave measured for different zones across the slope model surface for each test series. The natural soil series showed the greatest amount of heave in the 12° slope

(12D/NS) with heave being evenly distributed across the middle portion of the model, Series 8D/NS had a similar distribution of heave but with 43% less overall upward surface expansion, whereas Series 4D/NS had 12% less heave but a high concentration of activity to the left-side of the slope model which resulted in a large range of total heave across the model surface (see fig. 5.3.2).

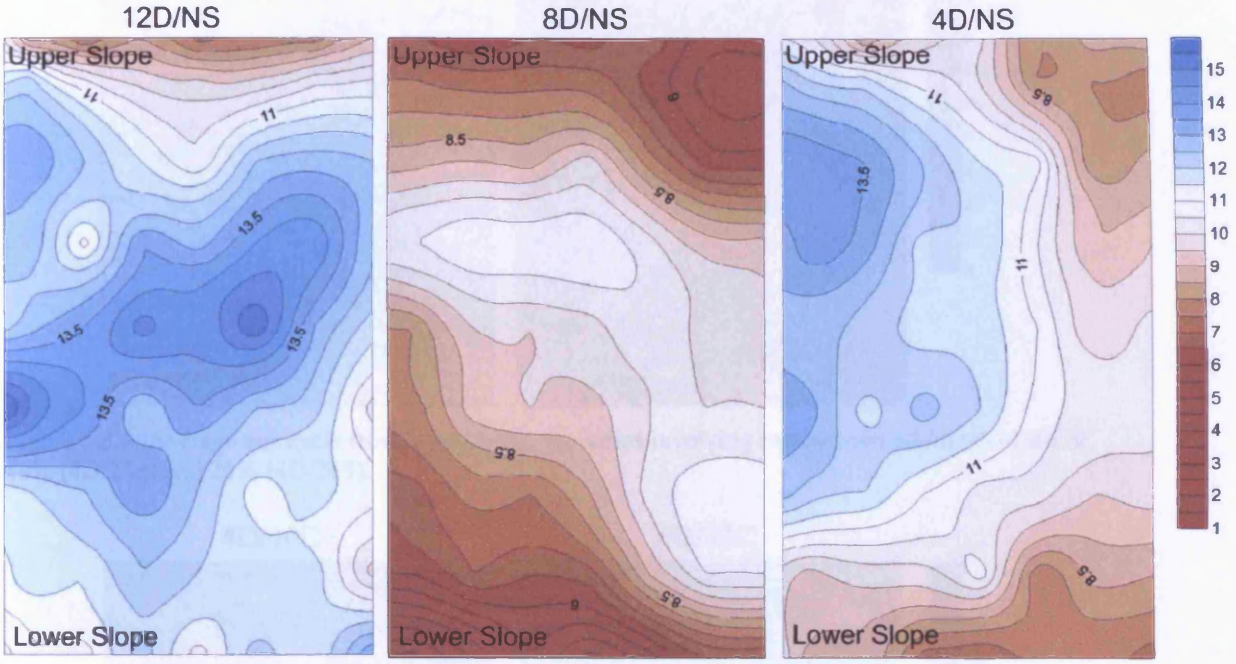

Figure 5.3.2. Average per cycle frost heave (mm) for series involving natural soil.

The models series using modified soil showed patterns of frost heave that were unlikely to be related to sediment granulometry. Series 4D/10S showed a concentration of high frost heave towards the foot of the slope and an overall 6% increase in heave when compared to the natural soil (4D/NS), whereas the additional ten percent silt added into Series 4D/20S appeared to restrict frost heave activity with a 73% decline being distributed across the whole model surface (see fig. 5.3.3). Series 4D/10C showed a relatively small overall amount of frost heave (63% of the natural soil average) with the majority of activity being concentrated towards the bottom right portion of the slope model. In comparison, Series 4D/20C underwent relatively high amounts of frost heave with a 27% increase in activity being concentrated towards the head of the slope model-which was the closest zone to the water inlet within the most impermeable soil (see fig. 5.3.4). The enhanced rates of frost heave within the upper slope region of 4D/20C may be associated with the fact that the basal water supply was fed from beneath this end of the slope model.

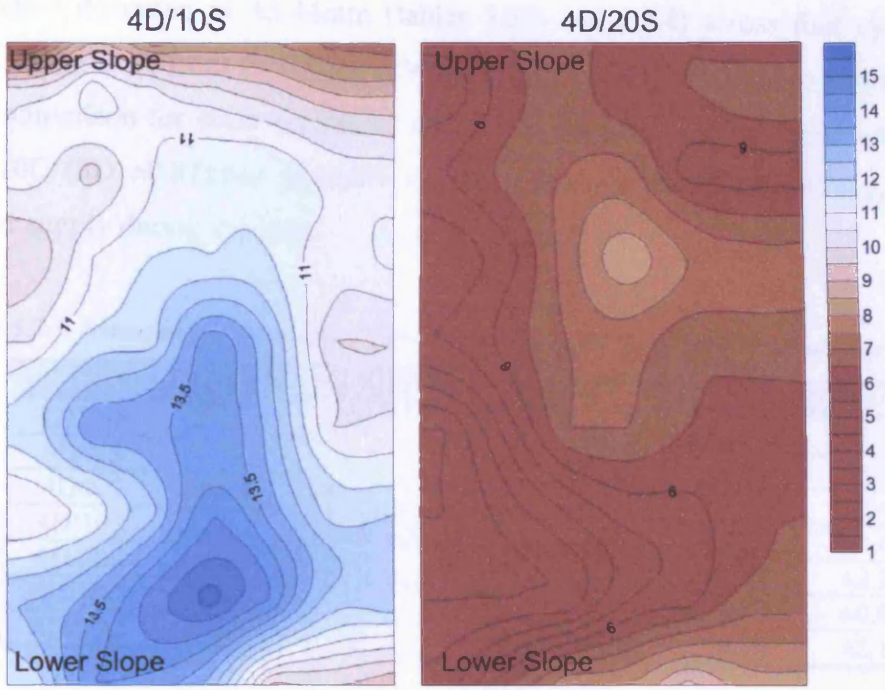

Figure 5.3.3. Average per cycle frost heave (mm) for series involving incremental additions of silt of 10% (4D/10S) and 20% (4D/20S).

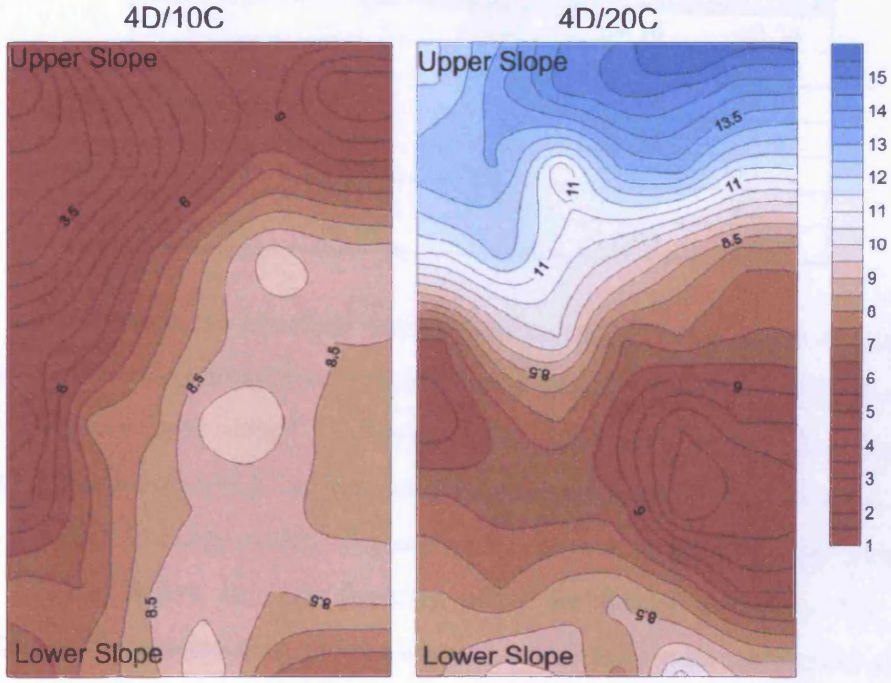

Figure 5.3.4. Average per cycle frost heave (mm) for series involving incremental additions of clay (10% and 20% respectively).

Table 5.3.3 clearly indicates that the slope models across a full series of four freezing phases appeared to react independently and were therefore not consistently influenced by the two controlled variables of soil grain size and slope gradient (see figs. 5.3.2-5.3.4). Series 4D/10S showed greatest variation in frost heave, with a

standard deviation of ±3.44mm (tables 5.3.3 and 5.3.4) across four cycles – this variability arose from variations in water supply between successive freezing phases. In comparison the most consistent reaction to freezing was measured within Series 4D/10C (SD ±0.87mm), possibly reflecting relatively uniform soil properties and water supply during freezing.

Table 5.3.3. Average frost heave (mm) for each cycle at model scale. SD = Standard Deviation.

Series	Cycle 1	Cycle 2	Cycle 3	Cycle 4	Average	SD
12D/NS	7.86	15.88	12.76	13.17	12.42	±3.34
8D/NS	4.38	9.62	9.24	11.40	8.66	±3.01
4D/NS	10.19	9.07	14.52	10.24	11.01	±2.41
4D/10S	8.88	14.26	8.67	15.14	11.74	±3.44
4D/20S	9.43	3.83	5.29	5.54	6.02	±2.39
4D/10C	6.71	5.60	7.69	7.00	6.75	±0.87
4D/20C	12.29	7.29	8.81	8.81	9.30	±2.12

Table 5.3.4. Standard deviation for frost heave (mm) values recorded from the spot-height matrix.

Series	Cycle 1	Cycle 2	Cycle 3	Cycle 4
12D/NS	±3.36	±2.25	±4.38	±2.54
8D/NS	±2.51	±2.53	±2.71	±2.89
4D/NS	±2.31	±2.81	±4.00	±1.91
4D/10S	±2.78	±2.88	±2.94	±3.65
4D/20S	±3.06	±2.51	±1.55	±1.72
4D/10C	±3.15	±1.91	±2.53	±2.41
4D/20C	±4.85	±6.10	±2.80	±3.56

Table 5.3.4 presents the standard deviation of recorded heave values to examine the amount of variation shown between individual models and between freezing phases within the same test series. Tables 5.3.3 and 5.3.4 indicate that frost heave behaviour was inconsistent for most slope models with a large variability in recorded values between freezing cycles. Figure 5.3.5 illustrates in plan view the independent nature of frost heave in each freezing phase for Series 4D/10S – this diagram highlights both intra-freezing phase variation across the model surface but also inter-series variations existing as a function of the consolidation characteristics determined through the previous thaw phase. For example, the third freezing phase of Series 4D/10S showed a 17mm range of frost heave values across the slope surface compared to just a 6mm range within the first freezing cycle (see fig. 5.3.5). However, both the first and third freezing phases showed an average of 41% less frost heave when compared to the other two frost cycles.

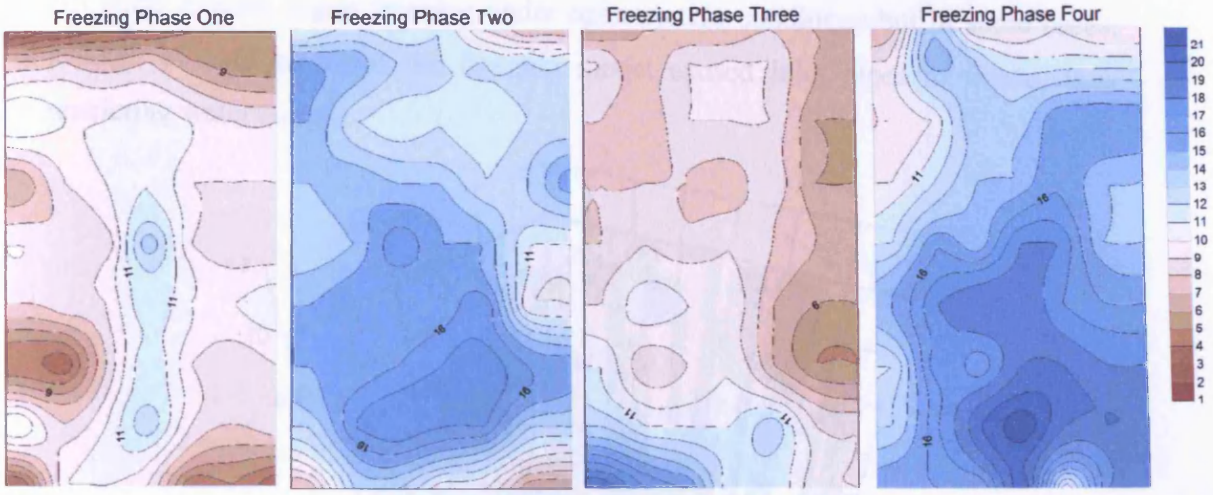

Figure 5.3.5. Frost heave (mm) for each freezing cycle for Series 4D/10S (see fig. 5.3.3).

It can be noted that these patterns of frost heave are highly variable and cannot be explained by conventional theories regarding the potential frost susceptibility of host sediment (e.g. classifications undertaken by Beskow, 1935 and Taber, 1930). For example, Tester and Gaskin (1996) reported that frost heave increased linearly with an increase in content of fine material within the host sediment, however, the current study has not simulated an analogous relationship between grain size and frost heave. However, the dynamic process of ice segregation (frost heave) is highly dependent upon localised changes to thermal and hydraulic variables (Section 2.1.8), and it may not be entirely valid to use average values to represent a complex scenario exclusively driven by small-scale thermodynamic variations (Feldman, 1988; Konrad & Morgenstern, 1980). These small scale variations can influence the generation of cryosuction pressure gradients driving moisture towards the freezing plane (e.g. Williams, 1966; 1972) whilst Smith and Williams (1990) have noted that variations in soil density and other mechanical properties of the host sediment have a major influence on water supply and rate of freezing and therefore upon ice segregation potential (Konrad & Morgenstern, 1981; Lunardini, 1998).

During freezing of the models the water supply was maintained by a large reservoir tank. However, slight variations in water level within this reservoir tank did take place as laboratory safety regulations meant it was logistically difficult to maintain continuous daily monitoring during periods of centrifuge operation and maintenance. Hence, it is likely that variation in heave in successive cycles were largely determined by variations in the water supply to the models (e.g. Lunardini, 1991).

All slope models began freezing under open system conditions but in some cases, leakage of cold air from the freezing model caused inlet pipes to freeze, thus restricting water supply.

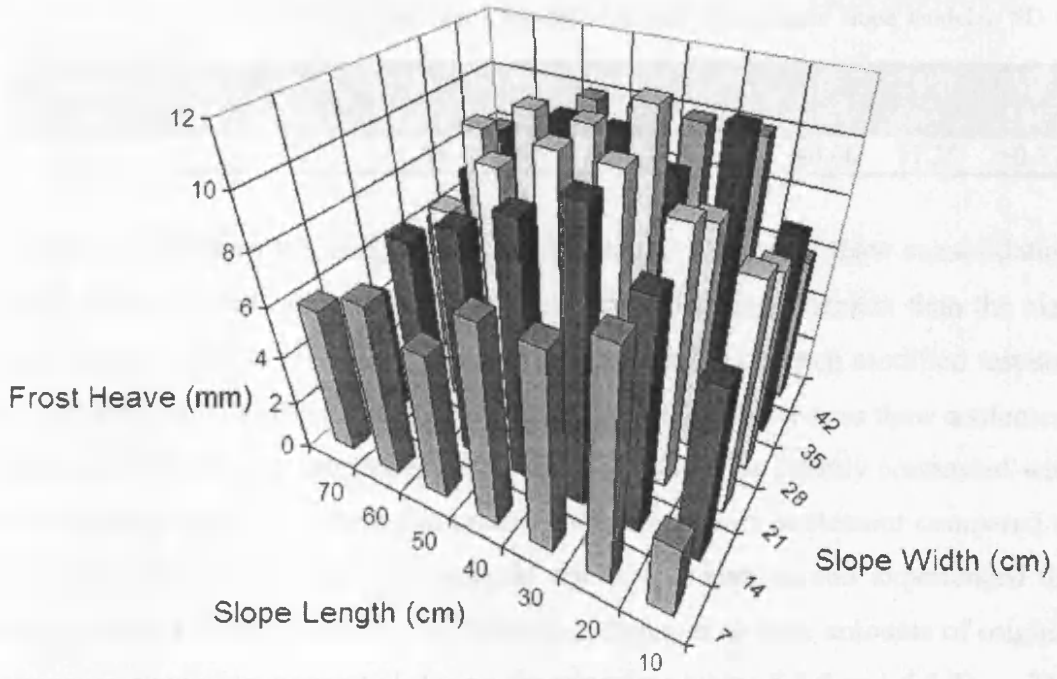

Figure 5.3.6. Measured frost heave from the second freezing phase of Series 4D/NS.

The freezing plate surface temperature was consistent, though slight irregularities in the model surface may have led to perturbations in the freezing front, thus partially explaining the small scale within-model heave variations. Differential patterns of heave may have progressively exacerbated this problem across single freezing phases. Slight spatial variability in soil density and granulometry were also probably partially responsible for within model heave variation across individual models (e.g. fig. 5.3.6).

5.3.2. Thaw Settlement

The melting of segregated ice held within the soil caused the model surface to consolidate during each thaw phase. Table 5.3.5 presents the overall average amount of thaw settlement measured within each test soil in the 4° slope models. The natural soil, twenty percent clay and the ten percent silt soils underwent the similar amounts of thaw settlement; although they experienced more subsidence

when compared to the twenty percent silt (-71%), ten percent clay (-38%) (see table 5.3.5).

Table 5.3.5. Average thaw settlement (mm) for each test soil (four degree slope models). SD = Standard Deviation.

Natural Soil	SD (NS)	10% Silt	SD (10S)	20% Silt	SD (20S)	10% Clay	SD (10C)	20% Clay	SD (20C)
11.88	±1.83	12.01	±1.89	6.95	±2.12	8.60	±0.66	11.28	±0.87

Overall, the modified test soils experienced a similar amount of thaw consolidation with the silt soils only encountering 4% more overall thaw settlement than the clay soils (see table 5.3.5). However, the individual behaviour of each modified test soil was different with the ten percent silt soil showing a 42% increase in thaw settlement compared to the twenty percent silt soil, this pattern can be directly contrasted with the ten percent clay soil which produced a 24% decrease in settlement compared to the twenty percent clay soil. In general, the ten percent silt soil experienced the largest overall average amount of settlement in response to large amounts of original volumetric expansion generated during freezing (see tables 5.3.5 and 5.3.3). The twenty percent silt soil reacted to thaw front progression with the largest overall range of settlement values across the model surface (SD ±2.12mm), whilst both the clay soils appeared to react to thaw penetration with the most consistency.

Table 5.3.6. Average thaw settlement (mm) for each slope gradient (Natural Soil). SD = Standard Deviation.

12°	SD (12°)	8°	SD (8°)	4°	SD (4°)
13.71	±3.11	10.05	±1.69	11.88	±3.07

Table 5.3.6 highlights that the amount of thaw settlement was not related to slope angle. Series 12D/NS experienced the largest average amount of thaw consolidation with the 8° model (8D/NS) undergoing 36% less settlement and the 4° model undergoing 15% less. The test series using natural soil/clay and natural soil/silt mixes mostly experienced less thaw settlement than the natural soil – with only 4D/10S (1% increase) showing the same magnitude of subsidence during thaw (see table 5.3.7). The NS and CL slope models whilst showing the two highest amounts of thaw subsidence also reacted with the most inconsistency – as both models have recorded relatively large ranges in settlement values between individual thaw cycles (see SD in table 3.5.7).

Table 5.3.7. Average thaw settlement (mm) for each thaw phase. SD = Standard Deviation.

Series	Cycle 1	Cycle 2	Cycle 3	Cycle 4	Overall Average	SD
12D/NS	9.33	16.69	14.17	14.64	13.71	±3.12
8D/NS	7.52	11.17	10.81	10.71	10.05	±1.70
4D/NS	10.52	9.69	16.43	10.88	11.88	±3.07
4D/10S	9.38	12.90	12.00	13.74	12.01	±1.89
4D/20S	10.07	5.48	6.45	5.78	6.95	±2.12
4D/10C	9.12	7.64	8.95	8.70	8.60	±0.66
4D/20C	12.17	11.29	10.10	11.59	11.28	±0.87

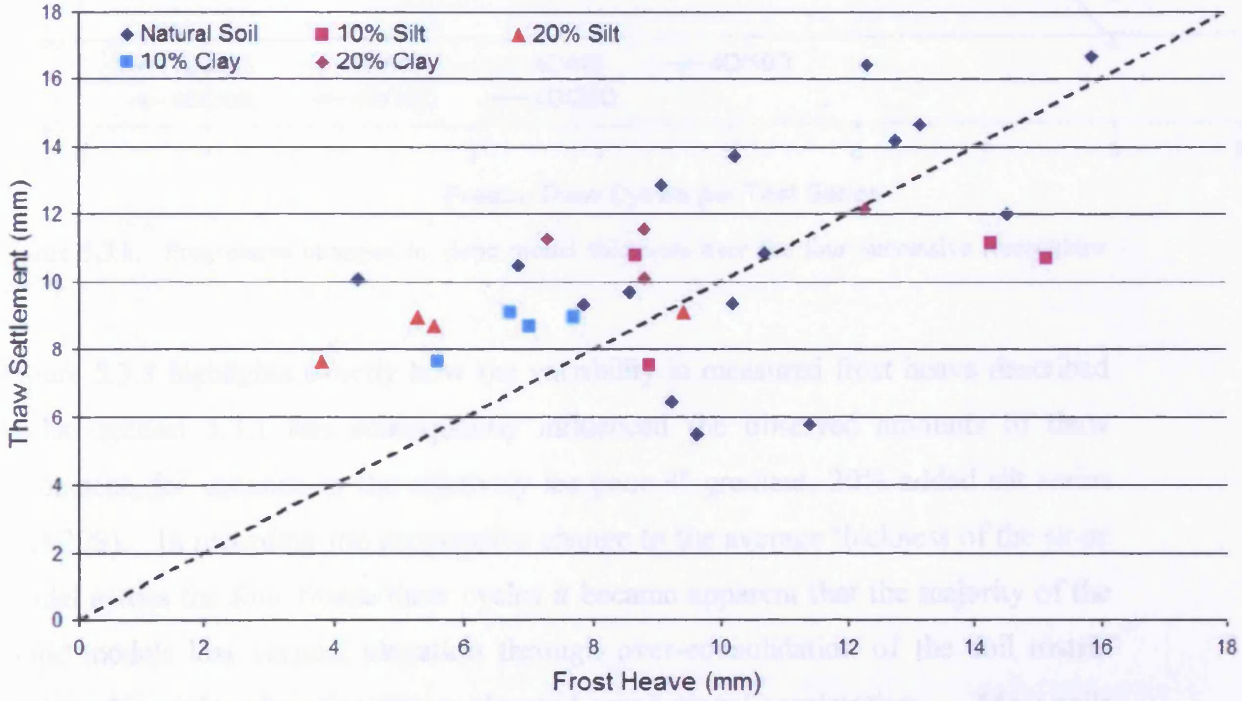

Figure 5.3.7. Relationship between average thaw settlement and average frost heave for every phase. The dashed straight line indicates the 1:1 ratio.

Figure 5.3.7 illustrates the relationship between thaw settlement and the amount of frost heave during the preceding freezing phase for each test soil, for example the range of heave and settlement values recorded for Series 4D/10C and 4D/20C in tables 5.3.3 and 5.3.7. As anticipated, thaw settlement during a given thaw phase was largely a function of the amount of frost heave recorded in the previous freezing phase although the majority of test series appear to show a greater amount of thaw settlement than frost heave. It may be inferred from this that slope models lost volume during thaw through both the melting of ice lenses and the consolidation of the test soil under self weight.

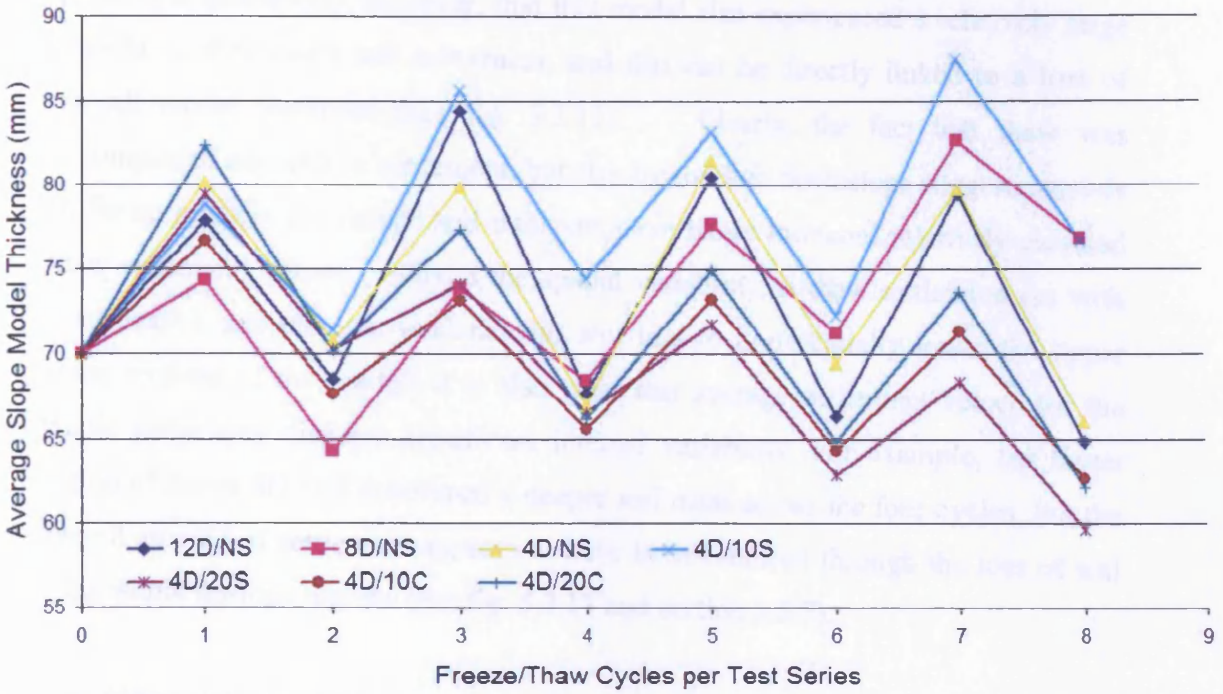

Figure 5.3.8. Progressive changes in slope model thickness over the four successive freeze/thaw cycles.

Figure 5.3.8 highlights exactly how the variability in measured frost heave described within section 5.3.1 has subsequently influenced the observed amounts of thaw settlement, for instance in the relatively ice-poor 4° gradient, 20% added silt series (4D/20S). In recording the progressive change to the average thickness of the slope model across the four freeze/thaw cycles it became apparent that the majority of the slope models lost vertical elevation through over-consolidation of the soil matrix under self weight when thawing at elevated gravitational acceleration. Most soils acted consistently except the last thaw phases of Series 4D/10S and 8D/NS (e.g. fig. 5.3.7). Series 4D/10S showed a loss of vertical elevation in its third thaw cycle but despite settling by the same amount in the fourth thaw cycle it did not regain its original thickness, while Series 8D/NS showed a net loss in overall model thickness after the first thaw cycle but showed a consistent gain in model thickness across the subsequent freeze/thaw phases.

In most cases a large amount of frost heave lead directly to a greater amount of settlement during thaw consolidation, see for example Series 12D/NS and Series 4D/NS. The greatest loss in model thickness was recorded within the relatively ice-poor Series 4D/20S which showed a reduction in vertical elevation after each thaw

cycle. It is noteworthy, however, that this model also experienced a relatively large amount of downslope soil movement, and this can be directly linked to a loss of overall model thickness (see fig. 5.3.13). Clearly, the fact that thaw was accompanied not only be settlement, but also by soil loss downslope suggests models suffering greatest downslope soil transport were likely to record relatively elevated thaw settlement values. Given the spatial variability in thaw settlement (as with frost heave), and also the tendency for soil loss to preferentially lower the upper slope sections of the models it is also clear that average settlement values for the whole slope may disguise significant internal variability. For example, the lower region of Series 4D/10S developed a deeper soil mass across the four cycles, but the overall amount of settlement appears to have been balanced through the loss of soil mass within upslope regions (see fig. 5.3.11 and section 5.5.7).

The consolidation parameters of each test soil played an important role in determining the relative amounts of thaw settlement (see fig. 5.3.8). The addition of fine silt/clay material would have impacted upon soil permeability and therefore the rate at which consolidation could occur, i.e. the coefficient of consolidation (C_V). The low C_V of the 4D/20S, 4D/10C and 4D/20C soils mean they would require a longer time for complete primary consolidation under self weight (see fig. 4.4.3). Figure 5.3.9 and Table 5.3.8 highlight this relationship because the soil with the highest C_V value was the only material to show a net gain in thickness over four freeze-thaw cycles, with a ratio of 1.17. The other test soils all showed negative volume strain during repeated frost heave and thaw consolidation. Series 4D/20S showed the largest amount of consolidation relative to frost heave, probably as a result of a low C_V and because the series was relatively ice-poor so that net thaw settlement is relative to low initial frost heave values. It is possible that in the ice-rich models, development of hydraulic cryosuction and frost heaving pressures may have combined to increase effective stress between ice lenses, consolidating the inter-lens soil, imprinting a cryofabric and reducing soil volumes, thereby allowing greater amounts of overall soil consolidation under self weight during thaw – especially as thawing ice lenses have been shown to increase overall hydraulic conductivity (e.g. Chamberlain & Gow, 1978; Dyke & Eggington, 1993; Burt & Williams, 1976).

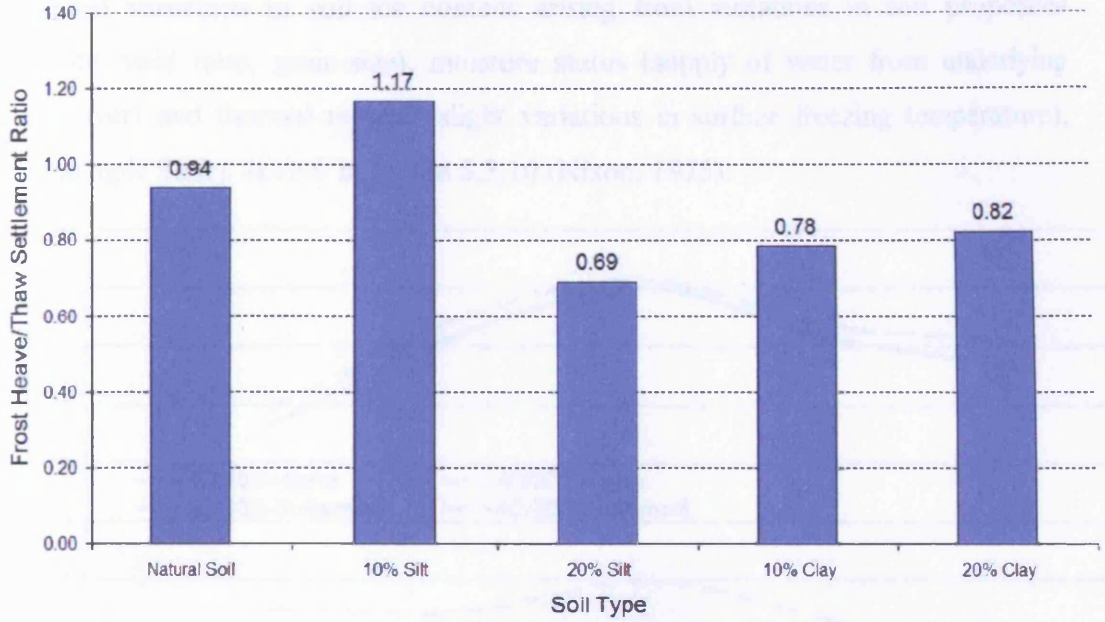

Figure 5.3.9. Ratio of average frost heave/thaw settlement for each soil type.

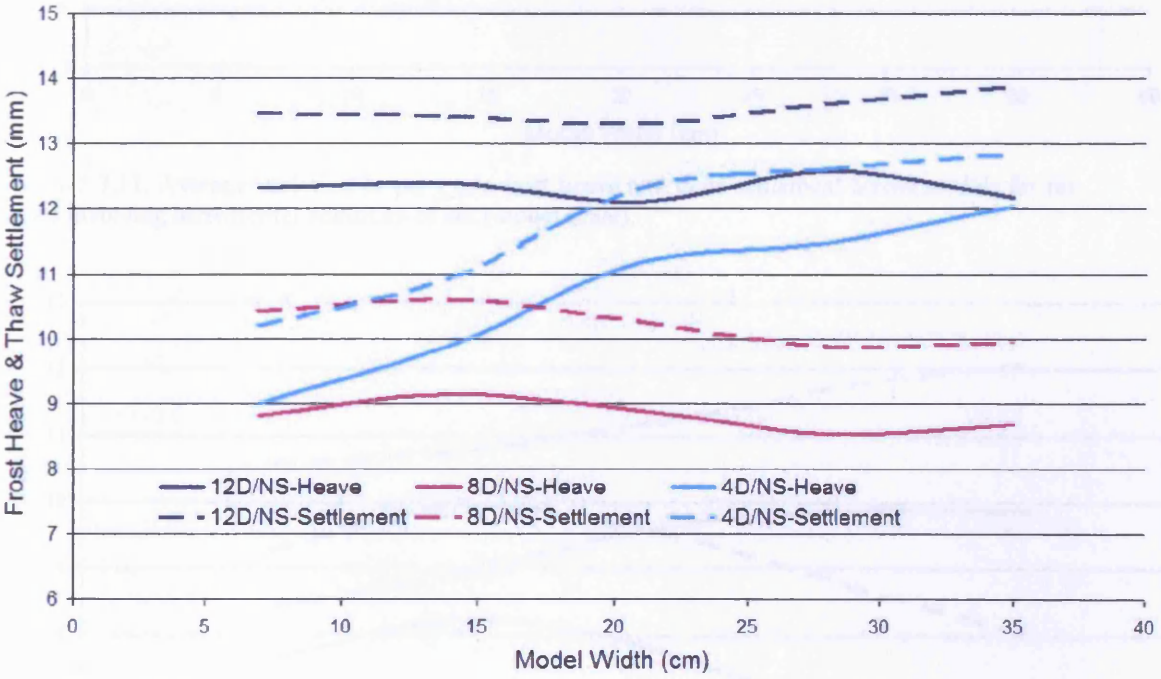

Figure 5.3.10. Average variation in per cycle frost heave and thaw settlement across models for the series involving natural soil (model scale).

The spatial linkage between zones of high frost heave and areas of enhanced thaw settlement can be identified within all of the test soils. Figures 5.3.10-5.3.12 indicate how variation in the distribution of average frost heave was directly related to subsequent patterns of settlement on the model surface. Patterns of average thaw settlement have varied spatially across the models and were probably the result of

localised variations in soil ice content arising from variations in soil properties (density, void ratio, grain-size), moisture status (supply of water from underlying sand layer) and thermal regime (slight variations in surface freezing temperature), for example Series 4D/NS in Figure 5.3.10 (Nixon, 1975).

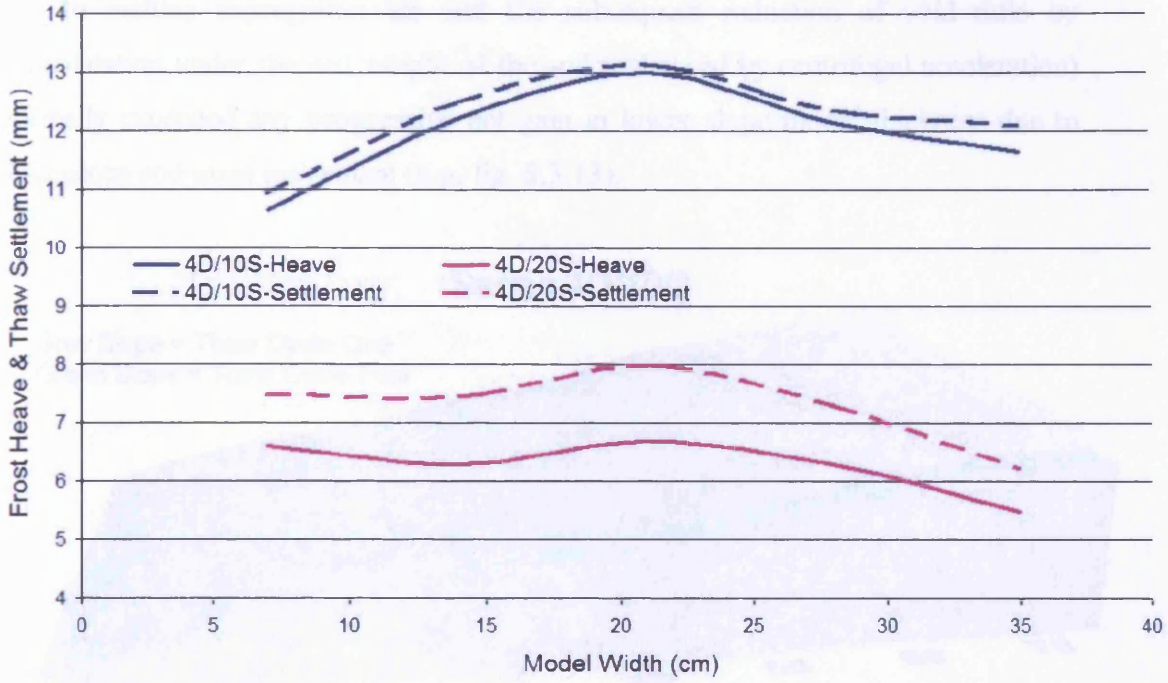

Figure 5.3.11. Average variation in per cycle frost heave and thaw settlement across models for the series involving incremental additions of silt (model scale).

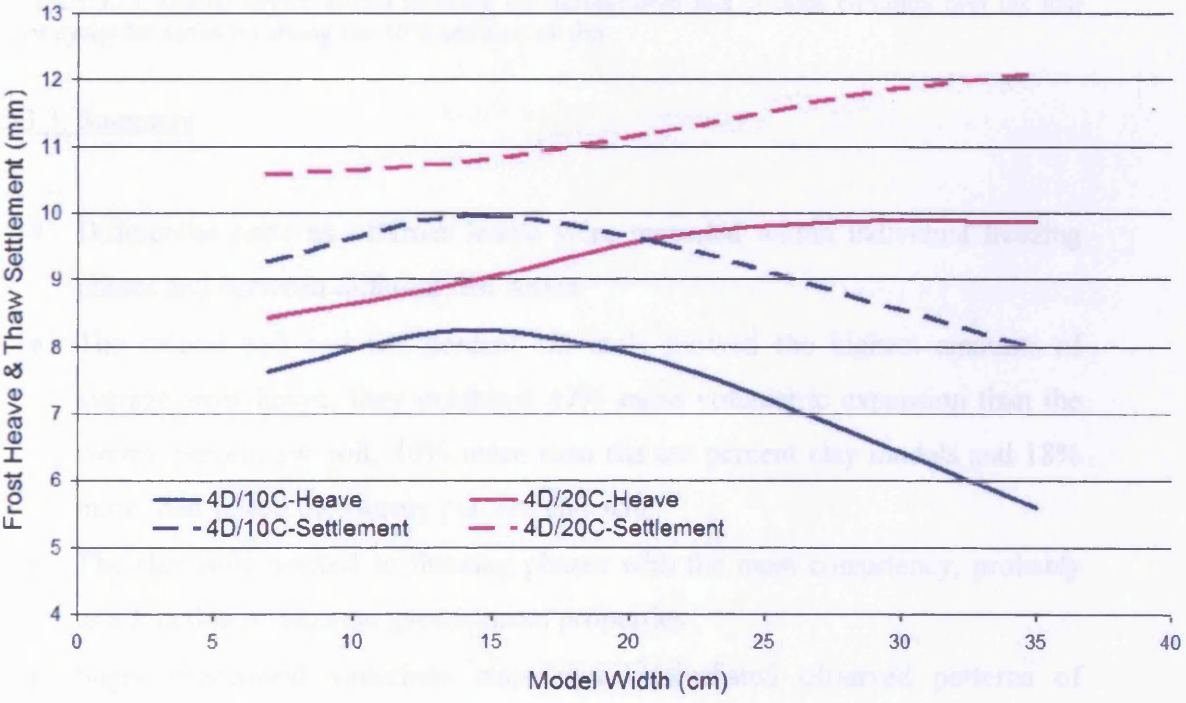

Figure 5.3.12. Average variation in per cycle frost heave and thaw settlement across models for the series involving incremental additions of clay (model scale).

Overall, net consolidation occurred in most slope models in response to both thaw settlement and the downslope displacement of soil mass, i.e. as the planar slope became flattened by transfer of soil from the upper slope to the lower slope, for examples see section 5.3.7. However, during individual thaw cycles, settlement due to melting segregation ice and the subsequent reduction of void ratio by consolidation under the self weight of the soil (enhanced by centrifugal acceleration) normally exceeded any progressive net gain in lower slope model thickness due to downslope soil mass movement (e.g. fig. 5.3.13).

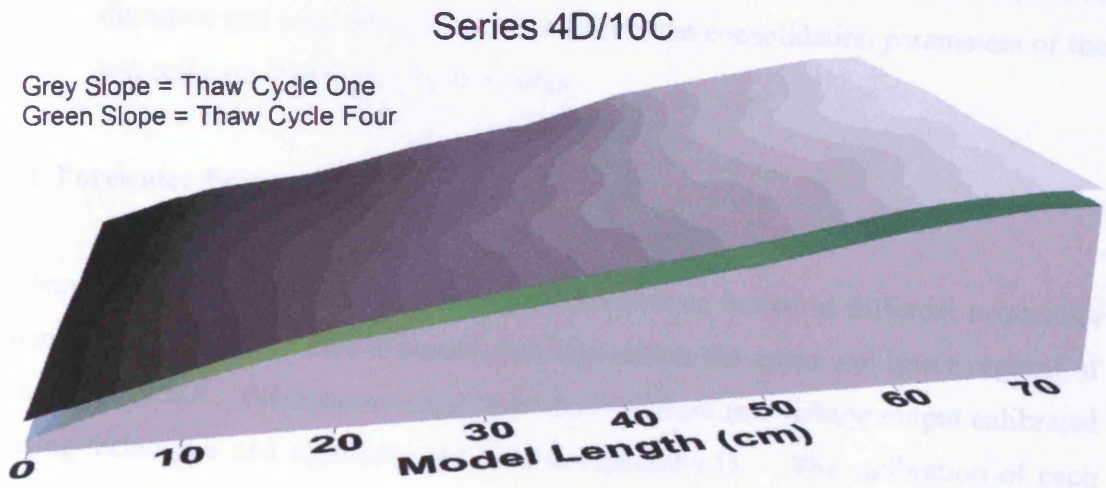

Figure 5.3.13. Digital terrain model showing the accumulated loss of slope elevation over the four thaw cycles for series involving the 10% addition of clay.

5.3.3. Summary

- Differential patterns of frost heave were recorded within individual freezing phases and between different test series.
- The natural soil and ten percent silt soils showed the highest amounts of average frost heave, they exhibited 47% more volumetric expansion than the twenty percent silt soil, 40% more than the ten percent clay models and 18% more than within the twenty percent clay soil.
- The clay soils reacted to freezing phases with the most consistency, probably as a function of inherent geotechnical properties.
- Slight procedural variations may have exacerbated observed patterns of differential heave.

- Amounts of thaw settlement commonly exceeded the amount of frost heave in the preceding freezing cycle.
- Thaw settlement was greatest within the ten percent silt and natural soils and exceeded that in the twenty percent silt soil by 71%, the twenty percent clay by 5% and the ten percent clay soil by 38%.
- Downslope soil mass movement affected the measured amount of thaw settlement by progressively lowering the slope profile.
- The consolidation parameters of each test soil were key to initial amounts of thaw settlement, but ice segregation within the slope model may have disturbed soil microstructure and modified the consolidation parameters of the test soil over four freeze/thaw cycles.

5.4. Porewater Pressure

Porewater pressures were measured using six probes buried at different sequential depths in two separate instrumentation strings within the upper and lower regions of the slope model. Pressure readings were derived from raw voltage output calibrated using techniques and equations outlined in Appendix D. The calibration of each probe generated an R^2 value for that calibration, and this was used to determine any progressive deterioration in transducer performance, that might ultimately lead to instrument failure. Compromised data commonly showed patterns of inconsistent noise or drift – suspicious values have been highlighted within the presented dataset.

The Druck PDCR81 pressure transducers were not manufactured for use within cryogenic environments and to protect each transducer the porous tips were filled with ethylene glycol (antifreeze). The performance of the PDCR81 transducers became compromised towards the end of Series 8D/NS (thaw cycles 22-25) (see table 5.4.1). As a direct consequence there was a lack of useable pressure data recorded for certain modified soil types (see fig. 5.4.1). In response to falling probe performance, the transducers were serviced in July 2002 (after thaw cycle 25) and began to provide a greater proportion of clean useable data for the following thaw cycles. The transducers provided the highest quality data during the initial thaw cycles of each test series, it was felt that the progressively poorer operation within

later cycles of a series was a result of both air penetration into the transducers and the dilution of the protective solution across sequential moisture rich thaw phases. Air penetration tended to create noisy or drifting values. The effectiveness of the antifreeze solution may have lessened across some test series, and on occasion this was observed to lead to a higher proportion of transducers presenting 'noisy' data where 'clean' data had been recorded in a previous thaw cycle (see section 5.7).

Table 5.4.1. Average useable pore pressure readings per thaw cycle.

Series	12D/NS	4D/NS	4D/10S	8D/NS	4D/20S	4D/10C	4D/20C
Date	Dec-00	Sep-01	May-02	Jun-02	Aug-02	Nov-02	Dec-02
Average	5.3	5.3	1.8	0.8	2.0	3.5	3.0

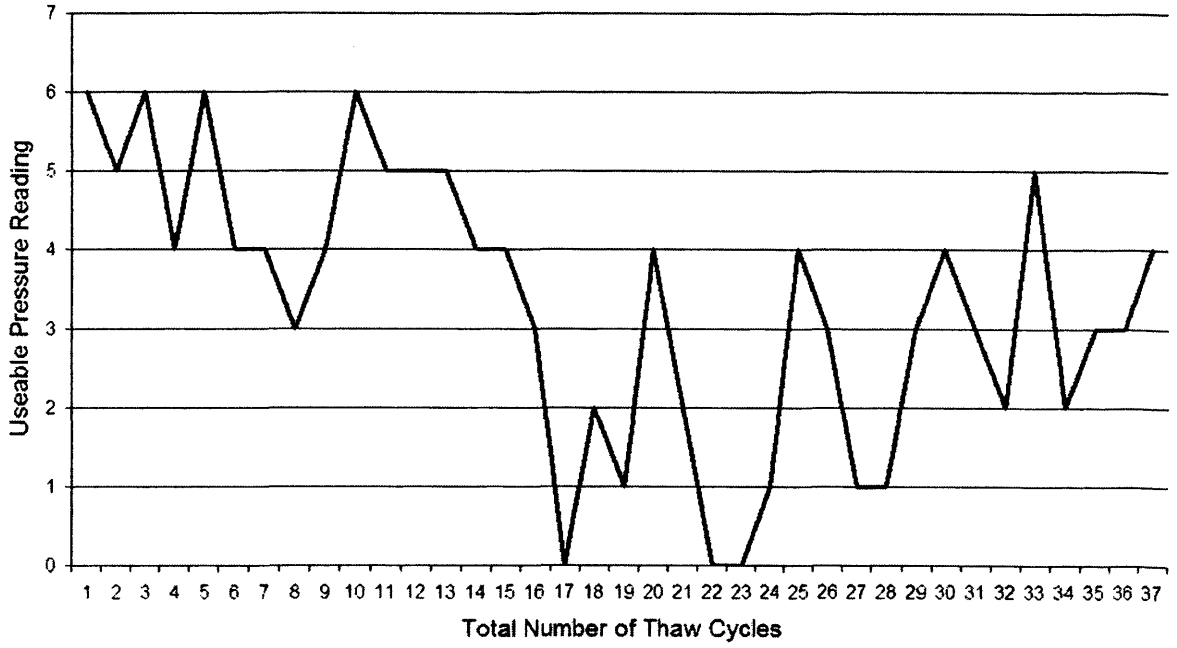

Figure 5.4.1. The number of PDCR81 pressure transducers producing useable data after probe calibration (see appendix D).

However, it should be noted that consistent patterns of probe reaction were achieved for the majority of thaw phases within all test series. Figure 5.4.2 demonstrates an excellent example of consistent patterns of pressure response being recorded across a complete four cycle test series. For this reason it was possible to systematically apply a data reduction technique to capture useable values from most datasets. The filtering technique involved removing the negative and fluctuating patterns that existed in the frozen soil prior to the arrival of the thaw plane as it was felt these values did not reflect clearly identifiable pore pressure conditions (see section 5.4.1

and fig. 5.4.3 for a full explanation). Full unmodified data are included in Appendix A.1.

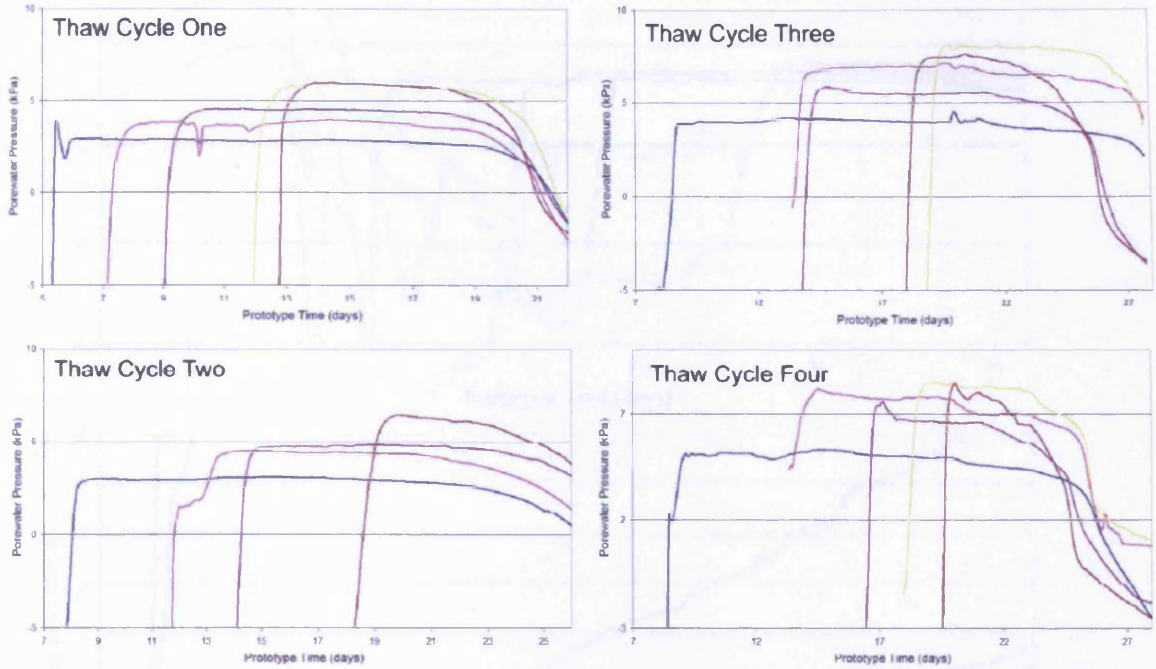

Figure 5.4.2. Porewater Pressure across four thaw cycles of Series 4D/NS. Note: Transducer depths given in model scale.

Reliable pressure probe response was also observed within individual thaw cycles, where it was important to note consistent patterns of probe reaction at similar depths within each adjoining instrument string. For example, Figure 5.4.3 presents the fourth thaw phase for Series 4D/20S where the pattern of pore pressure reaction is similar for both upper and lower slope regions (e.g. at 30mm depth). The following section will present data from single instrumentation strings to prevent comparison of non-synchronous pressure patterns measured across different regions of the model slope. This is important because section 5.2 has illustrated an intermittent but occasionally significant delay within the rate of thaw penetration between the upper and lower slope instrumentation zones (e.g. table 5.2.2).

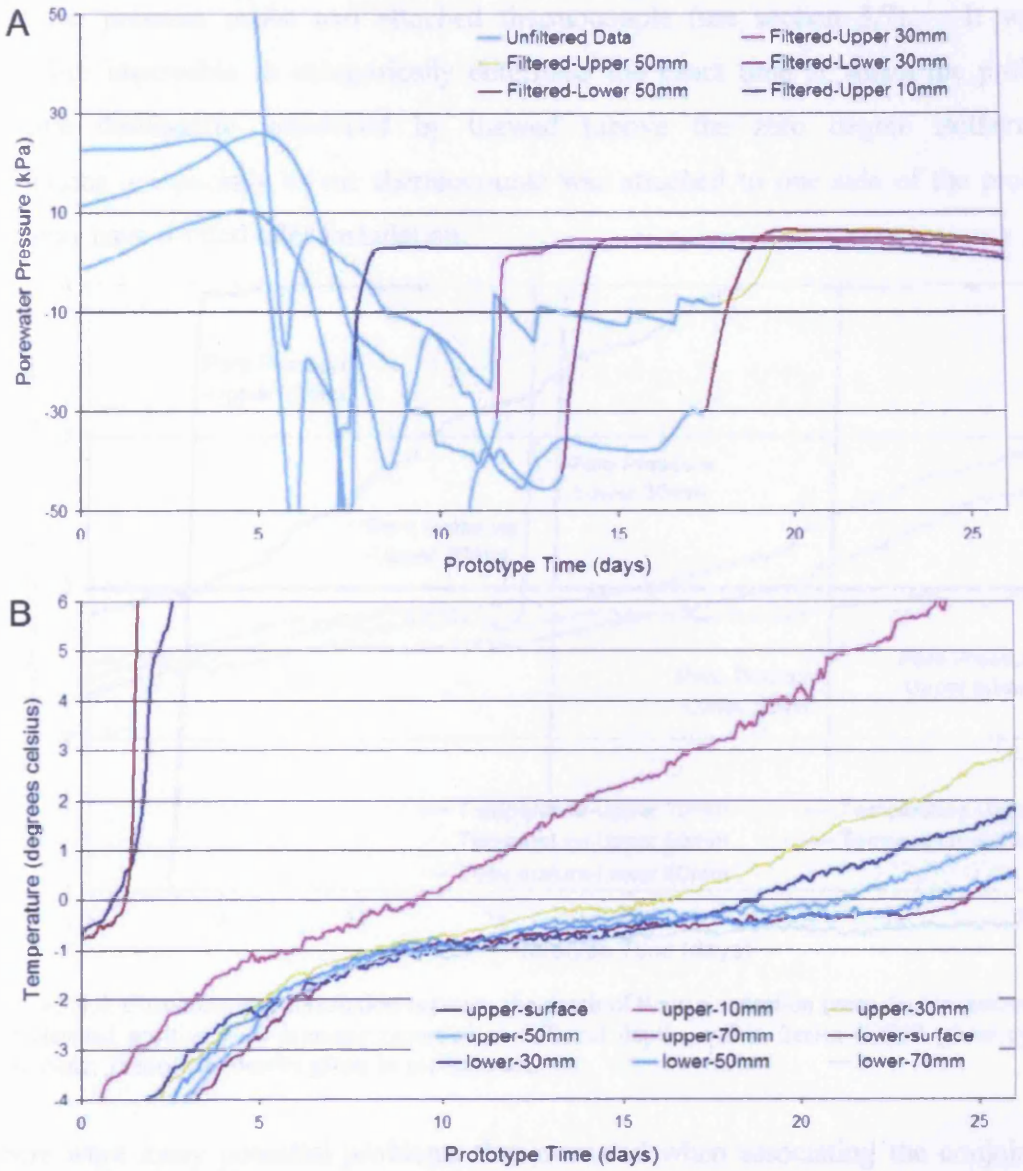

Figure 5.4.3. (A) An example of the applied data reduction technique for Series 4D/NS (thaw cycle two) and (B) the thermal data recorded during that thaw phase. Note: Transducer depths given in model scale.

A simple correlation between the inferred depth of the thaw plane, as defined by the zero degree isotherm, and a response in recorded pore water pressure was not always apparent, despite both pressure probe and thermocouple being positioned together at specific depths (see fig. 3.3.3). The premature or delayed response of specific pressure probes may have been due to phase change in finer soil pores taking place ahead of the zero degree isotherm. Additionally, the scaled diameter of each miniature pressure probe was increased under centrifugal force. The 6.5mm (model scale) diameter of the Druck PDCR81 became equivalent to 0.065m under prototype stress conditions. A transitional time-period existed as the thaw plane progressed

past the pressure probe and attached thermocouple (see section 3.7). It was therefore impossible to categorically determine the exact time at which the probe became dominantly influenced by thawed (above the zero degree isotherm) conditions – especially as the thermocouple was attached to one side of the probe and may have rotated after installation.

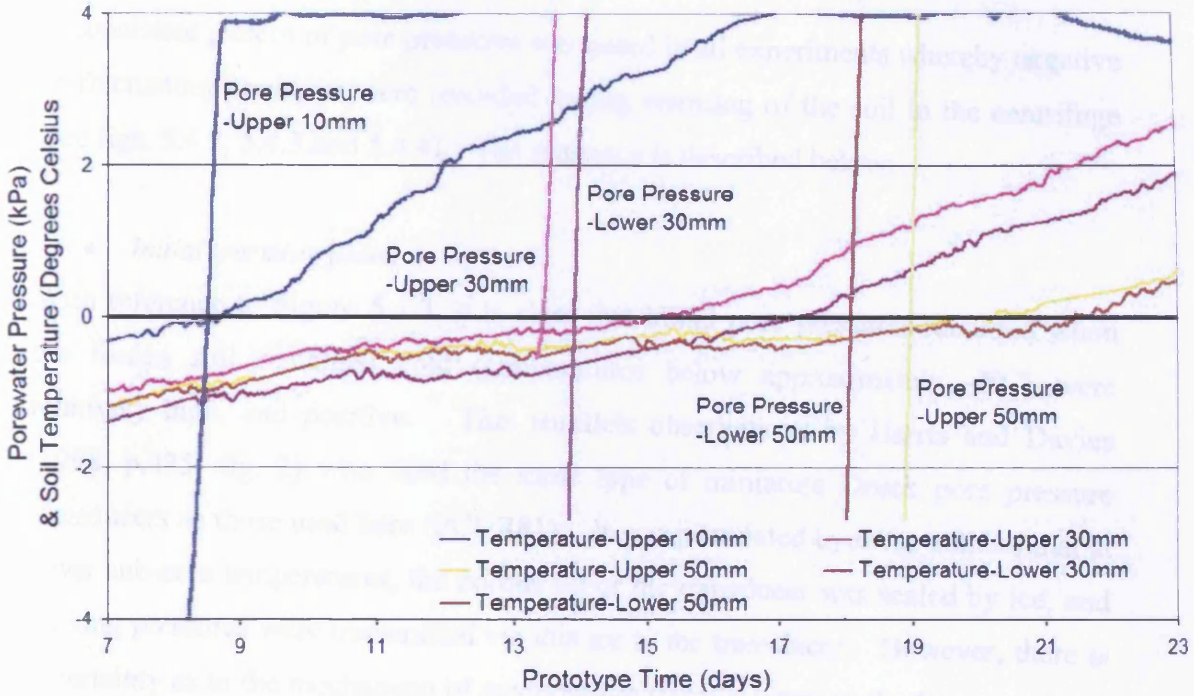

Figure 5.4.4. Chronological correlation between the depth of thaw penetration (zero degree isotherm) and elevated positive pore pressure recorded at different depths within Series 4D/NS (thaw cycle two). Note: Transducer depths given in model scale.

There were many potential problems that occurred when associating the conjoined thermal and pore pressure datasets for each sequential depth. On particular occasions both variables can show a good correlation, for example the upper 10mm pressure probe in Figure 5.4.4 shows an immediate reaction to passing the zero degree isotherm. However, within the majority of datasets the masking effect of the 'zero curtain' made it difficult to identify the exact freeze/thaw phase chronology for the pressure probes. The situation becomes complex because pore pressure probes have been commonly observed to react (activate) before the thaw plane has passed across the attached thermocouple, for example, the four day (prototype scale) premature reaction of the pressure dataset within the upper and lower-30mm probes in Figure 5.4.4. The effect of the zero curtain when combined with the scaling issue involving the probes makes assessment of exactly when the excess pore water released by thaw penetration had begun to dominate the pressure probe at the

thawing front. Clearly, depression of the freezing point in these fine soils may have allowed interstitial meltwater to influence probes before the above-zero isothermal conditions were established.

5.4.1. Pattern of variation of pore pressure in response to thawing of frozen models

A consistent pattern of pore pressures was noted in all experiments whereby negative or fluctuating pressures were recorded during warming of the soil in the centrifuge (see figs. 5.4.2, 5.4.3 and 5.4.4). The sequence is described below:

- *Initial warming phase*

With reference to Figure 5.4.3, it is clear that initial pore pressures recorded when the frozen soil remained cold (temperatures below approximately -2°C) were relatively high, and positive. This parallels observations by Harris and Davies (1998, p.435, fig. 2) who used the same type of miniature Druck pore pressure transducers as those used here (PCDR81). It was postulated by these authors that at lower sub-zero temperatures, the porous tip of the transducer was sealed by ice, and heaving pressures were transmitted via this ice to the transducer. However, there is uncertainty as to the mechanism of any pressure transfer between the frozen soil and so pressure readings during this period cannot be used to accurately reflect ice pressures (e.g. O'Neill & Miller, 1985; Take & Bolton, 2002).

- *Early Part of the "Zero Curtain" Phase*

Further warming of the still frozen soil led to temperatures approaching the "zero curtain" condition, and this period was associated with a sharp fall in pressure in all models, pressures often falling to low negative values (see figs. 5.4.3 and 5.4.5). Harris and Davies (1998) argued that during this period, the transducers occupied the partially frozen fringe at the thaw front, and were influenced by unfrozen pore water under cryogenic suction (Sutherland & Gaskin, 1973). Smith and Onysko (1990) have shown that that the pressure within an ice lens must equal the overburden pressure and tensile strength (cohesion) of the host sediment, and the difference between pore ice pressure and pore water pressure can be described via the Clausius-Clapeyron equation:

$$(P_i - P_w) = (T\text{-}T_o)\, L_f\, V_i / V_w\, T_o \qquad (5.1)$$

where $(P_i - P_w)$ represents the difference in pore ice pressure and pore water pressure (the matric potential), T is the temperature (K), T_o is the freezing point of pure water, L_f is the latent heat of fusion and V_i and V_w are the specific volumes of water and ice (Williams, 1988). This matric potential is maintained by development of negative pore water pressures or "cryosuction" within the pore water and this was recorded by the transducers (Perfect & Williams, 1980). At this time it is assumed that the soil matrix remained rigidly bound by ice, but unfrozen pore water was sufficiently abundant to form a hydraulic continuity with the pore pressure transducers. The simple change in phase from ice to water is associated with a 9% loss in volume, so that if the soil matrix remained rigid, this would also tend to generate suction within the unfrozen pore water. The pressure data recorded during each thaw cycle thus provided an insight into the temperature dependent status of both ice and water content within the slope model at each sequential depth during warming (fig. 5.4.5).

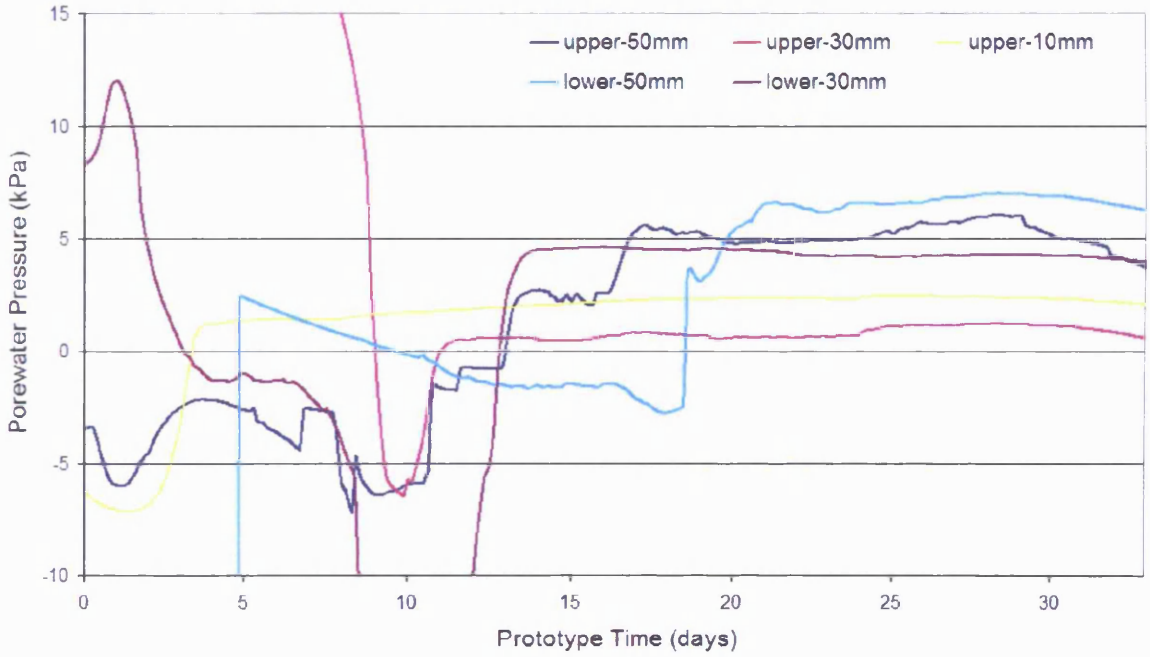

Figure 5.4.5. An example of fluctuating patterns of pore pressure before the penetration of the zero degree isotherm from Series 12D/NS (second thaw cycle). Note: Transducer depths given in model scale.

- *Final thawing and subsequent consolidation of the soil*

Continued thawing of soil ice during the period of the zero curtain eventually led to complete phase change. Release of meltwater from segregation ice left a saturated low density soil mass containing large water-filled voids, and a partial transfer of

total overburden stress to the soil pore water giving a rapid rise to positive pore pressures (see figs. 5.4.6, 5.4.7 and 5.4.8). The transition period between negative and positive pore pressures occurred between –1°C and 0°C for all depths (e.g. see fig. 5.4.4). Closure of voids and overall reduction in soil void ratio accompanied the thaw consolidation phase, so that the final period in this pore pressure history is associated with consolidation of a completely thawed soil, raised pore water pressures, progressive expulsion of excess pore water and progressive reduction in soil volume (thaw settlement). It was during this phase that downslope soil movements (solifluction) took place. In this thesis, therefore, the focus will be on this period of high pore pressures and the transducer readings observed during earlier warming of the still frozen soil will not be discussed in any detail.

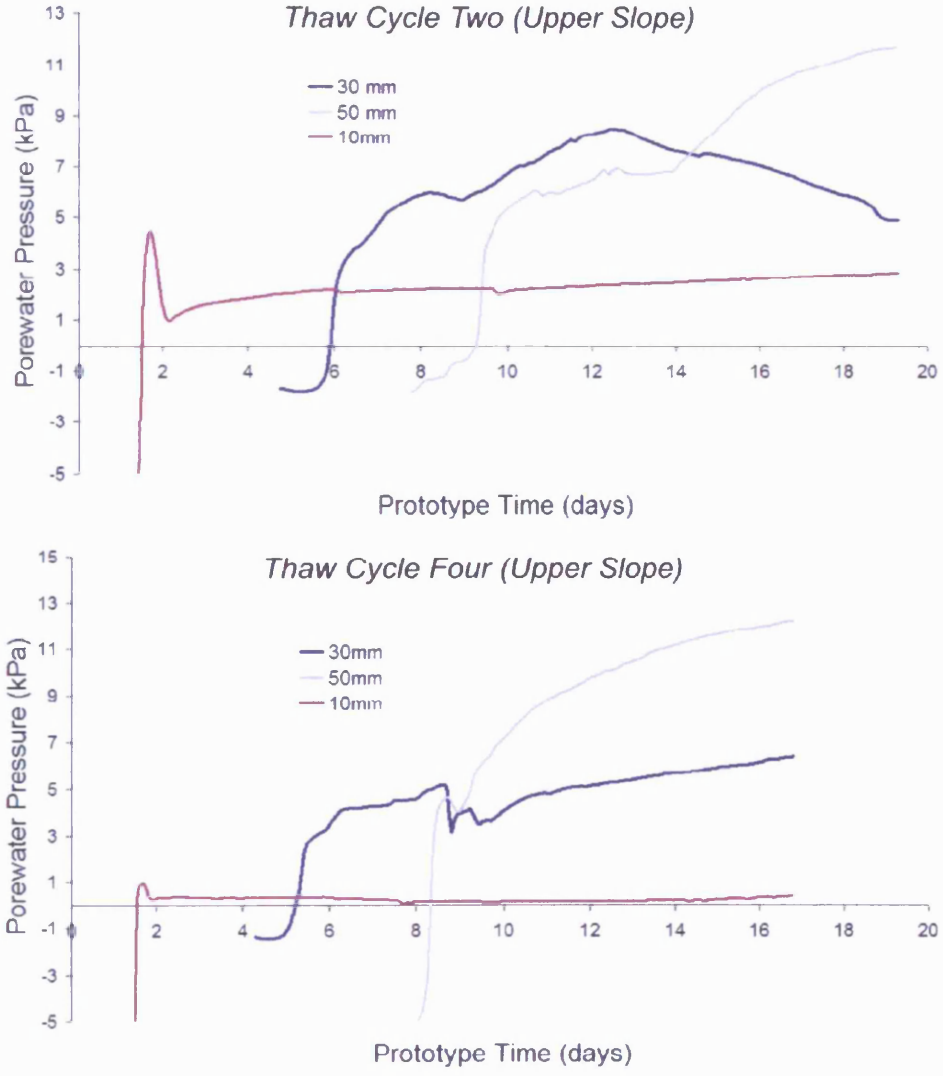

Figure 5.4.6. Pressure recorded during phases of soil thawing for Series 4D/10C. Note: Transducer depths given in model scale.

The sequence of pore pressure transducer readings described above replicates observations in earlier scaled centrifuge modelling of thawing silty soils (Harris *et al.*, 2000, 2001, 2003a; Murton & Harris, 2003) as well as in the full-scale modelling experiments by Harris *et al.* (1997) and Harris & Davies (1998).

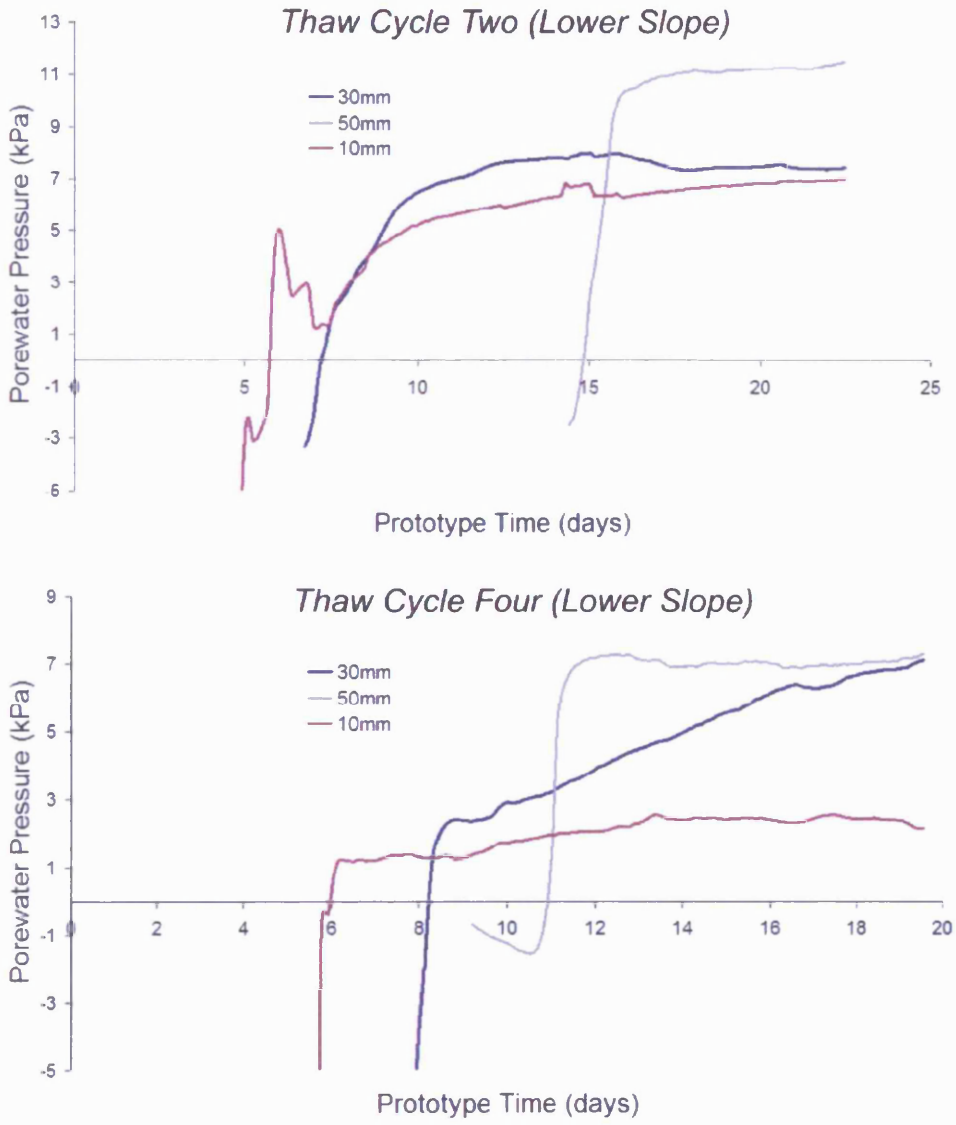

Figure 5.4.7. Pressure recorded during phases of soil thawing for Series 4D/10S. Note: Transducer depths given in model scale.

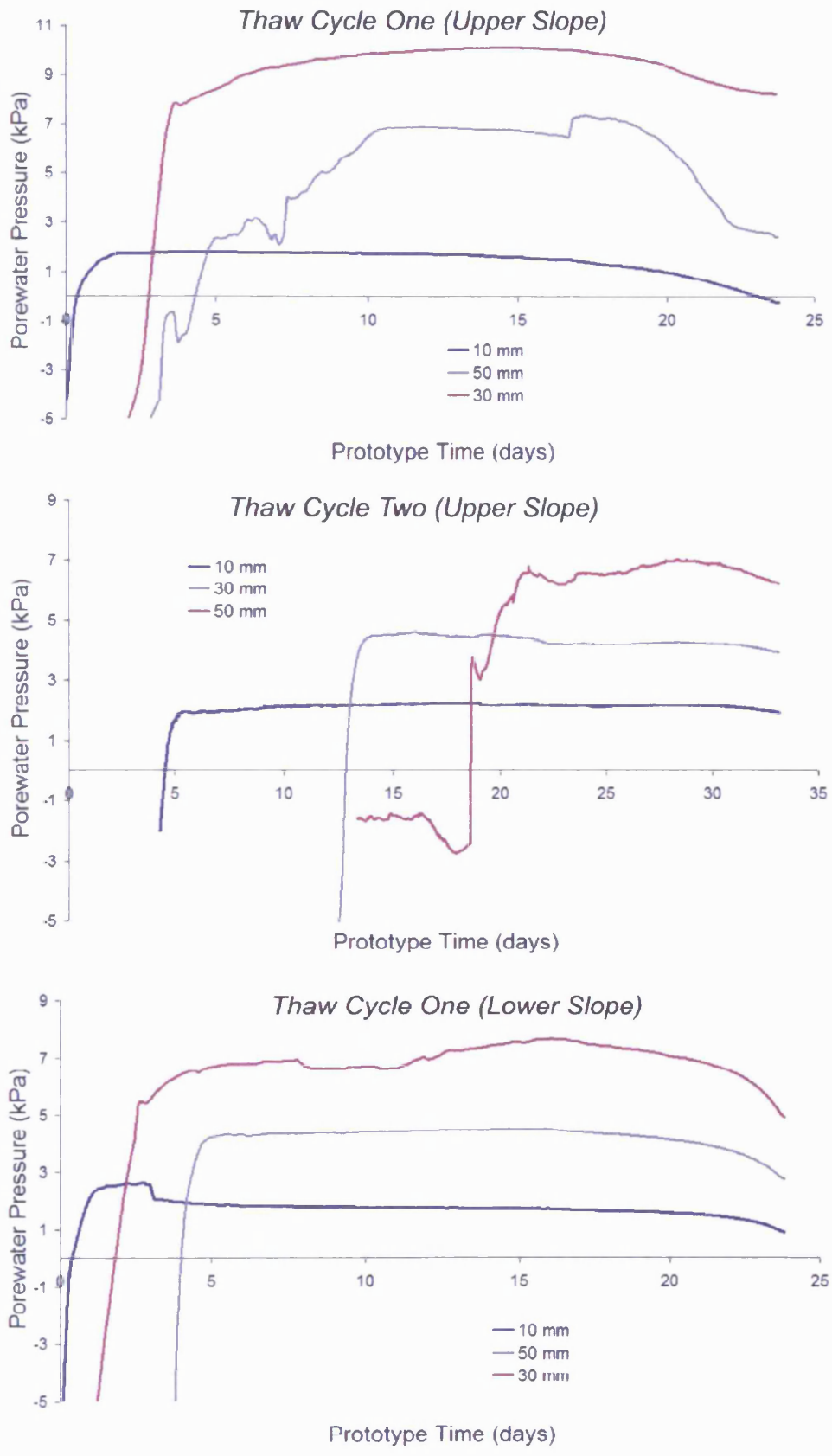

Figure 5.4.8. Pressure recorded during phases of soil thawing for Series 12D/NS. Note: Transducer depths given in model scale.

5.4.2. Style of pore pressure change during thaw consolidation

Figures 5.4.6 – 5.4.10 show a generally smooth, gradual evolution of pore water pressures during thaw consolidation. In most cases too, the highest pore pressures were recorded at the deepest depths within the soil profile and occurred at the latest stage in response to the downward progression of the thaw front through the slope model (see section 5.4.2) (Hallet & Waddington, 1992).

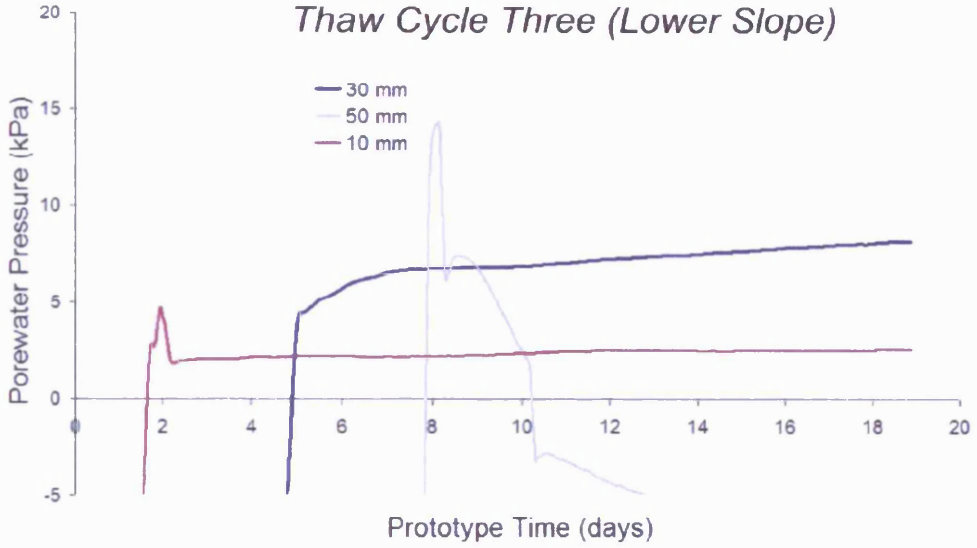

Figure 5.4.9. Pressure recorded during phases of soil thawing for Series 4D/20S. Note: Transducer depths given in model scale.

Figure 5.4.10 presents some clear examples of the dissipation of porewater pressure as the soil consolidated from Series 4D/NS. The fall in pore pressure would have been accompanied by a parallel increase in effective stress within the soil and a consequent increase in frictional strength via grain-to-grain contacts (e.g. thaw cycle two – fig. 5.4.10). A comparison of the pressure values between the three thaw phases highlights a high level of consistency with regard to pressure response to thaw penetration and soil consolidation.

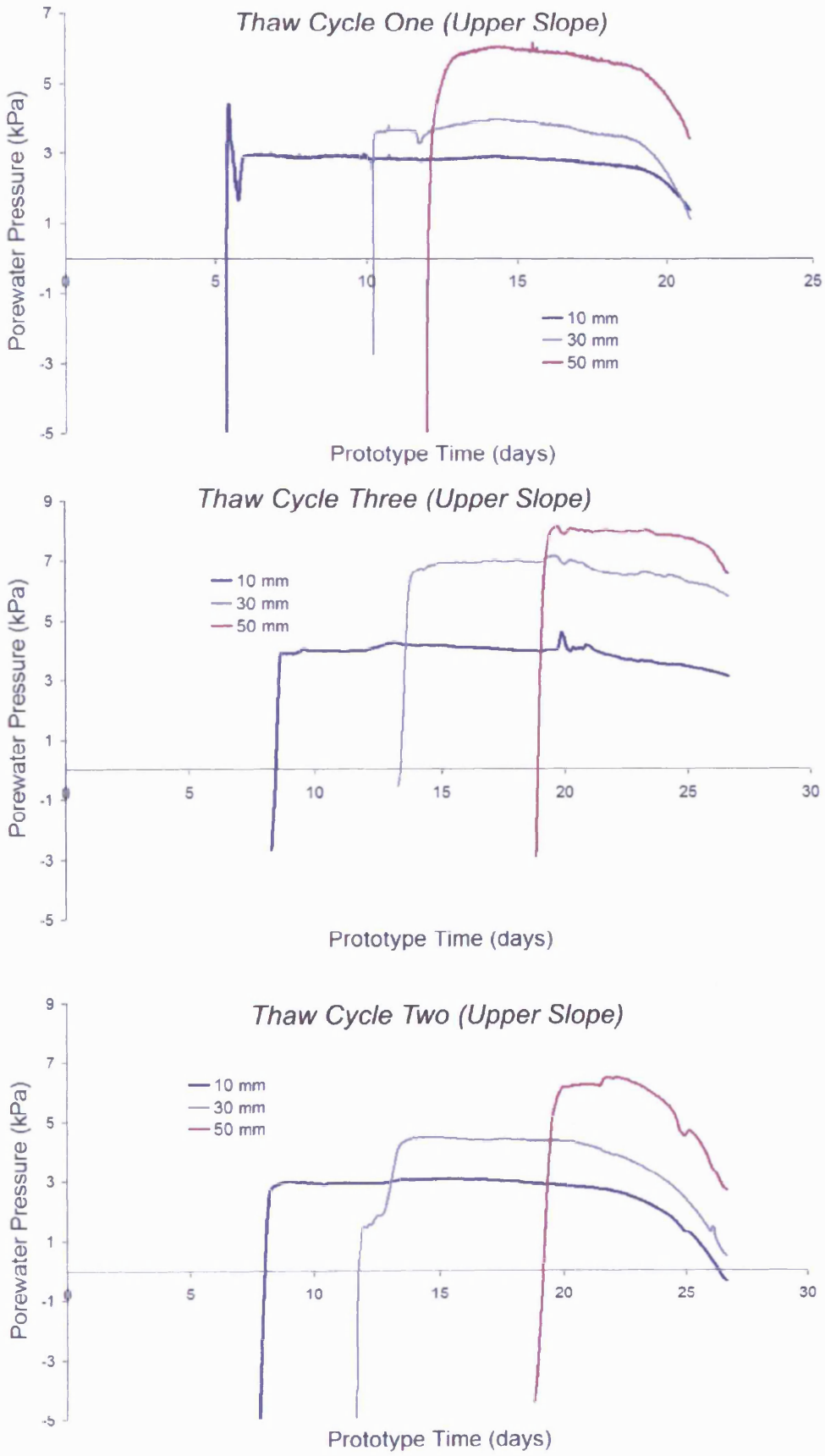

Figure 5.4.10. Pressure recorded during phases of soil thawing for Series 4D/NS. Note: Transducer depths given in model scale.

All the examples discussed above are from either the natural soil models (fig. 5.4.7, 5.4.10) the silt-enhanced soil (figs. 5.4.8, 5.4.9) or the natural soil plus 10% clay (fig. 5.4.6). However, in the model experiment using an admixture of 20% clay with the natural soil, pore pressure variation revealed a contrasting style (fig. 5.4.11). During thaw of this model experiment, pore pressures rose smoothly, but the rises were interrupted by repeated sharp falls in pressure, giving a "spiky" or "saw tooth" style of pore pressure change. It is felt this pattern may be a result of intermittent water escape events occurring within the clayey soil as a result of its low permeability and low strength. Thus, upward or lateral drainage of excess meltwater was severely impeded, allowing sharp rises in pore pressure to develop. Very similar saw tooth patterns of pore pressure change were observed by Harris *et al.* (2000) in their centrifuge simulation of thawing ice-rich clay soils and by Harris *et al.* (2003b) during slope simulation of solifluction processes in frozen overconsolidated silty clays soils.

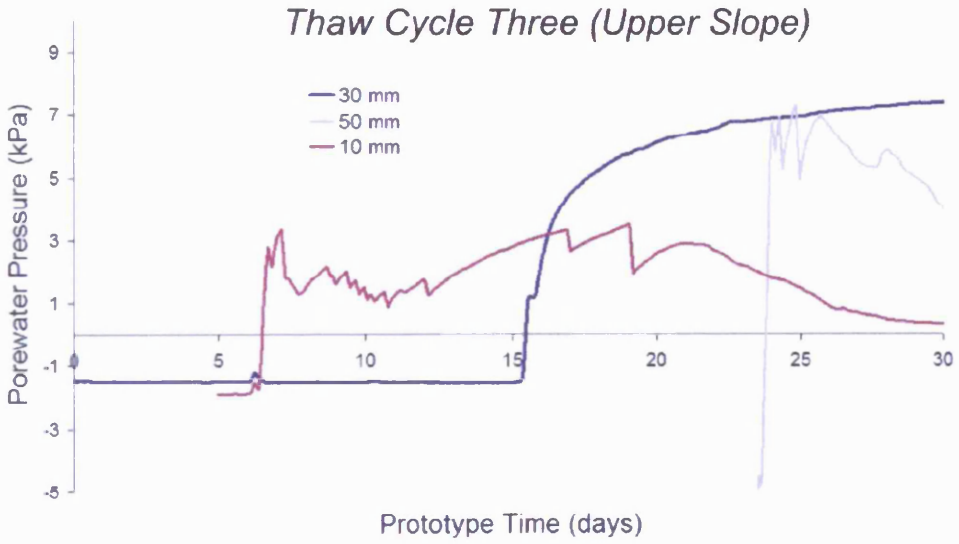

Figure 5.4.11. Pressure recorded during phases of soil thawing for Series 4D/20C. Note: Transducer depths given in model scale.

It is instructive to assess the ratio of pore water pressure to the total stress in Figure 5.4.12, since this provides an indication of whether pore water pressures were sufficient to lift the overlying soil mass and allow rapid water escape. If it is assumed that during thaw the soil bulk density was between 1.8 and 2.0 Mg/m^3, total stress at 0.1m depth prototype scale would have been between 1.75kPa and 1.96kPa and at 0.5m between 8.7kPa and 9.8kPa. Careful inspection of Figure 5.4.12(a)

shows that pore pressures peaked at just over 3 kPa in the 0.1m depth transducer, and between 7kPa and 8kPa at 0.5m depth, so that at the shallower transducer, pore pressures were in excess of geostatic and at 0.5m depth approximately equal to geostatic (if soil densities were lower, as they may have been, pore pressures may also have exceeded geostatic at 0.5m depths). This suggests strongly that sufficient pore pressures were generated to lift the overlying soil mass and allow water escape events to occur.

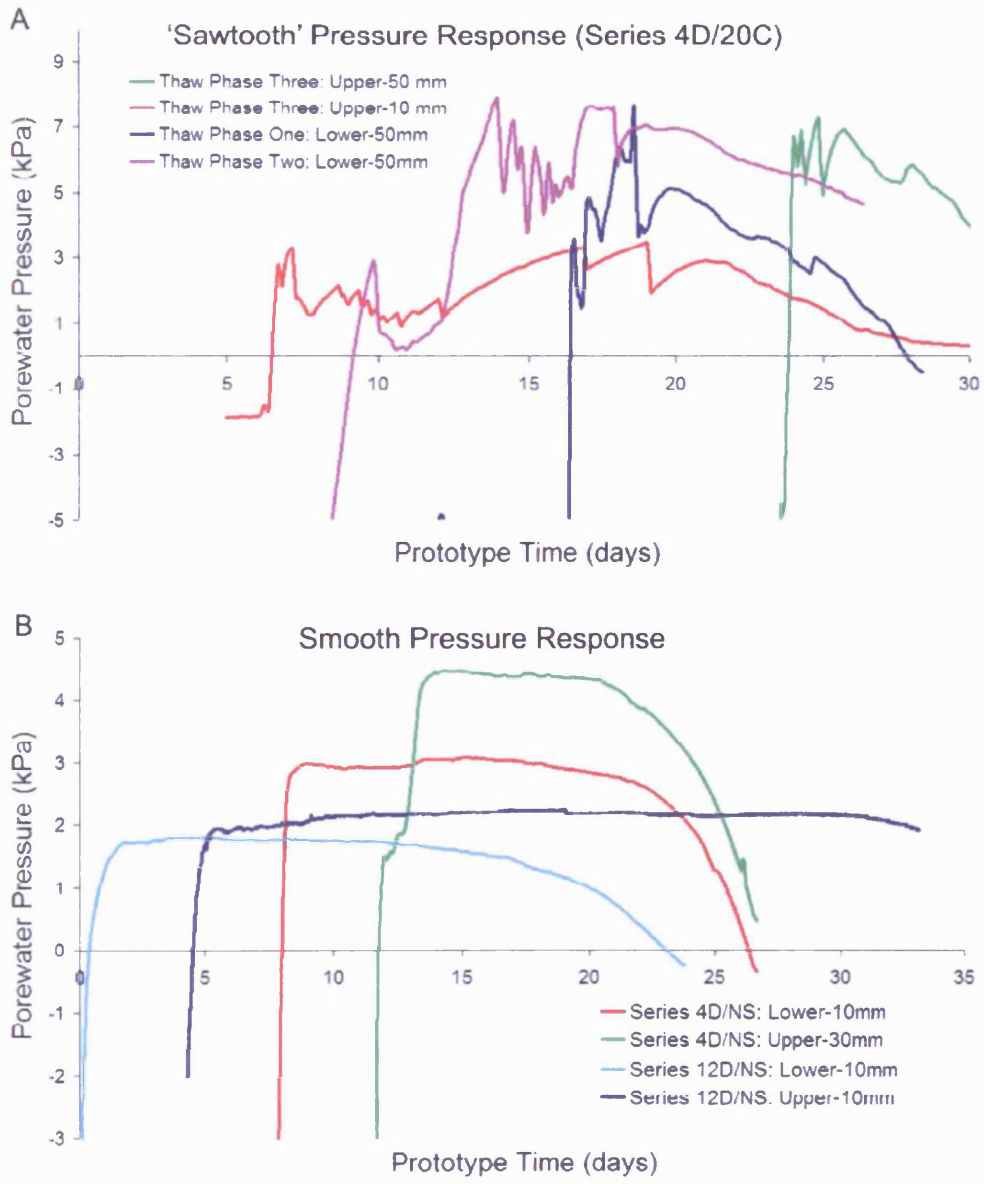

Figure 5.4.12. (a) Saw-tooth style of positive porewater pressure variation in the 20% clay soil model. (b) smooth pore pressure changes typical of all other soil models. Note: Transducer depths given in model scale.

A consistent near surface pattern of pressure response was noted within the majority of test series for all soil types (see fig. 5.4.13). Both the upper and lower 10mm transducer were observed to register very high positive porewater pressures during the initial stages of thaw consolidation. Exaggerated near surface pressure patterns have been previously reported by Harris *et al.* (1997) and Harris & Davies (1998). It is felt that these may have occurred in response to the greater thermal gradient in the near surface zones leading to faster thaw consolidation. The observed rise in near surface porewater pressures may also have been encouraged by the observed concentration of surface ice crystals formed underneath the freezing plate during model cooling periods.

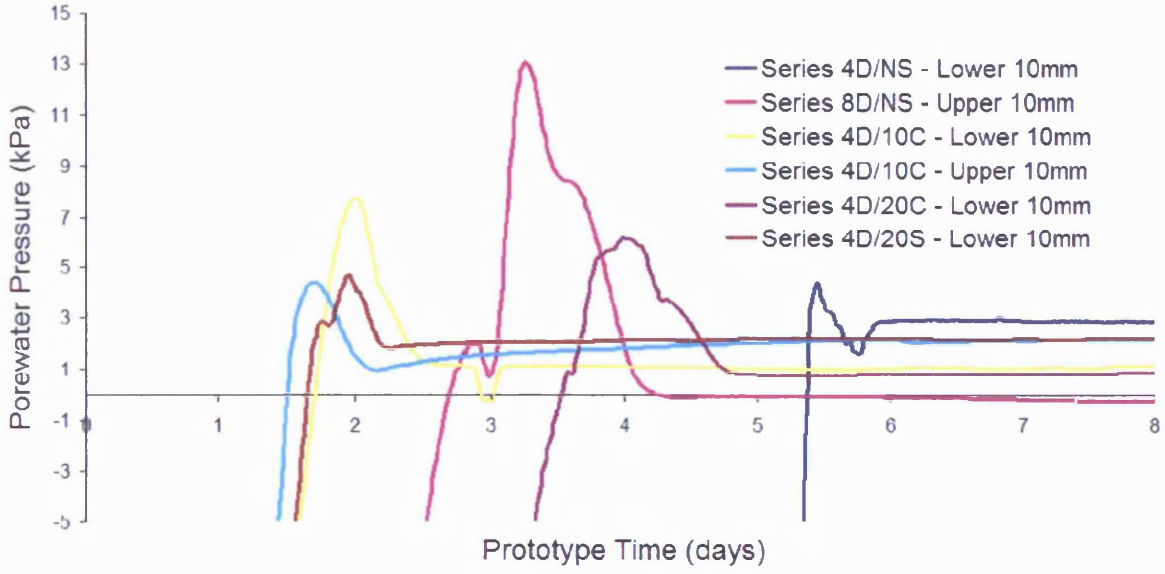

Figure 5.4.13. Near surface patterns of porewater pressure. Note: Transducer depths given in model scale.

5.4.3. Porewater Pressure Values

Pressure data were gathered from most datasets through recording the first discernible positive trend after the zero degree isotherm had passed the probe (see fig. 5.4.4). Data was not recorded if there was no discernible positive trend after thaw penetration had progressed through the depth of the buried probe.

The average maximum positive pressure at every depth for both slope regions are summarised within Tables 5.4.2.

Table 5.4.2. Average maximum values of porewater pressure at different model depths (kPa). Note: Transducer depths given in prototype scale.

Series	Lower Slope			Upper Slope		
	0.1m	0.3m	0.5m	0.1m	0.3m	0.5m
12D/NS	+2.66	+4.89	+6.43	+2.70	+5.41	+6.58
8D/NS	+7.98	n/a	+9.94	+8.61	+5.96	n/a
4D/NS	n/a	+5.44	+6.91	+3.71	+5.80	+7.20
4D/10S	+4.63	+8.78	+8.33	+6.65	+6.80	+9.94
4D/20S	+4.09	+7.89	+13.58	+5.84	+7.82	+13.52
4D/10C	+2.78	n/a	+7.60	+3.06	+6.63	+11.54
4D/20C	+5.20	n/a	+6.73	+1.89	+6.53	n/a

As expected, there was a general increase in pore pressure with depth during most thaw phases (fig. 5.4.14). This reflects the progressive increase in hydrostatic head above deeper transducer locations. Maximum pore pressures at the 10mm depth, are in some cases anomalously high (e.g. lower and upper slope in 8D/NS, and upper slope in 4D/10S and 4D/20S). These values relate to the unexplained short-duration peak values registered immediately after thaw (see fig. 5.4.13).

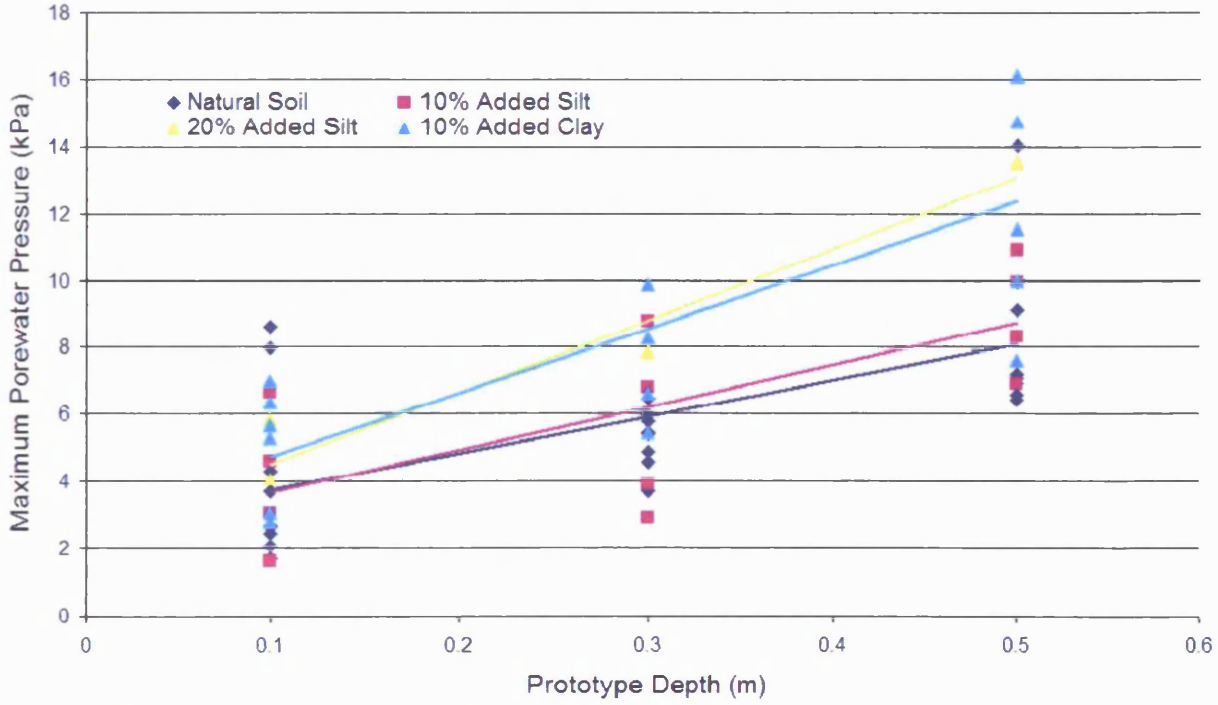

Figure 5.4.14. Maximum pore pressures recorded at different depths for each test soil. Note: Series 4D/20C not presented due to lack of useable data.

The trend lines suggest that pore pressures were generally similar in the natural soil and the natural soil plus 10% silt, but significantly higher in the models with 10% added clay and 20% added silt. This is thought to reflect the lower permeability of

the latter soils, allowing greater pore pressures to develop. Note that the relatively high pore pressures observed during thaw of the 20% silt model occurred despite the relatively limited ice segregation and frost heave recorded during each of the four freezing phases in this test. Thus, it appears that the 20% silt soil may be particularly susceptible to generation of thaw-induced excess pore pressures. The style of pressure variation in the 20% clay model discussed above suggests that water escape events occurred before pore pressures reached their potential maximum values. This change in style of pore pressure dissipation may well be a critical factor affecting slow pre-failure deformation of thawing clay slopes, and in controlling the factor of safety against rapid failure.

5.4.4. The significance of the Thaw Consolidation Ratio

The positive porewater pressures recorded during model thawing resulted from the thaw-consolidation process whereby the rate of thaw released porewater at a rate exceeding that at which it could flow from the soil. The individual characteristics of each test soil can therefore have an effect on porewater pressures during thaw by influencing the ice content, ice distribution, permeability, compressibility, etc. The second major control on thaw-induced pore pressures is the rate of thaw. The generation of porewater pressures therefore depends upon the ratio between rate of thaw (meltwater release) and rate of consolidation (rate of meltwater expulsion) as the voids left by the melting of segregated ice can only be closed if excess meltwater is expelled from the soil (McRoberts & Morgenstern, 1974). This ratio forms the basis for the Thaw Consolidation Ratio (R) (McRoberts and Morgenstern, 1974; Nixon and Ladanyi, 1978; Morgenstern, 1981; see Section 2.1.9 for details) where:

$$R = \frac{1}{2}\left[\frac{\alpha}{\sqrt{C_v}}\right] \qquad (5.2)$$

where

$$\alpha = \frac{X_t}{\sqrt{t}} \qquad (5.3)$$

X_t is depth of thaw in time t and C_V is the coefficient of consolidation. An important factor justifying the centrifuge modelling technique is that there are no scaling conflicts when modelling thaw consolidation at elevated gravitational

acceleration, so that the R value is the same when calculated at model scale and at prototype scale (see Section 2.5.2 and equations 2.8-2.9). Calculated R values are presented in Table 5.4.8.

Table 5.4.8. Thaw consolidation ratio for test series involving gelifluction processes. Note: that the mean thaw rate for each of the four freeze thaw cycles is used to calculate R in this table.

Series	α (m/year^{½})	Cv (m^2/year)	Thaw Consolidation Ratio (R)
12D/NS	2.51	12.74	0.35
8D/NS	2.91	12.74	0.41
4D/NS	2.66	12.74	0.37
4D/10S	2.96	14.95	0.38
4D/20S	3.35	10.74	0.51
4D/10C	2.86	6.63	0.56
4D/20C	2.53	5.60	0.53

The thaw consolidation theory suggests that pore pressures during thaw are directly related to the thaw consolidation ratio R. To investigate this, average pore pressure data from Table 5.4.2 have been compared with the average thaw consolidation ratios presented in Table 5.4.8 for transducer depths of 0.3m and 0.5m (prototype scale) (see figs 5.4.15 and 5.4.16).

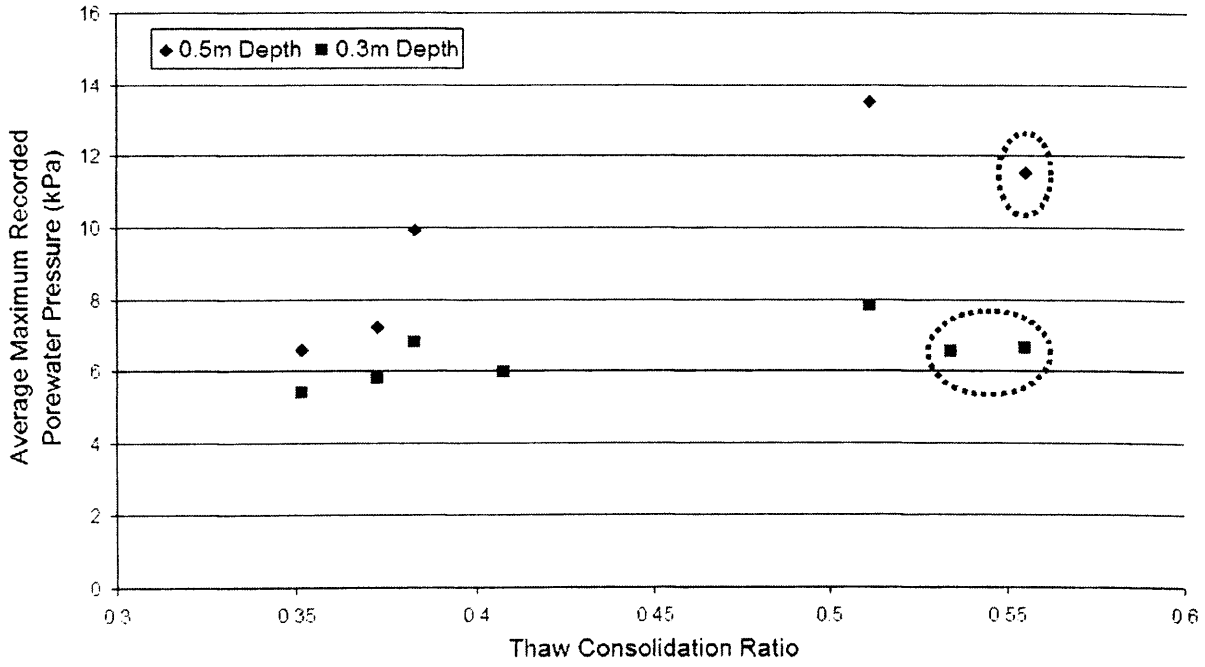

Figure 5.4.15. Influence of thaw consolidation ratio upon maximum porewater pressure within the upper slope region of slope models. Note: circled datapoints represent the clay-enriched soils.

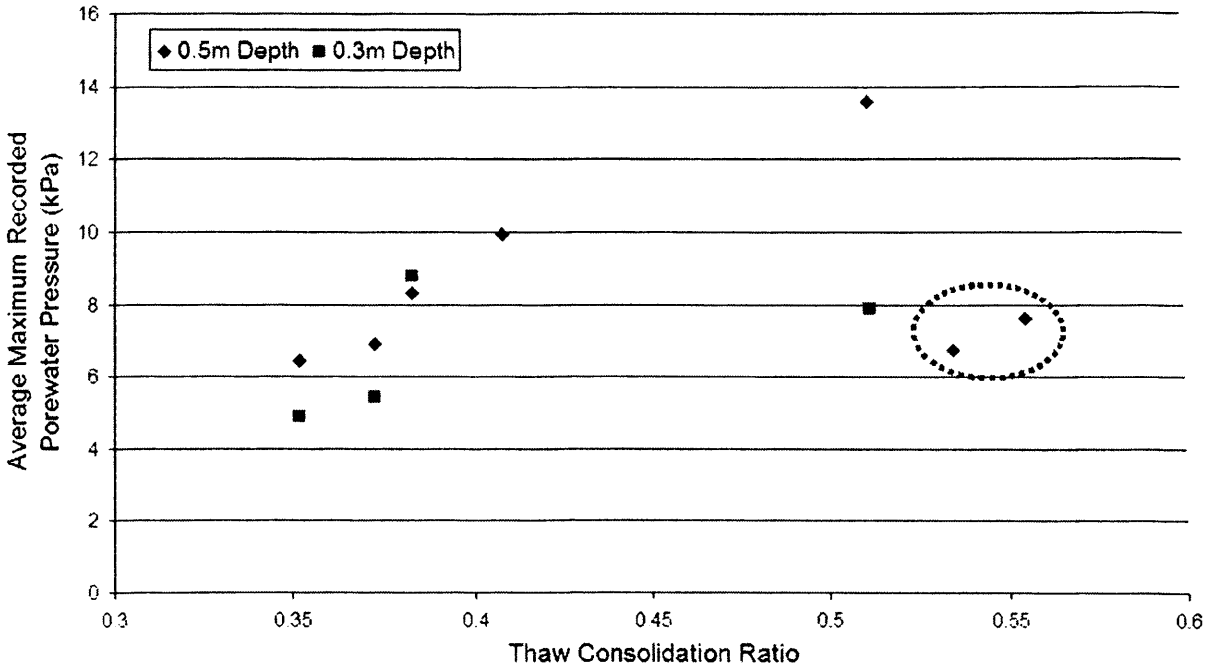

Figure 5.4.16. Influence of thaw consolidation ratio upon maximum porewater pressure within the lower slope region of slope models. Note: circled datapoints represent the clay-enriched soils.

There is a clear trend for increasing maximum pore pressures with increasing value of R, with the main controlling variable being the rate of thaw (determining the α value). This is particularly well shown for the 0.5m depth transducers in the natural soil and soil + silt models. In Figures 5.4.15 and 5.4.16 above, the data for the models constructed with clay enhanced soils are circled. In all cases the recorded average maximum pore pressures within the clay models are lower than might be anticipated. It was proposed that the observed "saw tooth" pore pressure fluctuation in the 20% clay model arose from water escape events, and threshold values of pore pressure were observed beyond which rapid water escape drainage occurred. It is likely, therefore, that pore pressures in the clay-rich models did not reach their potential values, because before this water escape was triggered, rapidly draining the soil.

5.4.5. Summary

- Overall, a steep rise in positive porewater pressure was recorded in most test series and as a result of phase change from ice to water
- There is a slight uncertainty as to the precise relationship between thermocouple temperature data and the moment at which pressure

transducers responded to rising pore pressures. This was due to the dimensions of the pore pressure transducer, and the complexity of the soil-ice-meltwater-transducer interactions.

- This pore pressure response to thaw commonly followed a period of negative pressures (suction) within the unfrozen water films created by the reduction of water volume during phase change.
- Water pressures during thaw consolidation showed a general increase with depth.
- Pore pressures rose and then slowly fell through the thaw consolidation period as overburden stress from the consolidating soil was transferred from the soil water to the soil matrix.
- Pore pressure response differed markedly in the 20% clay model (4D/20C), since the rise in pore pressures following thaw was repeatedly interrupted by sharp falls, giving a "saw-tooth" pattern. This was interpreted as resulting from water escape events whereby water occupying voids left by ice lenses drained rapidly.
- The average thaw consolidation ratio was below unity, but directly influenced the maximum pore pressures recorded, particularly in the natural soil and silt enhanced soils.
- In the clay-enhanced soils, pore pressures may not have reached their maximum potential values due to water escape events.

5.5. Downslope Movement

The following section will outline the style and rate of downslope soil deformation in terms of surface movement and subsurface volumetric displacement, the former being derived from surface marker displacements recorded following every thaw phase and the latter, deformation of plastic columns excavated at the end of each test series.

5.5.1. Surface Movement

Surface displacement was measured through fifteen markers embedded into the upper layer of the slope model (see fig. 5.5.1). The surface markers were placed onto the model surface away from the key instrumentation zones as these areas were subject to additional surface disruption through the pressure probe and thermocouple installation process and cabling associated with the transducers (see fig. 3.3.1). The aerofoil attached to the strongbox masked specific zones of the slope model – the aligned positioning of the markers therefore allowed the centrally-housed digital camera to record progressive movement of all markers (see fig. 5.5.2). Images were automatically acquired every twenty minutes.

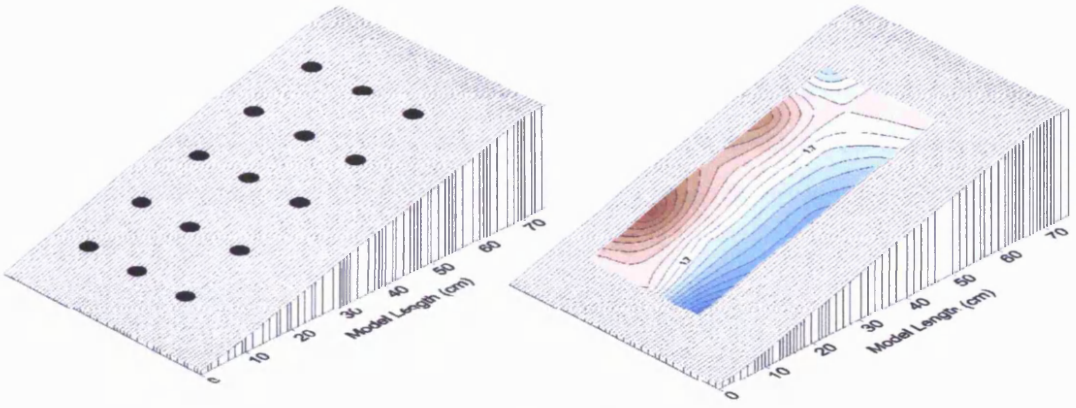

Figure 5.5.1. Surface movement markers and the derived zone of contoured downslope movement.

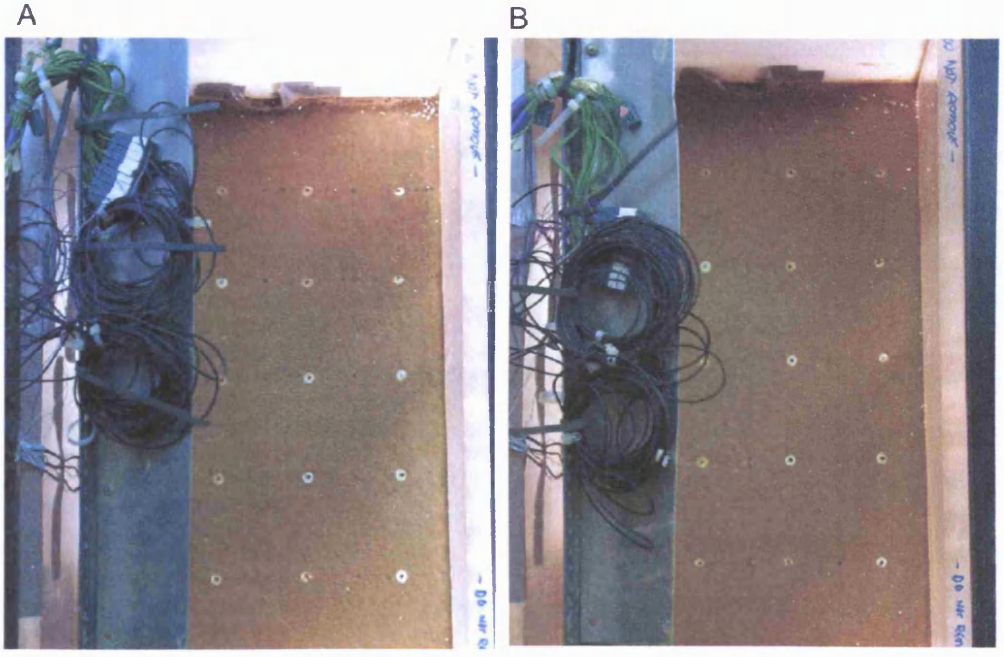

Figure 5.5.2. Inflight position of surface markers on model captured via the centrally mounted digital camera. Note: Photograph A taken at 20 minutes from Series 8D/NS (thaw cycle two). Photograph B taken at 120 minutes from Series 8D/NS (thaw cycle three).

Ice crystals were observed to grow underneath some markers during certain freezing phases. This appeared to be the result of water accumulating underneath the markers as a result of transfer of vertical pressure exerted via the freezing plate and expulsion of pore water during the resulting consolidation process. Surface markers underlain by the excess ice occasionally gave exaggerated movement readings during thaw and it is assumed that this was caused by gliding across the model surface as ice beneath the marker melted.

5.5.2. Patterns of Surface Movement

Downslope surface movement was consistent between the four thaw cycles for each slope model (see table 5.5.1 and fig. 5.5.3). The spatial consistency of slope model and test soil behaviour therefore allowed surface movement to be described as an across model average for every individual thaw cycle (for example see table 5.5.3 and figure 5.5.9).

Table 5.5.1 illustrates that the initial thaw cycle was generally associated with a relatively large average surface movement, but in many cases average movement rates were as large if not larger in one or more later cycles. After the initial thaw period the natural soil showed incremental increases in the amount of surface deformation for each thaw cycle, perhaps through the development of a cryogenic and mass movement related soil fabric. The silt enhanced soils had a consistent response to thaw and showed minor variations in movement after the initial thaw phase. The clay soils showed a progressive decline in surface movement, except for cycle 4 in the 10% clay model (4D/10C) in which the final cycle surface movement rate was the largest recorded in the series. Sections 5.2 and 5.3 have mentioned that the clay soil test series had relatively little segregated ice within the upper profiles and showed the largest amount of volumetric compression during thaw – both of these factors might increase stiffness in the upper layers by decreasing void ratio and consolidation.

Table 5.5.1. Average per cycle downslope surface movement (mm) for each thaw cycle for different test soils.

Test Series	Thaw Cycle One	Thaw Cycle Two	Thaw Cycle Three	Thaw Cycle Four
12D/NS	5.60	3.40	3.60	4.06
8D/NS	1.80	1.60	2.80	3.60
4D/NS	1.53	1.00	2.80	3.33
4D/10S	1.60	3.33	2.26	3.80
4D/20S	6.93	3.80	4.60	3.40
4D/10C	1.93	1.40	1.20	2.26
4D/20C	3.40	2.73	1.53	1.20

The average rate of surface movement was observed to vary downslope. In the natural soil models this was particularly marked in the 12° and 4° slope gradients, where movement was greatest in the central slope zone, and least apparent in the 8° slope model, where average movement rates increased progressively downslope (table 5.5.2 and figs. 5.5.3 and 5.5.4).

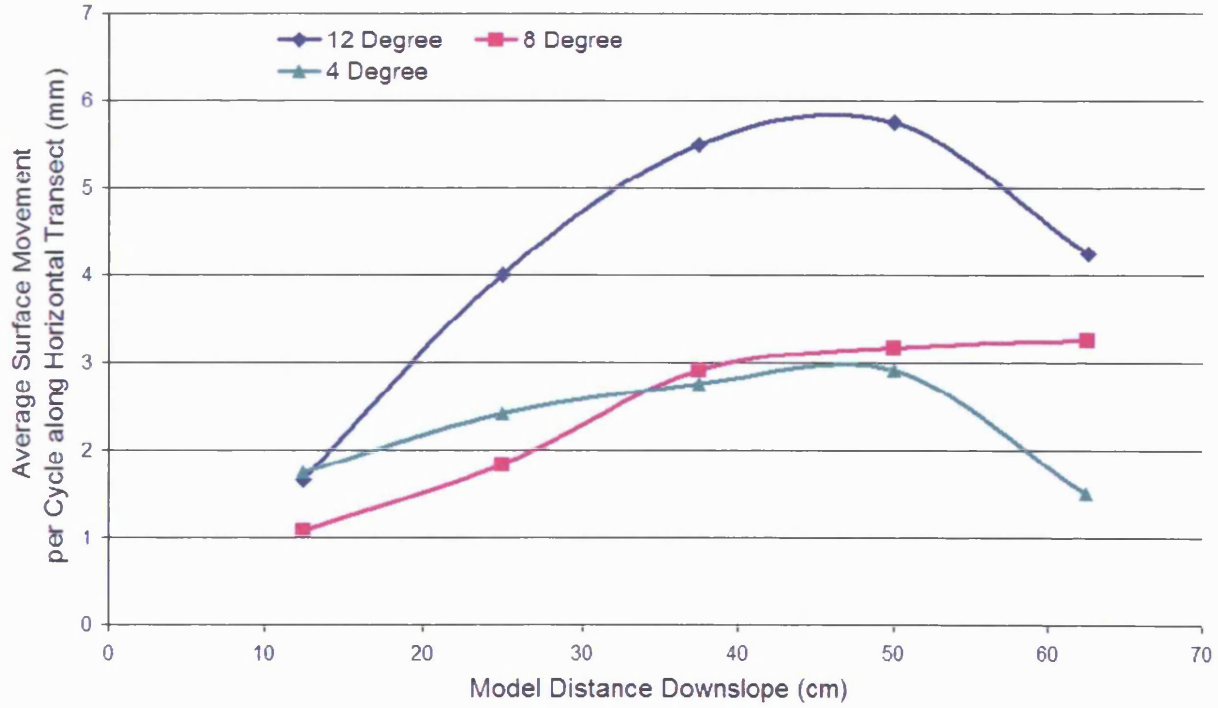

Figure 5.5.3. Average per cycle surface movement for each marker transect within test series involving natural soil.

Figure 5.5.4 illustrates the consistency of downslope deformation between thaw cycles for Series 8D/NS with a less than 6mm range of marker movement across the four cycles. Series 8D/NS reiterates the relationship shown in Table 5.5.1 by providing an example of surface movement becoming slightly more pronounced in

lower slope regions across the four cycles, it is felt this pattern may be the result of cryogenic fabric development through repeated freezing, thawing and pre-failure soil strain (Chamberlain & Gow, 1978; Dyke & Eggington, 1990).

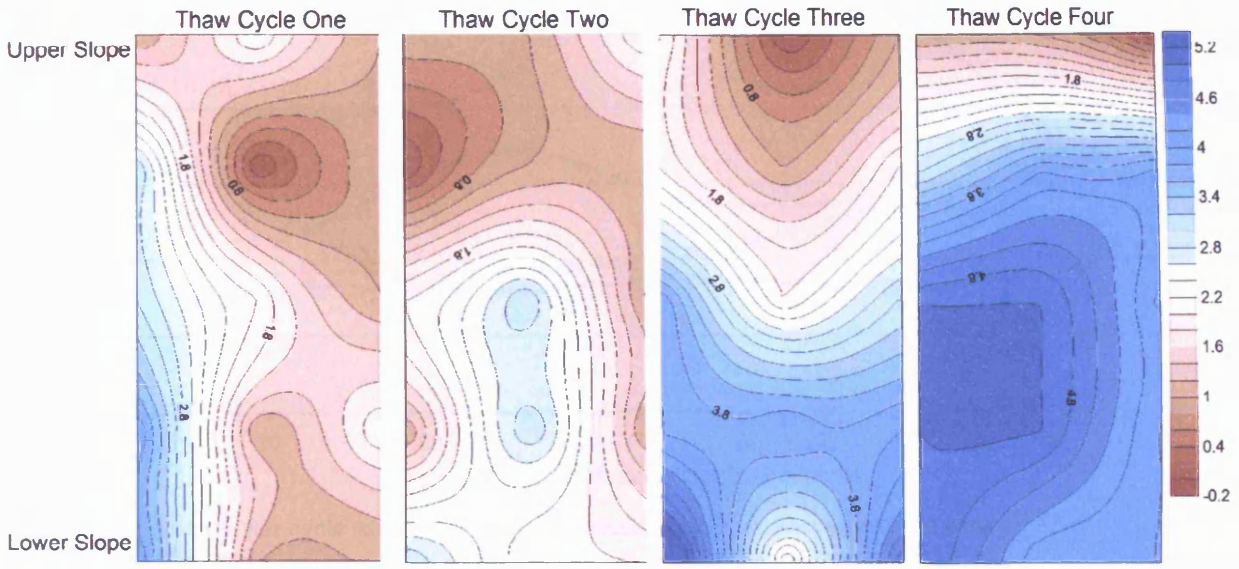

Figure 5.5.4. Average per cycle downslope surface displacement for each thaw cycle of Series 8D/NS.

Surface movement became more pronounced towards the foot of the model, with an average 28% increase in per cycle surface movement from the uppermost to lowest marker transect (see table 5.5.2).

Table 5.5.2. Average per cycle downslope surface movement (mm) for each three marker horizontal transect (see fig. 5.5.1 for context).

Series	Distance Downslope				
	12.5cm	25cm	37.5cm	50cm	62.5cm
12D/NS	1.67	4.00	5.50	5.75	4.25
8D/NS	1.08	1.83	2.92	3.17	3.25
4D/NS	1.75	2.42	2.75	2.92	1.50
4D/10S	2.42	3.42	2.75	2.75	2.42
4D/20S	3.75	4.42	6.83	5.33	3.08
4D/10C	1.67	1.58	1.75	1.58	1.92
4D/20C	1.83	1.83	2.08	2.75	3.25
Average	2.02	2.79	3.51	3.46	2.81

The difference in movement pattern cannot be ascribed to the change in model gradient and it is likely that the distribution of frost heave and thaw settlement across the slope profile may have played a significant role in determining the observed movement patters in Series 8D/NS, 4D/NS and 12D/NS

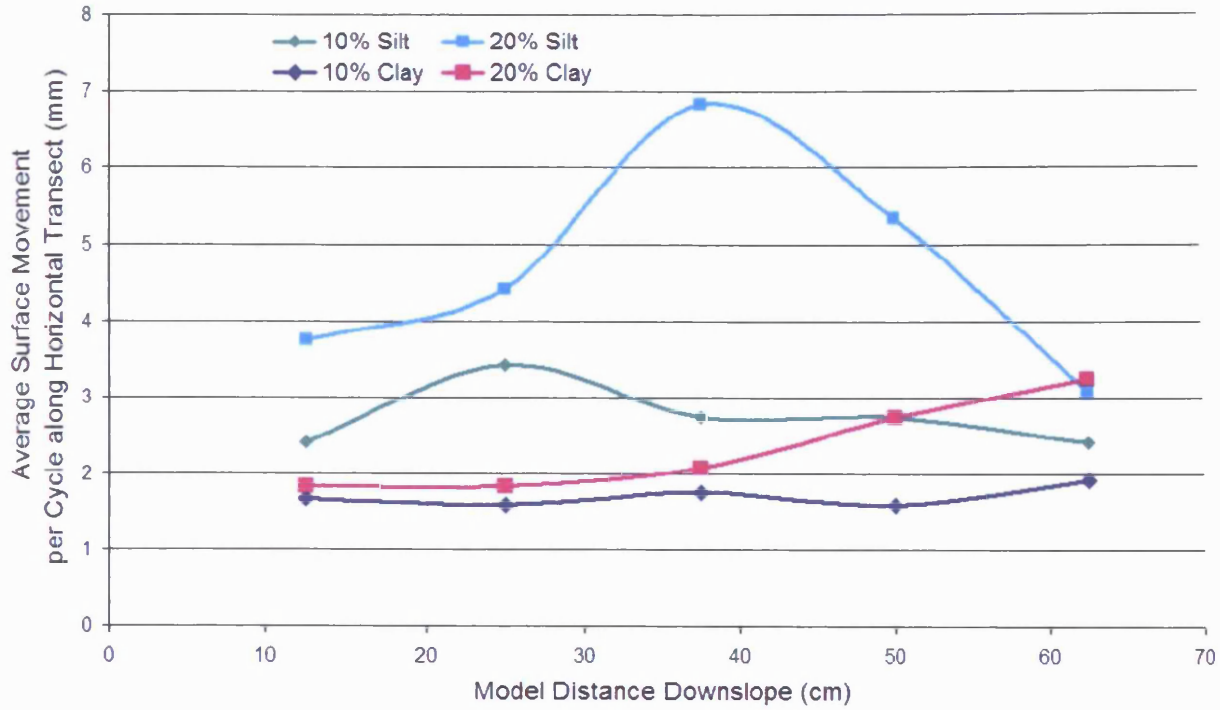

Figure 5.5.5. Average per cycle surface movement for each marker transect within test series involving modified soils.

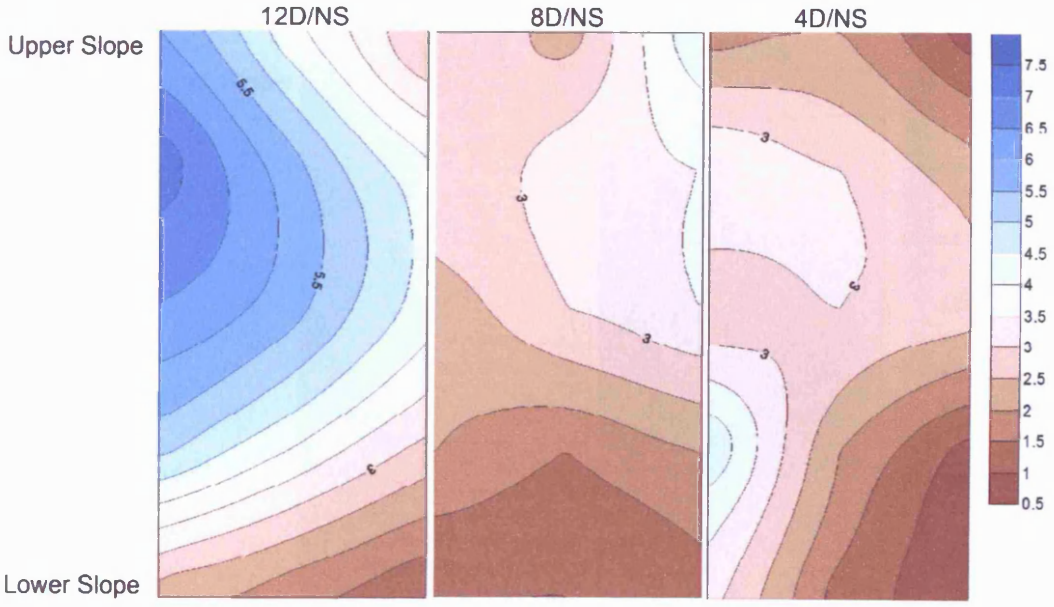

Figure 5.5.6. Average per cycle surface movement (mm) within test series using natural soil.

Comparing the distribution of average surface movement rates across the slope models in the 4° slope models formed in different soil types, reveals greatest spatial consistency in the clay-enriched soils and much greater spatial variation in the silt-enhanced soils (fig. 5.5.5). The clay-enriched soils showed an increase in movement in the lower slope regions, but in the silt-enhanced soil models,

movement was greatest in the upper mid-slope zones. The distribution of frost heave and thaw settlement undoubtedly had an influence in these patterns, but it is also likely that in the more cohesive clay models the downslope transmission of strain through the entire catenary sequence was facilitated in comparison with the silt-enriched soil models in which shear strain during thaw represented a more localised response to soil ice content, leading to a larger spatial variation in surface movement.

The spatial variation in surface movement was greatest within the slope models showing the largest overall amount of deformation (see section 5.5.2). Figure 5.5.6 highlights this pattern where the twelve degree model (12D/NS) has shown a large variance across the model with movement being concentrated within the central and upper left slope zones, whereas the eight and four degree slopes (8D/NS and 4D/NS) show slightly less overall movement and smaller spatial variation, with a pronounced lack of movement at the foot of the slope.

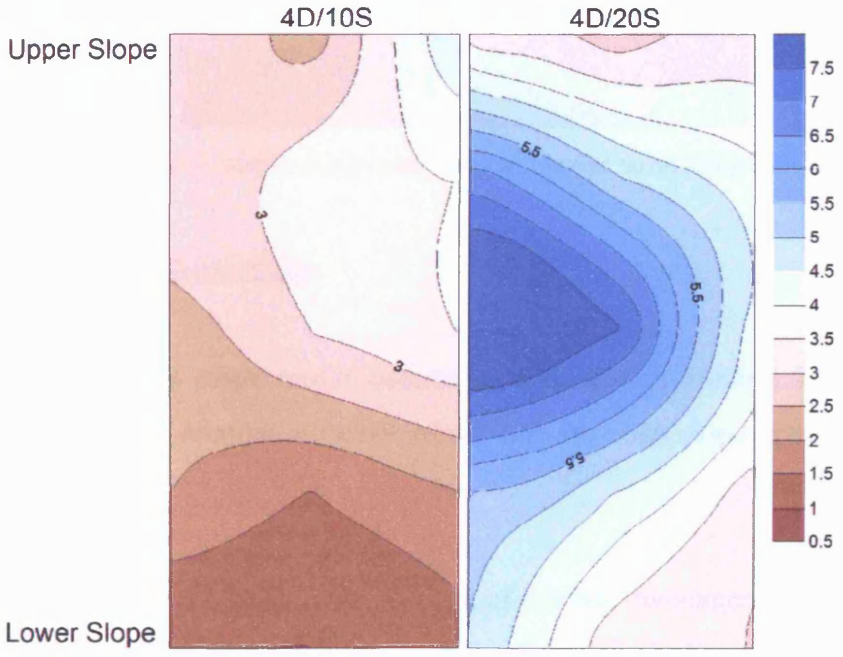

Figure 5.5.7. Average per cycle surface movement (mm) within test series using additions of silt.

Soil granulometry would appear to have had a direct influence on the spatial variability of surface movement. Figure 5.5.7 shows that the addition of the ten percent silt to the natural soil has had little impact and patterns have replicated those seen within Series 4D/NS. However, the addition of another ten percent silt within

Series 4D/20S has generated a large response with considerably more movement within the central slope region, the spatial distribution of this movement is possibly related to segregated ice development and patterns of thaw settlement and this relationship will be examined within section 6.2. The large amount of surface movement within the central and upper left slope zones for Series 4D/10S & 4D/20S has led to the possible generation of the infant landforms described in Section 5.5.8.

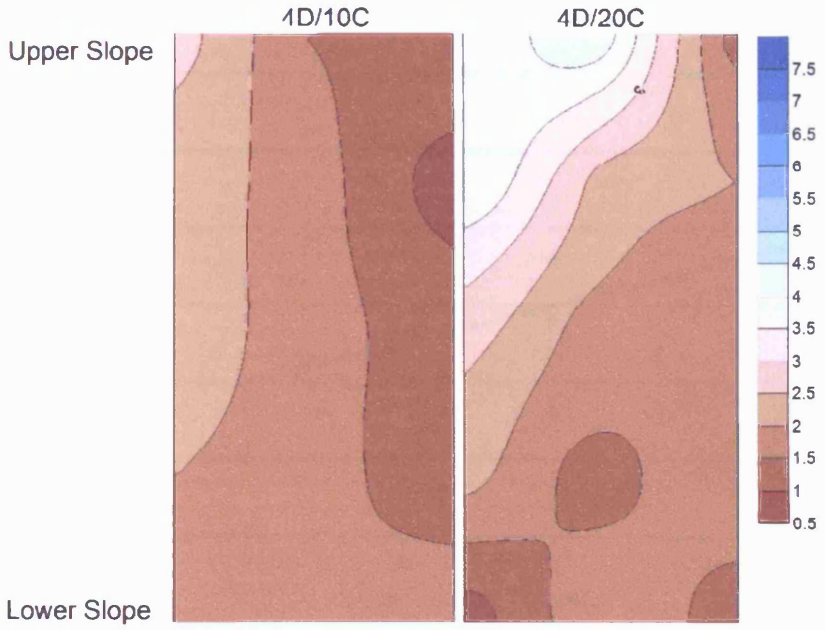

Figure 5.5.8. Average per cycle surface movement (mm) within test series using additions of clay.

5.5.3. Rates of Surface Movement

The coherent nature of slope model behaviour described in Table 5.5.1 allowed a clear assessment of the relative influence of the two variables slope gradient and soil grainsize.

Table 5.5.3 emphasises that the overall rate of surface movement was consistent between different thaw cycles of the same test series with the Standard Deviation of movement not exceeding ±1mm for all markers across a test series. In comparing the natural soil models, the largest amount of movement was recorded on the twelve degree natural soil slope (12D/NS) with an average per cycle movement of 4.17mm. This was 70% more than that exhibited within the 8 degree model and 92% more than that recorded during the four degree model thaw phases. Figure 5.5.9

illustrates that there is a clear positive relationship between a greater slope angle and an increased amount of surface movement during thaw consolidation.

Table 5.5.3. Average per thaw cycle surface movement at model scale (mm) for each slope gradient in natural soil models. SD = Standard deviation.

12°	SD (12°)	8°	SD (8°)	4°	SD (4°)
4.17	±1.00	2.45	±0.93	2.17	±1.08

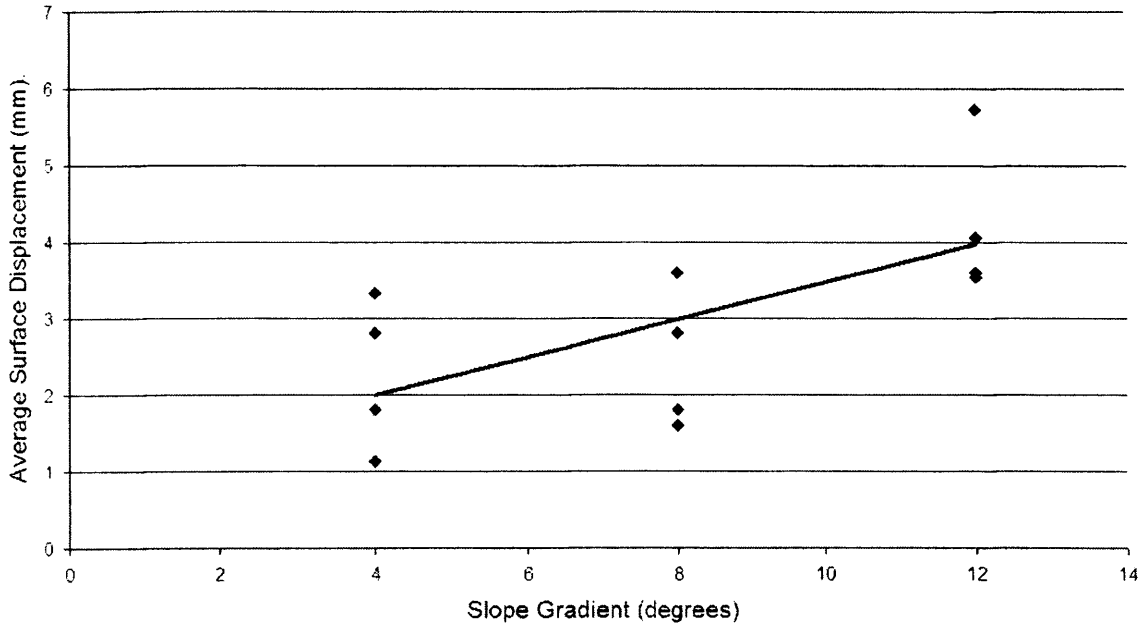

Figure 5.5.9. Influence of slope model gradient upon surface movement for test series involving the natural soil.

Table 5.5.4 illustrates that progressive changes to the soil grainsize directly impacted on observed rates of surface movement without creating inconsistent model behaviour, for example Series 4D/10C had a standard deviation of just ±0.49mm for all surface markers across a four thaw phase series. The most inconsistent surface displacement (SD ±1.58mm) was measured within Series 4D/20S, however this occurred in response to the largest average overall surface movement (4.68mm/cycle) and probably represents different zones of the model deforming in response to localised frost heave and thaw consolidation (see section 6.5.1).

Table 5.5.4. Average per thaw cycle surface movement at model scale (mm) for each soil type. SD = Standard deviation.

Natural Soil	SD (NS)	10% Silt	SD (10S)	20% Silt	SD (20S)	10% Clay	SD (10C)	20% Clay	SD (20C)
2.17	±1.08	2.75	±1.00	4.68	±1.58	1.70	±0.49	2.22	±1.03

The addition of silt into the natural soil caused an increase in surface movement. The addition of ten percent silt caused a 21% increase whilst the twenty percent silt increment caused a 54% increase when compared to the 4° natural soil slope model (4D/NS). The twenty percent silt soil reacted with 70% more movement than the ten percent silt soil despite the fact that the heaving ratio in this model series was the lowest of all models (see table 5.3.1). This almost certainly indicates a behavioural threshold with the 10% silt enhancement causing only a slight increase in flow susceptibility, but increasing this to 20% causing a significantly greater response to thaw consolidation (see fig. 5.5.10).

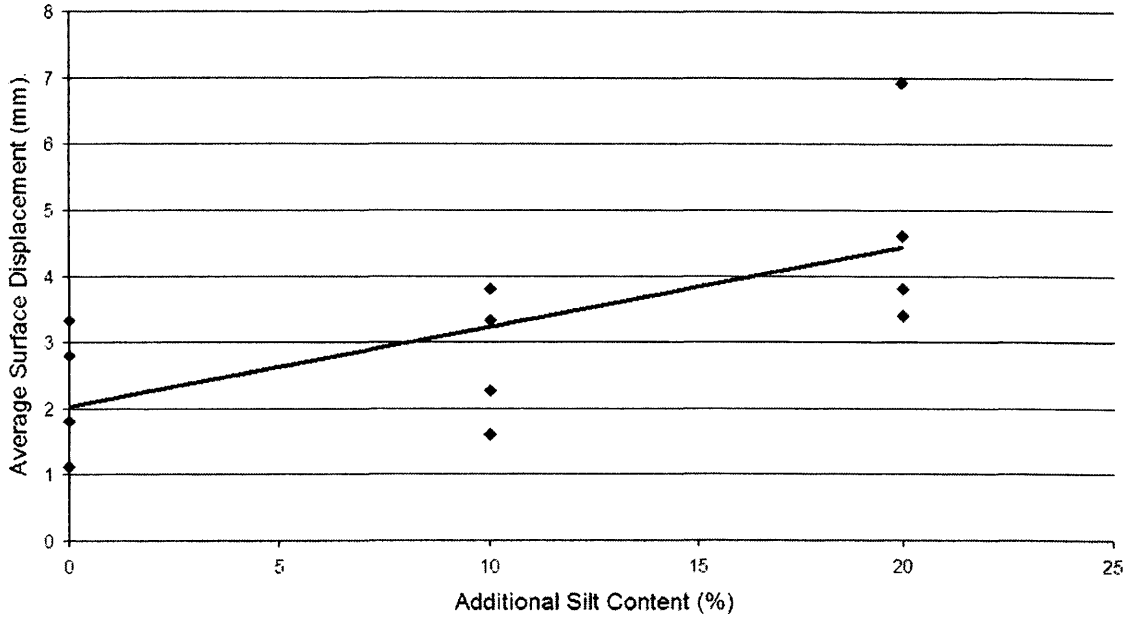

Figure 5.5.10. Influence of additional silt content upon surface movement within four degree slope models.

The addition of clay had a mixed effect on surface movement with the ten percent clay soil being associated with a 28% reduction, whilst the twenty percent clay caused a 2% increase in measured average surface displacements when compared with the natural soil of Series 4D/NS (see table 5.5.4). The addition of the extra ten percent clay within Series 4D/20C therefore caused a 30% increase in overall surface movement when compared with Series 4D/10C.

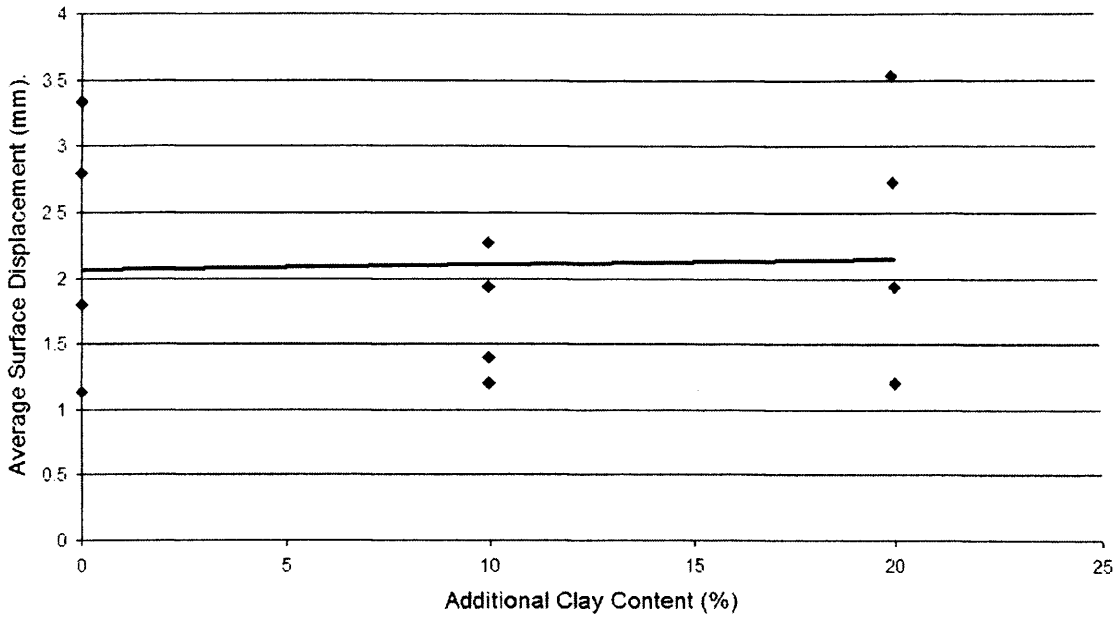

Figure 5.5.11. Influence of additional clay content upon surface movement within four degree slope models.

5.5.4. Subsurface Movement

Subsurface marker columns were excavated along two distinct transects after the final thaw phase of each series (see fig. 5.5.12 & 3.6.1). Five sets of marker columns were placed into each transect and these created a geo-referenced subsurface 'slice' across the slope model (see fig. 5.5.12). The starting position of each marker column was identical between each slice.

A 'key area' for measurement was established within the central portion of the slope model (slices 2 to 4) as this area remained least affected by boundary conditions, for example it is felt that Slice 5 may have been influenced by the impermeable end-wall and the lack of a run-off zone towards the foot of the slope model. Unless explicitly stated all results presented within this section will use values collected from the defined key area of measurement.

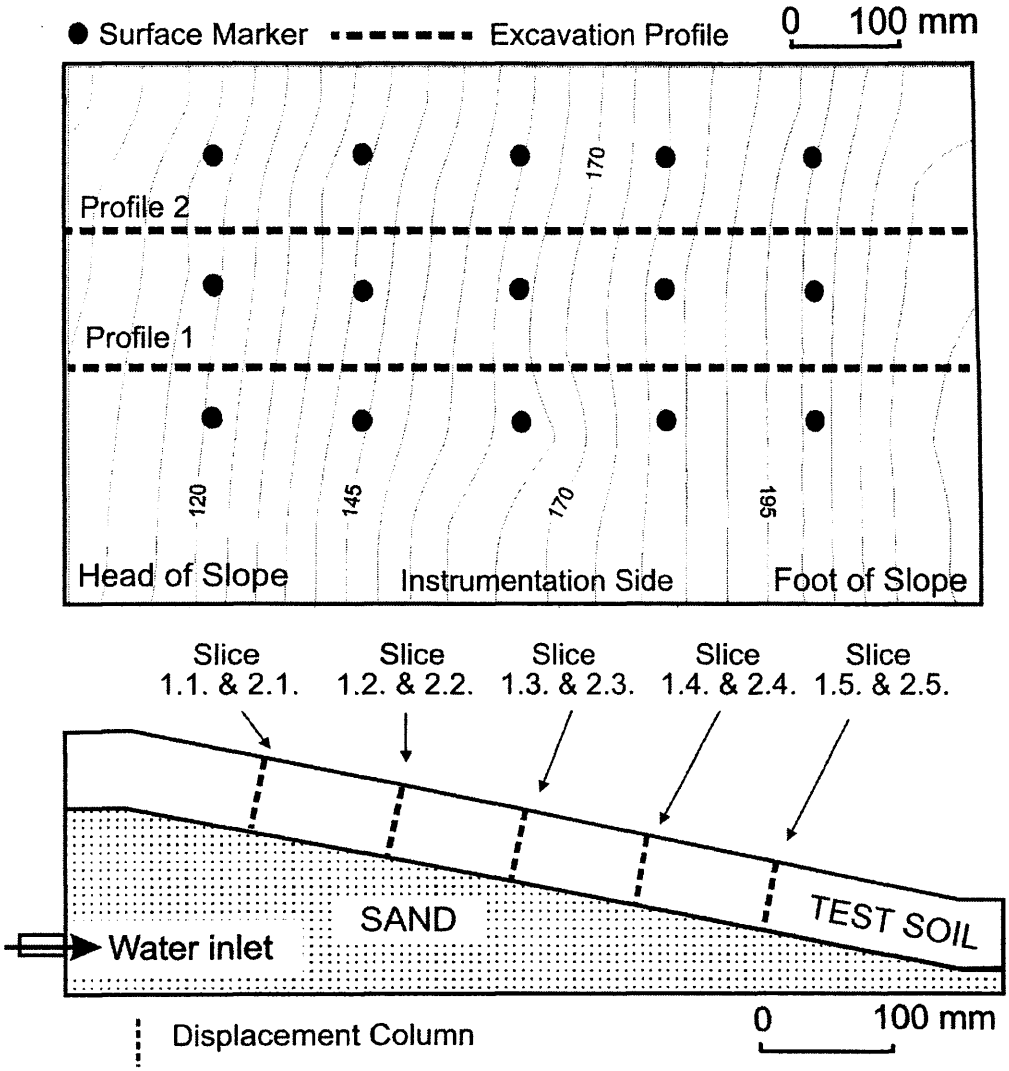

Figure 5.5.12. Subsurface transects and position of each slice upon the slope model.

5.5.5 Excavation Profiles

The following section presents photographic evidence illustrating the subsurface downslope deformation that occurred during each test series. The marker profiles from the key area of interest have been highlighted within each excavated transect. A discussion on the patterns of subsurface deformation is included in section 5.5.6.

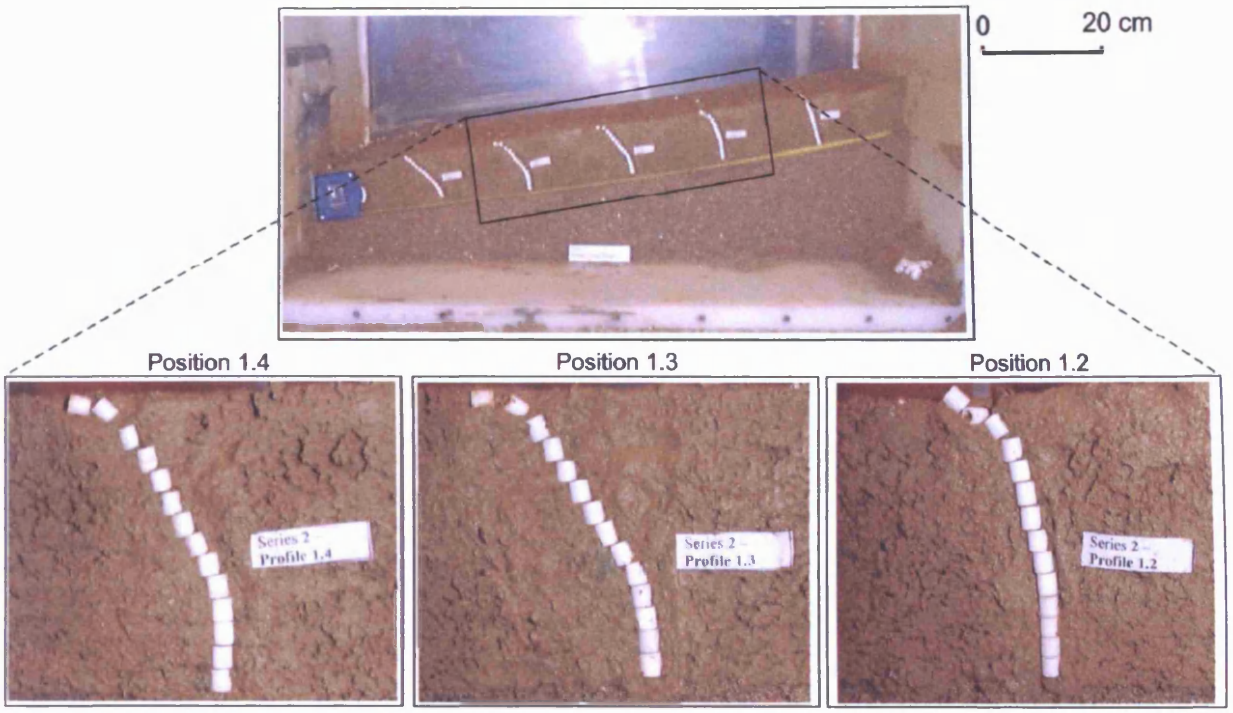

Figure 5.5.13. Subsurface movement from excavation profile one of Series 12D/NS.

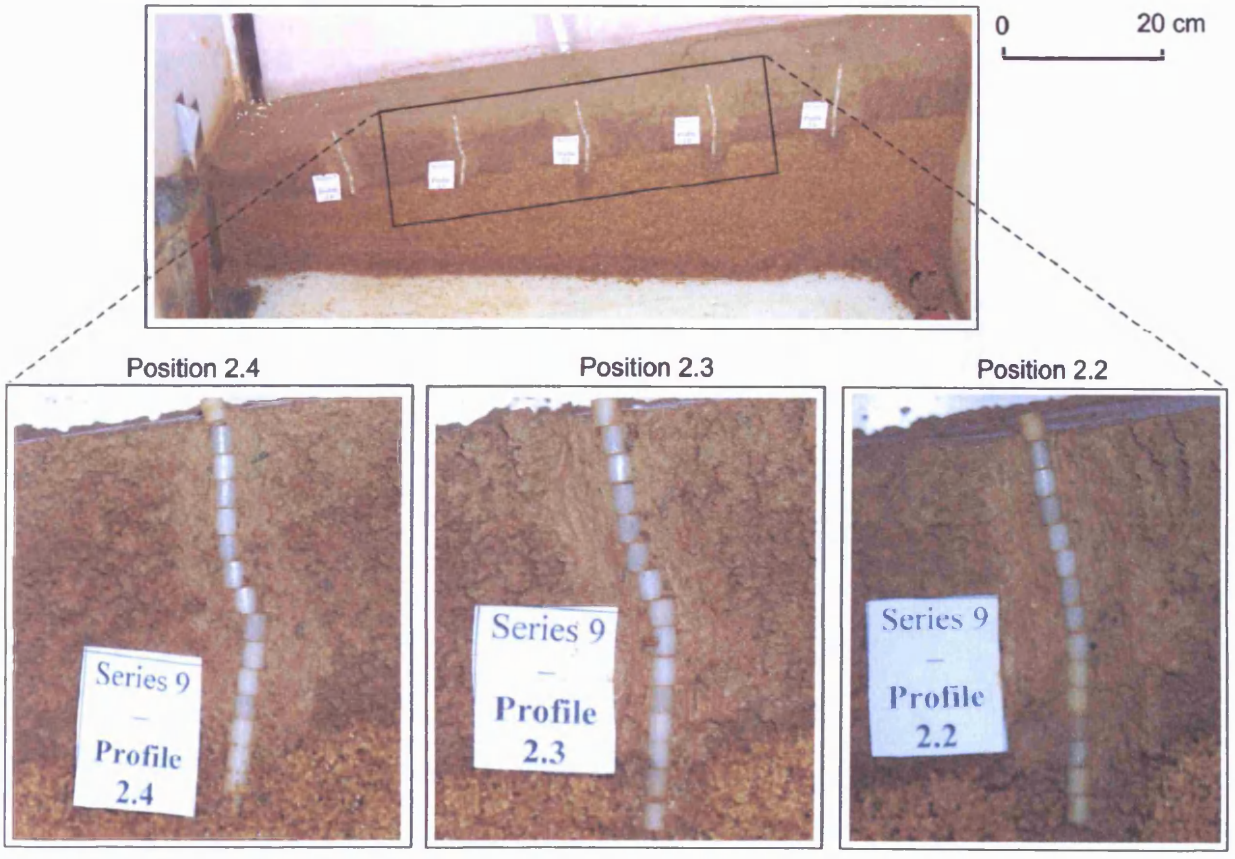

Figure 5.5.14. Subsurface movement from excavation profile two of Series 8D/NS.

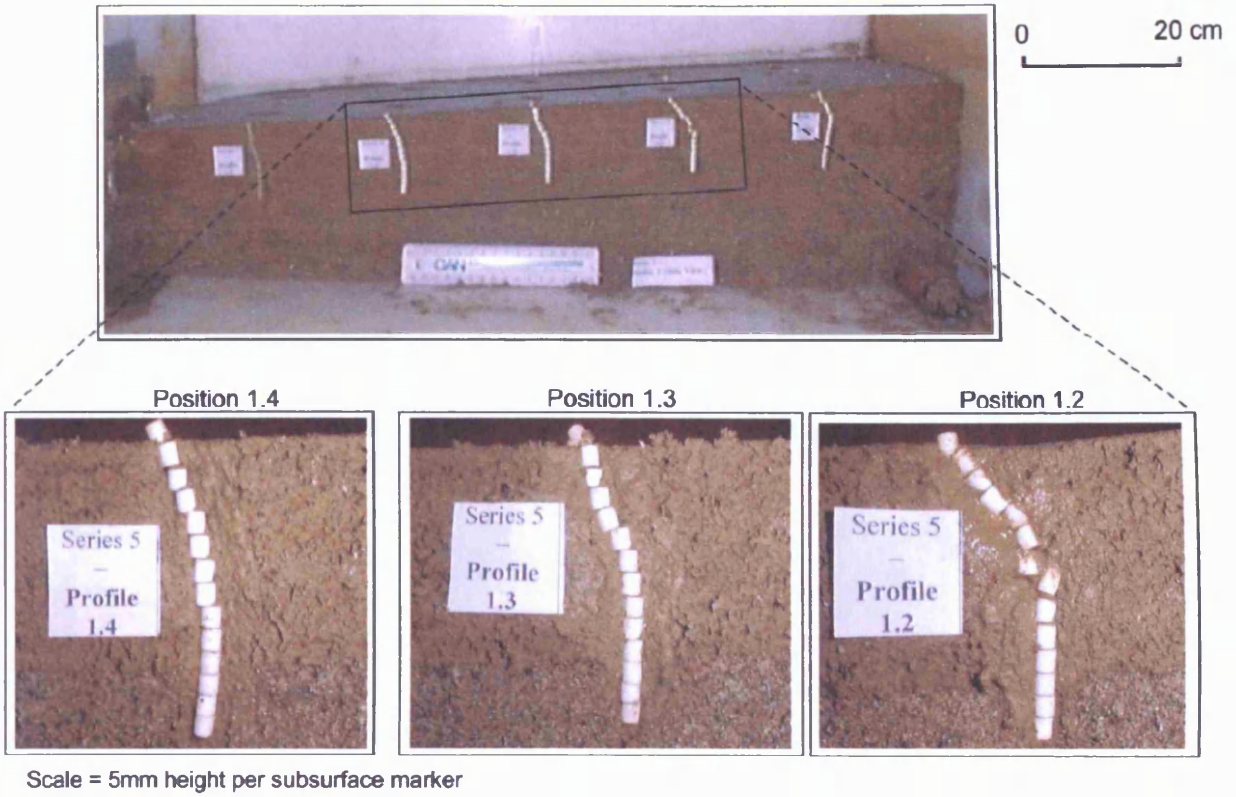

Figure 5.5.15. Subsurface movement from excavation profile one of Series 4D/NS.

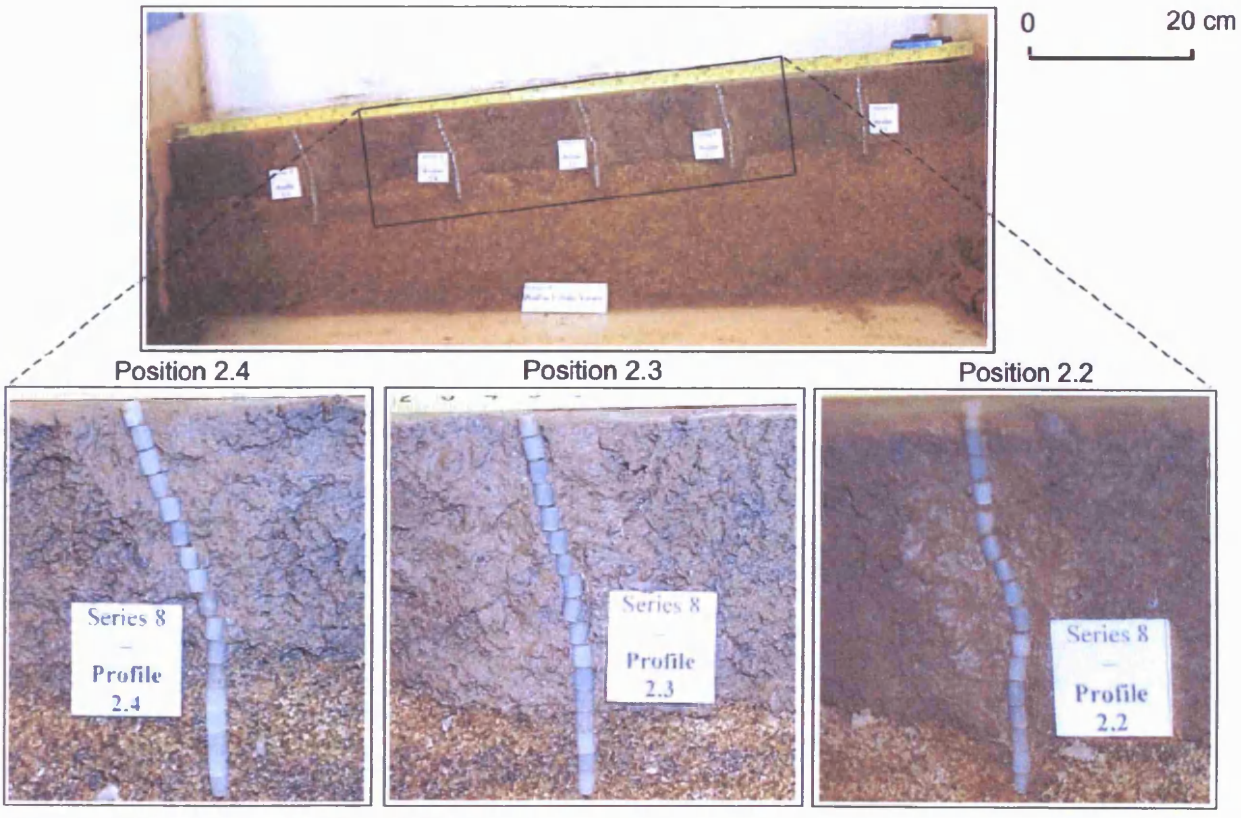

Figure 5.5.16. Subsurface movement from excavation profile one of Series 4D/10S.

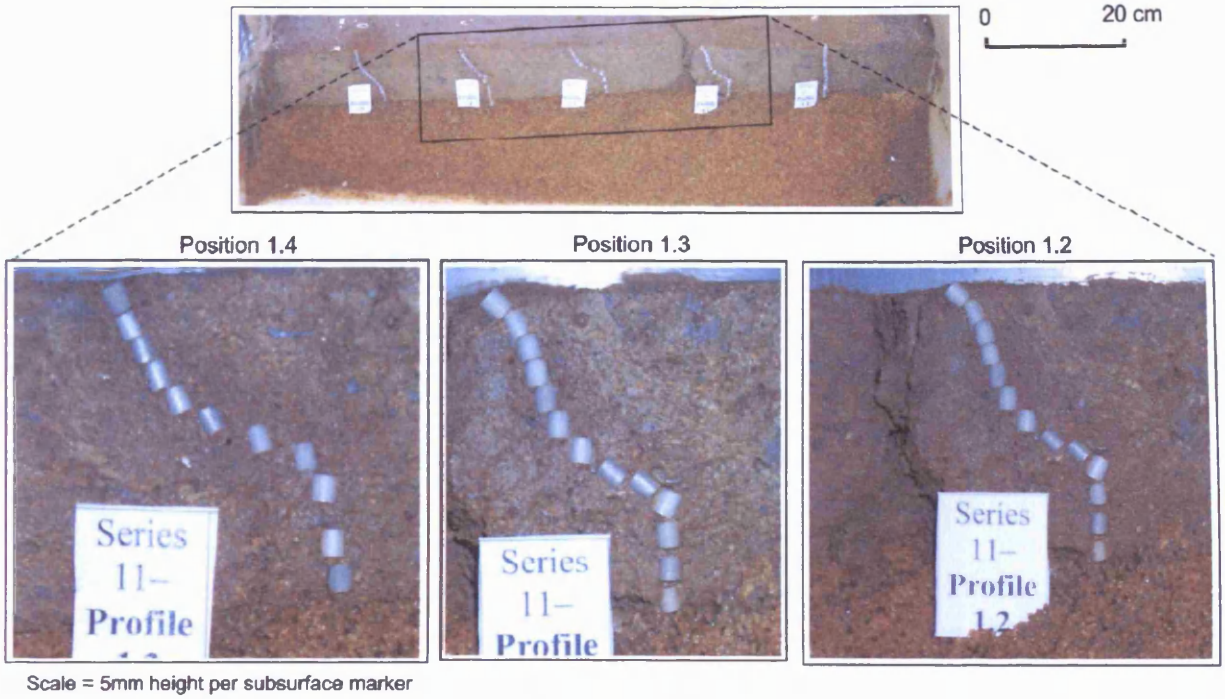

Figure 5.5.17. Subsurface movement from excavation profile one of Series 4D/20S.

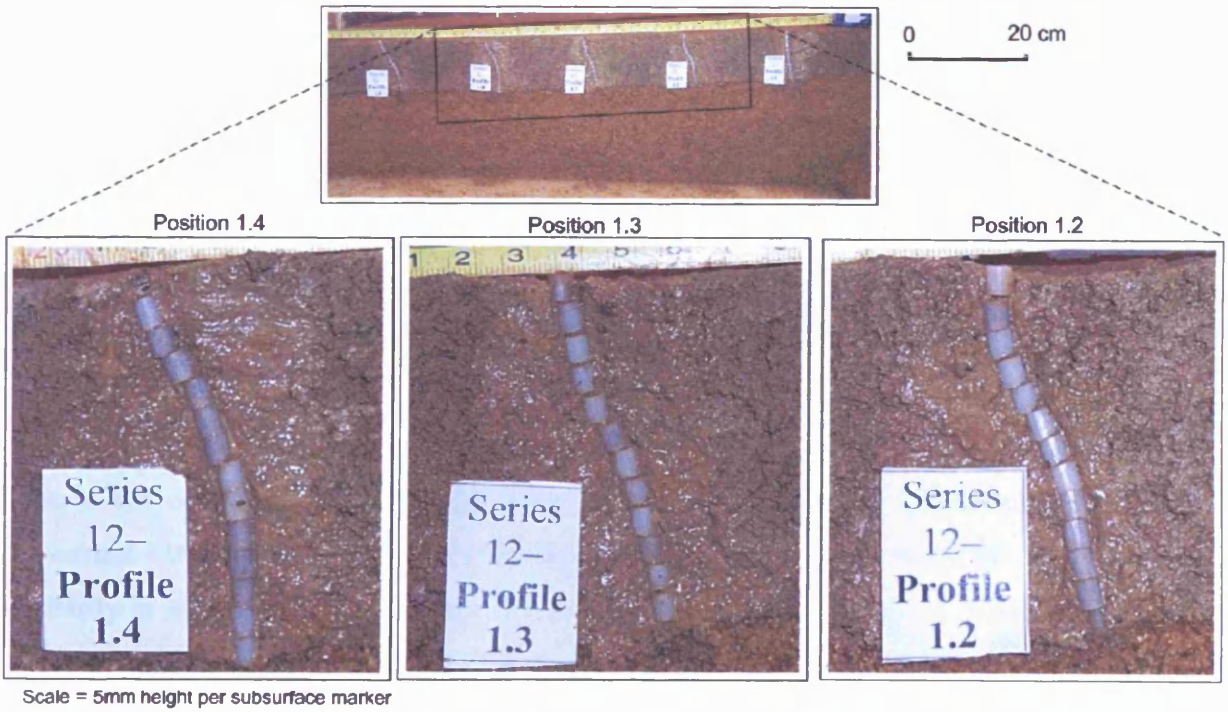

Figure 5.5.18. Subsurface movement from excavation profile one of Series 4D/10C.

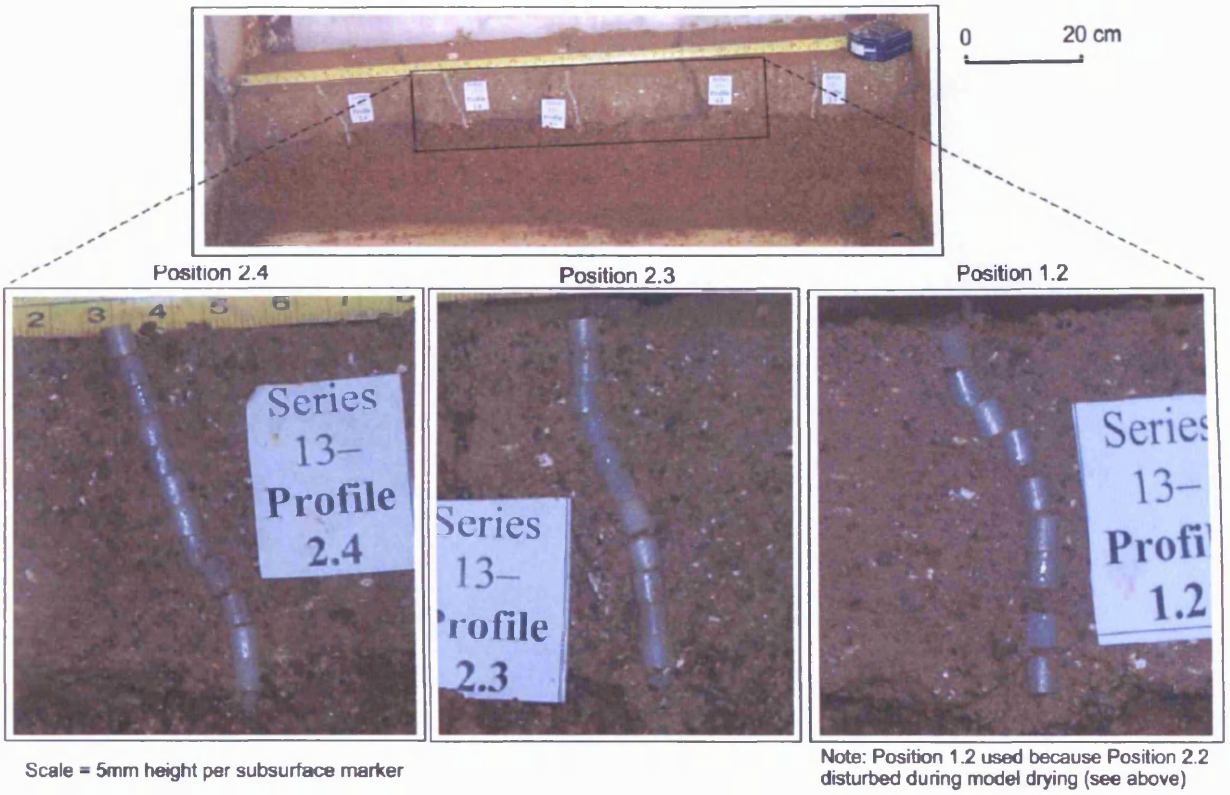

Figure 5.5.19. Subsurface movement from both excavation profiles one and two of Series 4D/20C.

The subsurface marker profiles presented in Figures 5.5.13-5.5.19 were very similar to marker profiles excavated during previous full-scale and model-scale research into gelifluction processes (Harris *et al.*, 1997; Harris *et al.*, 2003a). Figure 5.5.20 highlights that similar excavated patterns of displacement were observed after four freeze/thaw cycles within series 12D/NS (positions 1.3 & 1.4) when compared to buried columns of unglazed tiles from seven cycles of soil freezing and thawing undertaken upon within Vire silt at the CNRS laboratories (Caen, France) (Harris *et al.*, 1997, p.861, fig. 10).

Clearly the centrifuge model scaled experiments generated styles of sub-surface movement very similar to equivalent full-scale prototypes (see section 8.4.5). The similarity in style of mass movement gives confidence in the analysis of movement volumes obtained in the present research project. In order to quantify this volumetric movement, data was gathered from each slice through the measurement of marker movement against the datum of straight, undeformed columns of markers as originally installed, with the base set within the stable basal sand layer (see fig. 5.5.21).

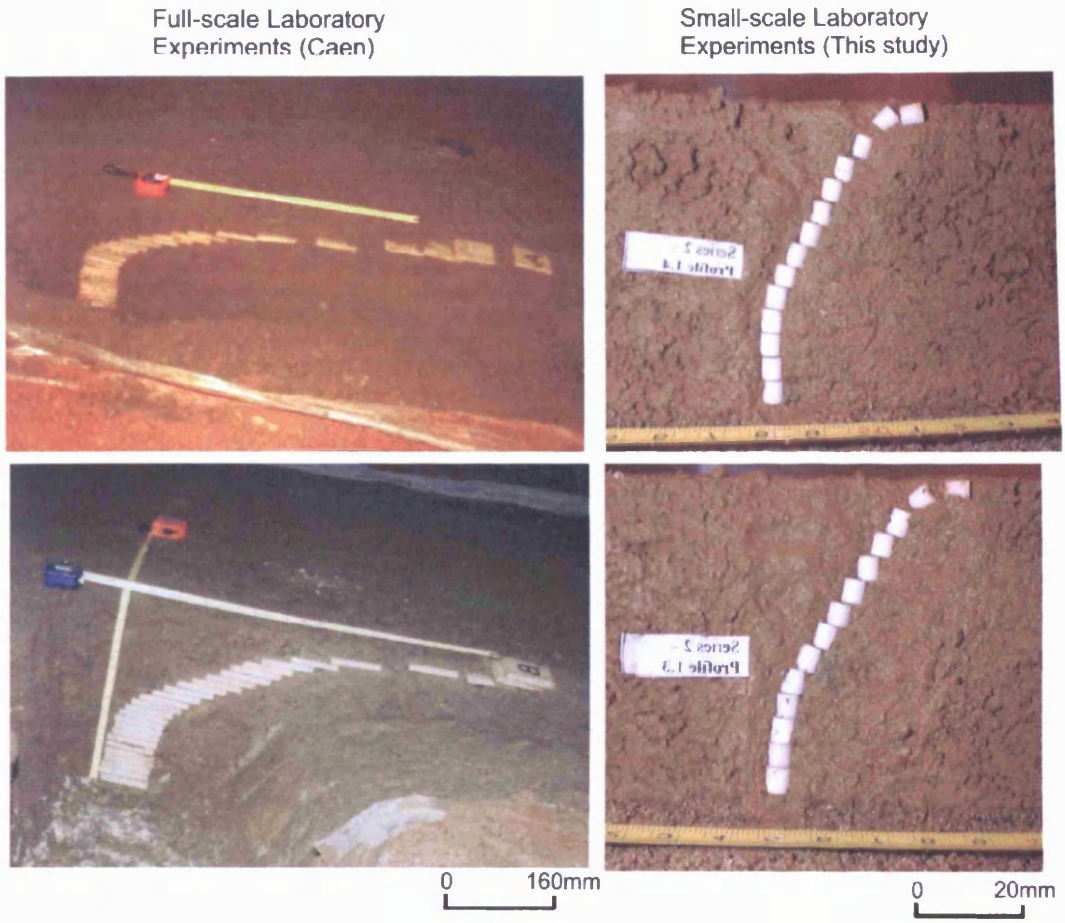

Figure 5.5.20. Subsurface velocity profiles from two different laboratory simulations of gelifluction processes. Note: Excavation of full-scale experiment from seven cycles of freeze/thaw within central region of a 12° slope model (positions A & B) (Harris *et al.*, 1997, 851, fig. 1). Excavation of small-scale experiment from four freeze/thaw cycles series 12D/NS (positions 1.3 & 1.4). (CNRS Photograph: Charles Harris).

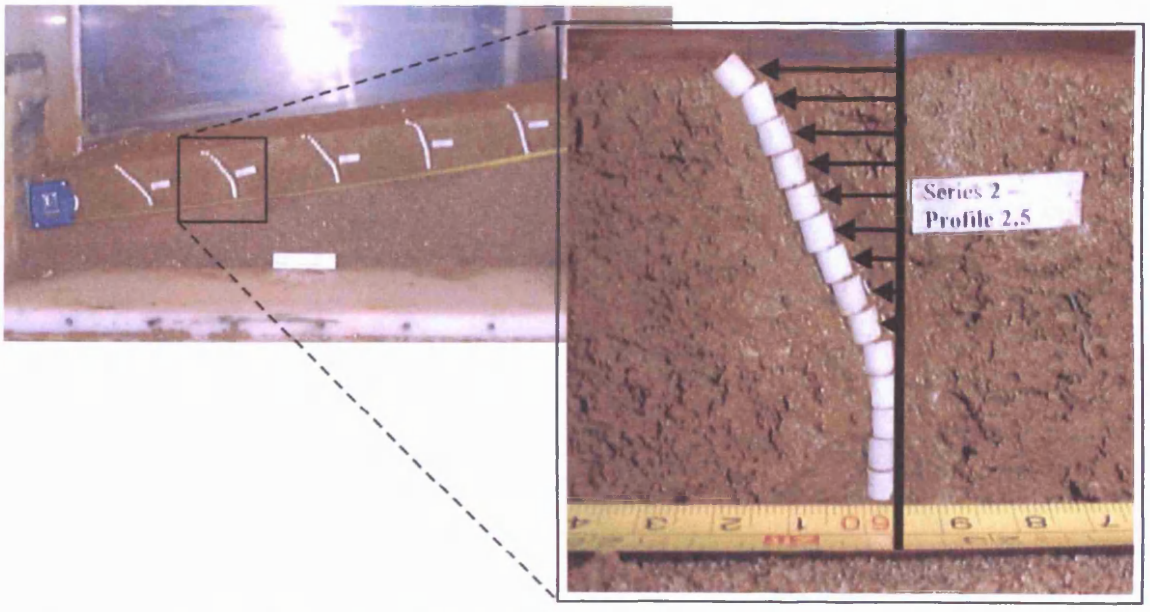

Figure 5.5.21. Method of volumetric/horizontal displacement measurement for each subsurface marker column.

5.5.6. Patterns of Subsurface Deformation

The displacement of key area marker profiles from both slope transects were measured using the technique exemplified in Figure 5.5.21. The information presented below is directly linked to the excavation profiles outlined in section 5.5.5 but by presenting the information in graphical form it allows both transects to be examined in each slope model to illustrate the variability of movement occurring in all regions of the slope (see fig. 5.5.22).

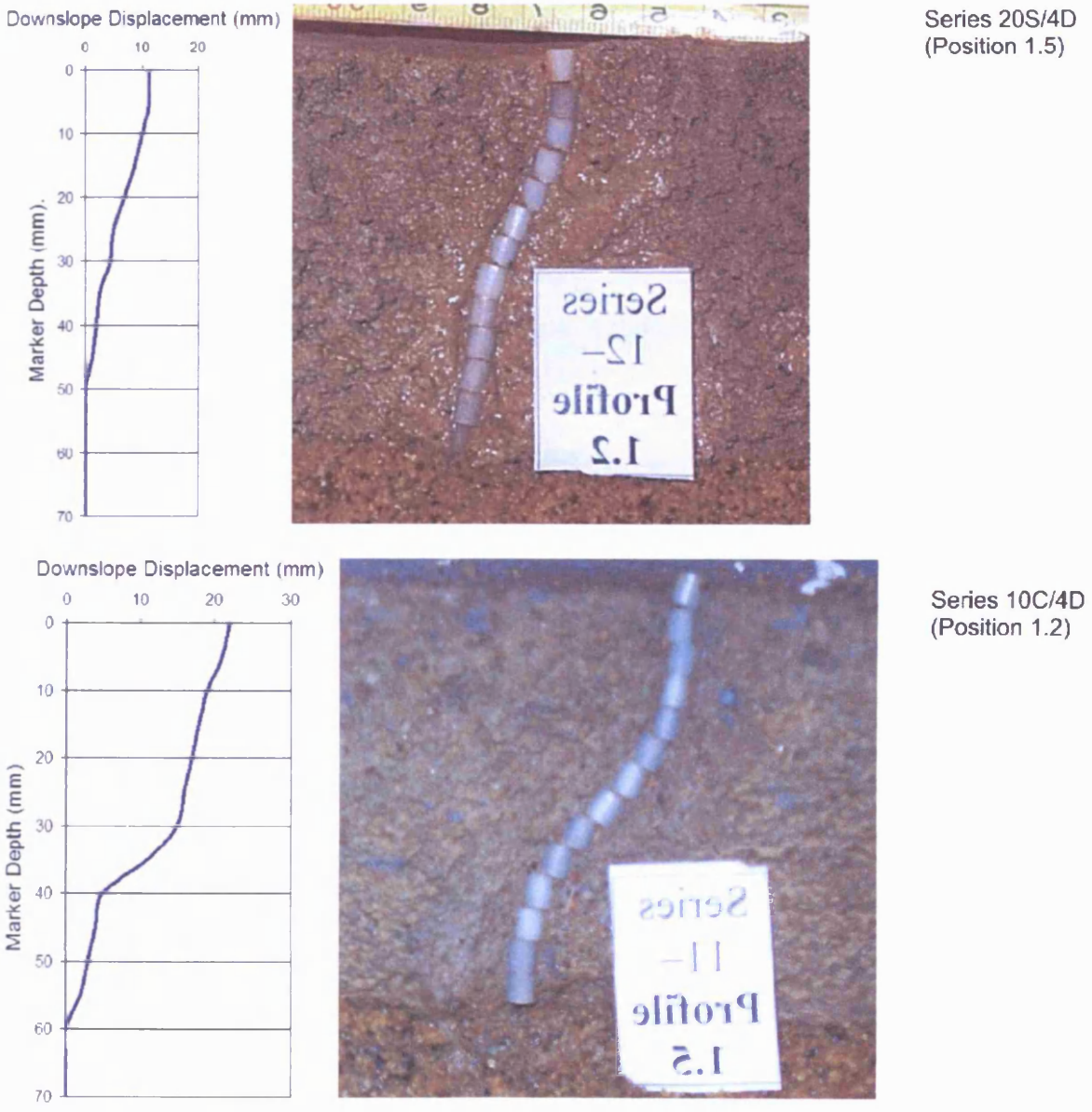

Figure 5.5.22. Example of the conversion of subsurface marker profiles into numeric data.

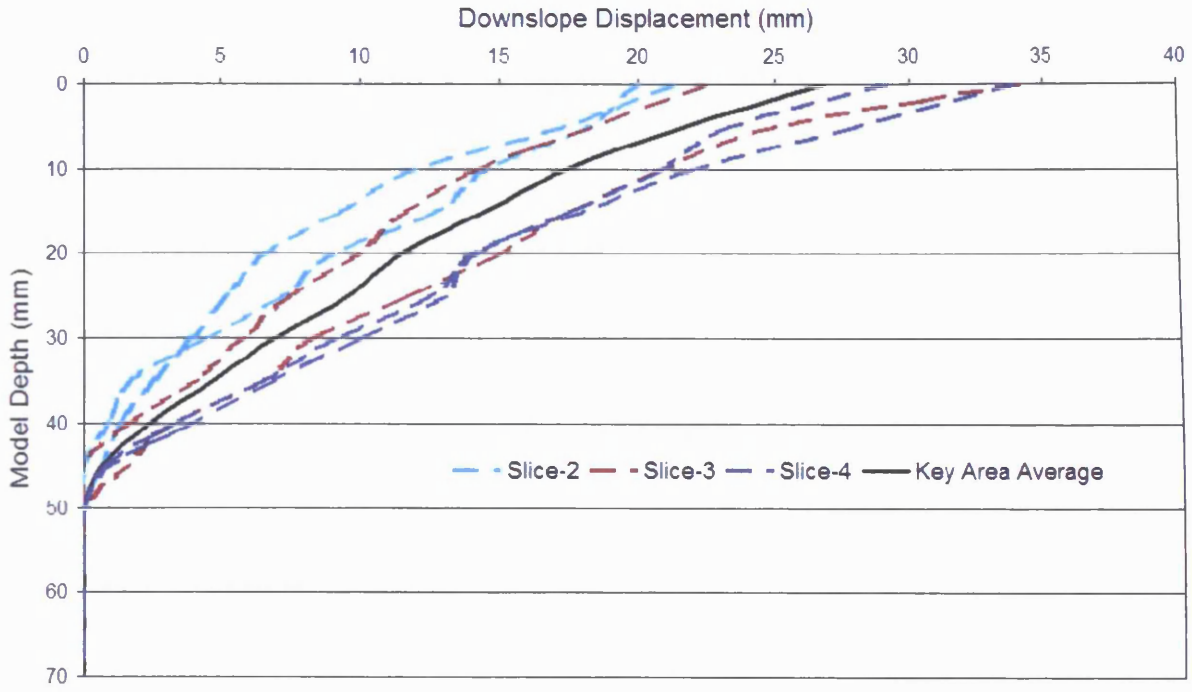

Figure 5.5.23. Subsurface downslope displacement for the key area of Series 12D/NS.

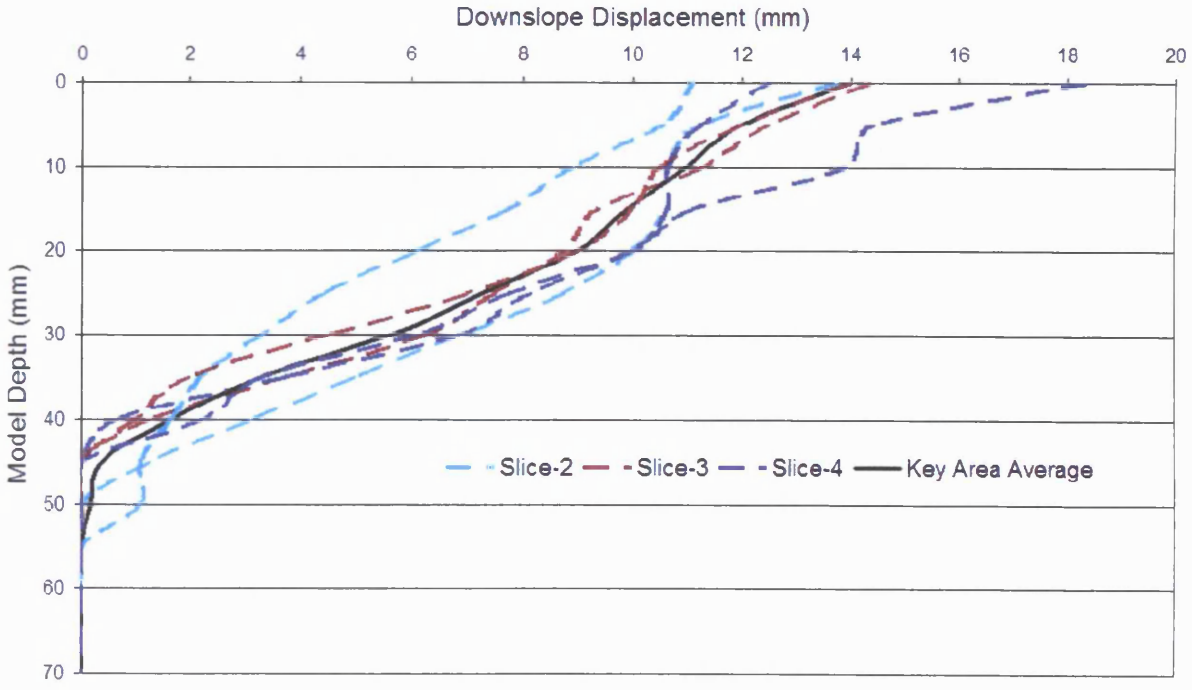

Figure 5.5.24. Subsurface downslope displacement for the key area of Series 8D/NS.

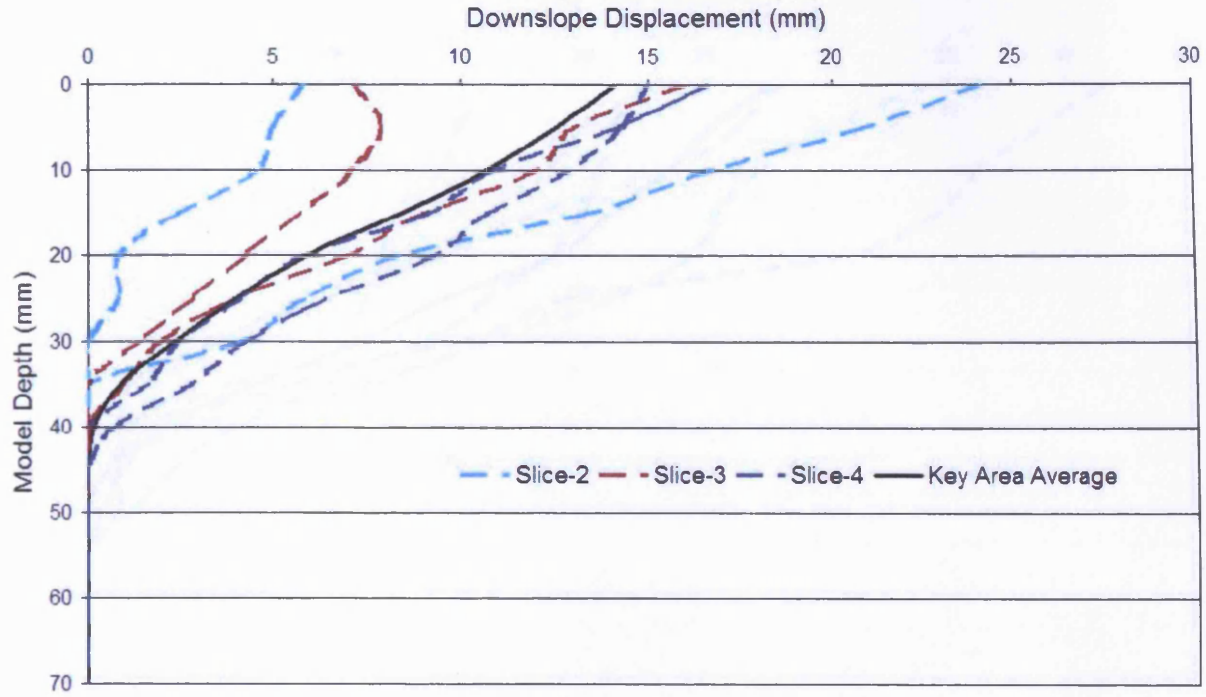

Figure 5.5.25. Subsurface downslope displacement for the key area of Series 4D/NS.

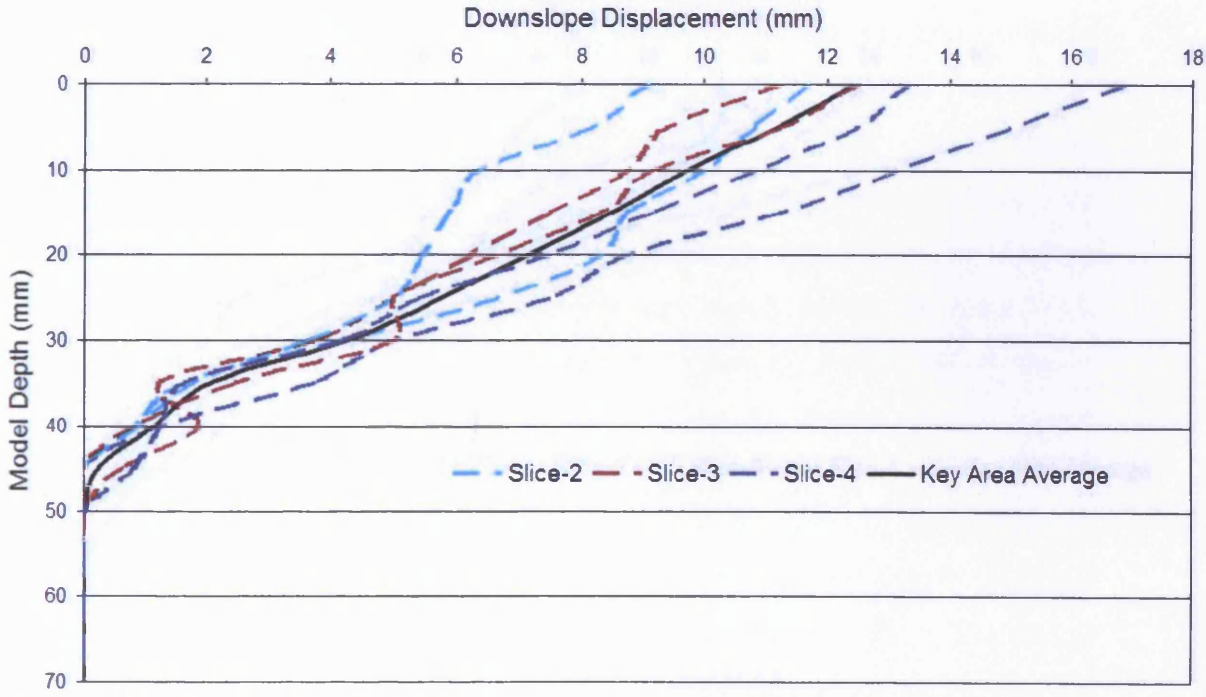

Figure 5.5.26. Subsurface downslope displacement for the key area of Series 4D/10S.

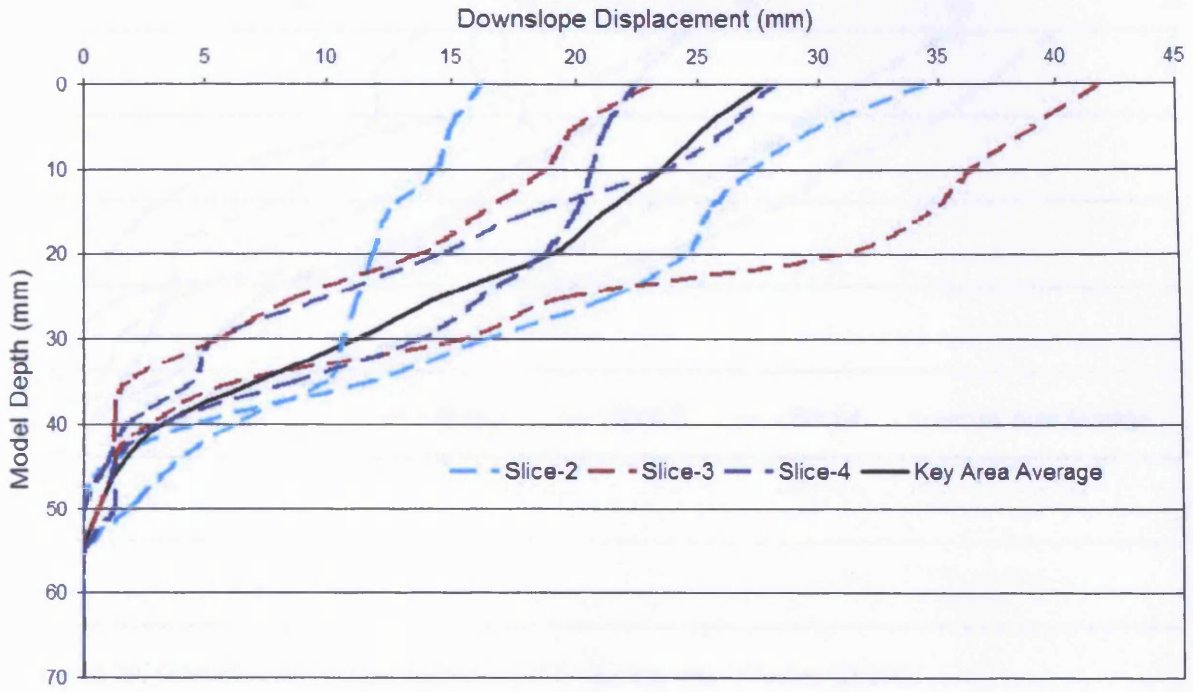

Figure 5.5.27. Subsurface downslope displacement for the key area of Series 4D/20S.

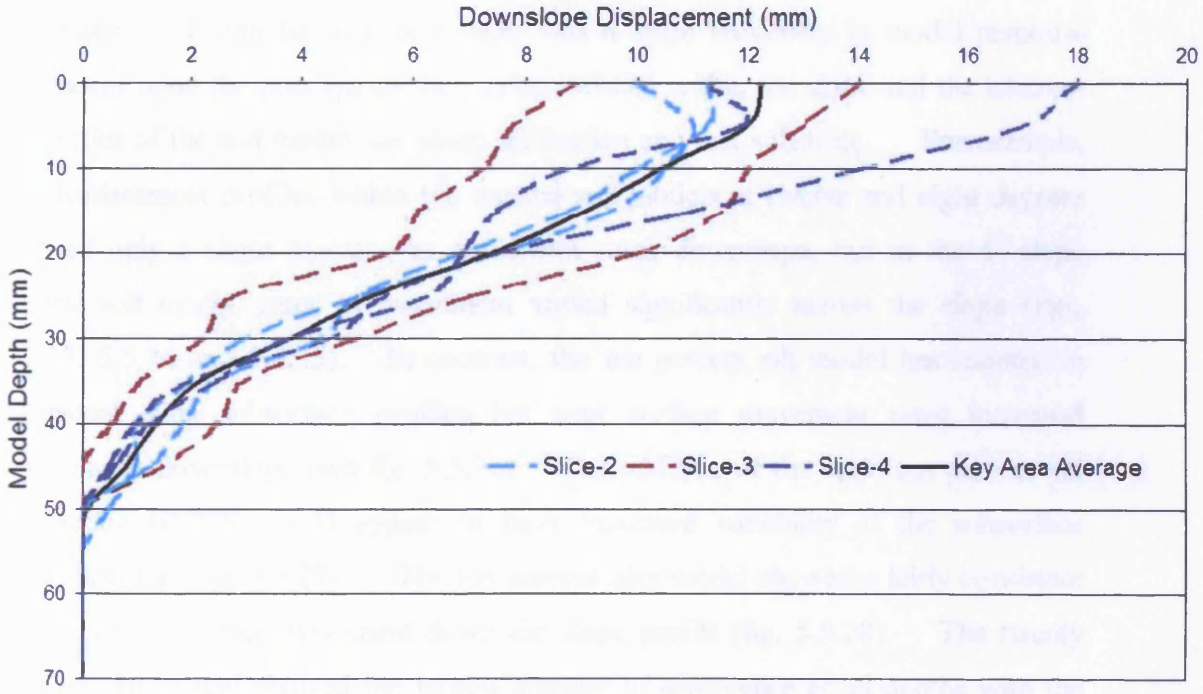

Figure 5.5.28. Subsurface downslope displacement for the key area of Series 4D/10C.

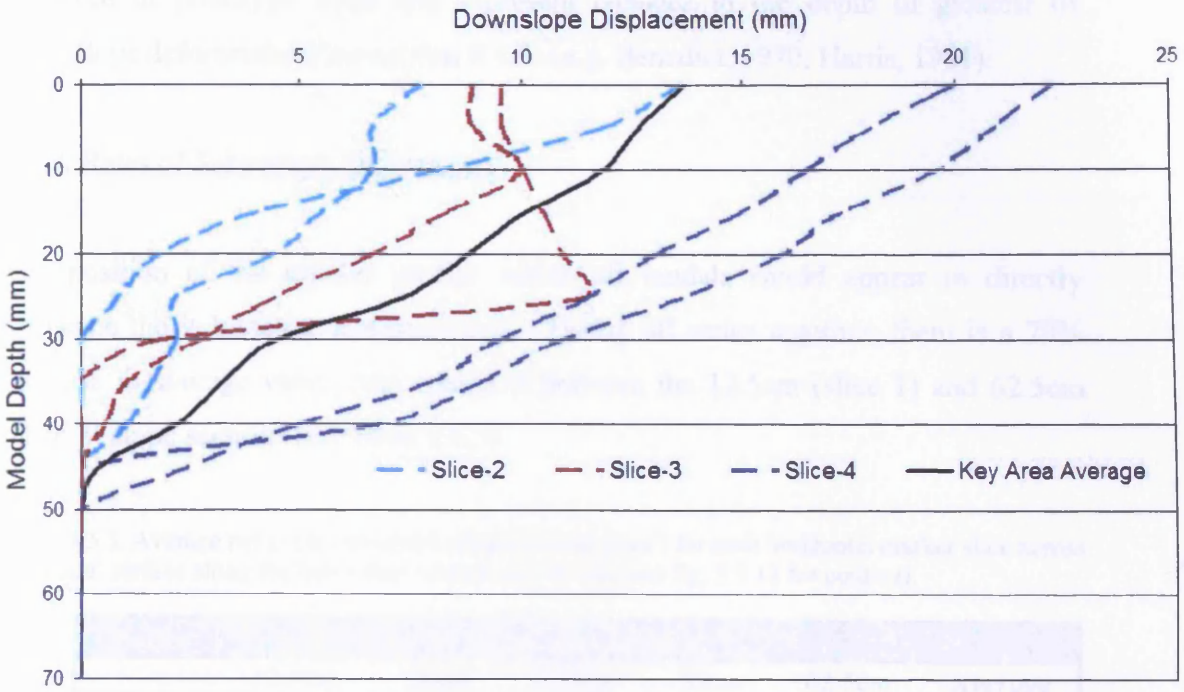

Figure 5.5.29. Subsurface downslope displacement for the key area of Series 4D/20C.

Figures 5.5.23-5.5.29 illustrate the patterns of downslope displacement generated during four freeze/thaw cycles within the slope models undergoing gelifluction processes. It can be seen that there was a large variability in model response dependent upon the position of the marker column within the slope and the inherent properties of the soil model, i.e. slope inclination and test substrate. For example, the displacement profiles within the natural soil models at twelve and eight degrees showed only a slight increase in movement rates downslope, but in the 4° slope natural soil model, rates of movement varied significantly across the slope (figs. 5.5.23, 5.5.24 and 5.5.25). In contrast, the ten percent silt model has resulted in consistent deep subsurface profiles but near surface movement rates increased significantly downslope (see fig. 5.5.26). The addition of the extra ten percent silt for Series 4D/20S would appear to have increased variability of the subsurface movement (see fig. 5.5.27). The ten percent clay model showed a fairly consistent pattern of subsurface movement down the slope profile (fig. 5.5.28). The twenty percent clay model showed the largest amount of divergence at all depths with the amount of subsurface displacement being related to the slope position of the marker column within the model. It is notable that in the 20% clay model there appear to be zones of localised shearing. The current simulation would appear to have recreated

convex and concave subsurface movement profiles – these forms have been observed at prototype scale and represent changes to the depth of greatest of downslope deformation (see section 8.4.5) (e.g. Benedict, 1970; Harris, 1981).

5.5.7. Rates of Subsurface Deformation

The position of the marker profile within all models would appear to directly influence the volumetric displacement. Taking all series together, there is a 70% increase in average volumetric transport between the 12.5cm (slice 1) and 62.5cm (slice 5) slope sections (see table 5.5.5).

Table 5.5.5. Average per cycle volumetric displacement (mm^2) for each horizontal marker slice across the model surface along the horizontal excavation transect (see fig. 5.5.12 for context).

Series	Transect Length					
	12.5cm	25cm	37.5cm	50cm	62.5cm	*Average*
12D/NS	178.27	424.39	600.00	721.25	732.74	*531.33*
8D/NS	239.32	348.96	362.50	403.99	372.81	*345.52*
4D/NS	108.33	282.29	251.07	353.57	219.64	*242.98*
4D/10S	153.03	273.20	292.19	372.92	349.48	*288.16*
4D/20S	203.13	776.42	847.44	702.84	884.77	*682.92*
4D/10C	136.39	310.31	304.31	354.06	462.50	*313.51*
4D/20C	84.20	196.97	288.26	638.41	647.39	*371.05*
Average	*157.52*	*373.22*	*420.82*	*506.72*	*524.19*	

As expected, slope gradient would appear to affect the volumetric soil transport rates occurring with distance downslope. Figure 5.5.30 shows that increasing model slope gradient in the natural soil models leads to progressively larger amounts of subsurface movement. Series 12D/NS showed a 75% greater volumetric movement in the lowest slice compared with the uppermost and lowest slices. This pattern can be compared to a 35% increase downslope for the eight degree model and a fluctuating 50% increase downslope on the four degree gradient. Taking the overall average volumetric transport for each slope category, there is a clear increase with increasing slope gradient (Table 5.5.5). It would appear that the volumetric movement rate is a function of slope angle and at the higher slope angles shows a progressive downslope increase, but the lowest gradient model shows no such systematic trend (see fig. 5.5.30).

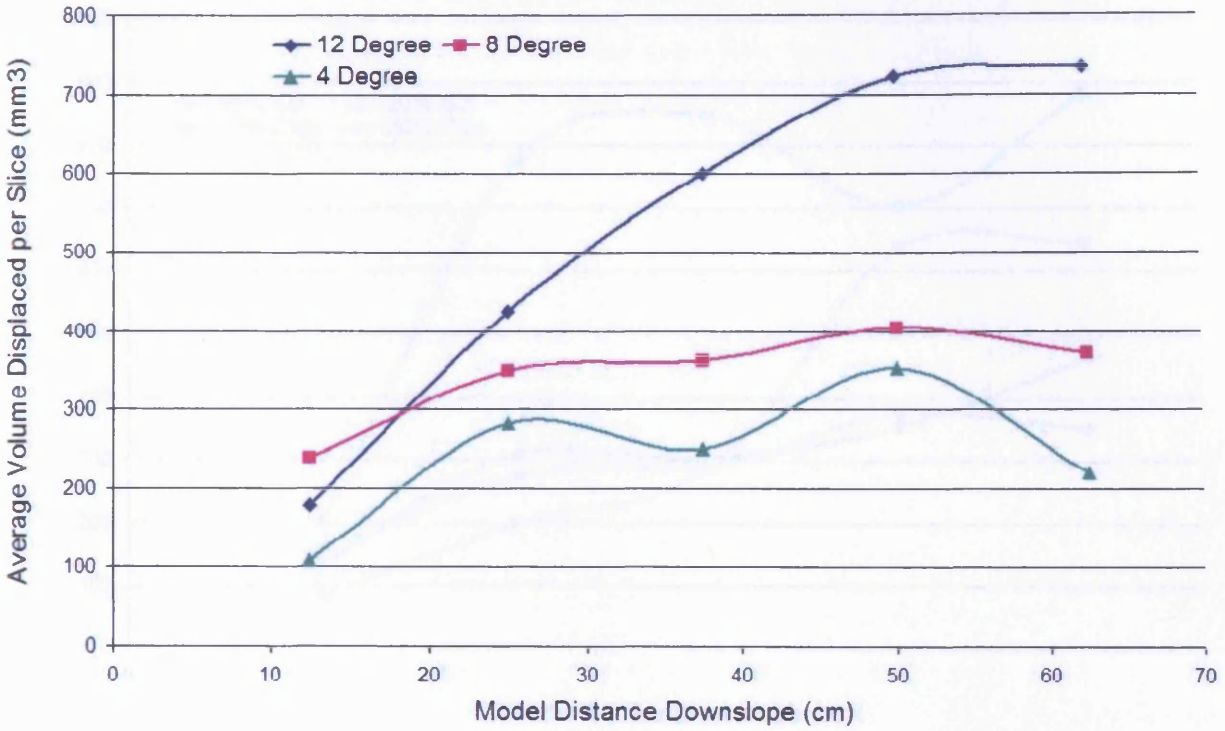

Figure 5.5.30. Average subsurface volumetric displacement for each marker slice within test series involving natural soil.

The addition of silt and clay to the natural soil lead to a greater more systematic downslope increase in volumetric displacement, with Series 4D/10S showing a 56% increase from uppermost to lowest marker columns and Series 4D/20S showing 77% more movement within the lowest columns when compared to the uppermost columns. Similarly, the ten percent clay increment model reacted with a 70% increase in volumetric transport from upper to lower slope whilst the twenty percent clay model showed an 86% increase in transport rate in the lower slope relative to the uppermost zone. Turning to the overall average volumetric transport, clearly on the 4° slope models, addition of silt and clay to the soil increased average volumetric transport compared with the natural soil (table 5.5.5). The greatest increase came between the 10% silt and 20% silt models, with a doubling in the average volumetric displacement. In the clay models, the overall average volumetric transport was greater in the 20% increment model than the 10%, but the greater transport rate was entirely in the lower slope region.

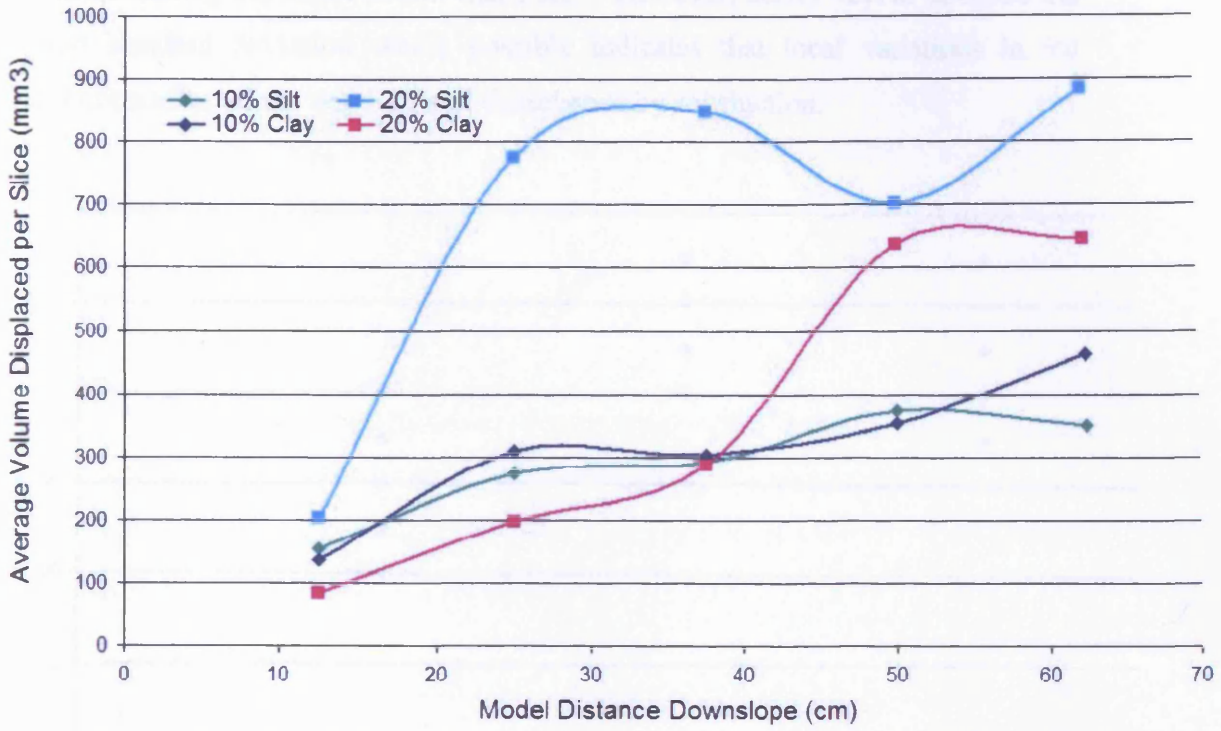

Figure 5.5.31. Average subsurface volumetric displacement for each marker slice within test series involving modified soils.

The maximum depth of subsurface movement (D_M) was also affected by changes to slope gradient and soil type (see fig. 2.3.2 for definition). D_M can be used to describe differential patterns of subsurface movement presented within figures 5.5.24-5.5.29 – and for this reason D_M values have been collated within Table 5.5.6.

Table 5.5.6. Greatest depth of subsurface movement (mm) for each test series. SD = Standard deviation.

Series	Slope Position						Average	SD
	1.2	*2.2*	*1.3*	*2.3*	*1.4*	*2.4*		
12D/NS	45	40	45	40	45	45	43.33	±2.58
8D/NS	45	50	40	40	40	40	42.50	±4.18
4D/NS	30	25	35	30	35	40	32.50	±5.24
4D/10S	40	40	40	45	40	40	40.83	±2.04
4D/20S	45	50	45	50	45	50	47.50	±2.74
4D/10C	50	45	45	40	45	45	45.00	±3.16
4D/20C	25	40	30	40	40	45	36.67	±7.53

Figure 5.5.32 illustrates that model slope angle influenced the maximum depth of subsurface movement. There was little difference in D_M between the eight and twelve degree natural soil models but the four degree model generated a 33% shallower movement profile. Overall, there appeared to be a behavioural threshold between the eight degree and four degree slope models with the decreasing slope

gradient reducing the depth of soil transport. However, Series 4D/NS also had the highest standard deviation which possibly indicates that local variations in ice distribution affected the depth of soil disturbance by solifluction.

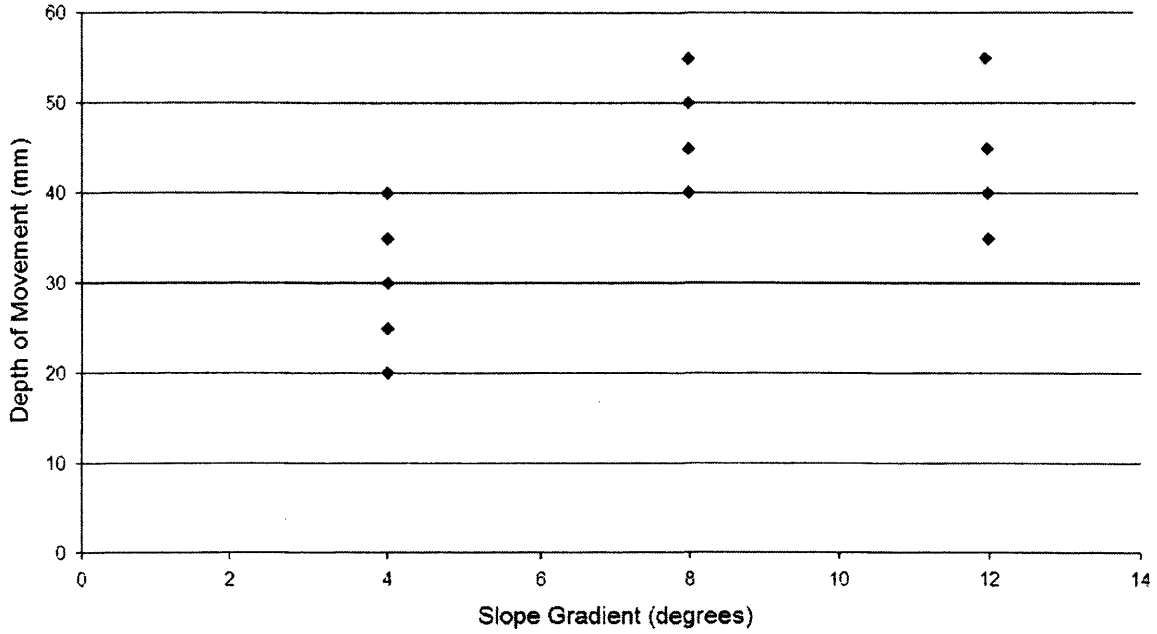

Figure 5.5.32. The influence of slope angle on the depth of subsurface movement.

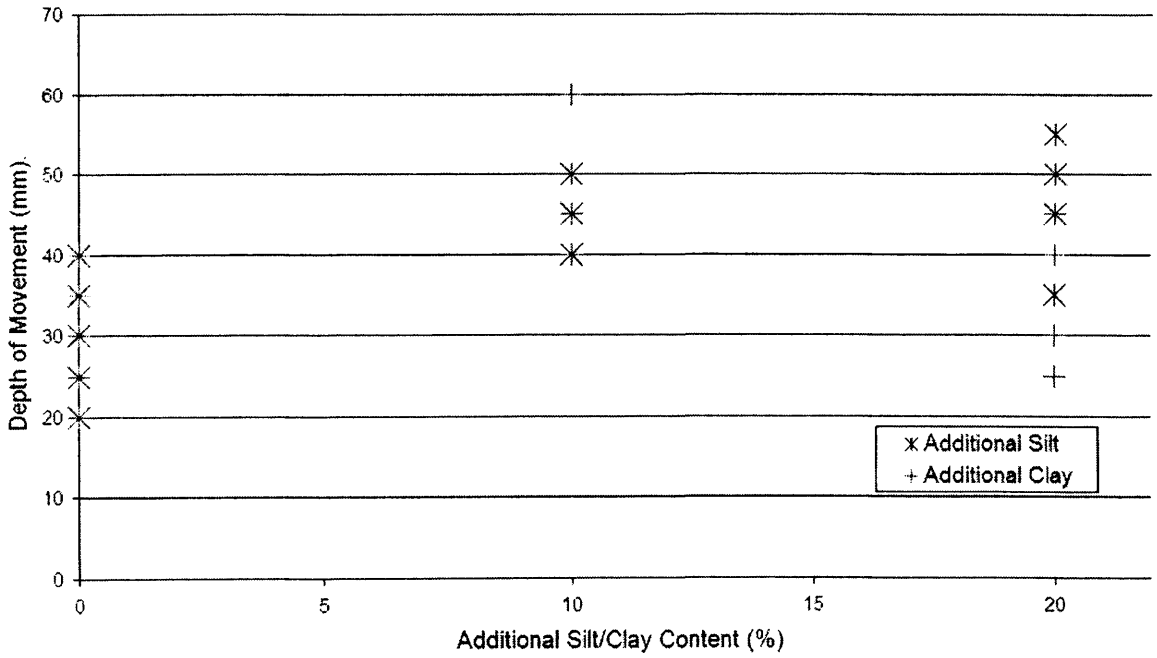

Figure 5.5.33. The influence of additional silt and clay content upon the depth of subsurface movement.

Figure 5.5.33 indicates that the addition of silt to the natural soil increased D_M by 20% within the ten percent increment and by 32% within the twenty percent silt model when compared to Series 4D/NS. In comparison the addition of clay generated a more pronounced effect within the ten percent model with a 27% deepening of D_M compared to the twenty percent clay model which recorded an average 11% deeper profile of subsurface movement when compared to the natural soil.

Table 5.5.7 presents the net volumetric displacement which occurred across the four freeze/thaw cycles of each test series for each subsurface marker position. Table 5.5.8 further reduces this information and infers the total amount of subsurface deformation for each individual thaw cycle.

Table 5.5.7. Total subsurface displacement (mm^2) for each marker profile (see fig. 5.5.12 for spatial context).

	12D/NS	8D/NS	4D/NS	4D/10S	4D/20S	4D/10C	4D/20C
Marker Position							
1.1	161.50	340.00	191.70	147.73	268.75	95.00	65.91
1.2	403.30	406.25	466.70	158.33	1138.64	397.50	318.18
1.3	720.80	375.00	320.00	314.58	1004.55	525.00	602.27
1.4	755.00	371.88	325.00	231.82	568.75	315.63	191.67
1.5	932.10	378.13	214.30	278.13	737.50	303.13	595.00
2.1	195.00	138.64	25.00	306.25	984.09	305.00	202.27
2.2	445.50	291.67	97.90	412.50	668.18	405.00	681.82
2.3	479.20	350.00	182.10	333.33	137.50	177.78	102.50
2.4	687.50	436.11	382.10	378.13	556.25	211.11	258.33
2.5	533.30	367.50	225.00	320.83	765.00	400.00	692.50

Table 5.5.8. Inferred per cycle subsurface displacement (mm^2) for each marker profile (see fig. 5.5.12 for spatial context).

	12D/NS	8D/NS	4D/NS	4D/10S	4D/20S	4D/10C	4D/20C
Marker Position							
1.1	40.38	85.00	47.93	36.93	67.19	23.75	16.48
1.2	100.83	101.56	116.68	39.58	284.66	99.38	79.55
1.3	180.20	93.75	80.00	78.65	251.14	131.25	150.57
1.4	188.75	92.97	81.25	57.95	142.19	78.91	47.92
1.5	233.03	94.53	53.58	69.53	184.38	75.78	148.75
2.1	48.75	34.66	6.25	76.56	246.02	76.25	50.57
2.2	111.38	72.92	24.48	103.13	167.05	101.25	170.45
2.3	119.80	87.50	45.53	83.33	34.38	44.44	25.63
2.4	171.88	109.03	95.53	94.53	139.06	52.78	64.58
2.5	133.33	91.88	56.25	80.21	191.25	100.00	173.13

The average rate of subsurface volumetric displacement occurring per thaw cycle has been inferred for profiles 2, 3 and 4 (the model key area) in both downslope transects (tables 5.5.9).

Table 5.5.9. Average volumetric velocity for each subsurface profile within the key area at both model and prototype scale.

Series	Model Scale		Prototype Scale
	Volumetric Displacement (mm^2)	Volume Per Cycle (mm^2/cycle)	Volume Displaced (cm^2/year)
12D/NS	582	145.5	145.5
8D/NS	372	93	93
4D/NS	296	74	74
4D/10S	313	78.25	78.25
4D/20S	776	194	194
4D/10C	323	80.75	80.75
4D/20C	375	93.75	93.75

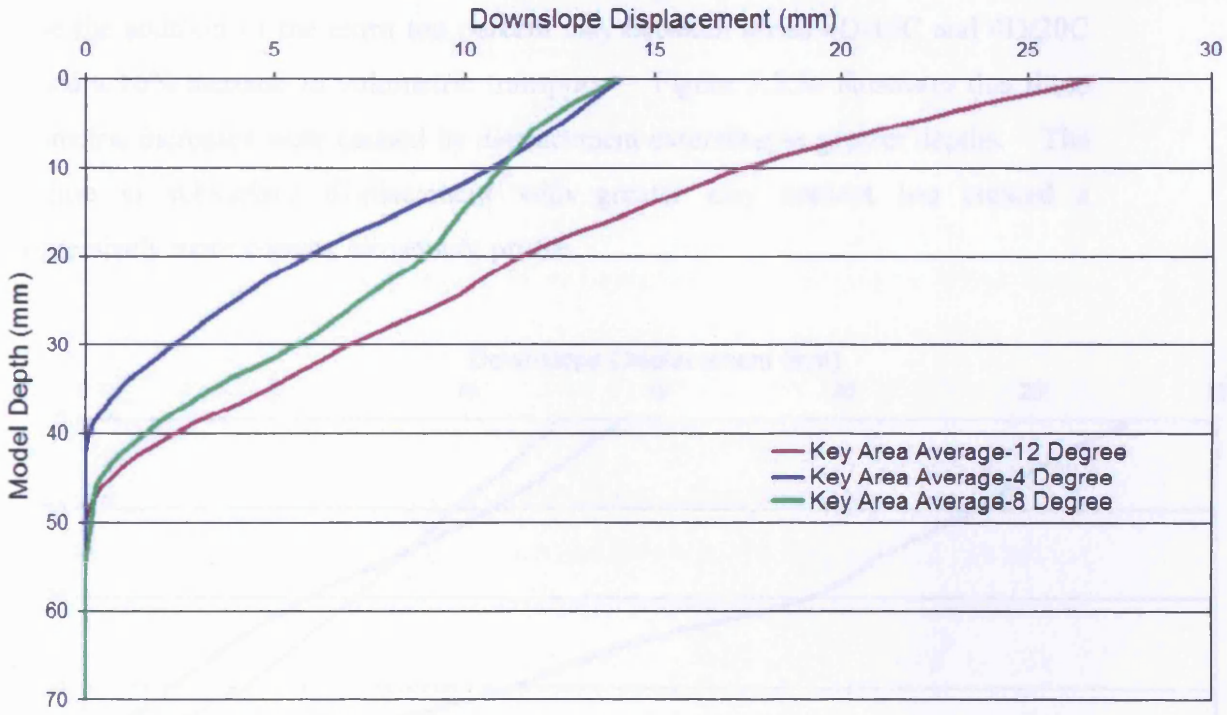

Figure 5.5.34. Average downslope displacement profile for the key area of the test series involving natural soil.

It can be observed within Figure 5.5.34 that increasing model slope gradient has generated larger amounts of subsurface movement. The influence of slope gradient appeared to increase with slope angle, for example the increase in deformation between the four and eight degree slopes was only 18% compared to the 56% between the eight and twelve degree slopes. Figure 5.5.34 illustrates how the four

and eight degree models have experienced different amounts of subsurface deformation despite similar near surface amounts of movement, the impact of gelifluction processes within the lower soil zones has created an average marker profile for Series 8D/NS that is slightly convex downslope (see fig. 5.5.15 for illustration).

Figure 5.5.35 illustrates the impact of increasing soil silt content on the overall rate of subsurface movement. Clearly a threshold occurred between the ten and twenty percent silt soils whereby Series 4D/10S generated 5% additional volumetric velocity but the extra ten percent silt within Series 4D/20S caused a 61% increase in volumetric movement when compared to the natural soil The addition of clay to the natural test soil had a less dramatic effect than the addition of silt. The 10% clay model showed 8% greater volumetric transport than the equivalent natural soil slope, while the addition of the extra ten percent clay between series 4D/10C and 4D/20C caused a 16% increase in volumetric transport. Figure 5.5.36 illustrates that these volumetric increases were caused by displacement extending to greater depths. The increase in subsurface displacement with greater clay content has created a progressively more convex movement profile.

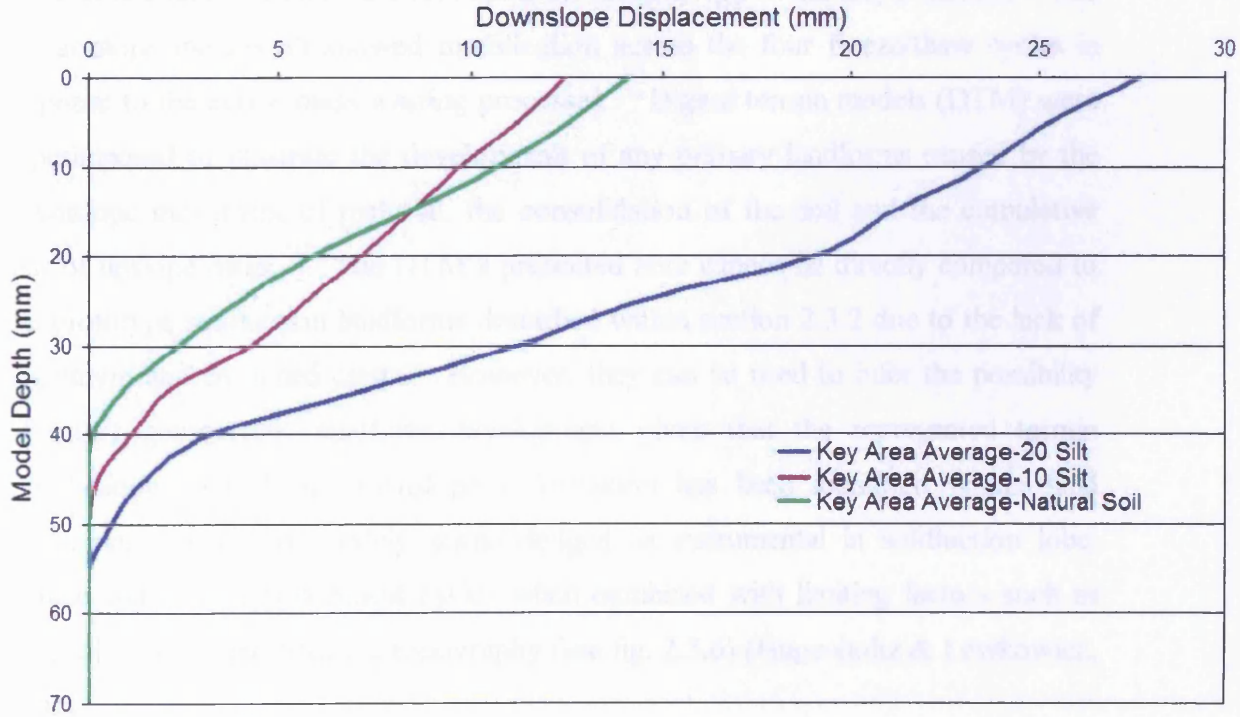

Figure 5.5.35. Average downslope displacement profile for the key area of the test series involving additions of silt to the natural soil.

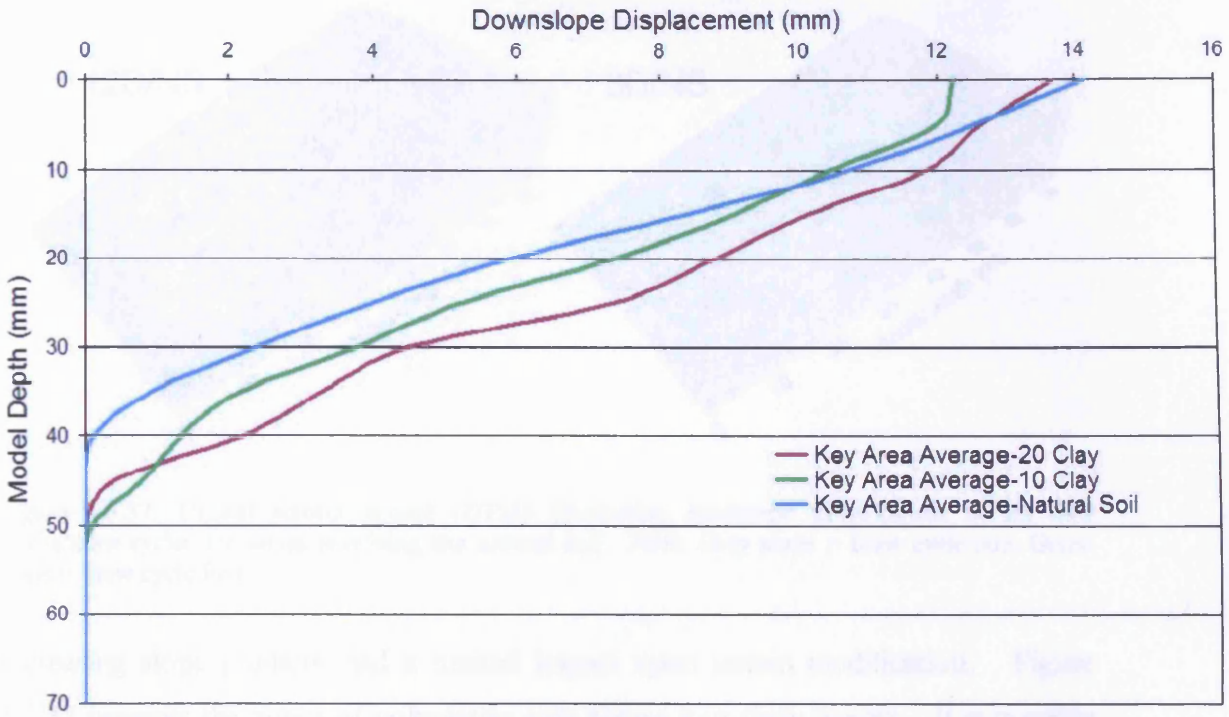

Figure 5.5.36. Average downslope displacement profile for the key area of the test series involving additional clay content.

5.5.8. Terrain Development

The style and rate of surface and subsurface movement recorded within the previous sections had an accumulative effect upon the morphology of the slope models. The planar slope models all showed modification across the four freeze/thaw cycles in response to the active mass wasting processes. Digital terrain models (DTM) were superimposed to illustrate the development of any primary landforms caused by the downslope movement of material, the consolidation of the soil and the cumulative loss of upslope mass. The DTM's presented here cannot be directly compared to the prototype solifluction landforms described within section 2.3.2 due to the lack of vegetation and entrained clasts. However, they can be used to infer the possibility of future geomorphic landform development given that the represented terrain modification created by downslope deformation has been identified within field monitoring studies and widely acknowledged as instrumental in solifluction lobe, terrace and sheet development cycles when combined with limiting factors such as vegetation cover and bedrock topography (see fig. 2.3.6) (Hugenholtz & Lewkowicz, 2002).

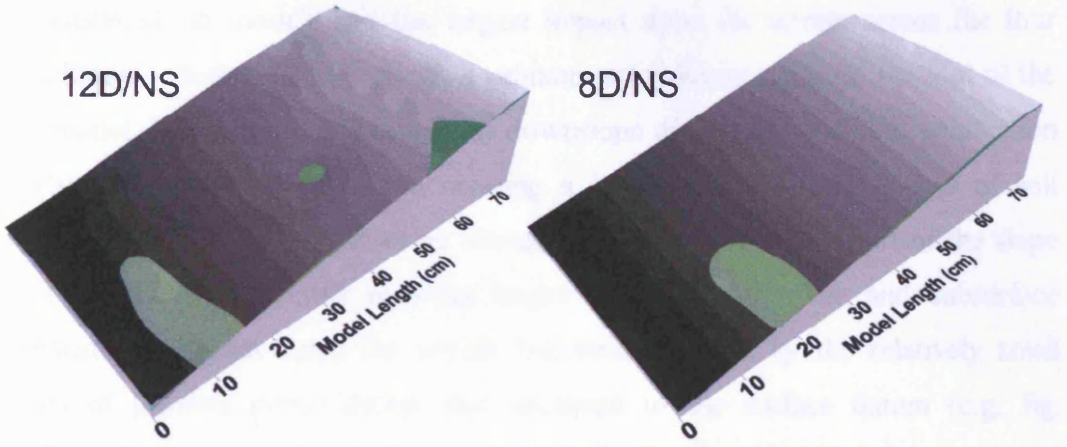

Figure 5.5.37. Digital terrain model (DTM) illustrating landscape development across four freeze/thaw cycles for series involving the natural soil. Note: Grey slope = thaw cycle one, Green slope = thaw cycle four.

Increasing slope gradient had a limited impact upon terrain modification. Figure 5.5.37 presents the zones of volumetric gain across four thaw phases. It is possible that the primary landforms seen within the bottom right section of the slope model within both series 12D/NS and 8D/NS would develop into gelifluction landforms given the correct limiting field conditions and sufficient freeze/thaw cycles. An interesting feature is the small circular extrusion within the central portion of Series 12D/NS as this landform may be a direct analogue for an infant stage solifluction lobe which given sufficient sediment supply from upslope regions during additional thaw phases may have shown further stages of development.

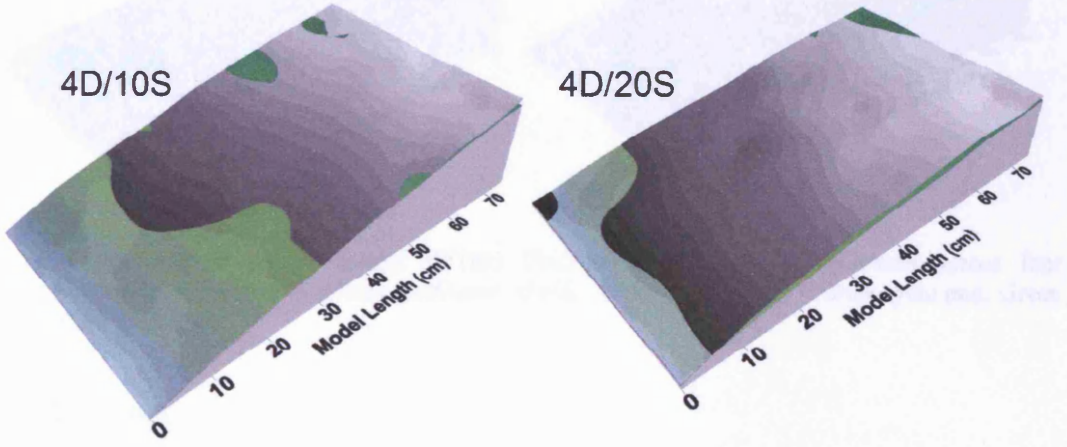

Figure 5.5.38. Digital terrain model (DTM) illustrating landscape development across four freeze/thaw cycles for series involving additions of silt. Note: Grey slope = thaw cycle one, Green slope = thaw cycle four.

The additional silt models had the largest impact upon the terrain across the four thaw phases. Series 4D/10S shows a pronounced volumetric gain at the foot of the slope model. This occurred through (a) downslope displacement due to gelifluction and (b) progressive consolidation creating a lower void ratio and a loss of soil volume. Series 4D/20S shows an increase in soil volume at the foot of the slope model – despite the series showing larger amounts of surface and subsurface movement the impact upon the terrain has been lessened by the relatively small amount of physical consolidation that occurred to the surface datum (e.g. fig. 5.3.10). However, within field environments the limiting of surface movement is a common cause for solifluction lobe development, it is therefore felt that the accumulation of sediment as the base of the model could potentially form a solifluction sheet given sufficient physical space and further freeze/thaw cycles.

The impact of subsurface and surface deformation could not be shown within the clay models because of the large amount of volumetric loss due to the progressive consolidation described within Figure 5.3.8. However, it has been shown within sections 5.5.7 and 5.5.3 that the clay models acted as a complete cohesive unit and that greater amounts of subsurface movement occurred through increasing clay content.

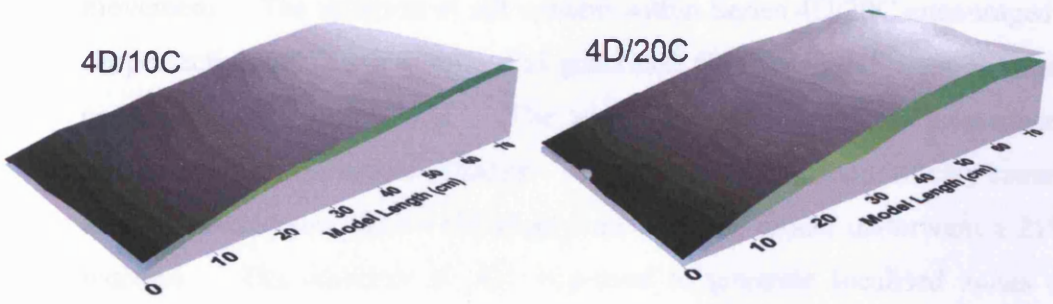

Figure 5.5.39. Digital terrain model (DTM) illustrating landscape development across four freeze/thaw cycles for series involving additions of clay. Note: Grey slope = thaw cycle one, Green slope = thaw cycle four.

5.5.8. Summary

- Rates of surface movement were consistent between individual thaw phases.

- Surface movement progressively increased towards the foot of the slope within all slope models. Progressive downslope acceleration was consistent within the cohesive clay test soils but variations in soil ice content may have created localised patterns of displacement within the silt test soils.
- Increasing model slope gradient encouraged greater amounts of surface displacement. Series 12D/NS showed 70% more surface displacement than Series 8D/NS and 92% more surface movement when compared to Series 4D/NS.
- Soil granulometry had an influence upon surface displacement. Increasing silt content had a consistent effect. A ten percent increase in silt lead to a 21% increase whilst a twenty percent increase caused a 54% increase in surface movement. The addition of clay had a varied effect. A ten percent increase in clay generated a 28% reduction in movement whilst the twenty percent increment caused a 2% increase.
- Subsurface deformation patterns were consistent and replicated data gathered from previous full-scale and model-scale simulations of solifluction.
- Subsurface volumetric velocity increased with model slope gradient. The twelve degree slope model generated 56% more than the eight degree model and 96% more when compared to the four degree model.
- Modifications to soil grainsize influenced the rate and style of subsurface movement. The addition of silt content within Series 4D/20C encouraged a deeper active gelifluction zone and generated 62% more deformation when compared to the natural soil. The addition of clay had a less pronounced influence upon volumetric velocity – the ten percent increment of clay caused a small 8% increase whilst the twenty percent clay model underwent a 21% increase. The addition of clay appeared to generate localised zones of shearing and thereby created a convex subsurface movement profile.
- Behavioural thresholds were identified between the different clay and silt test soils. Test soil granulometry had a distinct influence upon the style and rate of surface and subsurface movement.
- All planar slope models were subjected to landscape development with the degree of terrain modification being causally determined by variations in soil grainsize or slope model gradient.

5.6. Micromorphology of Test Soils

In order to investigate the development of soil fabrics, thin sections were prepared from undisturbed samples collected during the excavation of models at the end of each centrifuge test sequence (see fig. 3.6.1). The use of soil micromorphology is a widely accepted geomorphic analytical tool (Kemp, 1985; Ballantyne & Harris, 1994, p.109). Several conceptual models describing soil particle arrangements have been proposed to classify micromorphology arising from sediment deposition, reworking and pedogenesis (for a comprehensive review see Collins & McGown, 1974). Geologists and engineers can use these models to examine soil microstructure to determine either the past history of a material or the past environmental conditions; for example an indurated layer (fragipan) can be used to indicate the former presence of permafrost (Bertran & Texier, 1999; Van Vliet-Lanoë & Langohr, 1981). Researchers are able to infer historical conditions based upon the assumption that particle arrangement and microstructure is a function of the mode of deposition (e.g. water-lain, glacial, in-situ weathering, etc.), subsequent stress history (e.g. consolidation, shearing, cryosuction-induced stresses (Harris, 1998), and the electrochemistry of the pore fluid at the time of deposition (Bertran & Texier, 1999). These influence the physical constitution (microfabric) of a soil material through the spatial arrangement of solid particles and associated voids (Anderson *et al.*, 1978).

It should be noted that there are several other factors known to influence the microfabric of a soil deposit; such as particle shape/size/gradation, clay mineralogy, organic content, rate of deposition, etc. Specific suites of these factors influence the site-specific microstructural characteristics of periglacial gelifluction deposits (Harris, 1985). General interpretation requires the identification of diagnostic features; within periglacial sediments these can indicate cryogenic processes and/or cryogenic history (e.g. active layer thickness, the presence of absence of permafrost and/or the dominant mass wasting process - see Harris, 1985 for a full description). However, any environmental reconstruction should take into account the possibility of equifinal behaviour, in that similar microfabric or macroscopic features may be produced by different processes, for example the overall combined effect of wetting, drying, freezing and thawing (Van Steijn *et al.*, 1995).

The development of new electron microscopy technology and precise cryogenic laboratory techniques has allowed greater experimental investigation into minor alterations within the microstructure of freezing or frozen soils (e.g. Jiacheng & Yujie, 1998; Kumai, 1988; Grechishchev *et al.*, 1992; Jianming *et al.*, 1998). These advanced techniques have created the potential to model specific scenarios and examine the microstructural significance of particular environmental changes, for example the influence of a buried chilled pipeline on micromorphological development and consequent soil behaviour (White & Williams, 1993; Dore *et al.*, 1998).

The major micromorphological components of a periglacial soil include; *plasma* which has been defined as fine-grained material liable to translocation, *skeletal grains* that are relatively stable larger grains and are not easily translocated, and *pore spaces* which are the air-filled voids between the plasma/skeletal matrix. Harris (1985) defined four main micromorphological components developed under periglacial regimes. Interpretation of sediment samples from slope models within the centrifuge-modelling program involved analytical evaluation for the presence of these elements.

- Grain Coatings;

Solifluction and cryogenic processes can be result in the formation of cappings of fine matrix material coating the upper surfaces of sand grains and soil aggregates. Such cappings are frequently smooth and contain micro-laminations suggesting incremental growth (Harris, 1985; Van Vliet-Lanoë, 1985, 1988). Plasma caps coating the top faces of skeletal grains and larger clasts have been widely reported in seasonally frozen ground and permafrost, for example Harris and Ellis (1980) observed gelifluction grain coatings within the active layer at Okstindan, northern Norway. Silt coatings have also been reported upon both the top and bottom of soil particles, with laminations forming due to grain rotation during gelifluction, such grain coatings are termed *cutans* (Ballantyne & Harris, 1994; Harris, 1981). The caps of fine material upon clasts and/or sand particles form due to the downward translocation of clay/silt sized material (Bertran & Texier, 1999, p.114, fig. 17).

This illuviation occurs through soil moisture flows generated by high soil moisture contents associated with periglacial thaw events, although such illuviation could not occur within continuous permafrost zones where vertical drainage is impeded and thermal gradients greatly influence moisture pathways (Harris, 1998; Harris, 1984).

- Platy/Lenticular Structure;

The growth of segregated ice leads to platy structures forming within the soil profile within both permafrost and seasonally frozen ground (Bertran & Texier, 1999; Ballantyne & Harris, 1994). It has been noted by some researchers that platy microstructures have the tendency to become prismatic as the soil profile reaches permanently frozen ground (e.g. Van Vliet-Lanoë, 1985). Dense platy peds containing both skeletal grains and plasma separated by planar voids have been ascribed to consolidation during soil freezing through porewater cryosuction and ice-lens nucleation and growth (Bertran, 1993). Thawed permafrost soils inherit platy structures from the former presence of ice lenses, as saturated conditions during thaw consolidation encourages fine material to settle through the water filled voids and form plasma concentrations on lower void surfaces and lenses of denser matrix associated with cryosuction and heaving pressures (Harris, 1984; Van Vliet-Lanoë, 1985).

- Grain Fabric;

Microfabrics can become well developed within gelifluction-derived soils due to the combined action of frost sorting and solifluction (e.g. Corte, 1966; Benedict, 1970). Fabrics are commonly created through the reorientation of elongate granular material along the axes of dominant transport, i.e. during the thaw-induced soil shear strain involved with repeated solifluction mass wasting. Particle movement leads to soil or clast fabrics parallel to the flow direction and to the slope surface dip, giving a strong downslope-preferred orientation (Nelson, 1985, Harris, 1998). In some cases an imbricated structure may form where the long axes of mineral particles will overlap as they become increasingly inclined in the direction of the former depositional current (Harris, 1983).

- Vesicular Voids;

The formation of smooth-walled bubble-like voids can be caused by air being expelled from the soil mass through either an advancing ice front or immediately following thaw through the action of thixotropic liquefaction (Harris, 1983). Liquefaction will occur as skeletal structures rapidly collapse during thaw consolidation leading to the formation of vesicular structures in zones where the rate of consolidation exceeds the air removal rate and traps soil gases within the newly formed matrix.

5.6.1. Sample Preparation

Sediment samples were collected during post-thaw excavation from the eleven slope models involved in the primary and secondary modelling phases (see fig. 3.14). Soil samples were removed by pushing a small plastic box (6cm x 6cm x 3cm) with a chamfered basal cutting edge into the slope model. Three samples were removed from each excavated section with each sample containing a complete profile of subsurface markers. Thin-section samples were geo-referenced to allow back-analysis of observed microstructures with respect to slope location (see fig. 5.6.1). The orientation of the sample was noted with respect to the slope of the model to ensure thin-sections were manufactured along the correct axes referenced to the slope azimuth. The collected samples were allowed to fully air dry. The low clay content of the experimental soils ensured that structural shrinkage was not a significant problem and did not alter soil sample micromorphology during the drying procedure.

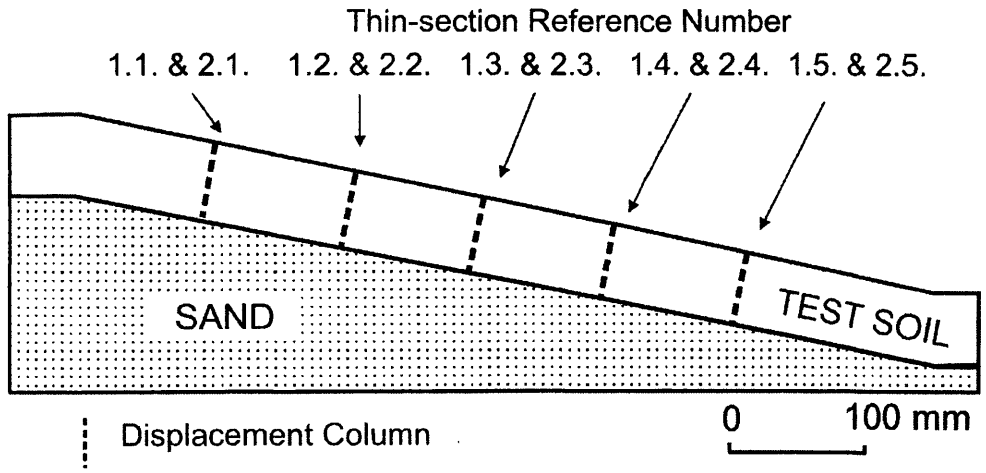

Figure 5.6.1. Thin-section reference system for each potential sample removal point within the two excavation transects. Note: Three samples were removed per slope model.

Soil samples were impregnated with a plastic resin to protect sample microfabric during thin-section preparation. The dried samples were placed in bath of Araldite resin for impregnation. The resin was mixed with acetone to reduce viscosity and promote movement through all accessible intra-pore spaces. To encourage complete resin impregnation the full Araldite bath was then placed in a vacuum oven for a 24-hour period. Excess resin was then removed from the impregnated soil samples and the resin cured within a warm drying cabinet. The hardened resin-impregnated samples were then cut into oriented sections using a diamond saw. These were lapped on a Logitech LP30 precision lapping machine. The impregnated sections were then cleaned by immersion in an ultrasonic bath and mounted on glass slides using epoxy resin within a Logitech bonding jig. The slides were subsequently mounted in a vacuum chuck where a cut off saw then trimmed the sample to a slide thickness of approximately 300μm. In this analysis, all samples were cut in the vertical plane. The glass slides were then lapped using a precision jig to the final 30μm soil section thickness. The completed slides were then available for full visual inspection using a petrological microscope.

5.6.2. Microfabric Analyses

Sedimentary fabric defines the orientation and dip of individual particles within a deposit. Fabric can be defined as any components of a sediment that behave as single discrete units with respect to an applied force (Harris, 1981). The presence or absence of resulting patterns of alignment will characterise differing processes of transport. Harris (1981), Van Vliet-Lanoë (1985, 1988) and Douglas & Harrison (1987) have recognised characteristic microfabrics for periglacial sediments, and have described modern and relict periglacial sediments via analyses of microfabric orientation and internal structures. This approach has allowed researchers to differentiate between Quaternary sediments on the basis of their particle fabrics, for example the analysis of glacigenic sediments conducted by Lawson (1979) or paraglacial deposits by Harris (1998). In this context, the nature of solifluction microfabrics will reflect both flow and creep processes and be a function of moisture content, duration of mass wasting transport, and underlying slope angle (Nelson, 1985).

Sediment microfabric was assessed using a modification to the method outlined by Harris and Ellis (1980). The direction of predominant particle arrangement within the microfabric of the derived samples was analysed with a Nikon Optiphot 2 transmitted/reflected light stereomicroscope using a measurement eyepiece and rotational jig. Two vertical plane thin sections were used for each of the three test series investigated (4D/NS, 8D/NS and 12D/NS). Particles where chosen randomly within a section of undisturbed sediment. Each particle was elongate, blade or rod shaped, i.e. displayed an A/B axis ratio greater than 2:1. These particles were then measured to determine the azimuth and dip of the A axis. Measurements were recorded for 100 randomly selected particles for each slope model. Orientation data were combined from the two thin sections measured for each model, and summarised using rose diagrams (see fig. 5.6.2), the full dataset is presented within Appendix A.

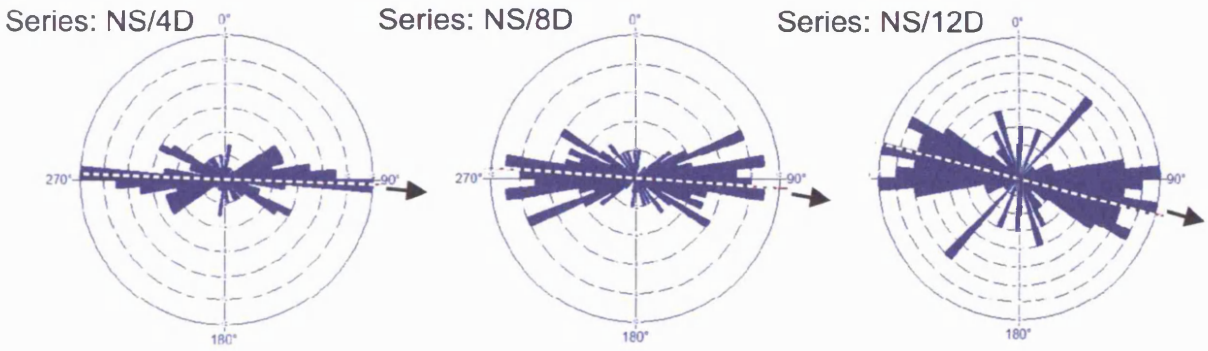

Figure 5.6.2. Preferred orientation of elongate sand particles from thin-sections of geliflucted sediment derived from series using natural soil. Note: the annotated white dotted line indicates mean average orientation for each series and the black arrow highlights model slope angle.

Fabric patterns indicate a relationship between preferred particle dip and slope angle, where the predominant alignment of particle A axes dips increases as the slope gradient increases. The observed pattern is similar to that observed by macroscopic analyses where preferred clast orientations have occurred parallel to the measured slope angle within prototype lithofacies (e.g. Nelson, 1985; Benedict, 1970; Washburn, 1979, p.217). Harris and Ellis (1980) have recorded similar sand grain dips within field-derived solifluction and cryogenically altered soil samples. It should be noted that the evaluation of skeletal grain orientations in thin-sections is complicated by the potential for recording an experimentally modified grain shape.

The sample preparation procedure can potentially alter perceived grain shape by cutting through a particle B axis and creating an apparent two-dimensional view of a soil fabric.

5.6.3. Microscopic Thin-section Observation

Thin-sections were systematically examined for the main diagnostic cryogenic microfabric criteria outlined by Harris (1984). Sediment microfabric was visually assessed using a Leica MZ12.5 transmitted light stereomicroscope used with a twin fibre optic light source with polariser and fitted transmitted light base with polariser. The photomicrography was captured using a colour digital camera that moved images into a Leica Qwin image processing software suite for further analysis and measurement. A summary of observed microstructures is given in Table 5.6.1 and examples are illustrated and briefly described below:

Table 5.6.1 Summary of microstructures observed via optical microscopic analyses.

Test Series	Slope Position	Grain Fabric	Cutan/ Coating	Lenticular Structures	Vesicles	Shear/Flow Structures
12D/NS	1.3	X	X			
12D/NS	2.4	X	X			
16D/NS	1.2	X	X			
16D/NS	1.5	X	X		X	X
16D/NS	2.3	X				X
8D/NS	1.2	X	X			
8D/NS	2.2	X			X	X
4D/NS	1.3	X	X			
4D/NS	1.4	X				
8D/10S	1.2	X				X
8D/10S	1.3	X	X		X	X
12D/10C	1.2	X	X			
4D/10S	1.3	X			X	X

- *Preferred Orientation of Elongate Sand Grains*

Typical vertical plane thin sections are shown in Photomicrographs 5.6.3 and 5.6.4. In both sections the preferred orientation of elongate sand grains is apparent, with grains oriented around the slope azimuth (fig. 5.6.3). Also apparent are poorly developed grain coatings and cappings, together with occasional small vesicular voids.

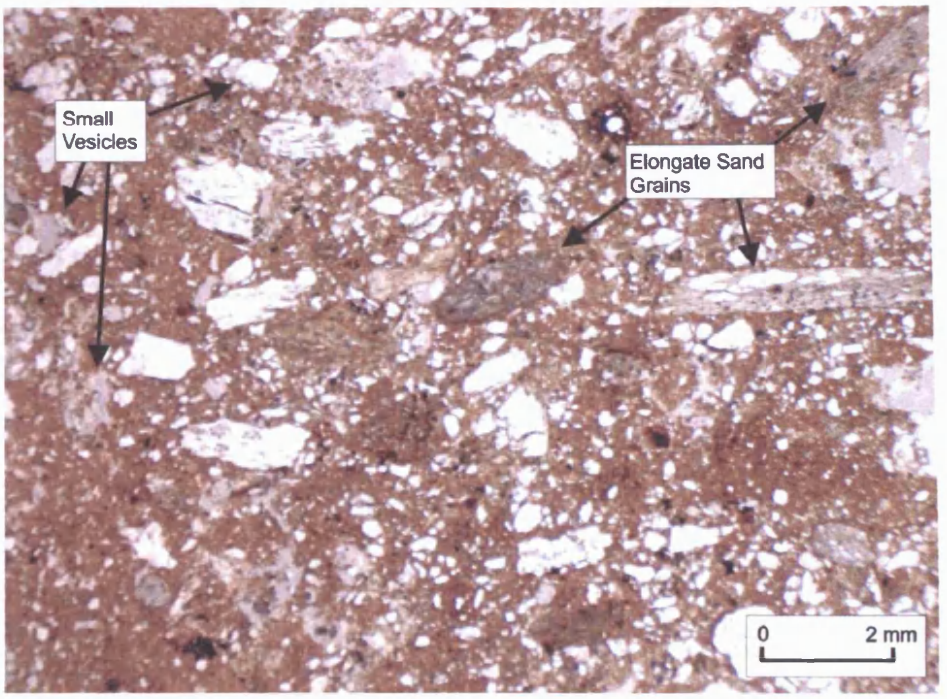

Figure 5.6.3. Vertical thin-section from slope model 8D/NS (transect position 1.2) after four freeze/thaw cycles. Thin-section showing general soil skeletal matrix with defined orientation of larger particles and the presence of small vesicular structures. Note: Photomicrograph taken with partially crossed polarised light.

- *Grain Coatings or Cutans*

These were observed in soil thin sections from all primary phase slope models (see table 5.6.1). Examples of thin sections showing fine matrix coatings on soil grains are shown in Figures 5.6.4 and 5.6.5.

Figure 5.6.4 shows a vertical thin section from test series 12D/NS after four freeze-thaw cycles. Here the upper surfaces of two skeletal grains are coated with translocated silt/clay, forming silt cappings or cutans. The capping material comprises a dense aggregate of fine silt flakes and clay particles. In the upper grain the cutan surface is smooth and fairly sharp, while upon the lower grain coating is thicker and has a slightly more diffuse boundary. The maximum cutan thickness is approximately 400μm. Very similar grain coatings were also observed in other vertical sections (figs. 5.6.5a & 5.6.5b). In the case of Figures 5.6.5c & 5.6.5d from series 8D/NS, grains show coatings of finer soil on all surfaces, suggesting grain rotation during thaw consolidation. Slides have also shown a flecked texture to the silt coating, resulting from larger silt flakes and fine sand grains, and these appear to show streamlining around the grain (figs. 5.6.5c & 5.6.5d).

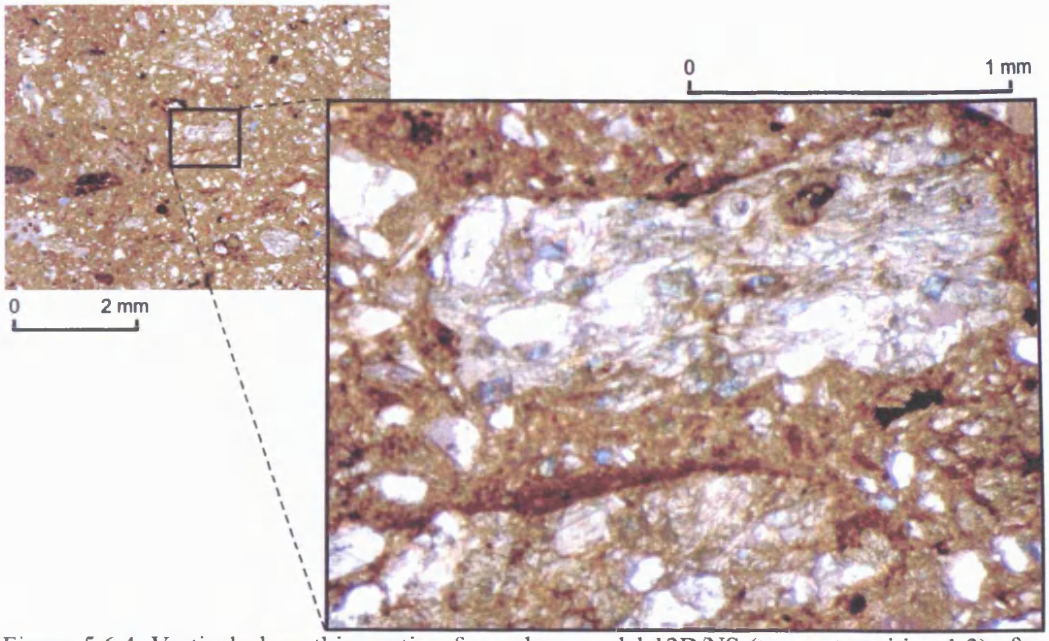

Figure 5.6.4. Vertical plane thin-section from slope model 12D/NS (transect position 1.3) after four freeze/thaw cycles. Thin-section showing skeletal grains with top face silt capping (cutans). Note: Photomicrograph taken with partially crossed polarised light.

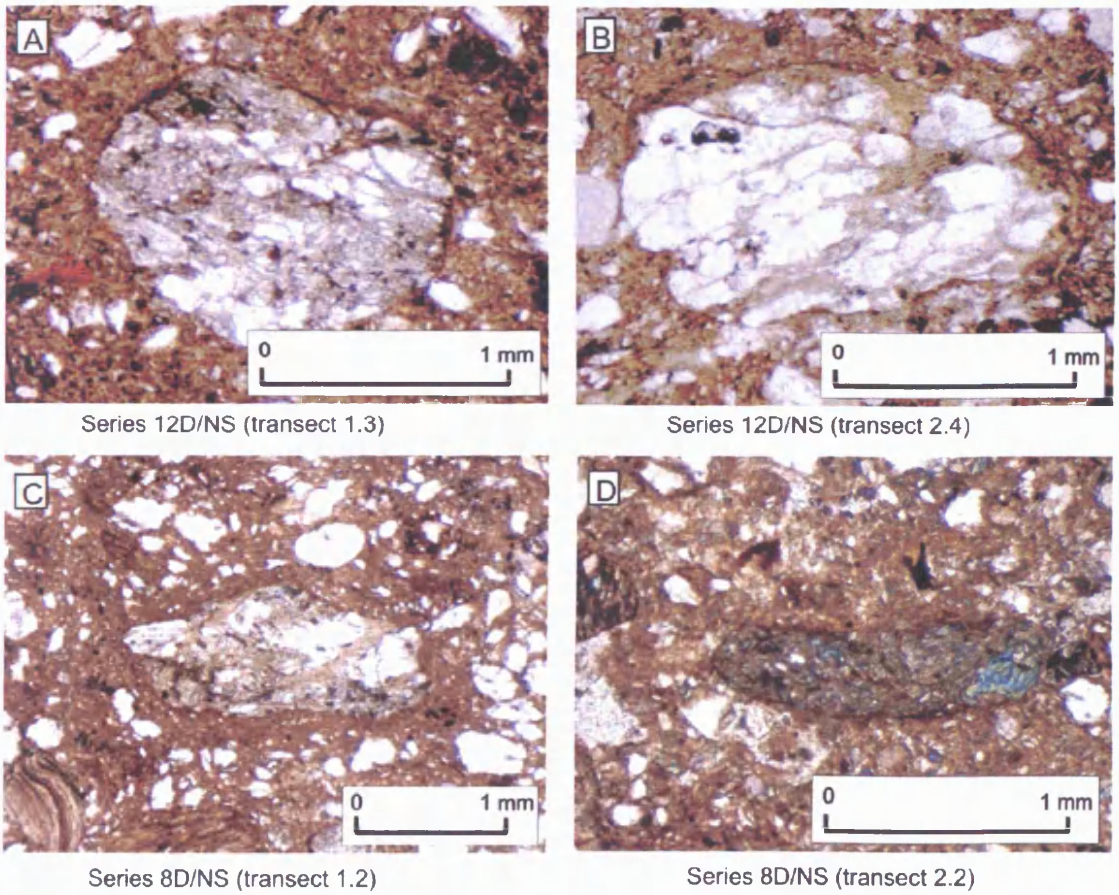

Figure 5.6.5. Vertical thin-sections from various slope models after four freeze/thaw cycles. Thin-sections showing rounded and slightly elongate sand grains with complete microlaminations of silt and clay. Note: Photomicrographs taken with partially crossed polarised light.

- *Shear-related Structures*

Irregular discontinuities within the general soil fabric were observed in several slides (table 5.6.1). These consisted of either areas with a linear or irregular "ropey" flecked pattern, or zones where silt and fine sand grains show a striated pattern under partially polarised light (see fig. 5.6.6). These areas suggest some localised accentuated shearing within the finer matrix, possibly associated with thawing of ice lenses within the soil (Van Vliet-Lanoë *et al.*, 1984).

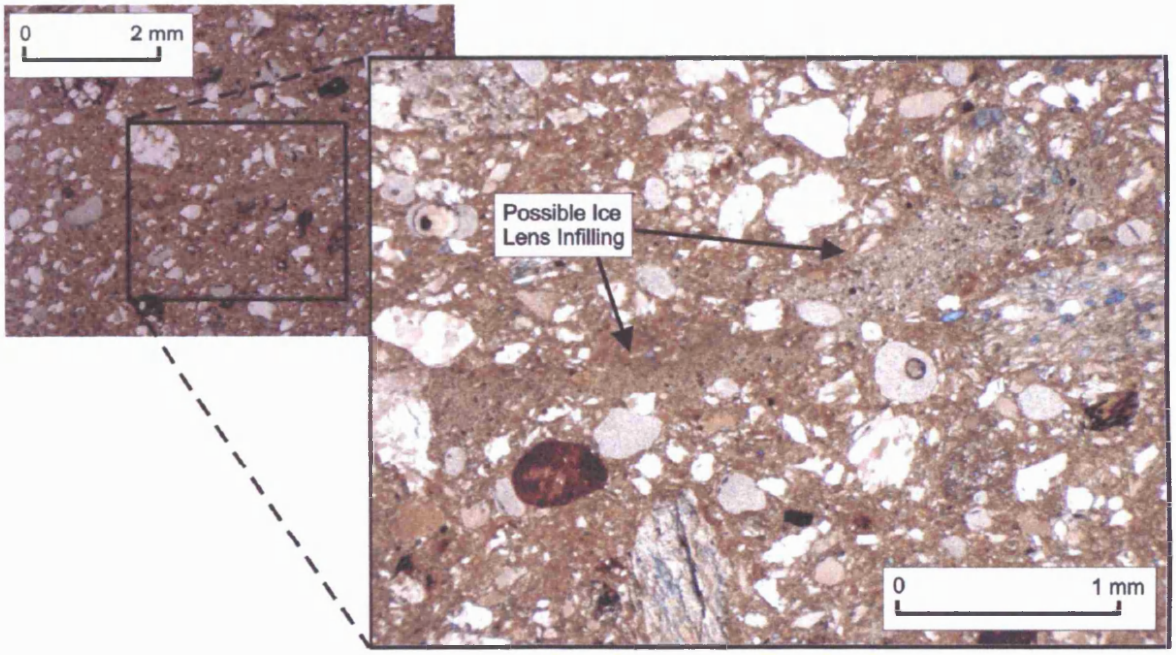

Figure 5.6.6. Vertical thin-section from slope model 8D/10S (transect position 1.3) after two freeze/thaw cycles. Thin-section showing a site of possible ice lens infilling or zone of solifluction microshear as described by Van Vliet-Lanoë (1985). Note: Photomicrograph taken with partially crossed polarised light.

- *Vesicles*

Smooth-walled bubble-like voids, or vesicles were observed in several thin sections, though not in all (e.g. fig. 5.6.3). These voids ranged up to approximately 600μm in diameter and their walls were clean. It appeared that they developed during thaw, but were probably destroyed in subsequent freezing cycles, so that no fines accumulated within them. These structures resemble closely those described by Harris (1983).

5.6.4. Discussion

The microstructures identified within the laboratory thin-sections would appear to be analogous to prototype field structures described as common within periglacial solifluction deposits (Ballantyne & Harris, 1994, Van Vliet-Lanoë, 1985). Skeletal grains have been observed to be both uniformly encased within fine material (see fig. 5.6.5d) and capped on their upper particle surfaces (see fig. 5.6.4). The completely encased structures appear analogous to pressure cutans created by fine material accumulating through grain rotation during downslope displacement. The upper-surface cutans would appear to reflect direct plasma settlement during thaw consolidation, with fine material moving onto the particle surface through evaporating downslope meltwater movement along thermal gradients. Flattened patches of matrix enrichment (e.g. Harris and Ellis, 1980) were widely observed. The presence of zones with flecked ropy patterns within the matrix may well reflect micro-shear structures associated with the thawing of segregation ice. Small vesicular structures suggest small isolated air bubbles trapped within a thixotropic soil formed during thaw consolidation, as suggested by Harris (1983).

Grain orientation was sometimes relatively weakly developed, though in some cases distinct modal grain orientations were roughly parallel to the slope gradient in vertical sections. This is very similar to the fabrics reported by Harris (1981) and Harris and Ellis (1980) from modern solifluction lobes in Norway. Thin-sections taken from the upper portions of the slope exhibited less orientation than lower slope zones that had greater amounts of particle rotation.

Many features would appear to be in an early stage of development. This is clearly not surprising since the experimental soils had suffered only four cycles of freezing and thawing. However, relatively small-scale micromorphological elements have been identified and verified; and are considered as being indicative of ice segregation during soil freezing and thawing, pore water flux during thaw and slope shear strain within the slope materials due to solifluction (Bertran & Texier, 1999). The experimental centrifuge-modelling program has successfully simulated microstructural and microfabric characteristics previously described within both full-scale laboratory experiments (e.g. Van Vliet-Lanoë *et al.*, 1984) and prototype field analogues (e.g. Benedict, 1970; Harris, 1981).

5.7. Experimental Issues and Complications

The following section will record some of the problems that occurred when applying the laboratory methodology described in chapter 3. These complications may have influenced slope model behaviour and therefore some of the results presented from the centrifuge program in sections 5.2-5.6.

- *Sediment deformation during initial and inter-cycle consolidation*

Prior to the first thaw cycle for test series 16D/NS, 4D/20S and 4D/20C the model was saturated and consolidated following the standard procedures described in sections 3.2 and 3.4. However, the weight of the freezing plate and confining load when initially applied resulted in some sediment deformation around the edge of the plate. This created an upward displacement of wet sediment around the plate edge and following consolidation the sediment was manually removed to create a smooth plane aligned with the consolidated main slope surface. The removal of displaced sediment created a small net loss of soil mass from the slope model. It was felt that this problem did not significantly impact upon observed measurements for surface movement, frost heave or thaw consolidation as the majority of measurements were recorded within a central zone upon the model surface (e.g. fig. 5.5.1). Over the four freeze-thaw cycles, the more plastic host sediments used within Series 4D/20S and 4D/20C created a convex model profile due to downslope material displacement during each thaw cycle (see section 5.5.7). The weight of the freezing plate and confining load created a minor distortion of the convex surface as the displaced soft sediment moved from the centre of the model towards the crown and toe of the slope. This effect was noted during the consolidation phase that followed the first thaw cycle and became less prominent through the introduction of a lag rest period to the experimental procedure after each thaw cycle for Series 4D/10C, 4D/20S, and 4D/20C. The additional lag phase allowed model moisture conditions to equilibrate before the confining load and freezing plate were placed back upon the model surface. The model was therefore able to regain pre-thaw shear strength and this lessened the impact of the freezing plate load on the convex slope profile.

- *Water supply problems during freezing*

The external water supply pipelines may have become frozen for several individual tests within a given series (see fig. 3.4.2). It is felt that the freezing of the pipelines was caused by cold air flowing underneath the insulating lid and sinking between the sidewall of the Perspex model liner and polystyrene insulating casing (see fig. 3.4.3). It was difficult to quantify the exact impact of pipeline freezing - although it was felt this intermittent problem could have influenced the water flux towards the freezing front towards the end of some freezing phases and therefore reduced ice segregation by limiting water supply. This problem within the experimental design may explain the intra-series inconsistencies observed in measured amounts of frost heave, (see section 5.3). However, there may have been occasions whereby pipeline freezing did not fully commence until the downward freezing front had passed through the soil model and reached the sand basal layer. The problem within the experimental design was not fully recognised until after the completion of both phases of centrifuge testing. A modification to the experimental design has been proposed in Chapter 9 to alleviate water supply issues.

- *Centrifuge Malfunction*

The centrifuge had a malfunction during the third stage of initial acceleration during the first thaw cycle for 8D/10S. A short circuit within the control unit caused a complete power loss. The slope model was retrieved from the centrifuge after a thirty-five minute safety delay; the model had thawed to a depth of approximately 10mm so the complete thaw cycle was rescheduled. The model was allowed to thaw upon the laboratory floor and a complete freezing phase was undertaken with full re-measurement of all data. It was not felt that this delay created significant behavioural problems within the soil slope model.

- *Model drainage during centrifuge testing*

Several models experienced drainage problems during the thaw phase. This occurred because the central drainage channel became blocked with fine silt material carried in suspension by the melt water. On three occasions this created a sustained blockage that allowed melt water to pond at the foot of a slope model. It was impossible to directly remove the blockage from outside the test specimen as the thawed slope model was securely placed within the steel strongbox and centrifuge

gondola. Instead, surface water was removed via an industrial syringe and the external gauze protector was reshaped to recreate a free drainage path away from the model surface. This ponding of water at the foot of the slope is not thought to have materially affected behaviour of the soil in the instrumented zone further upslope. For example, water drainage problems occurred during the second thaw phase of test series 8D/10S where fine material was held in suspension by meltwater around a congested central drain. The test was suspended after 1hr 45m to siphon off excess surface water whilst widening the drainage channel and refilling it with coarse sand. Overall test suspension lasted for fifteen minutes and prevented further drainage problems during that thaw phase. It was not felt that the test delay unduly influenced slope model behaviour.

- *Measurement of subsurface movement profiles using scaled plastic columns*

It was observed that the subsurface profile column markers protruded above the model surface in certain test series due to frost heaving of the columns. The protruding effect within the uppermost markers was first noted during the fourth thaw phase of test series 4D/20S. It was also recognised that the protruding column sections were being pressed back into the soft sediment by the freezing plate during the subsequent consolidation phase. The weight of the confining load was therefore potentially disrupting the subsurface profile and any derived volumetric or displacement measurements. After the second thaw cycle of series 4D/10C any protruding column sections were removed post-thaw to prevent potential interference during the next consolidation phase. It is felt that this column disturbance may have affected the uppermost column markers and unduly reworked subsurface marker profiles in a limited number of tests, particularly Series 4D/20S (see for example position 1.2 in figure 5.5.18). It should be noted that the removal of protruding markers caused a smaller number of markers to remain during model excavation, especially within the test series undergoing large amounts of physical compression during thaw consolidation, for example position 1.2 in Series 4D/20C represented within Figure 5.5.20.

- *Noisy signals from transducers*

There was a frequent problem with noisy or erroneous signals from the thermocouples and miniature porewater pressure transducers. These problems occasionally coincided with probe failure and therefore could not be rectified once the series was in progress, for example the upper slope base thermocouple within Series 4D/10C. It was felt a problem within the internal wiring system of the interface boxes, centrifuge slip ring and Campbell CR7 data logger may have further compounded the problem for specific pore water pressure transducers.

There was a degree of uncertainty regarding the long-term accuracy of the K-type thermocouples used within the experimental program. Many of the thermocouples provided consistently noisy data due to the constant harsh conditions of use. This did not present a direct problem as the thermocouple array was mainly used as a time indicator of how the thaw front was progressing through each slope model. It is not felt thermocouple complications impacted upon the experimental procedure because where thermocouple failure occurred, the adjoining thermocouple from the adjacent string could be used to infer the progression of the freezing front through the model and therefore complete the thaw phase at the appropriate juncture.

CHAPTER SIX : Experimental Results – Discussion

In this chapter the interrelationships between the variables explored in Chapter 5 and resulting model responses in terms of mass movement mechanisms will be explored and discussed. Specifically, the factors influencing the style and rates of gelifluction will be investigated based on the data sets presented in Chapter 5. It is important to ascertain the basic relations between the rate and style of gelifluction and changes in soil granulometry and slope gradient in order to elucidate upon the complex set of interrelated variables that may influence gelifluction in the field.

6.1. Mechanisms of Slow Downslope Movement

The slow mass wasting processes observed within this study (see section 5.5) can be subdivided into frost creep occurring during model freezing and gelifluction occurring during subsequent thaw consolidation (see sections 2.2.3 & 2.2.4). It is necessary to separate these mechanisms in order to correctly assess their efficacy under different conditions of soil type and slope angle. An index of the relative importance of gelifluction and frost creep was determined from surface movement data via the calculation of the maximum potential frost creep (equation 2.6 on page 32).

Table 6.1.1. Potential frost creep and gelifluction components for the average per cycle amount of recorded surface movement. SD = Standard deviation.

Series	Potential Frost Creep (FC) (mm)	Gelifluction (G) (mm)	% Potential Frost Creep	G/FC Ratio	SD
12D/NS	2.00	3.09	39.3	1.53	±0.43
8D/NS	1.39	1.30	51.7	0.98	±0.58
4D/NS	0.80	1.90	29.6	2.34	±1.14
4D/10S	0.82	2.15	27.6	2.66	±0.76
4D/20S	0.42	5.11	7.6	12.78	±5.48
4D/10C	0.54	1.10	32.9	2.13	±1.35
4D/20C	0.53	1.69	23.9	3.28	±1.54

Table 6.1.1 and Figure 6.1.1 both show that the amount of frost creep was a function of slope gradient of the test series since frost heave is assumed to take place perpendicular to the slope surface gradient. In absolute terms, as expected, the

potential frost creep decreased with decreasing slope gradient in the natural soil slope models. However, in relative terms, series 8D/NS showed the largest component of frost creep, accounting for some 51.7% of the average surface movement. With a constant slope gradient (4°), frost creep was related to the amount of frost heave occurring within the slope model (fig. 6.1.2). Frost creep was ultimately a function of water supply, rate of freezing and the frost susceptibility of the soil (grain size), with secondary controls of permeability and capillarity. Series 4D/NS and 4D/10S showed the largest absolute amounts of potential frost creep within the 4° slope models, but as a percentage of the total surface movement rates, the 10% clay enhanced soil showed a larger relative proportion of movement as a result of potential frost creep, to reflect the low total surface movement recorded in this model. In Series 4D/20S, potential frost creep accounted for only 7.6% of the average surface soil movement rate, as a result of the high rates of surface displacement recorded, despite low frost heave values and a gentle slope gradient.

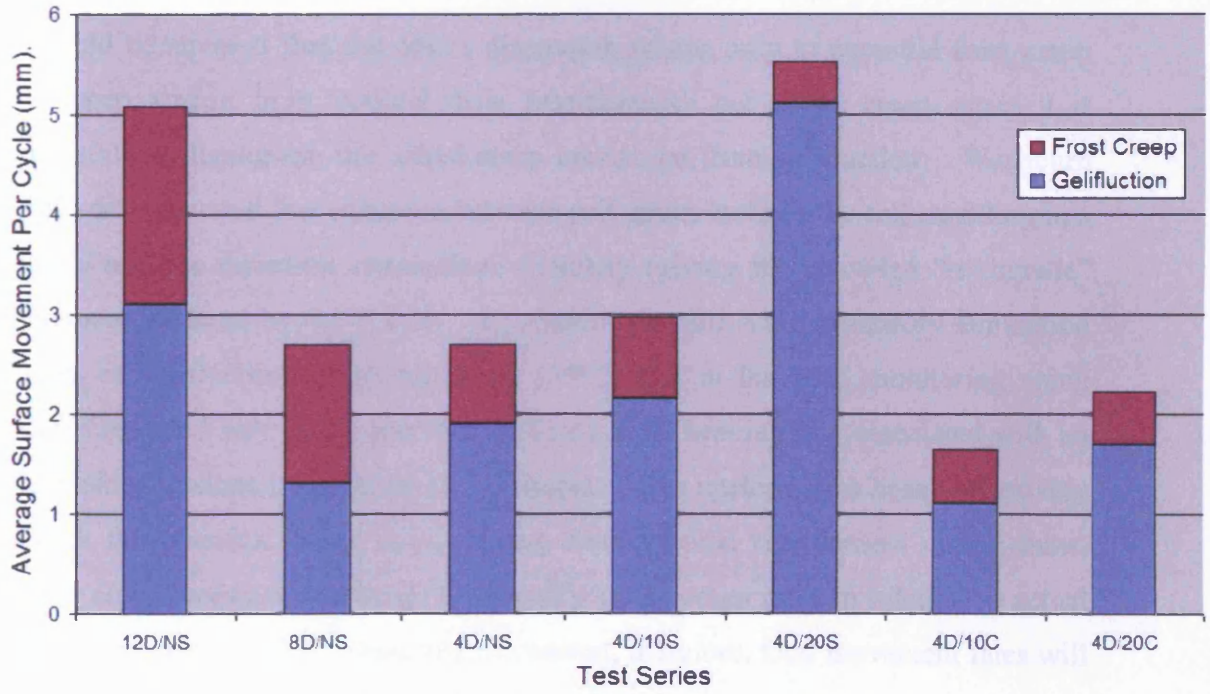

Figure 6.1.1. Relative components of gelifluction and potential frost creep for the average amount of surface movement per thaw cycle for each test series.

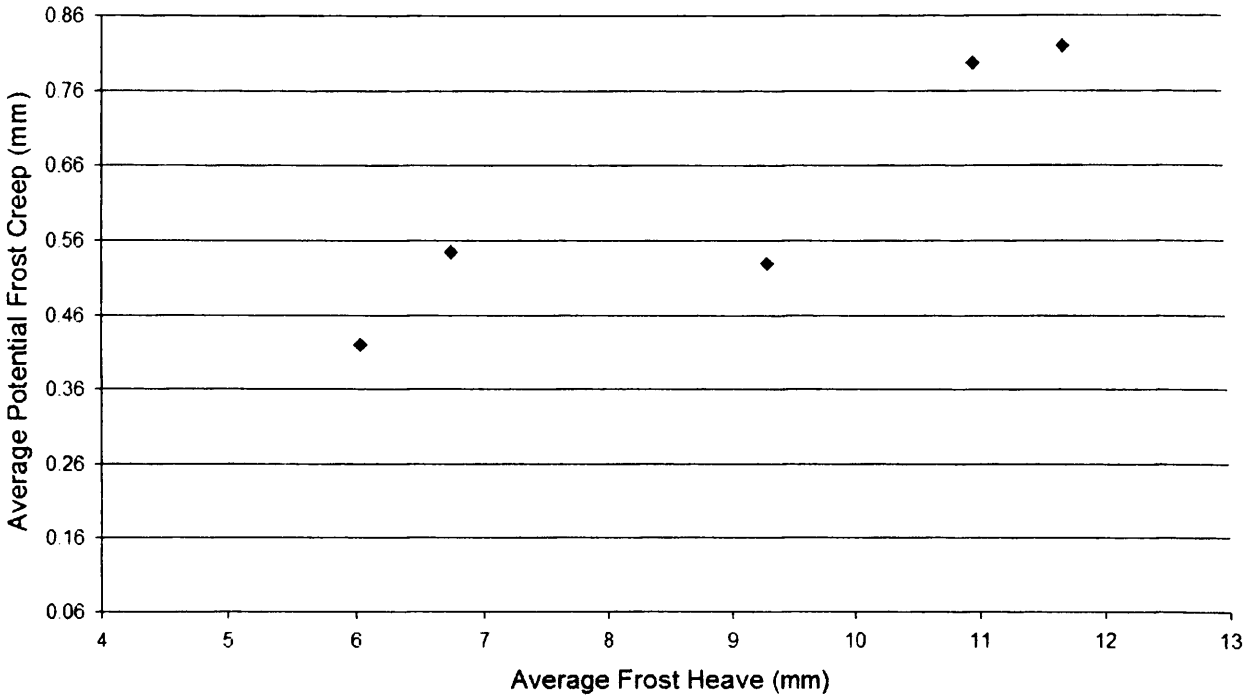

Figure 6.1.2. Potential frost creep and frost heave for four degree slope models. Note: the thickness of the frozen soil was constant in all models, so the relationship between total measured frost heave and heaving ratio was constant in all cases.

It should be stressed that the above discussion relates only to potential frost creep (the creep arising from vertical thaw resettlement), not actual creep, since it is impossible to distinguish the actual creep movement from gelifluction. Washburn (1967) demonstrated that cohesion between soil grains leads to the soil resettling in a slightly upslope direction rather than vertically (giving the so-called "retrograde" movement outlined in fig. 2.2.3). In addition, in full scale laboratory simulation studies of solifluction by Harris *et al.* (1997) and in the field monitoring using LVDTs reported here in Chapter 8 (fig. 8.3.6), frost heaving was associated with an unexplained upslope component of movement. This upslope frost heave effectively reduces the potential creep value arising from vertical resettlement during thaw, further complicating any attempt to quantify actual creep rates in relation to actual gelifluction rates. In the remaining discussion, therefore, total movement rates will be considered, that is, the combined effects of gelifluction and frost creep. Since in all experiments the measured surface movement rates exceeded (and in some cases greatly exceeded) the potential frost creep arising from vertical soil settlement, it can be concluded that in all cases gelifluction was significant and probably dominant (fig. 6.1.1).

It was anticipated that the thaw-induced surface movement rates should be directly related to slope angle. However, despite the twelve degree slope (12D/NS) showing the largest average amount of deformation, patterns were inconsistent with little difference revealed between Series 8D/NS and Series 4D/NS (fig. 6.1.1). This non-intuitive trend may have occurred through unexpected surface marker glide occurring as a result of thawing of ice that formed between the marker and the underlying soil, misrepresenting the actual amount of surface deformation within Series 4D/NS. Analysis of subsurface volumetric velocity clearly indicates that sediment transport by gelifluction was greater within Series 8D/NS than Series 4D/NS (fig. 5.5.34).

A consideration of the 4° slope models illustrates the role of changing soil granulometry. Figure 6.1.1 clearly illustrates the influence of silt content on the total measured surface movement rates, with addition of 10% and 20% silt leading to a 12% and 63% increase when compared to the natural soil. What is particularly striking, however, is that the increase in surface movement associated with the 20% silt enhanced model (4D/20S) occurred despite restricted frost heaving and therefore thaw settlement caused by a limited moisture supply during the freezing of this model. The role of thaw settlement in determining surface movement rates is discussed in detail below, but it is of note that the high surface movement values observed in the 4D/20S model were achieved despite an average heaving ratio of around 0.09, compared with values of 0.155 for the 4D/NS model and 0.162 for 4D/10S.

Table 6.1.2. Average ratio between total volumetric displacement (mm^3/mm) and surface displacement (mm) for the key area of the four degree slope models.

4D/NS	4D/10S	4D/20S	4D/10C	4D/20C
24.10	24.98	27.81	30.53	35.85

The addition of 10% and 20% clay to the natural soil did not increase rates of surface displacement – with Series 4D/10C showing a 28% reduction and 4D/20C a negligible change when compared to the natural soil (4D/NS). However, this relationship is misleading because both the clay enhanced models had a higher ratio of subsurface movement when compared to surface movement (see table 6.3.2)

which meant the actual volumetric soil transport occurring within the clay models was not completely represented by surface values.

6.2. Influences of Thaw Settlement on Downslope Movement

Laboratory and field studies have identified frost heave and thaw settlement as critical parameters determining the amount of periglacial solifluction (Harris, 1981; Matsuoka, 2001). Since the current investigation has restricted itself to an examination of soil movement relations during thaw consolidation, the discussion here will focus on the influence of thaw settlement on surface and volumetric velocities. Figure 5.3.7 has shown that in the experiments described here, frost heave and thaw settlement are intrinsically related. In this study, thaw consolidation generally exceeded frost heave as a result of post-thaw consolidation of the soil (see figs. 5.3.8 and 5.3.9).

6.2.1. Influence of Slope Gradient

Figure 6.2.1 illustrates the downslope variation in surface movement rates recorded in these experiments. It can be clearly seen that markers within the upper regions of the slope despite showing high amounts of thaw settlement in both 12D/NS and 4D/NS show little downslope movement when compared to markers lower down slope, where less thaw settlement was associated with higher surface displacements. However, it should be noted that Figure 6.2.1 presents an average per cycle amount of thaw settlement compared with the final surface marker position, perhaps masking the influence of a particular freeze/thaw phase in which differential heave might have been larger or smaller than the average.

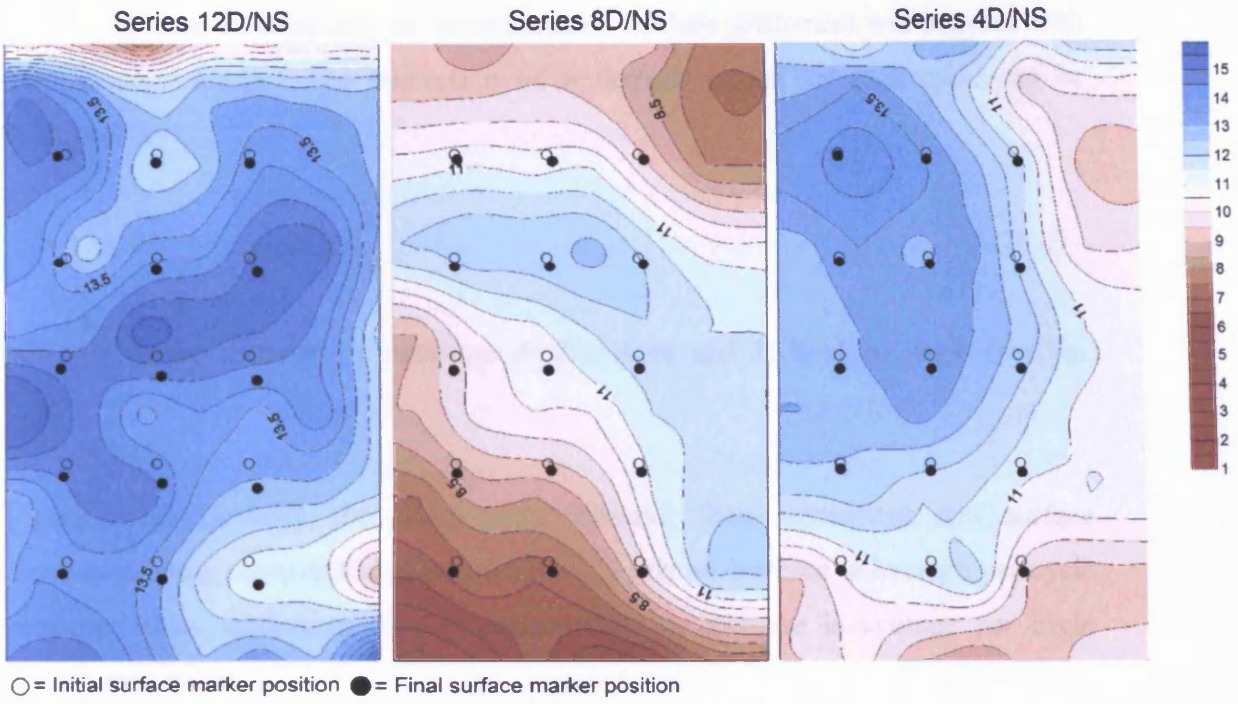

Figure 6.2.1. Spatial relationship between average per cycle thaw settlement (mm) and surface movement (mm) for the test series involving the natural soil. Note: all dimensions are model scale.

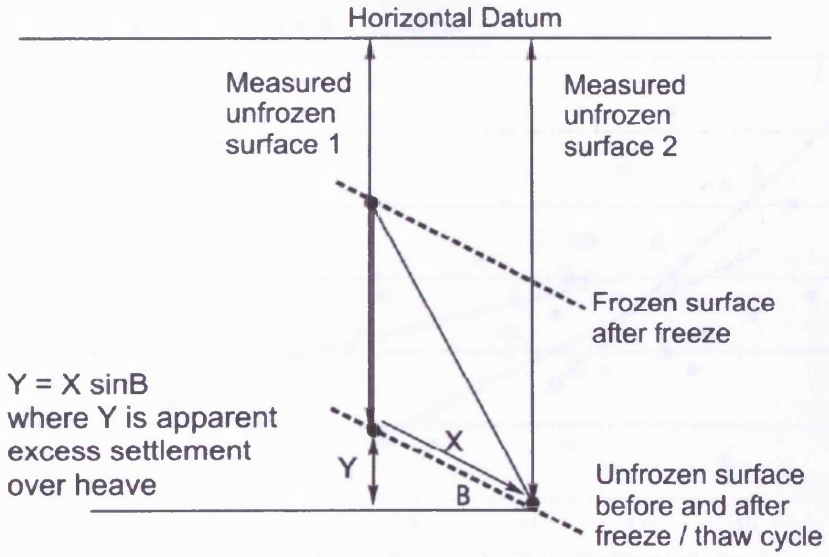

Figure 6.2.2. Thaw settlement correction technique. Note: that despite heave = settlement in this example, simple repeated measurement of markers leads to the conclusion that settlement > heave.

The measurement of the vertical heave of a marker against a reference datum leads to an over estimation of thaw settlement because the surface marker moves downslope. It is important to calibrate the dataset to remove this over estimation when attempting to accurately gauge the influence of thaw settlement upon surface

marker movement, especially as overestimation of thaw settlement will increase with greater slope angle. The correction of settlement values for each cycle can be calculated by:

$$y = x \sin B \qquad (6.1)$$

where x is the measured downslope displacement and B is slope angle (see fig. 6.2.2).

Figure 6.2.3 presents the relationship between thaw settlement and surface movement using uncorrected data values. Clearly an increase in average per cycle measured thaw settlement was associated with an increase in average per cycle surface movement.

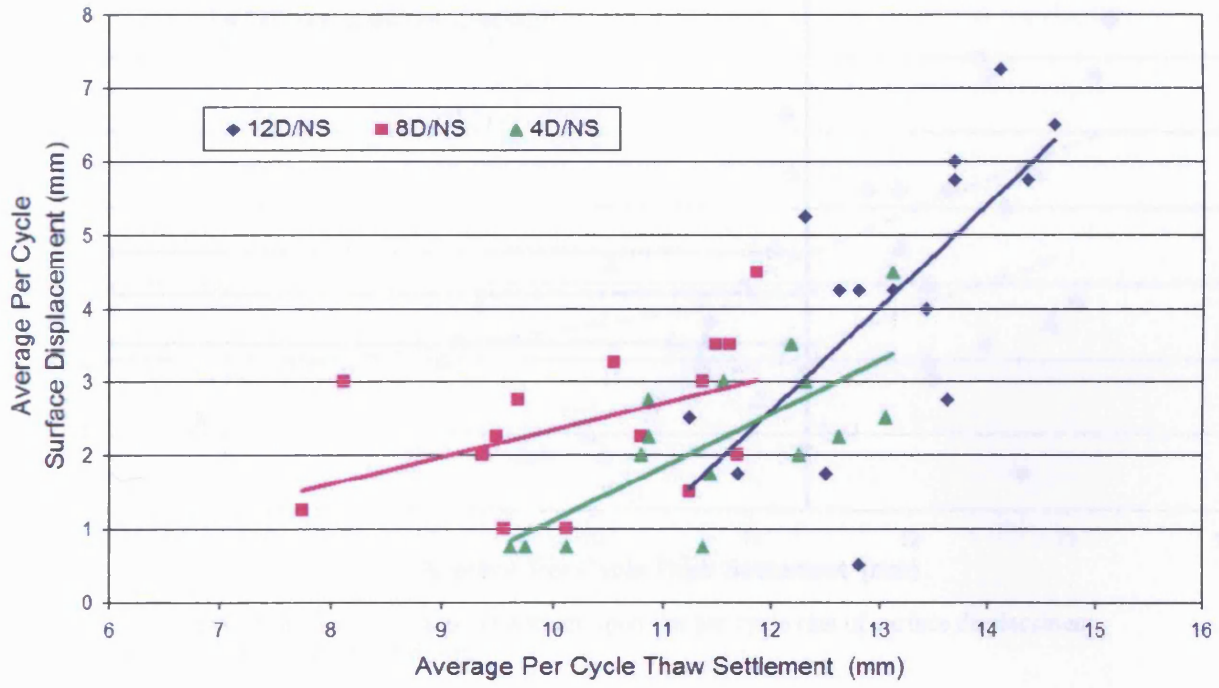

Figure 6.2.3. Non-calibrated influence of thaw settlement upon the per cycle rate of surface displacement within test series involving the natural soil.

Figure 6.2.4 presents calibrated average settlement values that account for downslope marker movement. Greater average per cycle surface movement is observed for a given frost heave value as slope angle increases. These were caused by a combination of increased downslope self-weight shear stress and a

progressively greater angle of inclination of ice lenses (formed parallel to the surface) within the steeper slope models. Ice lenses probably provided zones of micro-shearing causing greater material displacement on steeper slopes. The dilation of the soil by freezing processes left the thawed soil with a high void ratio, and pore pressures generated during consolidation decreased frictional grain-to-grain contacts within the pore matrix and therefore increased the efficacy of gravitational shear stresses acting upon the soil unit. In Figure 6.2.4 the average overall per cycle settlement of 11.2 mm is shown, with equivalent best estimates of average per cycle surface displacement rates based on the linear regression analysis. Predicted model scale rates are 2.2 mm/cycle (4° gradient), 2.9 mm/cycle (8° gradient) and 3.5 mm/cycle (12° gradient).

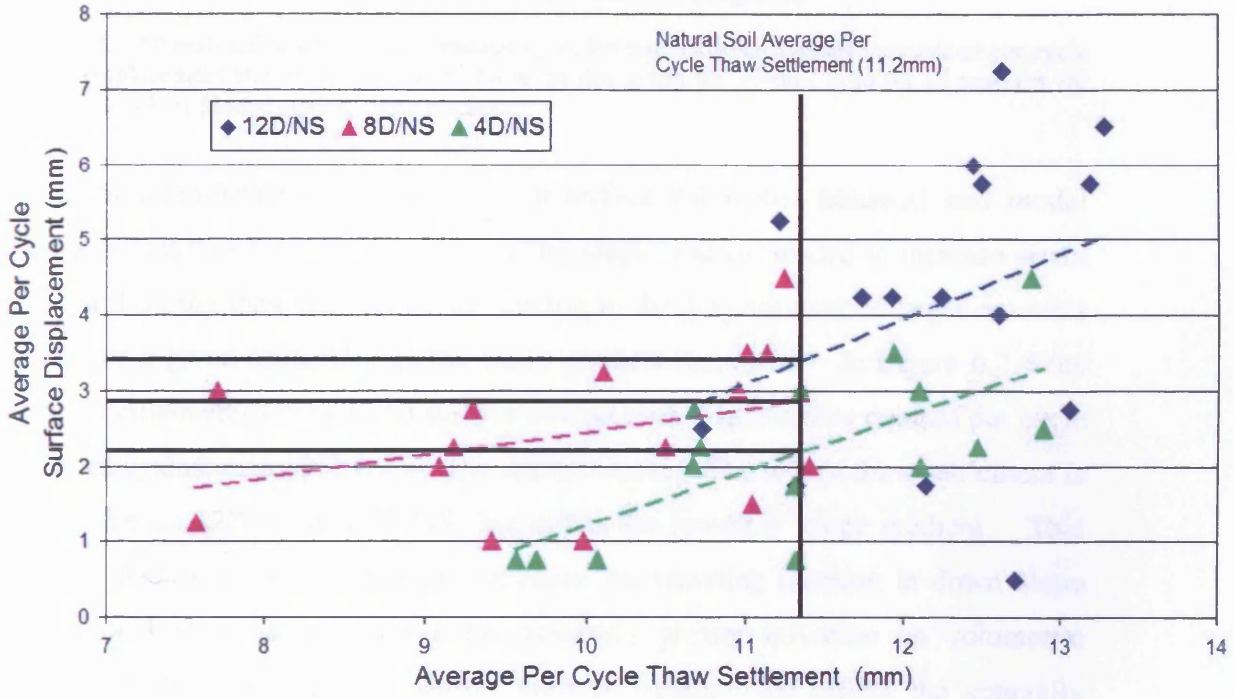

Figure 6.2.4. Calibrated influence of thaw settlement upon the per cycle rate of surface displacement within test series involving the natural soil.

Figure 6.2.5 shows clearly that the ratio between surface displacement to thaw settlement increases with slope angle, reinforcing the conclusion that keeping other variables approximately constant, the rate of surface movement is a function of downslope gravitational shear stress.

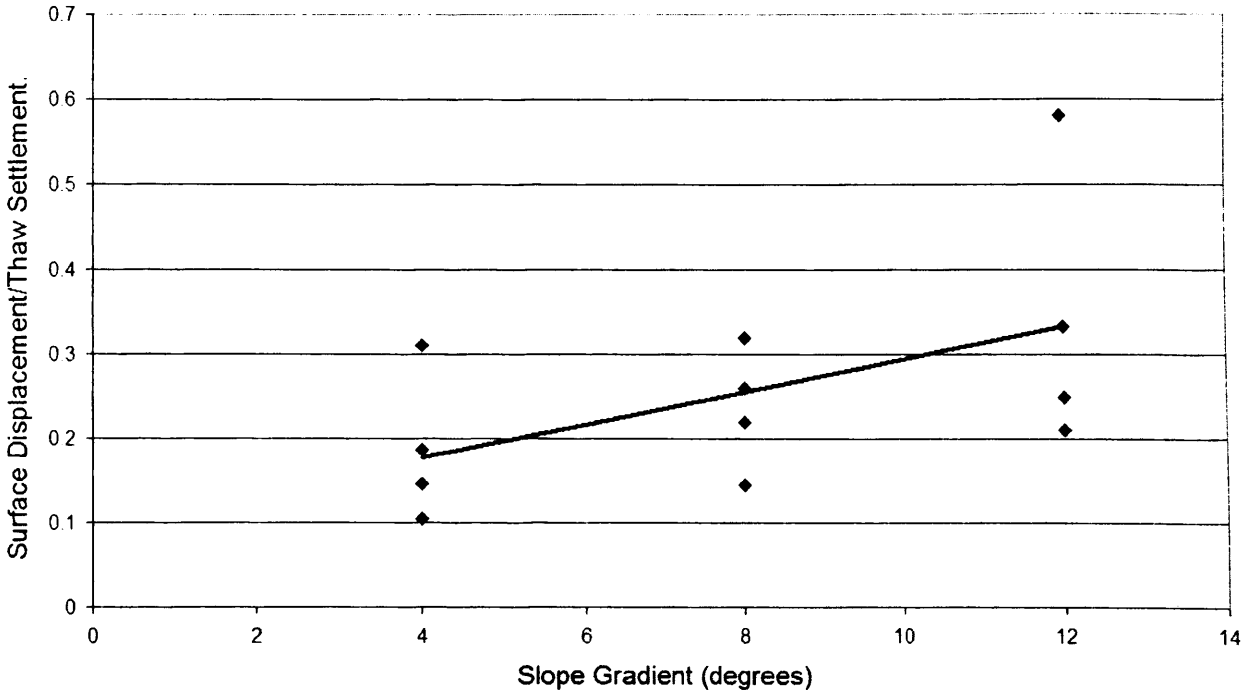

Figure 6.2.5. Overall influence of slope gradient upon the ratio between average amounts of per cycle surface displacement and thaw settlement. Note: in this graph the average ratio for all markers for each thaw cycle is plotted against slope gradient.

A similar relationship exists between subsurface volumetric transport and model slope gradient (see fig. 6.2.6). Increasing slope gradient tended to increase strain in the soil during thaw consolidation, leading to the displacement of larger amounts of soil for a given settlement as the slope gradient increased. In Figure 6.2.6 the average settlement of the ground surface around each displacement column per cycle is plotted against measured volumetric soil transport. The role of thaw settlement is clear in Series 12D/NS and 8D/NS, but not in the lowest 4° slope gradient. This suggests that as the slope gradient increases the resulting increase in down slope gravitational shear stresses has a progressively greater influence on volumetric transport rates. The scatter of points seen in Figure 6.2.6 reflect the generally observed trend for observed shear strain after four thaw cycles to increase downslope.

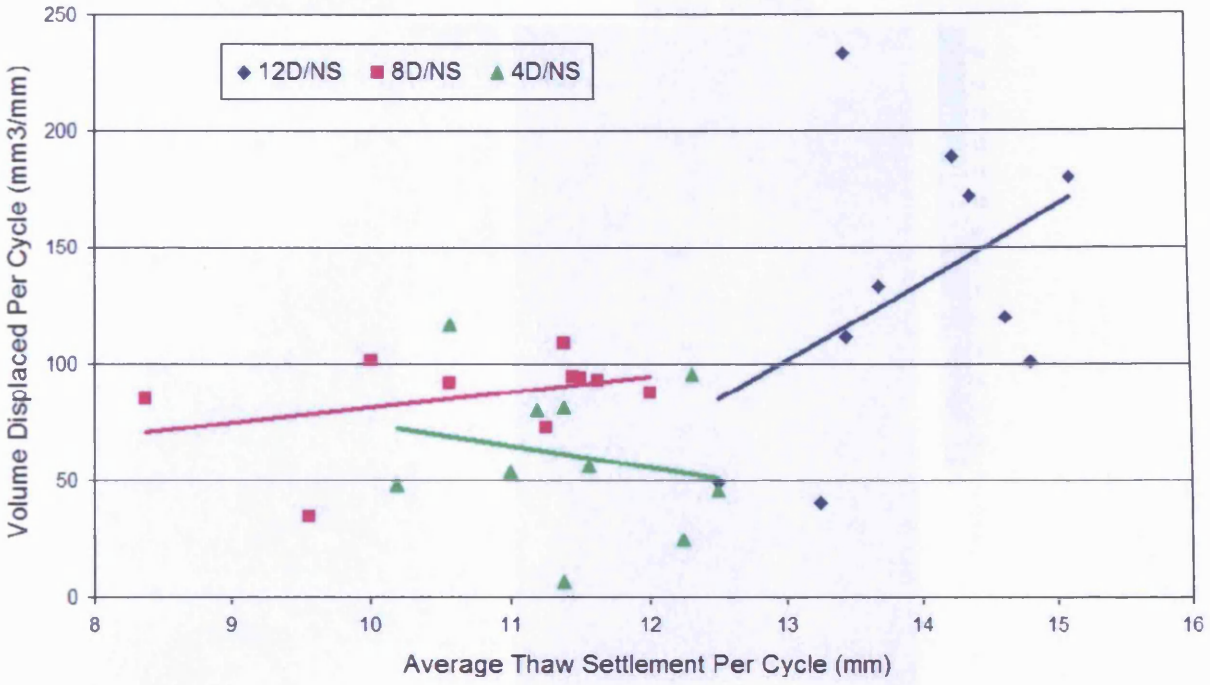

Figure 6.2.6. Calibrated influence of thaw settlement upon the per cycle rate of subsurface displacement within test series involving the natural soil.

6.2.2. Influence of Silt and Clay Content

There appears to be a spatial relationship between the pattern of average thaw settlement and surface marker movement within the modified silt models (see fig. 6.2.7). It can be clearly observed within the lower slope zone of 4D/10S that a zone of greater thaw settlement has encouraged downslope marker movement. The importance of these zones of greater settlement is again emphasised in Series 4D/20S where despite the overall lack of settlement due to the ice-poor nature of the model – surface movement can be observed to mirror settlement contours. For example, the upper central zone of high settlement has encouraged markers to traverse across the slope away from that central zone.

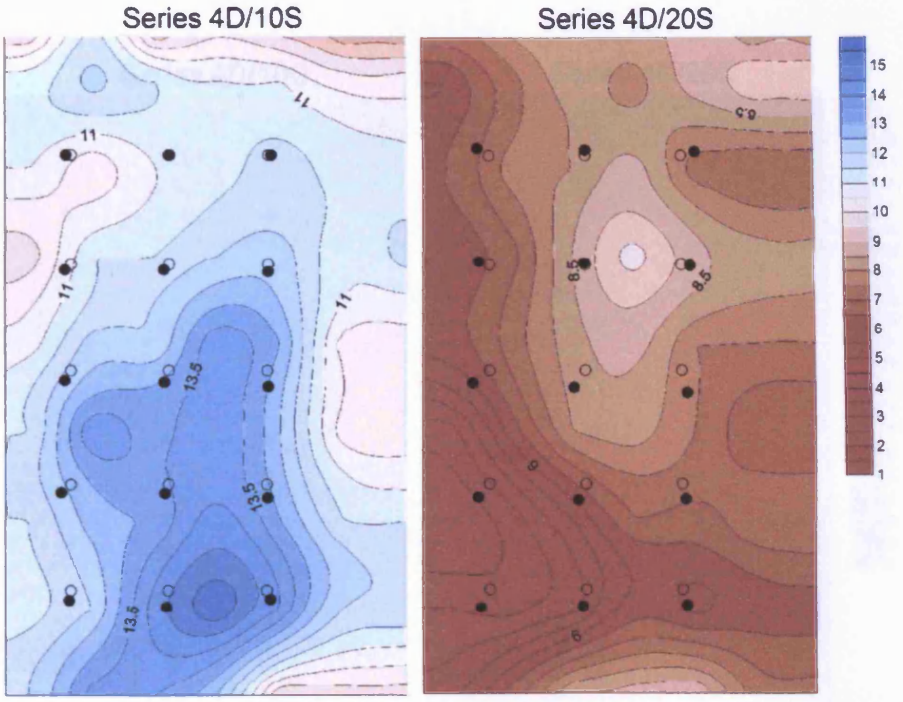

Figure 6.2.7. Spatial relationship between average per cycle thaw settlement (mm) and surface movement for the test series involving the increasing silt content. Note: all dimensions are model scale.

Figure 6.2.8 illustrates that a spatial linkage did not exist between zones of settlement and surface marker movement within the modified clay soils. It has been mentioned in section 5.5 that overall surface displacement increased between Series 4D/10C and 4D/20C and that movement rates were accelerated with greater distance downslope, however, it would appear that the cohesive nature of the clay soils has minimised the ability of separate slope zones to react independently to areas of greater soil settlement during consolidation. The uniform pattern within the modified clay soils may also represent the slow speed of thaw consolidation and the large amount of thaw consolidation that occurred within all regions of the modified clay slope models (e.g. see section 5.3.2). However, a pattern can be observed within the upslope zone of Series 4D/20C whereby a zone of exaggerated thaw settlement occurred in response to a region of concentrated frost heave explained within section 5.3.1. It is possible that the movement of the uppermost markers within the twenty percent clay model partly occurred in response to freezing plate pressure during successive freezing cycle, causing upslope movement of surface markers (see section 5.7 for explanation).

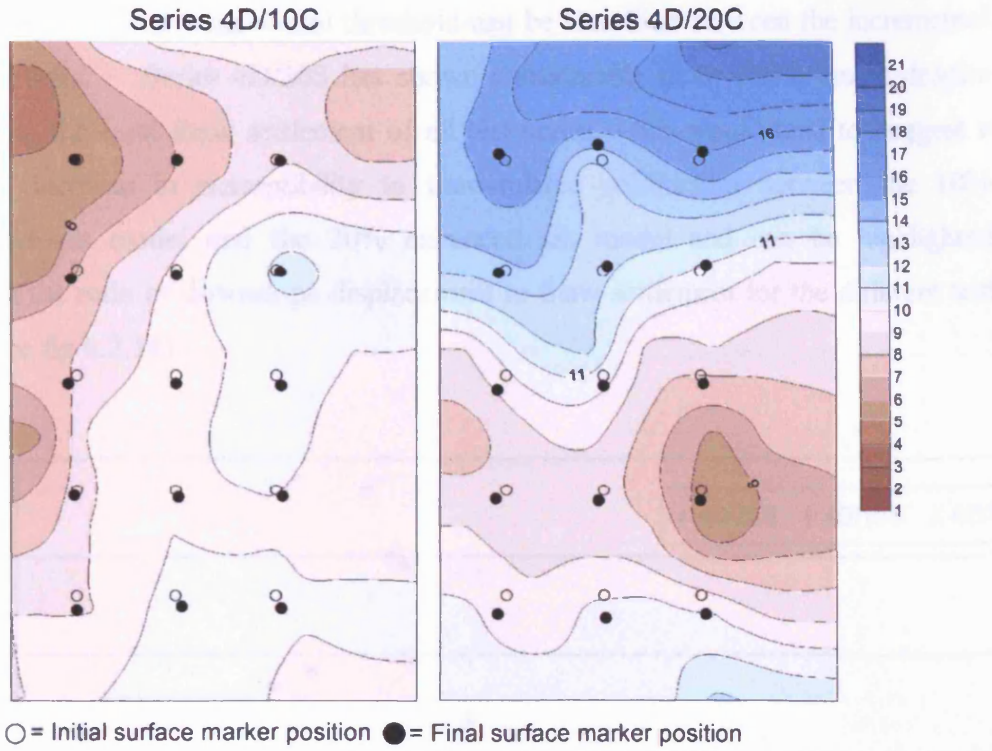

Figure 6.2.8. Spatial relationship between average per cycle thaw settlement (mm) and surface movement for the test series involving the incremental addition of clay. Note: all dimensions are model scale.

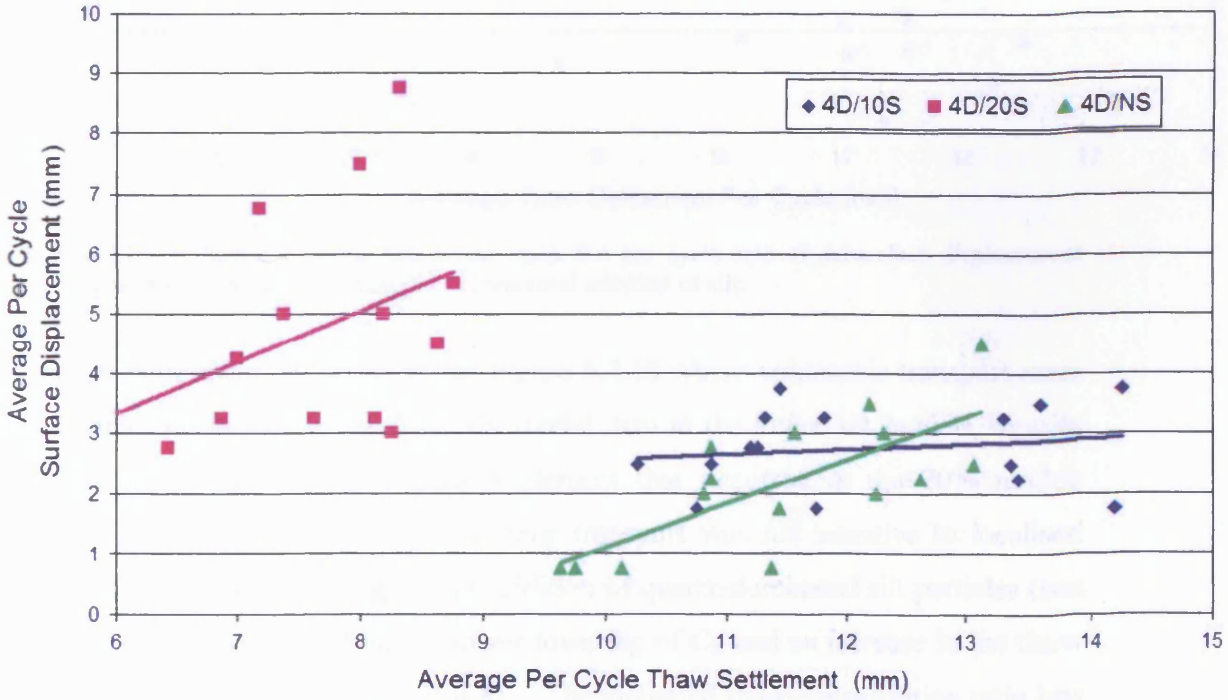

Figure 6.2.9. Influence of thaw settlement upon the per cycle rate of surface displacement occurring within test series involving the incremental addition of silt.

Figure 6.2.9 illustrates the overall relationship between thaw settlement and surface movement – a clear behavioural threshold can be identified between the incremental silt test soils. Series 4D/20S has shown considerably more displacement despite recording the least thaw settlement of all test series – this would tend to suggest a marked increase in susceptibility to thaw-related solifluction between the 10% enhanced silt model and the 20% enhanced silt model and can be highlighted through the ratio of downslope displacement to thaw settlement for the different test soils (see fig 6.2.14).

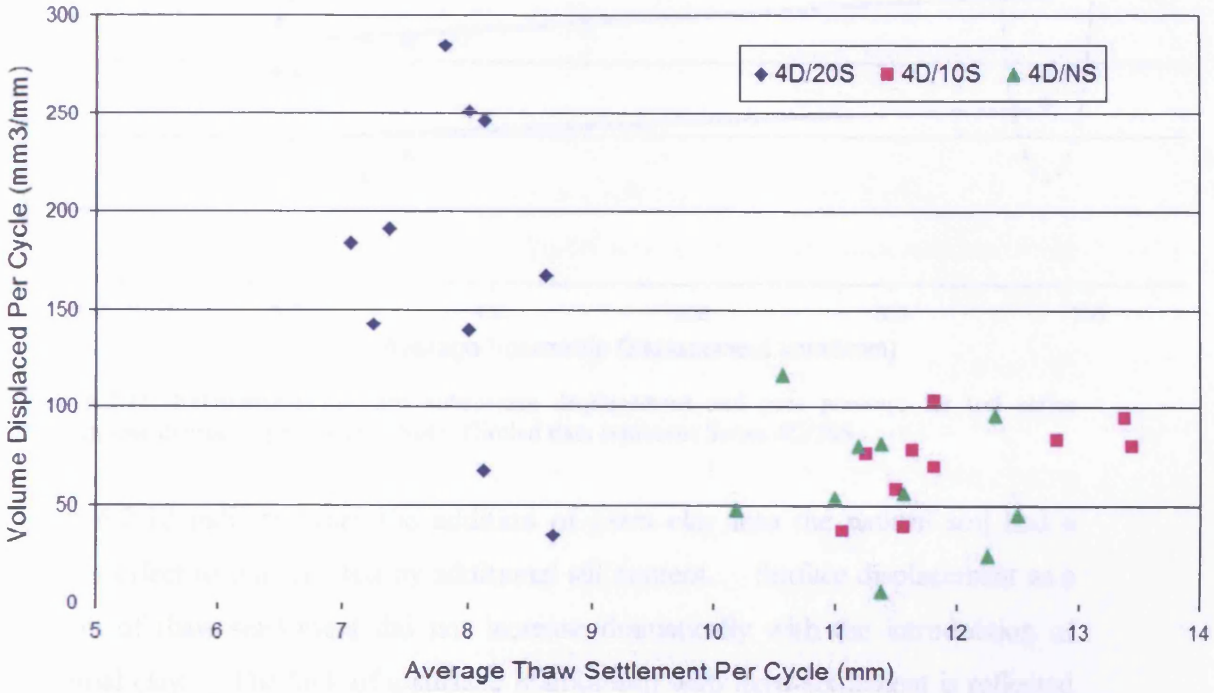

Figure 6.2.10. Influence of thaw settlement upon the per cycle rate of subsurface displacement occurring within test series involving the incremental addition of silt.

A similar pattern can be noted within Figure 6.2.10 where volumetric transport rates are significantly higher in the 20% silt model than in the lower silt models, despite the low heave and therefore thaw settlement that occurred in the 20% model. However, it is clear that localised volume transport was not sensitive to localised average thaw settlement values. The addition of quartz-dominated silt particles (see section 4.6) was associated with a lower lowering of C_V and an increase in the thaw consolidation ratio (R) (see table 5.4.8). The increased thaw consolidation ratio has lead Series 4D/20S to experience the highest positive porewater pressures of all test

series and therefore a longer duration of reduced frictional strength with a resultant increase in average volumetric displacement (see fig. 6.2.11).

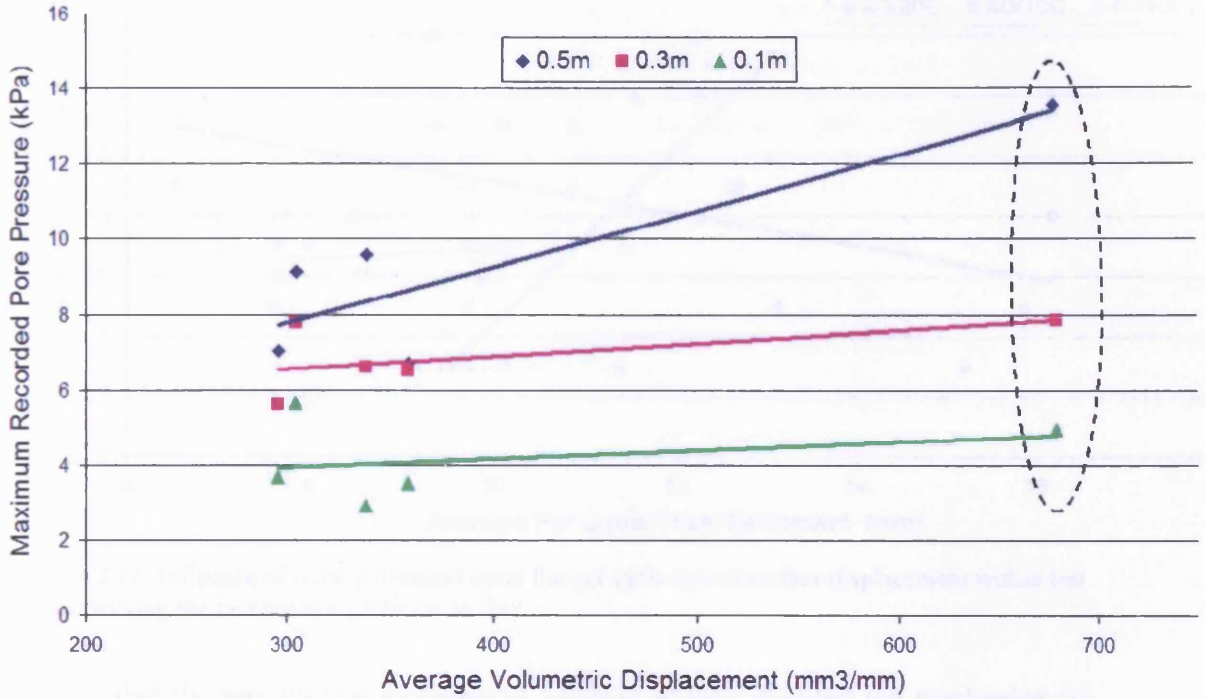

Figure 6.2.11. Relationship between subsurface displacement and pore pressure for test series involving four degree slope models. Note: Circled data represent Series 4D/20S.

Figure 6.2.12 indicates that the addition of extra clay into the natural soil had a different effect to that created by additional silt content. Surface displacement as a function of thaw settlement did not increase dramatically with the introduction of additional clay. The lack of a surface relationship with thaw settlement is reflected in Table 6.1.2 that shows that a higher proportion of material was displaced via subsurface movement for each additional increment of clay between Series 4D/NS and 4D/20C, despite an apparently insignificant 2% increase in surface displacement rates. The clay mineral added to these soils was kaolinite, which is a moderately inactive clay that does not absorb as much water into its structure as other clay minerals such as illite and montmorillonite, and probably had a lower impact on resulting geotechnical properties than these more active clay minerals might have had. Thus, it would be interesting to extend the current modelling procedure to test the influence of more active clay minerals on the susceptibility of soil to periglacial solifluction processes (see section 9.2 for further details).

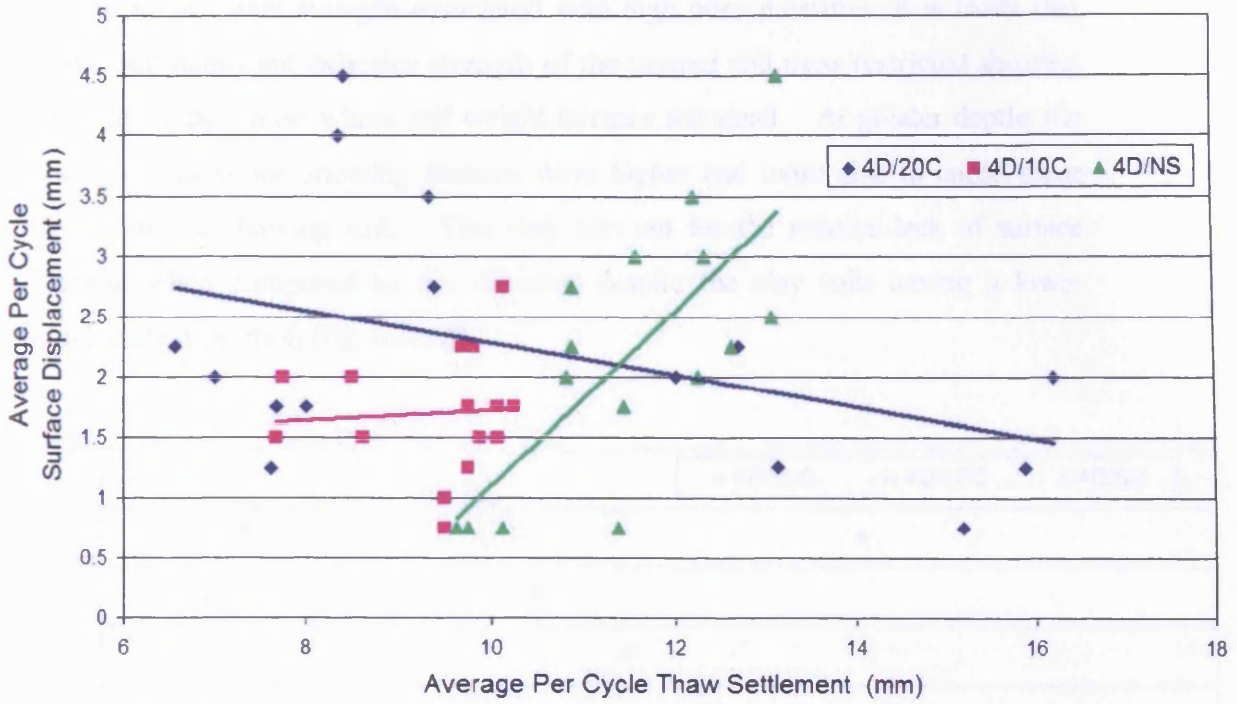

Figure 6.2.12. Influence of thaw settlement upon the per cycle rate of surface displacement within test series involving the incremental addition of clay.

It is felt that the progressive incremental addition of clay changed the mechanism of gelifluction through influencing the hydraulic properties of the soil during freezing. Increased clay content would have been associated with larger cryosuction during freezing. Leading to greater ice lens nucleation during freezing. However, once ice lens inception had occurred and ice crystals began to nucleate within the pore space at the freezing front then the low permeability of the soil would have limited the rate of water flux towards the ice lens. This probably encouraged the formation of a higher concentration of small ice lenses within the frozen soil than was the case in the silt enhanced soils of 4D/10S and 4D/20S.

The presence of a high number of these small ice bodies may account for the spatially more consistent amounts of frost heave recorded within the clay soils when compared to the natural soil (see section 5.3). However, it may also account for the different style of downslope displacement and porewater pressure recognised within the clay test soils. The maximum pore pressures observed in the highest clay content slope model were limited by initiation of water escape events through the very soft cohesive soil during thaw consolidation. It appears, therefore, that the clay models underwent a high number of intermittent positive pressure events. Despite

reduction in frictional strength associated with high pore pressures, it is likely that the low, but significant cohesive strength of the thawed soil mass restricted shearing in the near-surface zone where self weight stresses are small. At greater depths the self-weight downslope shearing stresses were higher and more able to cause shear strain within the thawing soil. This may account for the relative lack of surface movement when compared to the silt soils despite the clay soils having a lower internal angle of friction (fig. 6.2.12).

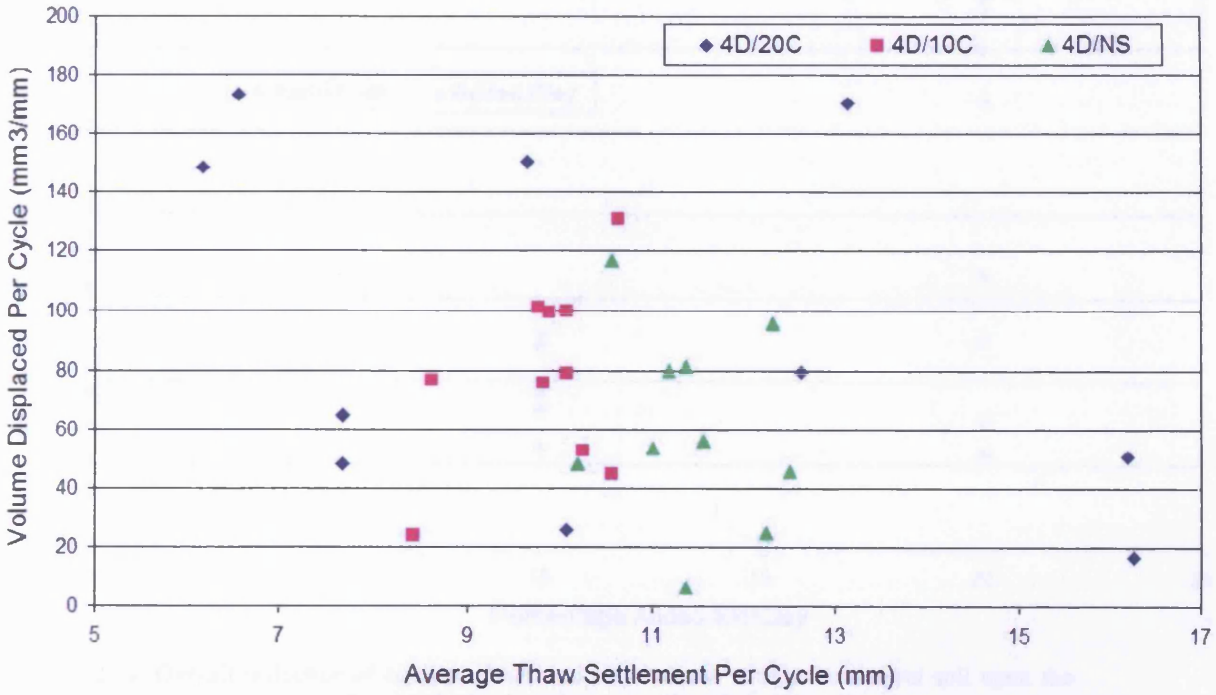

Figure 6.2.13. Influence of thaw settlement upon the per cycle rate of subsurface displacement within test series involving the incremental addition of clay.

It is felt that the silt soils generated large ice lenses during freezing as a result of their higher permeability, and hence created the localised spatial correlation between patterns of settlement and surface movement (fig. 6.2.7). In the clay soils it appears that the cohesive strength prevented localised excessive shearing, but rather transmitted a general shearing rate through much of the slope (fig. 6.2.13). As discussed above, this cohesive property may have limited near-surface shear, but it is also possible that the greater shear strain observed at depth in the clay soil was in part the response to a higher ice content at depth.

The combination of particle cohesion, smaller ice lenses, and the presence of water escape events limited the efficacy of gelifluction and created a stable set of behaviour within the modified clay soils. In comparison, the more frost susceptible modified silt soil appeared to show a behavioural threshold between the ten and twenty percent increment as a result of decreasing shear strength and decreased permeability (fig. 6.2.14).

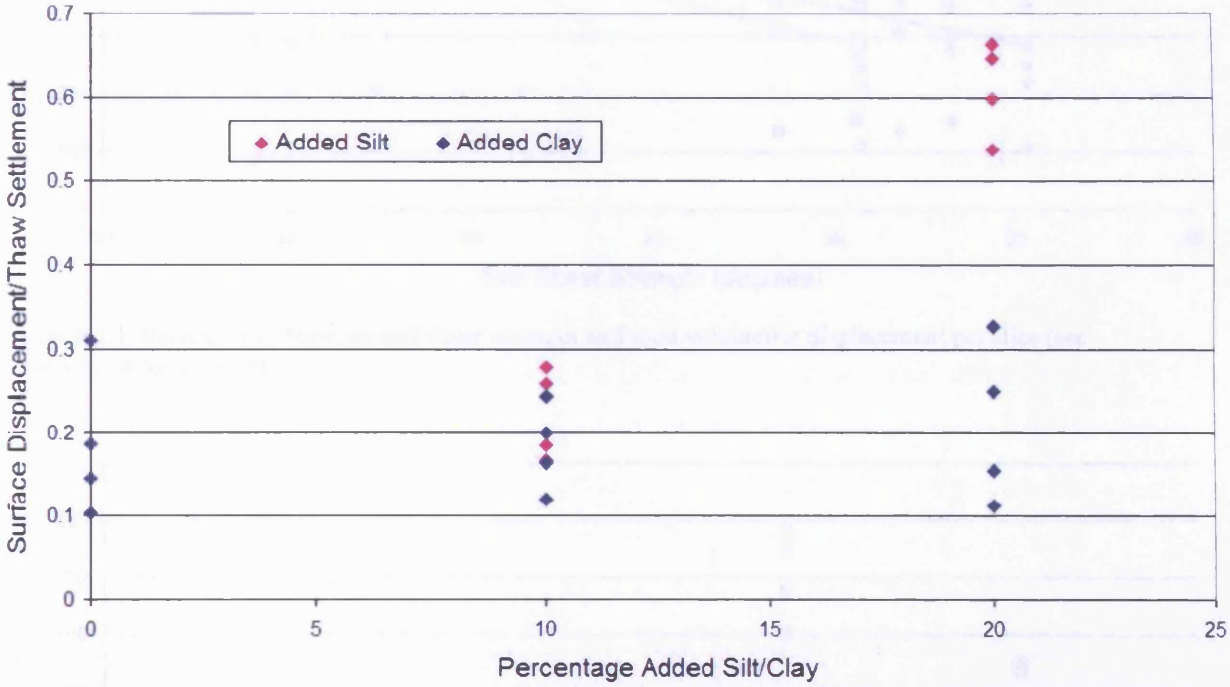

Figure 6.2.14. Overall influence of additional silt and clay content within the natural soil upon the ratio between average amounts of per cycle thaw settlement and surface displacement.

6.2.3. Overall Summary of Influence of Test Soil Geotechnical Properties

The impact of the addition of silt and clay to the soil used in constructing slope models on resulting solifluction can be clarified by comparing the change in geotechnical properties with the observed changes in volumetric transfer.

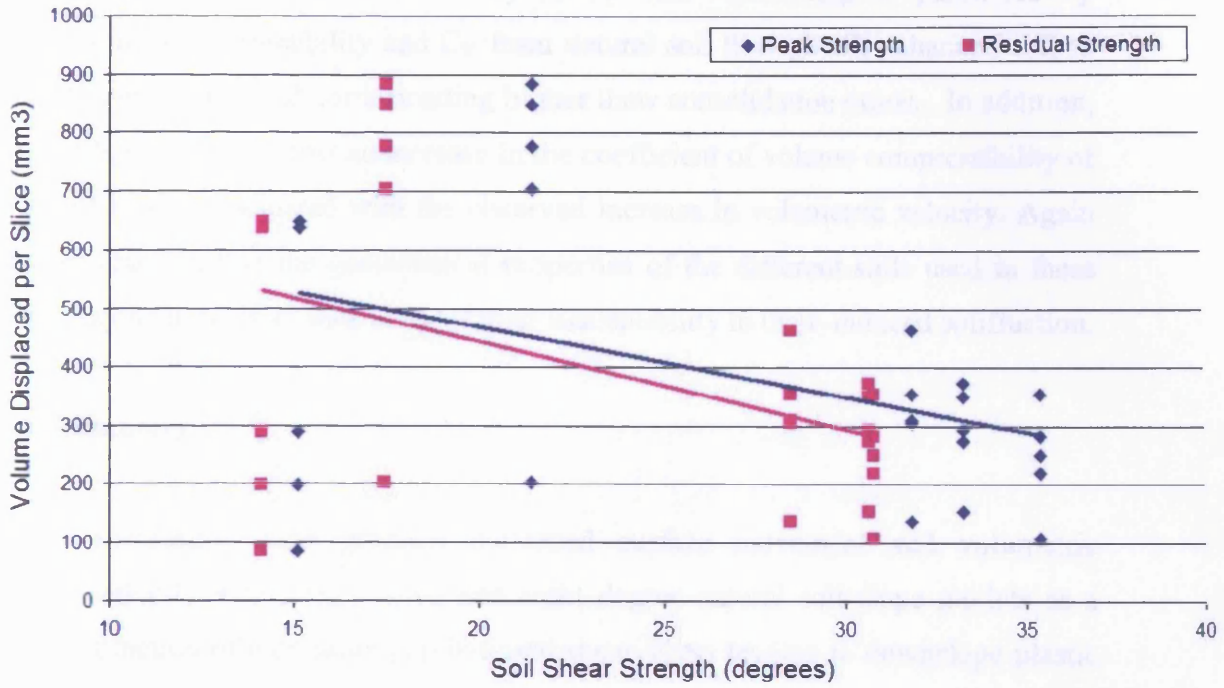

Figure 6.3.1. Relationship between soil shear strength and total volumetric displacement per slice (see section 5.5.4 for context).

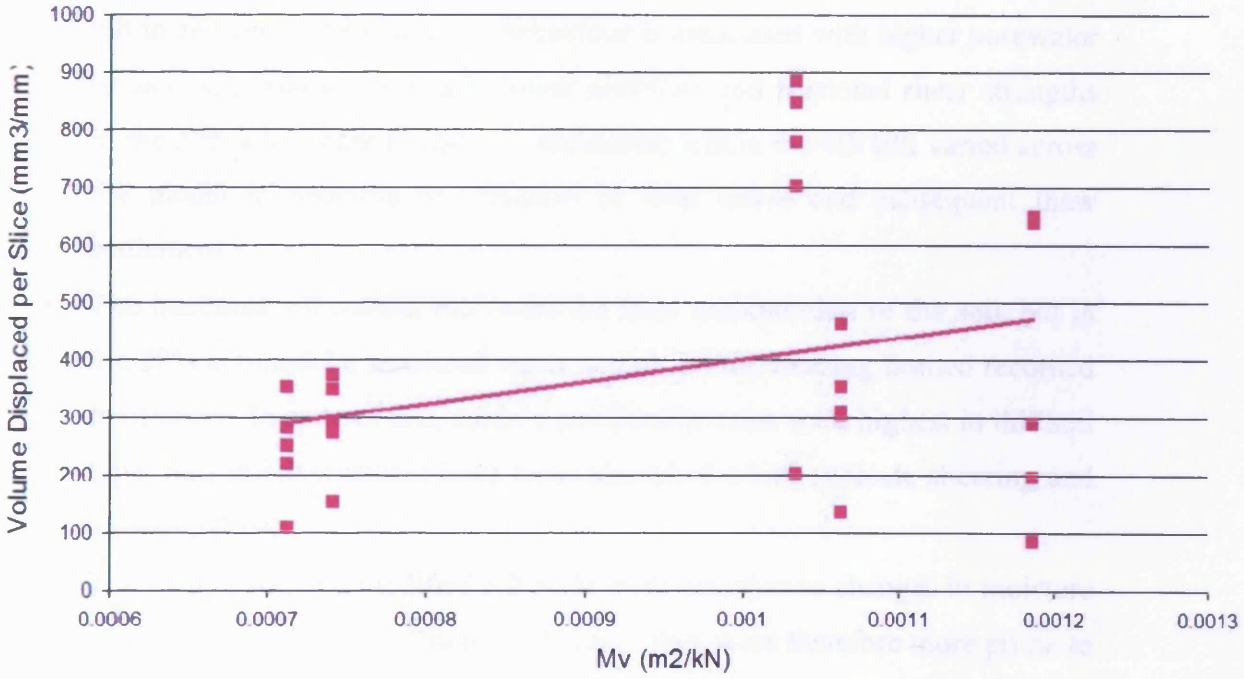

Figure 6.3.2. Relationship between M_V and total volumetric displacement per slice (see section 5.5.4 for context).

Figure 6.3.1 illustrates that volumetric transport reduces with increasing residual and peak frictional strength. The change in frictional strength correlates with soil granulometry, with the highest values corresponding to the natural soil and the

lowest with the 20% additional clay soil. This relationship is paralleled by decreasing soil permeability and C_V from natural soil through silt enhanced soil to clay enhanced soil, and corresponding higher thaw consolidation ratios. In addition, Figure 6.3.2 indicates that an increase in the coefficient of volume compressibility of the soil is also associated with the observed increase in volumetric velocity. Again this emphasises that the geotechnical properties of the different soils used in these tests may be used as an indication of their susceptibility to thaw-induced solifluction.

6.3. Summary

- Increasing slope gradient increased surface movement and volumetric velocity within the twelve and eight degree natural soil slope models as a function of increasing gravitational shear stress leading to downslope plastic deformation coupled with microshearing across thawing ice lenses.
- Increasing silt content increased both surface movement and volumetric movement. A behavioural threshold was noted between the 10% and 20% silt increments – the change in behaviour is associated with higher porewater pressures, a cohesive strength, lower plasticity and frictional shear strengths in the 20% silt enhanced soil. Gelifluction within the 4D/10S varied across the model in response to variation in frost heave and subsequent thaw settlement.
- The increased silt content increased the frost susceptibility of the soil, but in the 20% silt model a restricted water supply during freezing limited recorded frost heave. In spite of this, surface gelifluction rates were highest in this soil type. Soil microstructures have been identified which indicate shearing and localised flow.
- The natural soil and modified silt soils were sensitive to changes in moisture content due to their low Plasticity Index – they were therefore more prone to plastic deformation when localised meltwater release events intermittently raised moisture contents near to the Liquid Limit.
- The addition of clay to the natural soil generated a different inferred mechanism of downslope movement. The cohesive nature of the clay generated more uniform patterns of deformation throughout the slope profile.

- In the modified clay soils, a slightly cohesive behaviour gave low but significant shear strengths despite high pore pressures during thaw. This reduced shear strain to low values in the near-surface zone of low self-weight stresses.
- The clay soils also showed periodic water escape events, which probably limited the maximum pore pressures achieved. This may have had a direct bearing on observed solifluction rates.
- The addition of Kaolinite clay caused a change in style of soil displacement, with a more uniform shear strain concentrated lower in the profile, in contrast to the silt enhanced soils where shear strain increased towards the surface.
- The greatest influence on gelifluction would appear to have been silt content followed by slope gradient. The susceptibility to gelifluction was not linearly related to silt content, but increased markedly between the 10% silt increment and the 20% silt increment.

CHAPTER SEVEN : Centrifuge Modelling – Landsliding Processes

Although this thesis is concerned mainly with modelling solifluction processes, the experimental design, whereby models with different slope gradients were tested resulted in tests in which the threshold from slow thaw-related solifluction to rapid slope failures was crossed. This chapter describes data gathered from such slope models. Slope failure processes on thawing slopes are first reviewed, with particular reference to the thresholds and mechanisms of slope failure. The chapter presents movement and thermal data gathered from the slope model thaw phases of the four series that underwent rapid transitional failures. Pore water pressure data is synthesised in order to undertake back analyses of slope stability conditions during the transition from slow creep to rapid mass wasting. Finally, mechanisms of failure revealed during excavation of buried movement columns and analysis of microstructures within the failed soils are discussed.

7.1. Slope Stability

On slopes, shear stresses are developed within the soil mass due to gravitational acceleration. The response of a soil to shearing stress is determined by its shearing resistance or strength – this strength can be defined as it ability to resist deformation (see section 4.5). Slope failure will occur unless shearing resistance on every plane within the soil mass is greater than the shearing force (Bromhead, 1992). Failure in cohesive soils normally will occur in the form of movement of a large mass of soil along a more or less definite surface, with slope failure being principally associated with shearing strain (Brunsden & Prior, 1985) (see fig. 7.1.1). However, water saturated non plastic soils may fail by flow so that the profile of mass movement displays shear strain through much of the thickness of the slide. Slope stability assessments commonly apply a limit equilibrium approach to defining the stability of a slope – this approach adopts the concept of factor of safety (F_S) against failure by balancing shear stress against shear strength (Selby, 1993, p.276).

Slope materials are affected by gravitational stresses that can be represented as downslope shear (τ) and perpendicular normal (σ) components of stress, where an increase in slope gradient will cause an increase in τ and consequent decrease in σ

(Brunsden & Prior, 1985). The downslope or shearing stress (τ) gives rise to forces tending to cause downslope displacement, whereas the normal stress (σ) determines the frictional resistance through gravitational pressure on the base of the potential slide surface. Therefore τ can be considered a disturbing stress while σ multiplied by the coefficient of friction on a potential plane of failure generates the resisting stress (or strength of the soil) opposing the tendency for slope material to slide. Therefore, the normal stress determines the frictional resistance to sliding (r):

$$r = \sigma \tan \emptyset \qquad (7.1)$$

where σ depends on the weight of the landslide material being supported by intergranular contacts within the soil matrix.

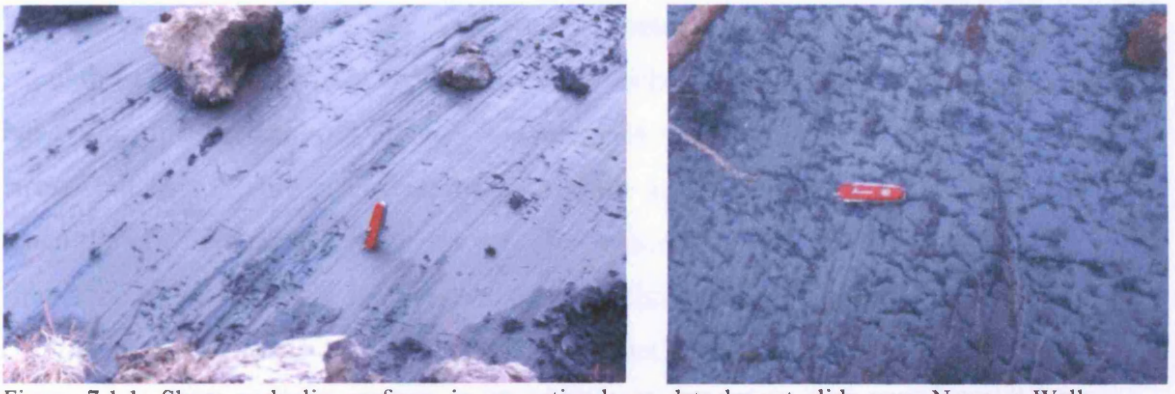

Figure 7.1.1. Shear and slip surfaces in an active-layer detachment slide near Norman Wells, Mackenzie Valley, Canada (1995). (Photographs: Charles Harris).

Slope instability frequently occurs when porewater pressure takes a proportion of the overburden stress from the intergranular contacts, thereby reducing the stress within the soil on a potential failure plane, and hence reducing frictional strength, i.e. pore fluid helps support the normal stress thus reducing the pressure between the mineral grains. The intergranular friction within a soil provides the resisting force preventing the generation of a slide – the intergranular pressure is termed the *effective stress*, and is given by:

$$\sigma' = (\sigma - u) \qquad (7.2)$$

where σ' is the effective normal stress on the potential slip surface, σ is the total normal stress on the potential slip surface and u is the pore water pressure on the

potential slip surface. Slope failure is therefore normally triggered by high pore pressures reducing intergranular friction and a consequent reduction in the strength of the soil (see fig. 7.1.1).

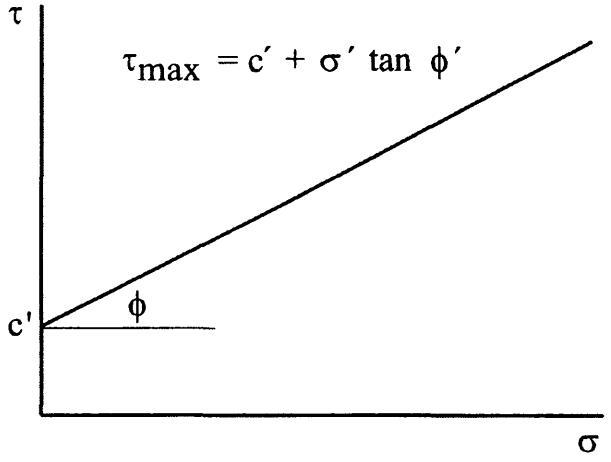

Figure 7.1.2. Mohr-Coulomb failure envelope.

Laboratory testing of soils has, however, suggested a second element of soil shear strength in clay soils known as *cohesion (c).* When representing the stress-strength behaviour of a typical soil, frictional strength is a function of the effective normal stress, but in cohesive soils there may remain an element of shear strength even when the effective normal stress on the slip surface is zero (fig. 7.1.2). Figure 7.1.2 shows the Mohr-Coulomb failure envelope, in which the slope is equal to the friction coefficient tan Ø' (measured with respect to effective stress) and the intercept on the vertical axis is the cohesion (c'), also measured with respect to effective stress. The equation for the Mohr-Coulomb envelope is give by:

$$\tau = c' + \sigma' \tan \emptyset' \qquad (7.3)$$

For a given shear stress (proportional to the sine of slope angle) a slope may be stable, (that is shear strength > shear stress), but if pore pressures are progressively increased, effective normal stress decreases, as does the frictional strength that can be mobilised, and failure may therefore ensue. The threshold for failure occurs where the Factor of Safety (F_S) is unity, where:

$$Fs = \left(\frac{c' + \sigma' \tan \phi'}{\tau} \right) \qquad (7.4)$$

7.2. Landslide Processes in Periglacial Environments

Slope failures are spatially and temporally discontinuous and periodic, in contrast to the slow mass wasting processes described in chapters 5 and 6. Slope failures normally involve relatively rapid or catastrophic downslope movements of material through various processes such as debris flows, rockfalls, avalanches, mudflows, landslides, etc (Varnes, 1978). Slope failures in permafrost regions normally involve shallow displacements of unfrozen active layer material across the underlying permafrost table (e.g. Lewkowicz, 1990). Classifications distinguish between flow and slide dominated failure mechanisms (Jahn, 1975; Ballantyne & Harris, 1994). McRoberts and Morgernstern (1974) termed flow based failures skinflows to reflect the shallow nature of the process. Skinflows occur where soil moisture exceeds the liquid limit during thaw consolidation leading to soil flowage; they therefore commonly occur in cohesionless silty soils that are highly frost susceptible and have low liquid limits (Harris & Lewkowicz, 2000) (see fig. 7.2.1).

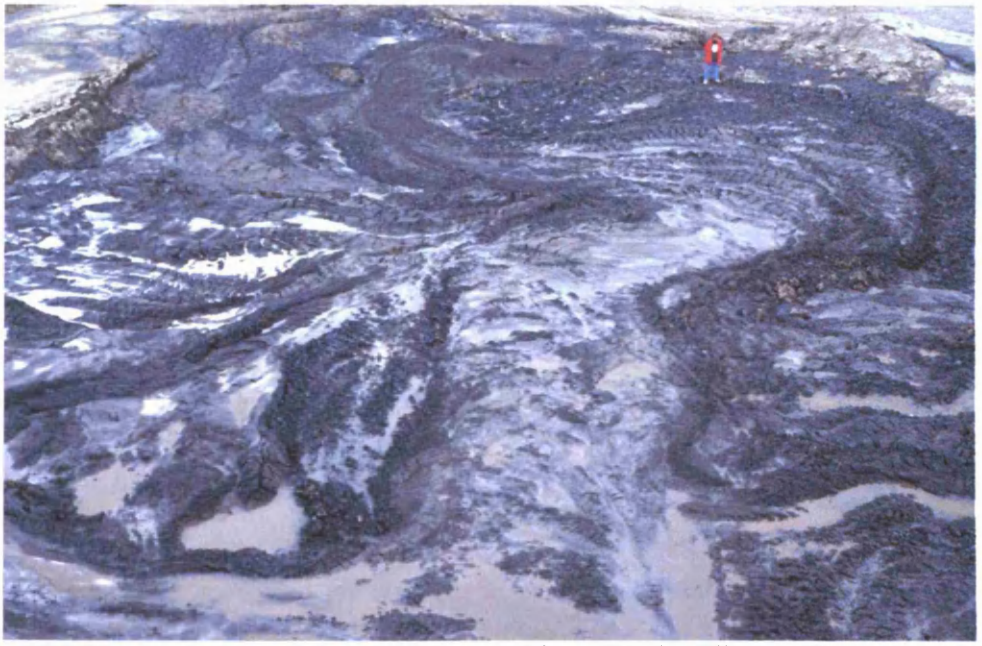

Figure 7.2.1. Mudflow associated with melting ground ice at Eureka, Ellesmere Island, Canadian Arctic (1990). (Photograph: Charles Harris).

Slide dominated failures have been termed active-layer detachment slides (French, 1996; AGCR, 1988). Earth slides are triggered by either an increase of shear stress due to factors such as the steepening of a slope by river undercutting; or by a

decrease in soil strength due to high pore water pressures, weathering or slow creep. In periglacial regions, slides are usually promoted by the thawing of ice-rich frozen soils within the active layer, or top of the permafrost, e.g. skin flows or active-layer detachment slides (Harris and Lewkowicz, 1993). Such periglacial failures often occur in response to extreme events related to high temperature (e.g. fire), rainfall, and permafrost degradation due to ground cover disturbance (e.g. removal of vegetation) (Viereck, 1982; Brown, 1963; Polemio & Petrucci, 2000). The trigger mechanisms cause rapid thawing of ice-rich sediment within the soil profile, near the base of the active layer, or in the topmost part of the permafrost (Mackay, 1983; Woo & Steer, 1983). For this reason some field studies have demonstrated that on steeper slopes, extreme events may trigger rapid slope failures within previously soliflucting active layers (Harris and Lewkowicz, 1993).

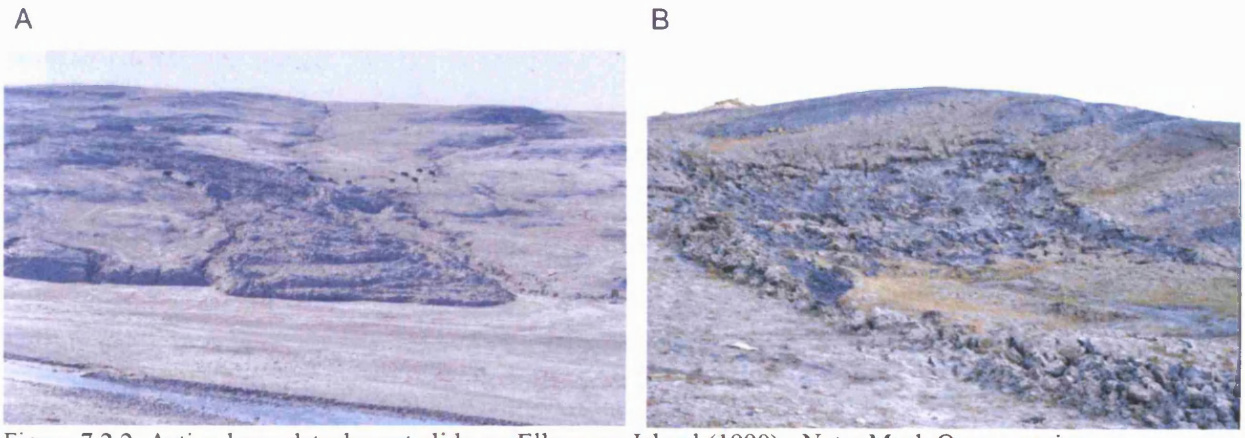

Figure 7.2.2. Active-layer detachment slide on Ellesmere Island (1990). Note: Musk Oxen crossing surface of landslide (A) and intact vegetation mat on upper surface of detached landslide mass (B). (Photographs: Charles Harris).

Active-layer detachment failures occur through a soil unit sliding over a distinct basal slip surface and may suffer little internal disturbance during movement (see fig. 7.1.1). Figure 7.2.2 (B) presents an example of a detachment failure where the unfrozen soil mass has slid across the underlying permafrost table and maintained cohesive unity, as indicated by the presence of relatively undisturbed vegetation cover. These detachment slides commonly occur in clay-rich (i.e. cohesive) soils or within desiccated and hardened soils such as those resulting from two sided freezing (see section 2.2.5) (Lewkowicz & Clark, 1988). Active-layer detachment failures therefore occur with a range of morphometric dimensions within specific regions in

response to localised geoenvironmental criteria such as climate, soil type, slope geometry, etc (Lewkowicz, 1990) (see fig. 7.2.3).

Figure 7.2.3. Aerial panorama of several active-layer detachment slides on Ellesmere Island (1992). (Photograph: A. Lewkowicz).

7.3. Centrifuge Modelling Data

In this section data from the four series of centrifuge flights that resulted in slope failure and simulated landsliding processes are presented. The section will present data recorded during each freeze-thaw test cycle to illustrate conditions thermal regimes, frost heave, thaw settlement, pore water pressure, surface movement and subsurface volumetric movement. The section will also outline the chronological progression of each landslide process as this will enable comparison between the simulation of rapid processes and the slow mass wasting processes associated with gelifluction. Mechanisms of failure are also explored within each slope failure through investigation of internal deformation geometry and landslide morphology (see for instance Lyndon and Schofield, 1970).

The four slope models discussed here are: Series 16D/NS (16° slope, natural soil), 8D/10S (8° slope, natural soil plus 10% silt), 12D/10C (12° slope, natural soil plus 10% clay), and 8D/10C (8° slope, natural soil plus 10% clay).

7.3.1. Distribution of Frost Heave

The amount of volumetric expansion during the freezing cycle was determined through a spot-height matrix across the model surface measured with reference to a horizontal datum. This created an accurate record of the distribution and amount of frost heave occurring across the slope model in the freezing phase prior to slope failure. Frost heave was variable across the model surface – in similar patterns to those described in Section 5.3 – it is likely that the amount of frost heave was related to the speed of frost penetration and the flux of water to the freezing front (see fig. 7.3.1).

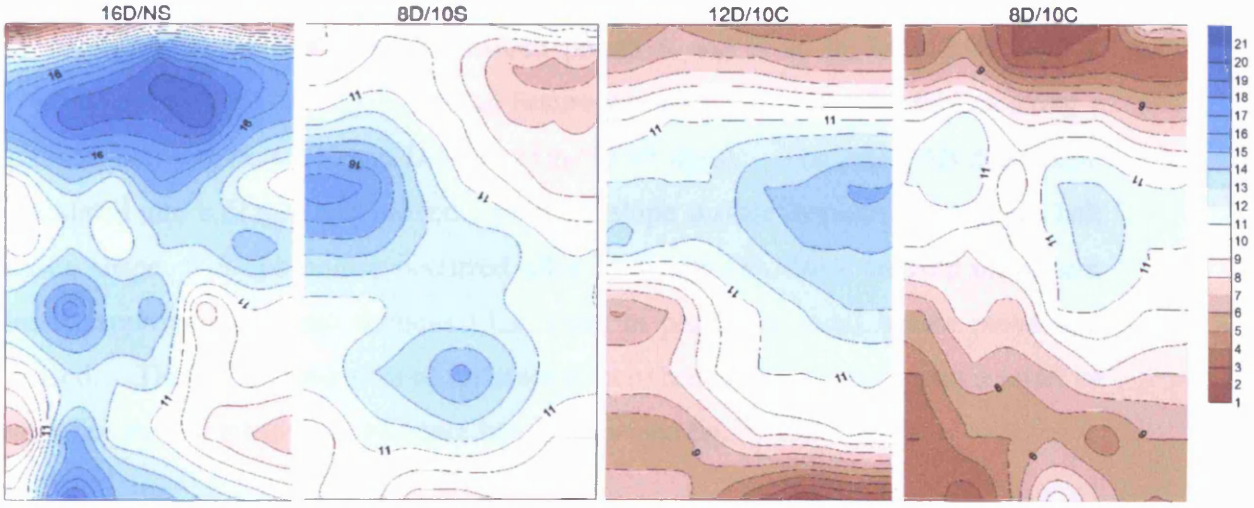

Figure 7.3.1. Amount of frost heave (mm) for the freezing cycle preceding slope failure (model scale).

Series 16D/NS had the highest frost heave prior to failure with the majority of ice segregation occurring in the upper portion of the slope. Series 8D/10S had the largest overall amount of frost heave with ice growth being widely distributed across the central zone of the slope. Series 12D/10C (33%) and 8D/10C (77%) experienced less frost heave when compared to the slope failure within the natural soil (table 7.3.1). The distribution of highest soil ice growth was found to be in the central portion of the slope model for both incremental clay failures. The distribution of soil ice can be spatially linked to the zone of failure inception within series 16D/NS and 12D/10C (e.g. figs. 7.3.4, 7.3.8 and 7.3.1).

Table 7.3.1. Average frost heave (mm) for each freezing cycle.

Series	Cycle 1	Cycle 2
NS/16D	13.48	n/a
10S/8D	8.12	14.93
10C/12D	10.10	n/a
10C/8D	7.88	n/a

7.3.2. Description of Landsliding Processes

The development of each slope failure will be outlined to provide an overall chronological context for the numerical data presented within sections 7.3.3-7.3.5.

- *Series 16D/NS*

A small depression first formed between points A and B at 3h 7m (12.98 days at prototype scale) (fig. 7.3.2). A small fissure was then formed on the surface along a transect between points C and D at 3h 21m (13.95 days). The initial AB depression translated into a fissure and moved across the slope surface to reach point E in a half moon shape. Slope failure occurred after 14.5 days (3h 29m); landslip movement lasted approximately two minutes (3.3 hours in prototype time) before movement ceased. The main active area of failure was between points F and G with a series of landslips leaving a toe zone of intact block units (see fig. 7.3.2).

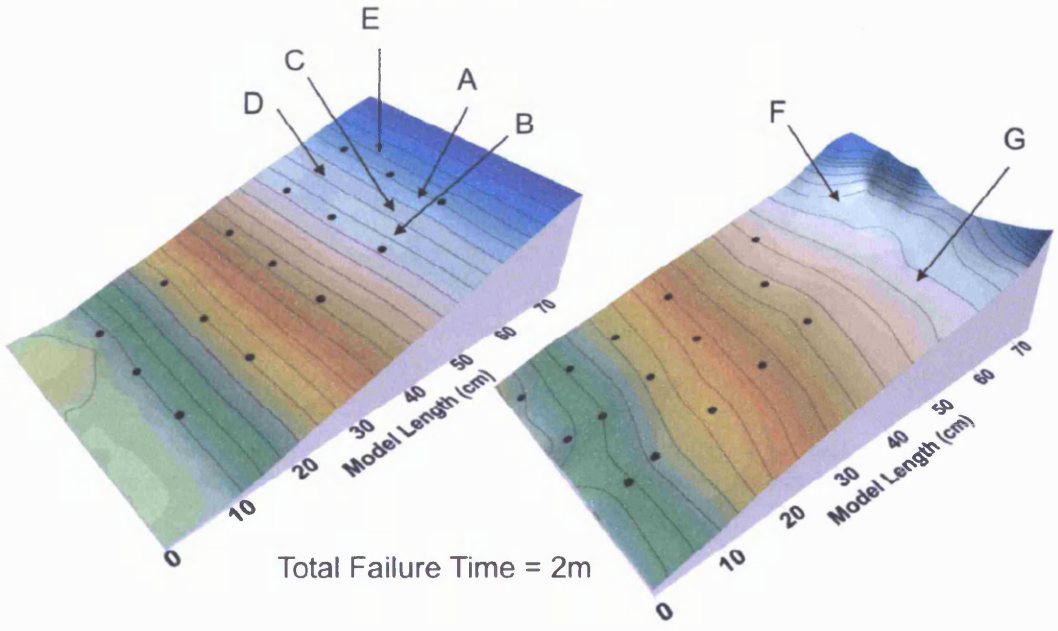

Figure 7.3.2. Pre-failure and post-failure DTMs for Series 16D/NS. Note: Black dots show locations of displacement markers on the slope surface.

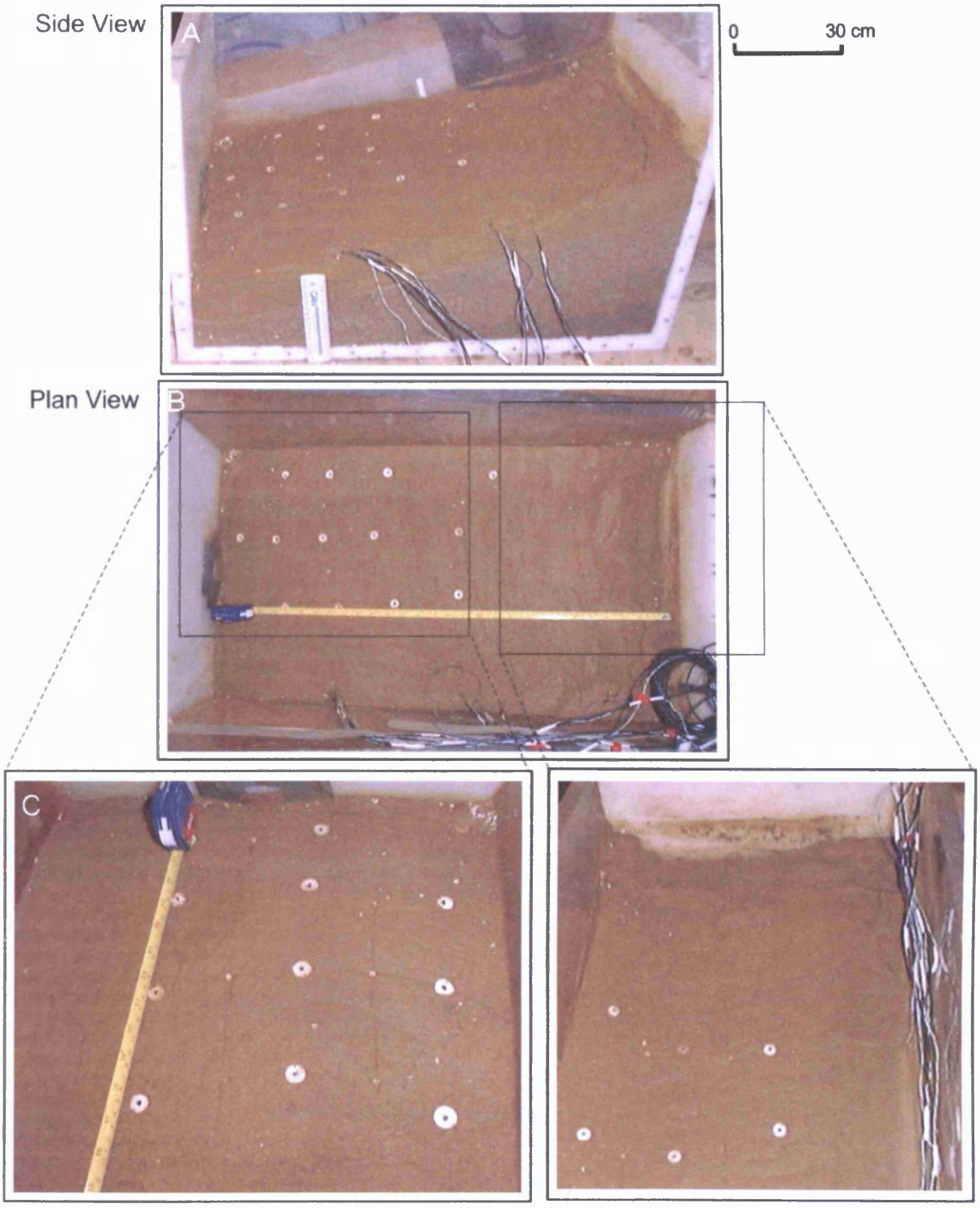

Figure 7.3.3. Pre-excavation record of slope failure within Series 16D/NS. Note: The lower slope in (c) is viewed in a downslope direction, the upper slope in an upslope direction.

- *Series 8D/10S*

A small amount of deformation appeared between points A and B at 4h 8m (17.2 days prototype time) and a small slip lead to a fissure opening up at the head of the slope at point C (4h 19m = 17.98 days prototype time). The localised slip deformed

the upper marker layer but the rest of slope remained unaffected. Exaggerated marker movement then occurred closest to points A and B, expanding the original fissure at point C across to point D at 4h 28m (18.6 days) (see fig. 7.3.4). Excess surface water observed at the toe of slope was possibly due to water seepage through the surface. The fissure between CD widened at 4h 59m (20.76 days) and lengthened at 5h 36m (23.3 days) to separate the displaced slope from the upper stable section. The centre markers moved downslope at 6h 02m (25.14 days) with little impact on the width of the upper CD fissure at the head of the slope. A slow intermittent failure was observed with long periods of stability – causing a gradual widening of an upper fissure and localised deformation of one transect of markers (see fig. 7.3.5). The main activity zones occurred between points E and F within Figure 7.3.4 across a period of 1h 15m (5.2 days prototype).

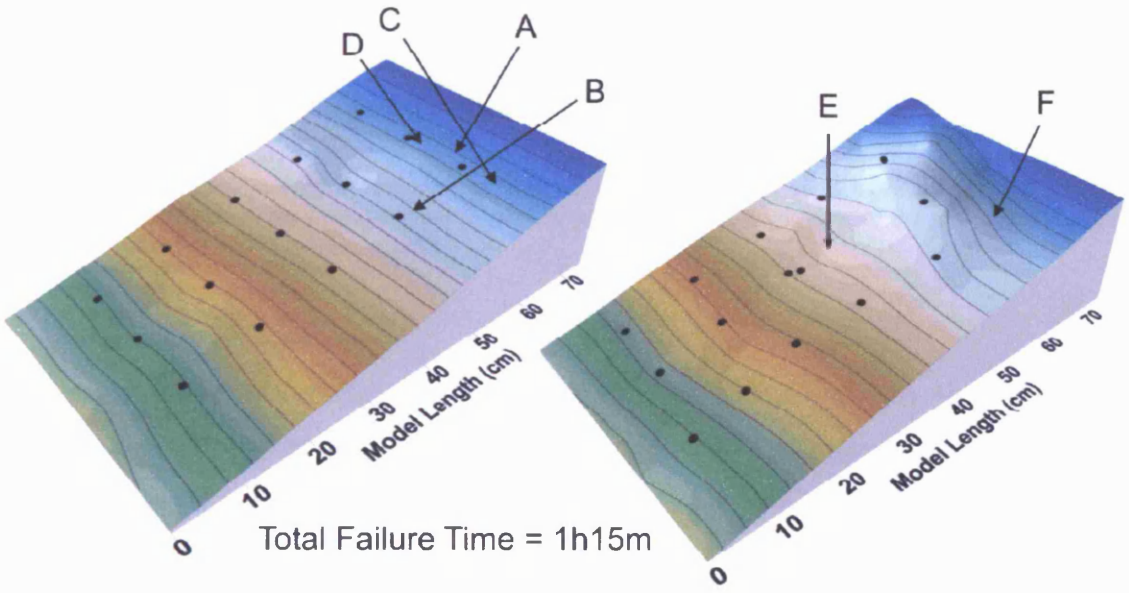

Figure 7.3.4. Pre-failure and post-failure DTMs for Series 8D/10S.

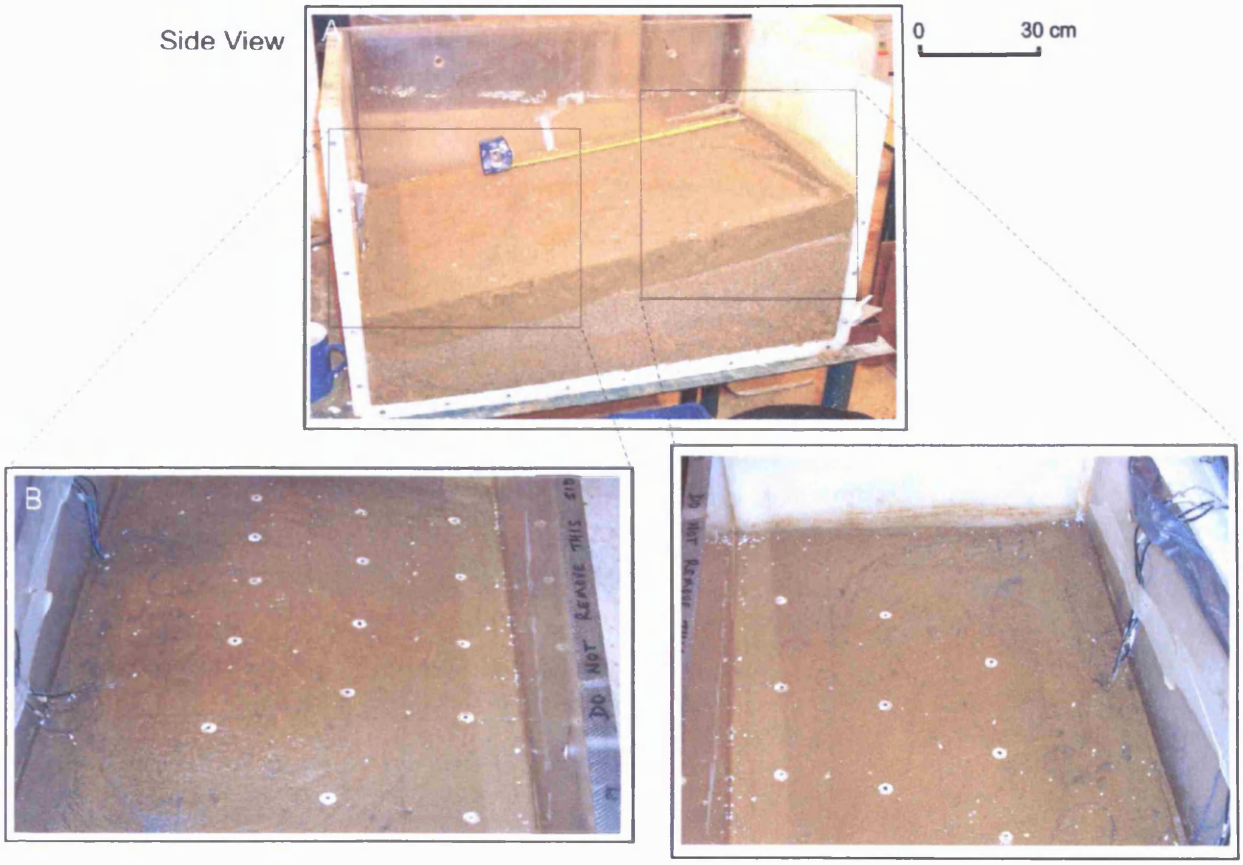

Figure 7.3.5. Pre-excavation record of slope failure within Series 8D/10S. The lower slope photographs (b) show an upslope view of the toe zone and an upslope view of the slide head. Note: the lobate toe and arcuate head scar.

- *Series 12D/10C*

A small fissure and surface depression formed around point A at 3h 40m – this fissure gradually widened across to point B by 3h 43m (15.27 days prototype). The development of the AB fissure moved downslope and was replicated by a smaller second fissure in the model surface between points C and D at 3h 44m (15.55 days prototype) (see fig. 7.3.6). Slope failure occurred as a single unit on the right side of the slope whereby the AB and CD fissures widened and created a series of block slides leading to a rapid collapse of the slope model at 3h 45m (15.62 days). The active failure zone is indicated by points E and F within Figure 7.3.6. However, the toe zone of the slope model remained intact (see fig. 7.3.7). After the initial landslide, additional reworking of the upper slope zone occurred at 3h 50m (15.97 days) to create the distinct headwall by lengthening the AB fissure until at 4h 11m (17.43 days prototype) when a large block separation moved downslope disrupting surface markers on the right side of the slope model. Excess meltwater was expelled in the zone around point G as the larger mass displacement took place.

The total time for slope failure was 20m (33 hours prototype time) with the initiation being concentrated within the upper right hand zone of the slope model.

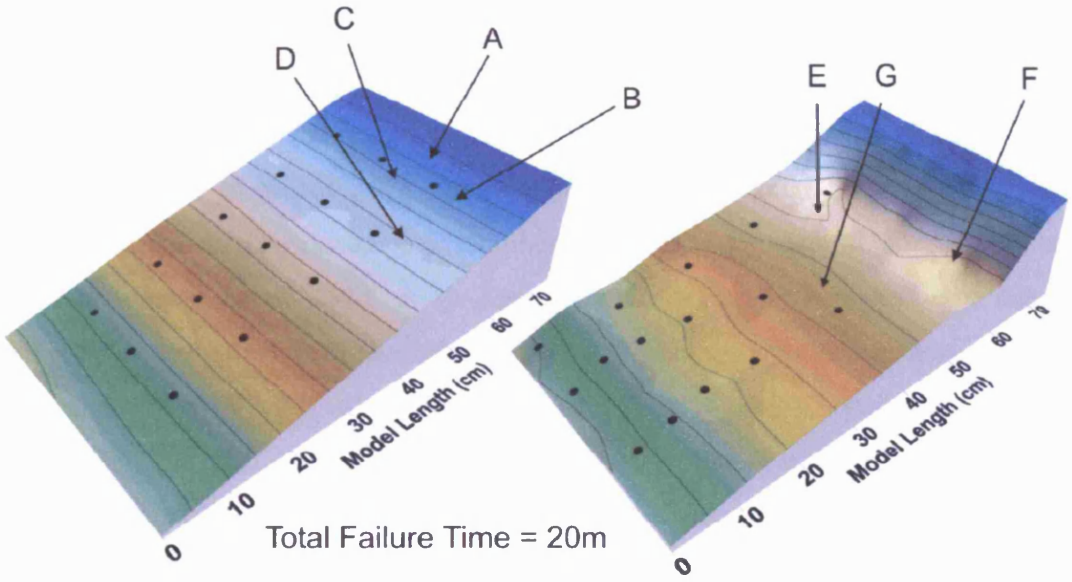

Figure 7.3.6. Pre-failure and post-failure DTMs for Series 12D/10C.

Figure 7.3.7. Pre-excavation record of slope failure within Series 12D/10C.

- *Series 8D/10C*

The model slope surface began to deform at 2h 17m (9.51 days prototype time) between points A and B with no visible surface fissures (see fig. 7.3.8). A surface depression quickly formed above point A at 2h 19m (3.3 hours later in prototype time) that transformed into a set of small surface fractures by 2h 20m (over a time period of 1.66 hours prototype). Slope failure occurred through the development of parallel fissures that widened and lengthened towards the central portion of the model between points B and C at 2h 22m (after a further 3.3 hours prototype time). The gradual development of the failure occurred within the upper slope zones – with the main activity being concentrated around the region of point D and E. Landsliding occurred at 2h 26m (10.13 days) with the downslope movement of markers occurring through the multiplication of the surface cracks towards point F and finally mudflow via the expulsion of surface water within the zone around point G. The toe zone of the slope model became saturated with excess meltwater during post-failure at 2h 37m (10.9 days) (see fig. 7.3.9).

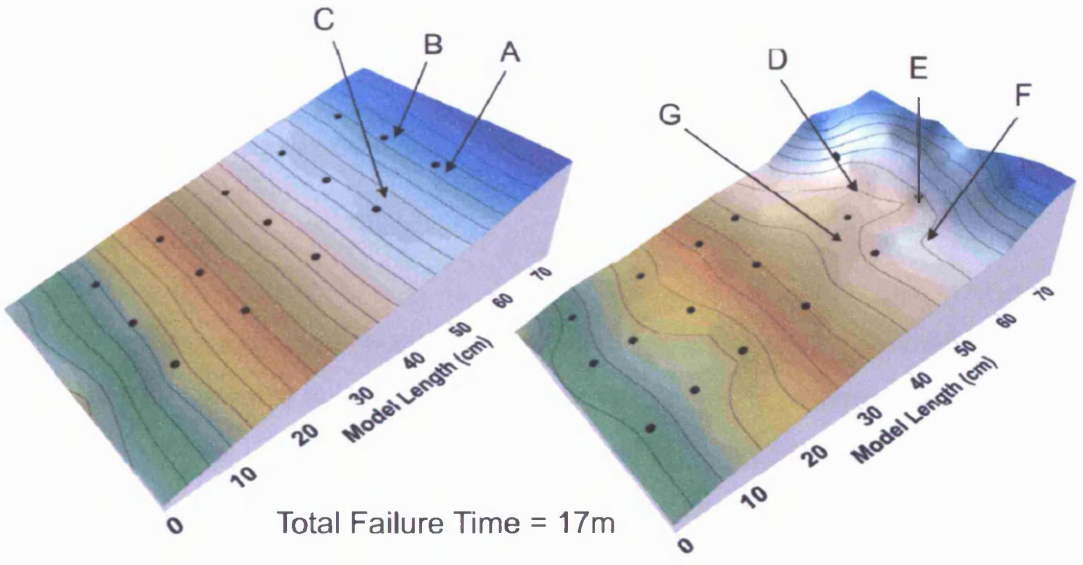

Figure 7.3.8. Pre-failure and post-failure DTMs for Series 8D/10S.

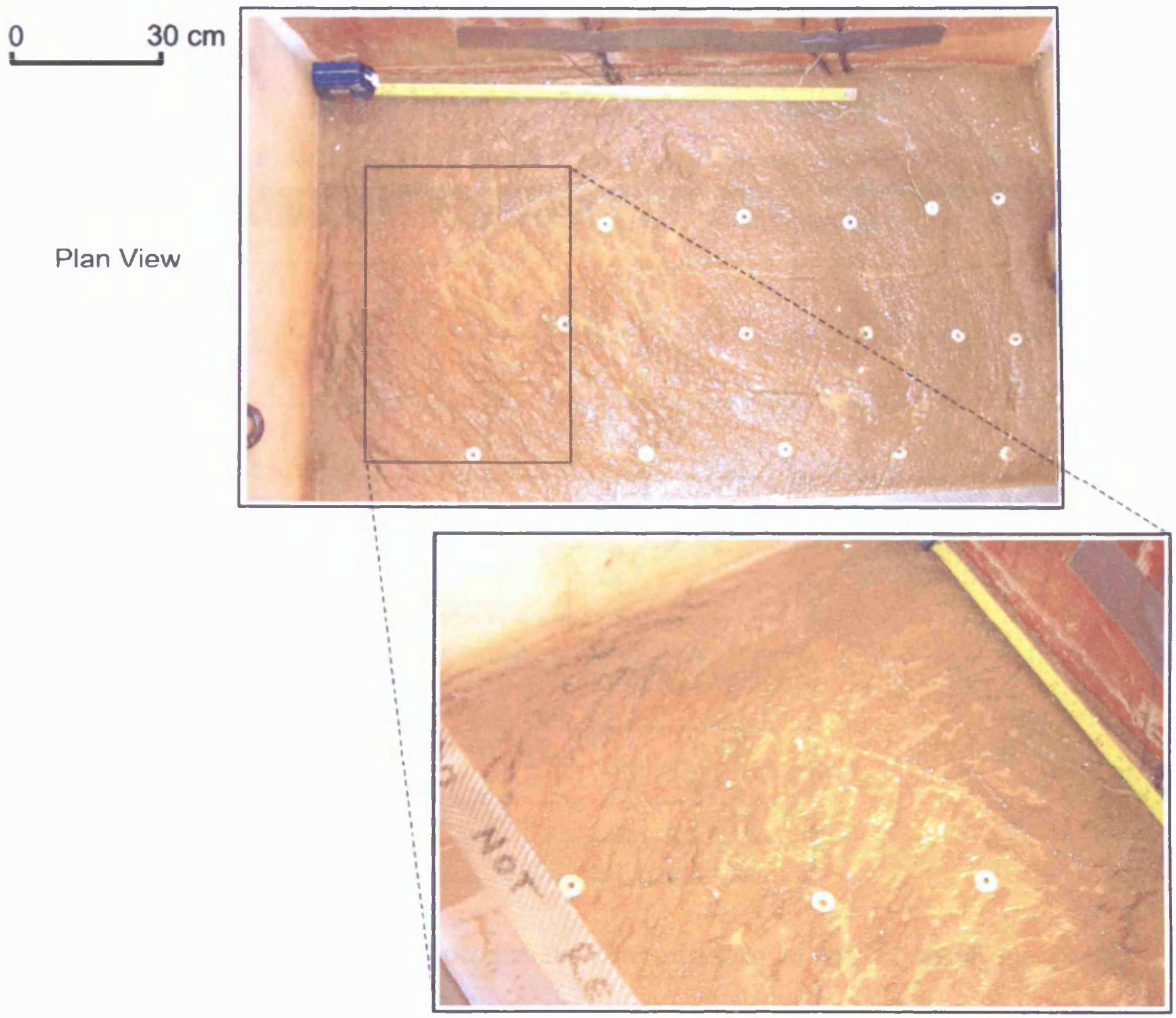

Figure 7.3.9. Pre-excavation record of slope failure within Series 8D/10C. Note: Slope to the right is enlarged view of the upslope source area.

7.3.3. Thermal Regime

Test conditions during thaw phases for all slope failure series are outlined in Table 7.3.2. It was noted in Section 5.1 that laboratory conditions remained consistent during thaw phases. Observed changes to thawed model response were therefore a function of variations in model parameters rather than experimentally induced response to external influences. The overall thaw rate for each slope failure remained roughly consistent between 'landslide' and 'non-landslide' test series – it is therefore inferred that failures occurred as a result of changes to model slope angle and soil strength during thaw (see tables 7.3.3 & 5.2.3). The style of thaw penetration was consistent with patterns recorded within Section 5.2 – with variation in warm front penetration at a particular depth being largely determined by localised segregated ice content. The fastest rate of thaw was recorded for Series 8D/10C

with 44mm/day (prototype scale) whilst the slowest rate of thaw front penetration was observed for Series 8D/10S at 23mm/day (see table 7.3.3).

Table 7.3.2. Centrifuge modelling test details for series involved in slope failure.

	16D/NS	8D/10S		12D/10C	8D/10C
Thaw Cycle	1	1	2	1	1
Minimum Pit Temperature (°C)	16.3	20.2	18.3	17.6	21.5
Maximum Pit Temperature (°C)	21.6	24.2	23.8	21.2	24.9
Rise in Ambient Air Temperature (°C)	5.3	4	5.5	3.6	3.4
Prototype Test Duration (days)	26.3	29.2	31.4	18.5	16.8

Table 7.3.3. Average rate of thaw penetration for each thaw phase.

	Prototype Scale	
Series	mm/day	m/day
16D/NS	27.01	0.027
8D/10S	23.76	0.024
12D/10C	28.10	0.028
8D/10C	44.27	0.044

The thermal data allowed an approximate determination of the depth of the thaw front at the time of slope failure for both the upper and lower slope regions (see table 7.3.4) in each model. By comparing this with profiles of movement it was possible to demonstrate the relationship between depth of slip surface and depth of thaw penetration. Figure 7.3.10 shows that thaw penetration was consistent throughout the 16D/NS model and that failure occurred on a frozen base roughly parallel to the slope surface. In model 12D/10C, failure occurred when the lower portion of the slope had completely thawed, but in the upper slope region, a frozen sub-surface provided the failure plane that initiated sliding (fig. 7.3.12). Figures 7.3.11 and 7.3.13 show thaw penetration at slightly different rates between the lower slope and the upper slope, creating a frozen plane with slightly different gradient to the model surface gradient. In that Series 8D/10S contained a thaw plane surface angle at the time of failure was approximately 5.5° (surface gradient 8°) whilst in Series 8D/10C the zero degree isotherm at the moment of failure had an approximate gradient of 9° (see table 7.3.4).

Table 7.3.4. Approximate depth of thaw plane (prototype scale) at time of slope failure.

Series	Lower Slope (m)	Upper Slope (m)
16D/NS	0.51	0.51
8D/10S	0.39	0.51
12D/10C	Model Base	0.39
8D/10C	0.58	0.53

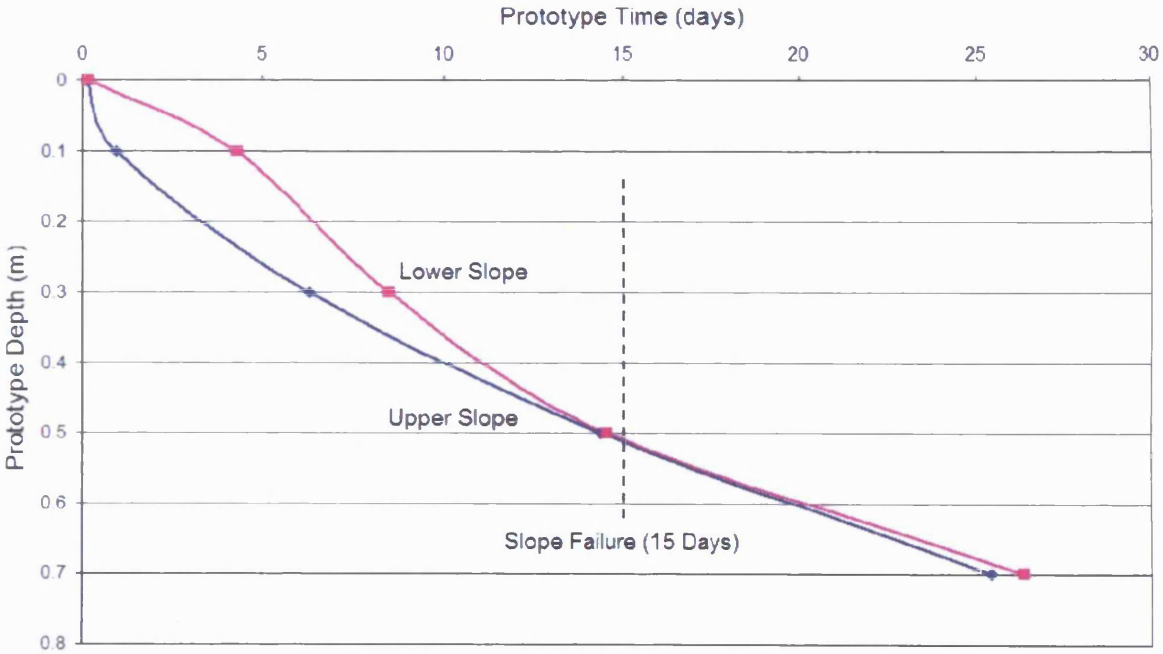

Figure 7.3.10. The progression of the zero degree isotherm within the landslide failure of 16D/NS.

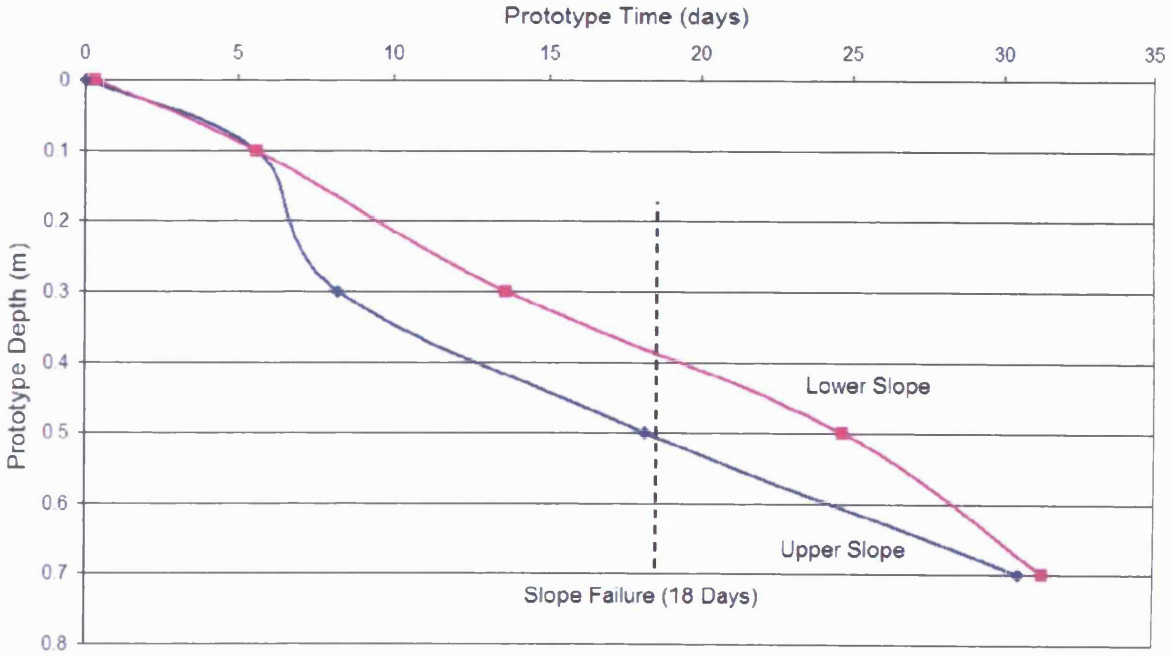

Figure 7.3.11. The progression of the zero degree isotherm within the landslide failure of 8D/10S.

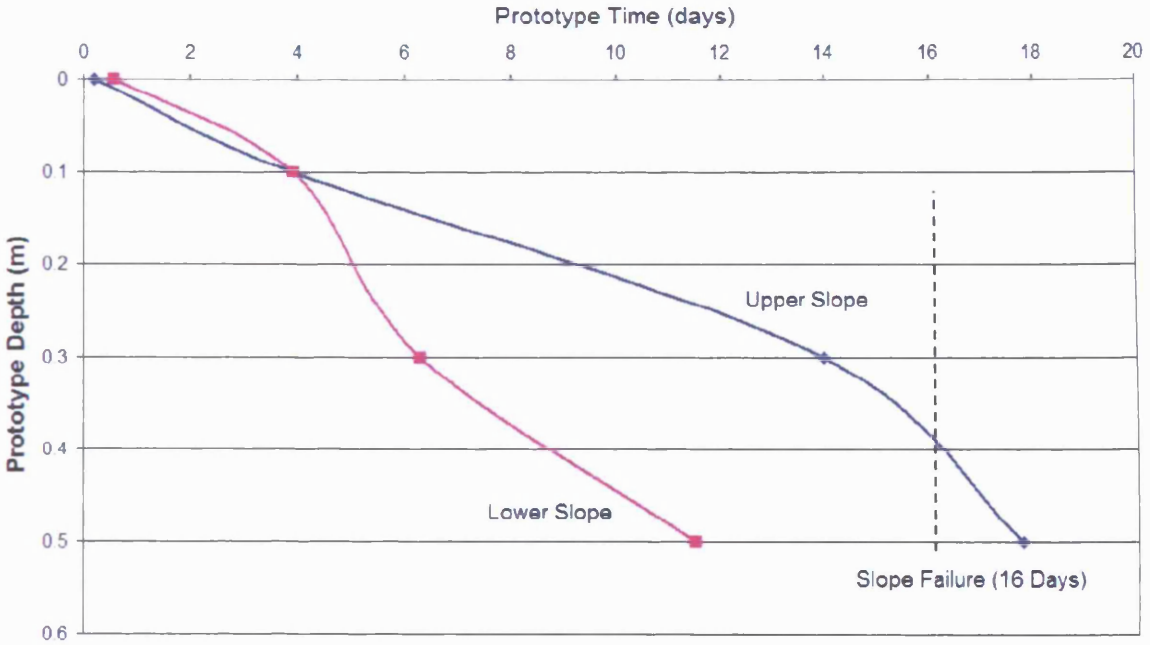

Figure 7.3.12. The progression of the zero degree isotherm within the landslide failure of 12D/10C.

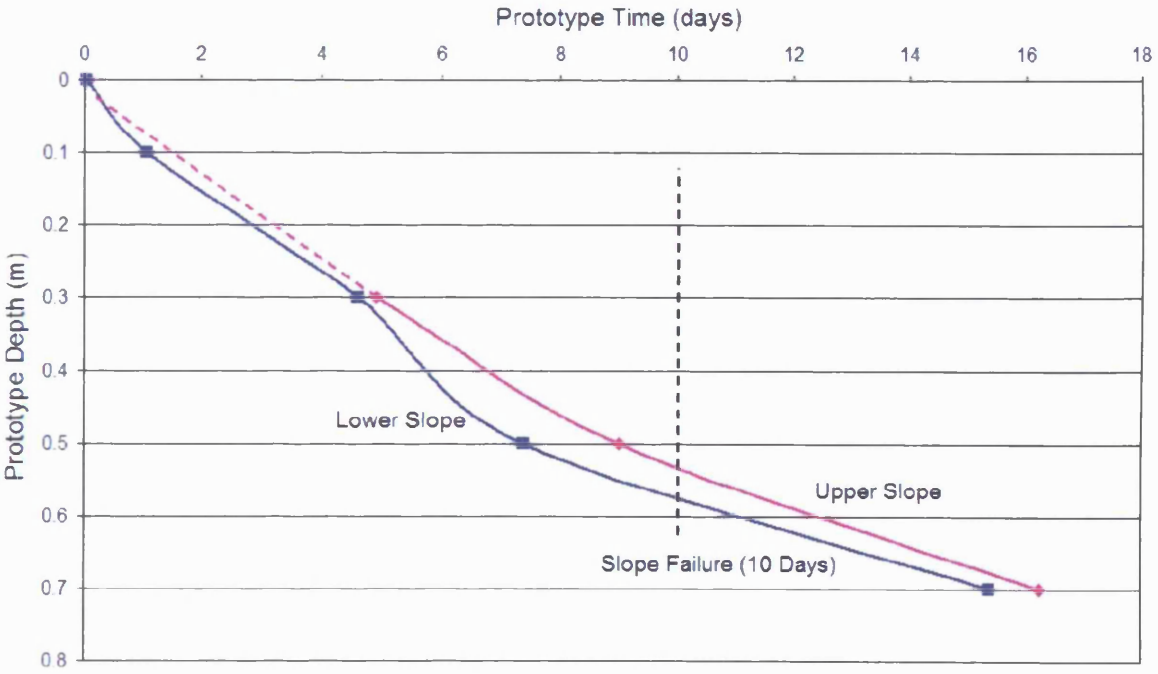

Figure 7.3.13. The progression of the zero degree isotherm within the landslide failure of 8D/10C.

However, Figures 7.3.10-7.3.13 represent the thermal conditions existing within the model during thaw and the zero degree isotherm may not accurately represent the actual depth of frozen material at the time of failure initiation, especially within the models containing percentages of additional fine material (i.e. 12D/10C, 8D/10C and 8D/10S), when some freezing point depression is to be anticipated. It has also been

assumed that a linear zero degree isotherm existed between the two instrument strings, whereas in reality the plane may have had irregularities due to localised variations in thermal properties caused by minor variations in ice content.

7.3.4. Porewater Pressure

Porewater pressure distribution is fundamentally important to the stability of a thawing slope (Bromhead, 1992). McRoberts and Morgernstern (1974) have shown that the thaw consolidation theory predicts that raised porewater pressures are associated with thaw consolidation of frozen soil (see sections 2.1.9 and 5.4). The thaw consolidation ratio was calculated for the models that underwent rapid failure (see table 7.3.5) – and these values were similar to the thaw consolidation ratios calculated for the gelifluction slope models. The natural soil and ten percent silt models allowed a faster expulsion of porewater whereas the more cohesive and fine-grained clay models had significantly slower drainage, reflected in a lower value of C_V. Although the Thaw Consolidation ratio did not approach unity, it was significantly higher in the clay model simulations.

Table 7.3.5. Thaw consolidation ratio (R) for models undergoing slope failure.

Series	α ($m/year^{½}$)	C_v (m^2/year)	Thaw Consolidation Ratio
16D/NS	2.63	12.74	0.37
8D/10S	2.46	14.95	0.32
12D/10C	3.17	6.63	0.62
8D/10C	3.36	6.63	0.65

Table 7.3.6 indicates that the maximum recorded pore pressures were progressively greater at increasing model depth within both the upper and lower slope zones of all models. The highest pore pressures were recorded within the ten percent clay soil, as a function of the higher thaw consolidation ratio reflecting the lower permeability of this soil (fig. 7.3.14). The lower slope pore pressure transducers experienced higher maximum porewater pressures than the upper slope; possibly as a result of pronounced meltwater percolation to the lower zone during thaw consolidation, and to thickening of the soil profile due to compression in the landslide toe zone.

Table 7.3.6. Maximum porewater pressures (kPa) at different prototype depths within the test series undergoing landsliding processes.

Series	Lower Slope			Upper Slope		
	0.1m	0.3m	0.5m	0.1m	0.3m	0.5m
16D/NS	2.07	4.59	9.11	1.70	3.69	7.09
8D/10S	1.61	2.91	10.92	3.07	3.89	6.93
12D/10C	5.69	5.46	16.09	7.01	9.88	9.97
8D/10C	6.37	n/a	16.10	5.29	8.28	14.73

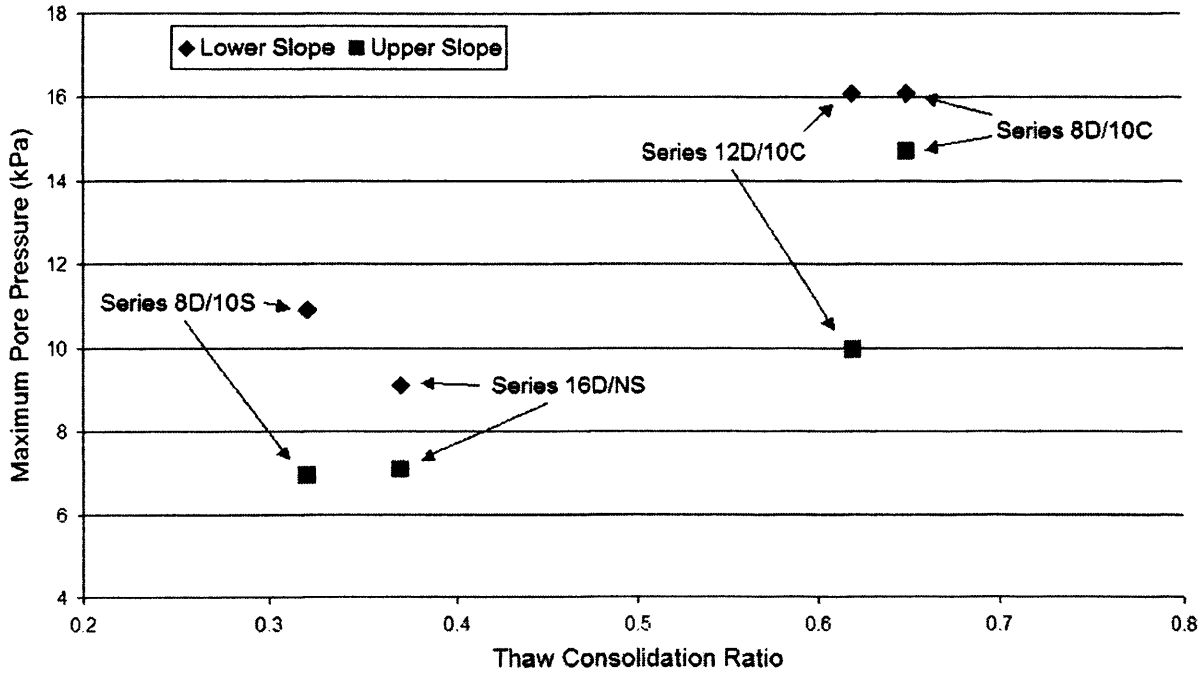

Figure 7.3.14. Relationship between Thaw Consolidation Ratio (R) and maximum pore pressure recorded at 50mm model scale (0.5m prototype scale).

Patterns of porewater pressure variation have been presented for both lower and upper instrumentation strings in all four slope models (figs. 7.3.15-7.3.17) because model failure involved movements across both instrument strings. The pore pressure data presented below indicate similar patterns to those discussed within Sections 5.4.1-5.4.2 with a transition from negative to positive pressures occurring during passage of the thaw front, and high pore pressures during thaw consolidation.

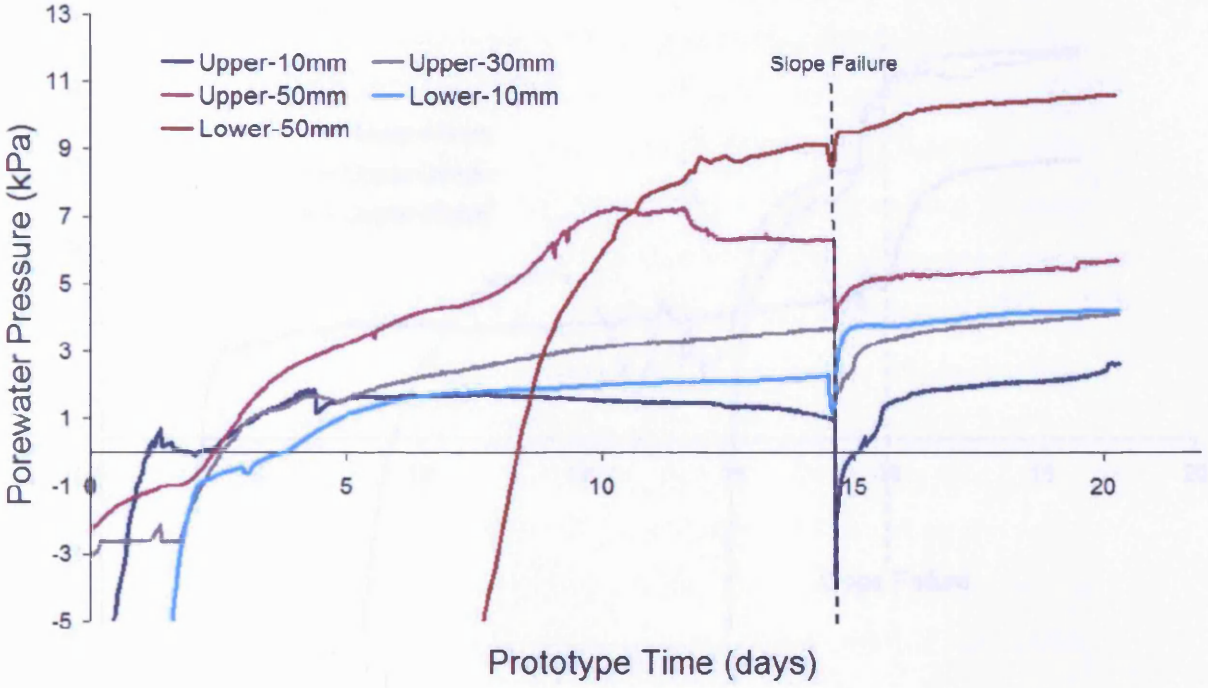

Figure 7.3.15. Porewater pressures recorded for Series 16D/NS. Note: Transducer depths given in model scale (equivalent prototype scale is x 10).

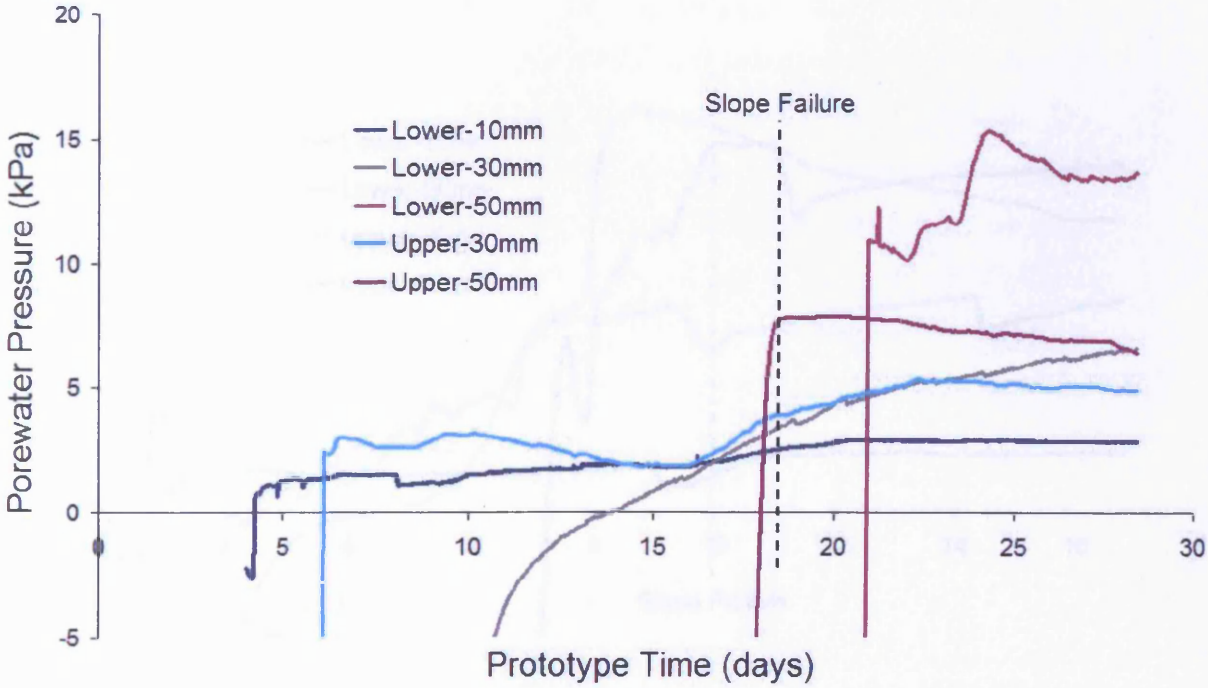

Figure 7.3.16. Porewater pressures recorded for Series 8D/10S. Note: Transducer depths given in model scale (equivalent prototype scale is x 10).

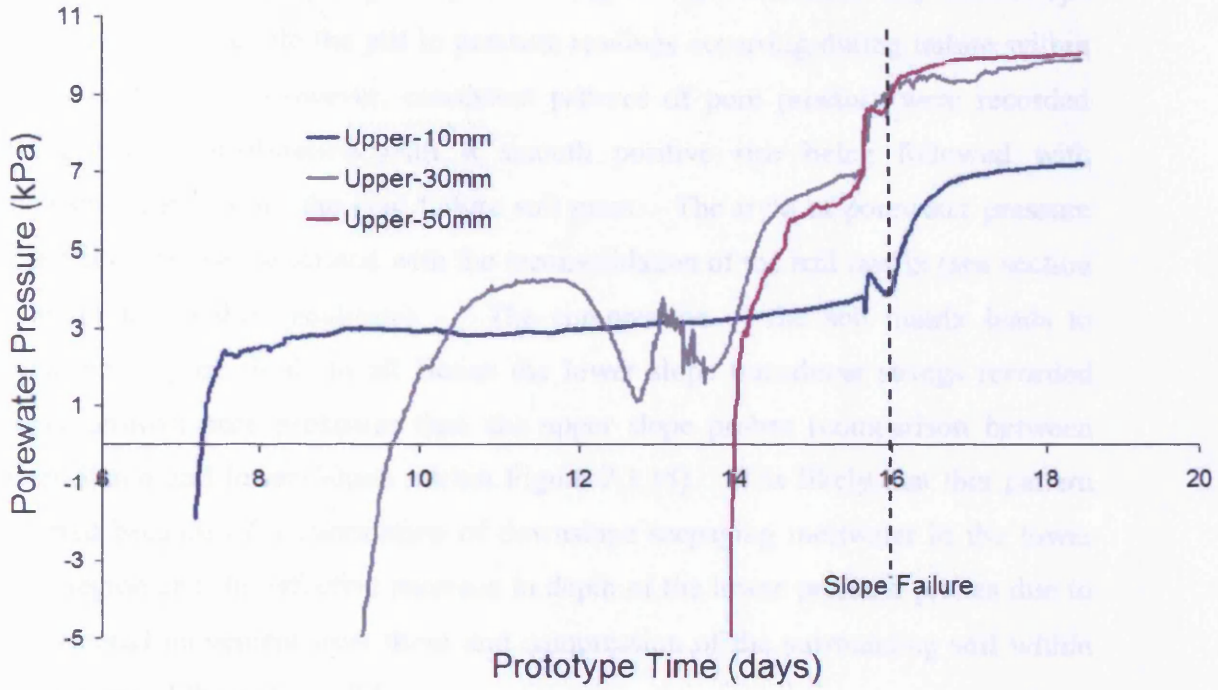

Figure 7.3.17. Porewater pressures recorded for Series 12D/10C. Note: Transducer depths given in model scale (equivalent prototype scale is x 10).

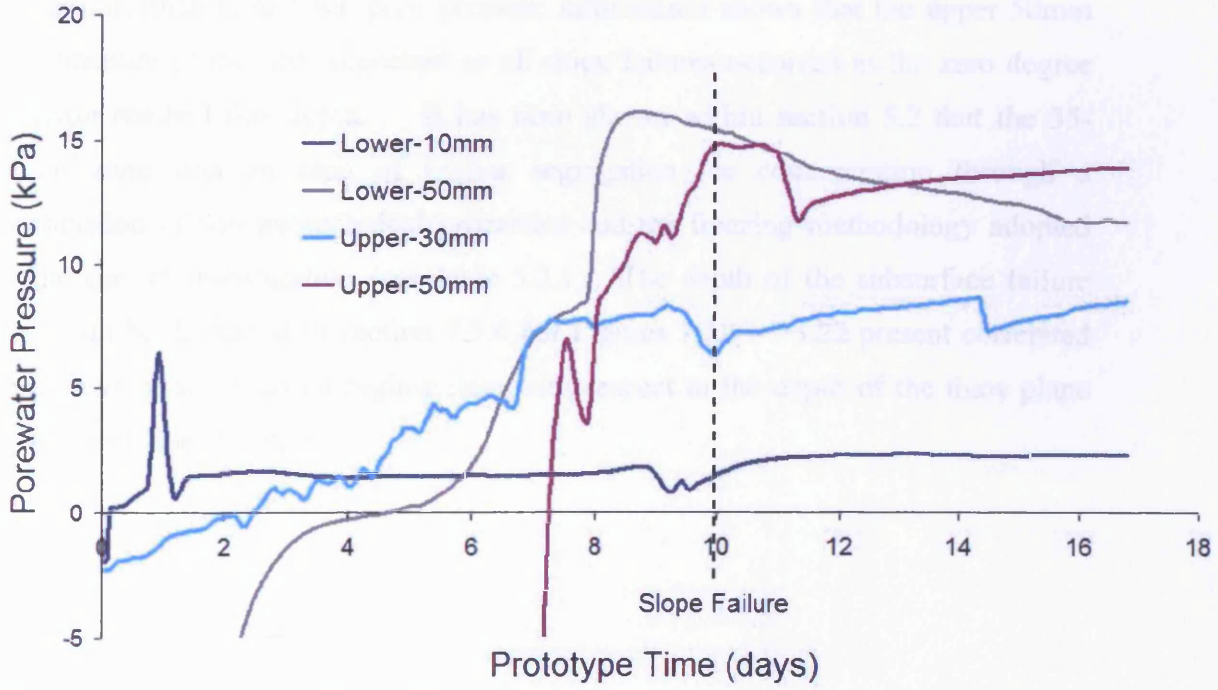

Figure 7.3.18. Porewater pressures recorded for Series 8D/10C. Note: Transducer depths given in model scale (equivalent prototype scale is x 10).

The data presented within Figure 7.3.15 show the difficulties associated with measuring pore pressure during slope failure as the translocation of material disrupts transducer location and depth by entraining the probe within any downslope movement, for example the jolt in pressure readings occurring during failure within Series 16D/NS. However, consistent patterns of pore pressure were recorded during thaw consolidation with a smooth positive rise being followed with fluctuating data within the post failure soil mass. The style of porewater pressure after failure can be associated with the reconsolidation of the soil matrix (see section 7.3.6 for microfabric analyses). The compression of the soil matrix leads to expulsion of pore fluid. In all Series the lower slope transducer strings recorded higher positive pore pressures than the upper slope probes (comparison between upper-50mm and lower-50mm within Figure 7.3.14). It is likely that this pattern occurred because of accumulation of downslope seepaging meltwater in the lower slope region and the effective increase in depth of the lower pressure probes due to soil material movement over them and compression of the surrounding soil within the toe zone of the slide.

It has been shown within section 5.4.2 that the style of pore pressure is related to thermal conditions during thaw consolidation. A comparison between the thermal regime information and the pore pressure information shows that the upper-50mm pore pressure probe was important as all slope failures occurred as the zero degree isotherm reached this depth. It has been shown within section 5.2 that the 35-50mm zone was an area of higher segregation ice concentration through a combination of soil geotechnical properties and the freezing methodology adopted by the current investigation (see table 5.2.1). The depth of the subsurface failure plane will be discussed in section 7.3.6 but Figures 7.3.19-7.3.22 present correlated pore pressure and thermal regime data with respect to the depth of the thaw plane during landslide initiation.

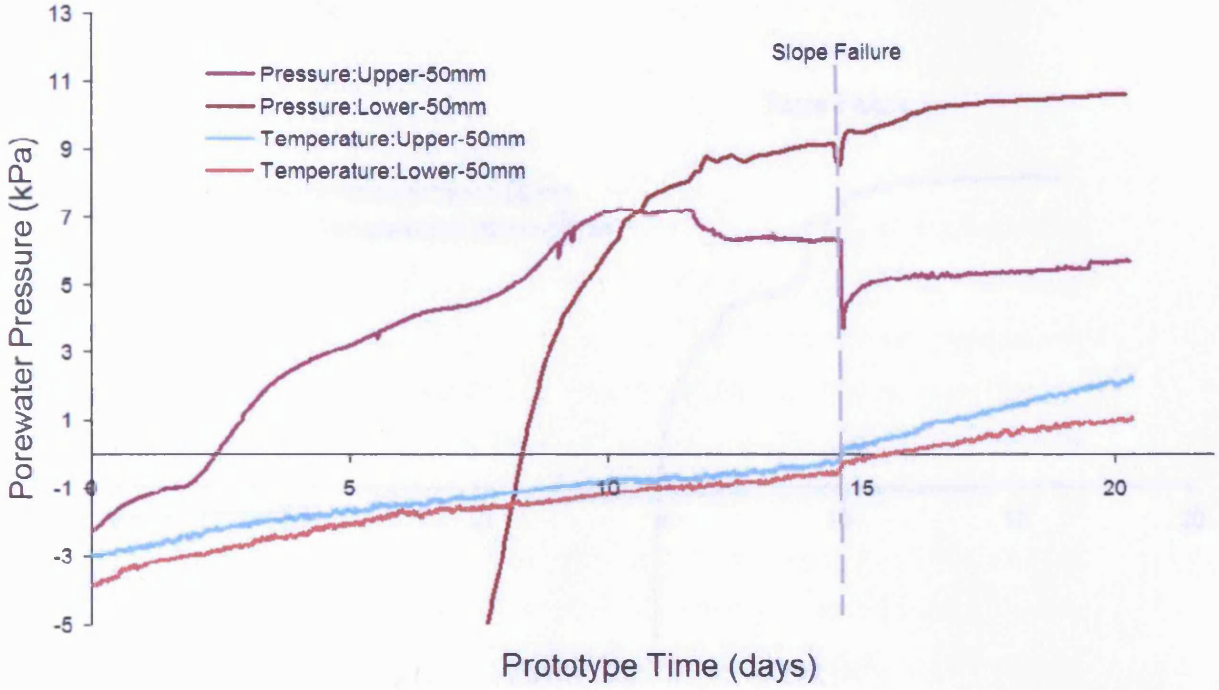

Figure 7.3.19. Correlation between thermal regime and porewater pressures recorded for Series 16D/NS. Note: Transducer depths given in model scale (equivalent prototype scale is x 10).

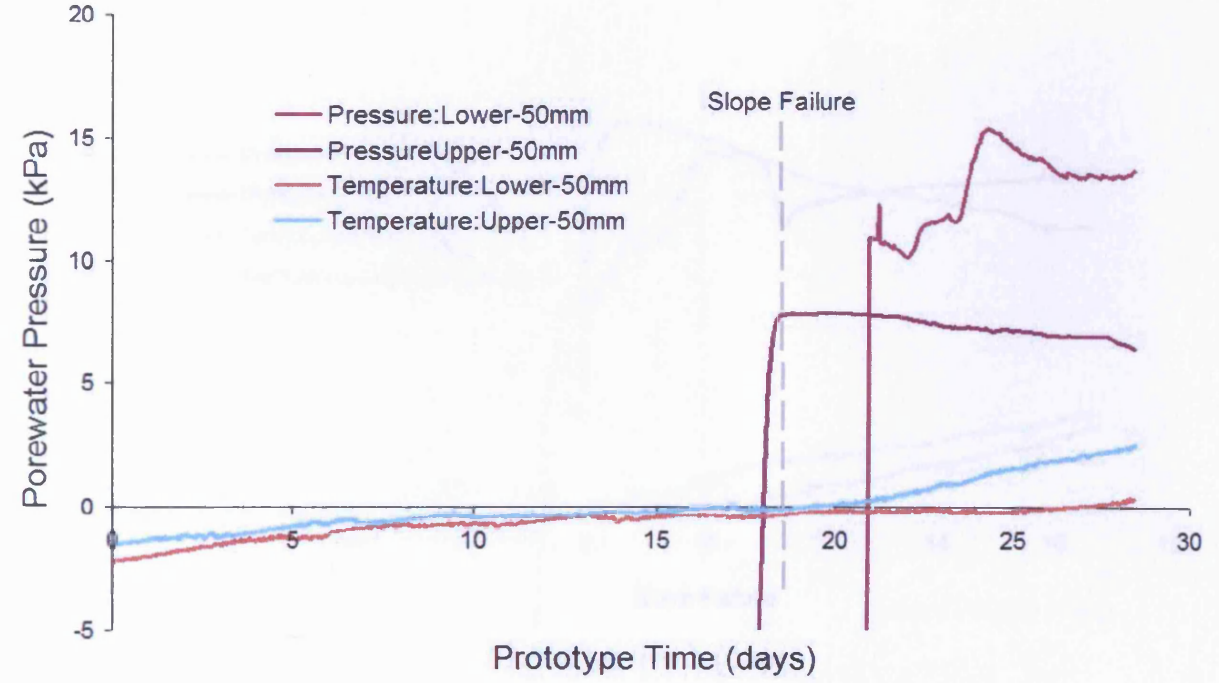

Figure 7.3.20. Correlation between thermal regime and porewater pressures recorded for Series 8D/10S. Note: Transducer depths given in model scale (equivalent prototype scale is x 10).

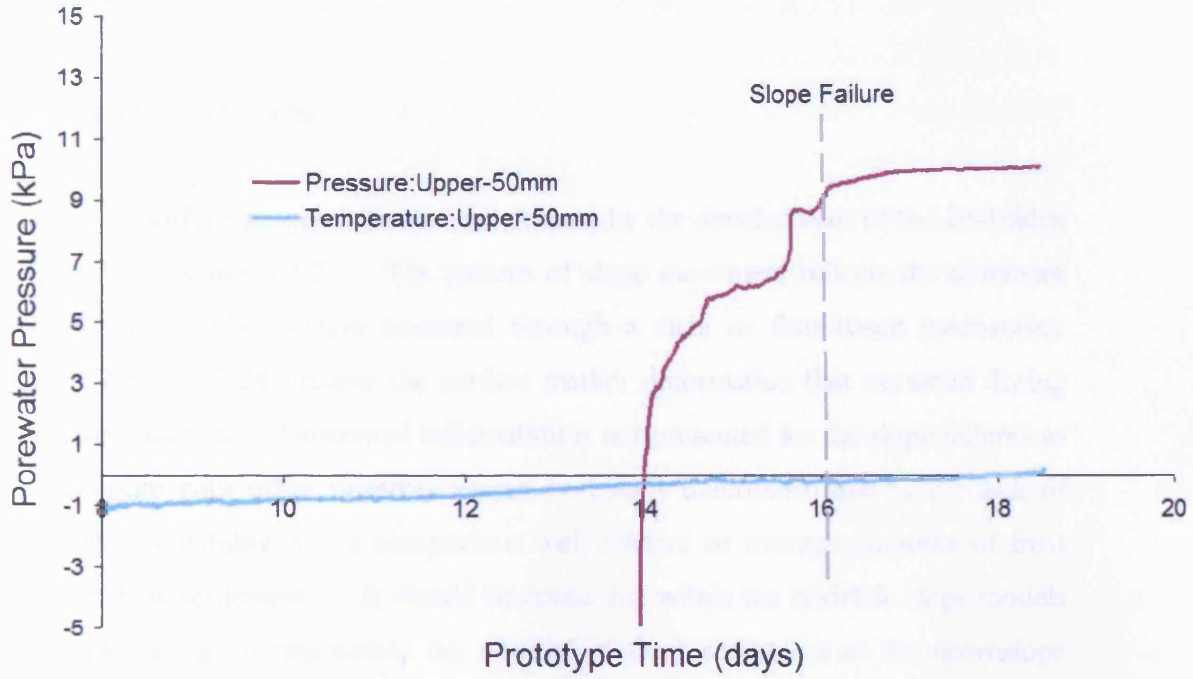

Figure 7.3.21. Correlation between thermal regime and porewater pressures recorded for Series 12D/10C. Note: Transducer depths given in model scale (equivalent prototype scale is x 10).

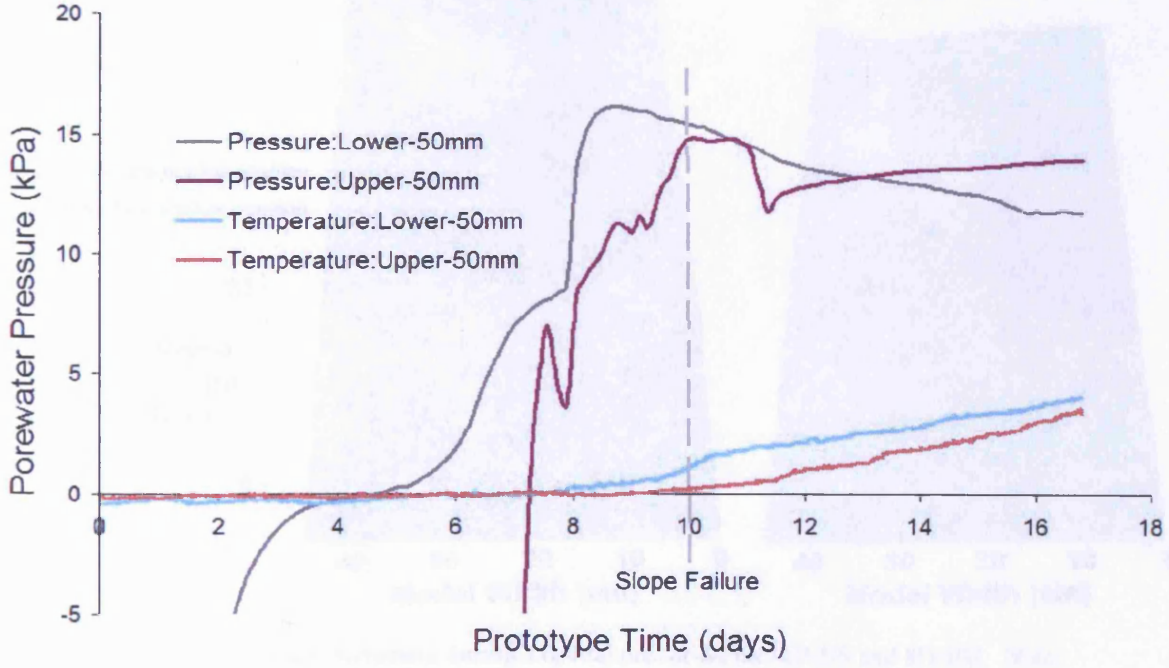

Figure 7.3.22. Correlation between thermal regime and porewater pressures recorded for Series 8D/10C. Note: Transducer depths given in model scale (equivalent prototype scale is x 10).

It is felt that slope failures were therefore directly related to the depth of thaw penetration impacting upon the potential maximum pore pressure value within the soil profile.

7.3.5. Surface Movement

Patterns of surface movement were determined by the development of the landslides described in section 7.3.2. The pattern of slope movement reflects the dominant process, i.e. whether failure occurred through a slide or flow-based mechanism. Figures 7.3.23-7.3.24 present the surface marker deformation that occurred during thaw consolidation. Numerical information is not presented for the slope failures as a relationship with other variables cannot be clearly determined due to the lack of inter-test repeatability, i.e. a comparison with relative or average amounts of frost heave or thaw settlement. It should be noted that within the landslide slope models it was impossible to recalculate the amount of thaw settlement as the downslope displacement of material disrupted the spot-height matrix (see for example section 7.3.8).

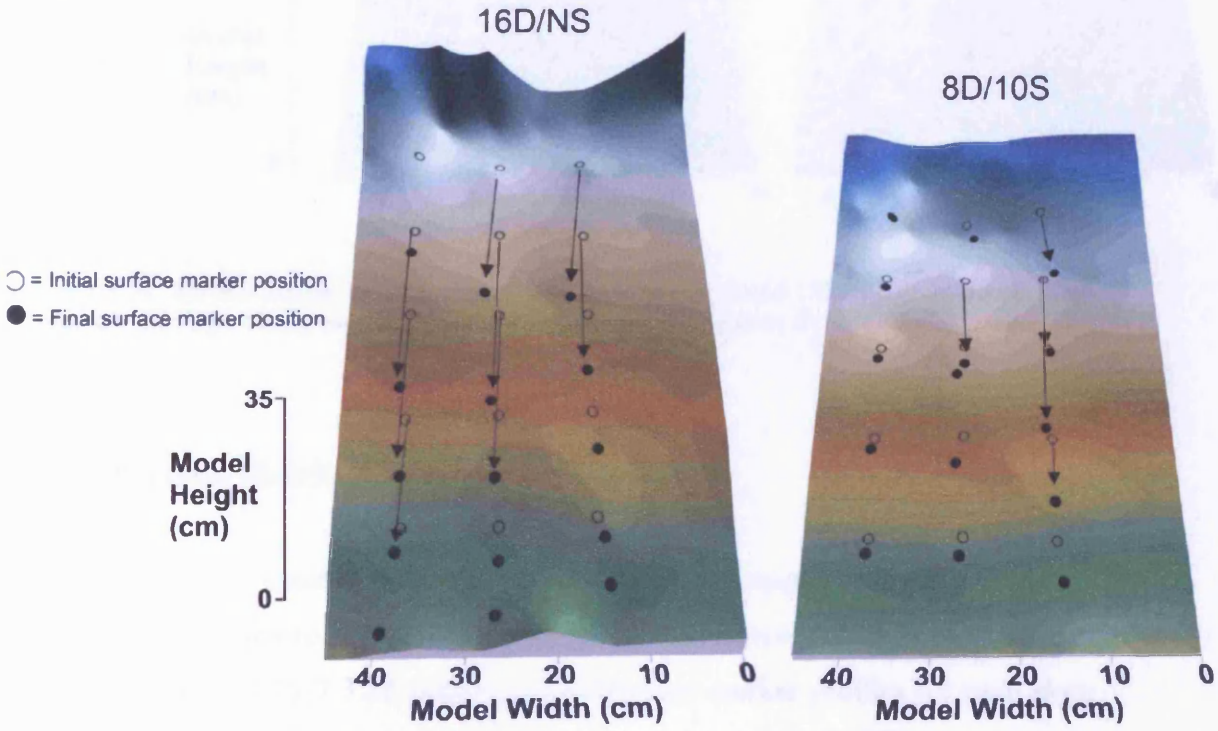

Figure 7.3.23. Surface marker movement during slope failure for Series 16D/NS and 8D/10S. Note: Contoured shading reflects surface deformation outlined in Figures 7.3.2 (16D/NS) and 7.3.4 (8D/10S).

Note that in many cases successive lines of markers moved past the original locations of the next line downslope, so that to match final location to original location in Figures 7.3.23 and 7.3.24 it is necessary to start with the lowermost markers and trace these back to the lowermost starting locations (see arrows). It is clear that movement was greatest on the 16° and 12° slopes, and in the case of model 8D/10S, most movement was concentrated within a bowl-shaped area in the upper right mid-slope. Landsliding was initiated and movement was greatest in the upper and central slope regions where frost heave and therefore soil ice contents were generally highest (see section 7.3.1).

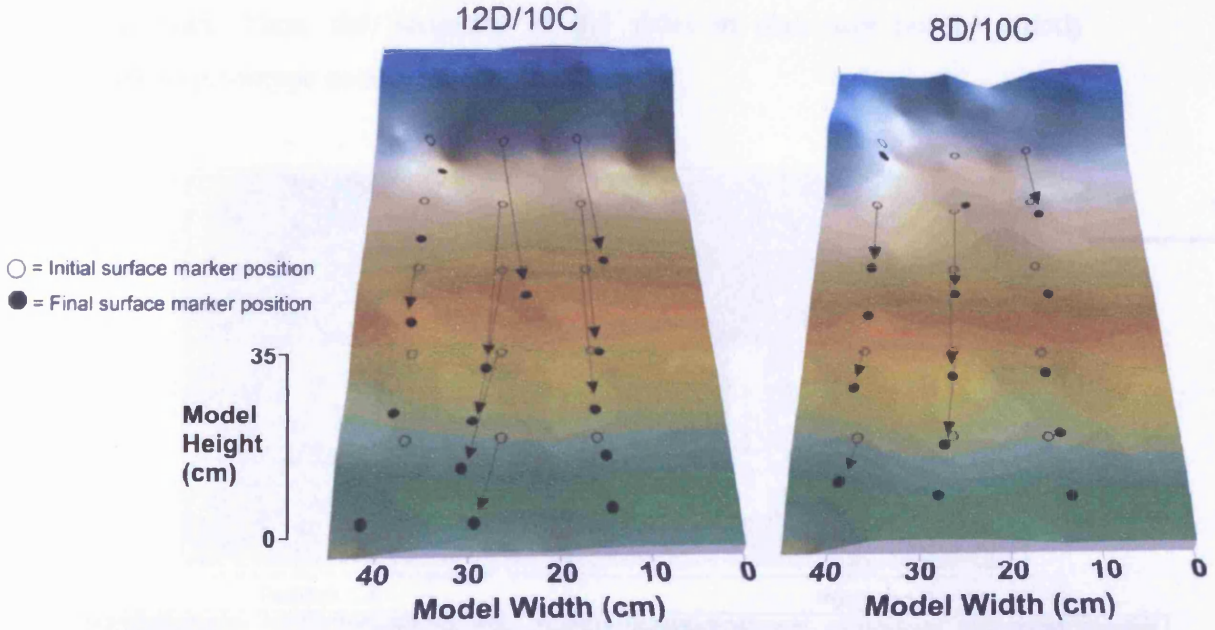

Figure 7.3.24. Surface marker movement during slope failure for Series 12D/10C and 8D/10C. Note: Contoured shading reflects surface deformation outlined in Figures 7.3.6 (12D/10C) and 7.3.8 (8D/10C).

7.3.6. Subsurface Movement

Slope models were excavated to analyse subsurface deformation patterns and collect samples for micromorphological analysis using the technique outlined in section 5.6.1. Figures 7.3.25-7.3.28 present the subsurface marker profiles for each slope failure. The large amount of subsurface disruption made it difficult to present complete profiles within the key area of interest defined within Figure 5.5.12 or to calculate the amount of volumetric displacement. Subsurface observations have

provided a key insight into the depth of the shear zone within each slope failure. The reorganisation of grain fabric can be clearly identified within all slope models as distinct slip surfaces have developed over which the slide mass has moved, as a planar slip. A shear zone occurred within all slope models at the model scale depth of between 40mm to 55mm (0.4m-0.55m). There is no clear correlation between the depth of model failure and slope gradient, soil geotechnical properties, rate of thaw, or the thaw consolidation ratio. However, the translational nature of sliding was clearly controlled by the geometry of the underlying still-frozen soil surface. It is likely that edge effects reduced displacement of the landslide adjacent to the container walls, and the landslide runout zone was limited by the presence of the lower end wall. Thus, the geometry of the slides in plan may not be strictly comparable to prototype conditions.

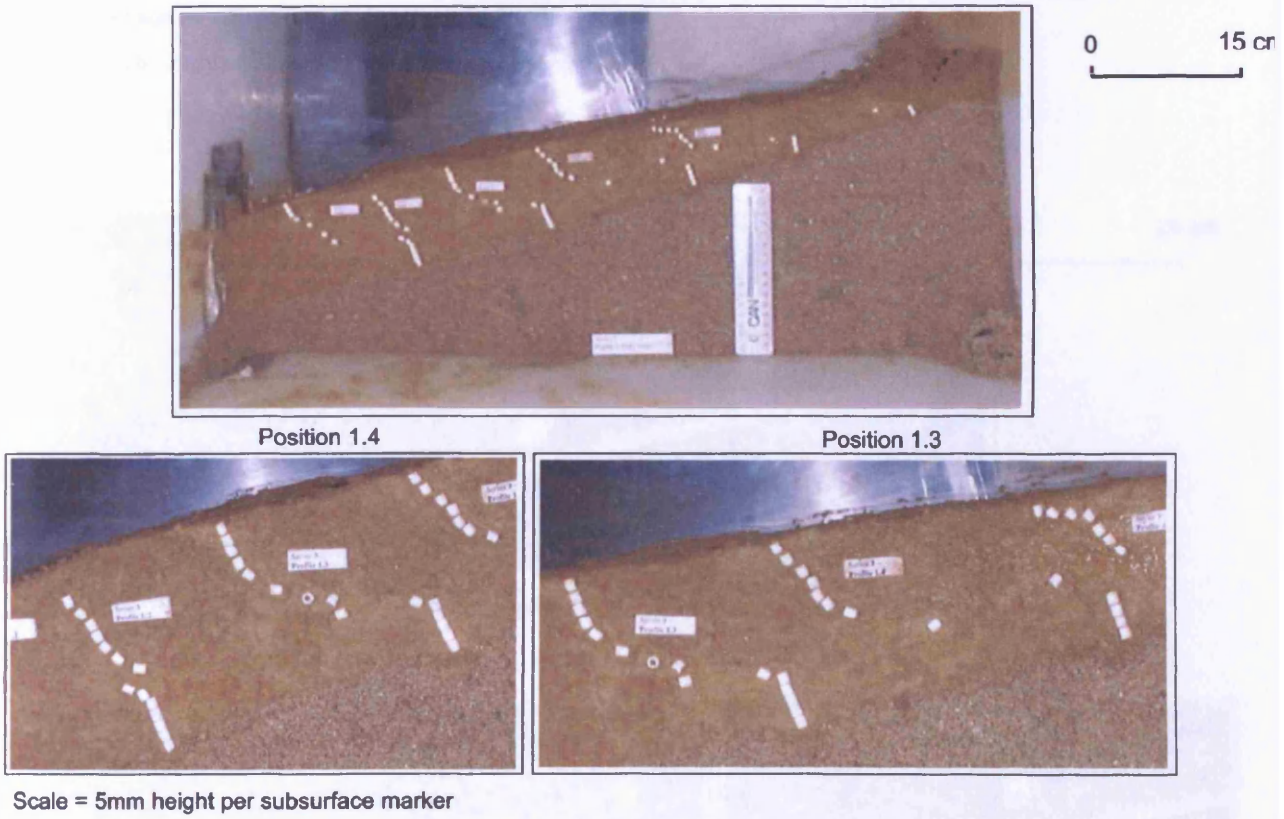

Figure 7.3.25. Subsurface movement from excavation profile one of Series 16D/NS.

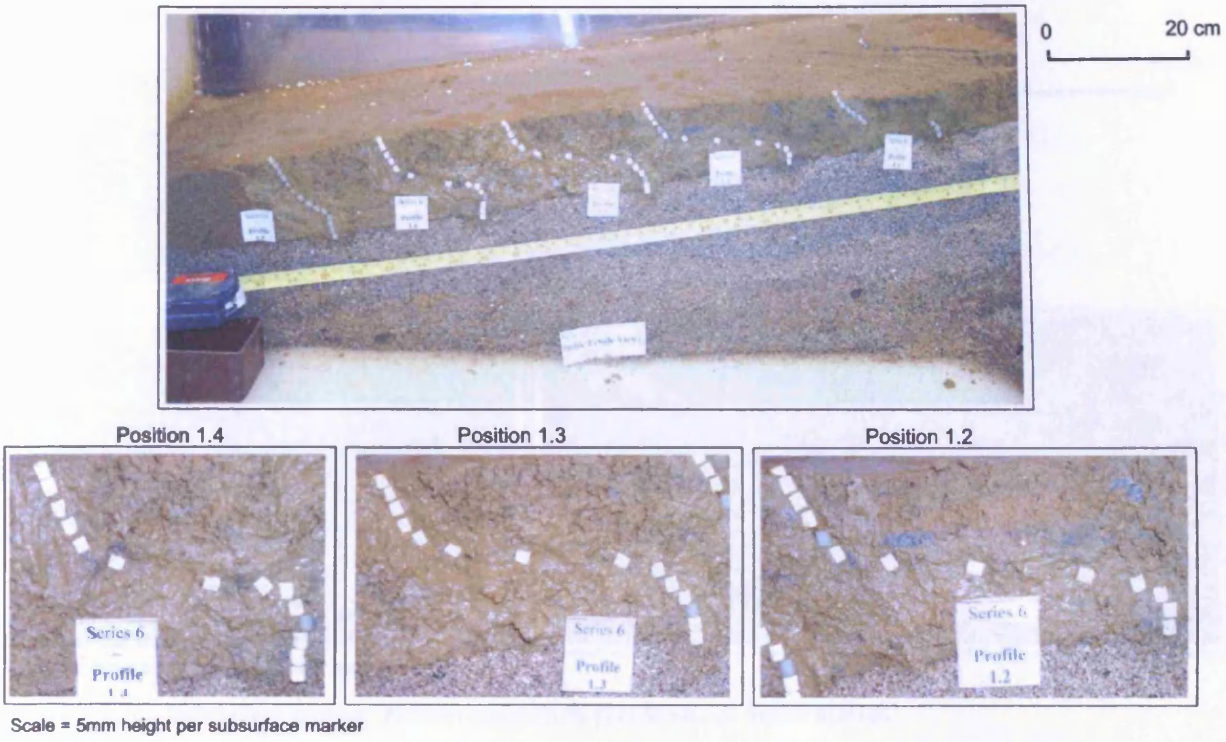

Figure 7.3.26. Subsurface movement from excavation profile one of Series 8D/10S.

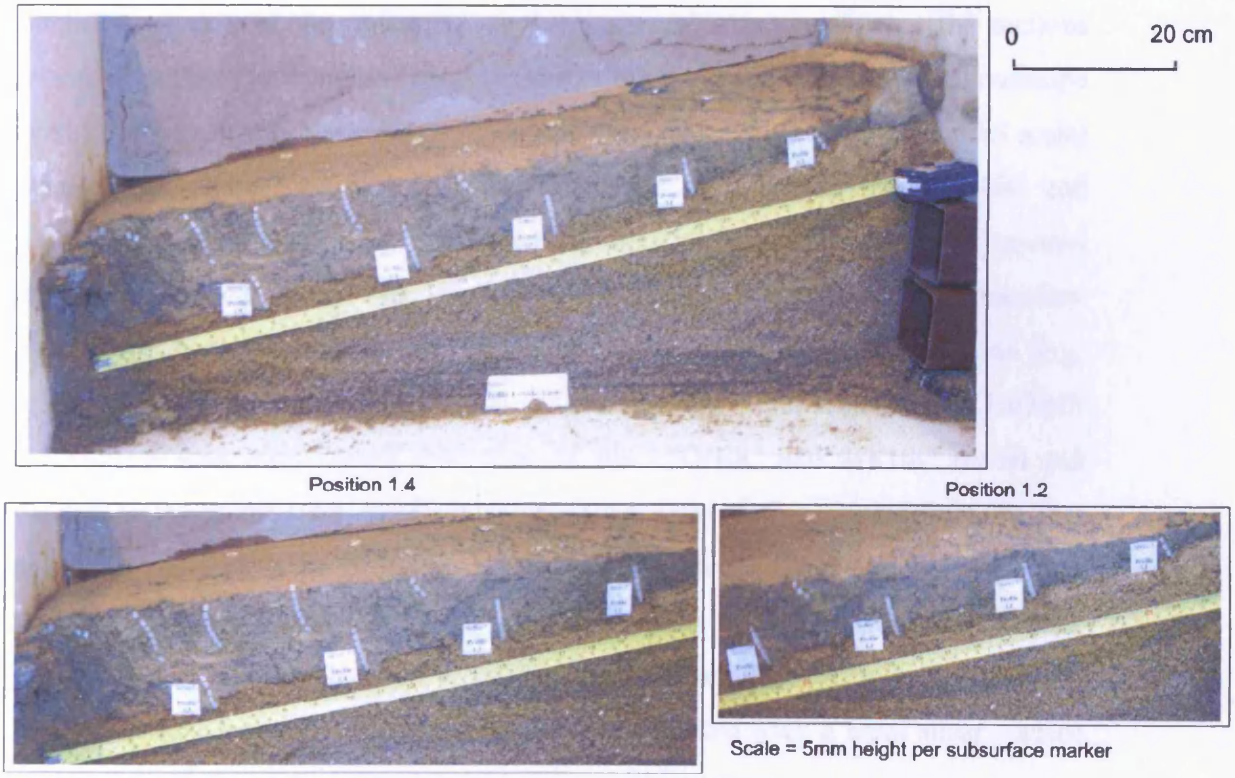

Figure 7.3.27. Subsurface movement from excavation profile one of Series 12D/10C.

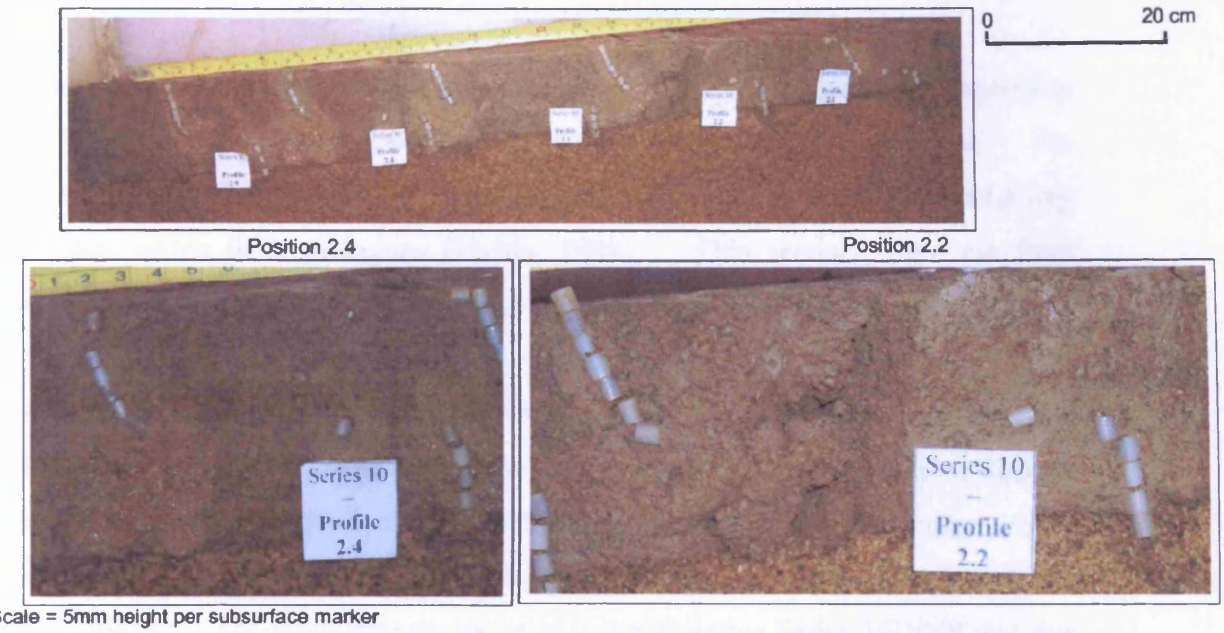

Figure 7.3.28. Subsurface movement from excavation profile one of Series 8D/10C.

The process of displacement was clearly somewhat different between the non-clay models 16D/NS and 8D/10S and the clay-enhanced models 18D/10C and 8D/10C. Careful inspection of the deformed displacement columns reveals that the sections embedded within the displaced mass of soil in the non-clay models show downslope convexity with strong attenuation of the columns in the lower 10mm (model scale) giving typical "flow" profiles (e.g. fig. 7.3.25). In contrast, the 12D/10C and 8D/10C models show relatively undeformed though slightly forward tilted column sections embedded within the slipped soil mass, with a clean sharp boundary between the displaced landslipped soil and the underlying undisturbed basal soil (e.g. fig. 7.3.28). It appears, therefore, that the fact that the Liquid Limits of the 16D/NS and 8D/10S soils were lower than that of the 12D/10C and 8D/10C model soil resulted in lower cohesive (undrained) shear strengths during slope failure, so that landsliding was by a combination of flow and slide. Thus the slope failures observed in models 16D/NS and 8D/10S are probably best described as flow-slides. In contrast, the failures observed in models 12D/10C and 8D/10C were more similar to planar landslides, with unit displacement concentrated over a basal shear surface and relatively little internal deformation of the displaced mass.

7.3.7. Soil Micromorphology

Microfabric analyses can provide an insight into the different mechanisms operating during slope failure (Van Vliet-Lanoë *et al.*, 1984; Van Vliet-Lanoë, 1985). The current investigation identified microstructures that are indicative of landsliding processes within field analogues (Harris, 1998). Thin sections were cut from undisturbed impregnated samples, with all sections in the vertical plane.

Figure 7.3.29 shows a potential shear surface within the lower shear zone of Series 16D/NS. The displaced soil above the slip surface has a high density of vesicles that are indicative of liquefaction of wet soils containing some air (Harris, 1983). The sample was taken from the lower slope in the region of rapid soil accumulation during failure. The slow-slide response of material within Series 16D/NS was due to the high Liquidity Index, relatively steep slope gradient and the high pore pressures generated during thaw – it has already been noted that this series showed a distinctive pore pressure pattern during post-failure reconsolidation.

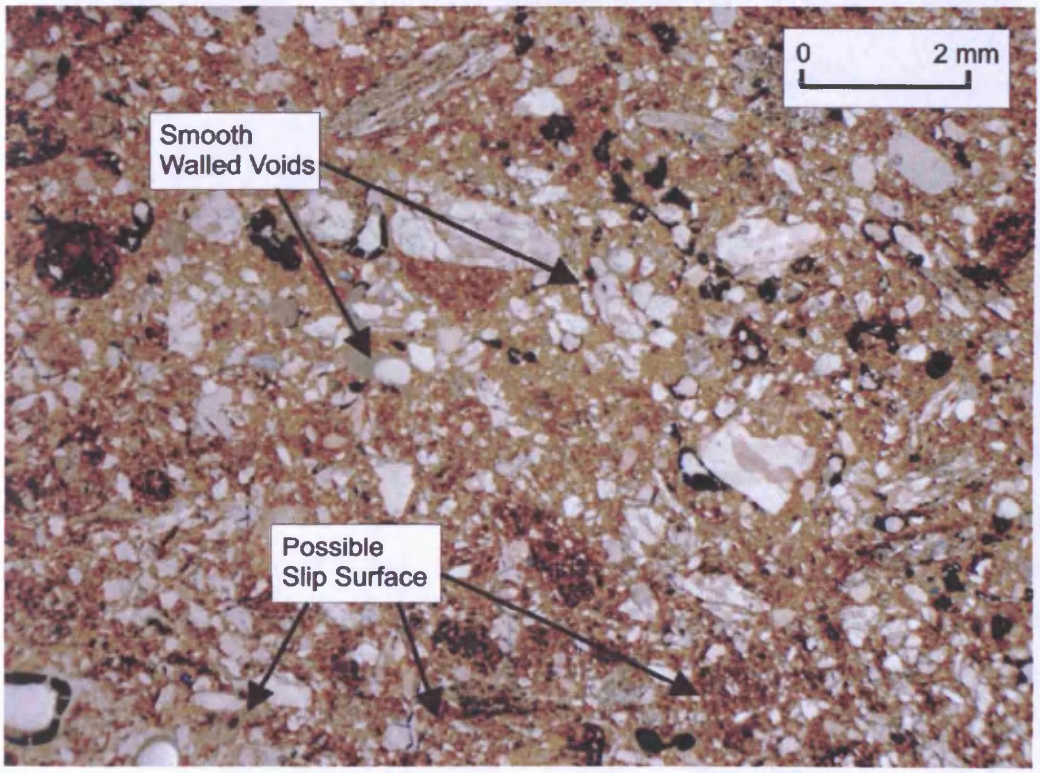

Figure 7.3.29. Vertical thin-section from slope model 16D/NS (transect position 1.5) after one freeze/thaw cycle. Note: Photomicrograph taken with crossed polarised light.

Figure 7.3.30 also presents evidence for soil flow from Series 8D/10S. Here a flow structure has developed surrounding an entrained clast, i.e. a disturbed wake of fine plasma around and behind the clast. This clear suggestion of matrix deformation around a sand grain, with a smooth streamlined leading side (lower left part of sand grain) and a more diffuse zone of denser matrix trailing to the right of the grain, gives excellent evidence for a flow-like deformation of the displaced soil. The rotation of sand grains during failure may have created further disruption features that may have become infilled with fine matrix during post-failure consolidation.

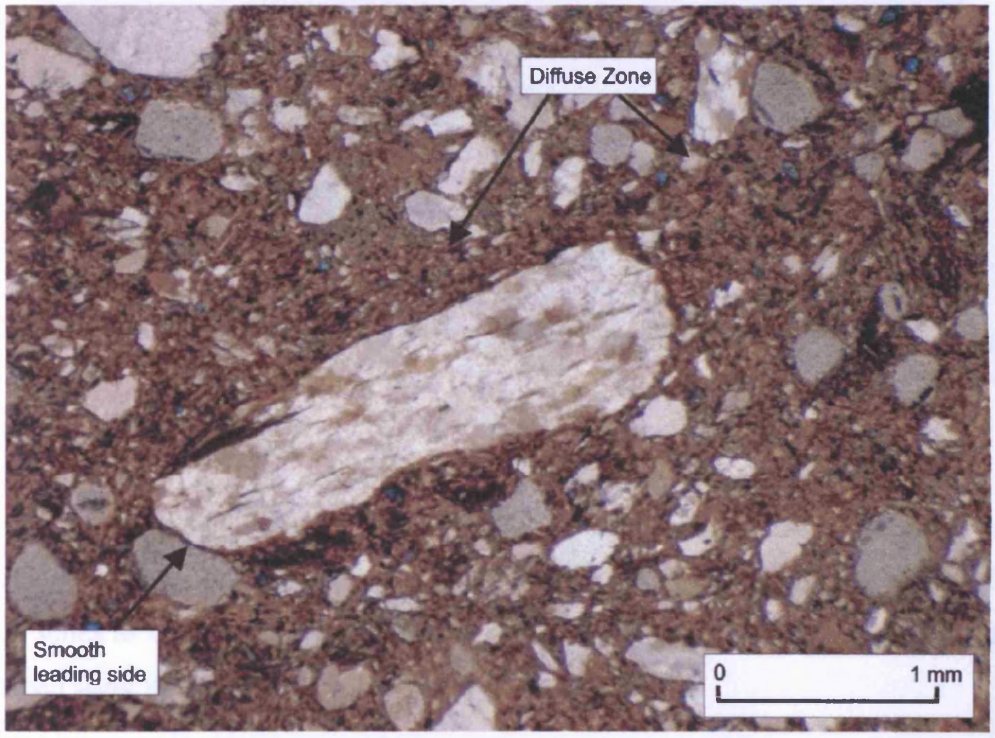

Figure 7.3.30. Vertical thin-section from slope model 8D/10S (transect position 1.3) after two freeze/thaw cycles. Note: Photomicrograph taken with partially cross polarised light.

Figure 7.3.31, taken from the base of the displaced soil in Series 8D/10S shows the accumulation of silt within a wavy planar discontinuity that is interpreted as a micro-shear over which the soil above has moved. Also visible are numerous smooth-walled vesicles, providing further evidence of matrix collapse and flow, trapping air as smooth-walled bubbles within the very soft soil. Thus, the micromorphological evidence may be used to support the contention that the observed slope failures in both models 16D/NS and 8D/10S may be classified as flow-slides over a still-frozen substrate. Due to problems with sample impregnation within the clay-enhanced soils, thin sections were not available for 12D/10C and 8D/10C.

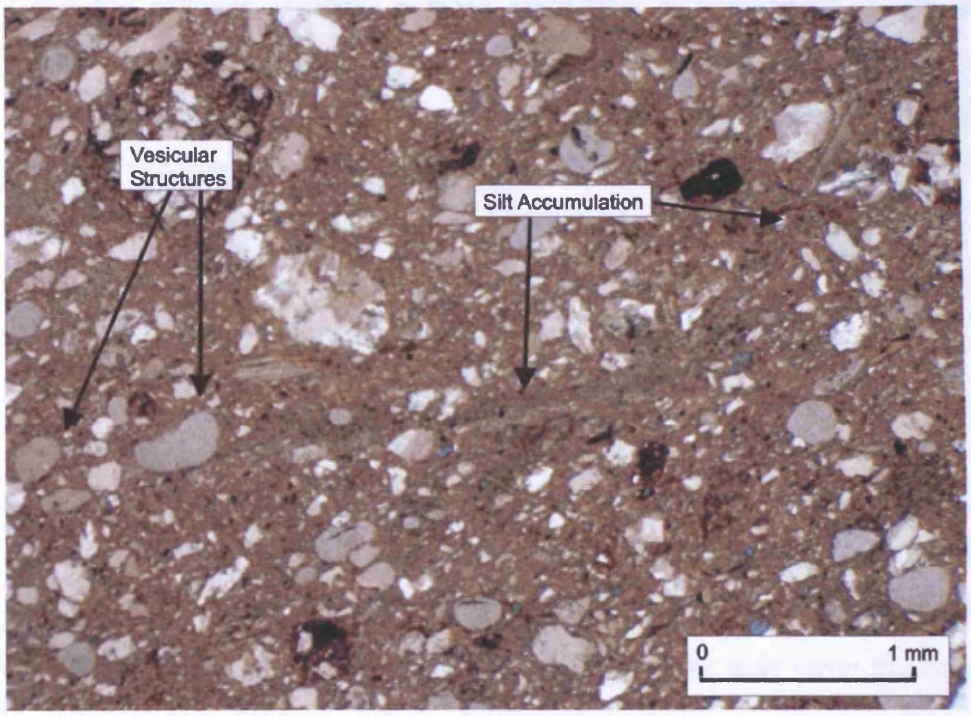

Figure 7.3.31. Vertical thin-section from slope model 8D/10S (transect position 1.3) after two freeze/thaw cycles. Note: Photomicrograph taken with partially cross polarised light.

7.4. Slope Stability Analysis

Slope movement will occur where destabilising driving forces (shear stress) exceed resisting forces (shear strength) at a particular location. Slopes can exist within three states as defined by the factor of safety (F_S) for a particular slope, i.e. the ratio between shear strength and shear stress described below:

$$F_S = s / \tau \qquad (7.5)$$

Where s is the total shear strength along a specific shear plane and τ the total amount of shear stress developed along the same plane. Where the shear strength is significantly greater than shear stress then the slope will be classified as stable (F_S >1.3), where shear strength is exceeded by shear stress then continuous or intermittent movement will occur and the slope is described as actively unstable (F_S < 1), the third classification is based upon a slope's response to transient changes in shear strength and is known as a conditionally stable slope with values of stable F_S between 1 and 1.3.

Slope stability analysis provides a good theoretical understanding of the factors which generate slope movements. However, soil parameters and pore water conditions may vary across a slope, so that most analytical solutions simplify the complexity of natural slopes. Given the slope geometry and internal structure of the landslides described in this chapter, the simplest approach to stability analysis is to apply an infinite planar slope model. This approach was used by Harris *et al.* (1995) in their analysis of full-scale modelling of gelifluction processes.

- *The Infinite Planar Slope Model*

Given an infinite planar slope of gradient β, with the potential slip surface at a depth Z and both slip surface and groundwater seepage parallel to the ground surface, soil internal angle of friction with respect to pore pressures $\emptyset'$, pore water pressure u and soil unit weight γ_s, for an effectively cohesionless soil we may write the Factor of Safety against failure as:

$$F = \frac{\tan\phi'}{\tan\beta}\left(1-\frac{u}{\gamma_s Z\cos^2\beta}\right) \qquad (7.6)$$

Since pore pressures at the time of failure were measured, we may substitute known values of $\emptyset'$, β, Z and γ_s in Equation 7.6 to determine the Factor of Safety when failure occurred in the four landslide models discussed above.

- *Series 16D/NS*

Figure 7.4.1 shows the relationship between pore pressure and depth for a Factor of Safety of 1. The critical location was the upper slope 0.5m depth (prototype) transducer. The recorded pore pressure suggests a Factor of Safety of less than unity, as do the maximum values at shallower depths. It may be that the shear strength of the soil was somewhat higher than the laboratory analysis suggested, but most likely the edge effects, which are not considered in this analysis, were contributing to the stability of this slope. The high pore pressures recorded for the 0.5m lower slope transducer are not explained. This may reflect very local seepage

pressures that were not generally applicable to the lower slope zone, or an error in calibration of this transducer.

- *Series 8D/10S*

Data for model 8D/10S is essentially identical to that for 16D/NS, with the stability model slightly under estimating soil shear strength, though again edge effects may be significant, particularly for the shallower transducer. The high maximum value in the 0.5m lower slope transducer was recorded post failure when the thawing transducer was buried by the displaced landslide mass (see fig. 7.4.2).

- *Series 12D/10C*

The stability analysis presented within Figure 7.4.3 suggests that pore pressures were all in excess of that necessary to cause a planar slope failure. The reason for this may be that the shear strength parameters measured for this soil may have under estimated cohesion (which was measured as zero). In shallow planar slides such as these, slight increments of cohesive strength have a major effect on increasing factor of safety, as was demonstrated for detachment slides in Ellesmere Island by Harris and Lewkowicz (2000). In addition, edge effects and the buttressing effect of the container end wall may have increased the stability of the thawing model slope and allowed these higher pore pressures to be generated.

- *Series 8D/10C*

The stability analysis undertaken within Figure 7.4.4 suggests that pore pressures were in excess of those necessary to cause a planar failure on this slope with the assumed soil properties. The model clearly behaved in a similar fashion to the 12° enhanced clay slope model, and the effects of cohesive strength and edge effects would have applied equally here.

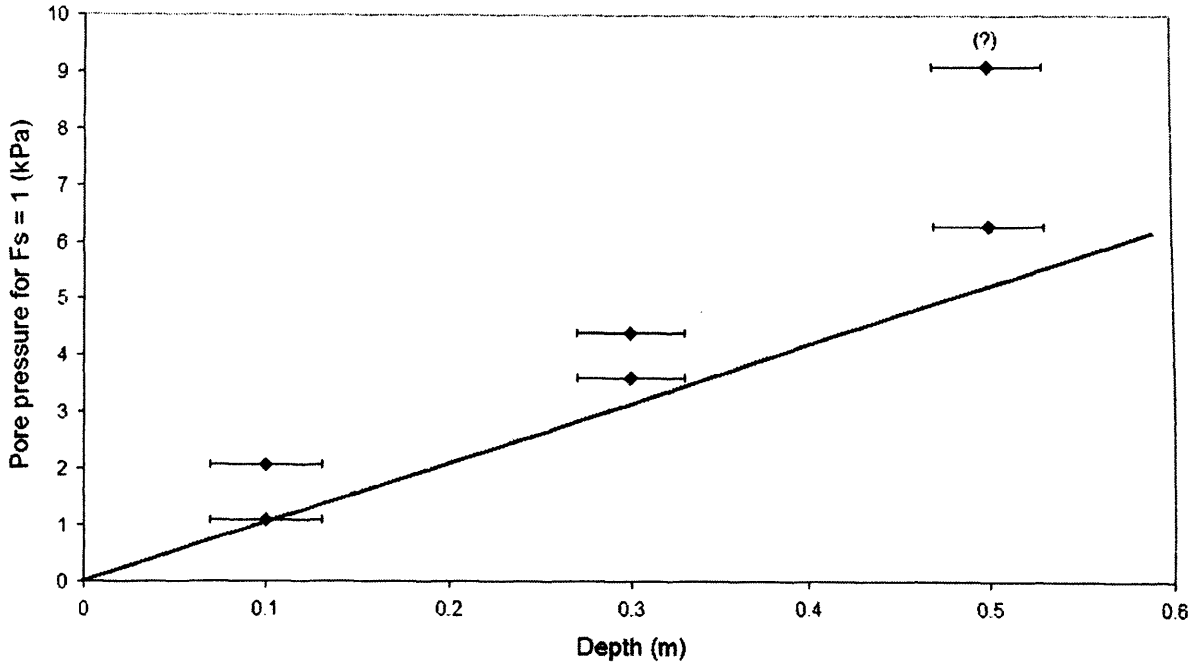

Figure 7.4.1. Slope stability analysis for Series 16D/NS. Assumed parameters: γ_s = 19.0 kN/m^3 Ø = 35°, Z = 0.5 m. The straight line indicates calculated pore pressure for F_s = 1 when the failure plane is at the transducer depth. Data points show highest pore pressures recorded at 0.1 m and 0.3 m (prototype scale), and the pore pressures at the time of failure at 0.5 m. In all cases the upper slope transducer recorded a lower value than the lower slope transducer.

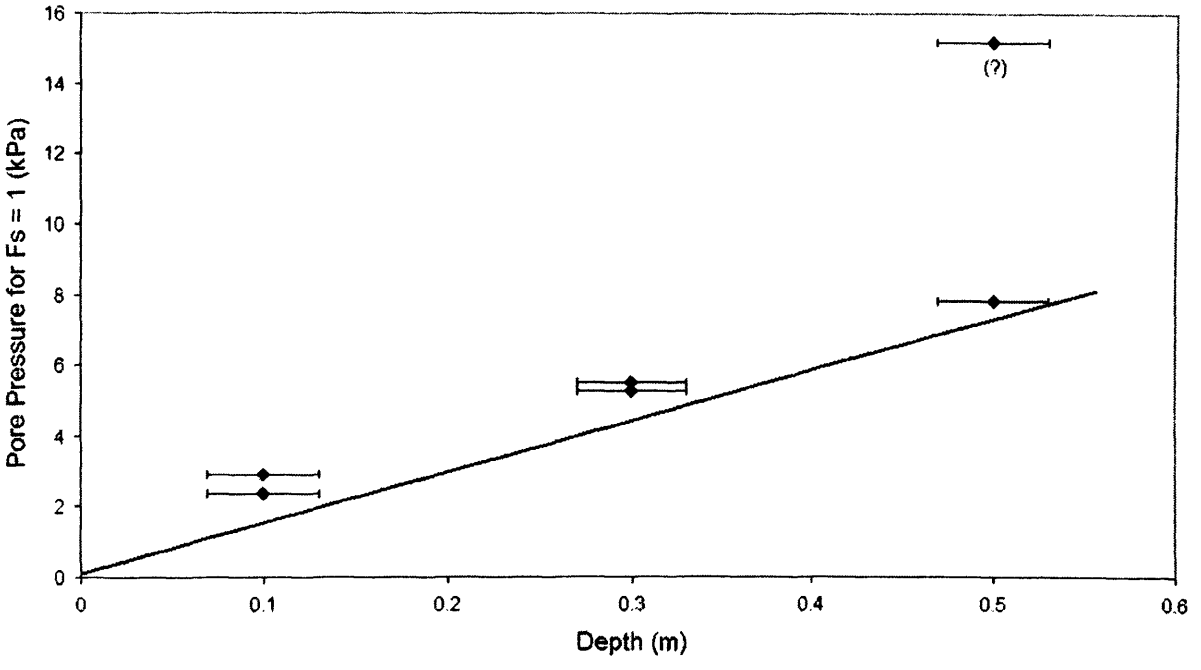

Figure 7.4.2. Slope stability analysis for Series 8D/10S. Assumed parameters: γ_s = 19.0 kN/m^3 Ø = 33°. The straight line indicates calculated pore pressure for F_s = 1 when the failure plane is at the transducer depth. Data points show highest pore pressures recorded at 0.1 m and 0.3 m (prototype scale), and the pore pressures at the time of failure at 0.5 m. In all cases the upper slope transducer recorded a lower value than the lower slope transducer.

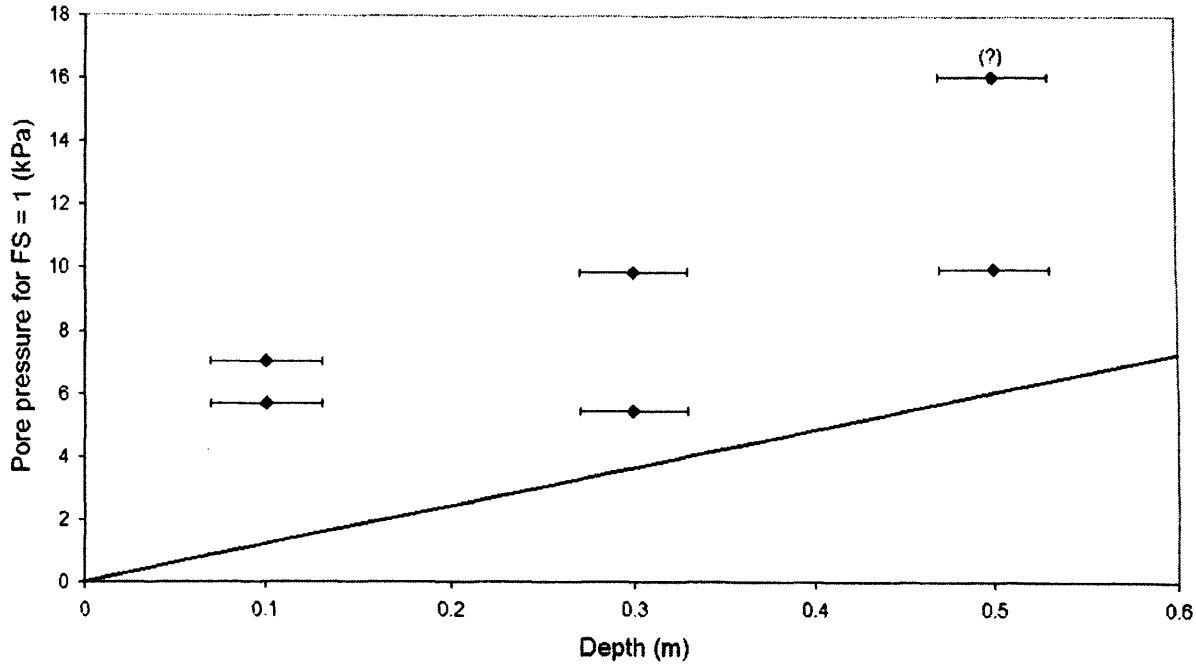

Figure 7.4.3. Slope stability analysis for Series 12D/10C. Assumed parameters: γ_s = 19.0 kN/m^3 Ø = 32°, Z = 0.5 m. The straight line indicates calculated pore pressure for F_s = 1 when the failure plane is at the transducer depth. Data points show highest pore pressures recorded at 0.1 m and 0.3 m (prototype scale), and the pore pressures at the time of failure at 0.5 m. In all cases the upper slope transducer recorded a lower value than the lower slope transducer.

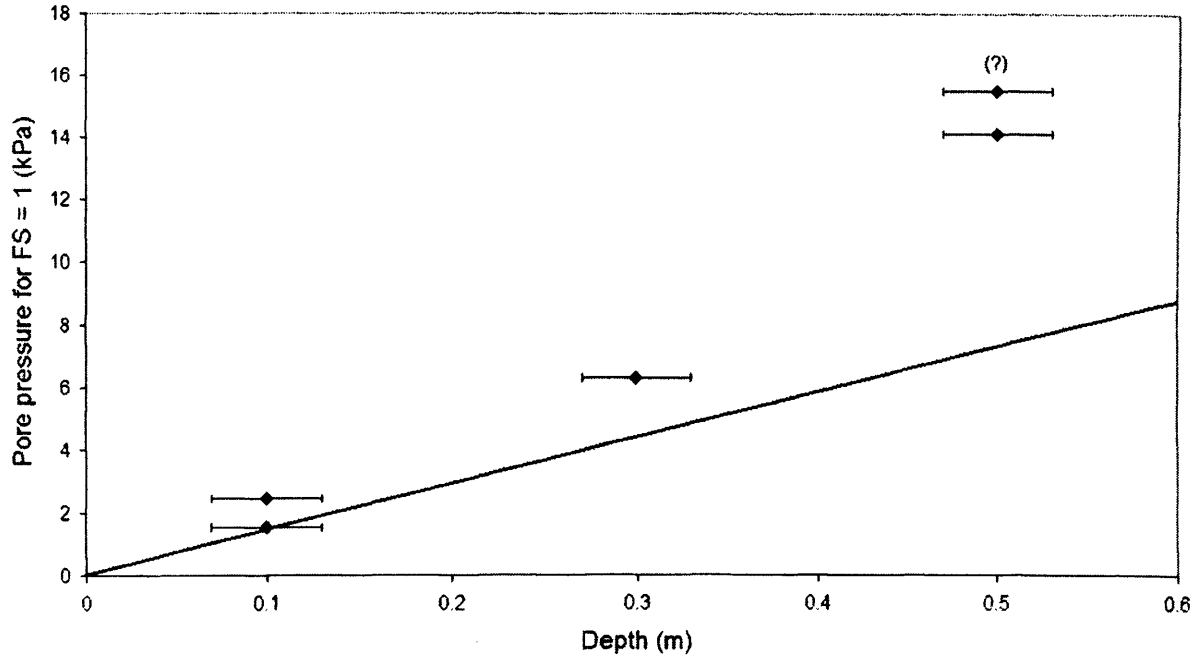

Figure 7.4.4. Slope stability analysis for Series 8D/10C. Assumed parameters: γ_s = 19.0 kN/m^3 Ø = 33°, Z = 0.5 m. The straight line indicates calculated pore pressure for F_s = 1 when the failure plane is at the transducer depth. Data points show highest pore pressures recorded at 0.1 m and 0.3 m (prototype scale), and the pore pressures at the time of failure at 0.5 m. In all cases the upper slope transducer recorded a lower value than the lower slope transducer.

7.5. Conclusions

- Relatively high pore pressures were recorded in all models, and an analysis of slope stability suggests that edge effects and the buttressing effect of the end wall may have enhanced the stability of these models.
- In all cases slope failure occurred when thawing had progressed to a model depth of around 50 mm (prototype depth 0.5m).
- Mechanisms of movement were consistent between Series 16D/NS and Series 8D/10S, which both failed as flow slides.
- Micromorphological analysis supported the evidence from excavated displacement columns that during failure in both these models the displaced soil mass underwent some flow-like shearing, particularly in the basal 10 mm (0.1 m).
- Series 12D/10C and 8D/10C exhibited failure profiles similar to a true planar slide-with much less internal deformation of the displaced slide blocks. Shearing was concentrated in the basal shear plane.
- Although the experiments described here were designed to model slow solifluction, the amount of data retrieved during landsliding, particularly the evolution of the slide as captured on the overhead video camera provides abundant detail on mechanisms of failure, information that is rarely available from field studies.
- If experiments are undertaken in future to model periglacial slope instability of this nature, it is recommended that models be tested at higher gravitational acceleration to increase the size of prototype modelled, and therefore allow the inclusion of a footslope run-out zone.

CHAPTER EIGHT : Field Monitoring and Data Validation

In this chapter the monitoring of an active gelifluction site in Dovrefjell, southern Norway is described. The chapter includes a summary of the characteristics of the chosen field site, and a description on the construction of the field apparatus. The chapter will also present preliminary data from a full year of field monitoring. The aim of the field-monitoring programme was to provide field data to validate the laboratory-modelling programme, and the significance of the data collected from Dovrefjell is discussed in this context.

The field monitoring station was instrumented to measure soil movement, surface frost heave, thaw consolidation, porewater pressure and thermal regime. To facilitate continuous automated electronic observations a well-engineered rigid structure was designed to support key instrumentation (see fig. 8.0.1). The complete field monitoring structure was planned to protect and maintain functional apparatus within the harsh mountain periglacial regime.

Figure 8.0.1. The fully constructed field-monitoring station. (Photograph: Charles Harris). Note: the turf-banked solifluction lobes with risers of 0.5 – 1.25 m.

Direct observation of natural processes provides the most useful source of information when formulating or testing theoretical hypotheses. For this reason field monitoring techniques have undergone rapid development towards high precision

approaches during the later 20th century (French, 2003). The major techniques for evaluating periglacial processes have evolved from mapping and describing geomorphic features towards more quantitative observation that captures large amounts of numerical data. Dynamic observations of solifluction were initially undertaken through geodetic survey (e.g. Washburn, 1967) or manual measurement via markers, strain probes, rods, etc (e.g. Rudberg, 1964; Williams, 1962). Such periglacial studies are required over long periods of time to enable inter-annual variation and long-term trends to be fully observed, but due to a lack of robust automated devices the majority of studies operated over intervals of several months or years (Matsuoka & Humlum, 2003).

The difficulties involved in gathering long-term field measurements within the periglacial regime led researchers to undertake laboratory simulations to reproduce the slow periglacial processes such as solifluction, frost sorting, frost weathering of rocks, and cryostructure formation (e.g. Corte, 1966; Harris *et al.*, 1997; Murton *et al.*, 2001). Laboratory investigations allowed direct observation and measurement of periglacial processes but necessitated the collection of corroborating field evidence to confirm that observed patterns were indicative of prevalent prototype processes. The coupling of laboratory investigation and field monitoring began in the 1990's; when the development of sophisticated electronic data-loggers permitted long-term, concurrent and continuous observation of both processes and atmospheric parameters (e.g. Matsuoka *et al.*, 1997; Lewkowicz, 1992). The use of automatic monitoring has therefore become a research standard for observing periglacial geomorphic processes such as frost wedging, frost heave, solifluction, frost sorting and ice-wedge cracking (e.g. Thorn, 2003).

The rate of solifluction displacement is dependent upon site-specific topographic and environmental conditions, and for this reason observed gelifluction movements are highly variable at all scales, e.g. even on a single lobe (Benedict, 1970). Soil moisture is a key factor controlling rates of gelifluction; where the moisture content of a particular site depends on small scale variables such as soil properties, ground ice accumulation, snowmelt, and surface/subsurface runoff (Jaesche *et al.*, 2003; Matsuoka, 2001). It has also been shown that solifluction activity is correlated to annual frost depth and mean annual air temperature (see fig. 2.3.4). It is therefore

necessary to monitor soil movement and concurrent localised thermal and hydrological conditions in order to calibrate existing theoretical models and laboratory simulations of the phenomena (Thorn, 2003). The year-round field monitoring described here will provide greater understanding of the role of ground freezing and soil hydrology, which when combined with other datasets will parameterise solifluction within different geoenvironmental environments (e.g. Smith, 1988; Yamada *et al.*, 2000; Matsuoka, 1996).

8.1. Field Site

The chosen field site was within a mountainous region of Southern Norway (62° 15'N, 9° 20'E). Dovrefjell is approximately 160km long and 40km wide and includes a protected National Park with an area of 256km^2. The field apparatus was installed during June 2001 in an area of active solifluction on the slopes of Steinhoi near Folldal, Dovrefjell (see fig. 8.1.1). Dovrefjell is an area rich in deglaciation landforms and contains well-developed moraines generated by the last activity of the Weichselian ice sheet in southern Norway.

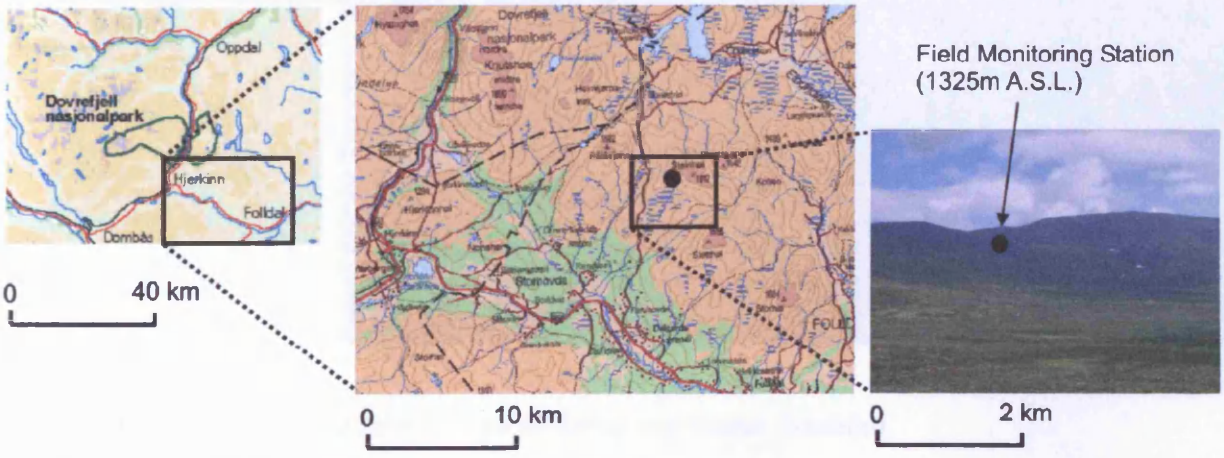

Figure 8.1.1. Location of field-monitoring site in Dovrefjell, Southern Norway.

Throughout the region there are variable thicknesses of surficial till and glacio-fluvial deposits, although weathered regolith and blockfields dominate the summit areas (see fig. 8.1.2) (Sollid *et al.*, 2003). The lower limit of the mountain permafrost on Dovrefjell has been mapped to approximately 1500m A.S.L, although zones of sporadic permafrost are present within palsa bogs at elevations down to

approximately 1000m A.S.L (Isaksen *et al.*, 2002). The mean annual air temperature (MAAT) for Dovrefjell was recorded as –0.1°C and the mean annual precipitation 435mm for the period 1961-1990 (Sollid *et al.*, 2003).

The overall research site was chosen as a good example of an active solifluction field (see fig. 8.1.2). The relative accessibility for technical support within Dovrefjell has allowed a number of research projects to be undertaken, and it was in this region that some of the pioneering field studies by Williams were undertaken (Williams, 1957a & 1957b). More recently, borehole monitoring of permafrost temperatures has been initiated (Sollid *et al.*, 2003). For logistical reasons the chosen field site was within 5km of the University of Oslo Hjerkinn field research station and within 1.5km of road access. The field monitoring station was established on a turf-banked lobe that suggested active contemporary movement.

Figure 8.1.2. Extensive active solifluction field at Stenhoi near Folldal, Dovrefjell.

8.2. Field Measurements and Monitoring

A variety of manual and electronic techniques were utilised to monitor the gelifluction lobe. The adopted methodology incorporated adaptations suggested by Smith *et al.* (1999) who utilised similar apparatus at Finse, central Norway. The approach attempted to collect both short and long-term datasets in order to

characterise movement for the current investigation whilst enabling field parameterisation for any future laboratory studies.

A manual survey was conducted to record local gelifluction lobe characteristics. The survey was conducted to examine the degree to which the chosen field station was indicative of local topography of the Stenhoi gelifluction field. The survey utilised a handheld Magellan Global Positioning System (GPS) in order to record lobe altitude and orientation, a clinometer determined lobe azimuth, and a measuring tape was used to assess lobe dimensions (width and height). The survey was conducted on sixty lobes within the local vicinity of the chosen field station. It should be noted that a single mobile GPS unit was used without a geostationary base station (e.g. Little *et al.*, 2003). The lack of a differential carrier-phase GPS measurement created an inherent nominal accuracy of approximately 100 metres within the captured dataset (Longley *et al.*, 1999; Rees, 2001). In addition the field station was completely surveyed and mapped using compass and tape (see fig. 8.2.1).

The selected electronic monitoring station consisted of a south-facing gelifluction lobe of gradient 13° at an altitude of 1325m A.S.L with approximate dimensions of 13.1m (width) by 19.8m (length) (see fig. 8.2.1). The monitoring station comprised a tubular steel frame with associated instrumentation. Soil and air temperatures were measured using 13 thermistor probes. Air temperatures were detected by 4 probes shielded from direct insolation by white plastic tubing, and fixed to the 2 m high vertical aluminium scaffold tube supporting the solar panel (fig. 8.2.1). The remaining thermistor probes were buried alongside six Druck PDCR81 transducers. Two strain gauges were placed on the horizontal bars of the support frame, to detect any distortion due to snow loading. Two 470 mm stroke water proof captive guided LVDTs were mounted on an aluminium track to form a fixed base triangle with the apex connected to an aluminium footplate attached into the ground surface via four 2cm deep anchor points. The footplate was securely embedded into the soil surface and progressive displacements due to frost heave, thaw consolidation, and gelifluction were detected by changes in the geometry of the LVDT triangle (for a laboratory example see Harris *et al.*, 1997).

Data were recorded by a Campbell CR23X data logger with multiplexer, with an average of ten readings per hour being recorded every hour. A mobile phone telemetry system allowed data download remotely, though problems with the aerial limited the success of this system. The monitoring station was powered through a solar panel that recharged a 12 volt lead-acid battery. Finally, five sets of Rudberg columns were installed to monitor long-term subsurface soil displacement (see fig. 2.3.1).

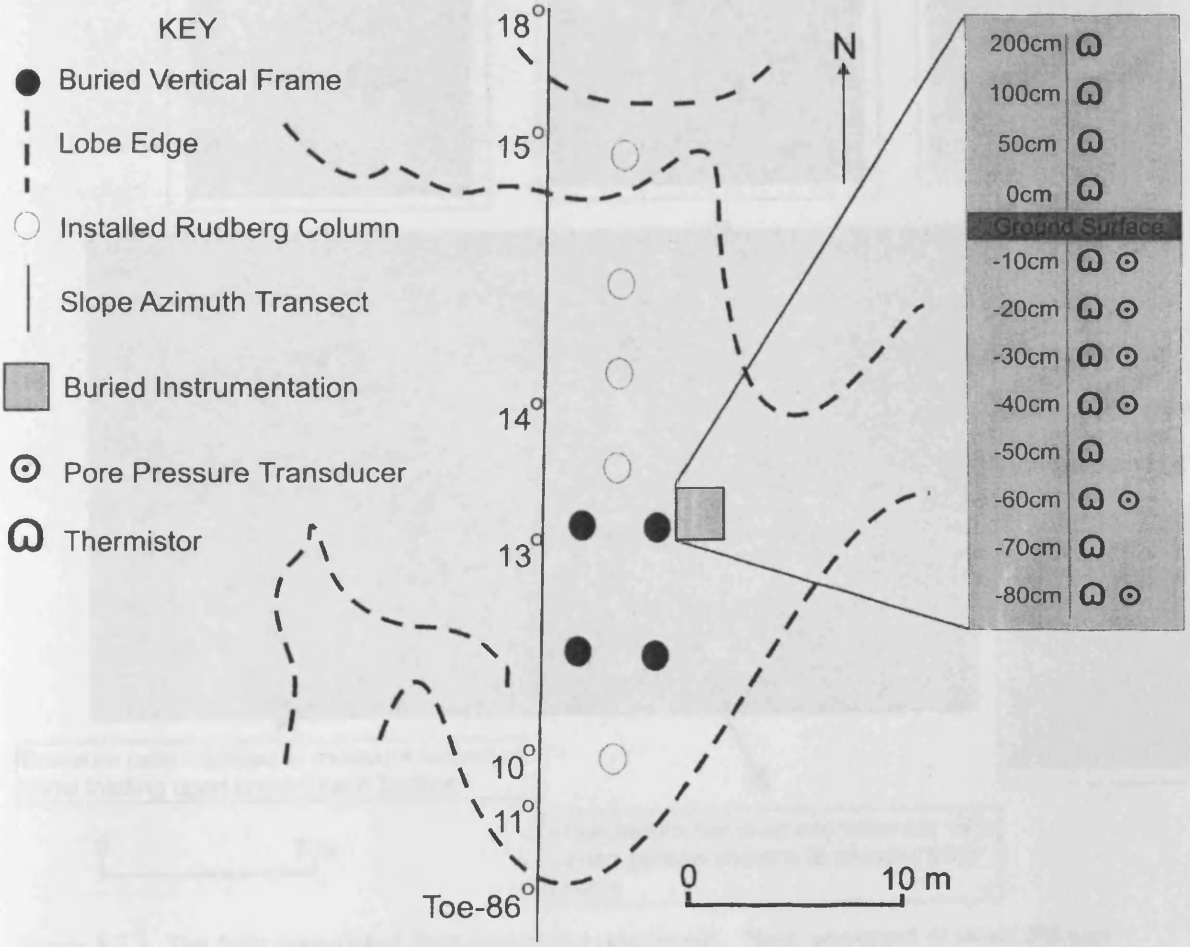

Figure 8.2.1. Sketch map of surveyed monitoring station.

The monitoring frame was fabricated from 48mm diameter steel tubing. Vertical members were installed into a 150mm borehole to a depth of 1.5m. The lower 0.5m was embedded into a concrete base and the upper 0.5m was lubricated with silicon grease and placed within a plastic sheath. The plastic sheath isolated the vertical steel member from the surrounding soil and minimised the effect of frost heaving upon the monitoring frame. The steel frame was assembled using pressed steel scaffold clips. The apparatus measured approximately 2m (width) by 3m (length)

(see fig. 8.2.2). The strain gauges allowed the effect of snow loading to be eliminated from any downslope displacement data.

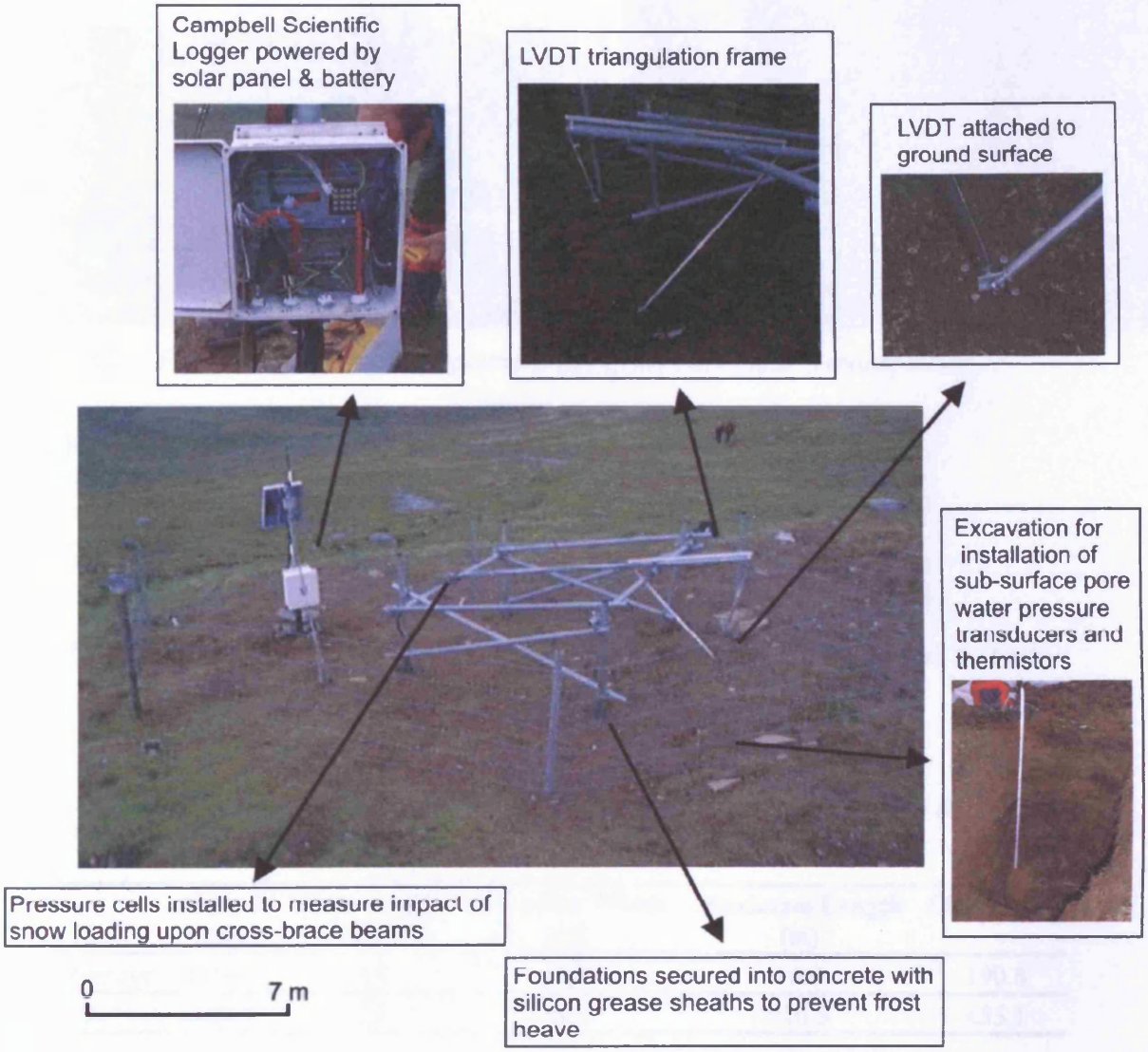

Figure 8.2.2. The fully operational field-monitoring equipment. Note: annotated to show different components.

It should be noted that a lightening strike caused equipment failure during November 2001. Heavy snowfall then resulted in breakage of an LVDT and loss of data between November 2001 and May 2002 (see fig. 8.2.3). However, a continuous record was obtained for the period May 2002 – July 2003, and the station continues to record at the present time.

Table 8.3.2. Soil grainsize for field monitoring site.

Gravel (%)	Sand (%)	Silt (%)	Clay (%)
23	54	21	2

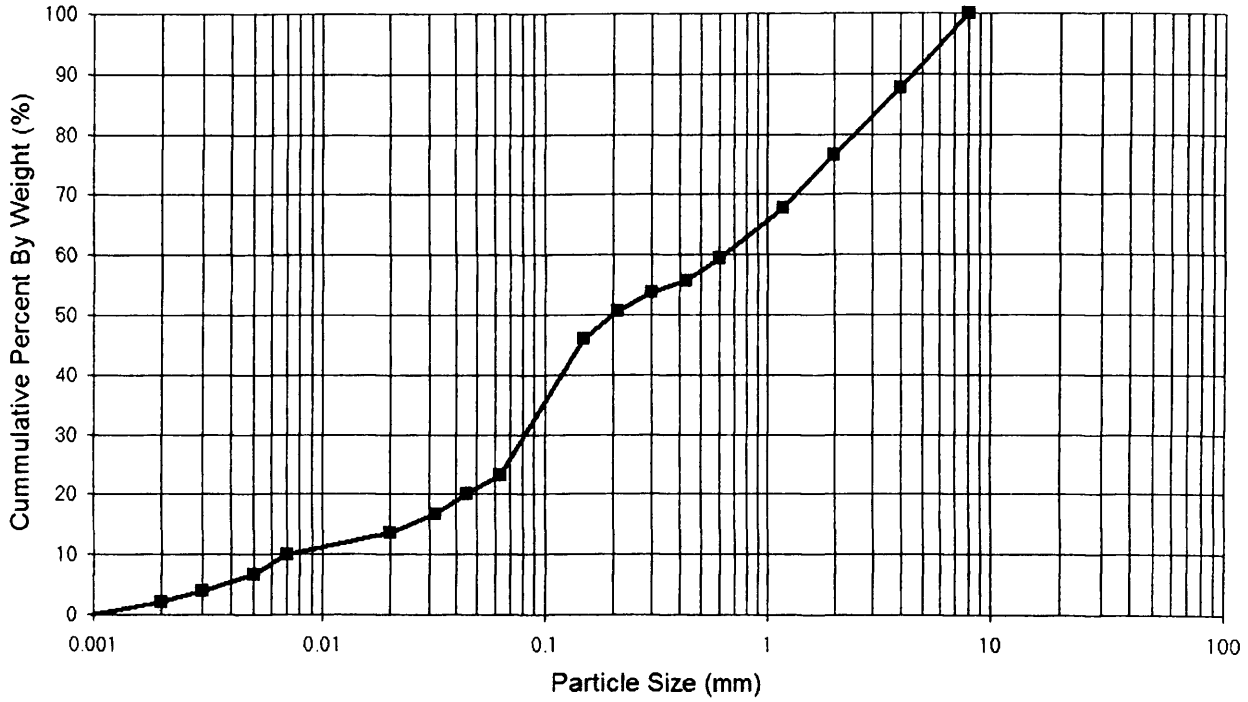

Figure 8.3.1. Cumulative frequency graph showing the particle size distribution for the field-monitoring site.

8.3.2. Electronic Field Monitoring (May 2002 – July 2003)

The electronic field study continuously monitored atmospheric conditions, ground thermal regime, subsurface pore pressure, and displacements of the ground surface for a total period of nineteen months. Results are summarised below.

- *Thermal Regime*

Tables 8.3.3 and 8.3.4 present the annual thermal regime measured for the atmospheric and subsurface thermocouple strings. The field site experienced low winter air temperatures of around –22°C (January 2003) and a summer high of 31°C (August 2002). It can be observed that there was a time lag between air temperature and soil temperature in the winter months associated with latent heat effects (the zero curtain) (see fig. 8.3.2). For example, the lowest minimum temperature was recorded above surface in January 2003 but the lowest soil

temperatures were recorded in February 2003 at 50cm depth and as late as March 2003 for the deepest thermocouple buried at 80cm depth. It should also be noted sub-zero ground temperature conditions only affected the upper 30cm of the soil profile. Snow cover was clearly a dominant factor in the observed ground thermal regime, severely limiting soil thermal response to atmospheric temperature fluctuations.

Table 8.3.3. Ground temperature readings gathered between May 2002 and July 2003. SD = Standard deviation.

	80 cm	70 cm	60 cm	50 cm	40 cm	30 cm	20 cm	20 cm	10 cm
Maximum (°C)	+8.85	+10.63	+9.93	+10.83	+11.57	+12.71	+13.38	+13.33	+16.16
Minimum (°C)	+0.27	+1.38	+0.35	+0.22	+0.04	-0.06	-0.04	-0.09	-0.27
Annual Average (°C)	+2.78	+4.05	+3.04	+2.98	+2.83	+2.89	+3.02	+2.97	+3.15
SD	±2.64	±2.72	±2.95	±3.27	±3.58	±3.92	±4.12	±4.12	±4.56

Table 8.3.4. Above surface temperature readings gathered between May 2002 and July 2003. SD =Standard deviation.

	0 cm (Surface)	50 cm (Air)	100 cm (Air)	200 cm (Air)
Maximum (°C)	+26.98	+31.84	+25.77	+26.58
Minimum (°C)	-4.13	-22.42	-22.21	-21.96
Annual Average (°C)	+3.11	+1.21	+0.27	+0.63
SD	±6.15	±9.48	±8.63	±8.80

Snow cover severely delayed frost penetration, insulating the soil from falling air temperatures in the autumn and early winter. For example, during January 2003 a temperature drop of 20.7°C did not modify thermal conditions within the upper 50cm of the soil profile and a 20°C range of air temperature in February 2003 was reduced to a 1°C range at 80cm depth (fig. 8.3.2). It is inferred from this data set that snow cover became established in the second week of September, since before this the ground surface temperatures responded rapidly to air temperature fluctuation, but after this date fluctuation was subdued and surface temperatures were below zero (fig. 8.3.3). Sixteen diurnal air temperature frost cycles were recorded prior to the arrival of snow cover, with five registering zero or sub zero temperatures at ground surface level (fig. 8.3.3), but none were reflected in significant frost penetration into the soil or frost heave although it is possible that needle ice formation occurred where sufficient soil moisture was available. Figure 8.3.4 highlights how ground temperatures within the lower soil profile continued to fall throughout the winter

period in a delayed response to the initial low temperature phases of winter, see for example at 70cm depth.

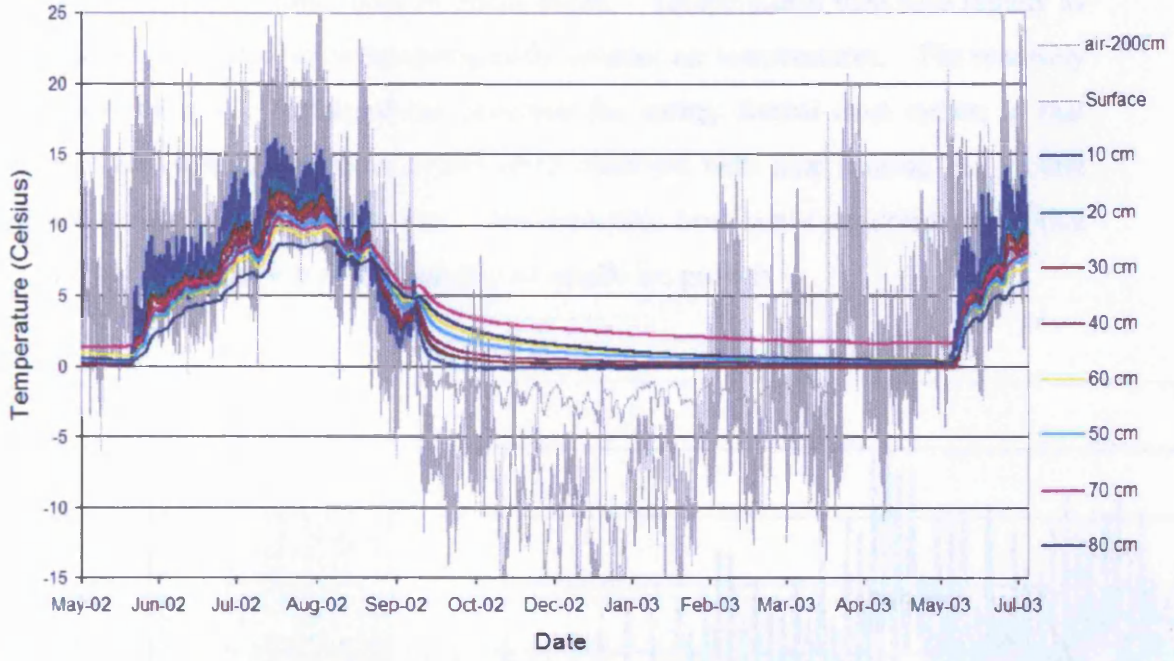

Figure 8.3.2. Ground and air temperatures recorded at the Dovrefjell field site from spring 2002 to summer 2003.

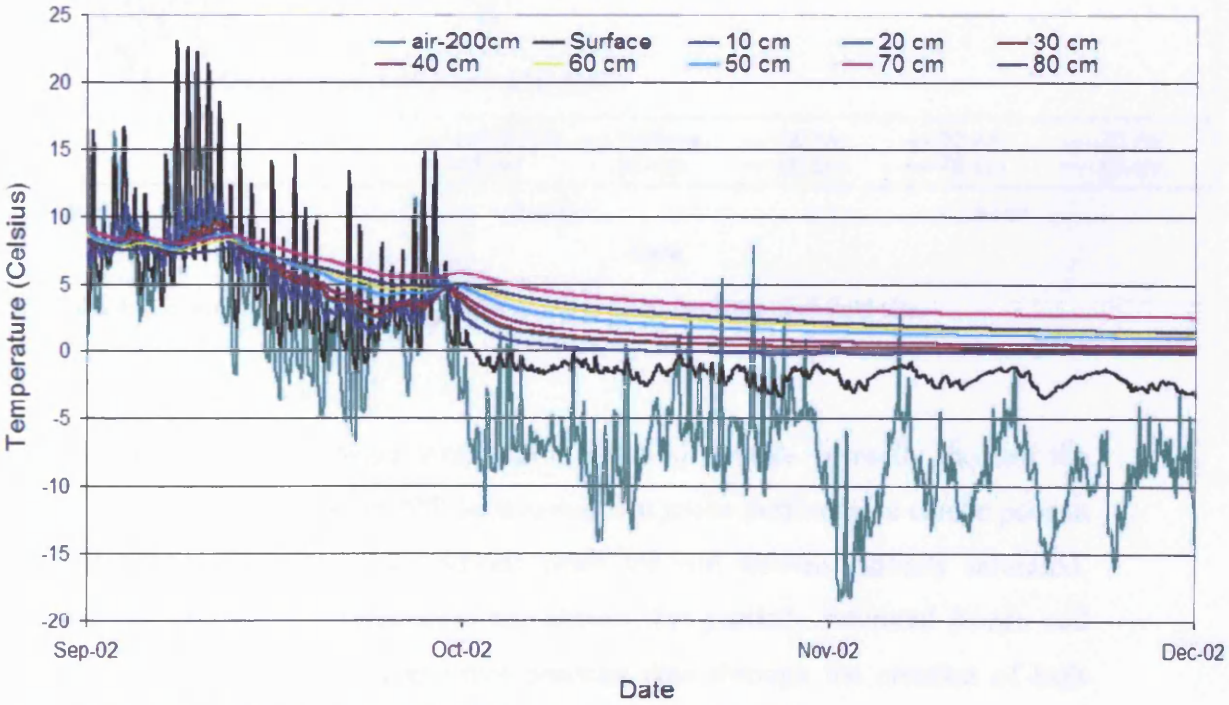

Figure 8.3.3. Autumn air and ground temperatures in at the Dovrefjell Site.

Clearance of snow on 21st April 2003 was marked by an immediate response in soil temperatures (see annotation to fig. 8.3.4). Thaw penetration accelerated through the upper 30cm of soil, taking 13 days to penetrate to 10cm depth, but only a further 4 days to penetrate from 10cm to 30cm depth. Temperatures then rose rapidly as the ground responded to rising spring/early summer air temperatures. The relatively late snow clearance restricted the potential for spring diurnal frost cycles; in that fourteen air temperature frost cycles were observed with nine causing the ground surface temperature to fall to zero. No detectible frost heave occurred during that period, but again there was a possibility of needle ice growth.

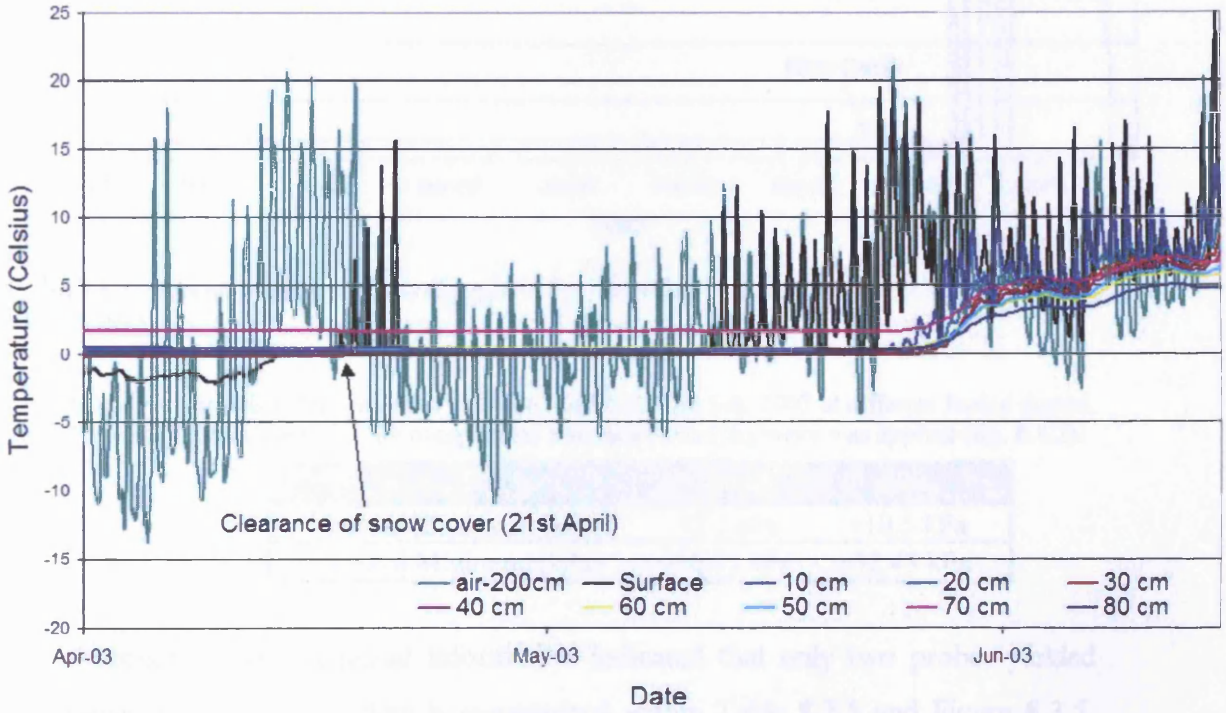

Figure 8.3.4. Air and soil temperatures in spring 2003 within the Dovrefjell field site.

- *Porewater Pressure*

The majority of pore pressure transducers failed to operate correctly through the winter period. Smith *et al.* (1999) have noted that probe performance can be poor in the field especially during long periods when the soil remains partially saturated. The current laboratory investigation has shown that partially saturated frozen soil can create fluctuating or unresponsive pressure data through the creation of high suction pressures, causing air entry into the transducer tip. It is also noted that noisy

data can result when the fragile PDCR81 transducer is exposed to the hostile soil cryotic environment (see fig. 3.3.4).

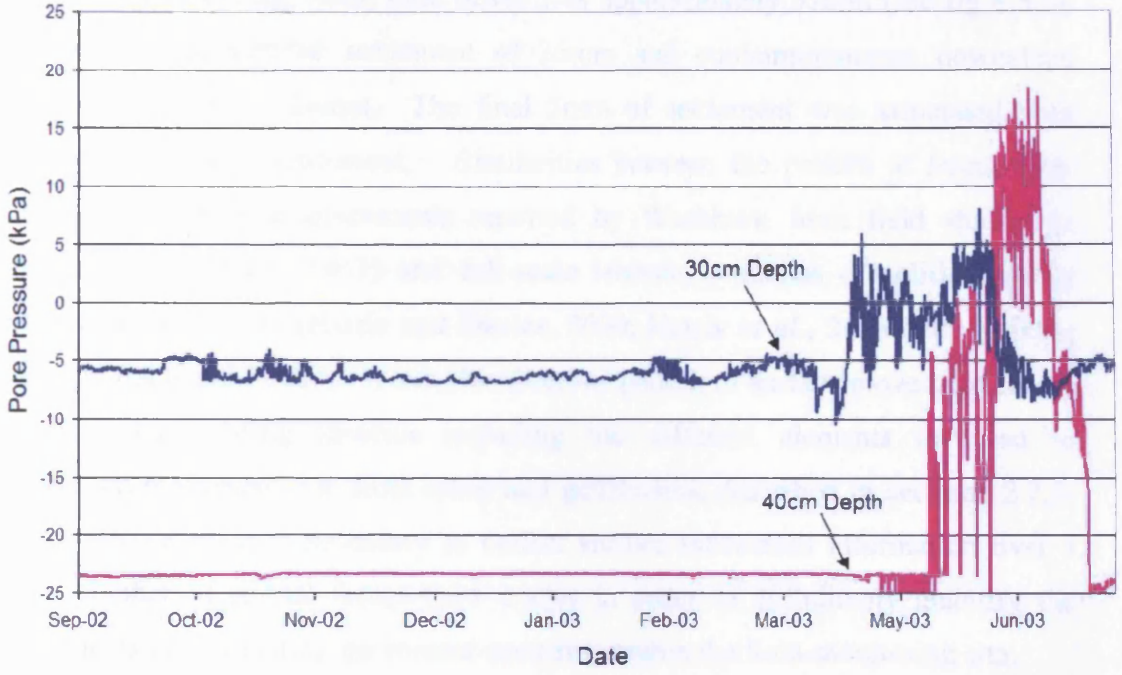

Figure 8.3.5. Porewater pressure recorded within the Dovrefjell field site between autumn 2002 and summer 2003.

Table 8.3.5. Pore pressure data recorded between May 2002 and July 2003 at different buried depths. Note: To remove the influence of the noisy signal a six-point running mean was applied (fig. 8.4.2).

	30cm	40cm
Annual Maximum (kPa)	+3.3 kPa	+10.5 kPa
Annual Minimum (kPa)	-10.55 kPa	-32.43 kPa

An assessment of the acquired information indicated that only two probes yielded discernible data patterns – data is summarised within Table 8.3.5 and Figure 8.3.5. The signal was extremely noisy, and was therefore smoothed using a 6 data point (half-day) running mean (see fig. 8.4.2). Captured information at 30cm depth indicated a steady negative pressure of approximately –5kPa occurred during winter months and thaw during March 2003 created a maximum positive pressure of 3.3kPa. A similar pattern occurred at 40cm depth during May 2003 where a steady negative pressure of approximately –23kPa was rapidly converted into a positive pressure of 10.5kPa.

- *Soil Movement*

Movement data indicated retrograde motion of the soil surface equivalent to 10mm during winter freezing, when frost heave was approximately 37mm (see fig 8.3.6). Thawing caused vertical settlement of 26mm and contemporaneous downslope surface movement of 24mm. The final 5mm of settlement was associated with upslope (retrograde) settlement. Similarities between the pattern of freeze/thaw related soil surface displacements reported by Washburn from field studies in Greenland (Washburn, 1967) and full-scale laboratory studies of solifluction by Harris and co-workers (Harris and Davies, 2000; Harris *et al.*, 2003a) are striking (e.g. figs. 8.4.6 and 5.5.20). Thus, the observed pattern of surface movement can be explained by existing theories regarding the different elements involved in solifluction movement, i.e. frost creep and gelifluction described in sections 2.2.3-2.2.4. However, it is necessary to collect surface movement information over a larger number of annual freeze-thaw cycles in order to definitively quantify the components of solifluction movement occurring within the field-monitoring site.

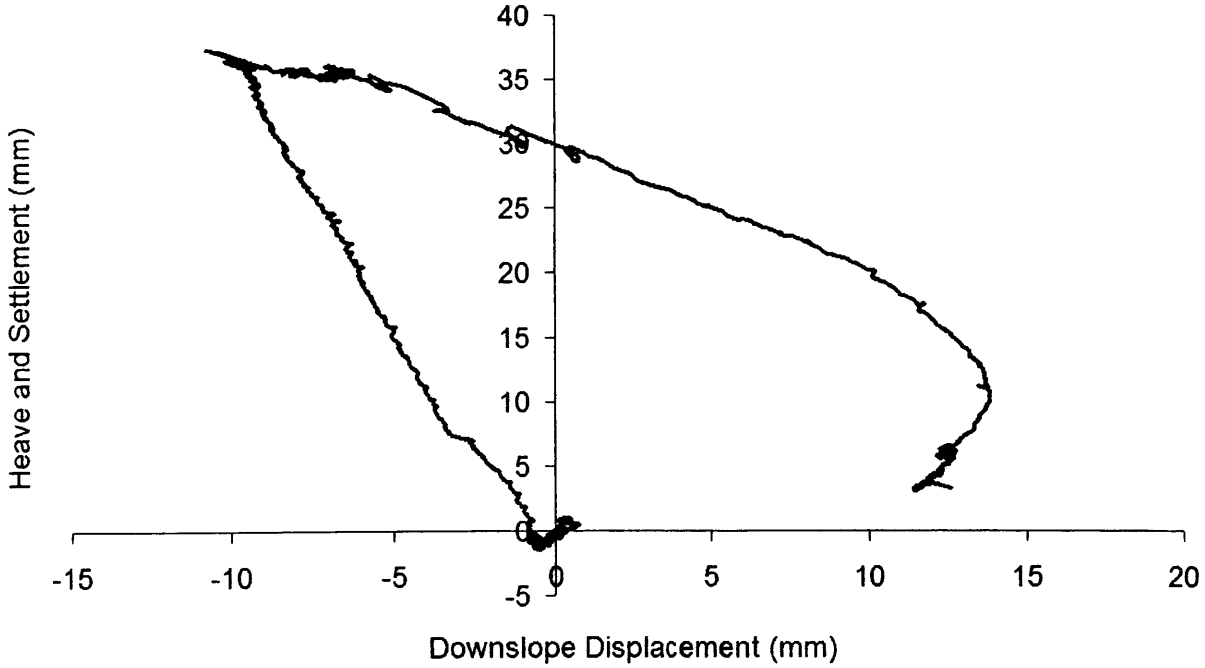

Figure 8.3.6. Surface displacement vectors continuously recorded via LVDTs at the Dovrefjell field site between autumn 2002 and summer 2003.

8.3.3. Summary

- Insulating snowfall dominated the ground thermal regime. Ground temperature conditions below 30cm remained above 0°C for the whole year despite air temperatures reaching a winter maximum of –22°C. Snowfall probably provided a large source of moisture during summer periods and possibly aided overall cryogenic processes (e.g. Lewkowicz & French, 1982).
- In the autumn sixteen diurnal freeze-thaw cycles of air-temperature were observed, and five were registered at the soil surface. After arrival of snow cover in September the soil surface temperatures stabilised and became negative.
- In the spring the late persistence of snow cover prevented diurnal freeze-thaw cycles affecting the soil surface temperature. When snow cleared in May, soil temperatures began to rise rapidly in response to air temperatures and radiation.
- Patterns of negative to positive pore pressure transition were recorded at 30cm and 40cm depths during the period of thaw consolidation in May/June 2003.
- Surface displacement patterns analogous to theoretical models of solifluction were recorded.
- The recording of pore pressure can be difficult within the field environment. However, continuous electronic monitoring of thermal conditions and surface movement is possible within harsh periglacial climatic regimes.

8.4. Field Prototypes for Current Laboratory Investigation

The centrifuge-modelling program collected primary data from an idealised and simplified replica of a prototype scenario. Large-scale field experiments have the advantage of modelling the total complexity of nature, but it is necessary to maintain monitoring over many years in order to determine the full range of variables and their interaction (Washburn, 1999). Laboratory experiments have the ability to model complex problems under repeatable experimental and boundary conditions but require careful interpretation because of their simplifying nature (Taylor, 1995). It is therefore necessary to evaluate the model-scale laboratory data with information gathered from comparative full-scale prototypes (see sections 1.3 and 1.4). The

comparison of model data and prototype field data is an essential part of the simulation exercise as it provides a method to parameterise data gathered during the small-scale replication of the full-scale event (Goodings & Gillette, 1991).

It should be remembered these small-scale laboratory models have used a specific soil type with a simplified geometry and thermal regime, and therefore did not attempt to replicate the intricacies of soil history within a natural prototype. Comparisons were therefore made to indicate whether the laboratory model response was comparable to the field situation.

Due to the small time-scale of the current field data collection programme it was not possible to quantitatively compare data from the field-monitoring site at Dovrefjell with the centrifuge modelling results. It was felt that the single season data gathered from Dovrefjell may have been unduly influenced by annual seasonal conditions and therefore failed to determine system variability across the slope. It was therefore necessary to collate a large body of published field sources and utilise secondary-source data in order to assess the current modelling program (e.g. Matsuoka, 2001). The published data had been recorded using different techniques across different time-scales from within a wide variety of periglacial monitoring sites, i.e. with localised and regional differences in ground cover, slope angle, soil type, active-layer thickness, mean annual air temperature, etc. However, it is felt the compilation of these datasets provide a useful global overview of gelifluction processes and provide an accurate means by which to assess the consistency of the model-scale data. It should be noted that all data used within this section was taken from monitoring studies indicating that gelifluction processes had occurred during single-sided freezing and thawing in zones of discontinuous permafrost.

8.4.1. Thermal Data

It is difficult to quantitatively compare the thaw phase within the field site with the thaw cycle simulated within the centrifuge because during winter the field site did not freeze to a comparable prototype depth (i.e. 70cm) (see fig. 8.3.4). It is also difficult to use published field studies because many field studies do not record the

localised micro-site conditions that may possibly impinge upon the influence of air temperature on rates of freezing and thawing.

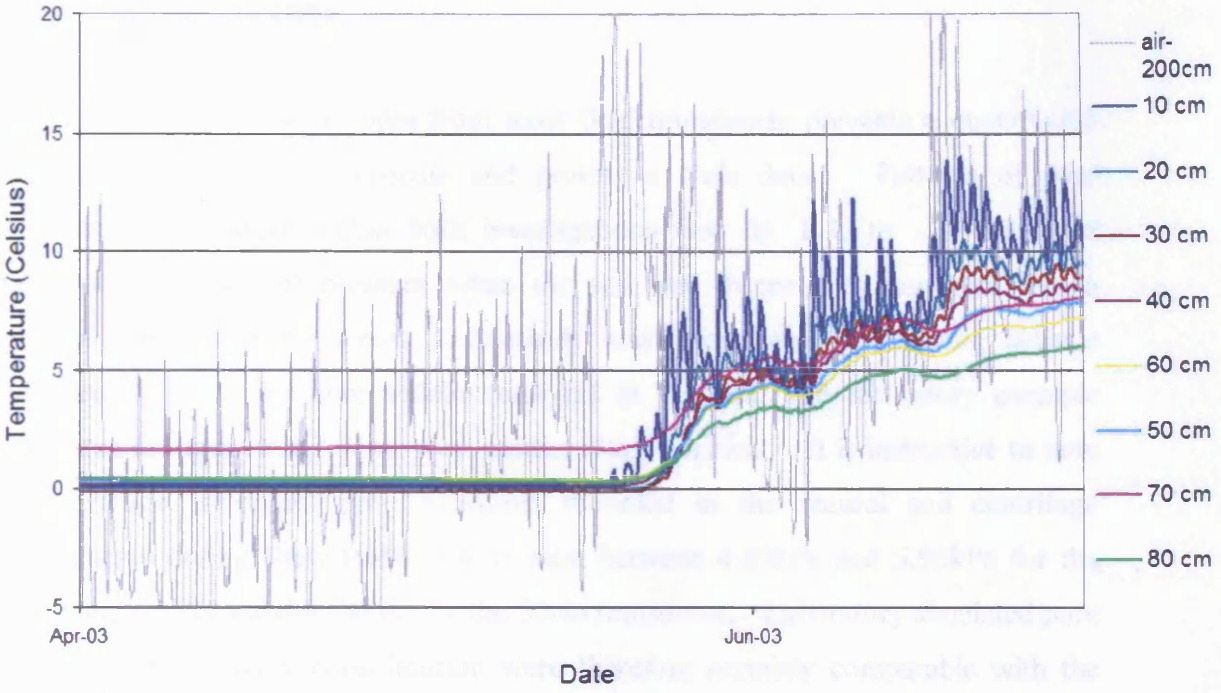

Figure 8.4.1. Thaw phase within the field-monitoring site. Summer ground temperatures recorded at the Dovrefjell field site between April 2003 and June 2003.

Air temperature conditions within the field site were dominantly influenced by the seasonal and diurnal climatic signal (see fig. 8.4.1). The resulting ground thermal regime within the field site was determined by micro-site variables such as topography but most importantly by winter snow cover. The influence of winter snow cover on ground thermal regime has been outlined in Figure 2.1.3 and section 8.3.2. In comparison, laboratory thaw phases consisted of single warm periods and were not inhibited or promoted by localised variations in single buffer layer factors. Figure 8.4.1 shows the thaw phase for the field site – unlike the majority of the laboratory thaw cycles there appears to be no pronounced zero curtain effect. The lack of a zero curtain may be due to the relatively high soil temperatures preventing high amounts of segregated ice formation within the soil profile. However, ground temperatures were observed to rise sequentially once summer air temperature had removed snow cover and allowed thaw penetration to commence. The pattern of ground warming was very similar to that observed within all laboratory thaw cycles. Overall, the style of soil warming was consistent between model and prototype scale

and therefore provides validation of the thaw phase methodology used during the centrifuge simulations.

8.4.2. Pore Pressure Data

The lack of pore pressure data from most field transducers prevents a quantitative comparison between model-scale and prototype scale data. Patterns of pore pressure were similar within both investigations (see fig. 8.4.2). A period of negative (soil tension) pressure when the soil was frozen was converted into a positive pore pressure across a relatively small timeframe as thawing became complete. Pore pressure values recorded in the field and laboratory example presented in Figure 8.4.2 were very similar, if not identical. It is instructive to note that average maximum pore pressures recorded in the natural soil centrifuge experiments during thaw (table 5.4.2) were between 4.89kPa and 5.96kPa for the 30cm and 6.58kPa and 9.94kPa for the 50cm transducer. Laboratory simulated pore pressures during thaw consolidation were therefore certainly comparable with the field pore pressure. Clearly the field site formed part of a slope continuum, with meltwater from snow patches upslope probably draining laterally through the monitored site (Woo & Steer, 1983; Stahli *et al.*, 1997). However, as in the scaled modelling experiments, raised pore pressures were restricted to the immediately post thaw period of thaw consolidation. It is therefore felt that the pattern of pressure conditions exhibited within the laboratory models were representative of pressure patterns generated at prototype scale.

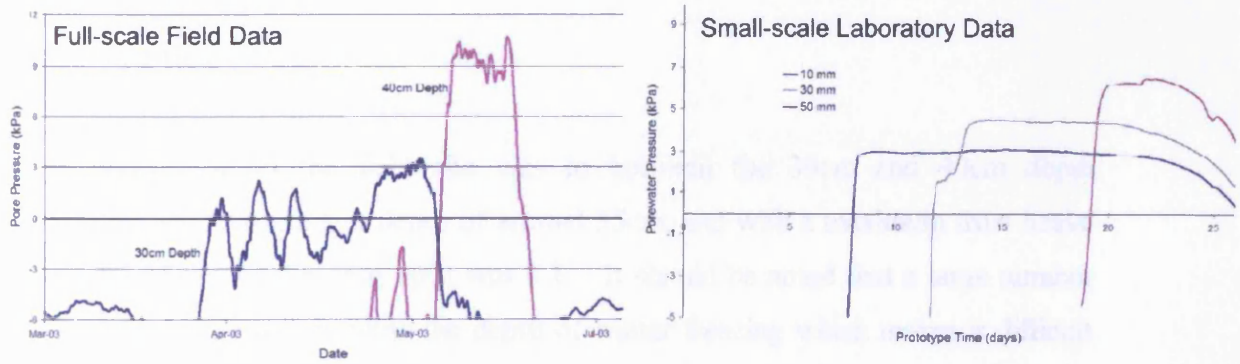

Figure 8.4.2. Comparison between full-scale and model-scale pressure data. Note: Small-scale data from Series NS/4D (thaw cycle three).

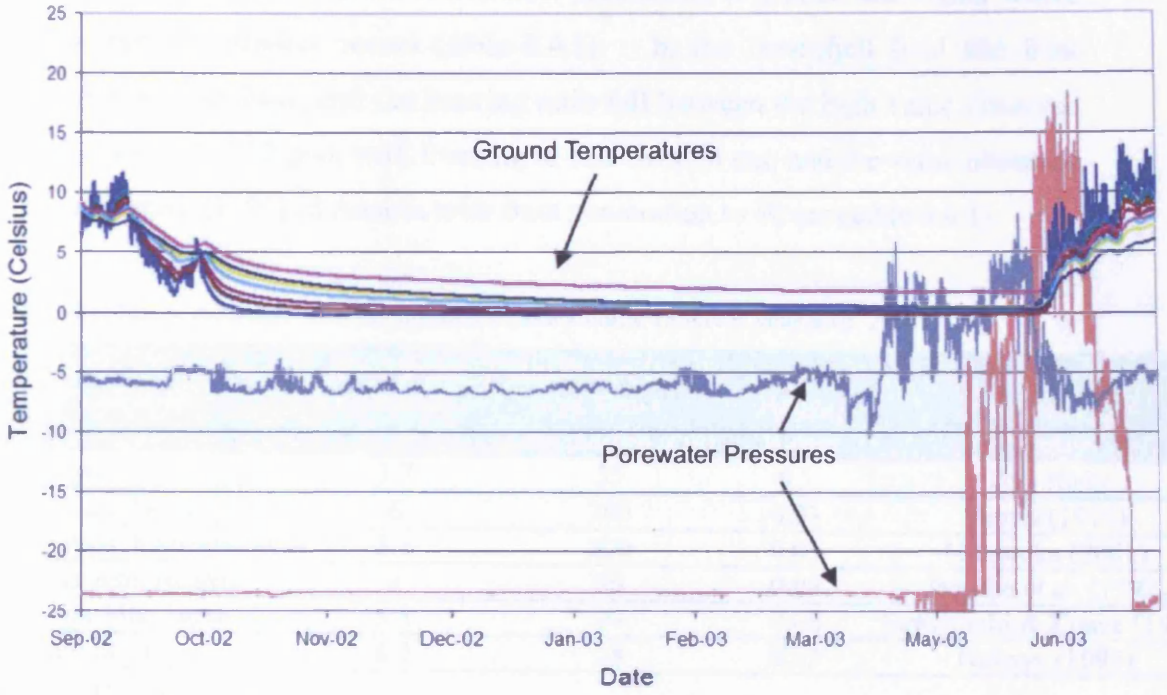

Figure 8.4.3. Ground temperature and Porewater pressure recorded at the Dovrefjell field site between autumn 2002 and summer 2003. Note: No scale for annotated pore pressure data. Information serves to highlight chronological correlation with recorded trends in ground temperature.

In detail it can be seen that in May 2003 pore pressure transducers actually responded before the soil temperatures reached 0°C (see fig. 8.4.3). This suggests that there was a slight freezing point depression, and/or that the beginning of the thaw settlement process occurred before the soil was fully thawed. Similar response of pore pressure transducers ahead of the zero degree isotherm were observed within the centrifuge models (see fig. 5.4.4). Overall, pore pressure response was observed to be temperature dependent and reactions remained consistent between both model and prototype scale.

8.4.3. Frost Heave Data

Frost penetration in the field site was to between the 30cm and 40cm depth thermistors, and assuming a depth of around 35cm, and with a maximum frost heave of around 35mm the heaving ratio was 0.1. It should be noted that a large number of field studies do not monitor the depth of winter freezing which makes it difficult to undertake accurate comparative analyses between the datasets. Table 8.4.1 outlines the calculated heave ratio for published field studies that logged both the maximum depth of winter freezing and the maximum amount of frost heave.

Clearly heaving ratios are lower where frost penetration is greater, and higher where shallow frost penetration occurs (table 8.4.1). In the Dovrefjell field site frost penetration was shallow, and the heaving ratio fell between the high value observed by Nakaya (1995) in Japan, with freezing to less than 30 cm, and the value observed by Jaesche *et al.* (1997) in Austria with frost penetration to 80 cm (table 8.4.1).

Table 8.4.1. Heave ratio derived from published field studies. (Source: Matsuoka, 2001).

Location	Maximum Frost Heave (cm)	Maximum Depth of Frost Penetration (cm)	Heave Ratio	Research Studies
Dovrefjell	3.7	35	0.1	This study
Okistindan, Norway	6	200	0.03	Harris (1972)
Swiss Alps, Switzerland	5.1	200	0.03	Matsuoka (2001)
Hohe Tauern, Austria	7	80	0.09	Jaesche et al. (1997)
Kitakami Mts, Japan	5.8	90	0.06	Sawaguchi & Koaze (1998)
Nagano, Japan	6.3	28	0.23	Nakaya (1995)
Average (Excluding This Study)	*6.04*	*119.6*	*0.09*	

Note: Field values always used the upper limit of any specified range.

The laboratory data generated higher heave ratios than those observed within many field environments (see table 8.4.2), though broadly comparable with the less deeply frozen examples in Table 8.4.1. The high heave ratio values in the laboratory datasets almost certainly relate to the conditions during model freezing, i.e. the continuous basal water supply and frost susceptible test soils. Under field conditions a number of factors would limit the heave ratio for a specific monitoring site – for example variations in soil type, clast concentration, vegetation and snow cover, terrain, altitude, diurnal temperature fluctuations, and ground water supply (Smith, 1975).

Table 8.4.2. Heave ratio for all freezing phases in centrifuge-modelling program.

Series	Freezing Cycle One	Freezing Cycle Two	Freezing Cycle Three	Freezing Cycle Four	*Average*
NS/12D	0.12	0.21	0.18	0.18	*0.17*
NS/8D	0.07	0.14	0.13	0.16	*0.12*
NS/4D	0.15	0.13	0.19	0.15	*0.15*
10S/4D	0.13	0.19	0.13	0.20	*0.16*
20S/4D	0.14	0.06	0.08	0.08	*0.09*
10C/4D	0.10	0.09	0.11	0.10	*0.10*
20C/4D	0.17	0.11	0.13	0.13	*0.13*

8.4.3. Surface Movement Data

The rate of surface movement was compared between the laboratory models and published field data derived from Matsuoka (2001) (see table 8.4.3).

Table 8.4.3. Surface velocity data from various field-monitoring studies. (Source: Matsuoka, 2001).

Location	Slope Gradient (°)	Surface Velocity (cm year $^{-1}$)	Research Studies
Melville Island, Canada	4.5	1.6	Bennett & French (1991)
Cornwallis Island, Canada	7	3	Washburn (1999)
Banks Island, Canadian Arctic	5	0.6	Eggington & French (1985)
Svalbard	18.5	3	Sawaguchi (1995)
Svalbard	11	2.2	Matsuoka & Hirakawa (2000)
SW Yukon,Canadian Arctic	16	1.3	Price (1991)
Svalbard	10	3.5	Jahn (1985)
Svalbard	10	5.1	Repelewska-Pekalowa (1993)
Svalbard	20	2.5	Matsuoka & Hirakawa (2000)
Svalbard	6	4.4	Akerman (1996)
Svalbard	8	3.5	Akerman (1996)
Kebnekaise, N. Sweden	16	1.9	Jahn (1991)
Abisko, N. Sweden	20	5.2	Nyberg (1993)
Okistindan, N. Norway	11	2.1	Harris (1972)
Iceland	8.5	0.9	Douglas & Harrison (1996)
N. Tibetian Plateau	20	1.65	Harris et al. (1998)
W. Tianshan, Kazakhstan	15	6.5	Gorbunov & Seversky (1999)
Daietsu Mts, N. Japan	19.5	3	Sone et al. (1998)
Colorado Front Range, USA	13	1.7	Benedict (1970)
Colorado Front Range, USA	12.5	2.2	Benedict (1970)
Colorado Front Range, USA	6.5	1	Benedict (1970)
Swiss Alps, Switzerland	7	3.4	Matsuoka (2001)
Swiss Alps, Switzerland	25	4.1	Gamper (1983)
Kitakami Mts, N. Japan	10	5.8	Sawaguchi & Koaze (1998)
Nagano, C. Japan	22	6.3	Nakaya (1995)

Note: Field values always used the upper limit of any specified range.

The field data were collected from regions of differing soil types and thermal regimes. Comparison with the laboratory results presented here reveals a similar pattern (see fig. 8.4.4) whereby an increase in slope gradient lead to higher rates of surface movement at both model and prototype scale. The centrifuge simulation studies produced a slightly higher average rate of surface movement at all slope angles, though the scatter of data between field and laboratory overlap. The extreme average surface movement rate at the 4° slope in the experimental data set corresponds to the natural soil plus 20% silt model which was observed to be particularly prone to solifluction (see section 5.5.6). All other values in the

corresponds to the natural soil plus 20% silt model which was observed to be particularly prone to solifluction (see section 5.5.6). All other values in the experimental data set are within the ranges of field values reported in the literature. The most significant differences between the laboratory and field conditions were probably the lack of surface vegetation and large clasts within the soil in the laboratory simulations. Under field conditions variations in surface movement would occur in response to localised variations in soil density, water supply and topography. Overall, the surface movement rates are comparable between both the field and laboratory datasets.

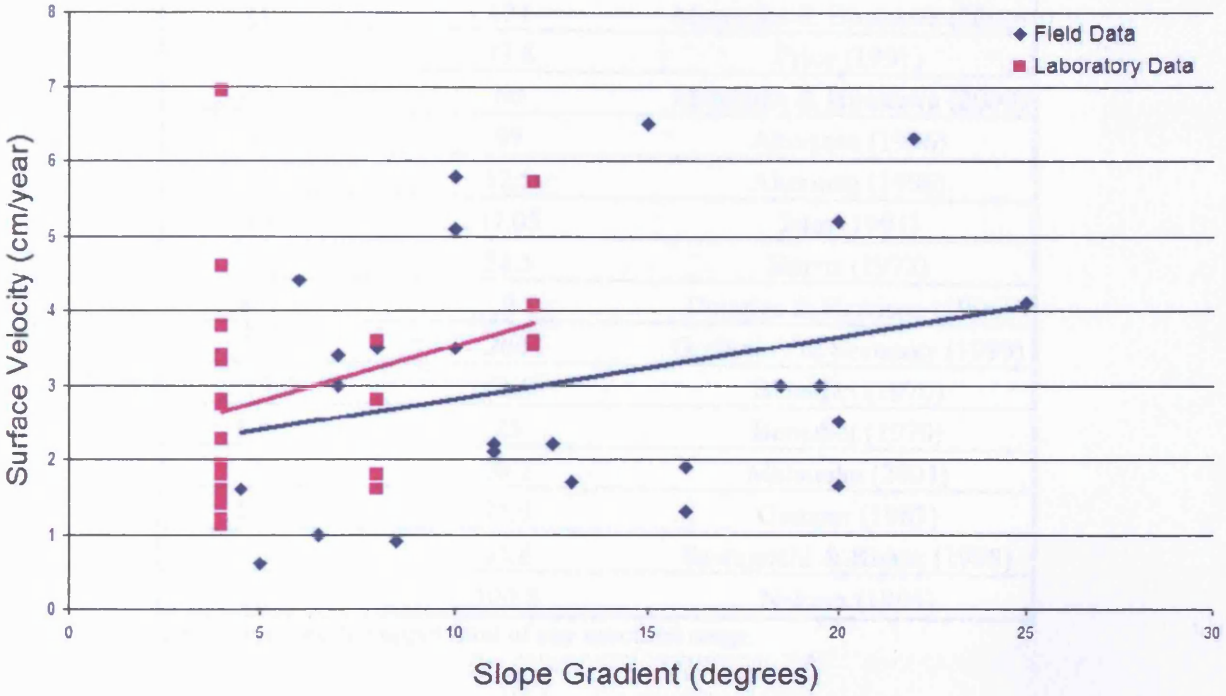

Figure 8.4.4. Influence of slope gradient upon annual surface velocity within both laboratory and field studies outlined in Table 8.4.3.

8.4.4. SubsurfaceVolumetric Movement Data

The rate of subsurface volumetric displacement was compared between the laboratory models and published field data derived from Matsuoka (2001) (see table 8.4.4). Subsurface displacement was estimated by Matsuoka from field data using values of surface velocity (table 8.4.3) and the depth of subsurface movement (table 8.4.4) where volumetric velocity was assumed to linearly decrease with depth (see fig. 2.3.2. Thus subsurface displacement was calculated by ½ V_S D_M where V_S is

Table 8.4.4. Annual volumetric displacement through gelifluction. Note: Field values are estimated.

Slope Gradient (°)	Volume Displaced (cm^3/yr)	Research Studies
12	145.5	12D/NS (This study)
8	93	8D/NS (This study)
4	74	4D/NS (This study)
4	78.3	4D/10S (This study)
4	194	4D/20S (This study)
4	80.8	4D/10C (This study)
4	93.8	12D/NS (This study)
4.5	52	Bennett & French (1991)
18.5	135	Sawaguchi (1995)
11	121	Matsuoka & Hirakawa (2000)
16	33.8	Price (1991)
20	60	Matsuoka & Hirakawa (2000)
6	99	Akerman (1996)
8	52.5	Akerman (1996)
16	37.05	Jahn (1991)
11	31.5	Harris (1972)
8.5	9	Douglas & Harrison (1996)
15	260	Gorbunov & Seversky (1999)
13	42.5	Benedict (1970)
6.5	25	Benedict (1970)
7	69.7	Matsuoka (2001)
25	77.9	Gamper (1983)
10	34.8	Sawaguchi & Koaze (1998)
22	100.8	Nakaya (1995)

Note: Field values always used the upper limit of any specified range.

Figure 8.4.5 indicates that a relationship exists where an increase in slope gradient generates larger amounts of subsurface displacement within both the field and laboratory datasets. The laboratory modelling simulated larger amounts of volumetric transport at lower slope gradient when compared to the field dataset. It is felt this resulted from high heaving ratios and rapid thawing within the slope models. Overall, a similar relationship between slope angle and subsurface movement has been generated and whilst field values are slightly lower it is felt that they have placed the laboratory data within an appropriate context.

movement has been generated and whilst field values are slightly lower it is felt that they have placed the laboratory data within an appropriate context.

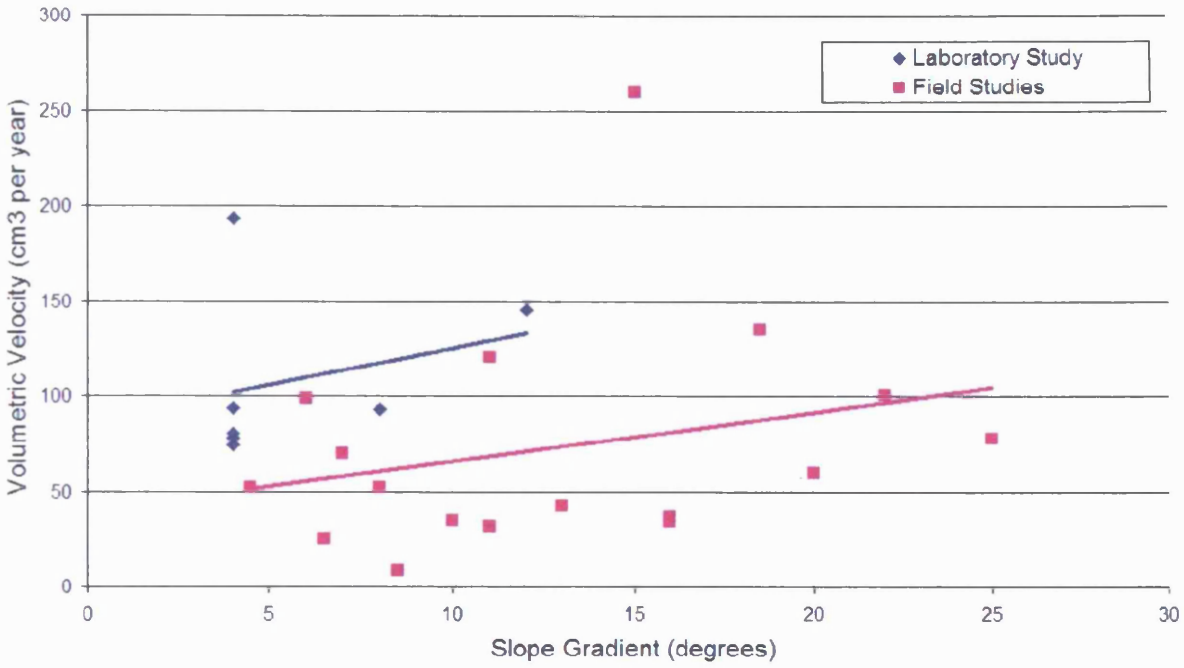

Figure 8.4.5. Subsurface volumetric displacement recorded during this study compared to the field studies outlined in Table 8.4.4.

The style of the subsurface displacement profiles revealed by excavation from the small-scale models were compared to velocity columns buried during full-scale field studies (e.g. Harris, 1977; Washburn, 1999). Figure 8.4.6 compares two sets of buried subsurface velocity columns. The field columns were excavated after five years and therefore five freeze/thaw cycles which made them comparable to the laboratory profiles which had undergone four freeze/thaw cycles. The laboratory simulation would appear to have successfully reproduced both convex and concave subsurface movement in response to the depth of greatest deformation (gelifluction). It can be clearly observed that the style of displacement created within the centrifuge simulation was similar to that exhibited under prototype conditions.

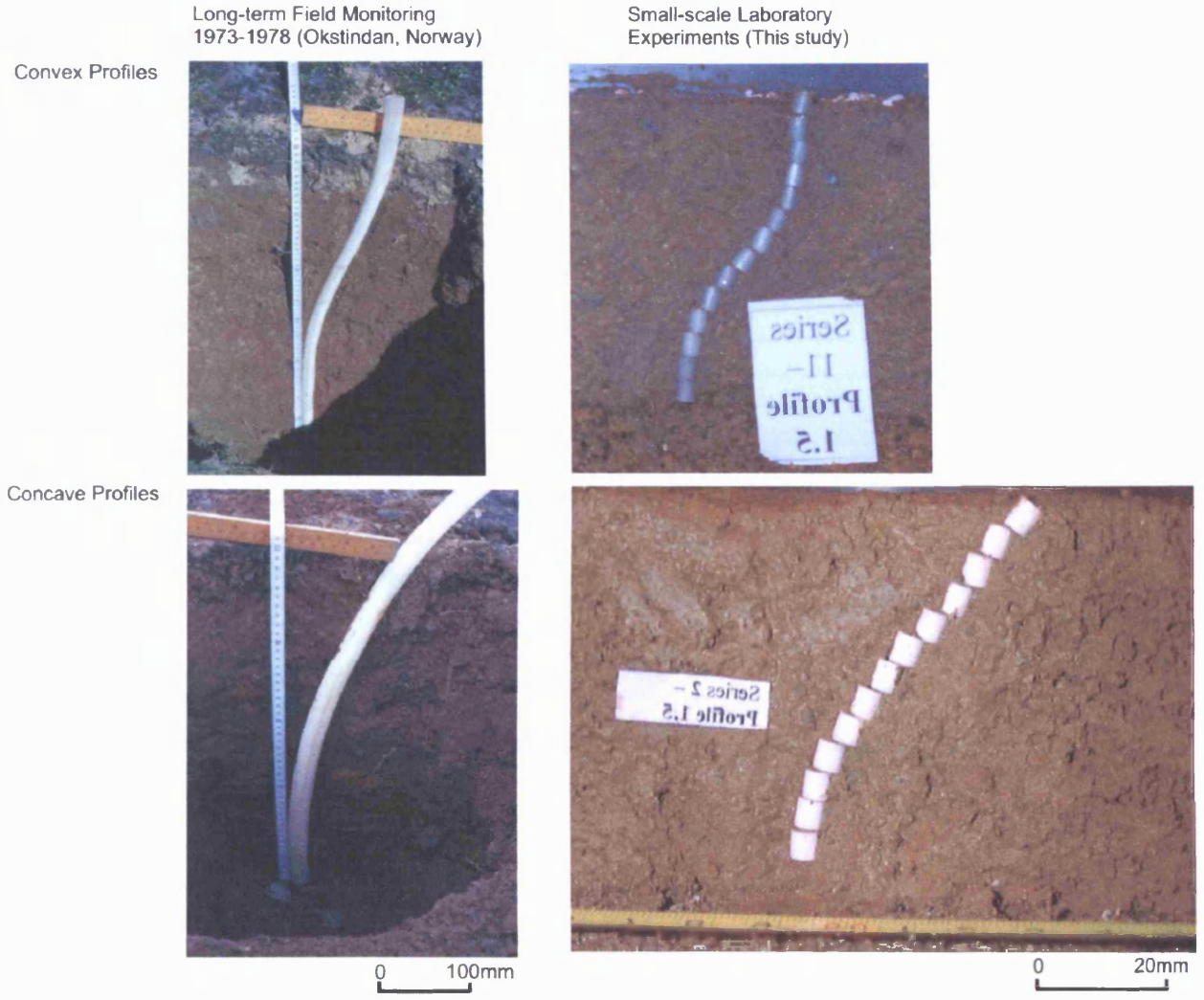

Figure 8.4.6. Subsurface velocity profiles after four freeze/thaw cycles within series 12D/NS (position 1.4) and 4D/10S (position 1.5) as compared to buried flexible tubes excavated after five annual thaw cycles upon Okstindan, northern Norway (1973-1978). (Okstindan Photograph: Charles Harris).

The depth of subsurface movement (D_M) was compared to selected field monitoring data collated by Matsuoka (2001) (see table 8.4.5). There was only a 2cm difference in average D_M with the current study having to an average D_M of 41cm compared to field studies measuring an average 39cm. It should be remembered that values of D_M principally reflect site-specific conditions of active layer thickness, micro-climate, etc. The site-specific nature of D_M can be indicated by the laboratory simulations having a small standard deviation of ±5.1cm compared to the field-based studies collated from different periglacial regions with a standard deviation of ±13.9cm. Overall, it is felt that the depth of subsurface movement was comparable between model scale and prototype scale but variations in field conditions, monitoring periods and the lack of additional micro-climatic or soil type data make further comparison difficult.

Table 8.4.5. The average depth of subsurface movement (D_M) recorded within the key area of each test series (prototype scale) compared to field data from various published studies. (Source: Matsuoka, 2001).

This Study	Freeze/Thaw Cycles	D_M (cm)	Field Research Studies	Freeze/Thaw Cycles	D_M (cm)
12D/NS	4	43.3	Bennett & French (1991)	3	65
8D/NS	4	42.5	Price (1991)	21	52
4D/NS	4	32.5	Matsuoka & Hirakawa (2000)	2	48
4D/10S	4	40.8	Akerman (1996)	23	45
4D/20S	4	47.5	Akerman (1996)	23	30
4D/10C	4	45.0	Jahn (1991)	8	39
4D/20C	4	36.6	Harris (1972)	1	30
			Douglas & Harrison (1996)	2	20
			Benedict (1970)	5	50
			Benedict (1970)	4	50
			Matsuoka (2001)	2	41
			Jaesche et al. (1997)	2	50
			Sohma et al. (1979)	2	22
			Gamper (1983)	4	38
			Sawaguchi & Koaze (1998)	2	12
			Nakaya (1995)	1	32

Note: Field values always used the upper limit of any specified range. The designated field monitoring period was directly translated into annual freeze/thaw cycles.

8.4.5. Summary

- The results from the laboratory slope models have been calibrated against field measurements. It is necessary to replicate the geotechnical properties and stress history of field sediments within a centrifuge model in order to manufacture a direct causal linkage between model scale and prototype scale.
- The style of thaw penetration was similar between field site and laboratory models. A 'zero degree curtain' effect was noted within both datasets.
- The style of porewater pressure response within the field site during spring soil warming was replicated on numerous occasions within laboratory models. Porewater pressure was noted to be temperature dependent within both datasets. A transition from negative to positive pressure was noted to occur as soil temperature approached 0°C, though often slightly before the arrival of the 0°C isotherm.
- Higher amounts of frost heave were generated within the laboratory models when compared to field datasets. Larger heave ratios probably occurred in

the laboratory models in response to the continuous freezing phase, the basal water supply and the homogenous host sediment.

- Higher amounts of surface movement were recorded within the laboratory simulation when compared to prototype scale field data. A similar pattern was noted within both datasets whereby surface movement increased with greater slope gradient.
- Higher amounts of subsurface movement were recorded within the laboratory study when compared to field sites, probably in response to the homogenous host substrate and the lack of soil stress history. A similar relationship was found within both datasets whereby greater slope gradient encouraged larger amounts of subsurface deformation.
- Similar depths of gelifluction movement were recorded within the laboratory simulation when compared to field studies conducted over a similar number of annual freeze/thaw cycles. The laboratory simulation of gelifluction also manufactured an appropriate simile for the style of prototype subsurface movement.
- It is felt necessary to maintain continuous electronic field monitoring to create a more extensive database for the direct calibration of future laboratory data with information gathered from the same test substrate.

CHAPTER NINE : Summary and Conclusions

The following chapter will synthesise information gathered within the investigation in response to the specific research questions addressed at the outset. It will also give a frame of reference with regards to future applications of centrifuge modelling techniques within cryogenic slope studies.

9.1. Research Questions

What is the effect of increasing silt content on the rate and style of gelifluction?

- Increasing silt content has been shown to increase the susceptibility of a soil to gelifluction processes. Increasing silt content is likely to increase the frost susceptibility of a soil, and therefore increase frost heaving and thaw settlement given an adequate supply of water. It has been suggested in the literature that both frost creep and gelifluction rates are primarily a function of slope gradient and the amount of frost heave/thaw settlement (e.g. Washburn 1967, Harris 1981, Harris *et al.*, 1995, Matsuoka, 2001), and the scaled centrifuge modelling experiments presented here have confirmed this to be the case (Chapters 5 and 6). However, in the present research, a limited water supply during freezing resulted in less frost heave and thaw settlement in the model constructed of natural soil enhanced with 20% silt than was observed in many other soil types during equivalent modelling. Despite this, the 20% silt enhanced soil still generated the greatest rate of solifluction. Clearly, therefore, the susceptibility of silt-rich soils to gelifluction is not simply a function of its frost susceptibility, but also of a significant reduction in shearing resistance within the thawing soil.

- When comparing the response of the 4° slope model constructed from natural soil and those constructed of natural soil enhanced with 10% silt and natural soil plus 20% silt, it was shown that the behaviour with respect to frost heaving and thaw settlement of the first two soil types differed only slightly. However, there appeared to be a threshold in susceptibility that induced solifluction between the 10% and 20% silt enhanced soils, the latter showing a marked increase in flow susceptibility, as discussed above.

- In exploring the reasons for this change in behaviour, several hypotheses may be presented. Firstly, increased amounts of silt may generate larger ice lenses - this may increase the amount of gelifluction by physically separating and weakening the soil matrix prior to thaw consolidation. Larger ice lenses may facilitate gelifluction by providing localised zones of low frictional shearing resistance, resulting in microshearing. In addition, the development of a fabric of aligned silt flakes during soil freezing and thawing may reduce frictional resistance and encourage flow, particularly where porewater pressures are raised above hydrostatic during thaw consolidation.

- The experiments reported in this thesis have demonstrated that relatively high pore pressures are generated during thaw of silt-enhanced soils. This is thought to be a function of reduced permeability associated with increasing silt content. This reduces the drainage rate of meltwater released by melting soil ice, giving a longer duration of higher pore pressures. Silt-rich soils also have a low Plasticity Index (e.g. Harris, 1981), so that the Liquidity Index of the soil is likely to approach unity during thaw consolidation, making the soil particularly flow susceptible. Micromorphological investigations reported in this thesis (Chapters 5 and 7) have shown clear evidence that the silt enhanced soils used in these experiments underwent flow-like soft sediment deformation during thawing. It should be noted, however, that recent research using scaled centrifuge modelling by Harris *et al.* (2003a) has shown that these very wet, very soft thawing soils behave as frictional materials with an elasto-plastic response to gravitational stress on slopes, rather than behaving as a viscous fluid.

What is the effect of increasing clay content on the rate and style of gelifluction?

- Increasing clay content in the centrifuge modelling experiments reported here led to an increase in volumetric transport by gelifluction, though with little increase in surface movement rates. The augmentation of the clay content of the test soils is thought to have increased cryosuction forces by increasing the unfrozen water content at sub zero temperatures close to 0°C. This in turn encouraged ice lens

nucleation and maintained ice lens growth over a longer period of time (see section 2.1.8 for discussion of the ice segregation process). The clay soils were associated with the generation of a large number of well-dispersed relatively small ice lenses when compared to the natural and modified silt soils (see Chapter 6).

- During thaw, excess ice contents led to a rise in pore water pressure following the passage of the thaw front. In the slope model constructed with the highest clay content soil (addition of 20% by weight kaolinite), thaw consolidation led to enhanced pore water pressures because of the reduction in permeability and hence coefficient of consolidation (C_V). Thus meltwater released from the thawing ice lenses was unable to drain, the Thaw Consolidation Ratio was higher, and pore pressures rose rapidly. Unlike in the natural soil and silt enhanced soils, however, the rise in pore pressures following thaw was repeatedly interrupted by sudden drainage, followed by further periods of pore pressure rise and further drainage events. Such a "spiky" pattern of pore pressure rise and fall during the period of thaw consolidation of clay-rich soils has been reported elsewhere (e.g. Harris *et al.*, 2001b, 2002), and is interpreted as the result of water escape events, possibly associated with the presence of discontinuities within the soil matrix marking the former location of ice lenses. It is likely, therefore, that the upper limit to thaw-generated pore pressures is provided by the stresses necessary to overcome the overburden pressures and allow water escape to occur. This is likely to relate to the geostatic pressure and therefore increase with depth.

- Enhancing the clay content of test soils led to an increase in plasticity, so that higher moisture contents were necessary to soften the soil during the thaw period than was the case for the silt enhanced soils. The thawing soil mass apparently retained an element of undrained cohesive strength. However, ice-rich bands or the presence of larger ice lenses apparently provided zones of weakness (possibly exploited in the water escape events) along which shearing was more intense. Since the self weight stress increased with depth, while it is assumed that the undrained shear strength was roughly constant through the soil profile, so that shear strain during thaw increased with depth. This accounts for the relatively large volumetric transport rate in the clay soils relative to surface movement rates in comparison to

the silt enhanced soils (see section 6.1). The clay-rich test soils displayed a tendency to produce convex downslope profiles of movement, indicating high shear strains at depth, while the silt enhanced soils displayed strongly concave downslope profiles, indicating increasing shear strain rates towards the surface.

What is the impact of slope geometry on the rate and style of gelifluction?

- Increasing slope gradient has been shown to enhance both surface movement and subsurface volumetric transport rates. In the experiments described in this thesis, freezing and thawing boundary conditions were maintained roughly constant, and the same natural test soil was used to construct slope models with increasing gradient. Thus it was possible to isolate the role of gradient. Clearly the downslope self weight shearing stress increases with the sine of the slope gradient, so that if a soil has a certain consistency and shearing resistance, it is likely that the amount of deformation will increase with increasing slope gradient. In addition, the potential soil creep value is a function of frost heave and the tangent of the slope angle, so that again, a steeper slope is likely to be associated with greater downslope soil displacement during thaw consolidation.

Under field conditions it is much more difficult to isolate the role of slope gradient within the wide range of environmental variables (Washburn, 1999). Evidence from the present series of experiments suggests that variation in soil type is likely to over-ride slope gradient as a controlling factor on solifluction rates and volumetric transport. For instance, even with a gradient of just 4°, the solifluction modelling using 20% additional silt caused average surface movement rate to increase by a factor of three when compared with the natural soil model.

Experimental data also demonstrated clearly that the amount of mass movement during a given freeze-thaw cycle was a function of the amount of frost heave and thaw settlement. Since soil moisture status is a major variable under field conditions, it is likely that the heaving ratio at a given site will outweigh the significance of slope gradient in determining solifluction rates (Matsuoka, 2001). This illustrates clearly one of the major advantages of adopting the scaled centrifuge

modelling approach, since it allows the operator to control both boundary conditions and soil properties, varying only selected parameters (e.g. soil type and frost heave) to quantify their relative importance.

Is it possible to accurately simulate prototype periglacial conditions using geotechnical centrifuge modelling?

- The centrifuge technique allows small-scale models to be frozen and thawed under prototype stress conditions. The use of increasingly sophisticated environmental simulation techniques can be combined with a geotechnical centrifuge to more accurately simulate prototype phenomena.

- To completely simulate prototype conditions requires the testing of undisturbed field samples that recreate the appropriate stress history when placed under an enhanced gravity field. Under the test conditions that applied to the present experiments, it was impossible to freeze models in the centrifuge under enhanced gravity. To attempt to recreate approximate stress conditions that prevailed during centrifuge thawing, models were frozen under an applied stress approximating the self weight at the centre of the models during flight. However, clearly the stress distribution on soil and water during freezing of the scaled models did not exactly recreate prototype conditions, and it is possible that ice lenses were somewhat larger in the tests reported here than would have been the case with in flight freezing.

- By accurately simulating gelifluction and cryogenic landsliding processes the current investigation has provided an additional element to the earlier phases of periglacial centrifuge modelling outlined in section 2.6. The validity of the geotechnical centrifuge technique has been reinforced by the current study; although special consideration must be made to the limitations of the technique when designing and implementing future simulation strategies (see sections 9.2 and 9.3).

- Centrifuge modelling has been proven to be a useful technique that enables the quantitative investigation of specific phenomenon under controlled conditions. The technique overcomes the limitations of field monitoring in harsh periglacial

environments and could potentially provide a large amount of value added data when combined with long-term field observation of prototype scale analogues.

Is it possible to validate laboratory data through comparative analyses of analogue field information?

- The centrifuge modelling technique increases the probability of generating large amounts of quantitative data from repeatable experiments. Once the appropriate scaling laws have been applied to the model scale information then field data can be used to test the validity of physical modelling outcomes. In this research programme, data from field monitoring in Dovrefjell, Norway was compared with that from the centrifuge experiments. Of particular interest was the pore pressure and thermal data, and on the basis of the 2002-2003 Dovrefjell data it appears that the scaled centrifuge modelling provided an accurate representation of pore pressures in the thawing soil. However, it is not possible to completely validate model scale data since these experiments did not use prototype soil material.

9.2. Methodological Developments

The methodology adopted within the current investigation has raised a number of technical and procedural issues. The following section will outline a number of improvements that may increase the efficacy of the centrifuge modelling methodology and augment the overall quality of any acquired data.

- *Water supply during freezing*

There were intermittent problems with the consistency of the water flux into the slope model during freezing phases (see section 5.7). The use of a constant head feeder tank would maintain designated hydraulic conditions for a complete freezing phase and allow monitoring of the volume of water moved into the slope model. The use of a tube attached to the exhaust outlet of the freezing plate would remove cold air away from the inlet pipes and therefore alleviate the previously observed water supply problems. However, the greatest consistency would be achieved through the use of a controlled environment chamber, although considerable

attention would be needed to maintain conditions of one-sided downward freezing of the slope model.

- *Intra-series subsurface measurement*

The current methodology prevented intra-series monitoring of subsurface movement. It is felt that the accurate non-invasive recording of subsurface response to individual test variations in heave and settlement should be a key component of any future research. The use of an embedded electronic strain gauge such as that used by Lewkowicz (1992) may allow intra-thaw phase monitoring; although there may be issues with regards to scaling, and the operation of the system, within the enhanced gravity environment. An alternative approach may involve the use remote sensing techniques, for example X-ray photography or sonograms derived from scanning ultrasound may be able to record subsurface marker movements after each centrifuge flight. Both of these techniques would rely upon the accurate measurement of buried reflective elements via either a high frequency directional sound-wave or the reflectance of the x-ray portion of the light spectrum. This approach has obvious logistical difficulties with regards to cost, access and the appropriate marker material providing the necessary spectral reflectance when buried within a mineral soil - but with adequate development it may provide the most appropriate non-invasive means of gathering such vital inter-test data (e.g. Kruse & Bezuijen, 1998; Konrad, 1988).

- *Test instrumentation*

It was necessary to filter the pore pressure dataset before any data analysis (see fig. 5.4.3). The data reduction technique removed fluctuating data and was consistently applied to probes registering negative pore pressures. It has been noted by other researchers that the Druck PDCR81 is a useful tool but has a high mortality rate when operating under conditions of tension (soil suction) (Take & Bolton, 2002). A number of modifications to the Druck PDCR81 probe have been suggested by Take and Bolton (2002) – the implementation of these design evolutions may allow an additional array of transducers to be installed to measure pressure conditions during freezing and the initial stages of each thaw cycle. It is felt this additional array may provide useable high quality data especially when combined with the methodological alterations designed to provide a more consistent freezing technique. The accurate

monitoring of positive (thawed) pressure and negative (frozen) pressure conditions through the mixture of specialised and non-specialised PDCR81 transducers would enable a more complete overview of in-situ pore space conditions.

It was mentioned within section 5.4 that several pore water pressure transducers began to provide consistently noisy data towards the latter stages of the experimental program (see fig. 5.4.1). It is felt that the use of antifreeze (ethylene glycol) solution did not completely suppress ice growth within the space between the porous stone and pressure diaphragm. The antifreeze solution possibly became diluted during successive moisture-rich thaw cycles and began to allow ice-crystal nucleation within the latter cycles of each test series. In hindsight, an alternative approach may have been to saturate the transducers in silicon oil. Murton *et al.* (2000, p.1286) have shown that silicon oil can offer greater long-term protection; for example within a recent study all but one of the thirty PDCR81 transducers embedded within a weathered chalk block survived 20 complete freeze-thaw cycles (Murton, *pers. comm.*). Silicon oil would therefore appear to provide a cryogenically stable solution that would completely prevent transducer re-airing by suppressing ice growth within the entry stone. This approach may have retained a higher quality of data acquisition and minimised the necessity for probe servicing towards the latter stages of the centrifuge program.

There were problems with the long-term accuracy of the K-type thermocouples used within the experimental program as many of the thermocouples provided consistently noisy data and required careful data reduction before analysis. The thermocouples appeared to react inconsistently within the constant harsh environment. If thermocouples are used within future cryotic experiments it is advised that they are serviced and calibrated at regular intervals to prevent numerical drift. Overall, it is recommended that an alternative temperature sensor be used in any future experimental programs. An array of thermally sensitive resistors (or thermistors) would appear to be a more robust and reliable substitute.

- *Measurement of model conditions during freezing phases*

It was noted in section 3.7 that the amount of frost heave and the rate of frost penetration were not continuously measured during the model freezing phase. It was also difficult to monitor rate of settlement during each thaw phase due to the enhanced gravity conditions, as any LVDT placed onto the thawing surface would penetrate into soil. A simple physical modification to the present methodology would allow the placement of an LVDT onto the freezing plate surface and the linkage of the embedded thermocouples into a continuous datalogging system during freezing. It is felt the development of the mobile Campbell CR7 logger throughout the current investigation will allow the monitoring of frost heave and thermal regime during the freezing cycles of future experiments (see fig. 4.5.1). However, in order to measure settlement during flight, it is necessary to utilise a remote sensor that records the distance of the soil surface from a fixed datum. A solution to this may be found through the development of a miniaturised version of the laser attenuation apparatus used during theodolite surveying of terrain. A modified laser device may be able to track a particular point upon the model surface and perhaps record in-flight changes to both the volume change and surface deformation of the soil body during thaw consolidation.

9.3. Future Applications

The current study has highlighted the value of centrifuge modelling techniques for investigating cryogenic phenomena. It is felt that centrifuge modelling presents an excellent opportunity for further research – a summary of potential future applications is presented with respect to both supplementary gelifluction research and other fields of cryogenic investigation.

9.3.1. Solifluction Modelling

- *Plug-like Flow*

Solifluction processes involving two-sided freezing of a slope within areas of continuous permafrost has been shown to result in distinctive ice distribution within the active layer and resulting plug-like displacements over the permafrost table (see section 2.2.5). The current methodology could be easily adapted to enable double

sided freezing of a soil model – this would allow accurate modelling of plug-like flow by presenting an opportunity to separate significant variables such as the rate of freezing and thawing, amount of fine clay/silt content, slope angle, etc and allow the recreation of unique phenomena such as the central desiccated zone (Mackay, 1981; Lewkowicz & Clark, 1988).

- *Modelling a specific prototype*

This would involve an investigation into solifluction processes with material excavated from a previously monitored field analogue. The current methodology would allow recreation of thermal and physical boundary conditions within the model. Derived results could then be directly parameterised to further validate the centrifuge modelling technique and extrapolate initial field results for predictive analysis. The technique could be modified to allow specific civil engineering scenarios to be explored – for example the impact of solifluction on newly constructed engineering structures (e.g. Bondarenko, 1993; Tart, 2003). The centrifuge-modelling technique allows high quality electronic data acquisition within the civil engineering field. It would be possible for strain gauges and pressure pads to be placed within the soil unit and buried engineering structures to measure the stress being exerted upon the soil/edifice interface through repeated freeze/thaw and downslope movement cycles under differing conditions of frost heave and thaw settlement.

- *Overconsolidated Material*

An investigation into solifluction processes acting on overconsolidated clays would allow reconstruction of Pleistocene slope processes in clay bedrock areas such as the Cotswold Escarpment, England. Careful model preparation may allow investigation of the significance of soil stress history on periglacial solifluction.

- *Influence of Vegetation and Clast Concentration*

The presence of vegetation and clasts can influence patterns of solifluction activity (see section 2.3.2). It would therefore be useful to utilise centrifuge modelling techniques to undertake an investigation into the influence of vegetation density and below ground biomass upon the rate and style of downslope movement and the

development of characteristic solifluction landforms (e.g. Gyssels & Poesen, 2003; Greenway, 1987). Vegetation has been identified as an important factor in determining the depth of the active layer and therefore defines the amount of potentially transportable material within any periglacial mass wasting system (Brown, 1963). The current methodology could be easily adapted to simulate the presence of vegetation within a slope model; loose carpet fibres could be mixed with the test soil and then placed to a particular depth to simulate the root network of vegetation cover. If a vegetative zone was placed adjacent to a non-vegetation zone then the relative influence of vegetation cover could be directly determined with respect to both subsurface and surface deformation. An investigation into the influence of buried clasts could be undertaken to assess the impact of clast density, clast mineralogy, and clast shape upon gelifluction related processes (Ballantyne & Harris, 1994, p.86; Mackay, 1984). Repeatable modelling could analyse the influence of clasts upon the thermal conductivity profile of the soil during both freezing and thawing and any resultant changes to the distribution of subsurface soil impacting upon relative patterns of displacement. A similar methodological approach could be used whereby adjacent zones of different specification are placed within the same slope model and concurrently tested to record relative behaviour with respect to the rate of soil warming, style of movement, and pore pressure conditions during consolidation. It is felt this would be useful with respect to quantifying the impact of clasts upon rates of movement – i.e. whether angular frost shattered clasts or rounded stones provide a preferential surface for downslope movement, etc. If these two separate simulations were successful then more complex scenarios could be investigated to analysis the relative influence of both vegetation and clast densities within mixed solifluction landforms.

- *Trigger Event Modelling*

The addition of rain or meltwater during seasonal periods of thaw has been identified within field studies as contributing to the raising of moisture levels and possibly promoting gelifluction (Matsuoka, 2001). An investigation into the influence of moisture status upon the rate of solifluction and the point source introduction of moisture upon the behavioural threshold between slow mass wasting and landsliding could be undertaken within the centrifuge using the current methodology. The

current technique could simulate the introduction of rainfall upon the model surface or meltwater within the active layer from an upslope snow patch (Woo & Steer, 1983). Repeatable modelling would enable direct observation of slope behaviour prior to moisture introduction and therefore a quantitative impact assessment of its influence upon slope stability and the rate and pattern of downslope displacement. The comparison between the impact of intra-soil moisture alongside externally introduced moisture would potentially provide an insight into the complexities of slope hydrology within the field prototype.

- *Remediation Techniques*

An investigation into the effectiveness of specific techniques designed to limit gelifluction related processes might take advantage of scaled modelling in a geotechnical centrifuge. The controlled boundary conditions would allow the testing of identical slope models to examine the relative influence of different remediation techniques on the rate and style of periglacial mass wasting. Techniques could range from the installation of vertical drains to rapidly dissipate excess pore pressures (Brennan & Madabhushi, 2002), the putting in place of a geocomposite hydrophilic capillary barrier to reduce subsurface frost heave (Henry & Holtz, 2001), to the geotextile reinforcement of buried structures to protect them from structural damage (Porbaha & Goodings, 1996). The impact of these techniques could be individually determined through repeat modelling between modified and non-modified slope models – centrifuge simulation would therefore allow an assessment of the relative efficacy of each technique and therefore identify any potential weaknesses before undertaking expensive prototype-scale trials under field conditions.

9.3.2. Further Cryogenic Studies

Geotechnical centrifuge modelling has been a recent advance within croygenic science because engineering and testing within periglacial regions is impractical, hazardous, and expensive (e.g. Smith, 1995). Section 2.6 has briefly outlined research areas already undergoing particular progress with regards to the application of centrifuge modelling techniques. The following section will briefly outline some

broad areas for future potential collaboration between cryogenic science and geotechnical civil engineering through enhanced gravity modelling:

- *Modern Periglacial Phenomena*

It may be possible to simulate other periglacial processes using modifications to the existing centrifuge technique outlined in Chapter 3. For example, using the current technique it would be possible to quantitatively investigate the related phenomena of ploughing boulders where solifluction lobes have been observed to entrain large boulders from frost weathered bedrock (see fig. 2.3.7). These large boulders are rafted upon the soil surface and move at a rate exceeding the surrounding soil mass with their undersides resting at or near the permafrost table (Ballantyne, 2001; Berthling *et al.*, 2001). A simulation of this process under controlled boundary conditions may reveal the specific factors which influence the efficacy of the phenomena within different field environments, i.e. an investigation into the role of the depth of annual thaw, the thermal conductivity of the boulder, boulder geometry, slope angle, surrounding vegetation density and root depth, the geotechnical properties of the host sediments, etc.

- *Numerical/GIS Modelling*

The current methodology facilitates the further collation of quantitative threshold data with respect to the amount of slow mass wasting that occurs within a soil unit with specific geotechnical properties upon a slope with a defined gradient. Further analyses can then examine the behavioural pore pressure thresholds between pre-failure strain and slope failure within those specific datasets. The information gathered from such an analysis may encourage hierarchical linear or finite element modelling to disaggregate the individual components influencing dynamic field-based gelifluction processes. The collation of large amounts of movement data within different host sediments and across variable slope gradients presents an opportunity to generate coarse computational models with respect to the potential for an area to generate gelifluction movements under simulated climatic regimes. The collation of movement threshold data within a GIS system would enable spatial

prediction of the distribution of slow mass wasting across large spatial zones through weighted overlay analysis (Burrough & McDonnell, 1998; Longley *et al.*, 1999). For example a DTM could be placed within the system to define the slope angle a specific location, geophysical surveying would determine the depth of regolith, local MAAT could be used to determine the climatic controls being placed upon the region, satellite remote sensing could be used to determine seasonal snow and vegetation cover, and a GPS or monitoring frame could be used to measure frost heave and thaw settlement (e.g. Little *et al.*, 2003). The spatial collation of this interrelated data may approximate the potential for pre-failure creep to occur at a specific location when combined with the behavioural movement data gained from centrifuge modelling under different prototype scenarios and conditions. The collation of disparate datasets into a single georeferenced database would enable further research into the potential regional impact of climatic warming upon slope instability.

- *Palaeoenvironmental Reconstruction*

The centrifuge modelling technique could be applied to palaeoenvironmental reconstruction in a number of ways. It can enable the back analysis of movement rates within head deposits, i.e. by removing soil samples and testing the amount of volumetric displacement occurring across a range of slope gradients and then reapplying that deformation data to the prototype scenario. This type of investigation would need to be coupled with a non-invasive geophysical (resitivity) survey to determine the thickness of the head deposit and the angle of underlying bedrock – back analysis would then allow a recalculation of past movement rates at that location. The technique would also allow the reconstruction of the formative processes occurring during the development of diagnostic features used to infer past climatic records (i.e. ice wedge casts, involutions, pingos, etc) (Huijzer & Vendenburghe, 1998; Isarin, 1997). By the repeated modelling of these processes within different host sediments of known geotechnical properties. The current methodology could therefore provide an approximation towards the ability of each material to form a physical record for the presence of the Quaternary feature, for example, to examine whether an ice-wedge cast or pingo rampart will be

preferentially preserved within a specific soil type. In that further simulations can determine the degree to which geotechnical soil properties may have imprinted an influence upon the distribution of Quaternary diagnostic features, and therefore potentially enable further discussion with reference to the distribution of previous Pleistocene estimations of MAAT (Huijzer & Isarin, 1997).

BIBLIOGRAPHY

Akerman, H.J. (1993) Solifluction and creep rates 1972-1991, Kapp Linne, West Spitsbergen. In: Frenzel, B. (ed.) *Solifluction and Climatic Variation in the Holocene.* Special Issue 6, European Science Foundation Project on European Palaeoclimate and Man. Stuggart, Akademie der Wissenschaften and Literature Mainz. Pg 225-249.

Akerman, H.J. (1996) Slow mass movements and climatic relationships, 1972-1994, Kapp Linne, West Spitsbergen. In: Anderson, M.G. & Brooks, S.M. (eds.) *Advances in Hillslope Processes* (volume two). Wiley, Chichester. Pg 1219-1256.

Alexander, C.S. & Price, L.W. (1980) Radiocarbon dating of the rate of movement of two solifluction lobes in the Ruby Range, Yukon Territory. *Quaternary Research*, **13**, pg 365-379.

Anderson, D.M., Pusch, R. & Penner, E. (1978) Physical and Thermal Properties of Frozen Ground. In: Andersland, O.B. & Anderson, D.M. (eds.) *Geotechnical Engineering for Cold Regions*. New York, McGraw-Hill. Pg 37-103.

Andersson, J.G. (1906) Solifluction, a component of subaerial denudation. *Journal of Geology*, **14**, pg 91-122.

Associate Committee on Geotechnical Research (1988) *Glossary of Permafrost and Related Ground-ice Terms*. Associate Committee on Geotechnical Research (Permafrost Subcommittee), Ottawa, National Research Council of Canada.

Atkinson, J.H. (1981) *Foundations and Slopes: an introduction to critical state soil mechanics*. McGraw-Hill, London

Auzet, A-V. & Ambroise, B. (1996) Soil creep dynamics, soil moisture and temperature conditions on a forested slope in the granitic Vosges Mountains, France. *Earth Surface Processes and Landforms*, **21**, pg 531-542.

Azizi, F. (1999) *Applied Analyses in Geotechnics*. E & FN Spon, London.

Ballantyne, C.K. (2001) Measurement and theory of ploughing boulder movement. *Permafrost and Periglacial Processes*, **12**, pg 267-288.

Ballantyne, C.K. & Harris, C. (1994) *The Periglaciation of Great Britain*. Cambridge University Press.

Barralos, P. (2000) *Cardiff School of Engineering: guidance on the completion of centrifuge balance calculation and test authorisation spreadsheet* (revision 5). Internal Publication, Cardiff University.

Barsch, D. (1993) Periglacial geomorphology in the 21st century. *Geomorphology*, **4**, pg 141-163.

Baulig, J. (1957) Peneplains and pediplains. *Bulletin of the Geological Society of*

America, **68**, pg 913-930.

BBC News (*Margaret Gilmore*) (2000) Meltdown in the Alps. **05/04/00**.

Benedict, J.B. (1970) Downslope soil movement in a Colorado alpine region: rates, processes and climatic significance. *Arctic and Alpine Research*, **2**, pg 165-226.

Benedict, J.B. (1976) Frost Creep and Gelifluction features: a review. *Quaternary Research*, **6**, pg 55-76.

Bennett, L.P. & French, H.M. (1988) Observations on near-surface creep in permafrost, Eastern Melville Island, Arctic Canada. *Proceedings of the 5th International Conference on Permafrost.* Trondheim, Norway, **1**, pg 682-688. Tapir Press.

Bennett, L.P. & French, H.M. (1991) Solifluction and the role of permafrost creep, eastern Melville Island, N.W.T., Canada. *Permafrost and Periglacial Processes*, **2**, pg 95-102.

Berthling, I., Eiken, T. & Sollid, J.L. (2001) Frost heave and thaw consolidation of ploughing boulders in a mid-alpine environment, Finse, southern Norway. *Permafrost and Periglacial Processes*, **12**, pg 165-177.

Bertran, P. (1993) Deformation-induced microstructures in soils affected by mass movements. *Earth Surface Processes and Landforms*, **18**, pg 645-660.

Bertran, P. & Texier, J-P. (1999) Facies and microfacies of slope deposits. *Catena*, **35**, pg 99-121.

Beskow, G. (1935) *Soil freezing and frost heaving with special application to roads and railroads*. The Swedish Geological Survey, C, **375** (3), Translated by Technological Institute, Northwestern University.

Black, R. F. (1976) Periglacial Features Indicative of Permafrost: Ice and Soil Wedges. *Quaternary Research*, **6**, pg 3-26.

Bondarenko, G.I. (1993) Prediction of stability of solifluction slopes and structures on them. In: *Proceedings of the 6th International Conference on Permafrost (Beijing, China)*, **1**, Lanzhou, South China University of Technology Press, pg 851-854.

Brennan, A.J. & Madabhushi, S.P.G. (2002) Liquefaction remediation by vertical drain groups. *Proceedings of the 1st International Conference on Physical Modelling in Geotechnics*, Newfoundland, Canada. Swets & Zietlinger Lisse. Pg 553-560.

British Standard 1377 (1990) & British Standard 5930 (1981) & British Standard S812-109 (1990). *Soil Testing Procedures*. HMSO.

Bromhead, E.N. (1992) *The Stability of Slopes*. Surrey University Press.

Brown, R.J.E. (1963) Influence of vegetation on permafrost. *Proceedings of the 1st International Conference on Permafrost*, Lafayette, Indiana, USA. Pg 20-24.

Brown, R.J.E. (1970) *Permafrost in Canada*. University of Toronto Press, Toronto.

Brown, R.J.E. (1978) Influence of climate and terrain on ground temperature in the continuous permafrost zone of northern Manitoba and Keewatin District, Canada. *Proceedings of the 3rd International Conference on Permafrost (Edmonton, Alberta)*, **1**, National Research Council of Canada, pg 15-21.

Brunsden, D. & Prior, D.B. (1985) *Slope Instability*. London, John Wiley & Son.

Burbidge, G. F.,French, H. M. & Rust, B. R. (1988) Water escape fissures resembling ice-wedge casts in Late Quaternary subaqueous outwash near St. Lazare, Quebec, Canada. *BOREAS*, **17**, pg 33-40.

Burn, C.R. & Smith, C.A.S. (1988) Observations of the "Thermal Offset" in near-surface mean annual ground temperatures at several sites near Mayo, Yukon Territory, Canada. *Arctic*, **41** (2), pg 99-104.

Burrough, P.A. & McDonnell, R.A. (1998) *Principles of Geographical Information Systems*. Oxford, Oxford University Press.

Burt, T.P. & Williams, P.J. (1976) Hydraulic conductivity in frozen soils. *Earth Surface Processes*, **1**, pg 349-360.

Campbell, S., Hunt, C.O., Scourse, J.D. & Keen, D.H. (eds.) (1998) *Quaternary of South-west England*. Chapman Hall, London.

Carver, S., Mikkelsen., N. & Woodward, J. (2002) Long term rates of mass wasting in Mesters Vig, northeast Greenland: Notes on a re-survey. *Permafrost and Periglacial Processes*, **13**, pg 243-249.

Casagrande, A. (1932) Research on the Atterberg Limits of soils. *Public Roads, Washington*, **13**, pg 121-136.

Chamberlain, E.J. (1981) Frost susceptibility of soil and review of index tests. *United States Army Cold Regions Research and Engineering Laboratory – Monograph 81-82*. Hanover, New Hampshire.

Chamberlain, E.J. (1987) A freeze-thaw test to determine the frost susceptibility of soils. *Cold Regions Research and Engineering Laboratory, Special Report*, **87**-1.

Chamberlain, E.J. & Gow, A.J. (1978) Effect of freezing and thawing on the permeability and structure of soils. *In: Proceedings of the International Symposium on Ground Freezing (Bochum, Germany)*. Ruhr University, pg 31-44.

Chen, X., Schofield, A.N. & Smith, C.C. (1993) Preliminary tests of heave and settlement of soils undergoing one cycle of freeze-thaw in a closed system on a

small centrifuge. *Proceedings of the 6th International Conference on Permafrost.* Beijing. **2**, pg 1070-1072.

Cheng, G. (1983) The mechanism of repeated ice-segregation for the formation of thick layered ground ice. *Cold Regions Science and Technology*, **8**, pg 57-66.

Chorley, R.J. (1978) Bases for theory in geomorphology. In: Embelton, C., Brunsden, D. & Jones, D.K.C. (eds.) *Geomorphology: Present Problems and Future Prospects*. Oxford University Press.

Clark, J.J. & Phillips, R. (2003) Centrifuge modelling of frost heave of arctic pipelines. In: M. Phillips, S.M. Springman and L.U. Arenson (eds.) *Proceedings 8th International Conference on Permafrost*, **1**, pg 151-156, Balkema, Lisse, The Netherlands.

Coelho, P.A.L.F., Haigh, S.K. & Madabhushi, S.P.G. (2003) Boundary effects in dynamic centrifuge modelling of liquefaction in sand deposits. *Proceedings of the 16th ASCE Engineering Mechanics Conference.* University of Washington, Seattle.

Collins, K. & McGown, A. (1974) The form and function of microfabric features in a variety of natural soils. *Geotechnique*, **24** (2), pg 223-254.

Corte, A.E. (1966) Particle sorting by repeated freezing and thawing. *Biuletyn Peryglacjalny*, **15**, pg 175-240.

Coutard, J.-P. & Mucher, H.J. (1985) Deformation of laminated silt loam due to repeated freezing and thawing cycles. *Earth Surface Processes and Landforms*, **10**, pg 309-319.

Coutard, J.-P., Van Vliet-Lanoe, B., Auzet, A.-V. (1988) Frost heaving and frost creep on an experimental slope: results for soil structures and sorted stripes. *Zeitschrift fur Geomorphologie*, Supplementbande, **71**, pg 13-23.

Craig, W.H. (1988) On the uses of a centrifuge. In: Corte, J-F (ed.) *Proceedings of the International Conference on Geotechnical Centrifuge Modelling '88.* Paris, **1**, pg 1-6. Rotterdam, Balkema.

Craig, W.H. (1989) Edouard Phillips (1821-1889) and the idea of centrifuge modelling. *Geotechnique*, **39** (4), pg 697-700.

Croce, P., Pane, V., Znidarcic, H., Yo, H.Y., Olsen, H.W. & Schiffman, R.L. (1985) Evaluation of consolidation theories by centrifuge modelling. In: Craig, W.H. (ed.) *Application of Centrifuge Modelling to Geotechnical Design*, pg 381-401. A.A. Balkema, Rotterdam.

Davies, J. L. (1972) *Landforms of Cold Climates; an introduction to systematic geomorphology*. Massachusetts Institute of Technology Press.

Davies, M.C.R., Hamza, O. & Harris, C. (2001) The effect of rise in mean annual temperature on the stability of rock slopes containing ice-filled discontinuities.

Permafrost and Periglacial Processes, **12**, pg 137-144.

Depountis, N. (2000) Geotechnical centrifuge modelling of capillary phenomena and contaminant migration in unsaturated soils. *Unpublished PhD Thesis.* University of Wales, Cardiff, UK.

Dore, G., Konrad, J-M. & Berube, M-A. (1998) The effect of consolidation on frost susceptibility of silty soils. *Proceedings of the 7th International Conference on Permafrost.* Yellowknife, Laval University, **1**, pg 239-244. Montreal.

Douglas, T.D. & Harrison, S. (1987) Late Devensian periglacial slope deposits in the Cheviot Hills. In: Boardman, J. (ed.) *Periglacial Processes and Landforms in Britain and Ireland*, Quaternary Research Association, Cambridge University Press.

Douglas, T.D. & Harrison, S. (1996) Turf-banked terraces in Oraefi, Southeast Iceland: morphometry, rates of movement, and enviromental controls. *Arctic and Alpine Research*, **28**, pg 228-236.

Druck Technical Report (1999) High Performance Pressure Transducers. *Miniature Series*. 06/1999.

Dyke, L. & Eggington, P.A. (1990) Influence of ice lens fabric on the hydraulic conductivity of thawing soil. In: *Proceedings of the Fifth Canadian Permafrost Conference*, Laval, Nordicana, **54**, pg 137-141.

Dylik, J. (1951) Some periglacial structures in Pleistocene deposits of Middle Poland. *Bulletin de la Societe des Sciences et des letters de lodz*, **3**, pg 1-6.

Dylik, J. (1964) The essentials of the meaning of the term 'periglacial'. *Biuletyn Peryglacjalny*, **15**, pg 1-19.

Eggington, P.A. & French, H.M. (1985) Solifluction and related processes, eastern Banks Island, N.W.T. *Canadian Journal of Earth Sciences*, **22**, pg 1671-1678.

Feldman, G.M. (1988) Formation problem of thick ice streaks in ice saturated horizons in permafrost. *Proceedings of the 5th International Conference on Permafrost.* Trondheim, Norway, **1**, pg 339-343. Tapir Press.

Folk, R.L. & Ward, W.C. (1957) Brazos River bar: a study in the significance of grain size parameters. *Journal of Sedimentary Petrology*, **27** (1), pg 3-26.

Francou, B. & Bertran, P. (1997) A multivariate analysis of clast displacement rates on stone-banked sheets, Cordillera Real, Bolivia. *Permafrost and Periglacial Processes*, **8**, pg 371-382.

Fredlund, D.G. & Rahardjo, H. (1993) *Soil Mechanics for Unsaturated Soils.* John Wiley & Sons. New York.

French, H.M. (1988) Active Layer Processes. In: Clark, M.J. (ed.) *Advances in*

Periglacial Geomorphology, pg 151-198. John Wiley & Sons.

French, H.M. (1996) *The Periglacial Environment* (second edition). Longman.

French, H.M. (2000) Does Lozinski's periglacial realm exist today? A discussion relevant to modern usage of the term 'periglacial'. *Permafrost and Periglacial Processes*, **11**, pg 35-42.

French, H.M. (2003) The development of periglacial geomorphology: 1- up to 1965. *Permafrost and Periglacial Processes*, **14**, pg 29-60.

Fukuda, M. (1982) Heat flow measurements in freezing soils with various freezing front advancing rates. *Proceedings of the 4th International Conference on Permafrost,* Fairbanks, Alaska, **1**, pg 445-452, Washington DC, National Academic Press.

Fukushima, S. & Tatsuoka, F. (1984) Strength and deformation characteristics of saturated sand at extremely low pressures. *Soils and Foundations*, **24** (4), pg 30-48.

Gallop, M. (1991) *Quaternary periglacial slope deposits in south-west England: field data and laboratory simulation.* Unpublished PhD thesis, University of Wales, Cardiff, UK.

Gamper, M.W. (1983) Controls and rates of movement of solifluction lobes in the Eastern Swiss Alps. *Proceedings of the 4th International Conference on Permafrost (Fairbanks, Alaska)*, **1**, pg 328-333, Washington DC, National Academic Press.

Gardiner, V. & Dackombe, R. (1987) *Geomorphological Field Manual.* Allen & Unwin, London.

Gengnian, L., Heigang, X. & Zhijiu, C. (1995) Gelifluction in the alpine periglacial environment of the Tianshan Mountains, China. *Permafrost and Periglacial Processes*, **6**, pg 265-271.

Gold, L.W. (1967) Influence of surface conditions on ground temperature. *Canadian Journal of Earth Sciences*, **4**, pg 199-208.

Gold, L.W. & Lachenbruch, A.H. (1973) Thermal conditions in permafrost – a review of North American literature. In: *Permafrost: North American Contribution, 2nd International Permafrost Conference (Yakutsk, USSR).* National Academy of Science, Washington. Pg 3-25.

Goodings, D.J. & Gillette, D.R. (1991) Grain and model size in centrifuge models of granular slope instability. In: Ko, H-K & McLean, F.G. (eds.) *Proceedings of the International Conference on Geotechnical Centrifuge Modelling '91.* Paris, **1**, pg 583-590. Rotterdam, Balkema.

Gorbunov, A.P. (1988) The alpine permafrost zone of the USSR. *Proceedings of the Fifth International Permafrost Conference*, Trondheim, Norway. **1**, pg 154-

158. Tapir Press.

Gorbunov, A.P. & Seversky, E.V. (1999) Solifluction in the mountains of Central Asia: distribution, morphology, processes. *Permafrost and Periglacial Processes*, **10**, pg 81-89.

Grab, S. (2001) Needle Ice Observations from the High Drakensburg, Lesotho. *Permafrost and Periglacial Processes*, **12**, pg 227-231.

Grechishchev, S.E., Pavlov, A.V. & Ponomarev, V.V. (1992) Changes in microstructure of fine-grained soils due to freezing. *Permafrost and Periglacial Processes*, **3**, pg 1-10.

Greenway, D.R. (1987) Vegetation and slope stability. In: Anderson, M.G. & Richards, K.S. (eds.) *Slope Stability*, pg 187-230. John Wiley & Sons.

Grober, H., Erk, S. & Grigull, U. (1961) *Fundamentals of Heat Transfer*. McGraw-Hill.

Gyssels, G. & Poesen, J. (2003) The importance of plant root characteristics in controlling concentrated flow erosion rates. *Earth Surface Processes and Landforms*, **28**, pg 371-384.

Haeberli, W. (2000) Modern research perspectives relating to permafrost creep and rock glaciers: a discussion. *Permafrost and Periglacial Processes*, **11**, pg 290-293.

Haeberli, W. & Burn, C.R. (2002) Natural Hazards in Forests: glacier and permafrost effects as related to climate change. In: Sidle, R.C. (ed.) *Environmental Change and Geomorphic Hazards in Forests*, pg 167-202. IUFRO Research Series **9**, CABI Publishing.

Hallet, B. & Waddington, D. (1992) Buoyancy forces induced by freeze-thaw in the active layer: implications for diapirism and soil circulation. In: Dixon, J.C. & Abrahams, A.D. (eds.) *Periglacial Geomorphology*. Wiley, Chichester, pg 251-279.

Harlan, R.L. & Nixon, J.F. (1978) Ground Thermal Regime. In: Andersland, O.B. & Anderson, D.M. (eds.) *Geotechnical Engineering for Cold Regions*. New York, McGraw-Hill. Pg 103-164.

Harris, C. (1972) Processes of soil movement in turf banked solifluction lobes, Okstindan, northern Norway. *Transactions of the Institute of British Geographers*, Special Publication **4**, pg 155-174.

Harris, C. (1977) Engineering properties, groundwater conditions, and the nature of soil movement on a solifluction slope in north Norway. *Quarterly Journal of Engineering Geology*, **10**, pg 27-43.

Harris, C. (1981) *Periglacial Mass Wasting – A Review of Research*. BGRG Research Monograph (**4**), Geobooks.

Harris, C. (1983) Vesicles in thin sections of periglacial soils from north and south Norway. *Proceedings of the 4th International Conference on Permafrost.* Fairbanks, Alaska, **1**, pg 445-449.

Harris, C. (1985) Geomorphological applications of soil micromorphology with particular reference to periglacial sediments and processes. In: Richards, K.S., Arnett, R.R.. & Ellis, S. (eds.) *Geomorphology and Soils*, George Allen & Unwin, London,

Harris, C. (1987) Mechanisms of mass movement in periglacial environments. In: Anderson, M.G. & Richards, K.S. (eds.) *Slope Stability*, pg 531-559. John Wiley & Sons.

Harris, C. (1993) The role of climate and soil properties in periglacial solifluction: evidence from laboratory simulation studies. In: Frenzel, B. (ed.) *Solifluction and Climatic Variation in the Holocene.* Special Issue 6, European Science Foundation Project on European Palaeoclimate and Man. Stuggart, Akademie der Wissenschaften and Literature Mainz, pg 295-308.

Harris, C. (1996) Physical modelling of periglacial solifluction: review and future strategy. *Permafrost and Periglacial Processes*, **7**, pg 349-360.

Harris, C. (1998) The micromorphology of paraglacial and periglacial slope deposits: a case study from Morfa Bychan, west Wales, UK. *Journal of Quaternary Science*, **13** (1), pg 73-84.

Harris, C. (2000) Geotechnical Centrifuge Modelling of Mass Movement Processes associated with Thawing Permafrost Soils. In: Bromhead, E., Dixon, N. & Ibsen, M.L. (eds.) *Proceedings of the 8th International Landslide Conference*, Cardiff, **1**, Thomas Telford, London. Pg 693-701.

Harris, C. & Davies, M.C.R. (1996) Processes of thaw-induced mass movement in non-cohesive soils: results of an instrumented slope simulation experiment. In: Anderson, M.G. & Brooks, S.M. (eds.) *Advances in Hillslope Processes* (Volume 2). John Wiley & Sons. Pg 1154-1171.

Harris, C. & Davies, M.C.R. (1998) Pressures recorded during laboratory freezing and thawing of a natural silt-rich soil. *Proceedings of the 7th International Conference on Permafrost.* Yellowknife, Laval University, **1**, pg 433-439. Montreal.

Harris, C. & Davies, M.C.R. (2000) Gelifluction: observations from large-scale laboratory simulations. *Arctic, Antarctic, and Alpine Research*, **32** (2), pg 202-207

Harris, C., Davies, M.C.R., & Coutard, J.-P. (1995) Laboratory simulation of periglacial solifluction: significance of porewater pressure, moisture contents and undrained shear strength during thawing. *Permafrost and Periglacial Processes*, **6**, pg 293-312.

Harris, C., Davies, M.C.R., & Coutard, J.-P. (1996) An experimental design for large-scale modelling of solifluction processes. *Earth Surface Processes and Landforms*, **21**, pg 67-76.

Harris, C., Davies, M.C.R., & Coutard, J.-P. (1997) Rates and processes of periglacial solifluction: an experimental approach. *Earth Surface Processes and Landforms*, **22**, pg 849-868.

Harris, C., M.C.R. Davies & Etzelmuller, B. (2001a) The assessment of potential geotechnical hazards associated with mountain permafrost in a warming global climate. *Permafrost and Periglacial Processes*, **12**, pg 145-156.

Harris, C., Davies, M. C. R., & Rea B.R. (2000) Geotechnical Centrifuge Modelling of Gelifluction: Validation of a New Approach to Cryogenic Mass Movement Process Studies. *Annals of Glaciology*, **31**, 417-421.

Harris, C., Davies, M.C.R. & Rea, B. (2002) Centrifuge modelling of slope processes in thawing ice-rich soils. In: Phillips, R., Guo, P. & Popescu, R. (eds.) *Proceedings of the International Conference on Physical Modelling in Geotechnics*, St Johns, Newfoundland, Canada. Balkema. Pg 297-302.

Harris, C., Davies, M.C.R., & Rea, B. (2003a) Gelifluction: viscous flow or plastic creep? *Earth Surface, Processes and Landforms*, **28** (12), pg 1289-1301.

Harris, C. & Ellis, S. (1980) Micromorphology of soils in soliflucted materials, Okstindan, northern Norway. *Geoderma*, **23**, pg 11-29.

Harris, C., Gallop, M. & Coutard J.-P. (1993) Physical modelling of gelifluction and frost creep: some results of a large-scale simulation experiment. *Earth Surface Processes and Landforms*, **18**, pg 383-398.

Harris, C., Haeberli, W., Vonder Muhll, D. & King, L. (2001c) Permafrost monitoring in the high mountains of Europe: The PACE Project in its global context. *Permafrost and Periglacial Processes*, **12**, pg 3-12.

Harris, C. & Haeberli, W. (2003) Warming permafrost in the mountains of Europe. *World Meterological Organization Bulletin*, July 2003, **52** (3).

Harris, C. & Lewkowicz, A. (1993) Micromorphological investigations of active-layer detachment slides, Ellesmere Island, Canadian Arctic. *Proceedings of the 6th International Conference on Permafrost.* Beijing. **1**, pg 232-237.

Harris, C. & Lewkowicz, A.G. (2000) An analysis of the stability of thawing slopes, Ellesmere Island, Nunavut, Canada. *Canadian Geotechnical Journal*, **37** (2), pg 449-462.

Harris, C., Murton, J. & Davies, M.C.R. (2000) Soft sediment deformation during thawing of ice-rich frozen soils: results of scaled centrifuge modelling experiments. *Sedimentology*, **47**, pg 687-700.

Harris, C., Rea, B. & Davies, M.C.R. (2001b) Scaled physical modelling of mass movement processes on thawing slopes. *Permafrost and Periglacial Processes*, **12**, pg 125-135.

Harris, C., Vonder Muhll, D., Isaksen, K., Haeberli, W., Sollid, L., King, L., Holmlund, P., Dramis, F., Guglielmin., M. & Palacios, D. (2003b) Warming permafrost in European mountains. *Global and Planetary Change*, **39**, pg 215-225.

Harris, S.A., Cheng, G., Zhao, X. & Yongqin, D. (1998) Nature and dynamics of an active block stream, Kunlun Pass, Qinghai Province, Peoples' Republic of China. *Geografiska Annaler*, **80A**, pg 123-133.

Harry, G. D. & Gozdzik, J. S. (1988) Ice wedges: growth, thaw transformation, and palaeoenvironmental significance. *Journal of Quaternary Science*, **3**, pg 39-55.

Head, K.H. (1992) *Manual of soil laboratory testing (Volume one: soil classification and compaction tests)*. Second Edition. Pentech.

Head, K.H. (1994) *Manual of soil laboratory testing (Volume two: Permeability, shear strength, and compressibility tests)*. Second Edition. Wiley, New York.

Henry, K.S. & Holtz, R.D. (2001) Geocomposite capillary barriers to reduce frost heave in soils. *Canadian Geotechnical Journal*, **38**, pg 678-694.

Higashi, A. & Corte, A.E. (1971) Solifluction: a model experiment. *Science*, **171**, pg 480-482.

Hirakawa, K. (1989) Downslope movement of solifluction lobes in Iceland: a tephrostratigraphic approach. *Geographic Report*, Tokyo Metropolitan University, **24**, pg 15-30.

Hugenholtz, C.H. & Lewkowicz, A.G. (2002) Morphometry and Environmental Characteristics of Turf-Banked Solifluction Lobes, Kluane Range, Yukon Territory, Canada. *Permafrost and Periglacial Processes*, **13**, pg 301-313.

Huijzer, A.S. & Isarin, R.F.B. (1997) The reconstruction of past climates using multi-proxy evidence; An example of Weichselian pleniglacial in northwest and central Europe, *Quaternary Science Reviews*, **16** (6), pg 513-533.

Huijzer, B. & Vendenberghe, J. (1998) Climate reconstructions of the Weichselian Pleniglacial in northwestern and central Europe. *Journal of Quaternary Science*, **13**, pg 391-418.

Hulme, M. (1999) Global warming. *Progress in Physical Geography*, **23** (2), pg 283-291.

Hutchinson, J.N. (1991) Theme lecture: Periglacial and slope processes. In: Forster, A., Culshaw, M.G., Cripps, J.C., Little, J.A. & Moon, C.F. (eds.) *Quaternary Engineering Geology*, Geological Society Engineering Geology Special Edition, **7**, pg 283-331.

Irving, D.H.B. (2000) Scaled physical modelling of permafrost creep processes with the geotechnical centrifuge. *Unpublished PhD Thesis*. University of Wales, Cardiff, UK.

Isaksen, K., Hauck, C., Gudevang, E., Odegard, R.S. & Sollid, J.L. (2002) Mountain permafrost distribution in Dovrefjell and Jotunheimen, southern Norway, based upon BTS and DC resistivity tomography data. *Norwegian Journal of Geography*, **56**.

Isarin, R. F. B. (1997) Permafrost distribution and temperatures in Europe during the Younger Dryas. *Permafrost and Periglacial Processes*, **8**, pg 313-333.

Jaesche, P-H., Viet, H., Huwe, B. & Stingl, H. (1997) Influence of water and heat dynamics on solifluction movements in a periglacial environment in the Eastern Alps (Austria). *Proceedings of the International Symposium on the Physics, Chemistry, and Ecology of Seasonally Frozen Ground.* Fairbanks, Alaska, **97-10**, pg 80-86. CRREL Extended Abstracts.

Jaesche, P-H., Veit, H. & Huwe, B. (2003) Snow Cover and Soil Moisture Controls on Solifluction in an Area of Seasonal Frost, Eastern Alps. *Permafrost and Periglacial Processes*, **14**, pg 399-410.

Jahn, A. (1975) *Problems of the Periglacial Zone.* PWN Polish Scientific Publishers, Warsaw.

Jahn, A. (1985) Experimental observations of periglacial processes in the Arctic. In: Church, M. & Slaymaker, O. (eds.) *Field and Theory: Lectures in geocryology*, pg 17-34. Vancouver: University of British Columbia Press.

Jahn, A. (1991) Slow soil movement in Tarfala Valley, Kebnekaise Mountains, Swedish Lapland, *Geografiska Annaler*, **73A**, pg 93-107.

Jiacheng, W. & Yujie, W. (1998) A study of the microstructure of frozen soils. *Proceedings of the 7th International Conference on Permafrost.* Yellowknife, Laval University, **2**, pg 1115-1118. Montreal.

Jianming, Z., Changqing, Z., Yafeng, L. & Tiande, M. (1998) Analyses of microstructure damage from the creep process in frozen soil using a scanning electron microscope. *Proceedings of the 7th International Conference on Permafrost.* Yellowknife, Laval University, pg 1213-1216. Montreal.

Jumikis, A.R. (1956) The Soil Freezing Experiment. *Highways Research Board Bulletin*, **135**, pg 150-165.

Jumikis, A.R. (1973) Effect of porosity on the amount of soil water transferred in a freezing silt. In: *Permafrost: North American Contribution, 2nd International Permafrost Conference (Yakutsk, USSR).* National Academy of Science, Washington. Pg 305-310.

Kalaugher, P.G. & Grainger, P. (1991) The influence of changes in sea level on coastal cliff instability in Devon. In: Forster, A., Culshaw, M.G., Cripps, J.C., Little, J.A. & Moon, C.F. (eds.) *Quaternary Engineering Geology*, Geological Society Engineering Geology Special Edition, **7**, pg 361-367.

Karte, J. (1987) Pleistocene periglacial conditions and geomorphology in north central Europe. In: Boardman, J. (ed.) *Periglacial Processes and Landforms in Britain and Ireland*, Quaternary Research Association (pg 67-77), Cambridge University Press.

Kasse, C. (1999) Can involutions be used as palaeotemperature indicators? *Biuletyn Peryglacjalny*, **38**, pg 95-110.

Keen, D.H. (1998) Start Point to Prawle Point. In: Campbell, S., Hunt, C.O., Scourse, J.D. & Keen, D.H. (eds.) *Quaternary of South-west England.* Chapman Hall, London. Pg 167-170.

Kemp, D.D. (1994) *Global Environmental Issues: a climatological approach.* Routledge, London.

Kemp, R.A. (1985) *Soil micromorphology and the Quaternary.* Quaternary Research Association Technical Guide No. 2, Cambridge.

Ketcham, S.A. & Black P.B. (1995) Initial results from small-scale frost heave experiments in a centrifuge. *U.S. Cold Regions Research and Engineering Laboratory Report*, **95-9**, 18pp.

Ketcham, S.A., Black, P.B. & Pretto, R. (1997) Frost heave loading of constrained footing by centrifuge modelling. *Journal of Geotechnical and Geoenvironmental Engineering*, September 1997, pg 874-880.

Kirkby, M.J. (1995) A model for variations in gelifluction rates with temperature and topography: implications for global change. *Geografiska Annaler*, **77A**, pg 269-278.

Ko, H-Y. (1988) Summary of the state-of-the-art in centrifuge model testing. In: Craig, W.H., James, R.G. & Schofield, A.N. (eds.) *Centrifuges in Soil Mechanics.* Balkema, Rotterdam. Pg 11-18

Konrad, J-M. (1988) Temperature of ice lens formation in freezing soils. *Proceedings of the 5th International Conference on Permafrost.* Trondheim, Norway, **1**, pg 384-389. Tapir Press.

Konrad, J-M. & Morgenstern, N.R. (1980) A mechanistic theory of ice lens formation in fine-grained soils. *Canadian Geotechnical Journal*, **17**, pg 473-486.

Konrad, J-M. & Morgenstern, N.R. (1981) The segregation potential of a freezing soil. *Canadian Geotechnical Journal*, **18**, pg 482-491.

Kruse, G.A.M. & Bezuijen, A. (1998) The use of CT scans to evaluate soil models.

In: Kimura, T., Kusakabe, O. & Takemura, J. (eds.) Proceedings of the International Conference. *Centrifuge 98*, Tokyo, Japan. Rotterdam, A.A. Balkema. Pg 79-84.

Kumai, M. (1988) Microstructure of frozen soils examined by SEM. *Proceedings of the 5th International Conference on Permafrost.* Trondheim, Norway, **1**, pg 390-395. Tapir Press.

Lawson, D.E. (1979) Sedimentological analysis of the western terminus region of the Matanuska Glacier, Alaska. *CRREL Report*, **79-9**.

Lewkowicz, A.G. (1988) Slope Processes. In: Clark, M.J. (ed.) *Advances in Periglacial Geomorphology*, pg 325-368. John Wiley & Sons.

Lewkowicz, A.G. (1989) Periglacial Systems. In: Briggs, D., Smithson, P, & Ball, T. (eds.) *Fundamentals of Physical Geography (Canadian Edition)*, pg 363-397. Copp Clark Pitman, Toronto.

Lewkowicz, A.G. (1990) Micromorphology, frequency, and magnitude of active-layer detachment slides, Fosheim Peninsula, Ellesmere Island, N.W.T. In: Burgess, M.M., Harry, D.G. & Sego, D.C. (eds.) *Proceedings of the 5th Canadian Permafrost Conference*, Quebec, Collection Nordicana No. **54**, pg 111-118.

Lewkowicz, A.G. (1992) A solifluction meter for permafrost sites. *Permafrost and Periglacial Processes*, **3**, pg 11-18.

Lewkowicz, A.G. (1992b) Factors influencing the distribution and initiation of active-layer detachment slides on Ellesmere Island, Arctic Canada. In: Dixon, J.C. & Abrahams, A.D. (eds.) *Periglacial Geomorphology*. Wiley, Chichester, pg 223-250.

Lewkowicz, A.G. & Clark, S. (1998) Late summer solifluction and active layer depths, Fosheim Peninsula, Ellesmere Island, Canada. *Proceedings of the 7th International Conference on Permafrost.* Yellowknife, Laval University, **1**, pg 641-646. Montreal.

Lewkowicz, A.G. & French, H.M. (1982) Downslope water movement and solute concentrations within the active layer, Banks Island, N.W.T. *Proceedings of the 4th International Conference on Permafrost.* Fairbanks, Alaska, **1**, pg 163-171.

Little, J.D., Sandall, H., Walegur, M.T. & Nelson, F.E. (2003) Application of differential global positioning systems to monitor frost heave and thaw settlement in tundra environments. *Permafrost and Periglacial Processes*, **14**, pg 349-357.

Loch, J.P.G. & Kay, B.D. (1978) Water redistribution in partially frozen, saturated silt under several temperature gradients and overburden loads. *Proceedings of Soil Science Society of America*, **42**, pg 400-406.

Longley, P., Goodchild, M., Maguire, D. & Rhind, D. (eds.) (1999) *Geographical*

Information Systems: Principles, Techniques, Applications and Management (second edition), New York, John Wiley & Sons.

Lunardini, V.J. (1998) Effect of convective heat transfer on thawing of frozen soil. *Proceedings of the 7th International Conference on Permafrost.* Yellowknife, Laval University, **1**, pg 689-695. Montreal.

Lunardini, V.J. (1991) *Heat Transfer with Freezing and Thawing.* Elsevier, Amsterdam.

Lyndon, A. & Schofield, A.N. (1970) Centrifugal model of a short term failure in London Clay. *Geotechnique*, **20** (4), pg 440-442.

Mackay, J.R. (1970) Disturbances to the tundra and forest environment of the western Arctic. *Canadian Geotechnical Journal*, **7**, pg 420-432.

Mackay, J.R. (1977) Changes in the active layer from 1968 to 1976 as a result of the Inuvik fire. *Geological Survey of Canada.* Paper **77-1B**, pg 273-275.

Mackay, J.R. (1981) Active layer slope movement in a continuous permafrost environment, Garry Island, NorthWest Territories, Canada. *Canadian Journal of Earth Sciences*, **18**, pg 1666-1680.

Mackay, J.R. (1983) Downward water movement into frozen ground, western arctic coast, Canada. *Canadian Journal of Earth Sciences*, **20** (1), pg 120-134.

Mackay, J.R. (1984) The frost heave of stones in the active layer above permafrost with downward and upward freezing. *Arctic and Alpine Research*, **16**, pg 439-446.

Mackay, J. R. (1986) The first 7 years (1979-1985) of ice wedge growth, Illisarvik experimental drained lake site, western Arctic coast. *Canadian Journal of Earth Sciences*, **23**, pg 1782-1795.

Mackay, J.R. (1992) The frequency of ice-wedge cracking (1967-1987) at Garry Island, western Arctic coast, Canada. *Canadian Journal of Earth Science*, **29**, pg 236-248.

Mackay, J.R. (1993) Air temperature, snow cover, creep of frozen ground, and the time of ice-wedge cracking, western Arctic coast. *Canadian Journal of Earth Science*, **30**, pg 1720-1729.

Mackay, J.R. (1997) A full-scale field experiment (1978-1995) on the growth of permafrost by means of lake drainage, western Arctic coast: a discussion of the method and some results. *Canadian Journal of Earth Sciences*, **34** (1), pg 17-33.

Mackay, J.R. & Mathews, W.H. (1974) Movement of sorted stripes, the Cinder Cone, Garibaldi Park, B.C. Canada. *Arctic and Alpine Research*, **6**, pg 347

Matsuoka, N. (1994) Continuous recording of frost heave and creep on a Japanese Alpine slope. *Arctic and Alpine Research*, **26** (3), pg 245-254.

Matsuoka, N. (1998) Soil moisture variability in relation to diurnal frost heaving on Japanese high mountain slopes. *Permafrost and Periglacial Processes*, **7**, pg 139-151.

Matsuoka, N. (1998b) The relationship between frost heave and downslope movement: field measurements in the Japanese Alps. *Permafrost and Periglacial Processes*, **9**, pg 121-134.

Matsuoka, N. (2001) Solifluction rates, processes and landforms: a global review. *Earth-Science Reviews*, **55**, pg 107-134.

Matsuoka, N. & Hirakawa, K. (2000) Solifluction resulting from one-sided and two-sided freezing: field data from Svalbard. *Polar Geoscience*, **13**, pg 187-201.

Matsuoka, N., Hirikawa, K., Watanabe, T. & Moriwaki, K. (1997) Monitoring of periglacial slope processes in the Swiss Alps: the first two years of frost shattering, heave and creep. *Permafrost and Periglacial Processes*, **8**, pg 155-178.

Matsuoka, N., Hirakawa, K., Watanabe, T., Haeberli, W. & Keller, F. (1998) The role of diurnal, annual and millennial freeze-thaw cycles in controlling Alpine slope stability. *Proceedings of the 7th International Conference on Permafrost.* Yellowknife, Laval University, **2**, pg 711-717. Montreal.

Matsuoka, N. & Humlum, O. (2003) Monitoring Periglacial Processes: New Methodology and Technology. *Permafrost and Periglacial Processes*, **14**, pg 299-303.

Matthews, J.A. & Berrisford, M.S. (1993) Climatic controls on rates of solifluction: variations within Europe. In: Frenzel, B. (ed.) *Solifluction and Climatic Variation in the Holocene.* Special Issue 6, European Science Foundation Project on European Palaeoclimate and Man. Stuggart, Akademie der Wissenschaften and Literature Mainz, pg 363-389.

Matthews, J.A., Harris, C., & Ballantyne, C.K. (1986) Studies on a gelifluction lobe, Jotunheimen, Norway: ^{14}C chronology, stratigraphy, sedimentology, and palaeoenvironment. *Geografiska Annaler*, **68A**, pg 345-360.

McRoberts, E.C. (1978) Slope Stability in Cold Regions. In: Andersland, O.B. & Anderson, D.M. (eds.) *Geotechnical Engineering for Cold Regions.* New York, McGraw-Hill. Pg 363-405.

McRoberts, E.C. & Morgenstern, N.R. (1974) The stability of thawing slopes. *Canadian Geotechnical Journal*, **11**, pg 447-467.

Mikkola, M. & Hartikainen, J. (2001) Mathematical model of soil freezing and its numerical implementation. *International Journal for Numerical Methods in Engineering*, **52**, pg 543-557.

Moore, C.A. & Mitchell, J.K. (1974) Electromagnetic forces and soil strength.

Geotechnique, **24** (4), pg 627-640.

Morgenstern, N.R. (1985) Recent observations on the deformation of ice and ice-rich permafrost. In: Church, M. & Slaymaker, O. (eds.) *Field and Theory: Lectures in geocryology*, pg 133-153. Vancouver: University of British Columbia Press

Morgenstern, N.R. & Nixon, J.F. (1971) One-dimensional consolidation of thawing soils. *Canadian Geotechnical Journal*, **11**, pg 447-469.

Mottershead, D.N. (1971) Coastal head deposits between Start Point and Hope Cove, Devon. *Field Studies*, **3**, pg 433-453.

Mottershead, D.N. (1976) Quantitative Aspects of Periglacial Slope Deposits in South-west England. *Biuletyn Peryglacjalny*, **25**, pg 35-57.

Mottershead, D.N. (1982) Coastal spray weathering of bedrock in the supratidal zone at East Prawle, South Devon. *Field Studies*, **5**, pg 663-684.

Muraleetharan, K.K. & Granger, K.K. (1999) The use of miniature pore pressure transducers in measuring matric suction in unsaturated soils. *Geotechnical Testing Journal*, **22** (3), pg 226-234.

Murton, J.B., Coutard, J-P., Ozouf, J-C., Lautridou, J-P., Robinson, D.A., Williams, R.G.B., Guillemet, G. & Simmons, P. (2000) Experimental design for pilot study on bedrock weathering near the permafrost table. *Earth Surface Processes and Landforms*, **25**, pg 1281-1294.

Murton, J.B., Coutard, J-P., Ozouf, J-C., Lautridou, J-P., Robinson, D.A. & Williams, R.B.G. (2001) Physical modelling of bedrock brecciation by ice segregation in permafrost. *Permafrost and Periglacial Processes*, **12**, pg 255-266.

Murton, J.B. & French, H.M. (1994) Cryostructures in permafrost, Tuktoyaktuk Coastlands, Western Arctic Canada. *Canadian Journal of Earth Sciences*, **31**, pg 737-747.

Murton, J.B. & Harris, C. (2003) The experimental simulation of ice-wedge casting. In: M. Phillips, S.M. Springman and L.U. Arenson (eds.) *Proceedings 8th International Conference on Permafrost*, **2**, pg 807-811, Balkema, Lisse, The Netherlands.

Murton, J.B. & Kolstrup, E. (2003) Ice-wedge casts as indicators of palaeotemperatures: precise proxy or wishful thinking? *Progress in Physical Geography*, **27** (2), pg 155-170.

Nakaya, A. (1995) The effect of vegetation types on mass movement caused by freezing and thawing (in Japanese). *Unpublished MSc Thesis*. University of Tsukaba, Japan.

Nelson, F.E. (1985) A preliminary investigation of solifluction microfabrics. *Catena*, **12**, pg 23-33.

Nelson, F.E., Anisimov, O.E. & Shiklomanov, O.I. (2001) Subsidence risk from thawing permafrost. *Nature*, **410**, pg 889-890.

Nesje, A., Knamme, M. & Rye, N. (1989) Neoglacial gelifluction in the Jostedalsbreen region, western Norway: evidence from buried palaeopodsols. *Earth Surface Processes and Landforms*, **14**, pg 259-270.

Nixon, J.F. (1975) The role of convective heat flow in the thawing of frozen soils. *Canadian Geotechnical Journal*, **12**, pg 425-429.

Nixon, J.F., Ellwood, J.R. & Slusarchuk, W.A. (1982) In situ frost heave testing using cold plates. In: French, H.M. (ed) *The Roger J.E. Brown memorial volume: proceedings of the Fourth Canadian Permafrost Conference (Calgary, Alberta)*. Associate Committee on Geotechnical Research, pg 466-474.

Nixon, J.F. & Ladanyi, B. (1978) Thaw Consolidation. In: Andersland, O.B. & Anderson, D.M. (eds.) *Geotechnical Engineering for Cold Regions*. New York, McGraw-Hill.

Nyberg, R. (1993) Freeze-thaw activity and some of its geomorphic implications in the Abisko Mountains, Swedish Lappland. *Permafrost and Periglacial Processes*, **4**, pg 37-47.

O'Neill, K. & Miller, R.D. (1985) Exploration of a rigid ice model of frost heave. *Water Resources Research*, **21** (3), pg 281-296.

Ohmura, A. & Beniston, M. (1996) Final Report: Thawing of ice and natural hazards in high mountains. *Swiss National Research Programme*, **31**.

Osterkamp, T.E. (1983) Response of Alaskan permafrost to climate. *Proceedings of the 3rd International Conference on Permafrost (Fairbanks)*, **1**, National Academy Press, Washington, pg 145-152.

Overpeck, J., Hughen, K., Hardy, D., Bradley, R., Case, R., Douglas, M., Finney, D., Gajewski, K., Jacoby, G., Jennings, A., Lamoureux, S., Lasca, A., MacDonald, G., Moore, J., Retelle, M., Smith, S., Wolfe, A., & Zielinski, G. (1997) Arctic environmental change of the last four centuries. *Science*, **278**, pg 1251-1258.

Palmer, A.C. (1967) Ice lensing, thermal diffusion, and water migration in freezing soil. *Journal of Glaciology*, **6** (47), pg 681-694.

Penner, E. (1970) Thermal conductivity of frozen soils. *Canadian Journal of Earth Sciences*, **7** (3), pg 982-987.

Penner, E. & Goodrich, L.E. (1980) Location of segregated ice in frost susceptible soil. In: *Proceedings of the 2nd International Symposium on Ground Freezing (Trondheim, Norway)*. Norwegian Institute of Technology, pg 626-639.

Perez, F.L. (1987) Downslope stone transport by needle ice in a High Andean area

(Venezuela). *Rev. Geomorphol. Dyn.*, **36**, pg 33-51.

Perez, F.L. (1992) Miniature sorted stripes in the Paramode Peidras Blancas (Venezuelan Andes). In: Dixon, J.C. & Abrahams, A.D. (eds.) *Periglacial Geomorphology*. Wiley, Chichester, pg 125-157.

Perfect, E. & Williams, P.J. (1980) Thermally induced water migration in frozen soils. *Cold Regions Science and Technology*, **3**, pg 101-109.

Phillips, R. (1995) Centrifuge Modelling: Practical Considerations. In: Taylor, R.N. (ed.) *Geotechnical Centrifuge Technology*. Blackie Academic and Professional, London. Pg 34-60.

Pissart, A. (1990) Advances in periglacial geomorphology. *Zeitschrift fur Geomorphologie*, Supplementband, **79**, pg 119-131.

Pissart, A. (1993) Understanding the controls on solifluction movements in different environments: a methodology and its application in the French Alps. In: Frenzel, B. (ed.) *Solifluction and Climatic Variation in the Holocene.* Special Issue 6, European Science Foundation Project on European Palaeoclimate and Man. Stuggart, Akademie der Wissenschaften and Literature Mainz, pg 209-215.

Platt, J.R. (1964) Strong Inference. *Science*, **146**, pg 347-353.

Polemio, M. & Petrucci, O. (2000) Rainfall as a landslide triggering factor: an overview of recent international research. In: Bromhead, E., Dixon, N. & Ibsen, M.L. (eds.) *Proceedings of the 8th International Landslide Conference*, Cardiff, **1**, Thomas Telford, London. Pg 1219-1226.

Porbaha, A. & Goodings, D.J. (1996) Centrifuge modelling of geotextile-reinforced cohesive soil retaining walls. *Journal of Geotechnical Engineering*, October 1996. Pg 840-848.

Powrie, W. (1997) *Soil Mechanics-Concepts and Application.* E & FN Spon, London.

Price, L.W. (1991) Subsurface movement on solifluction slopes in the Ruby Range, Yukon Territory, Canada: a 20-year study. *Arctic and Alpine Research*, **23**, pg 200-205.

Qiang, Z. (1988) On the distribution of frost heave with depth. *Proceedings of the 5th International Conference on Permafrost.* Trondheim, Norway, **2**, pg 1196-1199. Tapir Press.

Reanier, R.E. & Ugolini, F.C. (1983) Gelifluction deposits as sources of palaeoenvironmental information. *Proceedings of the 4th International Conference on Permafrost,* Fairbanks, Alaska, **2**, pg 1042-1047, Washington DC, National Academic Press.

Rees, W.G. (2001) Improving the accuracy of low-cost GPS measurements for

remote sensing applications. *International Journal of Remote Sensing*, **22** (5), pg 871-881.

Rein, R.G. & Burrous, C.M. (1980) Laboratory measurements of subsurface displacements during thaw of low-angle slopes of a frost-susceptible soil. *Arctic and Alpine Research*, **12**, pg 349-358.

Repelewska-Pekalowa, J. & Pekala, K. (1993) The influence of local factors on solifluction rates. Spitsbergen, Svalbard. In: Frenzel, B. (ed.) *Solifluction and Climatic Variation in the Holocene.* Special Issue 6, European Science Foundation Project on European Palaeoclimate and Man. Stuggart, Akademie der Wissenschaften and Literature Mainz. Pg 251-266.

Rouse, W.R. (1984) Microclimate of Arctic treeline: soil microclimate of tundra and forest. *Water Resources Research*, **20** (1), pg 67-73.

Rouse, W.R. (1993) Northern Climates. In: French, H.M. & Slaymaker, O. (eds.) *Canada's Cold Environments*. Pg 65-92. Montreal and Kingston, McGill-Queens University Press.

Rudberg, S. (1964) Slow mass movement processes and slope development in the Norra Storfjall area, southern Swedish Lapland. *Zeitschrift fur Geomorphologie*, **5**, pg 192-203.

Savidou, C. (1988) Centrifuge modelling of heat transfer in soil. *Centrifuge 88*, **1**, pg 583-591. A.A. Balkema, Rotterdam.

Sawaguchi, S. (1995) Rates and processes of mass movement on periglacial rubble slopes in Spitsbergen (in Japanese). *Journal of Geography*, **104**, pg 874-894.

Sawaguchi, S. & Koaze, T. (1998) Field experiment on periglacial mass movement and frost heave in the Kitakami Mountains, northeastern Japan (in Japanese). *Transactions of Japanese Geomorphological Union*, **19**, pg 221-242.

Schofield, A.N. (1978) Use of centrifugal model testing to assess slope stability. *Canadian Geotechnical Journal*, **15**, pg 14-31.

Schofield, A.N. (1980) Cambridge Geotechnical Centrifuge Operations, 20th Rankine Lecture. *Geotechnique*, **30** (2), pg 227-269.

Schofield, A.N. (1988) An introduction to centrifuge modelling. In: Craig, W.H., James, R.G. & Schofield, A.N. (eds.) *Centrifuges in Soil Mechanics*. Balkema, Rotterdam. Pg 1-11.

Schumm, S.A. (1979) Geomorphic Thresholds: the concept and its applications. *Transactions of the Institute of British Geographers*, NS **4**, pg 485-515.

Selby, M.J. (1993) *Hillslope materials and processes*. Oxford University Press, Oxford.

Shen, M. & Ladanyi, B. (1987) Modelling of coupled heat, moisture and stress field in freezing soil. *Cold Regions Science and Technology*, **14**, pg 237-246.

Skempton, A.W. (1953) Soil mechanics in relation to geology. *Proceedings of the Yorkshire Geological Society*, **29** (1), pg 33-62.

Skempton, A.W. (1988) Geotechnical aspects of the Carsington dam failure. *Proceedings of the 11th International Conference on Soil Mechanics*. Volume **5**. Balkema, Rotterdam. Pg 2581-2591.

Skempton, A.W., Norbury, D. & Petley, D.J. (1991) Solifluction shears at Carsington, Derbyshire. In: Forster, A., Culshaw, M.G., Cripps, J.C., Little, J.A. & Moon, C.F. (eds.) *Quaternary Engineering Geology*, Geological Society Engineering Geology Special Edition, **7**, pg 281-387.

Skempton, A.W. & Weeks, A.G. (1976) The Quaternary history of the Lower Greensand escarpment and Weald Clay vale near Sevenoaks, Kent. *Philosophical Transactions of the Royal Society of London*, **A 283**, pg 493-526.

Smith, C.C. (1995) Cold Regions Engineering. In: Taylor, R.N. (ed.) *Geotechnical Centrifuge Technology*. Blackie, London. Pg 264-292

Smith, D.J. (1987) Frost-heave activity in the Mount Rae area, Canadian Rocky Mountains. *Arctic and Alpine Research*, **19** (2), pg 155-166.

Smith, D.J. (1988) Rates and controls of soil movement on a solifluction slope in the Mount Rae area, Canadian Rockies. *Zeitschrift fur Geomorphologie*, Supplementbande, **71**, pg 25-44.

Smith, D.J. (1992) Long term rates of contemporary solifluction in the Canadian Rocky Mountains. In: Dixon, J.C. & Abrahams, A.D. (eds.) *Periglacial Geomorphology*. The Binghampton Symposia in Geomorphology: International Series, No. **22**, Chichester, Wiley.

Smith, F., Davies, M.C.R., Harris, C. & Rea, B. (1999) Monitoring of solifluction at Finse, Norway. In: Harris, C. (ed.) Permafrost and Climate in Europe: Climate Change, Mountain Permafrost Degradation and Geotechnical Hazard – Annual Report 1999. University of Giessen, Germany.

Smith, J. (1960) Cryoturbation data from South Georgia. *Biuletyn Peryglacjalny*, **8**, pg 73-79.

Smith, M.W. (1975) Microclimatic influences on ground temperatures and permafrost distribution, Mackenzie Delta, NorthWest Territories. *Canadian Journal of Earth Sciences*, **12**, pg 1421-1438.

Smith, M.W. (1985) Observations on soil freezing and frost heaving at Inuvik, NorthWest Territories, Canada. *Canadian Journal of Earth Sciences*, **22**, pg 283-290.

Smith, M.W. & Onysko, D. (1990) Observations and significance of internal pressures in freezing soils. In: *Proceedings of the Fifth Canadian Permafrost Conference, Nordicana*, **54**, pg 75-82.

Smith, M.W. & Patterson, D.E. (1989) Detailed observations on the nature of frost heaving at a field scale. *Canadian Geotechnical Journal*, **26**, pg 306-312.

Smith, S.L. & Williams, P.J. (1990) Ice lens orientation around a chilled buried pipe. *Proceedings of the Fifth Canadian Permafrost Conference, Nordicana*, **54**, pg 83-87.

Sohma, H., Okazawa, S. & Iwata, I. (1979) Slow mass movement processes in an alpine region of Mt. Shirouma Dake, the Japan Alps (in Japanese). *Geographical Review of Japan (Series A)*, **52**. pg 562-579.

Sollid, J.L., Isaksen, K., Eiken, T. & Odegard, R.S. (2003) The transition zone of mountain permafrost on Dovrefjell, southern Norway. In: M. Phillips, S.M. Springman and L.U. Arenson (eds.) *Proceedings 8th International Conference on Permafrost*, **2**, pg 1085-1090, Balkema, Lisse, The Netherlands.

Sone, T., Shiraiwa, T. & Kitahara, T. (1998) Surface stone movements on stone-banked lobes in a nivation hollow on the Daisetsu Mountains, Hokkaido, Japan (in Japanese). *Quarterly Journal of Geography*, **50**, pg 201-207.

Stahli, M., Jansson, P.-E., Lundin, L.-C. & Fluhler, H. (1997) Water infiltration and movement in seasonally frozen soils. In: Iskandar, I.K. *et. al.* (ed.) *Proceedings of the International Symposium of Physics, Chemistry and Ecology of Seasonally Frozen Soils (Fairbanks, Alaska)*. CRREL Special Report, **97-10**, pg 24-30.

Stromquist, L. (1983) Gelifluction and surface wash, their importance and interaction on a periglacial slope. *Geografiska Annaler*, **65A** (3-4), pg 245-254.

Sutherland, H.B. & Gaskin, P.N. (1973) Pore water and heaving pressures developed in partially frozen soils. In: *North American Contribution to the 2nd International Conference on Permafrost (Yakutsk)*. National Academy of Sciences, Washington DC. pg 409-419.

Taber, S. (1929) Frost Heaving. *Journal of Geology*, **37**, pg 428-461.

Taber, S. (1930) The mechanics of frost heaving. *Journal of Geology*, **38**, pg 303-317.

Take, W.A. & Bolton, M.D. (2002) A new device for the measurement of negative pore water pressures in centrifuge models. *Proceedings of the 1st International Conference on Physical Modelling in Geotechnics*, Newfoundland, Canada. Swets & Zietlinger Lisse. Pg 89-96.

Tart, R.G. (2003) Heave and solifluction on slopes. In: M. Phillips, S.M. Springman and L.U. Arenson (eds.) *Proceedings 8th International Conference on*

Permafrost, **2**, pg 1135-1140, Balkema, Lisse, The Netherlands.

Taylor, D.W. (1948) *Fundamentals of Soil Mechanics*. John Wiley, New York.

Taylor, R.N. (1995) Centrifuges in modelling: principles and scale effects. In: Taylor, R.N. (ed.) *Geotechnical Centrifuge Technology*. Blackie Academic and Professional, London. Pg 19-33.

Terzaghi, K. & Peck, R.B. (1967) *Soil Mechanics in Engineering Practice*. John Wiley & Sons, New York.

Tester, R.E. & Gaskin, P.N. (1996) Effect of fines content on frost heave. *Canadian Geotechnical Journal*, **33**, pg 678-680.

The Guardian (*Paul Brown*) (2001) Melting permafrost threatens Alps. **04/01/01**.

The Telegraph (*Charles Clover*) (2001) Alps may crumble as permafrost melts. **04/01/01**.

Thorn, C.E. (1992) Periglacial Gemorphology: what, where, when? In: Dixon, J.C. & Abrahams, A.D. (eds.) (1992) *Periglacial Geomorphology*. Pg 1-30. The Binghampton Symposia in Geomorphology: International Series, No. **22**, Chichester, Wiley.

Thorn, C.E. (2003) Making the Most of New Instrumentation. *Permafrost and Periglacial Processes*, **14**, pg 411-419.

Thornes, J.B. (1983) Evolutionary Geomorphology. *Geography*, **68**, pg 225-235.

Thornthwaite, C.W. (1961) The task ahead. *Annals of the Association of American Geographers*, **51**, pg 345-356.

Vallejo, L.E. & Mawby, R. (2000) Porosity influence on the shear strength of granular material-clay mixtures. *Engineering Geology*, **58**, pg 125-136.

Van Steijn, H., Bertran, P., Francou, B., Hetu, B. & Texier, J.P. (1995) Review of models for genetical interpretation of stratified slope deposits. *Permafrost and Periglacial Processes*, **6**, pg 125-146.

Van Vliet-Lanoe, B. (1985) Frost effects in soils. In: Boardman, J. (ed.) *Soil and Quaternary Landscape Evolution*. John Wiley Publications. Pg 115-156.

Van Vliet-Lanoë, B. (1988) *Le role de la glace de segregations dans les formations superficelles de l'Europe de l'Ouest*. Tome I-II, Editec, Caen.

Van Vliet-Lanoe, B., Coutard, J.-P. & Pissart, A. (1984) Structures caused by repeated freezing and thawing in various loamy sediments. A comparison of active, fossil and experimental data. *Earth Surface Processes and Landforms*, **9**, pg 553-566.

Van Vliet-Lanoe, B. & Langohr, R. (1981) Correlation between fragipans and permafrost with special reference to Weischsel silty deposits in Belgium and northern France. *Catena*, **8**, pg 137-154.

Vandenberghe, J., Kasse, K. & Coope, R. (eds.) (1998) Special Issue on Palaeoclimate of the Last Interglacial-Glacial Cycle in Western and Central Europe. *Journal of Quaternary Science*, **13** (5), pg 361-498.

Varnes, D.J. (1978) Slope movement types and processes. In: Schuster, R.L. & Krizek, R.J. (eds.) *Landslides-Analysis and control: Washington D.C.* National Academy of Sciences, Transportation Research Board Special Report 176, pg 12-33.

Viereck, L.A. (1982) Effects of fire and firelines on active layer thickness and soil temperatures in interior Alaska. *Proceedings of the 4th International Conference on Permafrost,* Fairbanks, Alaska, **1**, pg 445-452, Washington DC, National Academic Press.

Wang, B. & French, H.M. (1994) Climate controls and high-altitude permafrost, Qinghai-Xizang (Tibet) Plateau, China. *Permafrost and Periglacial Processes*, **5**, pg 87-100.

Washburn, A.L. (1967) Instrumented observations of mass-wasting in the Mesters Vig district, NE Greenland. *Meddelesler om Gronland*, **166**, pg 1-297.

Washburn, A.L. (1979) *Geocryology: A survey of periglacial processes and environments*. Edward Arnold.

Washburn, A.L. (1980) Permafrost features as evidence of climatic change. *Earth Science Reviews*, **15**, pg 327-392.

Washburn, A.L. (1999) A High Arctic frost-creep/gelifluction slope, 1981-89: Resolute Bay, Cornwallis Island, Northwest Territories, Canada. *Permafrost and Periglacial Processes*, **10**, pg 163-186.

White, I.D., Mottershead, D.N. & Harrison, S.J. (1992) *Environmental systems: an introductory text*. Second Edition. Chapman & Hall, London.

White, T.L. & Williams, P.J. (1993) Microstructural alteration of a frost heave susceptible soil adjacent to a buried chilled pipeline. *Proceedings of the 6th International Conference on Permafrost.* Beijing. **1**, pg 700-705.

Williams, P.J. (1957a) Some investigations in solifluction features in Norway. *Geographic Journal*, CXXIII, **1**, pg 42-58.

Williams, P.J. (1957b) The direct recording of solifluction movements. *American Journal of Science*, **255**, pg 481-490.

Williams, P.J. (1959) An investigation into processes occurring in solifluction. *American Journal of Science*, **257**, pg 42-58.

Williams, P.J. (1962) Quantitative investigations of soil movement in frozen ground phenomena. *Biuletyn Peryglacjalny*, **11**, pg 353-362.

Williams, P.J. (1966) Downslope soil movement at a Sub-Arctic location with regard to variations with depth. *Canadian Geotechnical Journal*, **3**, pg 191-203.

Williams, P.J. (1972) Use of ice-water surface tension concept in engineering practice. *Frost Action in Soils: National Academy of Science – National Academy for Engineering Highway Research*, Record **393**, Highway Research Board, pg 19-29.

Williams, P.J. (1979) *Pipelines and Permafrost: Physical Geography and Development in the Circumpolar North.* Longman, New York.

Williams, P.J. (1988) Thermodynamic and mechanical conditions within frozen soils and their effects. *Proceedings of the 5th International Conference on Permafrost.* Trondheim, Norway, **1**, pg 493-498. Tapir Press.

Williams, P.J. (1991) Thermal properties and the nature of freezing soils. *Proceedings of the 3rd International Symposium on Cold Regions Heat Transfer,* Fairbanks, Alaska, **1**, pg 57-67, American Society of Mechanical Engineers.

Williams, P.J. & Nickling, W.G. (1971) Ground thermal regime in cold regions. In: Yatsu, E. & Falconer, A. (eds.) *Proceedings of the 2nd Guelph Symposium on Geomorphology*, University of Guelph, Ontario and Geo Abstracts.

Williams, P.J. & Smith, M.W. (1989) *The Frozen Earth – Fundamentals of Geocryology.* Studies in Polar Research, Cambridge University Press.

Woo, M.K. & Gregor, D.J. (1992) *Arctic Environment: Past, Present and Future.* McMaster University Press.

Woo, M.K. & Steer, P. (1983) Slope hydrology as influenced by thawing of the active layer, Resolute, N.W.T. *Canadian Journal of Earth Sciences*, **20**, pg 978-986.

Worsley, P. (1993) Holocene solifluction at Okstindan, northern Norway: a reassessment. In: Frenzel, B. (ed.) *Solifluction and Climatic Variation in the Holocene.* Special Issue 6, European Science Foundation Project on European Palaeoclimate and Man. Stuggart, Akademie der Wissenschaften and Literature Mainz. Pg 49-57.

Yamada, S. Matsumoto, H. & Hirakawa, K. (2000) Seasonal variation in creep and temperature in a solifluction lobe: continuous monitoring in the Daisetsu Mountains, northern Japan. *Permafrost and Periglacial Processes*, **11**, pg 125-135.

Yang, D. & Goodings, D.J. (1996) Centrifuge modelling of frozen soil effects. *Geotechnical News*, March 1996, pg 34-36.

Yang, D. & Goodings, D.J. (1998) Climatic soil freezing modelled in centrifuge. *Journal of Geotechnical and Geoenvironmental Engineering*, Dec 1998, pg 1186-1194.

Zuidoff, F.S. (2003) Physical properties of the surface peat layer and the influence on thermal conditions during the development of palsas. In: M. Phillips, S.M. Springman and L.U. Arenson (eds.) *Proceedings 8th International Conference on Permafrost*, **2**, pg 1313-1317, Balkema, Lisse, The Netherlands.

APPENDICES
for

SCALED GEOTECHNICAL CENTRIFUGE MODELLING OF GELIFLUCTION

School of Earth, Ocean and Planetary Sciences
University of Wales, Cardiff

2004

APPENDICES - TABLE OF CONTENTS

Appendix D: Instrument Calibration

APPENDIX A : Supplementary Data

The appendix presents additional primary data gained during the centrifuge-modelling program. It highlights the comprehensive nature of the slope modelling methodology by portraying the large amount of data gathered on: thermal regime, pore water pressure, soil deformation, frost heave and thaw consolidation. The additional data was not included within the main body of the investigation. It was felt the extensive and complex nature of the information contained here would obscure the sequential theme of any arguments made within the main text. Section A.1 introduces unmodified pore pressure (section 5.4) and thermal data (section 5.2) gained from each thaw phase; the test series are not presented in chronological order. Section A.2 presents frost heave and thaw settlement data not included within Section 5.3. Supplementary surface and subsurface data fully discussed within section 5.5 and chapter 6 are presented in section A.3. Section A.4 introduces the raw data collected during the microfabric analyses discussed in section 5.7. Finally, Section A.5 outlines the data collected during the geodetic field survey undertaken at the Dovrefjell field site (presented in chapter 7).

A.1. Supplementary Thermal and Pore Pressure Data

A.1.1. Primary Test Series – Four Degree Slope, Natural Soil

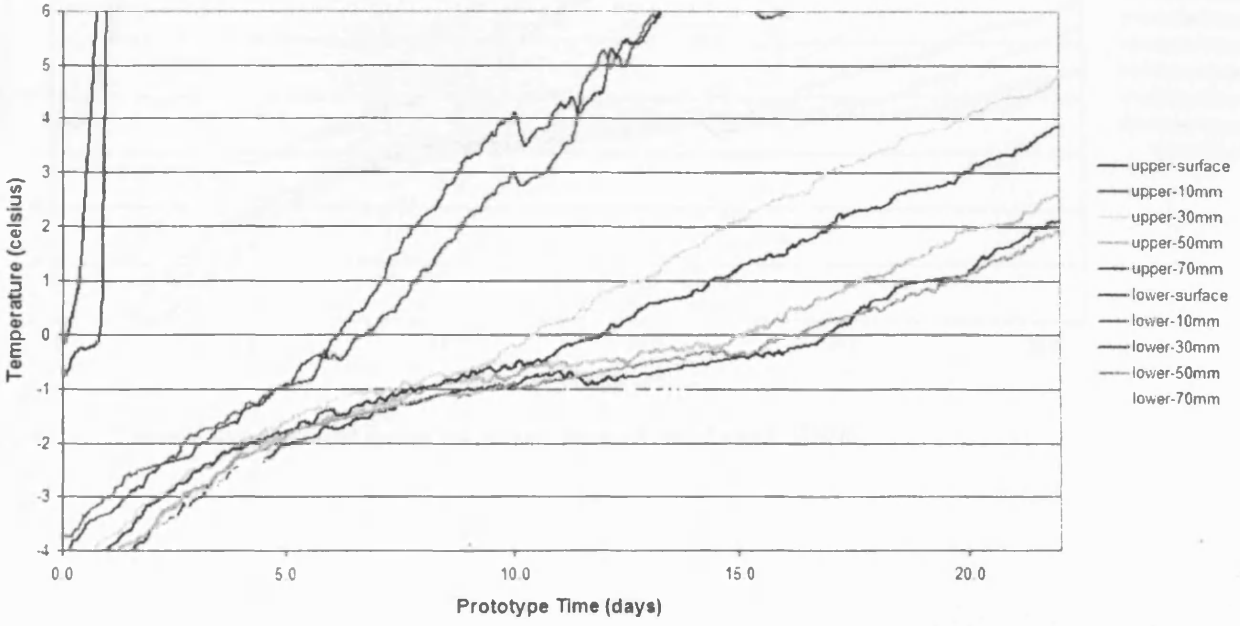

Figure A.1. Thermal data recorded during the first thaw phase of series 4D/NS.

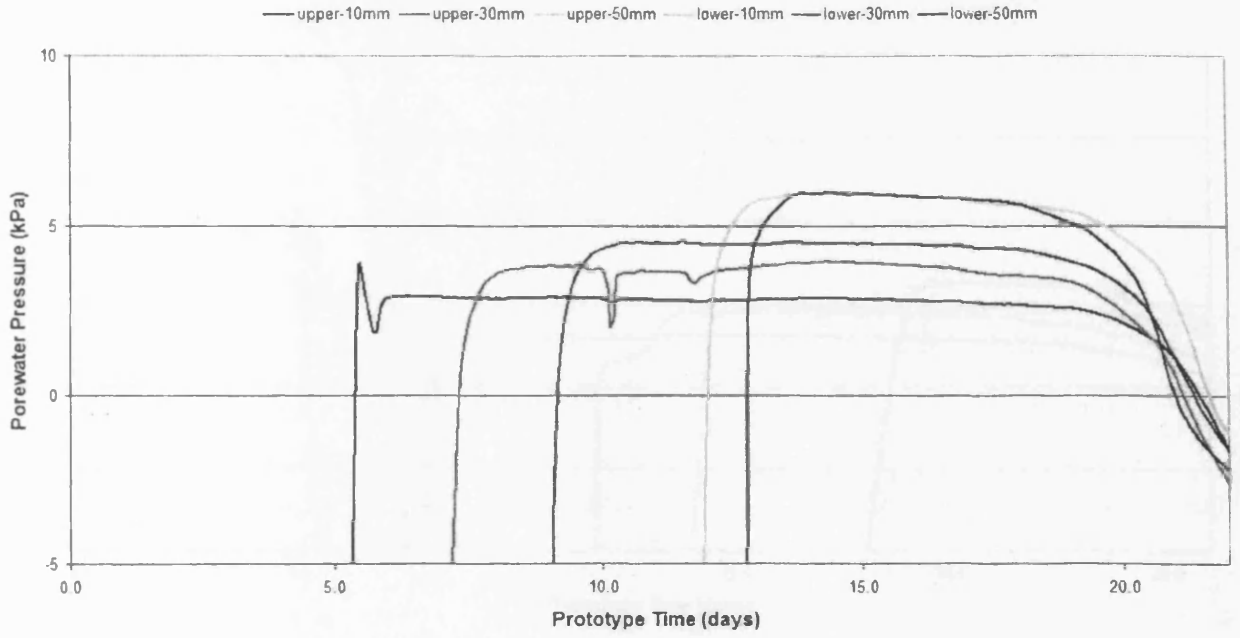

Figure A.2. Porewater pressure data recorded during the first thaw phase of series 4D/NS.

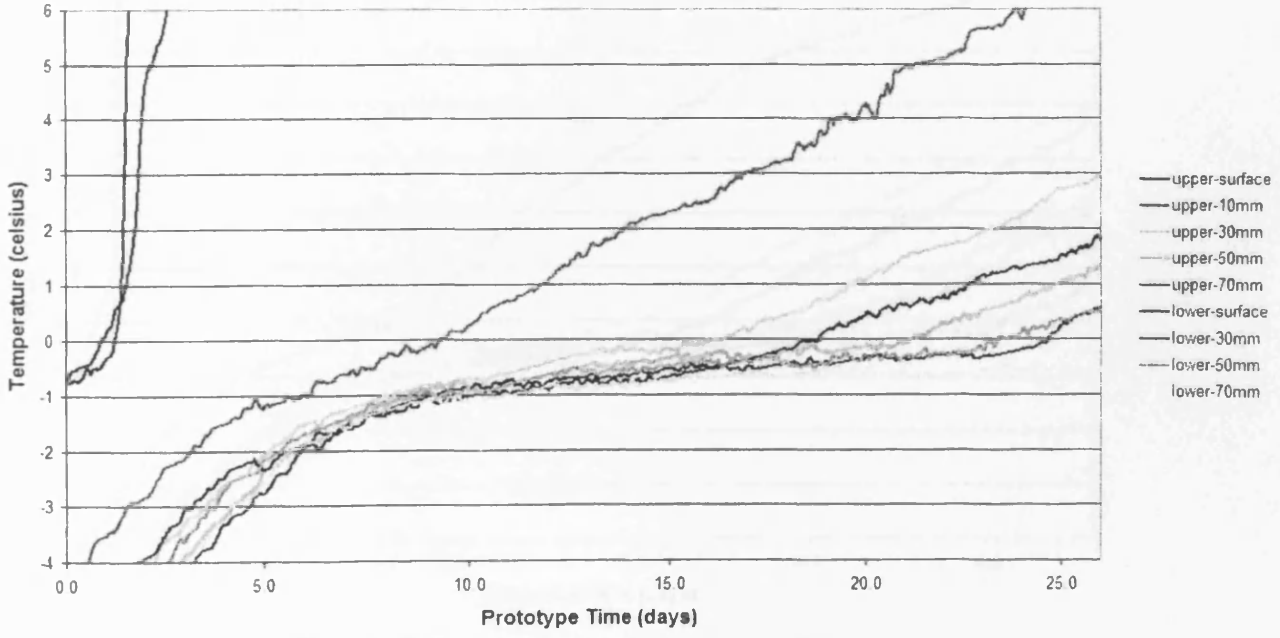

Figure A.3. Thermal data recorded during the second thaw phase of series 4D/NS.

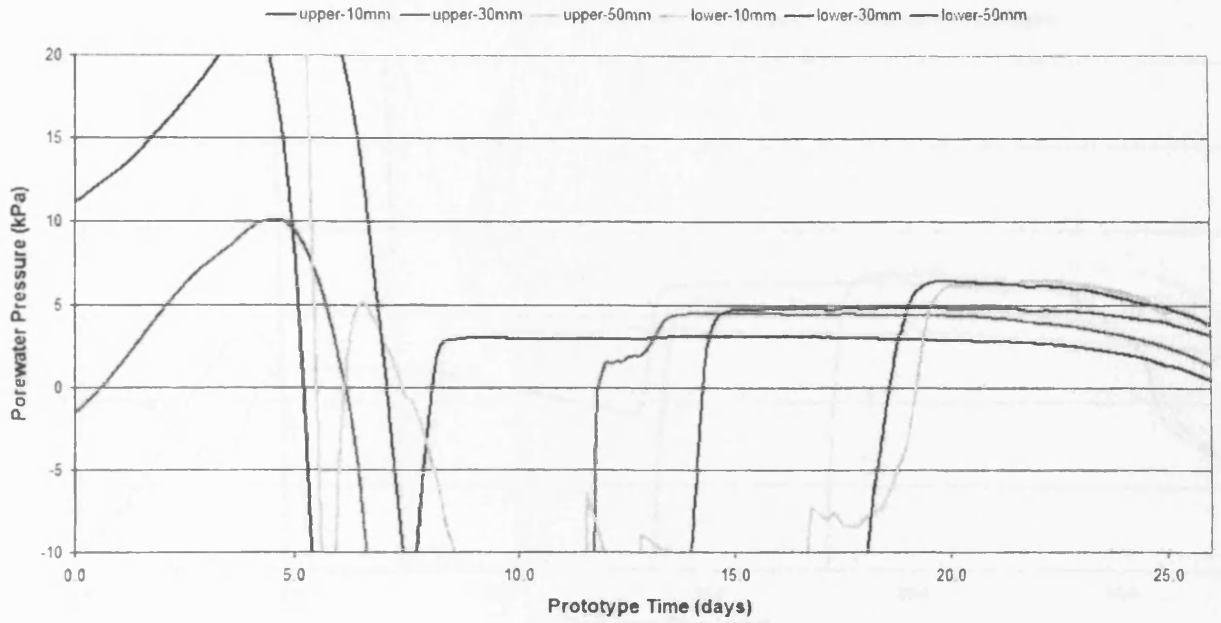

Figure A.4. Porewater pressure data recorded during the second thaw phase of series 4D/NS.

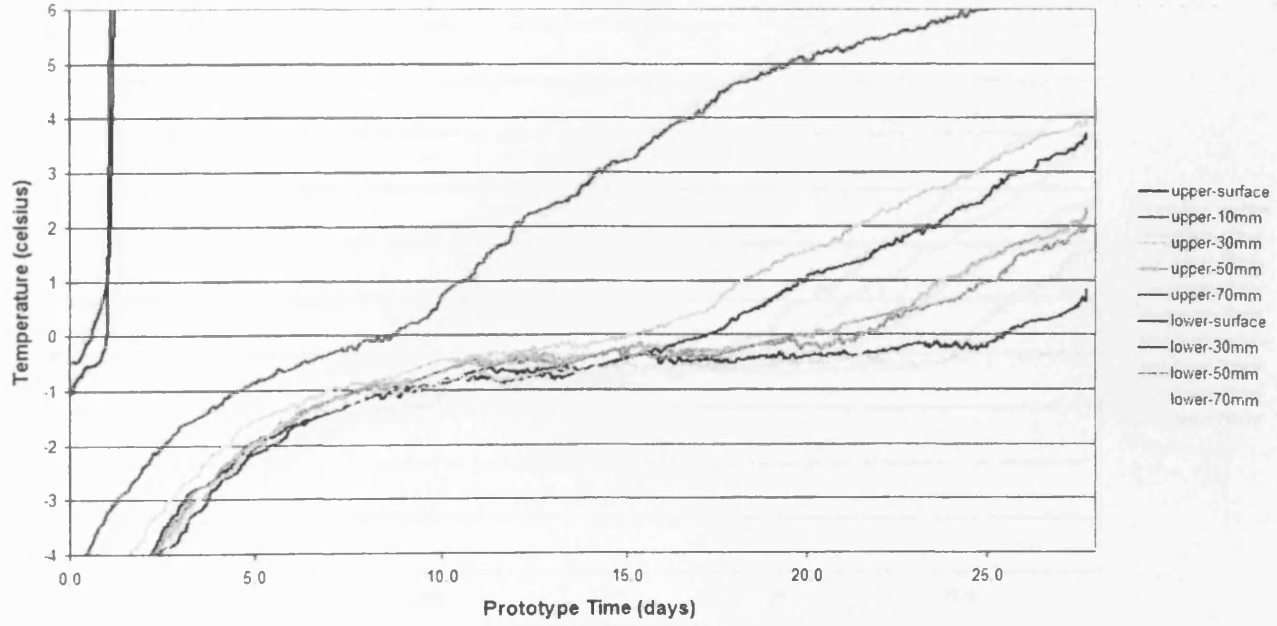

Figure A.5. Thermal data recorded during the third thaw phase of series 4D/NS.

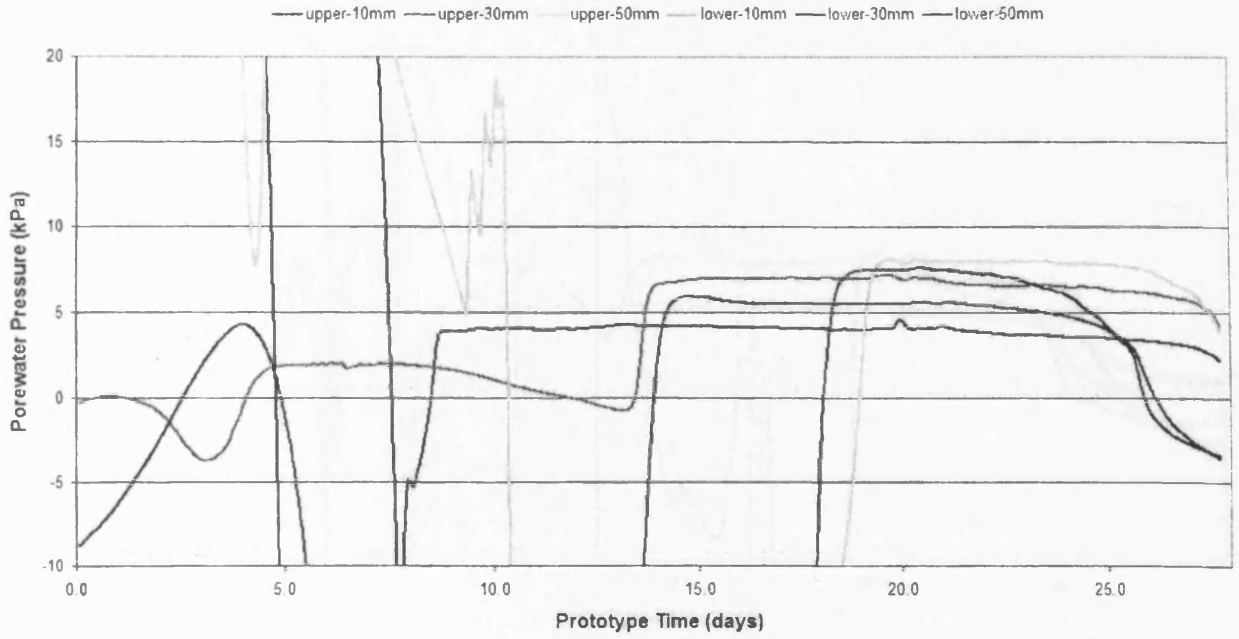

Figure A.6. Porewater pressure data recorded during the third thaw phase of series 4D/NS.

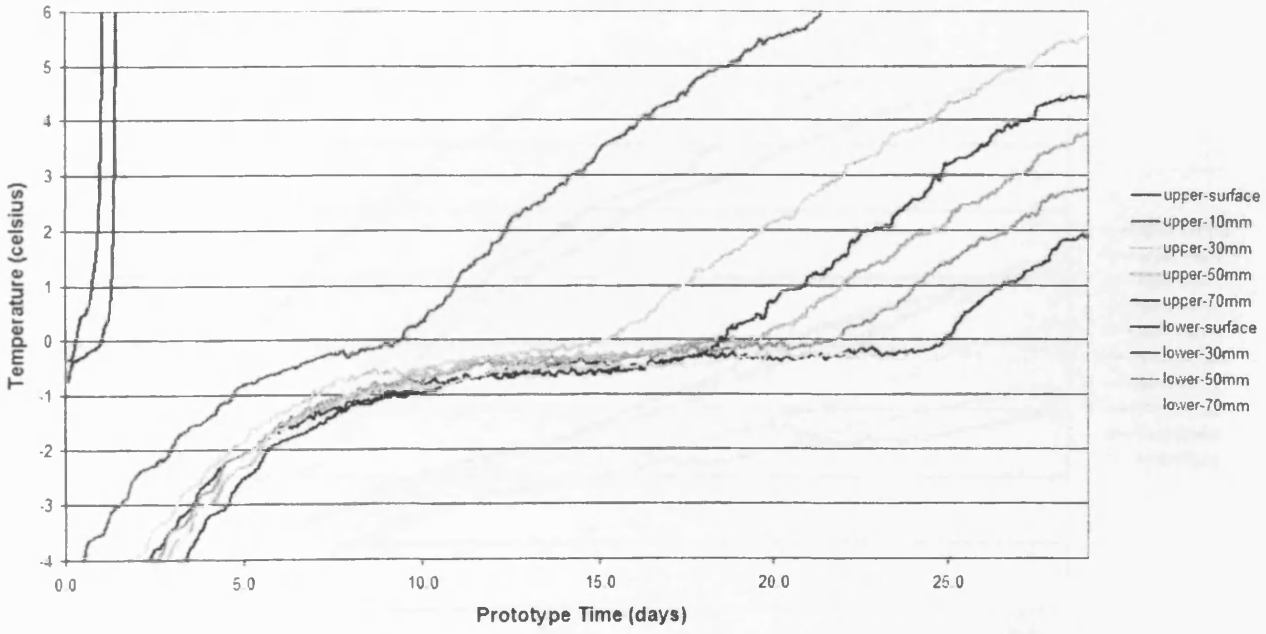

Figure A.7. Thermal data recorded during the fourth thaw phase of series 4D/NS.

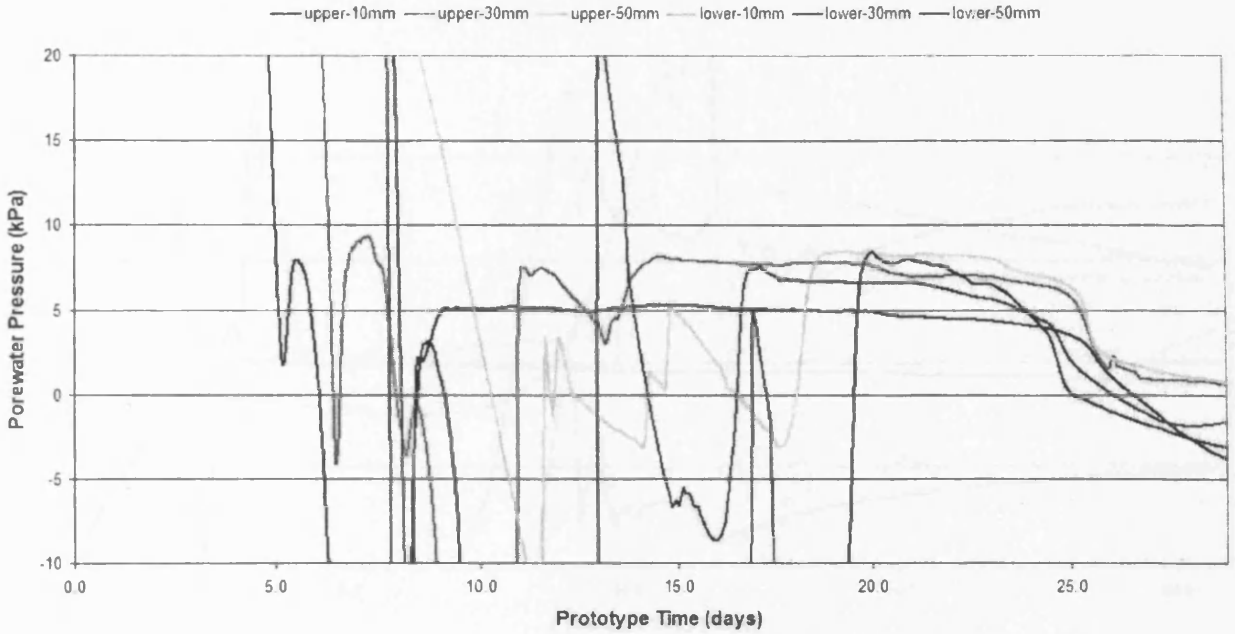

Figure A.8. Porewater pressure data recorded during the fourth thaw phase of series 4D/NS.

A.1.2. Primary Test Series – Eight Degree Slope, Natural Soil

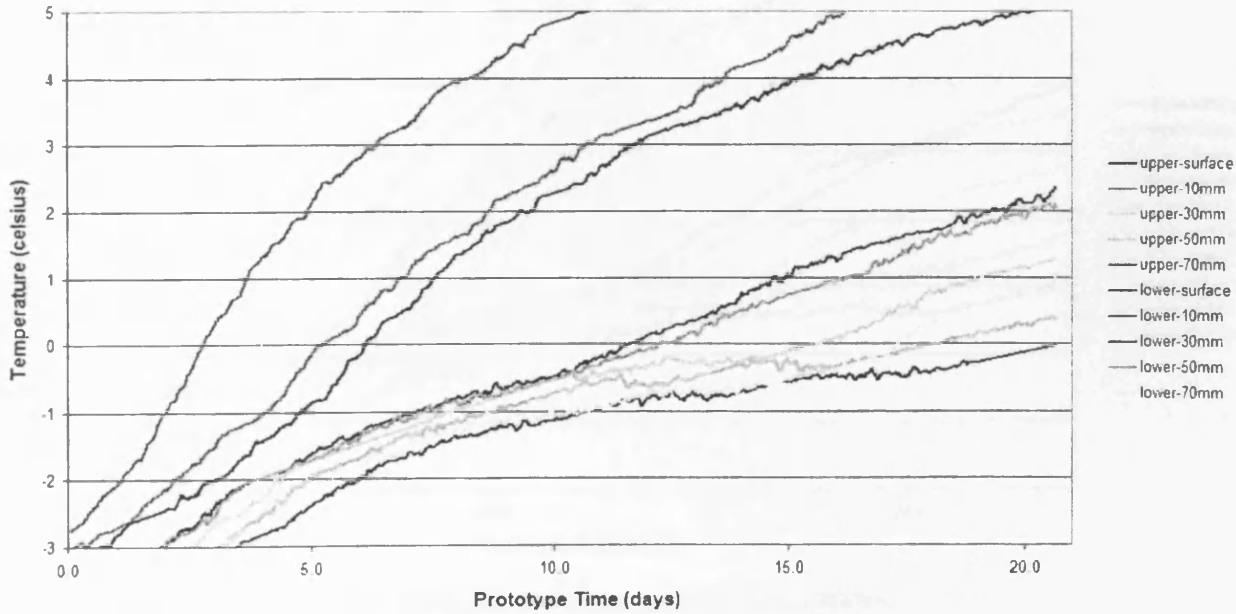

Figure A.9. Thermal data recorded during the first thaw phase of series 8D/NS.

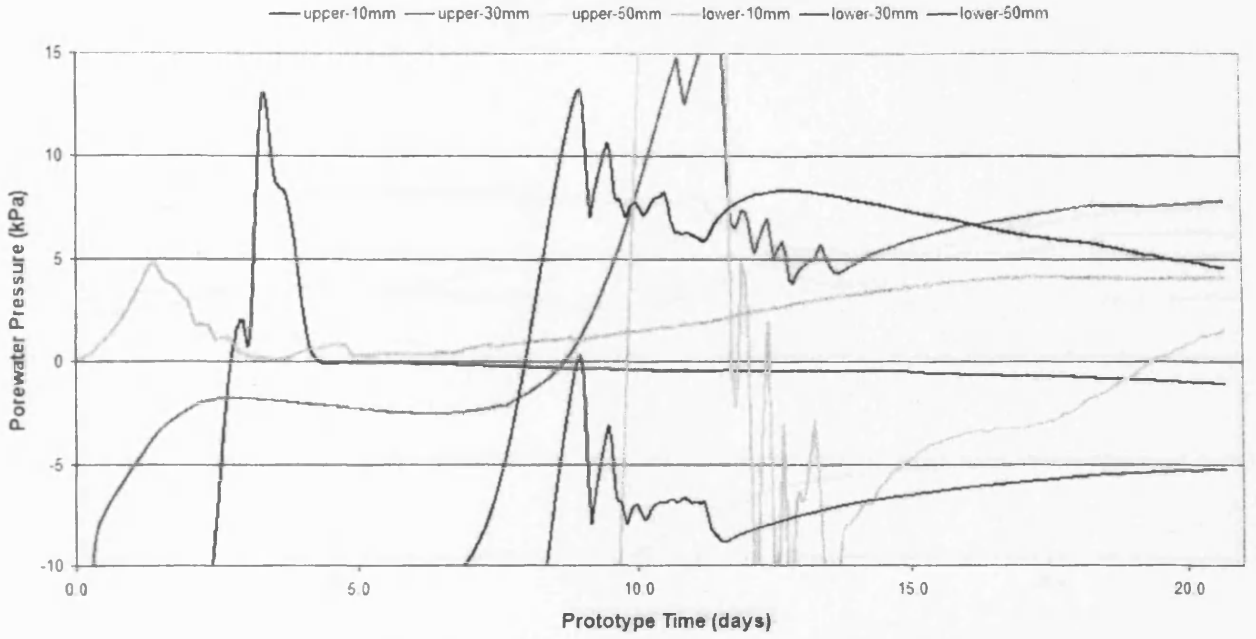

Figure A.10. Porewater pressure data recorded during the first thaw phase of series 8D/NS.

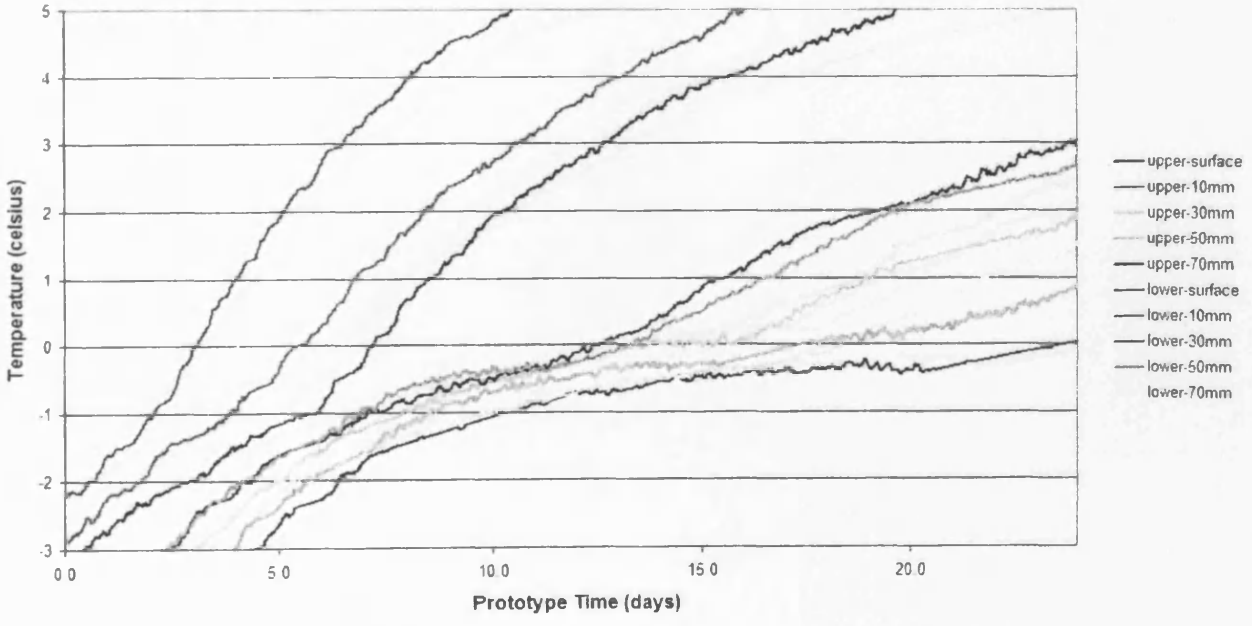

Figure A.11. Thermal data recorded during the second thaw phase of series 8D/NS.

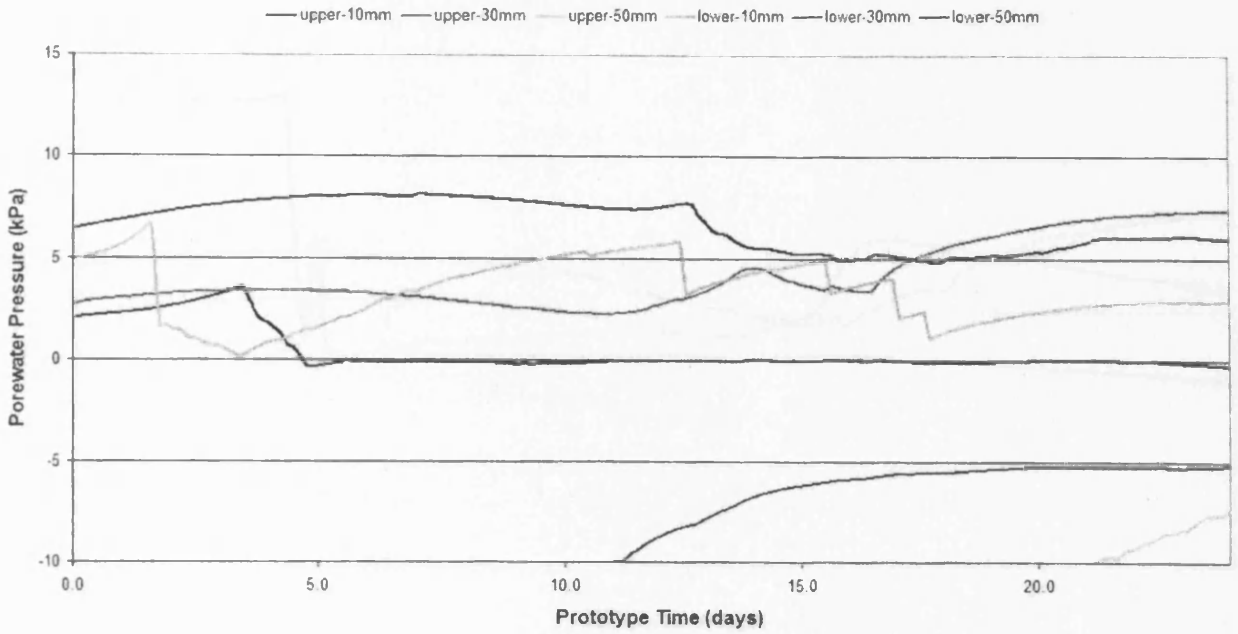

Figure A.12. Porewater pressure data recorded during the second thaw phase of series 8D/NS.

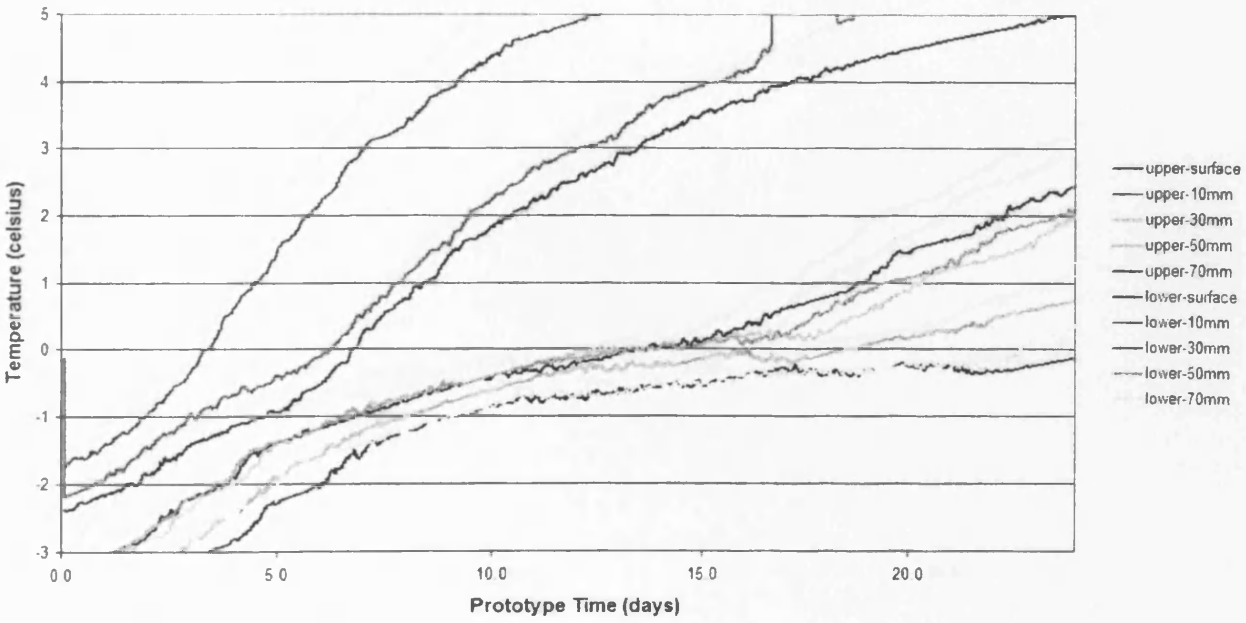

Figure A.13. Thermal data recorded during the third thaw phase of series 8D/NS.

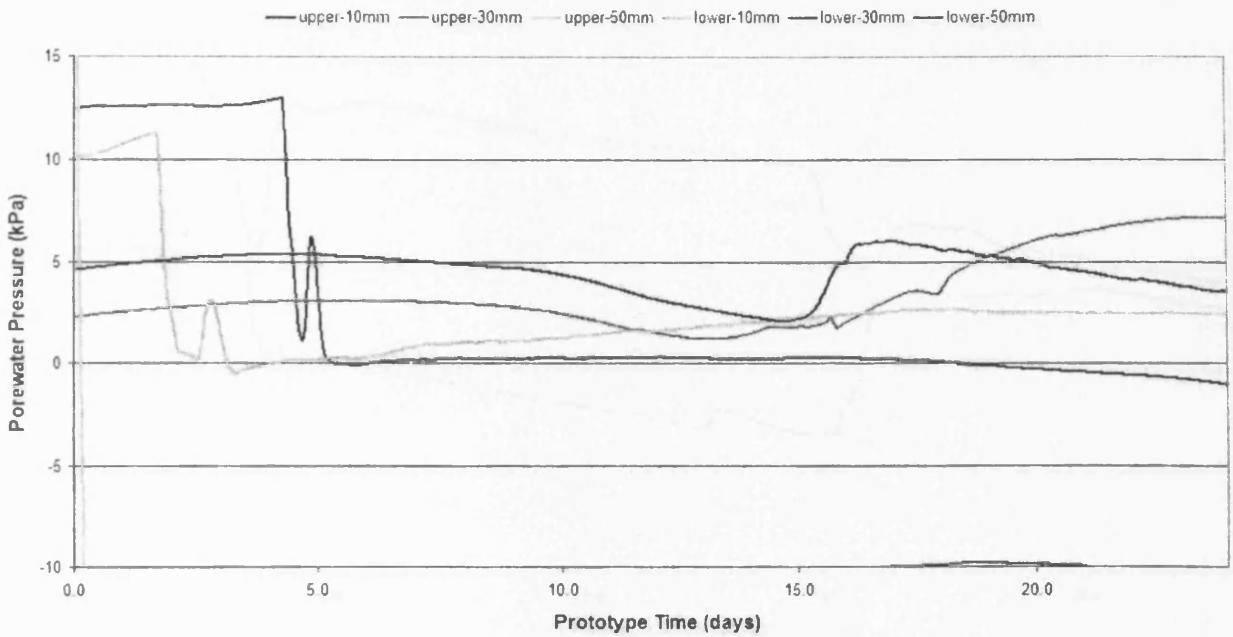

Figure A.14. Porewater pressure data recorded during the third thaw phase of series 8D/NS.

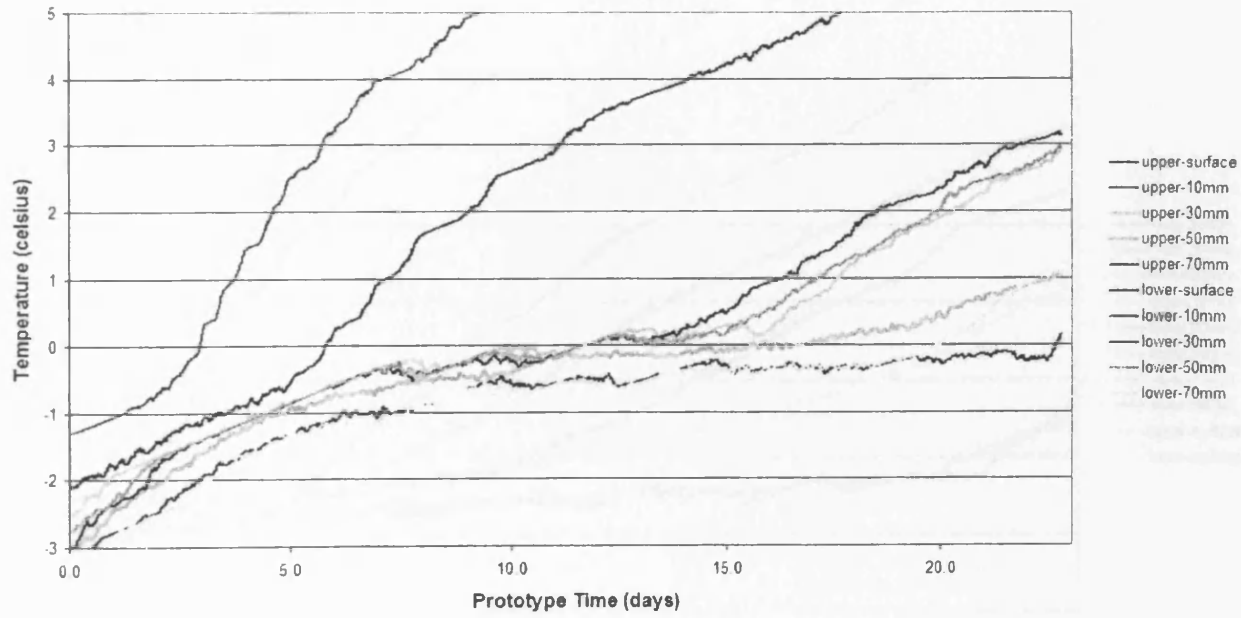

Figure A.15. Thermal data recorded during the fourth thaw phase of series 8D/NS.

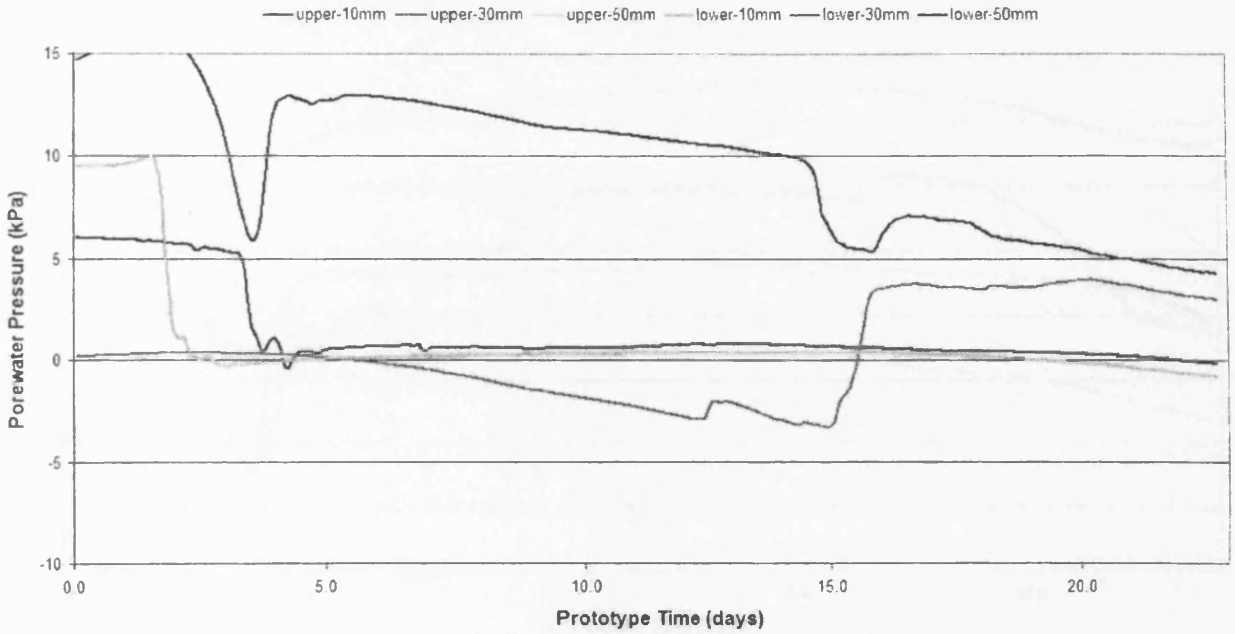

Figure A.16. Porewater pressure data recorded during the fourth thaw phase of series 8D/NS.

A.1.3. Primary Test Series – Twelve Degree Slope, Natural Soil

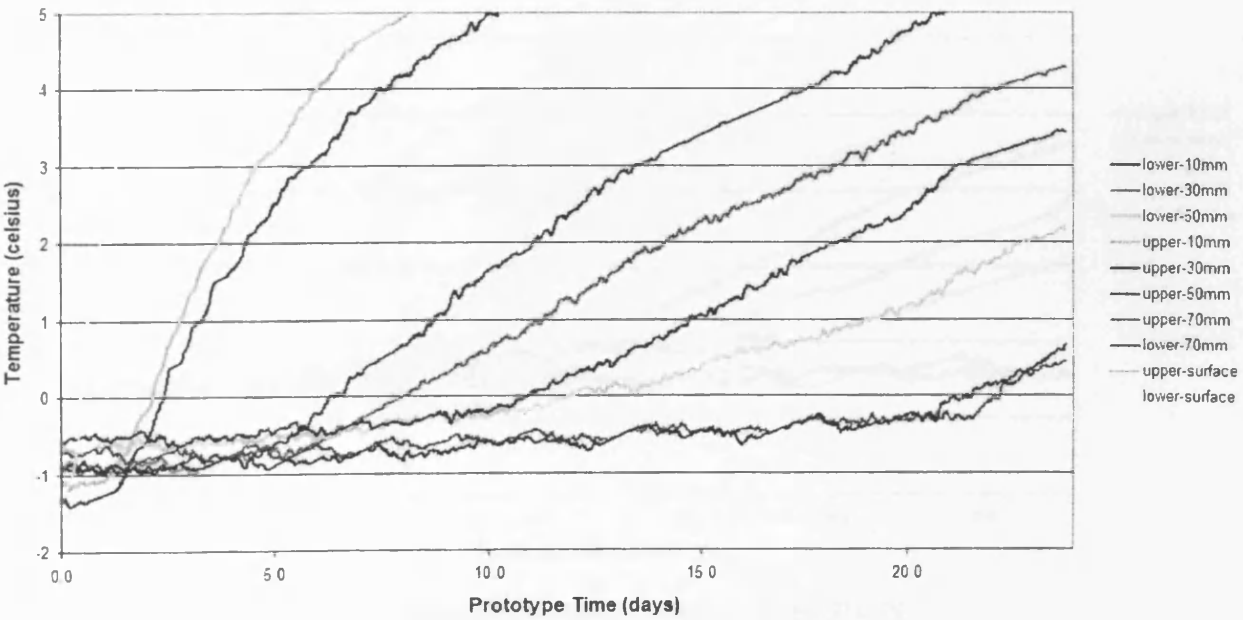

Figure A.17. Thermal data recorded during the first thaw phase of series 12D/NS.

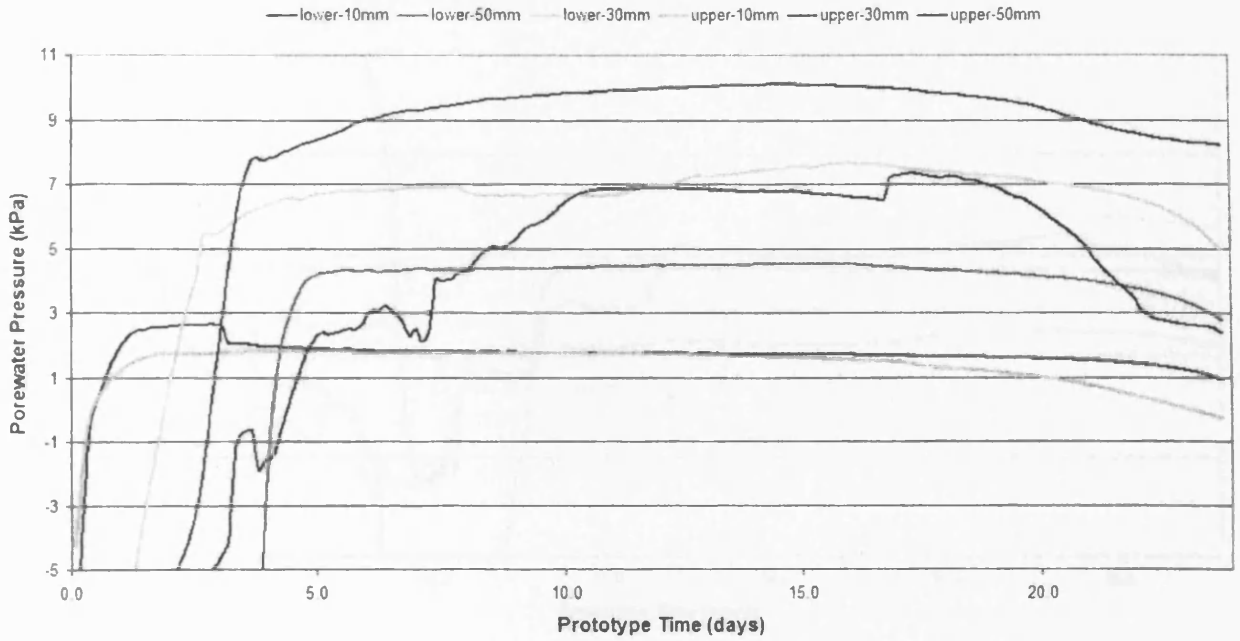

Figure A.18. Porewater pressure data recorded during the first thaw phase of series 12D/NS.

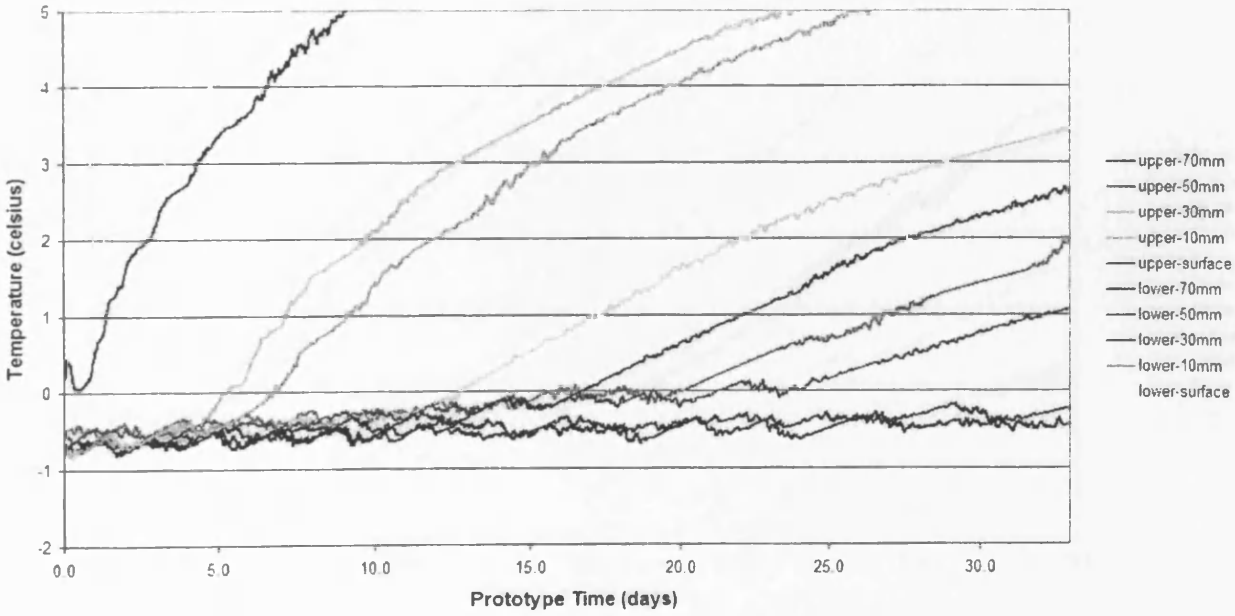

Figure A.19. Thermal data recorded during the second thaw phase of series 12D/NS.

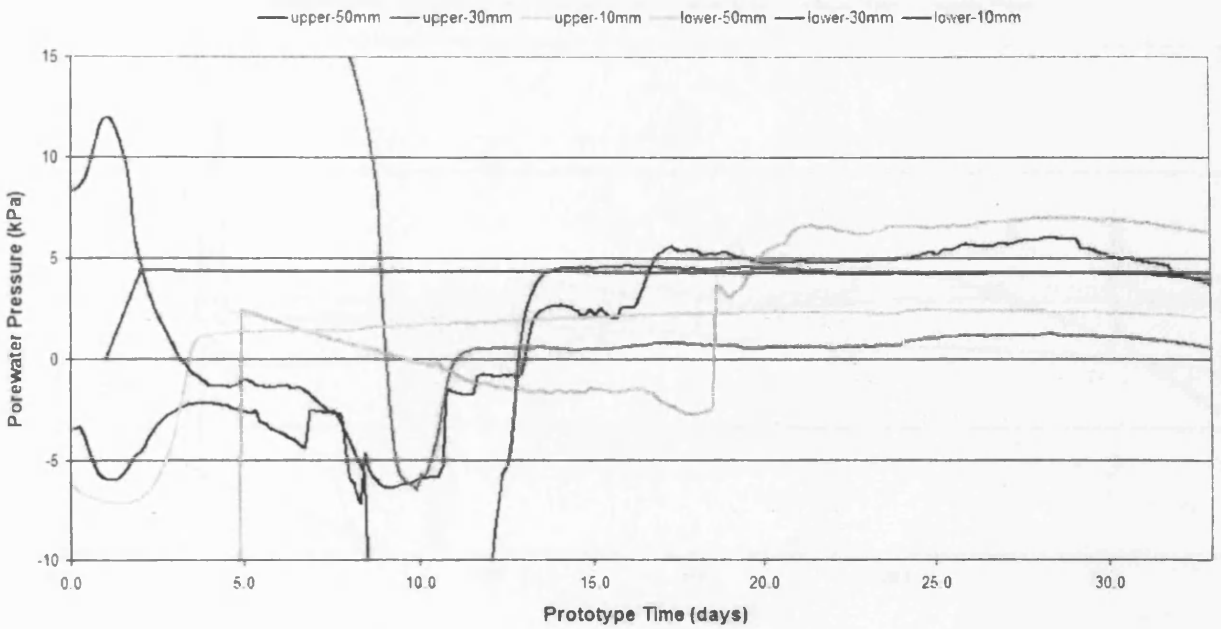

Figure A.20. Porewater pressure data recorded during the second thaw phase of series 12D/NS.

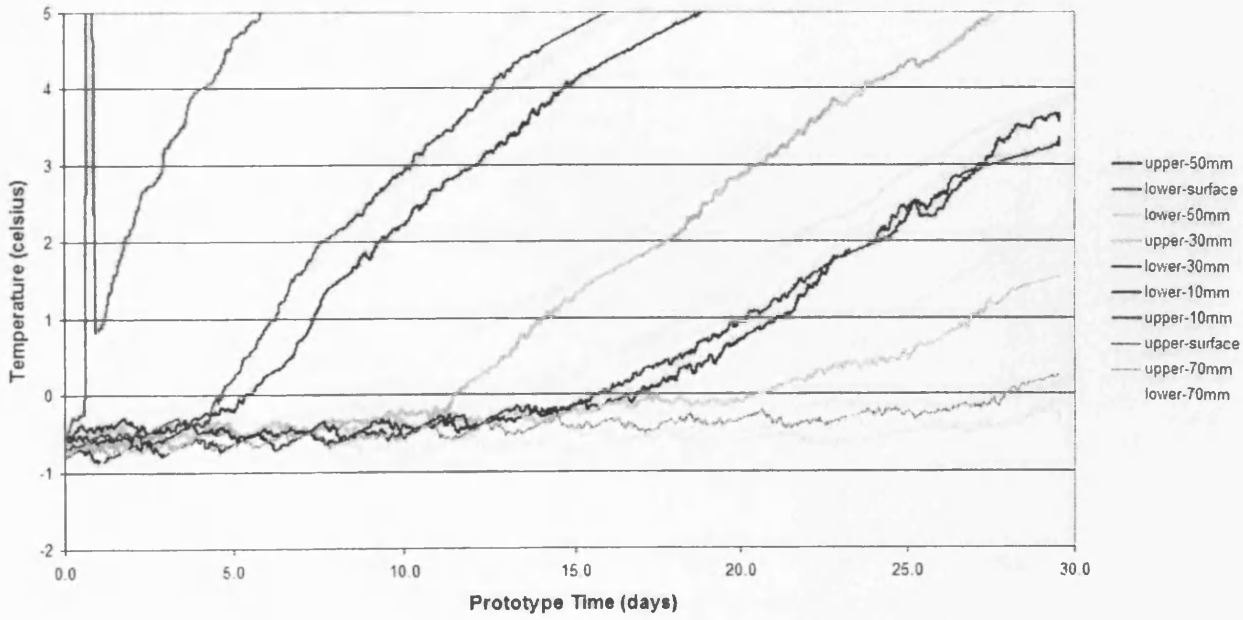

Figure A.21. Thermal data recorded during the third thaw phase of series 12D/NS.

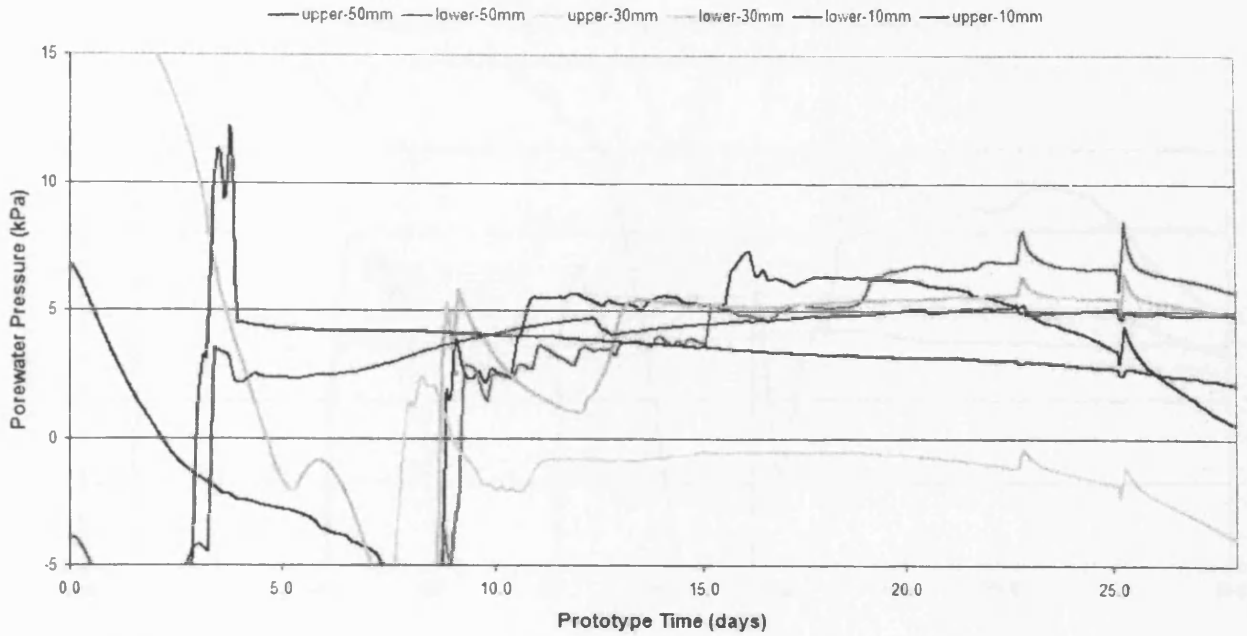

Figure A.22. Porewater pressure data recorded during the third thaw phase of series 12D/NS.

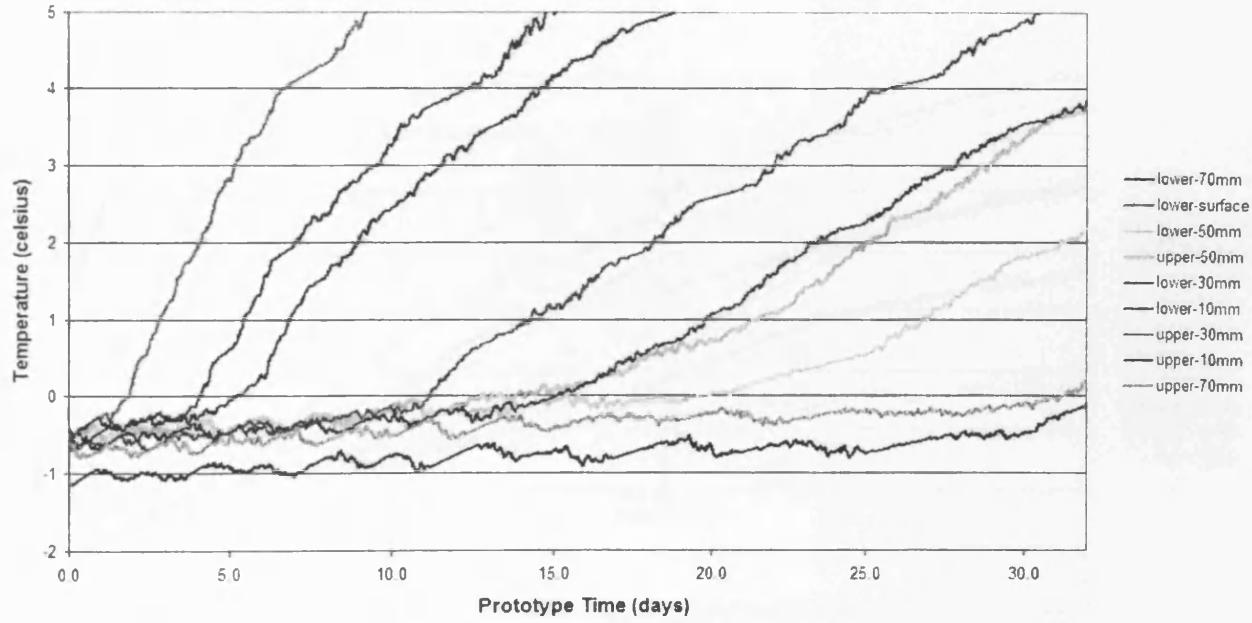

Figure A.23. Thermal data recorded during the fourth thaw phase of series 12D/NS.

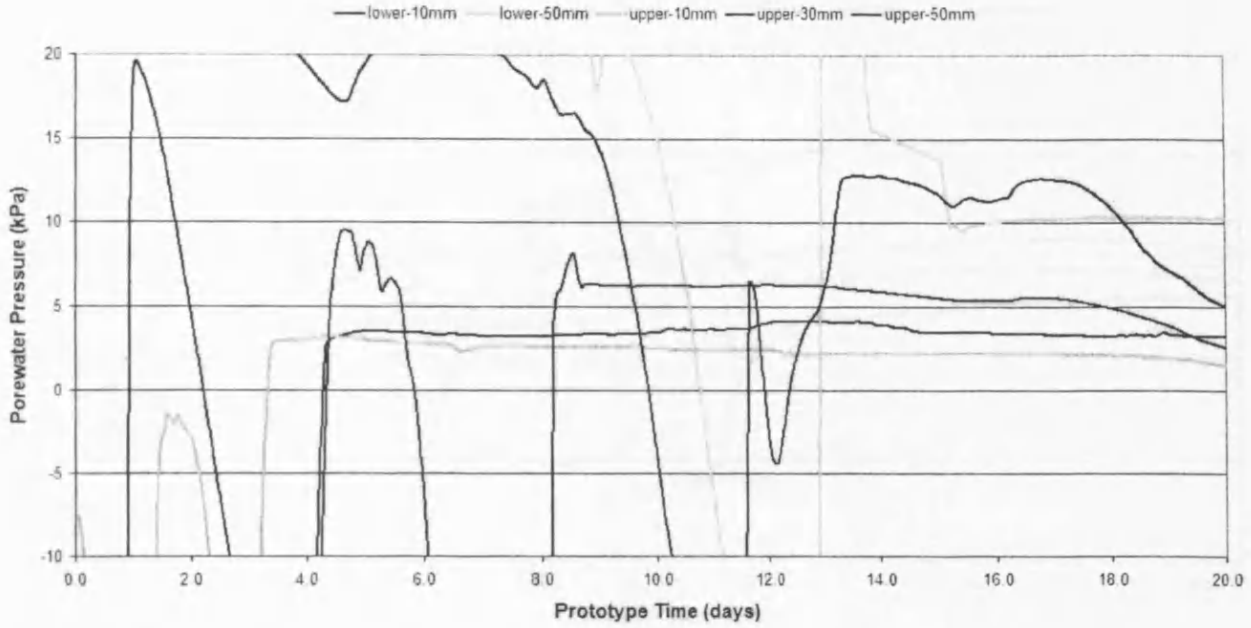

Figure A.24. Porewater pressure data recorded during the fourth thaw phase of series 12D/NS.

A.1.4. Primary Test Series – Sixteen Degree Slope, Natural Soil

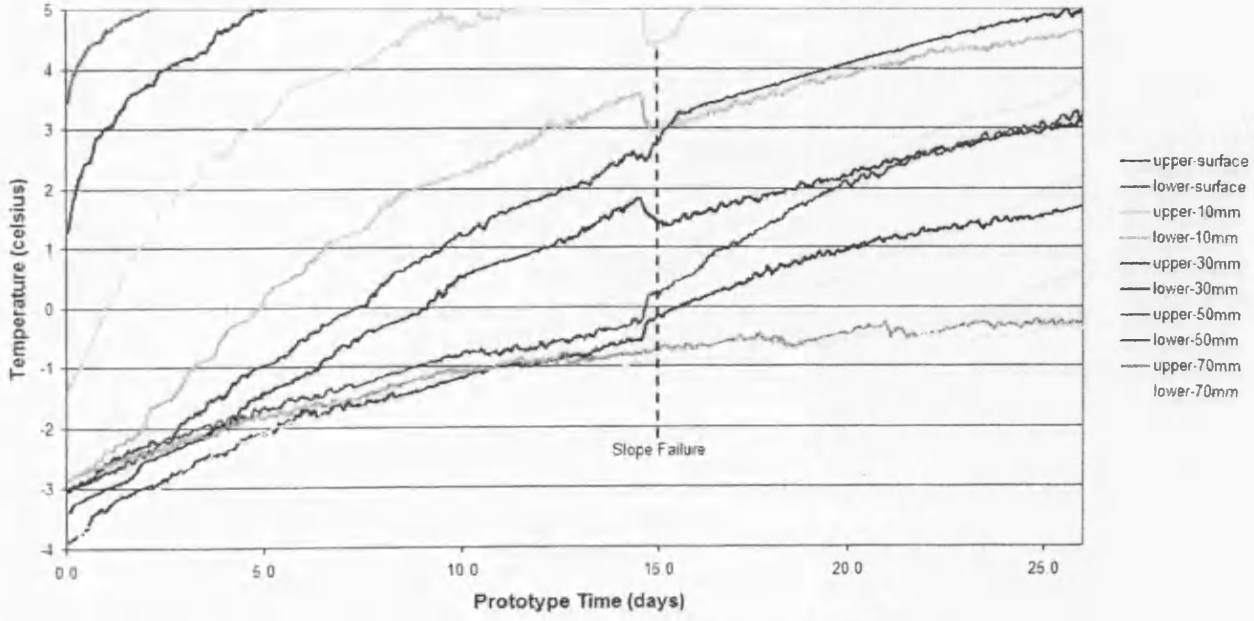

Figure A.25. Thermal data recorded during the first thaw phase of series 16D/NS.

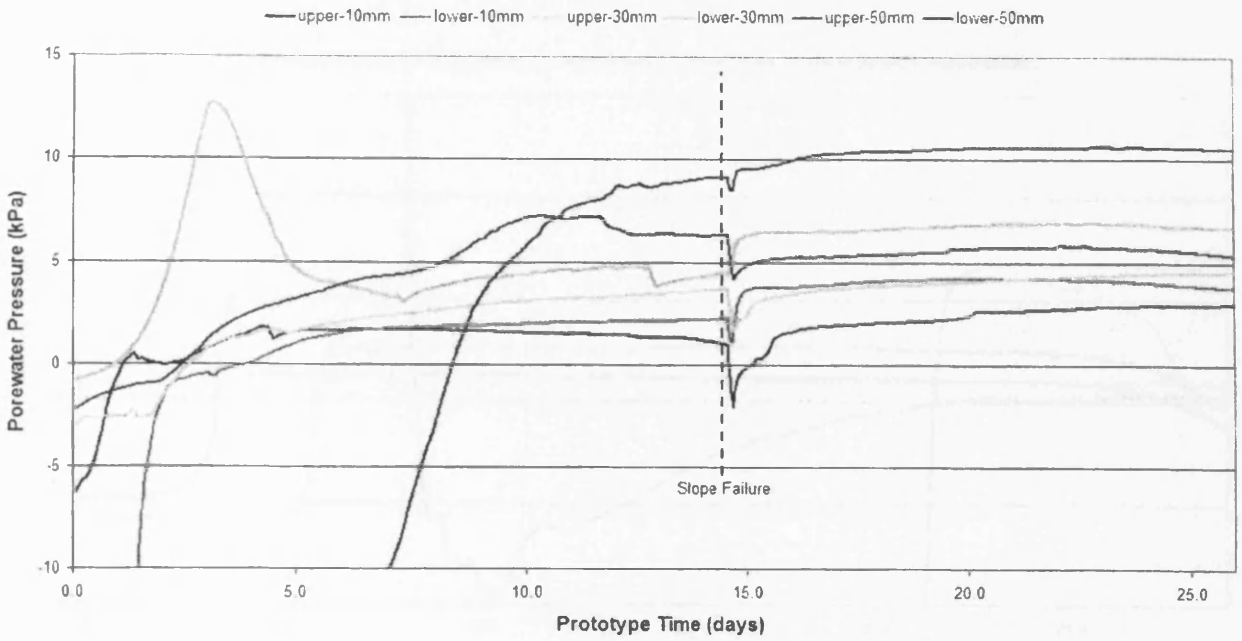

Figure A.26. Porewater pressure data recorded during the first thaw phase of series 16D/NS.

A.1.5. Test Series – Eight Degree Slope, Ten Percent Added Silt

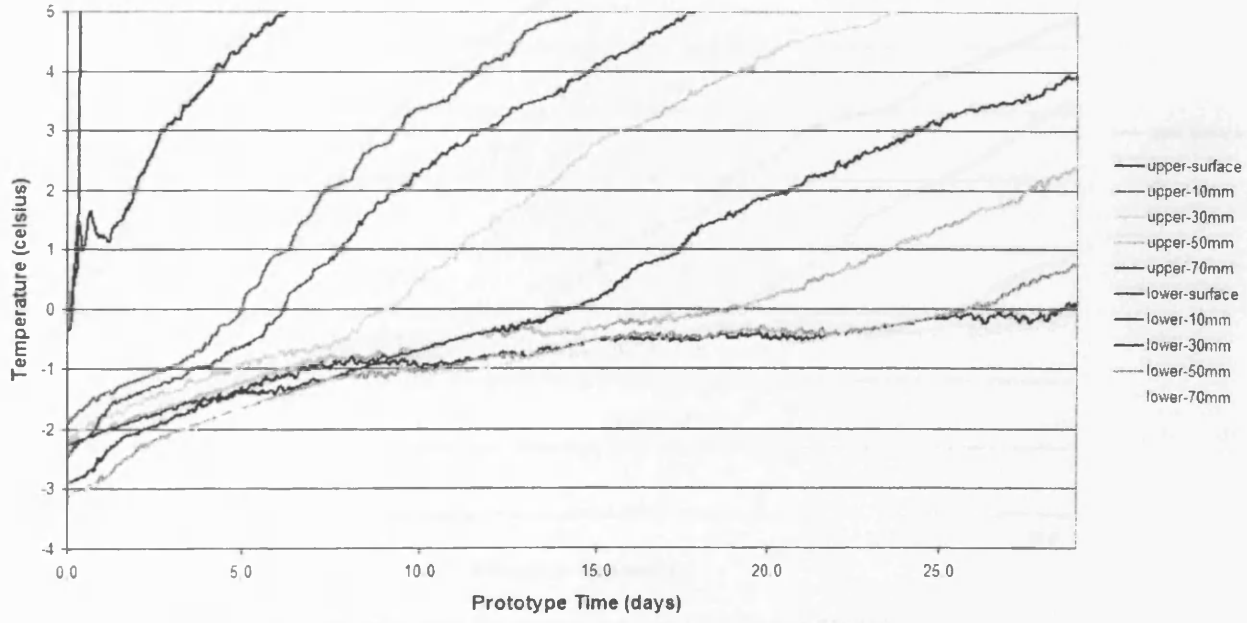

Figure A.27. Thermal data recorded during the first thaw phase of series 8D/10S.

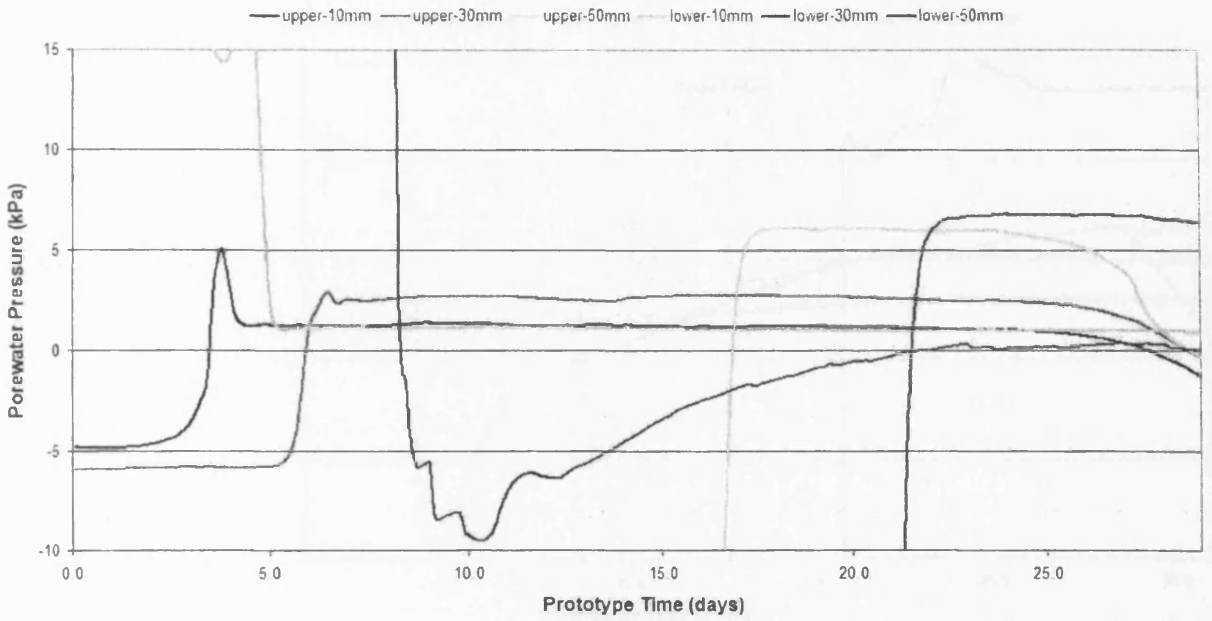

Figure A.28. Porewater pressure data recorded during the first thaw phase of series 8D/10S.

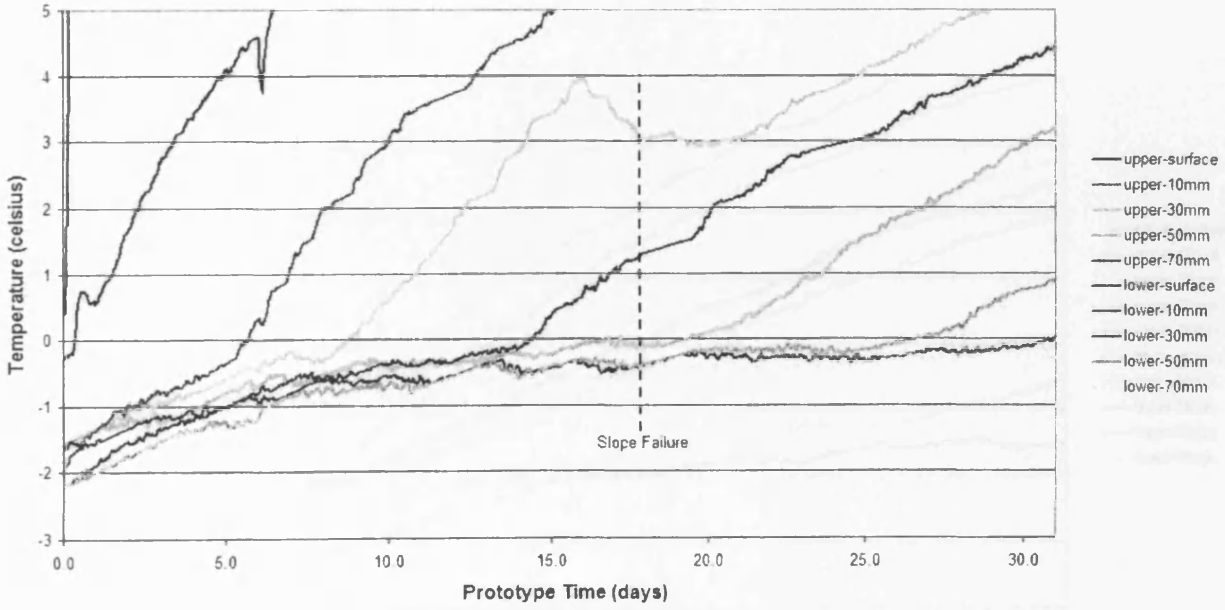

Figure A.29. Thermal data recorded during the second thaw phase of series 8D/10S.

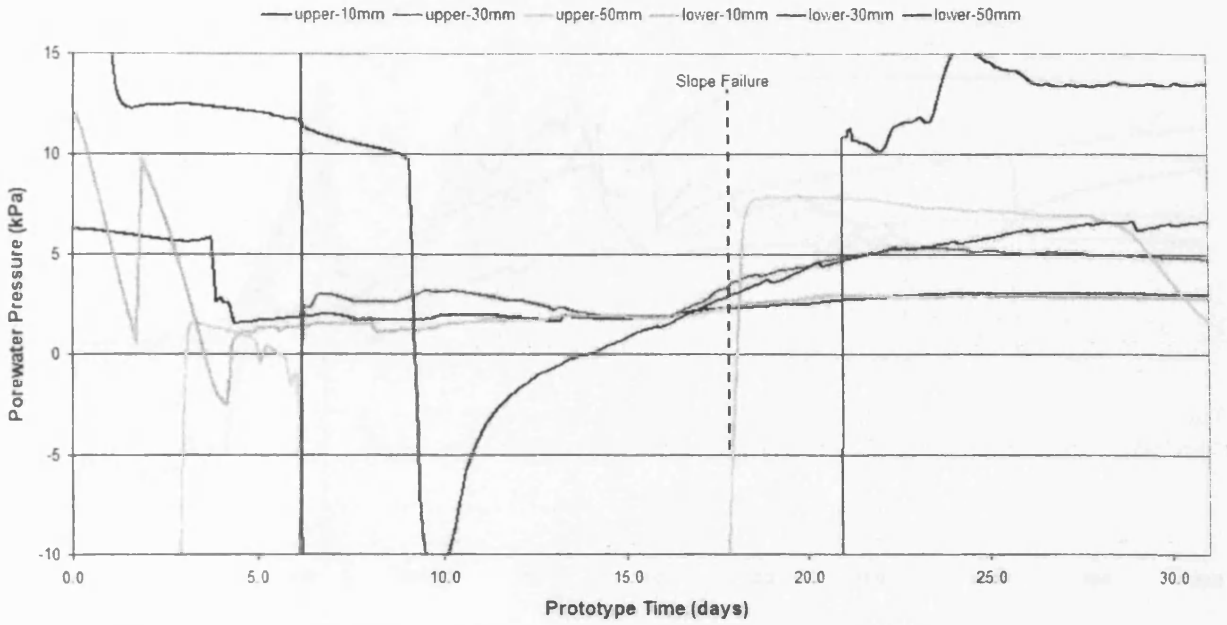

Figure A.30. Porewater pressure data recorded during the second thaw phase of series 8D/10S.

A.1.6. Test Series – Four Degree Slope, Ten Percent Added Silt

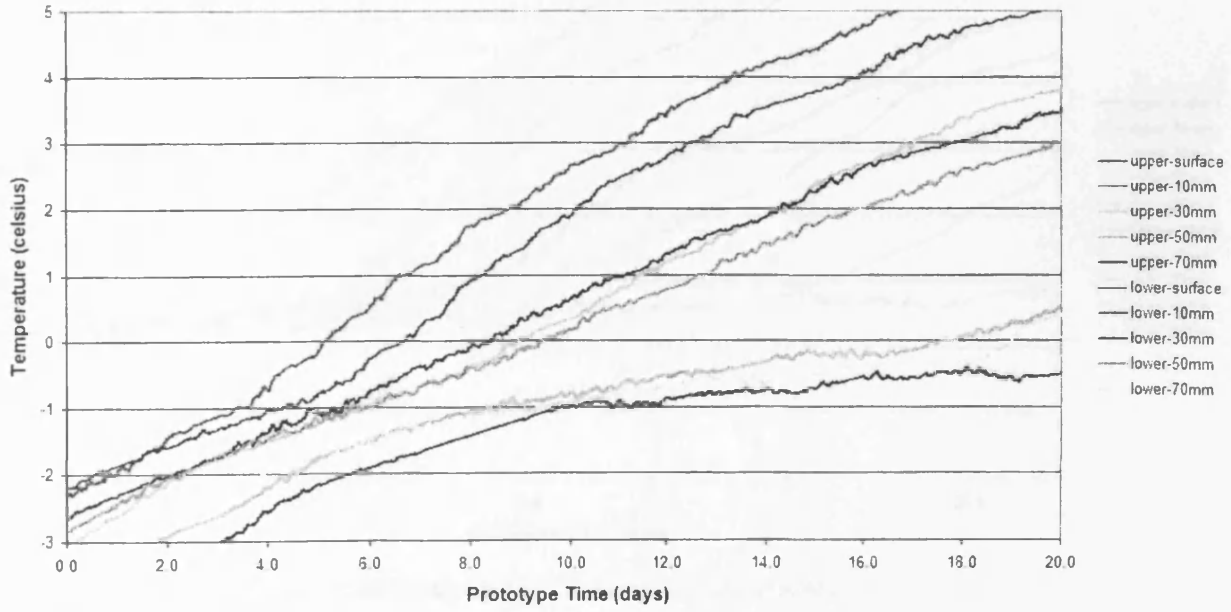

Figure A.31. Thermal data recorded during the first thaw phase of series 4D/10S.

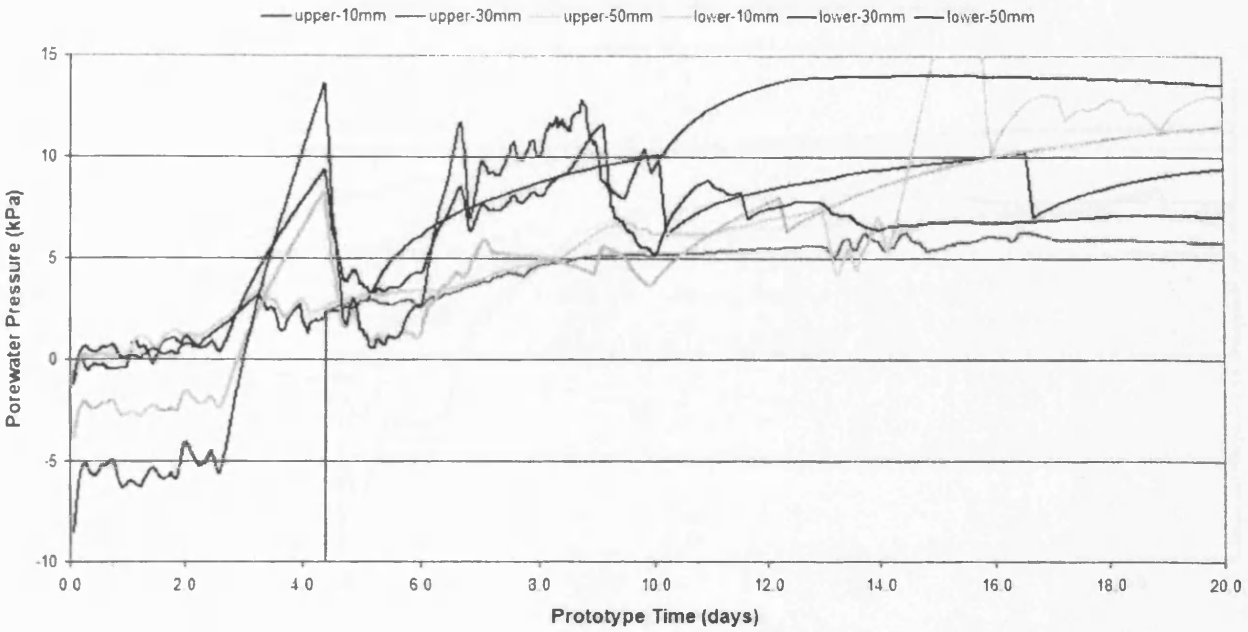

Figure A.32. Porewater pressure data recorded during the first thaw phase of series 4D/10S.

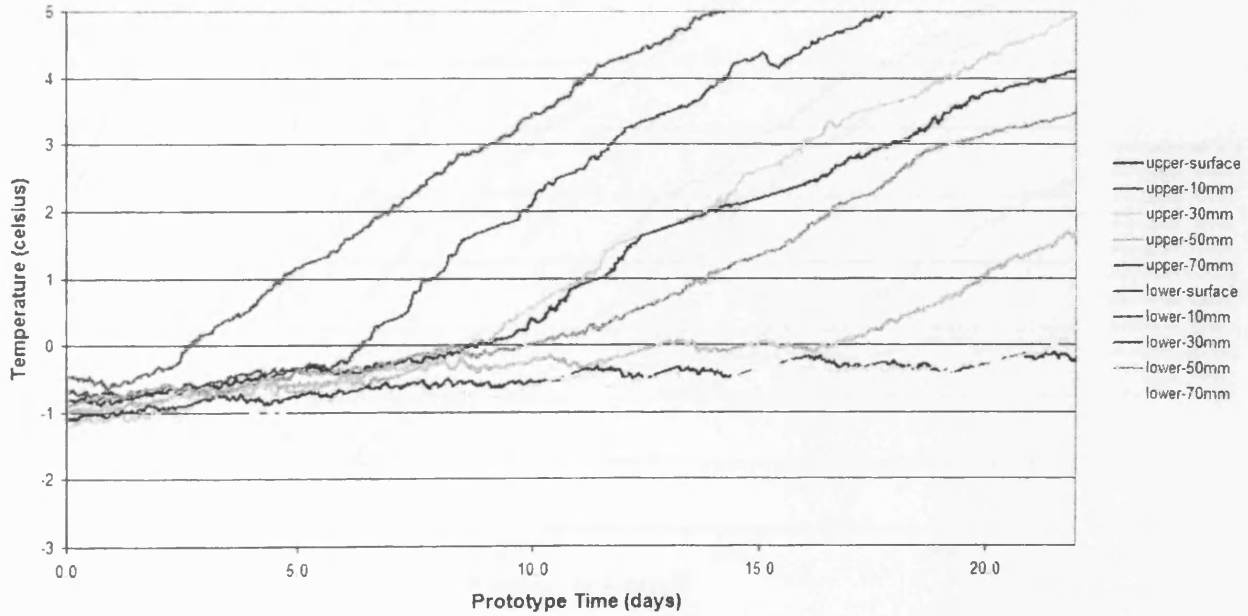

Figure A.33. Thermal data recorded during the second thaw phase of series 4D/10S.

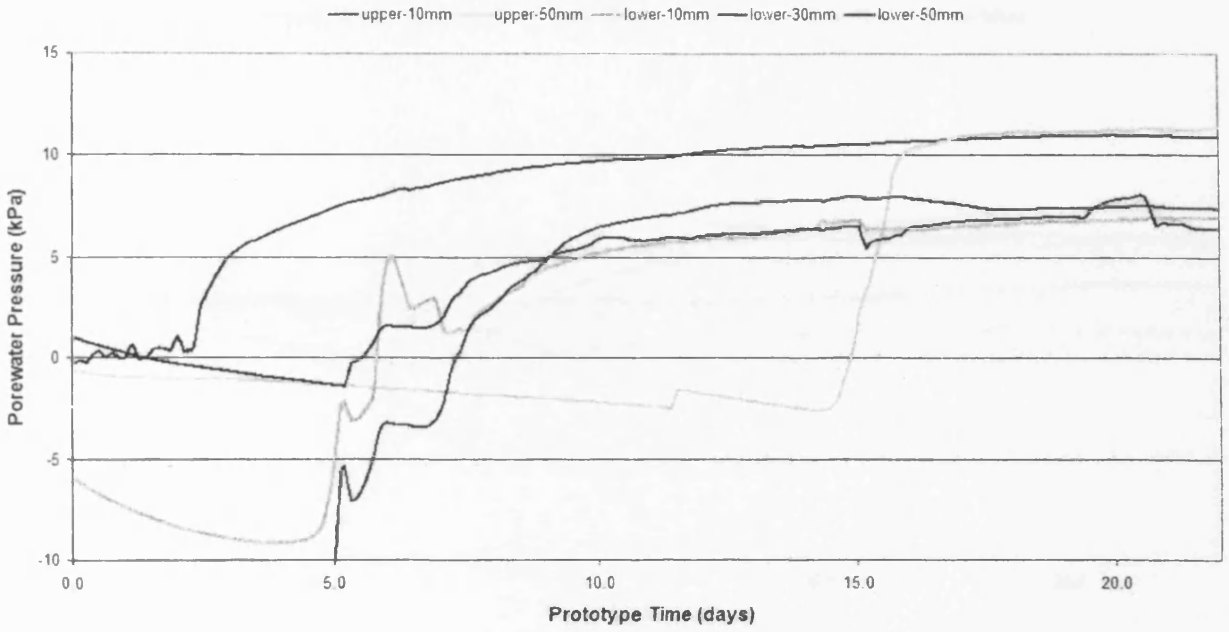

Figure A.34. Porewater pressure data recorded during the second thaw phase of series 4D/10S.

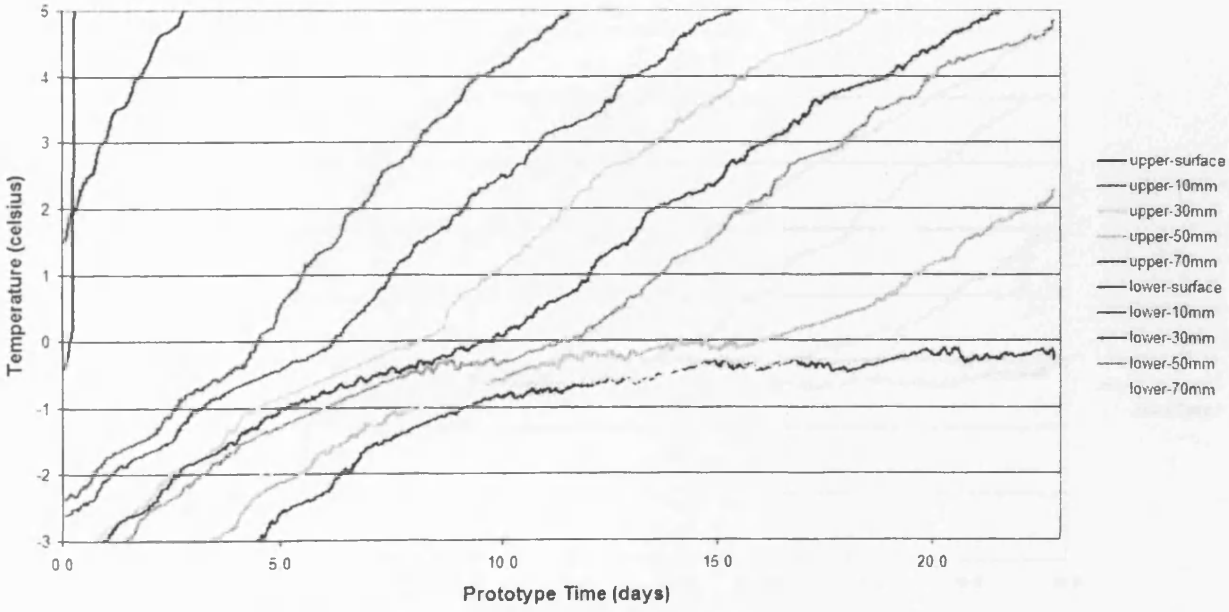

Figure A.35. Thermal data recorded during the third thaw phase of series 4D/10S.

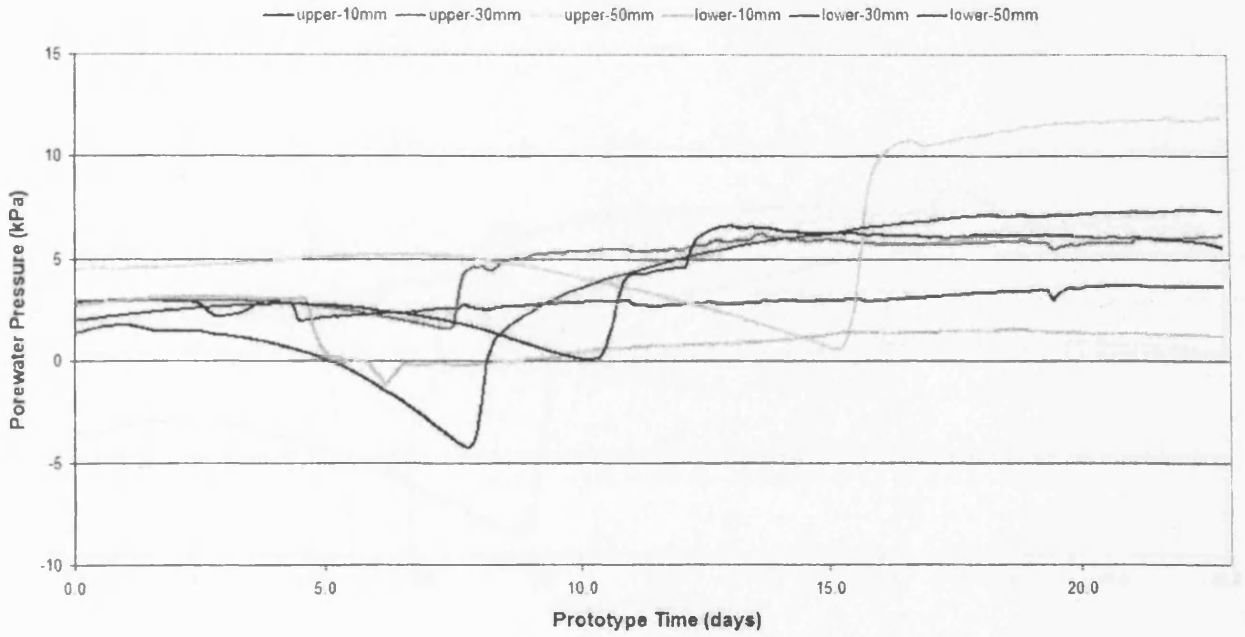

Figure A.36. Porewater pressure data recorded during the third thaw phase of series 4D/10S.

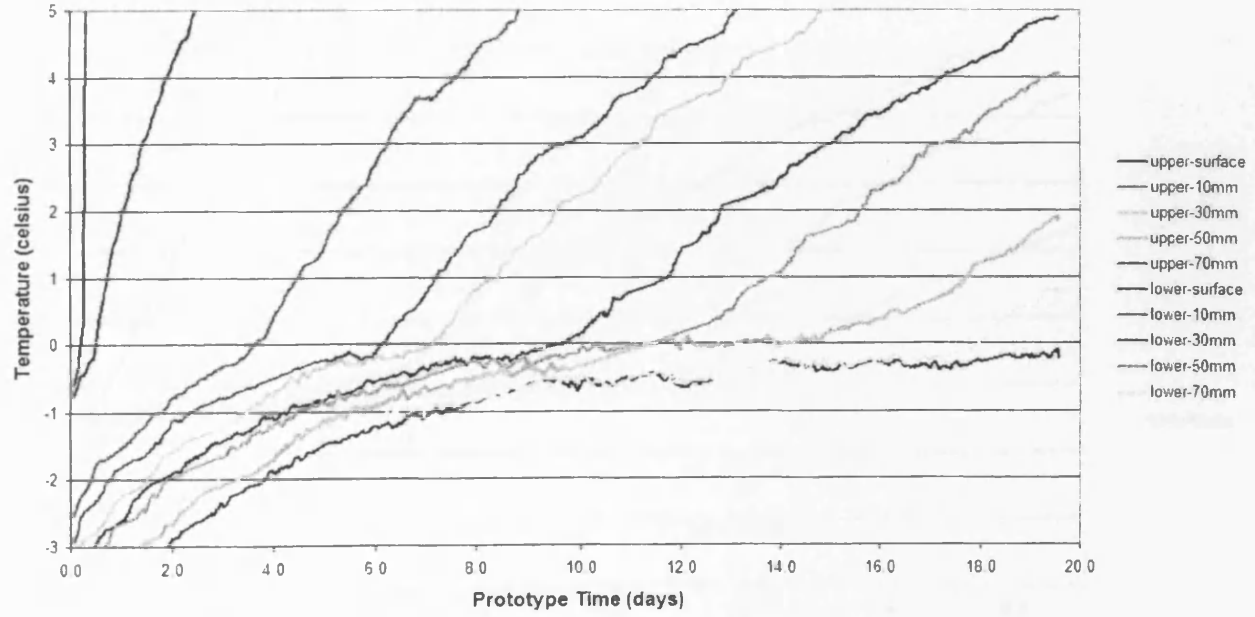

Figure A.37. Thermal data recorded during the fourth thaw phase of series 4D/10S.

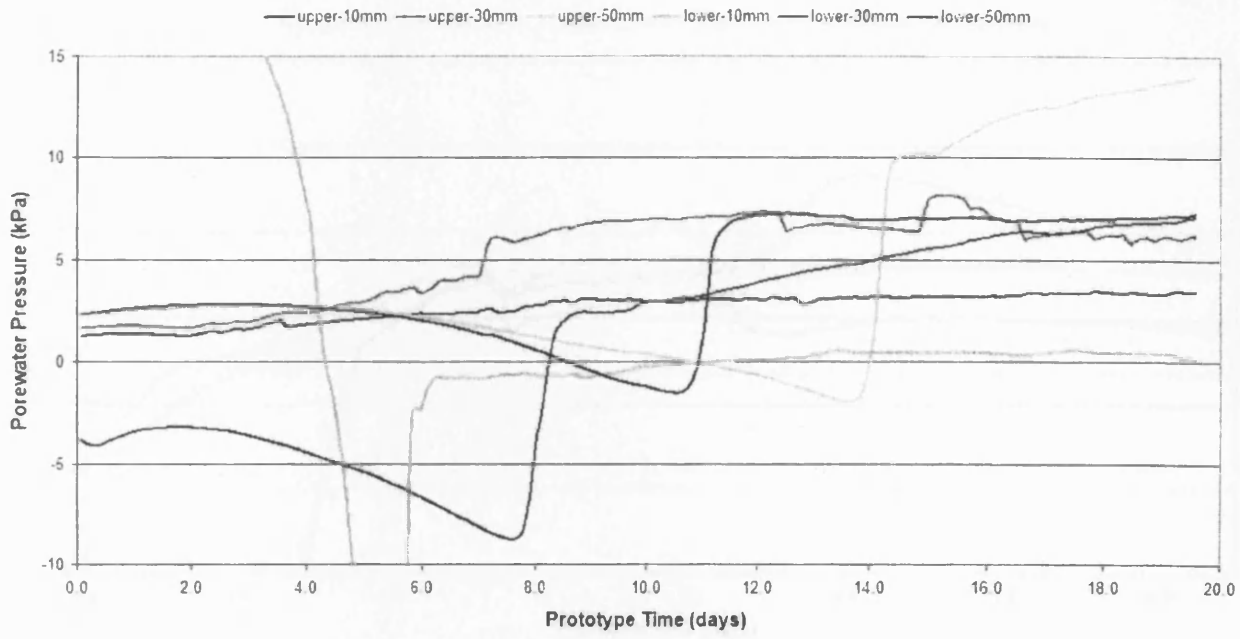

Figure A.38. Porewater pressure data recorded during the fourth thaw phase of series 4D/10S.

A.1.7. Test Series – Four Degree Slope, Twenty Percent Added Silt

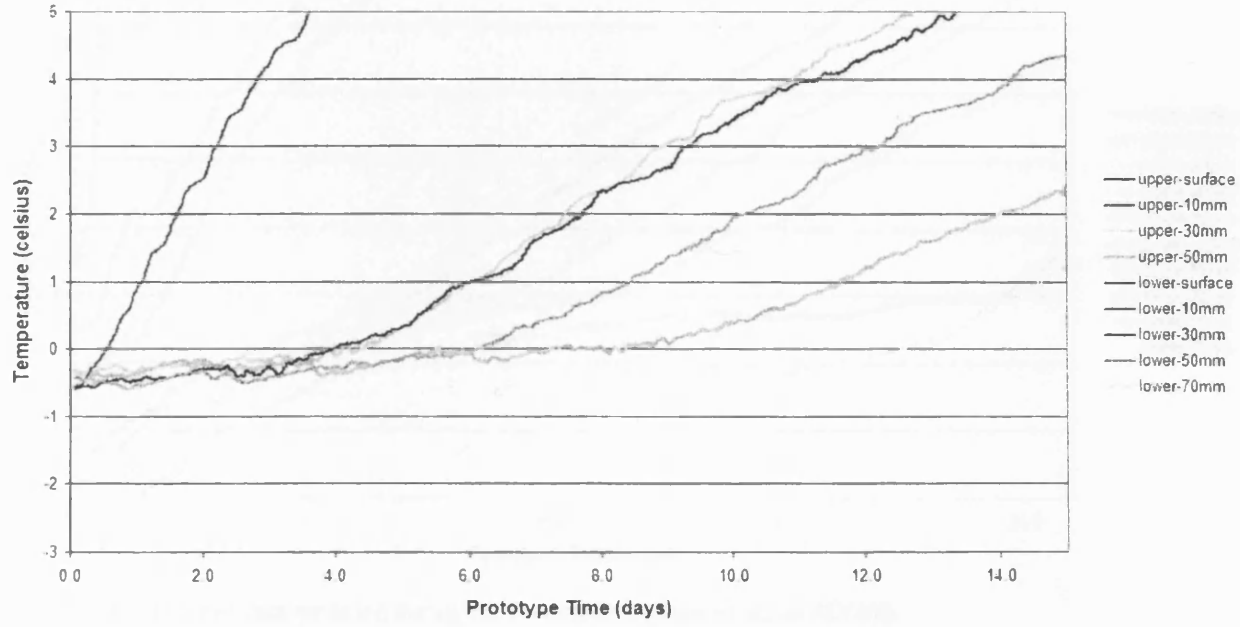

Figure A.39. Thermal data recorded during the first thaw phase of series 4D/20S.

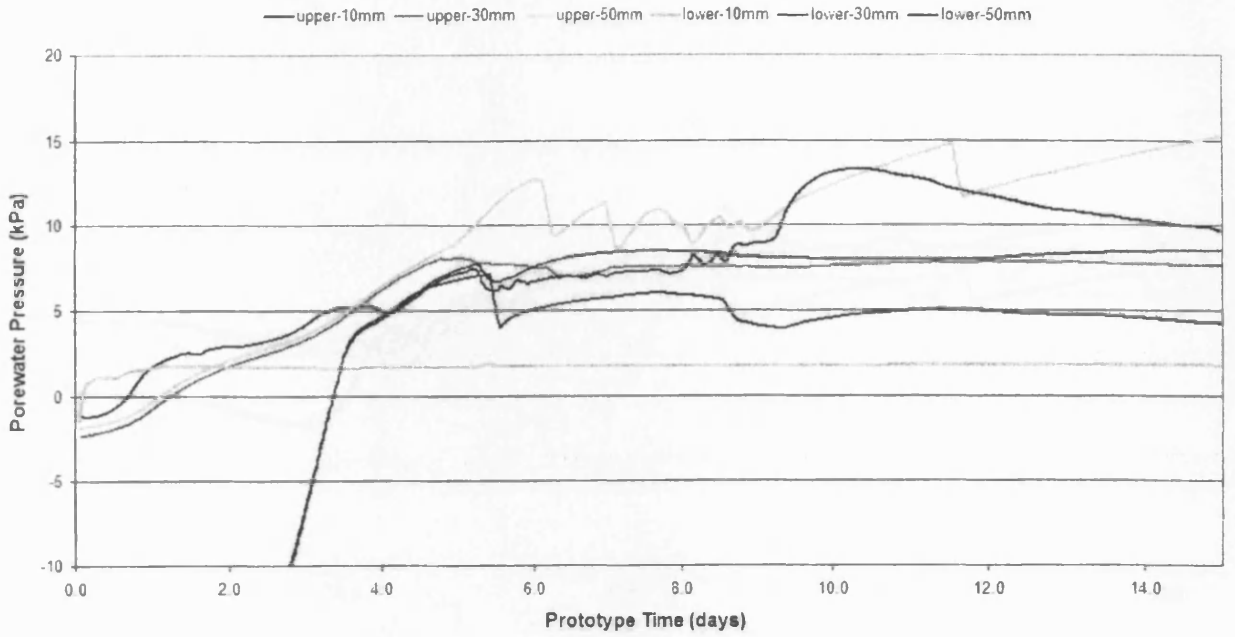

Figure A.40. Porewater pressure data recorded during the first thaw phase of series 4D/20S.

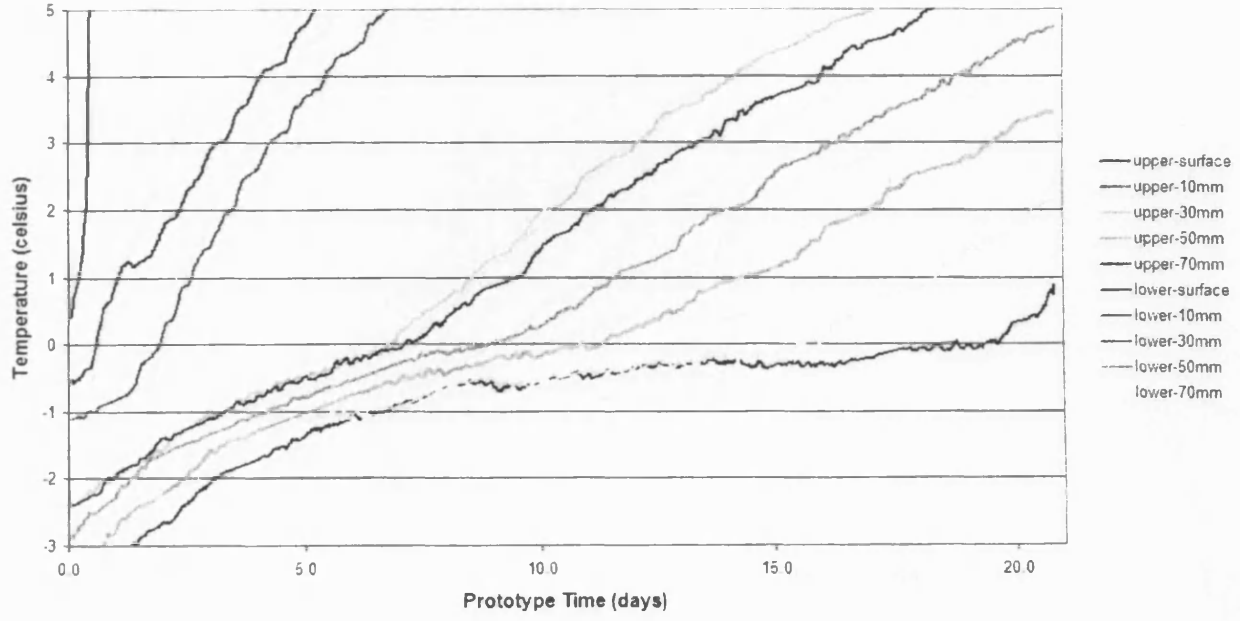

Figure A.41. Thermal data recorded during the second thaw phase of series 4D/20S.

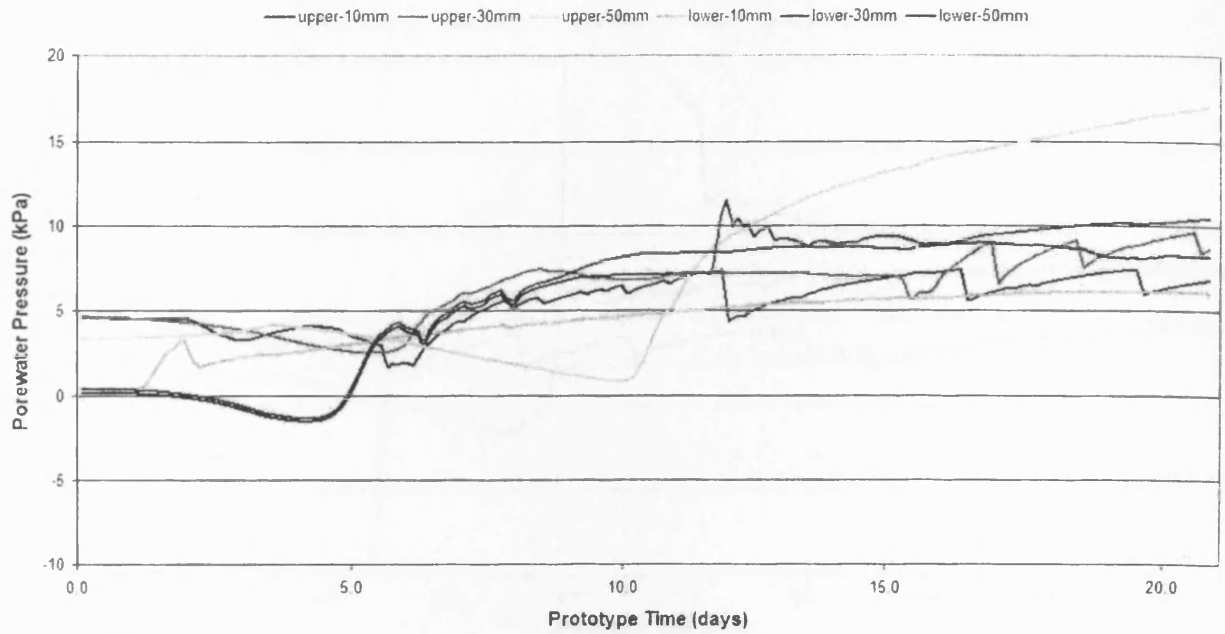

Figure A.42. Porewater pressure data recorded during the second thaw phase of series 4D/20S.

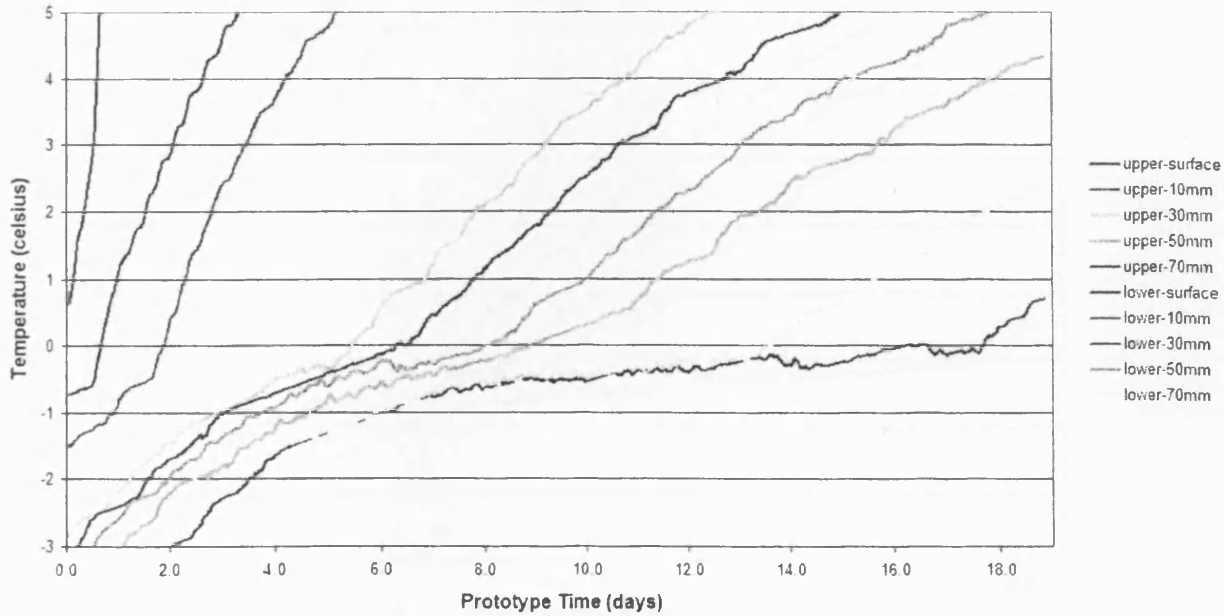

Figure A.43. Thermal data recorded during the third thaw phase of series 4D/20S.

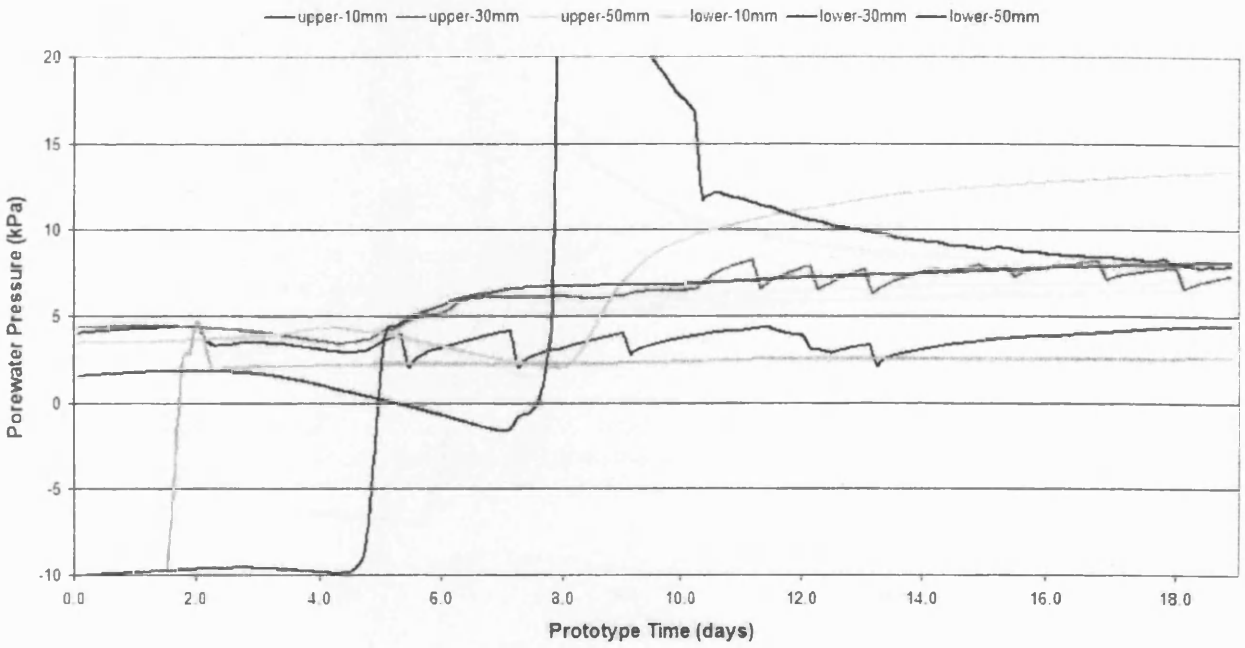

Figure A.44. Porewater pressure data recorded during the third thaw phase of series 4D/20S.

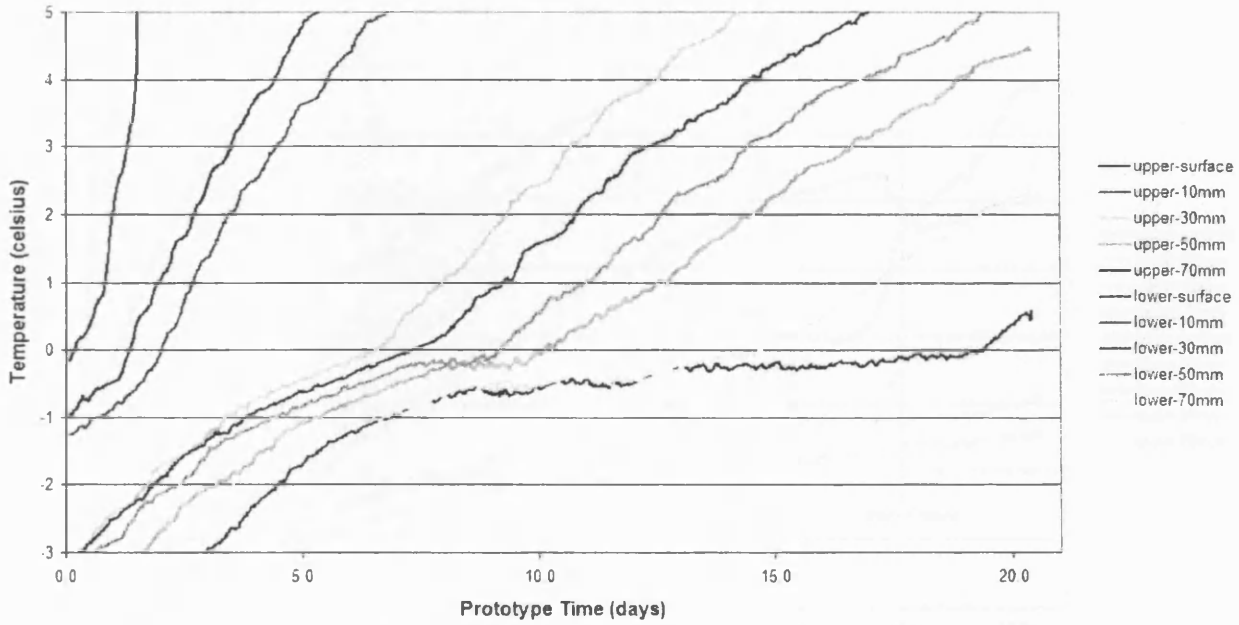

Figure A.45. Thermal data recorded during the fourth thaw phase of series 4D/20S.

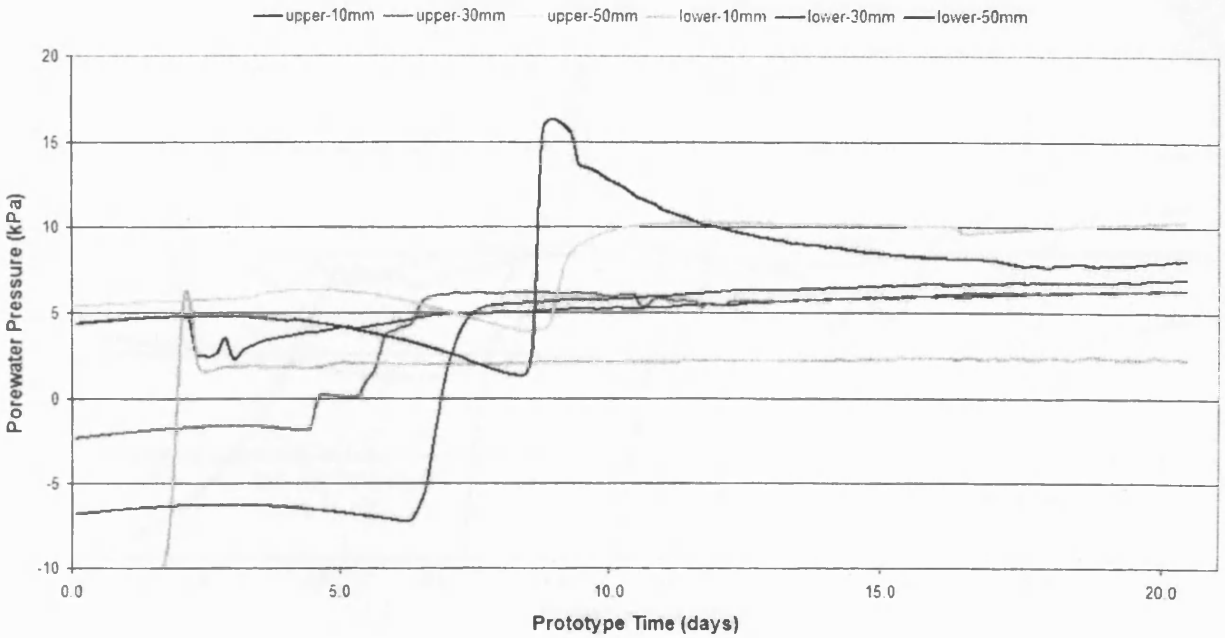

Figure A.46. Porewater pressure data recorded during the fourth thaw phase of series 4D/20S.

A.1.8. Test Series – Twelve Degree Slope, Ten Percent Added Clay

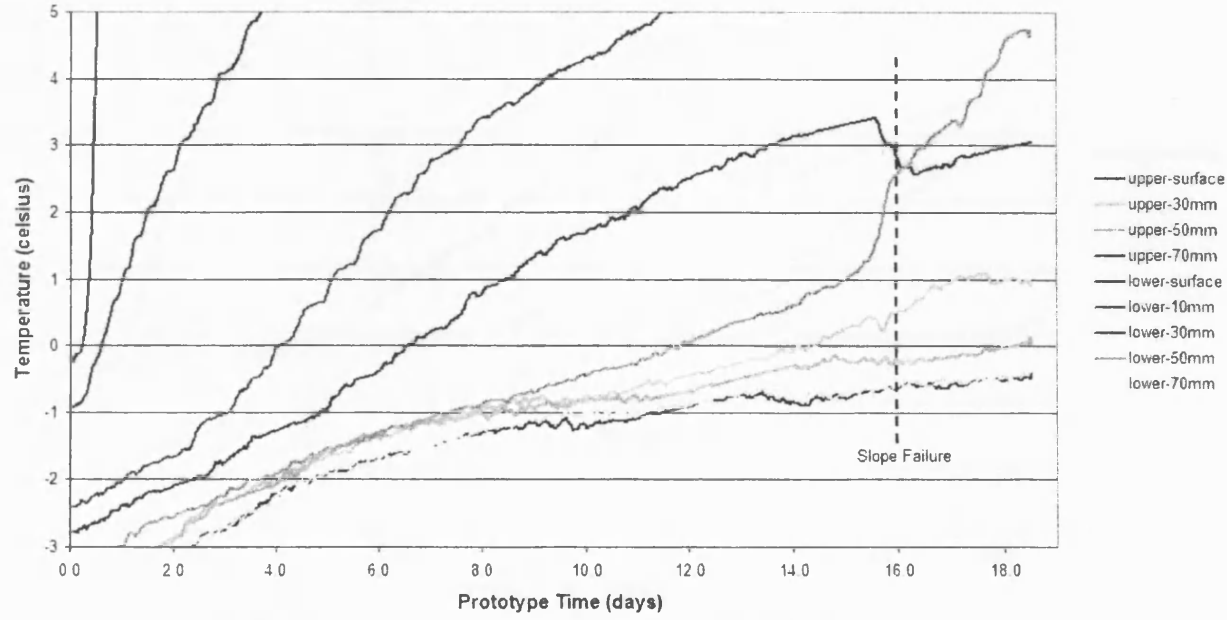

Figure A.47. Thermal data recorded during the first thaw phase of series 12D/10C.

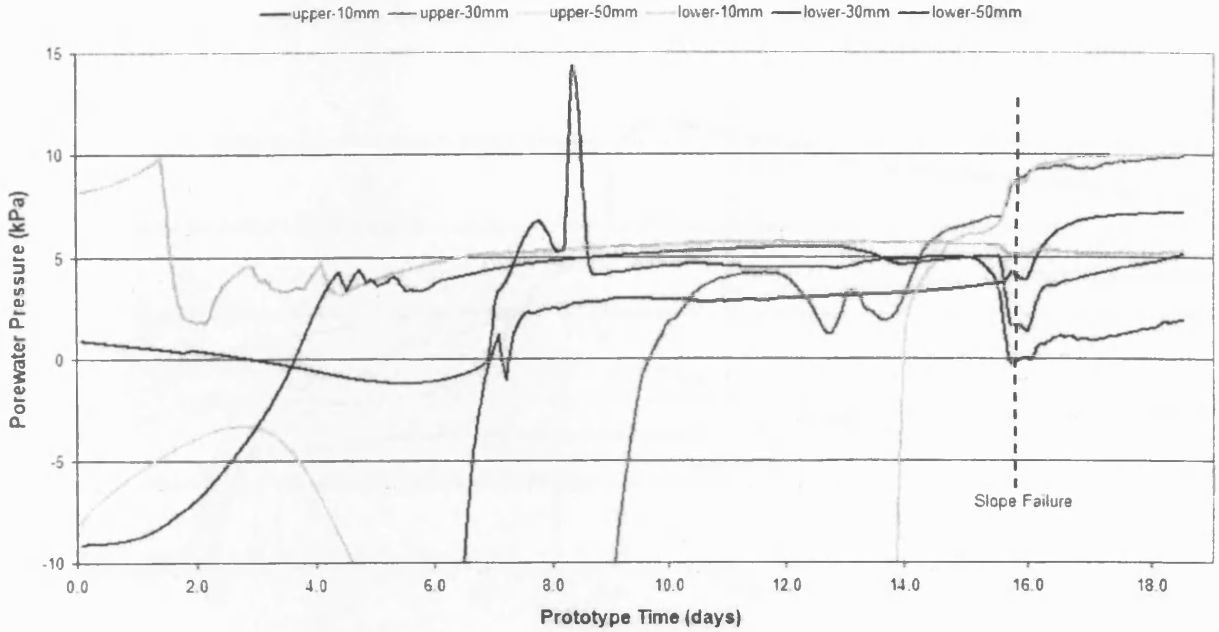

Figure A.48. Porewater pressure data recorded during the first thaw phase of series 12D/10C.

A.1.9. Test Series – Eight Degree Slope, Ten Percent Added Clay

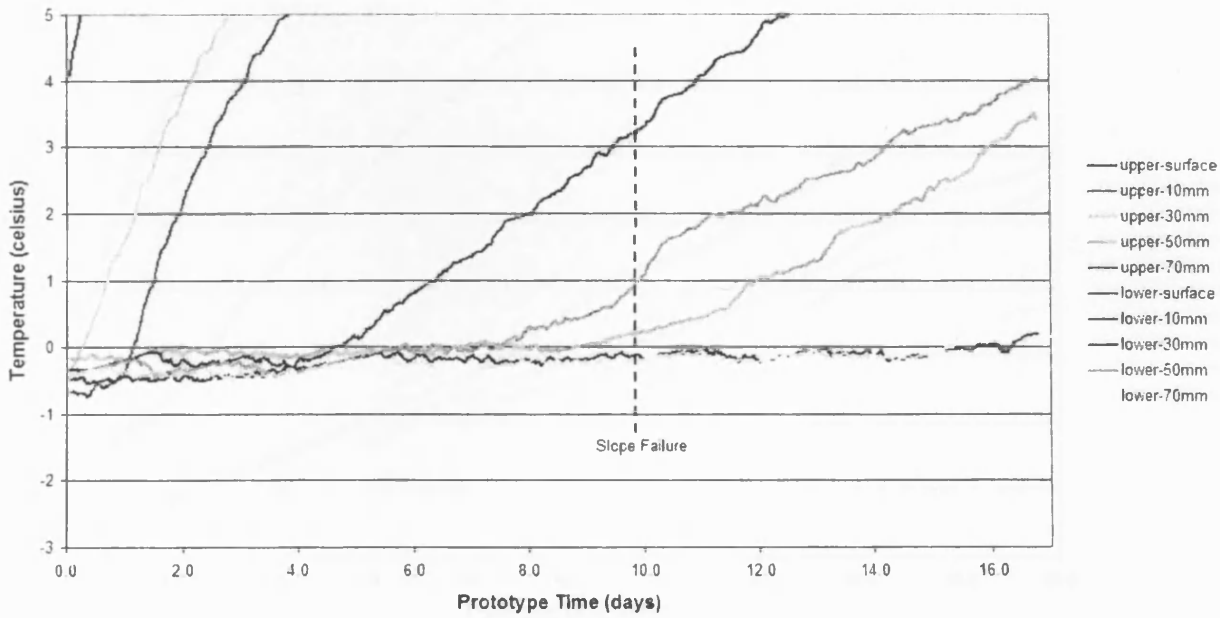

Figure A.49. Thermal data recorded during the first thaw phase of series 8D/10C.

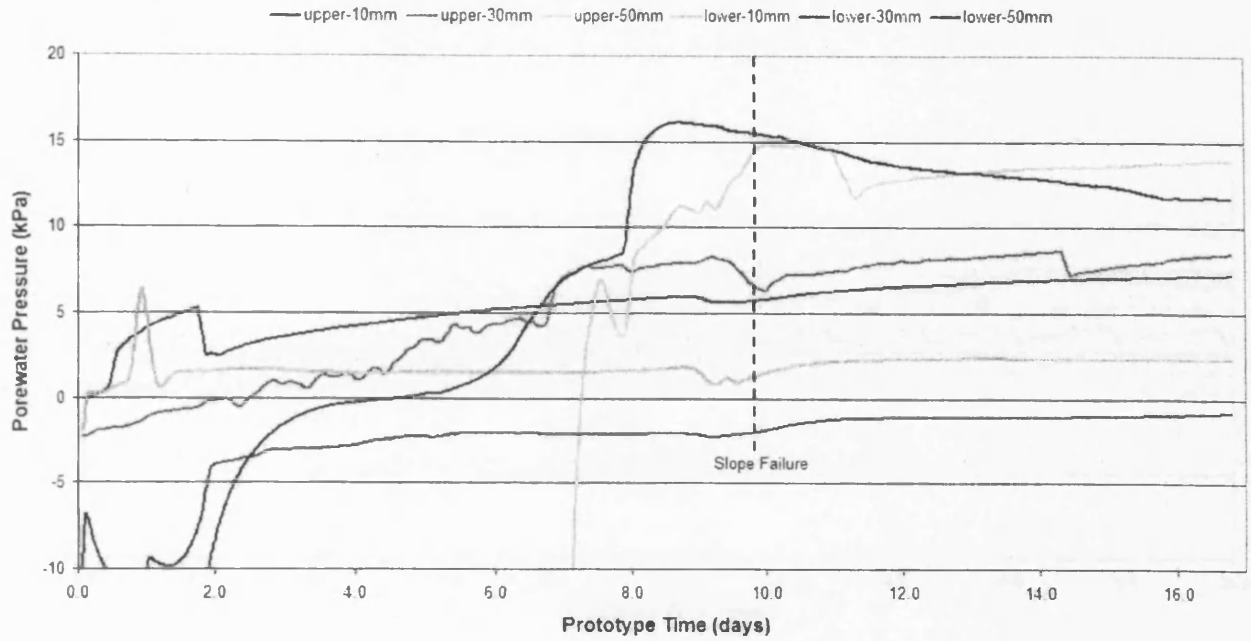

Figure A.50. Porewater pressure data recorded during the first thaw phase of series 8D/10C.

A.1.10. Test Series – Four Degree Slope, Ten Percent Added Clay

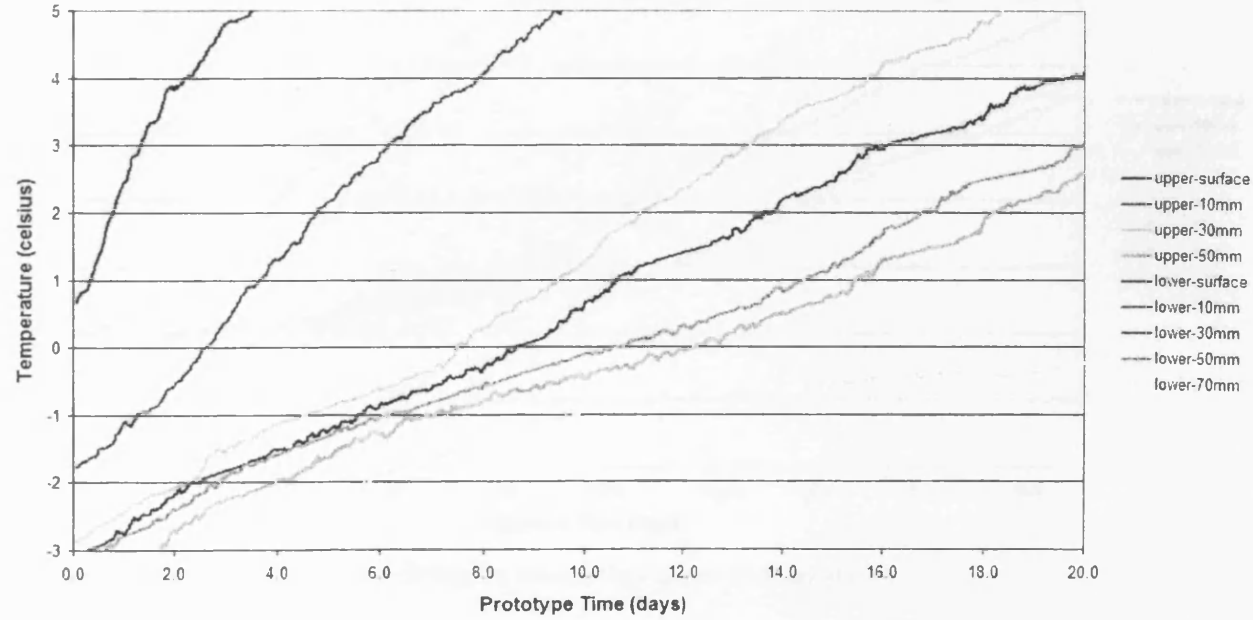

Figure A.51. Thermal data recorded during the first thaw phase of series 4D/10C.

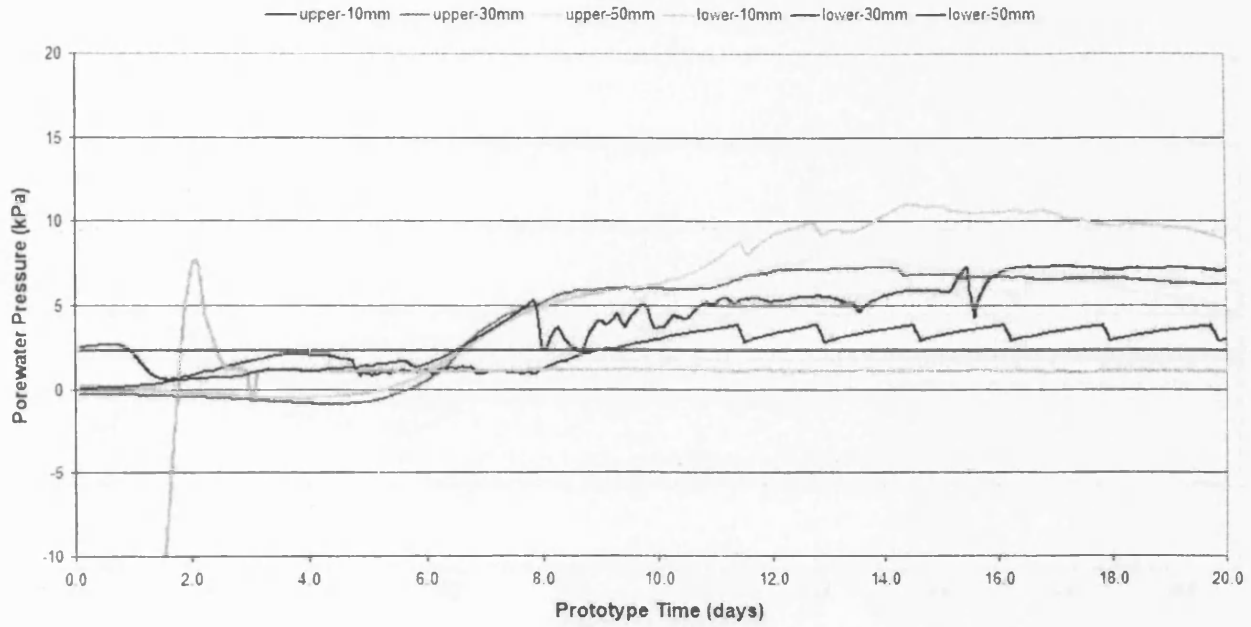

Figure A.52. Porewater pressure data recorded during the first thaw phase of series 4D/10C.

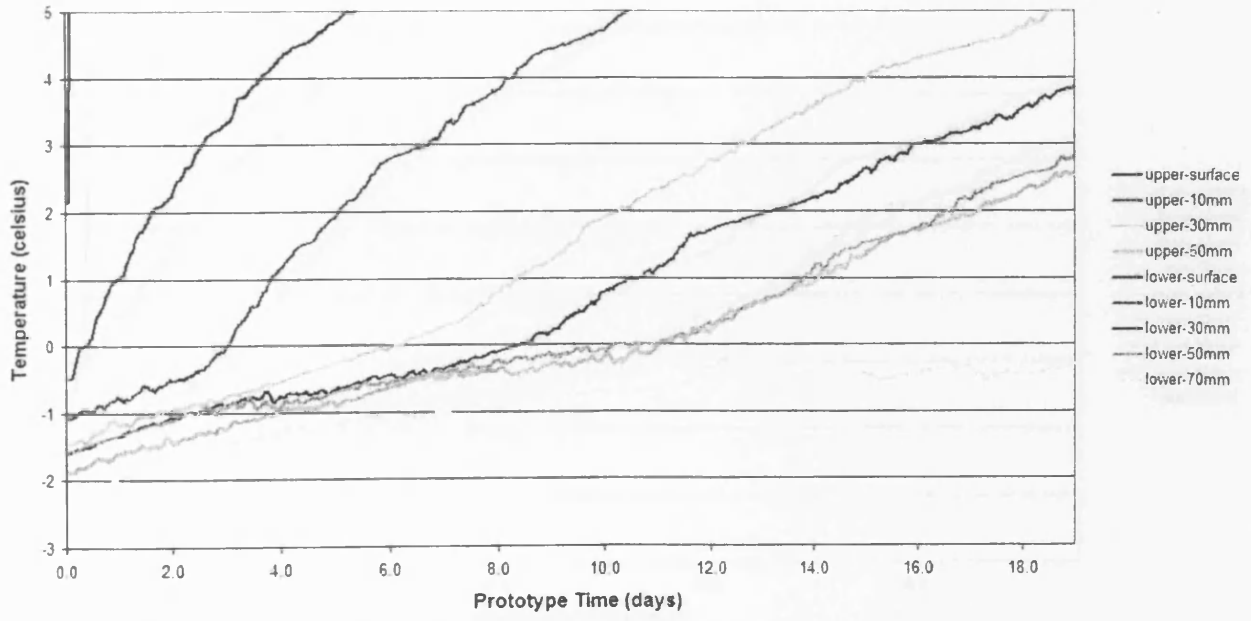

Figure A.53. Thermal data recorded during the second thaw phase of series 4D/10C.

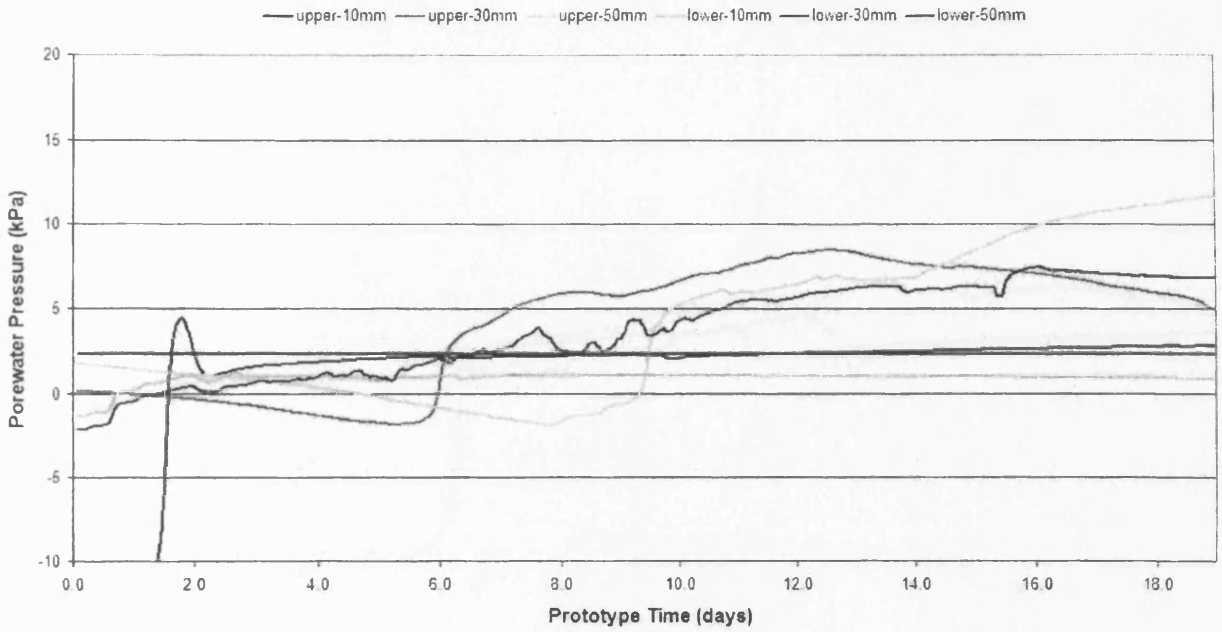

Figure A.54. Porewater pressure data recorded during the second thaw phase of series 4D/10C.

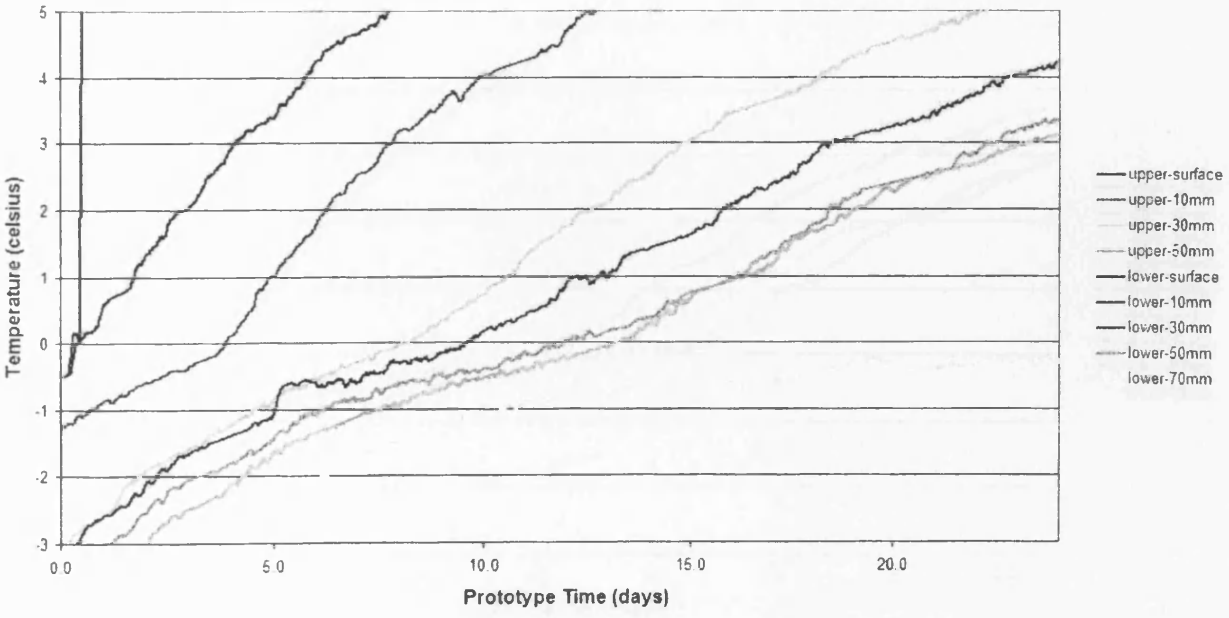

Figure A.55. Thermal data recorded during the third thaw phase of series 4D/10C.

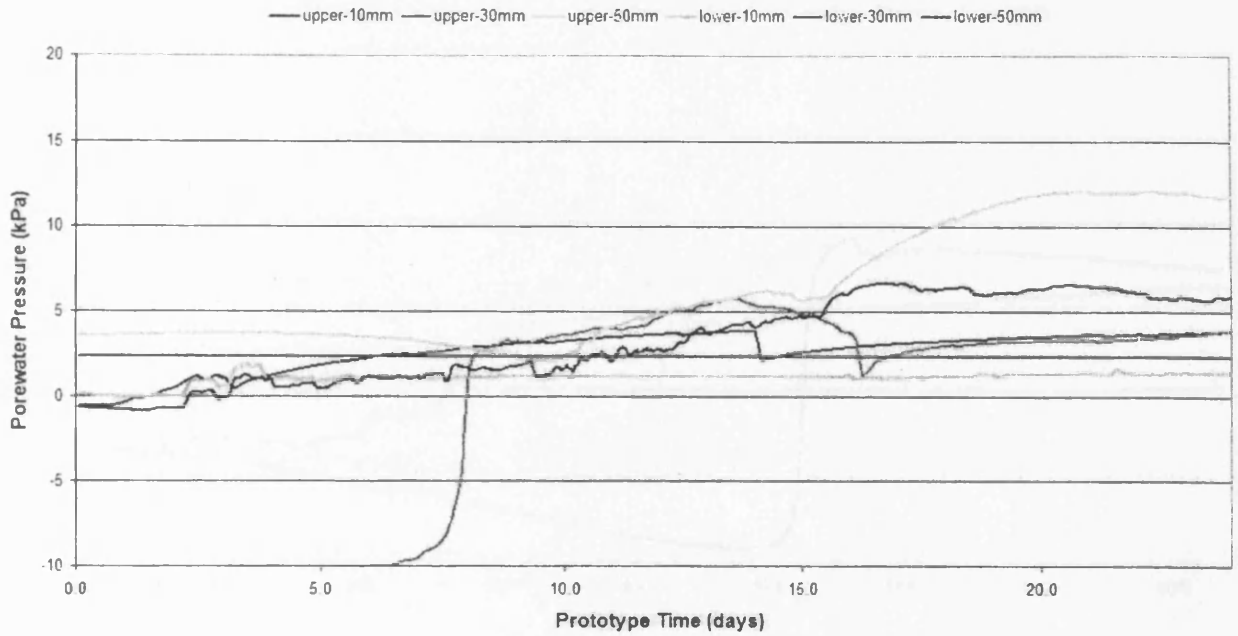

Figure A.56. Porewater pressure data recorded during the third thaw phase of series 4D/10C.

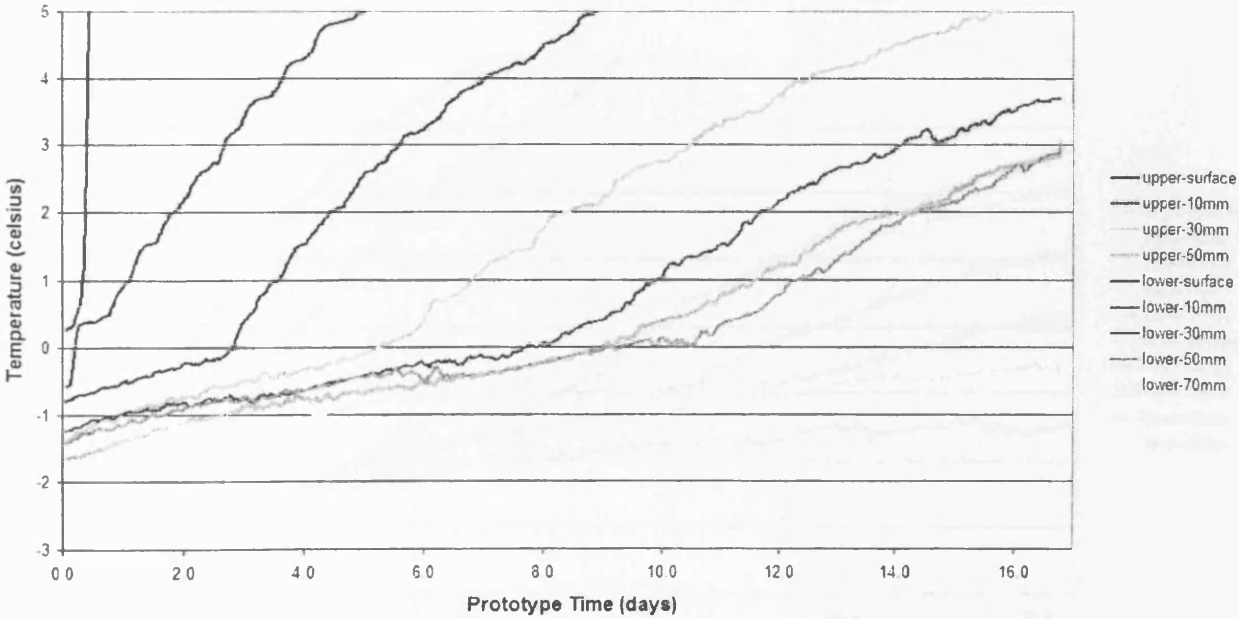

Figure A.57. Thermal data recorded during the fourth thaw phase of series 4D/10C.

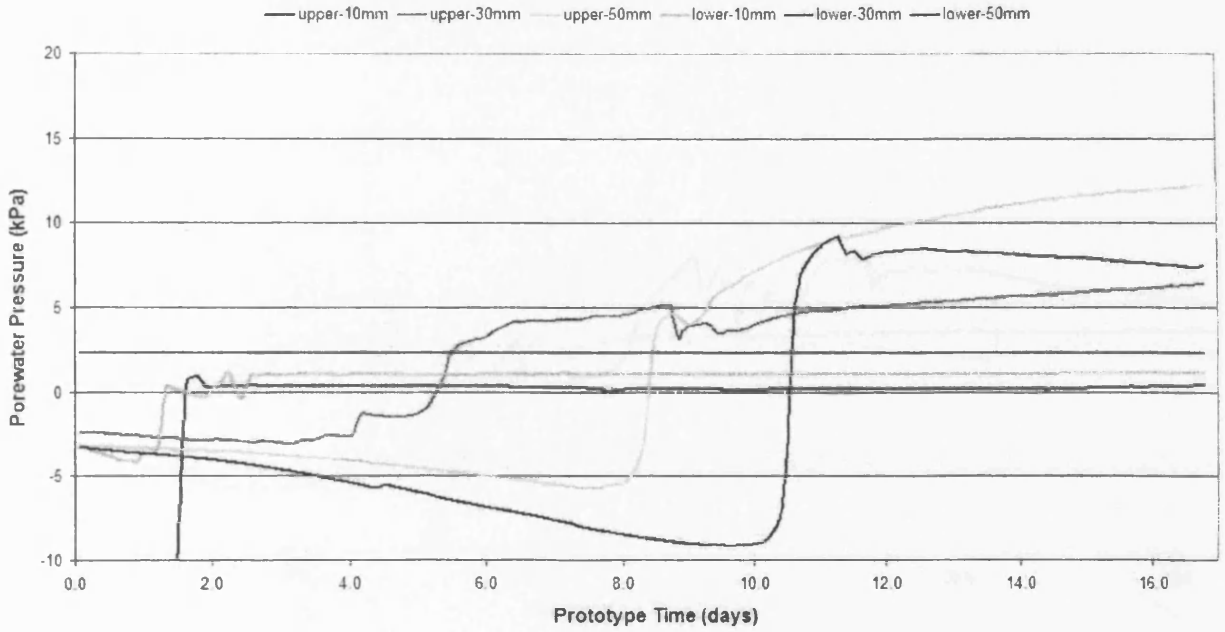

Figure A.58. Porewater pressure data recorded during the fourth thaw phase of series 4D/10C.

A.1.11. Test Series – Four Degree Slope, Twenty Percent Added Clay

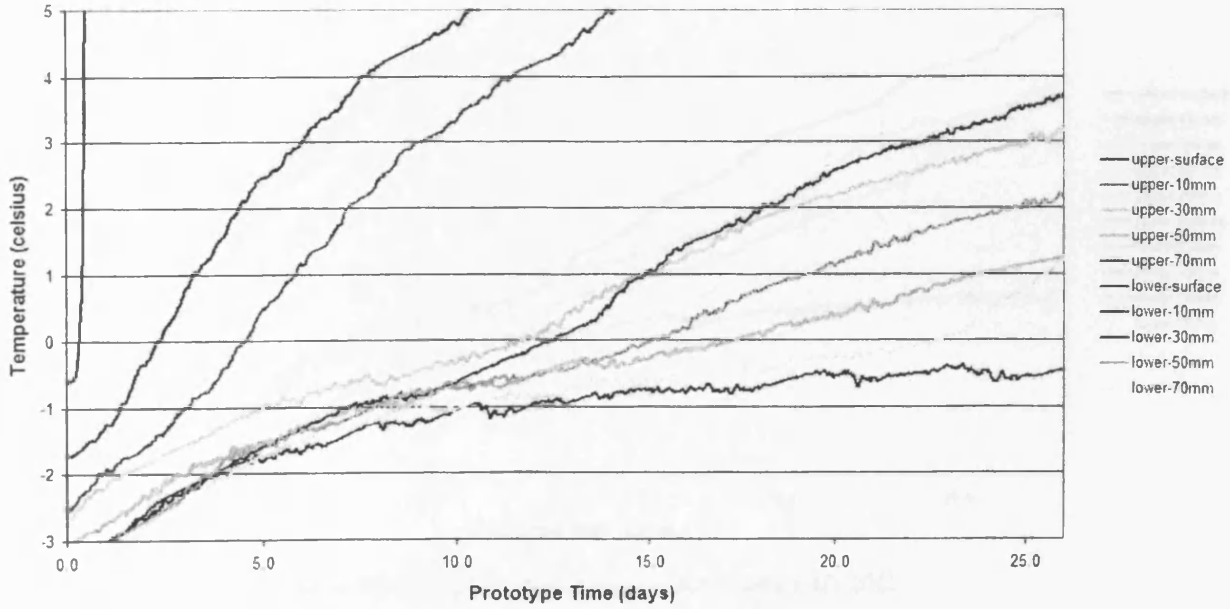

Figure A.59. Thermal data recorded during the first thaw phase of series 4D/20C.

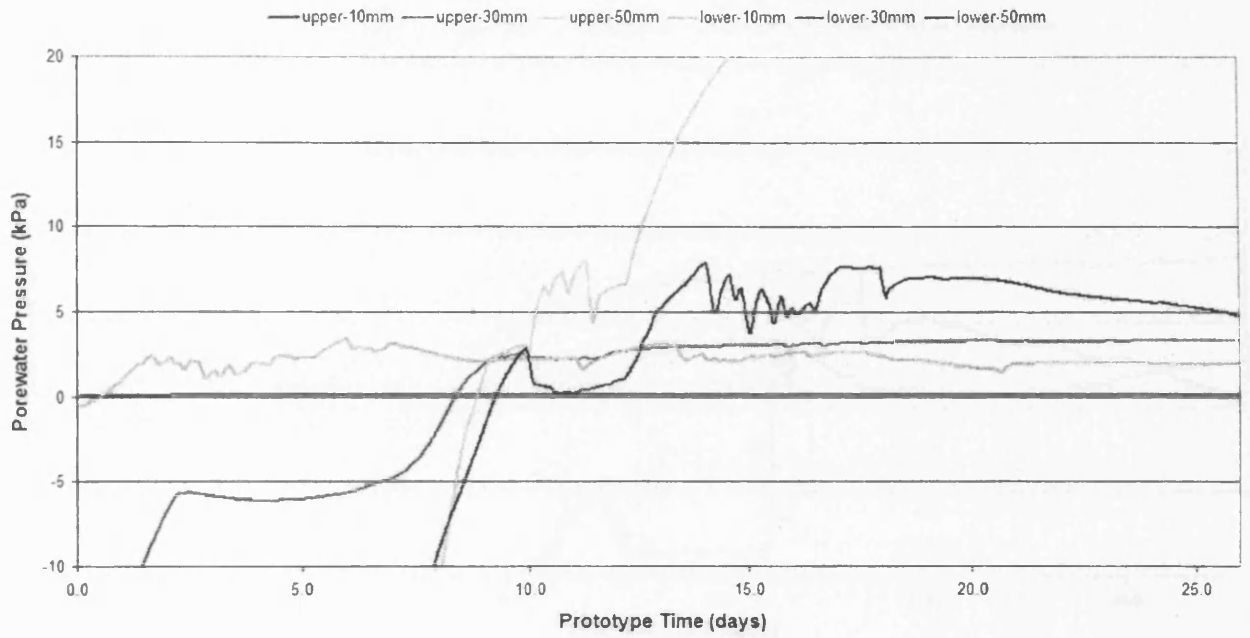

Figure A.60. Porewater pressure data recorded during the first thaw phase of series 4D/20C.

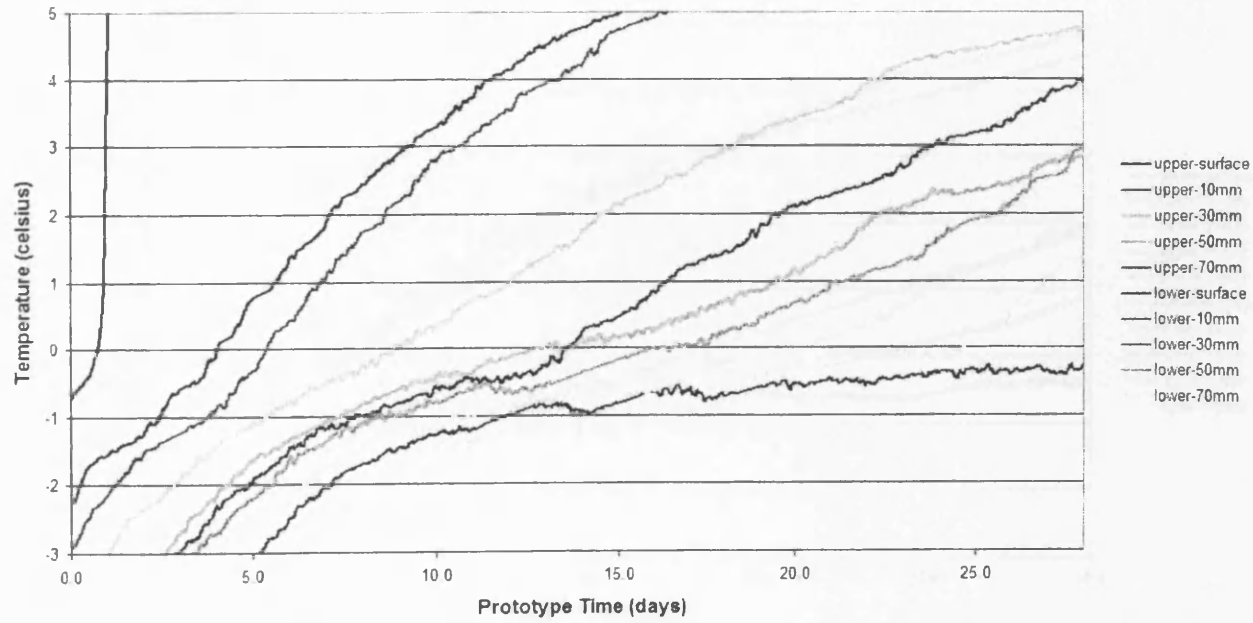

Figure A.61. Thermal data recorded during the second thaw phase of series 4D/20C.

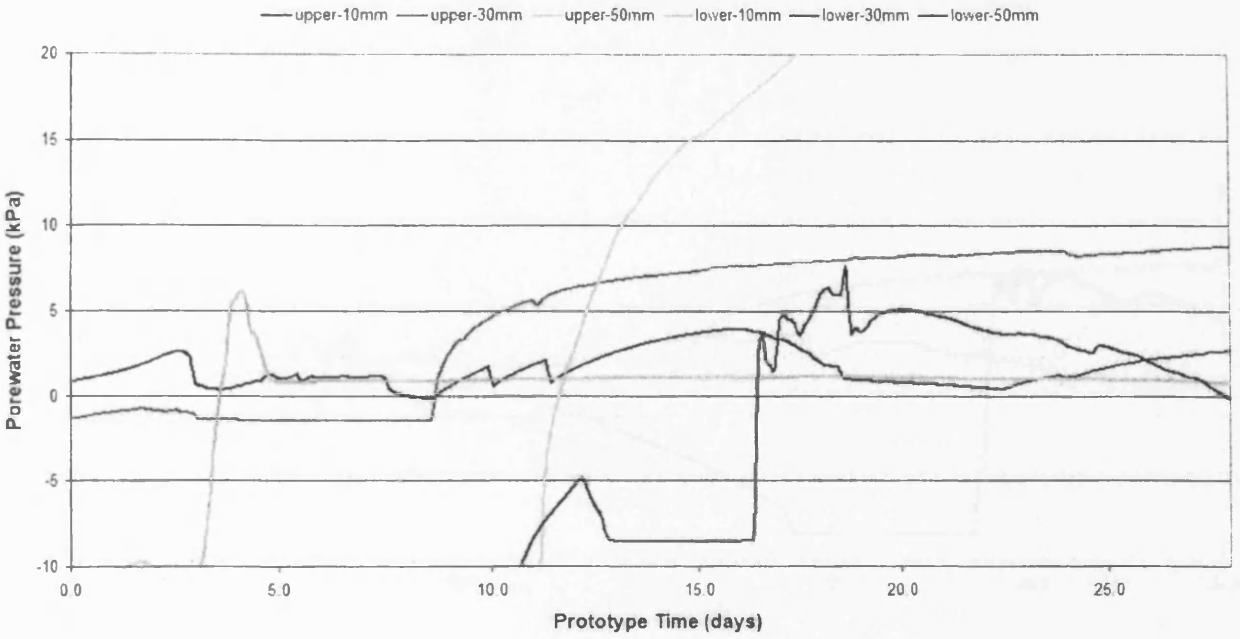

Figure A.62. Porewater pressure data recorded during the second thaw phase of series 4D/20C.

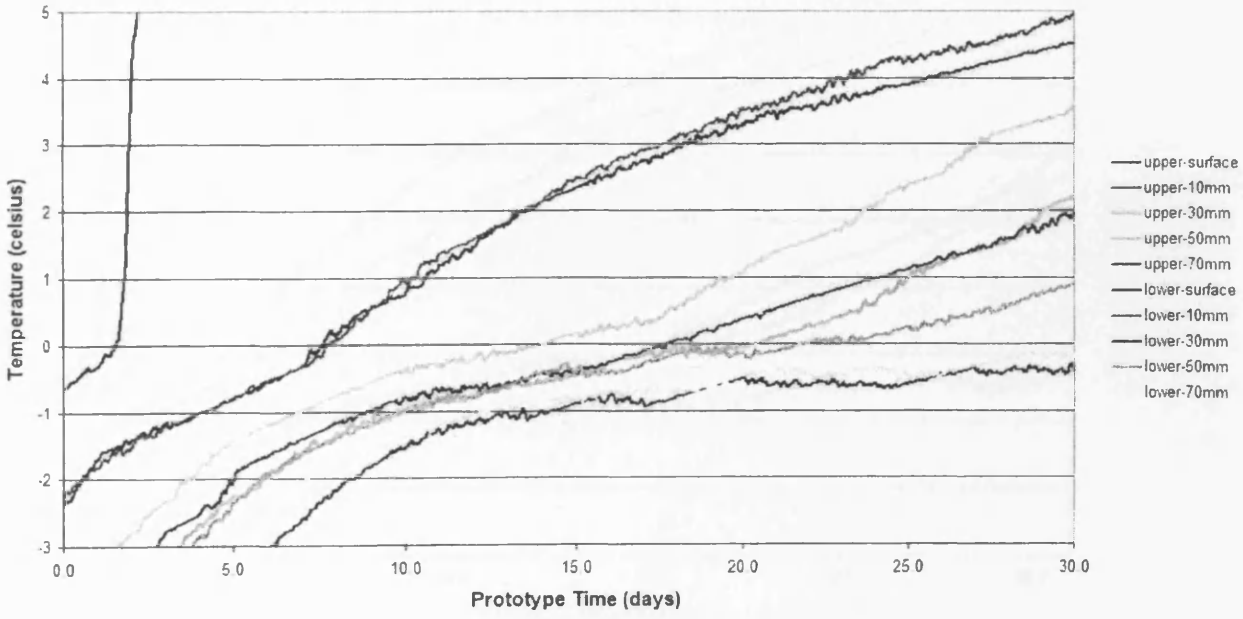

Figure A.63. Thermal data recorded during the third thaw phase of series 4D/20C.

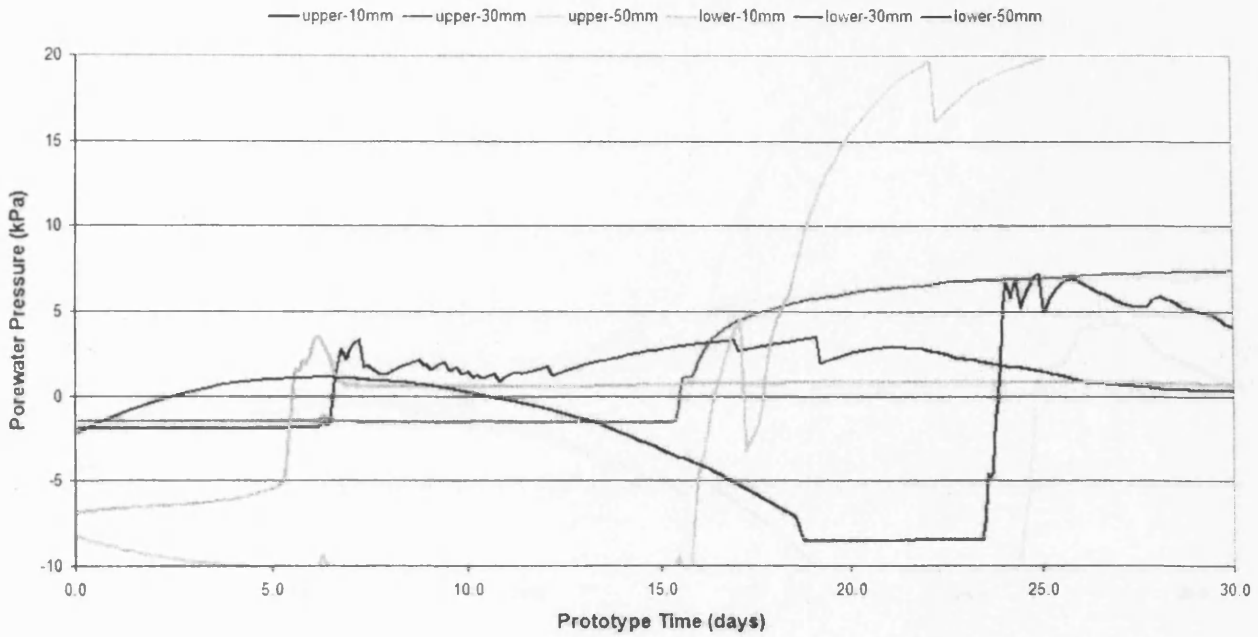

Figure A.64. Porewater pressure data recorded during the third thaw phase of series 4D/20C.

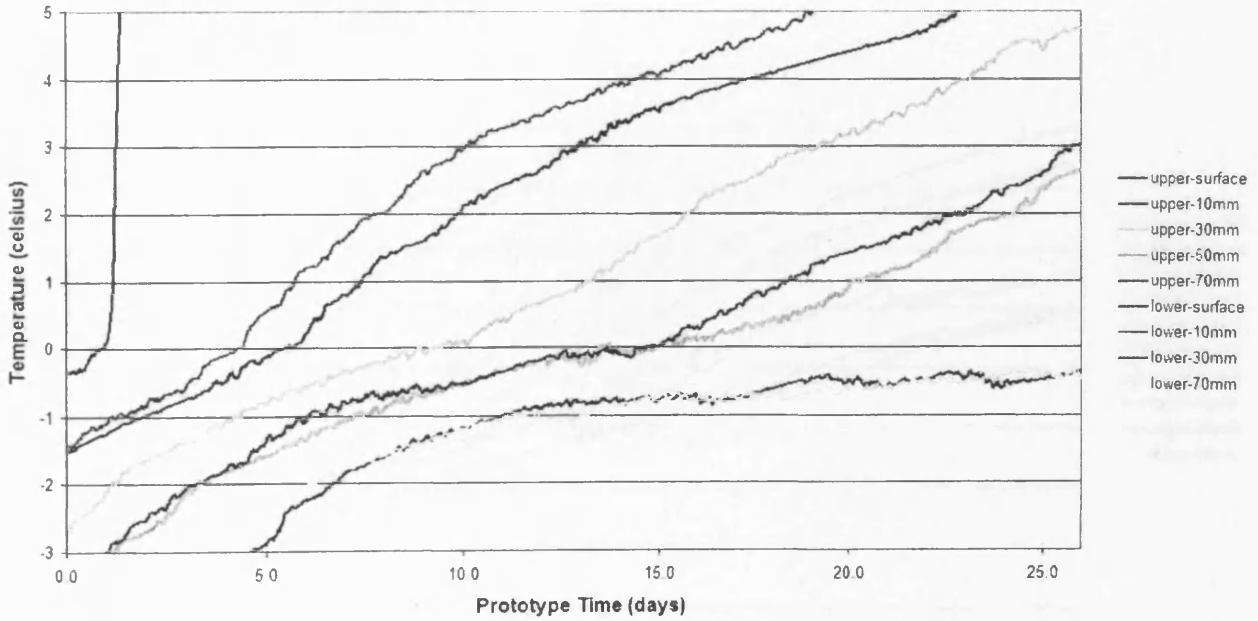

Figure A.65. Thermal data recorded during the fourth thaw phase of series 4D/20C.

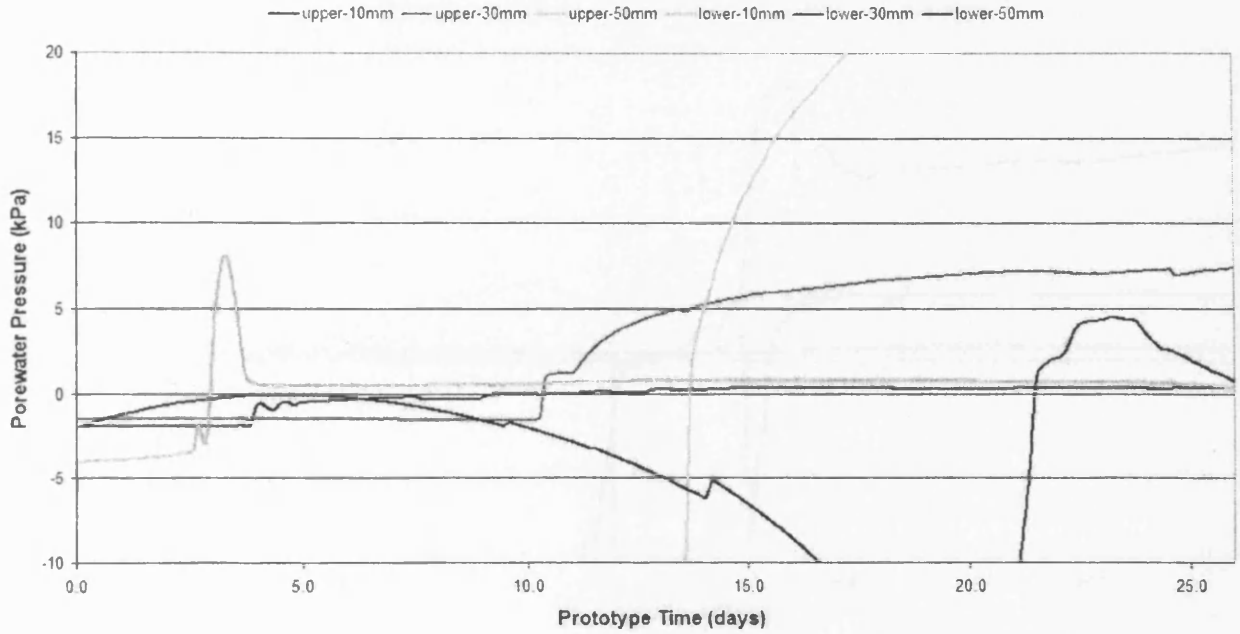

Figure A.66. Porewater pressure data recorded during the fourth thaw phase of series 4D/20C.

A.1.12. Primary Test Series – Eight Degree Slope, Natural Soil (FAULT)

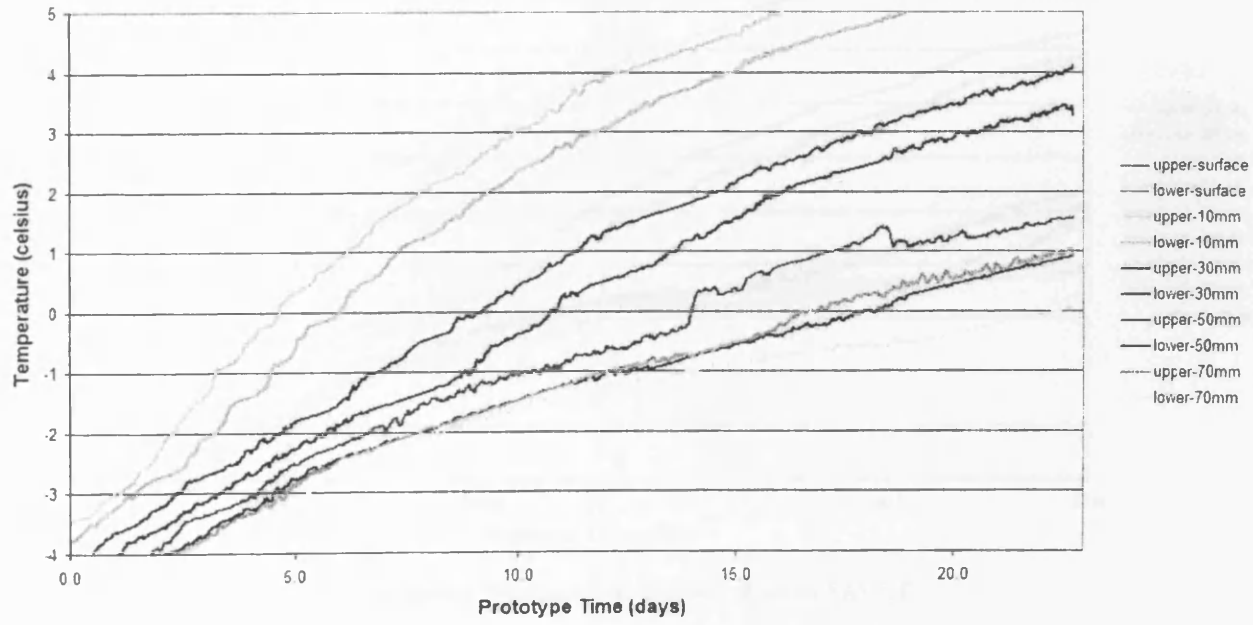

Figure A.67. Thermal data recorded during the first thaw phase of series FAULT.

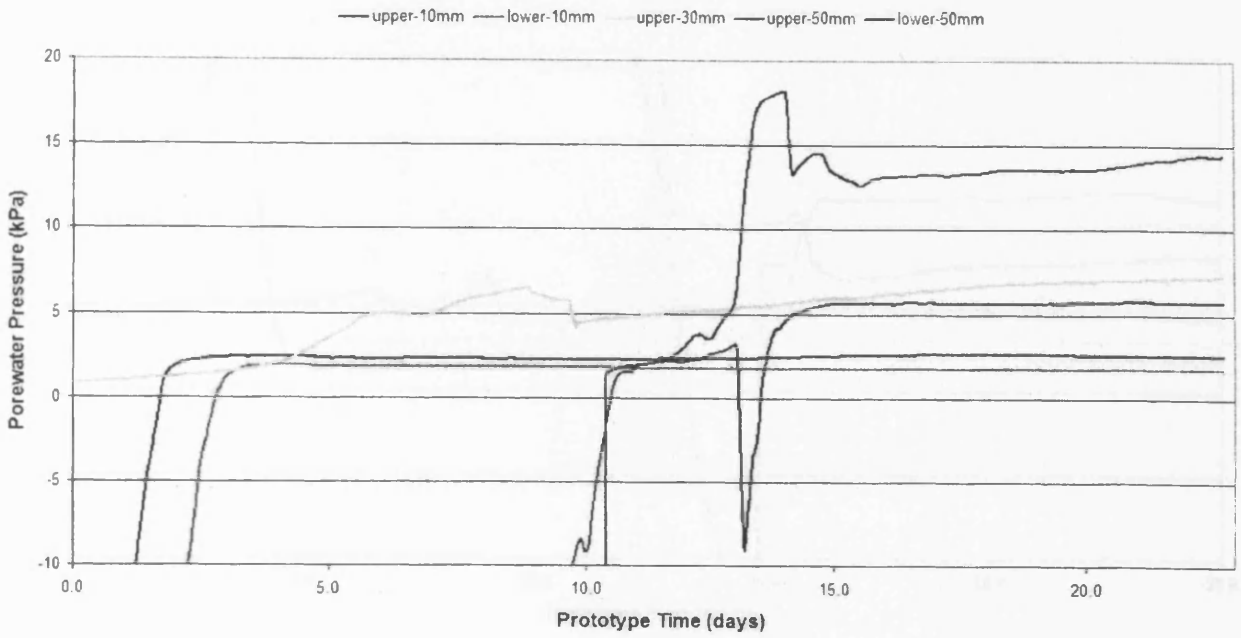

Figure A.68. Porewater pressure data recorded during the first thaw phase of series FAULT.

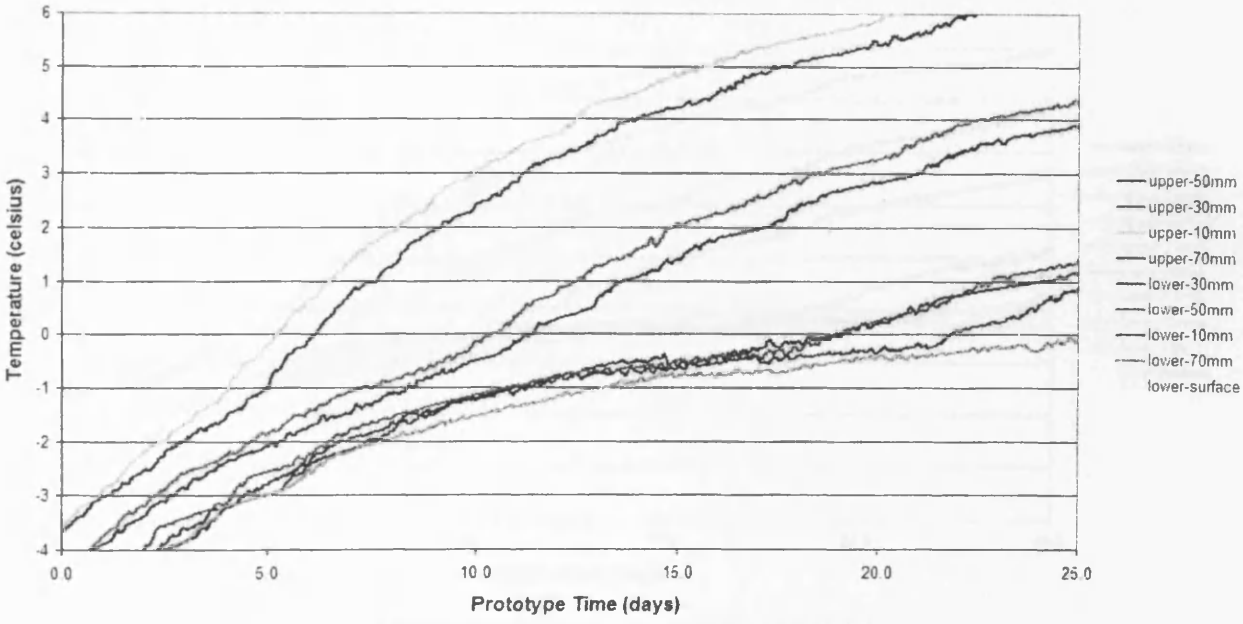

Figure A.69. Thermal data recorded during the second thaw phase of series FAULT.

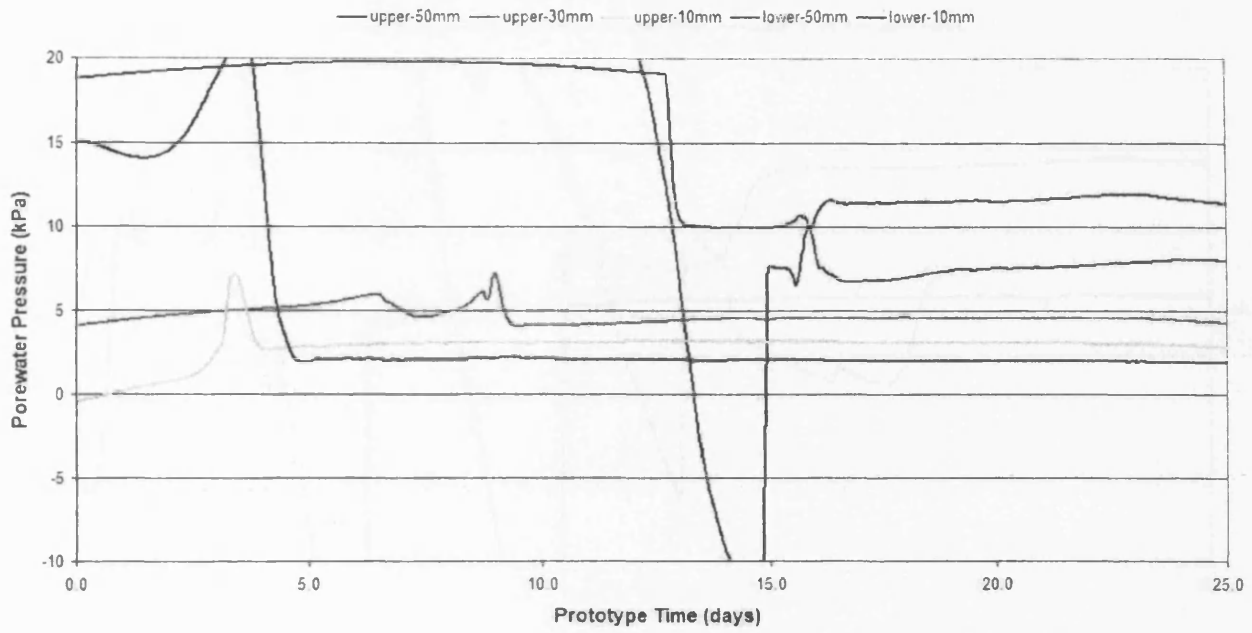

Figure A.70. Porewater pressure data recorded during the second thaw phase of series FAULT.

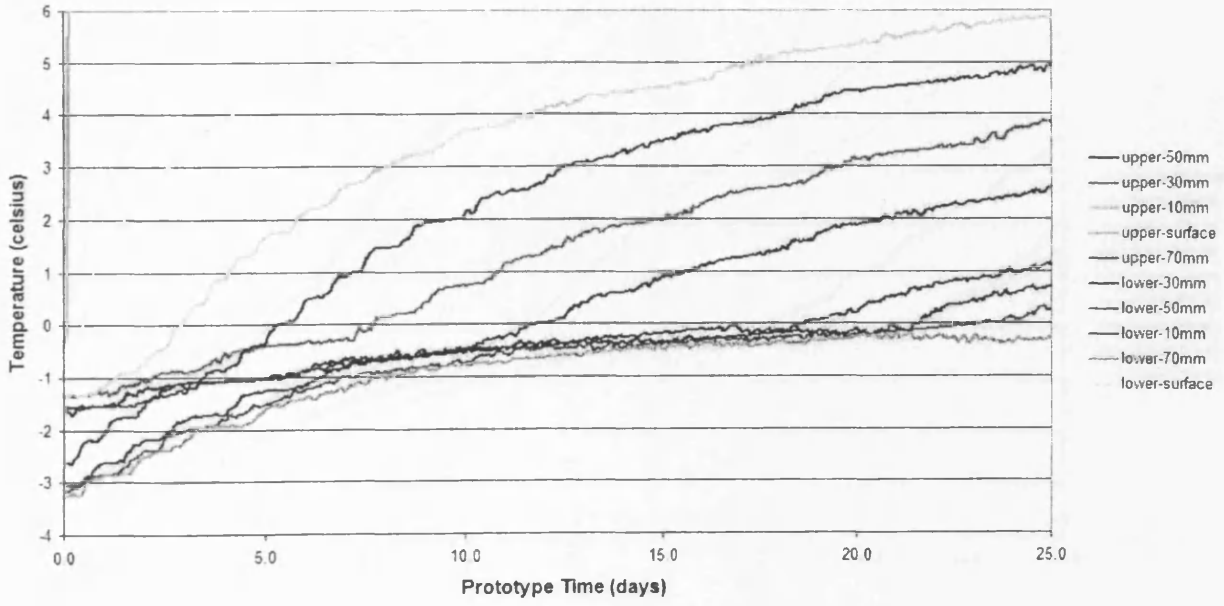

Figure A.71. Thermal data recorded during the third thaw phase of series FAULT.

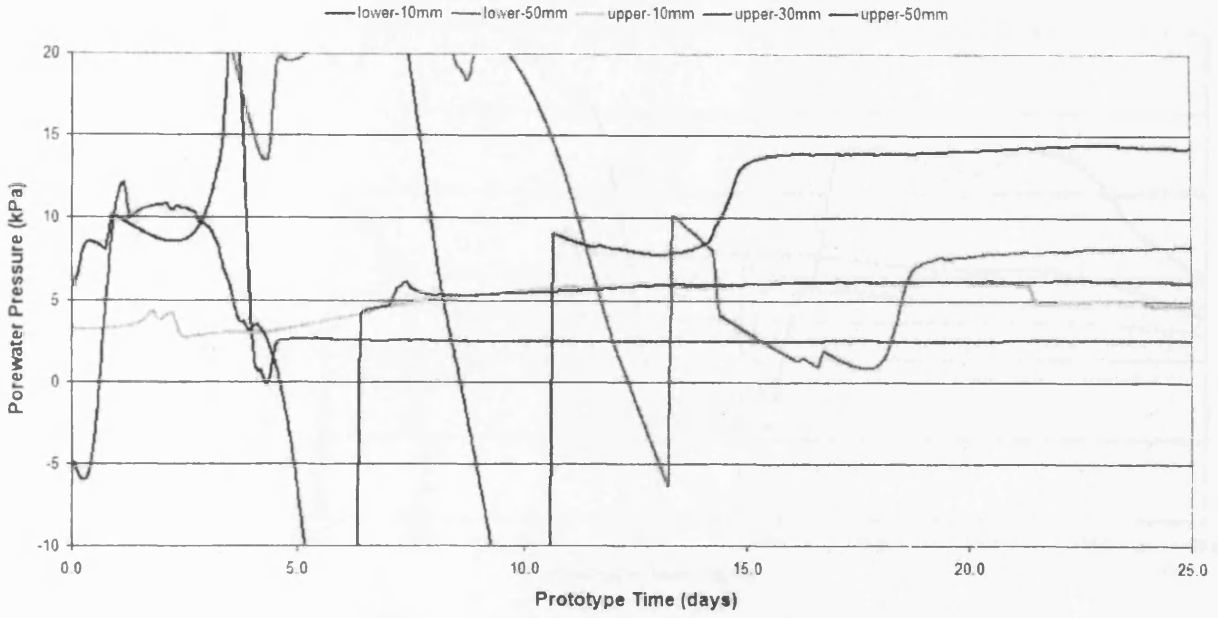

Figure A.72. Porewater pressure data recorded during the third thaw phase of series FAULT.

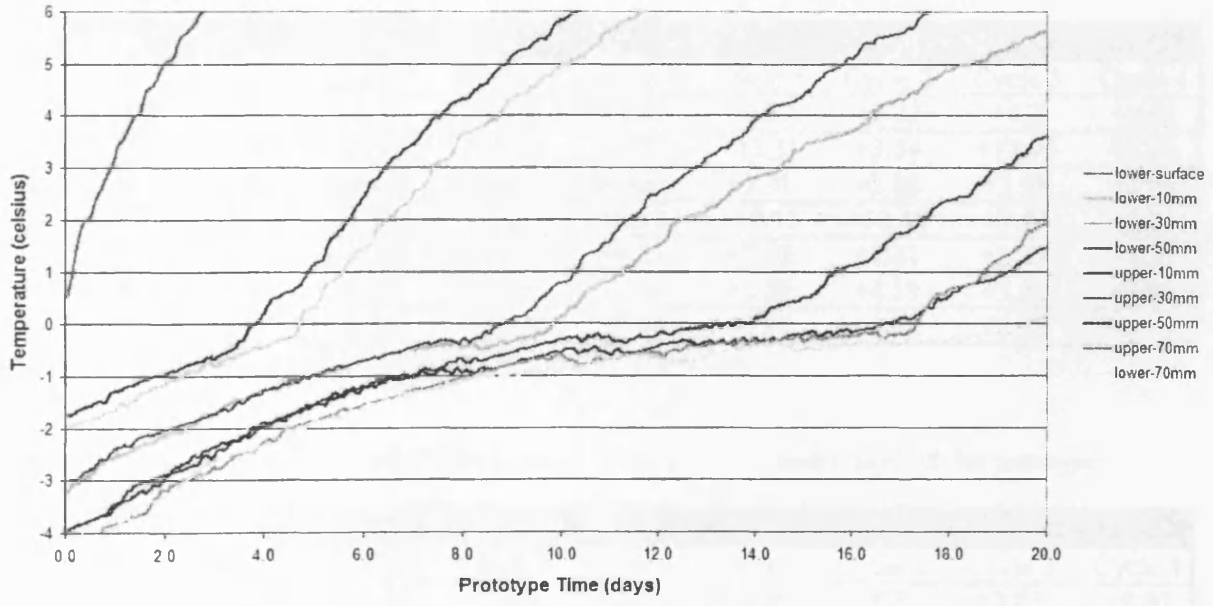

Figure A.73. Thermal data recorded during the fourth thaw phase of series FAULT.

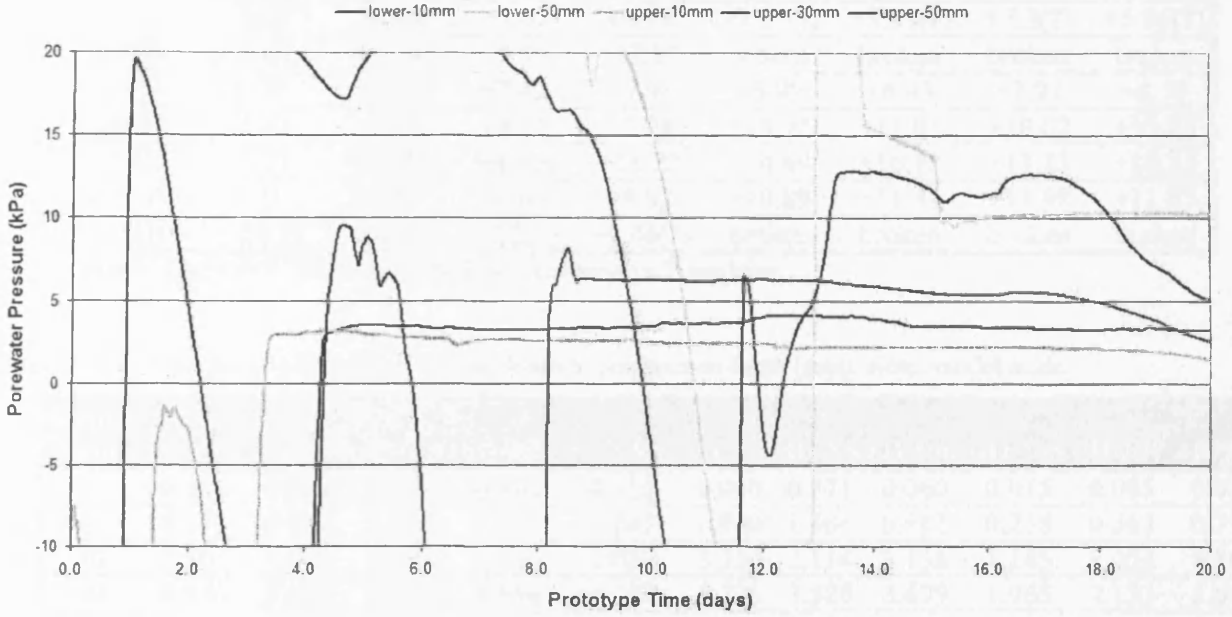

Figure A.74. Porewater pressure data recorded during the fourth thaw phase of series FAULT.

Table A.1.1. Maximum recorded porewater pressure (kPa) at 10mm model depth (0.1m prototype depth).

Series	Lower Slope				Upper Slope			
	Cycle 1	Cycle 2	Cycle 3	Cycle 4	Cycle 1	Cycle 2	Cycle 3	Cycle 4
NS/12D	+2.5	+2.12	+4.28	+1.72	+2.37	+2.22	+4.2	+2.02
NS/8D	+4.6	+6.44	+11.09	+9.77	+12.81	+3.54	+12.96	+5.13
NS/4D	broken	broken	broken	broken	+2.91	+2.88	+3.98	+5.05
10S/4D	+8.12	+6.81	+3.05	+0.52	+10.13	+10.48	+2.99	+3.01
20S/4D	+1.71	+3.96	+4.47	+6.21	+7.03	+7.41	+3.75	+5.18
10C/4D	+7.38	+1.09	+1.63	+1.02	+3.55	+4.19	+3.56	+0.95
20C/4D	+3.42	+6.05	+3.33	+7.99	+0.12	+3.92	+3.18	+0.33

(?) = Poorly Calibrated Transducer; Broken = Inoperative Transducer.

Table A.1.2. Maximum recorded porewater pressure (kPa) at 30mm model depth (0.3m prototype depth).

Series	Lower Slope				Upper Slope			
	Cycle 1	Cycle 2	Cycle 3	Cycle 4	Cycle 1	Cycle 2	Cycle 3	Cycle 4
NS/12D	+4.24	+4.55	+6.02	+4.76	+10.01	+0.8	+2.01	+8.80
NS/8D	broken	broken	broken	broken	broken	+7.08	+7.07	+3.73
NS/4D	+4.37	+4.59	+5.82	+6.99	+3.68	+4.48	+6.96	+8.09
10S/4D	+13.86(?)	+7.88(?)	+7.08(?)	+6.31(?)	+6.06	broken	+6.18	+8.17
20S/4D	+8.47	+10.18	+6.78	+6.13	+8.06	+8.99	+8.1	+6.12
10C/4D	broken	broken	broken	broken	+7.22	+8.44	+5.97	+4.89
20C/4D	broken	broken	broken	broken	+3.29(?)	+8.25(?)	+7.27(?)	+7.29(?)

(?) = Poorly Calibrated Transducer; Broken = Inoperative Transducer.

Table A.1.3. Maximum recorded porewater pressure (kPa) at 50mm model depth (0.5m prototype depth).

Series	Lower Slope				Upper Slope			
	Cycle 1	Cycle 2	Cycle 3	Cycle 4	Cycle 1	Cycle 2	Cycle 3	Cycle 4
NS/12D	+7.63	+6.93	+7.02	+4.13	+7.23(?)	+5.91(?)	+7.3(?)	+5.86(?)
NS/8D	+13.18	+7.64	+5.99	+12.95	broken	broken	broken	broken
NS/4D	+5.97	+6.33	+7.42	+7.93	+5.99	+6.43	+7.97	+8.39
10S/4D	+11.61	+7.94	+6.53	+7.24	+14.92	+11.05	+10.62	+13.23
20S/4D	+13.28	+11.24	broken	+16.22	+14.49	+16.12	+13.22	+10.23
10C/4D	+7.34	+7.45	+6.69	+8.92	+10.89	+11.41	+11.98	+11.87
20C/4D	+7.65(?)	+7.48(?)	+7.3(?)	+4.48(?)	broken	broken	broken	broken

(?) = Poorly Calibrated Transducer; Broken = Inoperative Transducer.

Table A.1.3. Time (hours) for zero degree isotherm to penetrate to depth (mm). Note: model scale.

Depth (mm)	12D/NS	16D/NS	4D/NS	8D/10S	12D/10C	4D/10S	8D/NS	8D/10C	4D/20S	4D/10C	4D/20C
0	0.196	0.035	0.040	0.165	0.015	0.050	0.171	0.060	0.015	0.085	0.036
10	1.079	0.635	1.093	1.559	1.245	0.940	1.384	0.961	0.258	0.363	0.733
30	2.801	1.780	2.316	3.434	2.030	3.350	2.114	3.136	1.145	1.456	1.860
50	4.026	3.470	4.173	4.650	4.385	4.270	3.528	3.679	1.965	2.133	2.686
70	6.835	6.220	5.061	6.066	7.070	n/a	4.910	5.074	3.795	3.821	5.258

A.2. Supplementary Frost Heave and Thaw Settlement Data

A.2.1. Frost Heave

Table A.2.1. Average per cycle frost heave (mm) from each downslope measurement transect using spot height matrix (see fig. 5.3.1 for context).

Series	7mm	14mm	21mm	28mm	35mm	42mm
12D/NS	12.32	12.39	12.11	12.57	12.18	12.93
16D/NS	12.57	13.00	15.14	13.43	15.43	11.29
FAULT	8.14	7.93	8.89	9.68	11.61	11.36
4D/NS	9.00	9.89	11.18	11.46	12.04	12.46
8D/10S	9.57	10.64	11.79	12.14	12.86	12.14
12D/10C	11.43	11.00	10.86	9.86	8.86	8.57
4D/10S	10.64	12.21	13.00	12.14	11.64	10.79
8D/NS	8.82	9.14	8.89	8.54	8.68	7.89
8D/10C	8.00	8.71	8.29	6.86	8.57	6.86
4D/20S	6.63	6.30	6.70	6.29	5.49	4.71
4D/10C	7.62	8.25	7.79	6.74	5.58	4.33
4D/20C	8.43	8.95	9.63	9.87	9.88	9.07

Table A.2.2. Average frost heave (mm) measured for each freezing cycle using spot height matrix.

Series	Cycle 1	Cycle 2	Cycle 3	Cycle 4	Average
12D/NS	7.86	15.88	12.76	13.17	12.42
16D/NS	13.48				13.48
FAULT	6.83	8.57	12.31	10.69	9.60
4D/NS	10.19	9.07	14.52	10.24	11.01
8D/10S	8.12	14.93			11.52
12D/10C	10.10				10.10
4D/10S	8.88	14.26	8.67	15.14	11.74
8D/NS	4.38	9.62	9.24	11.40	8.66
8D/10C	7.88				7.88
4D/20S	9.43	3.83	5.29	5.54	6.02
4D/10C	6.71	5.60	7.69	7.00	6.75
4D/20C	12.29	7.29	8.81	8.81	9.30

Table A.2.3. Average per cycle frost heave (mm) measured for each surface marker (see fig. 5.5.1 for overall context).

Marker	12D/NS	16D/NS	FAULT	4D/NS	8D/10S	12D/10C	4D/10S	8D/NS	8D/10C	4D/20S	4D/10C	4D/20C
A	6.25	12	9	8.75	7	9	9.5	6.5	8	5.75	5.75	11.25
B	6.5	15	11	10.5	8	10	11.75	10	13	7	5.75	11.75
C	6	13	13.75	13.25	10.5	9	11.5	12	13	6.5	4.25	11.25
D	6.75	14	8.25	9.75	7.5	11	10	9	12	6.5	8	6.5
E	7.25	13	8.75	11.5	10	11	11.5	11.5	14	8	8.5	9.25
F	7.5	11	10	13	9.5	9	11.5	11.5	14	5.25	5.5	9.25
G	9.5	11	13.75	11.5	9.5	11	10	9	13	7.25	8.25	6.75
H	11.25	9	12	12	10	10	13	10	14	6.5	8.5	7.25
I	11.5	9	13.75	13.25	12.5	12	12	10	11	5.75	7.75	8.25
J	9	9	8	9.5	9	12	11.5	9.5	12	5	7.5	6.75
K	10.25	11	11.5	10.75	9.5	13	12.75	9.5	7	5.25	9.5	6.5
L	11.5	10	13.5	11.25	11	9	13.25	9	11	4.5	6.5	7.5
M	6	10	12	9	8	9	10	9	6	4	7	8
N	8	11	11.75	9	9.5	7	12.25	7.5	8	6.25	8.25	8
O	8	11	11.5	11	10.5	6	14.5	7.5	8	4.75	7	8.25
Average	8.35	11.27	11.23	10.93	9.47	9.87	11.67	9.43	10.93	5.88	7.20	8.43

A.2.2 Thaw Settlement

Table A.2.4. Average per cycle thaw settlement (mm) measured for each downslope transect using spot height matrix.

Series	7mm	14mm	21mm	28mm	35mm	42mm
12D/NS	13.46	13.43	13.32	13.61	13.89	14.54
16D/NS	FAILURE					
FAULT	9.43	9.54	10.00	11.25	13.43	12.39
4D/NS	10.21	10.93	12.32	12.61	12.86	12.36
8D/10S	FAILURE					
12D/10C	FAILURE					
4D/10S	10.93	12.50	13.14	12.36	12.11	11.00
8D/NS	10.43	10.61	10.29	9.89	9.96	9.14
8D/10C	FAILURE					
4D/20S	7.50	7.46	8.01	7.31	6.23	5.31
4D/10C	9.28	9.96	9.58	8.78	8.00	6.36
4D/20C	10.59	10.78	11.22	11.77	12.12	11.27

Table A.2.5. Average thaw settlement (mm) measured for each thaw phase using spot height matrix.

Series	Cycle 1	Cycle 2	Cycle 3	Cycle 4
12D/NS	9.33	16.69	14.17	14.64
16D/NS	FAILURE			
FAULT	9.12	10.00	11.62	13.29
4D/NS	10.52	9.69	16.43	10.88
8D/10S	FAILURE			
12D/10C	FAILURE			
4D/10S	9.38	12.90	12.00	13.74
8D/NS	7.52	11.17	10.81	10.71
8D/10C	FAILURE			
4D/20S	10.07	5.48	6.45	5.78
4D/10C	9.12	7.64	8.95	8.70
4D/20C	12.17	11.29	10.10	11.59

A.3. Supplementary Surface and Subsurface Movement Data

A.3.1. Surface Movement

Table A.3.1. Average per cycle surface movement (mm) measured along horizontal surface marker transects. Note: model scale.

Series	12.5cm	25cm	37.5cm	50cm	62.5cm
12D/NS	1.67	4.00	5.50	5.75	4.25
16D/NS			FAILURE		
FAULT	2.50	3.42	5.08	5.42	6.00
4D/NS	1.75	2.42	2.75	2.92	1.50
8D/10S			FAILURE		
12D/10C			FAILURE		
4D/10S	2.42	3.42	2.75	2.75	2.42
8D/NS	1.08	1.83	2.92	3.17	3.25
8D/10C			FAILURE		
4D/20S	3.75	4.42	6.83	5.33	3.08
4D/10C	1.67	1.58	1.75	1.58	1.92
4D/20C	1.83	1.83	2.08	2.75	3.25

Table A.3.2. Average per cycle surface movement (mm) measured for each surface marker.

Marker	12D/NS	FAULT	4D/NS	4D/10S	8D/NS	4D/20S	4D/10C	4D/20C
A	1	2	0.75	1.75	1.25	3	2	1.25
B	1.75	1.75	1.25	2.75	1	3.25	1.5	2
C	2.25	3.75	3.25	2.75	1	5	1.5	2.25
D	2.75	4	0.75	3.25	2	3.25	1	2
E	4	3	2	3.25	1.5	4.5	1.75	1.25
F	5.25	3.25	4.5	3.75	2	5.5	2	2.25
G	4.25	5	2.75	2.5	3.5	4.25	1.25	1.75
H	5.75	4.75	3	2.5	3	7.5	1.75	1.75
I	6.5	5.5	2.5	3.25	2.25	8.75	2.25	2.75
J	4.25	6	2.25	2.5	3.5	4.25	0.75	2
K	5.75	5	3	2.25	3.25	5	1.75	2.25
L	7.25	5.25	3.5	3.5	2.75	6.75	2.25	4
M	2.5	5.75	0.75	1.75	4.5	3.25	1.5	1.75
N	4.25	5.75	2	1.75	2.25	2.75	1.5	4.5
O	6	6.5	1.75	3.75	3	3.25	2.75	3.5
Average	4.23	4.48	2.26	2.75	2.45	4.68	1.7	2.35

A.3.2. Subsurface Movement

Table A.3.3. Volume displaced (mm^3) at different model depths per subsurface slice for series involving natural soil (see fig. 5.5.14 for context).

Depth (mm)	8D/NS					12D/NS				
	Slice 1	*Slice 2*	*Slice 3*	*Slice 4*	*Slice 5*	*Slice 1*	*Slice 2*	*Slice 3*	*Slice 4*	*Slice 5*
0	36.59	62.15	70.94	77.08	74.06	53.85	103.33	141.67	157.92	143.75
5	34.09	54.51	61.25	64.24	62.81	31.73	88.79	108.33	128.33	122.62
10	30.45	48.78	54.38	61.28	54.38	24.04	66.36	87.50	107.08	107.44
15	26.70	46.01	48.44	54.34	48.75	20.19	55.15	72.92	88.75	94.05
20	21.82	40.28	44.38	50.00	44.38	15.77	39.39	62.50	70.42	79.17
25	19.32	32.99	36.25	39.76	35.63	11.35	31.52	47.92	63.75	62.20
30	16.93	25.52	26.88	32.47	29.06	9.42	21.36	35.42	47.92	47.02
35	14.55	18.06	14.38	17.71	16.56	6.92	11.21	27.08	34.17	35.71
40	13.30	11.98	5.63	7.12	5.63	2.50	5.61	12.50	18.33	24.40
45	10.91	5.90	0.00	0.00	1.56	2.50	1.67	4.17	4.58	11.01
50	7.27	2.78	0.00	0.00	0.00	0.00	0.00	0.00	0.00	3.57
55	4.89	0.00	0.00	0.00	0.00	0.00	0.00	0.00	0.00	1.79
60	2.50	0.00	0.00	0.00	0.00	0.00	0.00	0.00	0.00	0.00
65	0.00	0.00	0.00	0.00	0.00	0.00	0.00	0.00	0.00	0.00
70	0.00	0.00	0.00	0.00	0.00	0.00	0.00	0.00	0.00	0.00
Sum	239.32	348.96	362.50	403.99	372.81	178.27	424.39	600.00	721.25	732.74

Table A.3.4. Volume displaced (mm^3) at different model depths per subsurface slice for series involving Series 4D/NS.

Depth (mm)	4D/NS				
	Slice 1	*Slice 2*	*Slice 3*	*Slice 4*	*Slice 5*
0	39.29	75.00	57.86	79.17	51.79
5	30.95	64.58	52.14	71.13	41.07
10	18.45	53.13	47.86	59.23	37.50
15	12.20	39.58	36.79	49.70	32.14
20	3.87	22.92	28.21	37.80	25.00
25	1.79	16.67	17.14	26.49	17.86
30	1.79	10.42	8.57	16.96	8.93
35	0.00	0.00	2.50	11.31	3.57
40	0.00	0.00	0.00	1.79	1.79
45	0.00	0.00	0.00	0.00	0.00
50	0.00	0.00	0.00	0.00	0.00
55	0.00	0.00	0.00	0.00	0.00
60	0.00	0.00	0.00	0.00	0.00
65	0.00	0.00	0.00	0.00	0.00
70	0.00	0.00	0.00	0.00	0.00
Sum	108.33	282.29	251.07	353.57	219.64

Table A.3.5. Volume displaced (mm^3) at different model depths per subsurface slice for series involving incremental additions of silt.

Depth (mm)	4D/10S					4D/20S				
	Slice 1	*Slice 2*	*Slice 3*	*Slice 4*	*Slice 5*	*Slice 1*	*Slice 2*	*Slice 3*	*Slice 4*	*Slice 5*
0	21.59	51.89	59.38	75.52	79.17	36.88	126.99	162.36	126.70	118.64
5	20.64	47.54	51.56	68.75	68.75	32.81	112.50	147.73	119.03	115.00
10	21.78	40.91	44.79	59.90	58.33	30.00	104.12	137.78	110.65	108.86
15	19.51	36.65	39.58	51.04	43.75	25.94	94.89	126.99	95.45	104.09
20	17.42	34.47	32.29	40.63	35.42	23.13	91.05	111.65	83.24	99.32
25	14.11	29.17	25.00	32.29	26.04	18.75	81.53	70.74	65.63	92.27
30	13.07	19.51	21.88	22.92	17.71	14.38	67.47	52.70	48.01	101.14
35	10.89	8.71	9.38	13.54	10.42	10.31	54.55	20.60	33.24	61.59
40	7.58	4.36	6.77	6.25	6.77	6.25	26.99	9.94	12.36	35.23
45	4.36	0.00	1.56	2.08	3.13	3.13	11.65	5.40	5.40	23.64
50	2.08	0.00	0.00	0.00	0.00	1.56	4.69	1.56	3.13	15.45
55	0.00	0.00	0.00	0.00	0.00	0.00	0.00	0.00	0.00	9.55
60	0.00	0.00	0.00	0.00	0.00	0.00	0.00	0.00	0.00	0.00
65	0.00	0.00	0.00	0.00	0.00	0.00	0.00	0.00	0.00	0.00
70	0.00	0.00	0.00	0.00	0.00	0.00	0.00	0.00	0.00	0.00
Sum	153.03	273.20	292.19	372.92	349.48	203.13	776.42	847.44	702.84	884.77

Table A.3.6. Volume displaced (mm^3) at different model depths per subsurface slice for series involving incremental additions of clay.

Depth (mm)	4D/10C					4D/20C				
	Slice 1	*Slice 2*	*Slice 3*	*Slice 4*	*Slice 5*	*Slice 1*	*Slice 2*	*Slice 3*	*Slice 4*	*Slice 5*
0	10.56	53.13	57.22	73.13	90.63	21.70	53.54	46.09	105.68	119.32
5	11.94	55.63	51.94	72.19	84.72	16.82	46.21	46.09	97.27	109.77
10	14.58	51.25	48.06	56.88	71.53	13.18	37.12	50.00	90.11	98.98
15	13.33	45.63	44.03	46.25	64.06	9.55	24.12	46.97	80.68	87.05
20	14.72	35.94	38.89	35.94	51.22	6.02	15.66	43.94	72.27	71.59
25	14.72	25.00	24.44	29.38	40.97	4.66	7.83	39.52	62.84	58.64
30	12.08	18.44	18.06	20.63	29.17	4.77	5.56	11.49	51.02	44.20
35	9.44	11.25	10.28	11.25	17.36	5.00	4.17	2.78	42.73	31.14
40	10.69	7.19	7.64	5.63	8.68	2.50	2.78	1.39	29.55	19.20
45	9.31	5.63	3.75	2.81	2.78	0.00	0.00	0.00	6.25	7.50
50	8.06	1.25	0.00	0.00	1.39	0.00	0.00	0.00	0.00	0.00
55	4.17	0.00	0.00	0.00	0.00	0.00	0.00	0.00	0.00	0.00
60	2.78	0.00	0.00	0.00	0.00	0.00	0.00	0.00	0.00	0.00
65	0.00	0.00	0.00	0.00	0.00	0.00	0.00	0.00	0.00	0.00
70	0.00	0.00	0.00	0.00	0.00	0.00	0.00	0.00	0.00	0.00
Sum	136.39	310.31	304.31	354.06	462.50	84.20	196.97	288.26	638.41	647.39

Table A.3.7. Maximum subsurface displacement (mm) for each marker column (see fig 5.5.14 for context).

Series	1a	1b	2a	2b	3a	3b	4a	4b	5a	5b	Average
12D/NS	11.54	10.00	21.33	20.00	34.17	22.50	34.00	29.17	35.00	22.50	24.02
16D/NS	FAILURE										
FAULT	28.33	20.83	51.25	28.57	78.75	31.11	57.50	27.50	38.89	28.75	39.15
4D/NS	15.00	0.71	24.17	5.83	16.00	7.14	16.67	15.00	10.71	10.00	12.12
8D/10S	FAILURE										
12D/10C	FAILURE										
4D/10S	4.55	5.00	11.67	9.09	11.25	12.50	16.88	13.33	17.50	14.17	11.59
8D/NS	11.00	3.64	13.75	11.11	14.38	14.00	12.50	18.33	15.63	14.00	12.83
8D/10C	FAILURE										
4D/20S	8.75	6.00	34.55	16.25	41.82	23.13	28.18	22.50	25.45	22.00	22.86
4D/10C	2.50	3.89	11.00	11.25	14.00	8.89	18.00	11.88	20.00	16.25	11.77
4D/20C	3.18	5.50	13.64	7.78	11.36	10.00	22.27	20.00	22.73	25.00	14.15

Table A.3.8. Inferred per thaw cycle subsurface displacement (mm) for each marker column.

Series	1a	1b	2a	2b	3a	3b	4a	4b	5a	5b	Average
12D/NS	1.62	1.95	4.03	4.45	7.21	4.79	7.55	6.88	9.32	5.33	5.31
16D/NS	FAILURE										
FAULT	5.42	5.63	7.44	6.71	12.94	9.28	13.63	8.69	11.72	8.13	8.96
4D/NS	1.92	0.25	4.67	0.98	3.20	1.82	3.25	3.82	2.14	2.25	2.43
8D/10S	FAILURE										
12D/10C	FAILURE										
4D/10S	1.48	1.58	3.15	2.32	2.78	3.06	4.13	3.33	3.78	3.21	2.88
8D/NS	3.40	1.39	4.06	2.92	3.75	3.50	3.72	4.36	3.78	3.68	3.46
8D/10C	FAILURE										
4D/20S	2.69	1.38	9.84	5.69	11.39	5.56	6.68	7.38	10.05	7.65	6.83
4D/10C	0.95	1.78	3.05	3.16	3.98	2.11	4.05	3.03	5.25	4.00	3.14
4D/20C	0.66	1.03	2.02	1.92	3.18	2.58	6.82	5.95	6.02	6.93	3.71

A.4. Microfabric Data

Table A.4.1. Particle orientation (°) measured within thin-section slides collected from both upper and lower slope zones of test series involving natural soil.

4D/NS	4D/NS	8D/NS	8D/NS	12D/NS	12D/NS
Upper Slope	*Lower Slope*	*Upper Slope*	*Lower Slope*	*Upper Slope*	*Lower Slope*
91	90	90	90	90	91
92	92	92	92	92	92
92	92	94	92	95	92
94	94	95	92	96	93
98	94	96	93	98	94
100	95	100	95	98	99
101	97	101	96	99	100
103	97	102	96	102	102

4D/NS	4D/NS	8D/NS	8D/NS	12D/NS	12D/NS
Upper Slope	*Lower Slope*	*Upper Slope*	*Lower Slope*	*Upper Slope*	*Lower Slope*
106	99	103	96	103	103
109	110	106	96	103	107
115	111	106	98	104	108
116	113	110	98	106	109
117	117	112	99	107	111
117	119	112	101	109	113
120	122	113	102	117	113
121	129	117	106	118	114
122	142	121	112	119	115
122	145	123	114	119	115
123	148	123	120	125	118
126	171	129	123	125	118
134	189	130	123	125	119
148	191	135	125	133	121
151	344	143	128	138	128
152	10	145	145	147	129
174	50	151	180	159	142
311	53	153	184	164	142
3	57	160	188	165	151
10	62	164	190	173	167
20	65	165	194	176	161
29	66	175	235	177	183
34	68	180	235	123	203
56	69	222	236	150	224
57	70	235	240	154	225
59	72	245	244	154	225
59	73	246	245	164	225
61	75	248	245	181	234
63	75	248	248	182	240
65	79	253	249	204	243
67	80	253	250	205	253
75	81	255	250	206	254
79	85	259	250	225	259
79	85	263	258	225	261
85	85	264	259	246	262
85	86	264	259	250	264
85	87	264	261	260	265
86	88	264	261	261	267
88	88	265	263	261	268
89	89	266	266	267	268
93	92	267	266	269	269

A.5. Dovrefjell Field Survey

Table A.5.1. Measured solifluction lobe characteristics upon Folldal, Dovrefjell, southern Norway. Key: mi = mixed lobe, g = turf banked lobe, r = stone banked lobe.

Altitude (m)	Slope Angle (°)	Max Width (m)	Max Length (m)	Orientation	Lobe Type
1414	17	20.2	68	262	g
1424	14	29.3	42.2	261	g
1425	18	16.9	29.1	262	g
1440	15	21.5	30.3	240	g
1444	20	19.8	23.4	238	r
1450	18	11.4	25.6	244	r
1454	20	15.7	32.6	252	r
1468	16	8	16.8	255	r
1470	15	12.5	28.8	244	mi
1467	17	16.3	45.1	240	mi
1468	12	9.2	9.7	238	mi
1483	16	17	27.4	236	g
1481	14	14.1	23.8	230	g
1488	13	11.7	12.6	235	mi
1492	12	10.3	23.7	238	r
1492	16	11.3	23.4	230	r
1486	12	10.6	13	210	g
1491	14	10.4	11.1	218	r
1504	14	12.5	22.3	210	r
1497	18	18.9	21.4	200	r
1487	13	12.9	25.9	222	r
1485	15	13.5	14.5	214	mi
1480	16	9.1	14.6	215	g
1478	15	5.9	7.1	217	g
1480	14	9.1	9.3	216	mi
1474	15	17.2	14.9	214	g
1469	16	18.4	21.6	212	g
1461	15	10.7	11.4	220	g
1459	11	11.8	16.1	200	g
1461	10	12.4	16.5	198	g
1460	14	17.1	17.6	196	g
1459	15	8.5	10.8	218	g
1460	12	13.1	16.3	210	g
1466	11	8.7	10.4	200	mi
1472	12	10.3	10.1	200	mi
1471	12	11.9	14.4	184	g
1475	12	9.8	11.8	181	mi
1468	8	9.3	12.4	179	r
1463	9	14.9	27.8	184	mi
1451	10	13.7	34.1	184	g
1450	12	11.8	19.4	178	g
1442	12	9.2	20.1	173	g
1443	12	6.6	12.7	174	g
1452	14	10.1	23.6	159	mi

Altitude (m)	Slope Angle (°)	Max Width (m)	Max Length (m)	Orientation	Lobe Type
1460	10	9.1	7.5	183	g
1457	13	12.1	17.8	165	g
1453	14	6.2	18.1	174	g
1452	8	7.3	16.4	160	mi
1455	10	13	21.6	150	g
1450	12	9.2	15.2	164	g
1417	8	8.4	6.2	168	g
1413	8	5.1	7	110	mi
1410	12	6.8	14.8	164	g
1406	13	4.5	8.2	160	g
1405	12	8.4	7.2	161	g
1404	12	9.4	13.1	156	g
1402	12	8.9	12.6	160	g
1400	14	8.6	16.1	160	mi
1400	11	9.7	14.7	148	mi
1389	10	8	17.2	154	g

APPENDIX B : Test Program Documentation

The appendix highlights the experimental timetable for all electronic data collection carried out within the investigation, it also provides an example of the safety documentation used to ensure the centrifuge was functioning within its operating limits during all slope model thaw phases.

B.1. Testing Timetable

The following section outlines the testing schedule for electronic data captured during the geotechnical and centrifuge-modelling elements of the current experimental investigation.

Table B.1.1. The centrifuge-modelling test program used within the current investigation.

TEST SERIES	SLOPE ANGLE (°)	HOST MATERIAL	TEST PHASE	SERIES RESULT	F/T CYCLES	TEST DATE
1	12	Lacustrine Silt	Proof	Failure	1	Sep-00
2	12	Natural	Primary	Gelifluction	4	Dec-00
3	16	Natural	Primary	Failure	1	Mar-01
4	8	Natural	Primary	Gelifluction	4	Jun-01
5	4	Natural	Primary	Gelifluction	4	Sep-01
6	8	10 Silt	Secondary	Failure	2	Dec-01
7	12	10 Clay	Secondary	Failure	1	Feb-02
8	4	10 Silt	Primary	Gelifluction	4	May-02
9	8	Natural	Secondary	Gelifluction	4	Jun-02
10	8	10 Clay	Secondary	Failure	1	Jul-02
11	4	20 Silt	Secondary	Gelifluction	4	Aug-02
12	4	10 Clay	Secondary	Gelifluction	4	Nov-02
13	4	20 Clay	Secondary	Gelifluction	4	Dec-02

Table B.1.2. Oedometer test program used within the current investigation.

TEST SERIES	WEIGHT (kg)	HOST MATERIAL	NUMBER OF TESTS	TEST DATE
1	2	Natural	1	Sep-00
1	4	Natural	1	Dec-00
1	8	Natural	1	Mar-01
1	2	Natural	1	Jun-01
2	4	10 Silt	1	Sep-01
2	8	10 Silt	1	Dec-01
2	32	10 Silt	1	Feb-02
2	64	10 Silt	1	May-02
3	8	10 Clay	1	Jun-02
TEST	WEIGHT	HOST	NUMBER	TEST

SERIES	(kg)	MATERIAL	OF TESTS	DATE
3	16	10 Clay	1	Jul-02
3	32	10 Clay	1	Aug-02
3	64	10 Clay	1	Nov-02

Table B.1.3. Direct drained shear box test program used within the current investigation.

TEST SERIES	WEIGHT (kN)	HOST MATERIAL	NUMBER OF TESTS	TEST DATE
1	8	Natural	1	Oct-01
1	16	Natural	1	Nov-01
1	32	Natural	1	Dec-01
1	64	Natural	1	Jan-02
2	8	10 Silt	1	Oct-01
2	16	10 Silt	1	Nov-01
2	32	10 Silt	1	Dec-01
2	64	10 Silt	1	Jan-02
3	8	10 Clay	1	Oct-01
3	16	10 Clay	1	Nov-01
3	32	10 Clay	1	Dec-01
3	64	10 Clay	1	Jan-02
4	8	20 Silt	1	Mar-03
4	16	20 Silt	1	Mar-03
4	32	20 Silt	1	Mar-03
4	64	20 Silt	1	Mar-03
5	8	20 Clay	1	Apr-03
5	16	20 Clay	1	Apr-03
5	32	20 Clay	1	Apr-03
5	64	20 Clay	1	Apr-03

B.2. Centrifuge Counter Balance Equation

The following section describes the correct completion of the balance calculation and test authorisation spreadsheets necessary before model slope thaw phases within the Cardiff Geotechnical Centrifuge center.

The centrifuge package was centrally mounted upon the gondola platform (see chapter three). For the safety purposes the package was considered as a single unit that normally consisted of the strong box, the soil slope model, and additional items connected to or mounted on the strong box. The net gravity (g) level (net acceleration) in flight increases with the radius on a centrifuge, it was therefore necessary specify the point within the slope model to which the specified g level was to be calculated. For the purposes of the balance calculation the specified g point was assumed to lie on the line through the centre of the gondola platform and

perpendicular to the top of the platform. The specified G point was chosen by defining the distance from the top of the mat, towards the pivot, along the line that combined the centre of mass of the gondola and package.

The objective of the balance calculation was to provide an appropriate amount of counterbalance on the geotechnical centrifuge. Figure B.1 shows the in flight forces acting on the centrifuge due to the mass of the gondola and package, and those due to the counterbalance. At the geotechnical centrifuge operating speed of 10g, the horizontal inertial forces due to the rotation are much larger than the vertical forces due to the self-weight of the components mounted on the centrifuge beam (Barralos, 2000). The requirement for the current investigation was therefore to balance the force due to the sum of the inertial forces of the centrifuge gondola and the package (i.e. the two horizontal components outlined in fig. B.2.1).

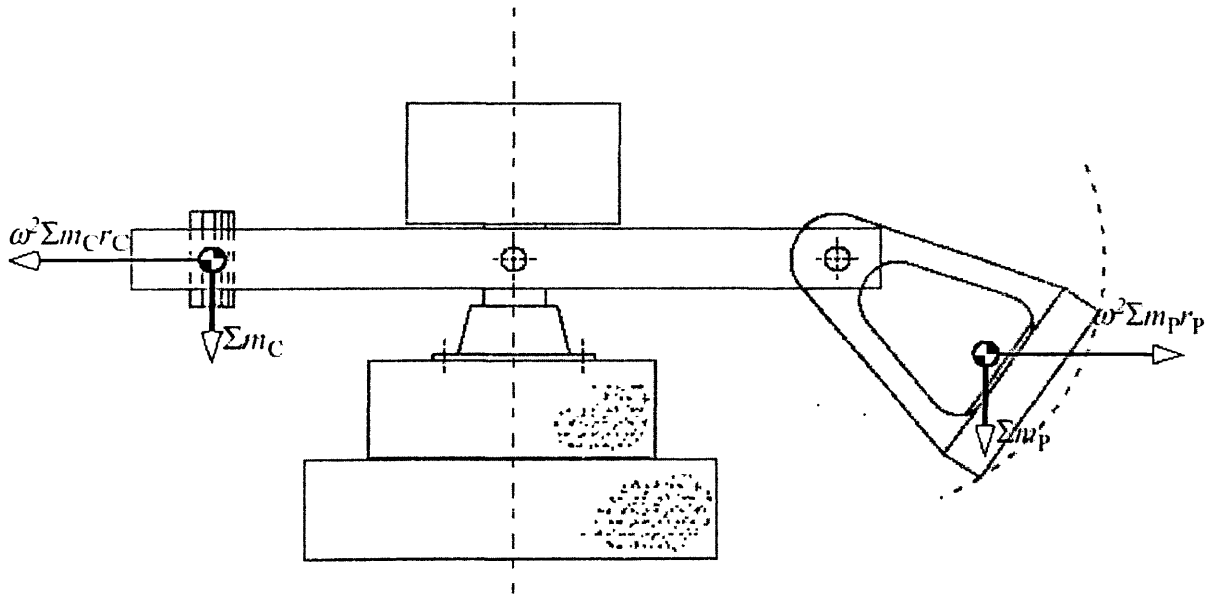

Figure B.2.1. Forces on the geotechnical centrifuge beam in flight (Source: Barralos, 2000, fig. 3)

The balance calculation and test authorisation form, plus sheets documenting the test package contents and procedure were available as a Microsoft Excel spreadsheets, these were used for all slope model tests as part of the general safety protocol. The safety spreadsheet suite was composed of three separate sections: the balance calculation and test authorization form, the package details, and test procedure forms. The purpose of the spreadsheets was to formalise the recording of all

elements being mounted on the geotechnical centrifuge, to document the proposed test procedure, and to indicate the most suitable amount of counterbalance weight.

The 'balance calculation and test authorisation form' outlined general test information such as the identification code for the proposed test, the date of proposed test, the net g level required, the distance above the gondola mat at which the required g level will act, and a short description of the test (see fig. B.2.2). The spreadsheet automatically calculated the slope angle of the gondola in flight, the radius to the point where the g level was specified, the two components of the net acceleration, and the required speed of the geotechnical centrifuge in revolutions per minute (RPM).

The centrifuge package consisted of the strong box, the model, and additional items connected to or mounted onto the strong box. The details of the test package were automatically updated within the multiple spreadsheets. The gondola mass was a constant, and the radius to the gondola centre of mass was calculated automatically through using gondola slope angle. The masses and locations of the instrument housing, the centrally mounted centrifuge operators camera, the pneumatic control valves, the stock bar on the end of the centrifuge arms on the counterbalance side, and the known imbalance in the centrifuge arms, were accounted for automatically when determining the appropriate counterbalance weight. The counterweights were made of steel. They all had the same cross-sectional shape; but through different thickness were able to make available different counterbalance masses. Prior to test authorization the correct amount of suitable counterweights were calculated to bring the load imbalance across the centrifuge arm into the permitted safety range.

BALANCE CALCULATION AND TEST AUTHORISATION FORM (Rev. 5, 11/02/00)

Test ID:	Smith 6a
Date of test:	12-Dec-01
Research worker:	James Smith

Net G level =	10.0
Dist. above mat of G point (m) =	0.297
Radius where G specified (m) =	2.3
Vertical G level =	1.0
Centripetal G level =	9.9
RPM =	62.4

TEST DESCRIPTION:	Twelve degree Slope. Prawle Point substrate + Ten percent added silt

CENTRIFUGE DETAILS

Radius to gondola pivot =	1.600 m	Distance pivot to top of mat =	0.983 m
Slope angle of gondola at G =	5.7 degrees	Radius to centre top of mat =	2.578 m

PACKAGE DETAILS

Package mass Σ M =	519.500 kg
Σ M_p x lever =	1222.619 kgm
Radius to package C_pM =	2.353 m

COUNTER WEIGHT DETAILS

Thickness (mm)	Area (m^2)	No of ?	Mass (kg)
0.5	0.3675	0	0.000
1	0.3675	1	2.922
2	0.3675	0	0.000
5	0.3675	0	0.000
10	0.3675	2	58.433
20	0.3675	0	0.000
50	0.3675	1	146.081
100	0.3675	2	584.325
		Total Mass (kg) =	791.760
		Total Thickness (mm) =	271.000

ADDITIONAL ELEMENTS

Element	Radius to C_pM (m)	Mass (kg)	Mass x C_pM (kgm)
Aerofoil	2.100	1.425	2.993

BALANCE CALCULATION

Element	Radius to C_pM (m)	Mass (kg)	Mass x C_pM (kgm)
Package	2.353	519.500	1222.619
Gondola	2.467	435.000	1072.986
Arm O.o.B			-232.000
Counter Weight	-1.715	791.760	-1357.473
Stock bar	-1.915	371.000	-710.465

Calculated package mass = 519.500 (kg)

Measured package mass = (kg)

Σ $m_{x/p}$ = 2066.60 kgm

Σ $m_{x/c}$ = -2067.94 kgm

Difference = -1.34 kgm

Signed (Research worker) Date:

Calculation check

Signed (Engineer) Date:

Measurement of mass

Signed (Centrifuge operator) Date:

Figure B.2.2. Balance calculation and test authorisation form. The sections of the spreadsheet intended for user input were shaded light grey. The rest of the spreadsheet was password protected, to maintain data integrity within the balance calculations. Information was automatically copied between the three different spreadsheets as required.

PACKAGE DETAILS

Test ID:	Smith 6a
Date of test:	12-Dec-01
Research worker:	James Smith

Net G level =	10.0
Dist. above mat of G point (m) =	0.297
Radius where G specified (m) =	2.3
Vertical G level =	1.0
Centripetal G level =	9.9
RPM =	62.4

TEST DESCRIPTION:	Twelve degree Slope. Prawle Point substrate + Ten percent added silt

Element	Mass of each, (kg)	No. Off	Mass, M (kg)	Dist above mat, d_B (m)	Lever arm (radius), d	Mass x lever (kgm)
STRONG BOX MANIFEST						
Strong box	345.500	1	345.500	0.227	2.352	812.689
CONTENTS MANIFEST						
Model	125.700	1	125.700	0.213	2.366	297.424
Additional liner	48.300	1	48.300	0.250	2.329	112.506
ADDITIONAL MANIFEST ITEMS						

TOTAL PACKAGE DETAILS

Mass of package Σ M (kg) = 519.500 **ΣMass x lever (kgm) = 1222.619**

Radius to Package C$_g$M (m) = 2.353

Figure B.2.3. Test package details form.

The package details sheet was an inventory of all elements of the package, it documented each test elements mass and the distance above the gondola mat for its centre of mass (see fig. B.2.3). For the purposes of the balance calculation each

element's centre of mass was assumed to lie on the line through the centre of the gondola platform and perpendicular to the top of the platform and located by its distance from the top of the mat, towards the pivot, along this line. The spreadsheet automatically calculated the radius to the centre of mass of each element. However, for some complex elements, such as the strong box or a profiled slope, it was necessary to undertake a detailed calculation via a separate element mass and centre of mass calculation spreadsheet (see fig. B.2.4).

ELEMENT MASS AND CENTRE OF MASS CALCULATION

MATERIAL DENSITIES

Material	Steel	Ally	Perspex	Dry sand	Wet sand	Clay	ZnCl	Wood	Ice	wet silt	
Density (kg/m³)	7830	2820	1300	1725	2100	2100	1725	600	920	2100	

Component	Depth (m)	Width (m)	Bl (m)	Area (m²)	Volume (m³)	Material	Density (kg/m³)	No. Off	Mass, M (kg)	Dist. above mat d_m (m)	Mass.w height (kg/m)
COMPONENT DETAILS FOR ELEMENT 1											
ELEMENT 1 DESCRIPTION											
Aluminium liner											
endplates x2	0.500	0.025	0.490		0.006125	ally	2820	2	34.545	0.326	11.262
baseplate	0.500	0.805	0.025		0.010063	ally	2820	1	28.376	0.076	2.142
feet	0.040	0.105	0.040		0.000168	ally	2820	8	3.790	0.043	0.163
Strongbox											
endplates x2	0.500	0.023	0.550		0.006325	steel	7830	2	99.050	0.275	27.239
baseplate	0.500	0.855	0.023		0.009833	steel	7830	1	76.998	0.115	8.854
Windows											
perspex x2	0.050	0.900	0.550		0.024750	perspex	1190	2	58.905	0.275	16.199
Frames: outer angle x2					0.000810	steel	7830	2	12.685	0.545	6.913
inner angle x2	0.008	0.780	0.060		0.000374	steel	7830	2	5.863	0.520	3.049
sideplates x4	0.008	0.060	0.550		0.000264	steel	7830	4	8.268	0.275	2.274
outer bottomplate x2	0.008	0.900	0.060		0.000432	steel	7830	2	6.765	0.030	0.203
inner bottomplate x2	0.008	0.780	0.060		0.000374	steel	7830	2	5.863	0.030	0.176
feet x4					0.000140	steel	7830	4	4.385	0.012	0.053
ELEMENT 1 SUMMARY						Mass of element ΣM (kg) =			345.486 kg	$\Sigma M \times d_m$ =	78.525 kgm
										Height above mat of $C_g M$ of element =	0.227 m
ELEMENT 2 DESCRIPTION											
COMPONENT DETAILS FOR ELEMENT 2											
Perspex box											
sides	0.025	0.800	0.435		0.008700	perspex	1300	2	22.620	0.306	6.910
ends	0.450	0.025	0.435		0.004894	perspex	1300	2	12.724	0.306	3.887
base	0.500	0.800	0.025		0.010000	perspex	1300	1	13.000	0.101	1.307
model											
sand base	0.448	0.750	0.138		0.023184	wet sand	2100	1	48.686	0.165	8.030
soil model	0.448	0.750	0.045		0.015120	wet silt	2100	1	31.752	0.213	6.763
ELEMENT 2 SUMMARY						Mass of element ΣM (kg) =			128.782 kg	$\Sigma M \times d_m$ =	26.900 kgm
										Height above mat of $C_g M$ of element =	0.209 m

Figure B.2.4. Element mass and centre of mass calculation form.

The manifest on the package details sheet is divided into three sections (see fig. B.2.3). The strong box manifest, where the strong box was entered as a single item; the contents manifest, where the various elements mounted in or on the strong box were listed; and the additional items manifest, which was for the elements that were associated with the strong box but not actually mounted within it, such as interface boxes that were directly bolted to the gondola frame. Taken together, the elements documented in these three sections constituted the overall test package, these were delivered to the centrifuge operator for weighing as a complete unit prior to being mounted within the centrifuge.

TEST PROCEDURE

Test ID:	Smith 6a
Date of test:	12-Dec-01
Research worker:	James Smith

Net G level =	10.0
Dist. above mat of G point (m) =	0.297
Radius where G specified (m) =	2.3
Vertical G level =	1.0
Centripetal G level =	9.9
RPM =	62.4

TEST DESCRIPTION:	Twelve degree Slope. Prawle Point substrate + Ten percent added silt

CHECKLIST

Item	Description	Check
1	Start video recorders & camera	
2	Start centrifuge	
3	Increase speed to 1.0g in 3.3g steps	
4	Observe experiment until end of test	
5	Stop centrifuge	
6	Remove and dismantle package	

Figure B.2.5. Test procedure documentation.

The test procedure documented the actions to be taken during the centrifuge test (see fig. B.2.5). In particular, it documented the centrifuge speeds in RPM to be set during each stage of the test, the approximate duration for acceleration and deceleration stages, the visual and electronic observations to be taken, and what instruments or actuators were to be operated within the test flight.

APPENDIX C : Centrifuge Data Logger Customisation

The appendix presents the machine code that instructed the Campbell CR7 logger a mode of handling the raw information derived from temperature and pore pressure probes. This program code defined the scan and refresh rate whilst also identifying which electronic ports carried the specific raw voltage information which eventually became converted into relevant units necessary for thermal, movement and pressure measurement.

C.1. Copy of System Code: Pace.dld

```
};CR7
;PACE1.DLD

;$
;:time
:pp7039#15:PP7039#16:pp7039#1
7:pp7039#18
;:pp7039#19:pp7039#20:reftemp
:thermoc#1:thermoc#2
;:thermoc#3:thermoc#4:thermoc
#5:thermoc#6:thermoc#7
;:thermoc#8:thermoc#9:thermo#
10:          :__________
;:__________:__________:_______
__:__________:__________
;:__________:__________:_______
__:__________:__________
;:__________:__________
;$
MODE 1
SCAN RATE 2.0

1:P18
1:00
2:100
3:1

2:P2
1:6
2:6
3:3
4:3
5:2
6:1.0
7:0.0

3:P14
1:10
2:6
3:5
4:5
5:3
6:8
7:9
8:1.0
9:0.0

4:P17
1:5
2:8

5:P89
1:1
2:4
3:.5
4:10

6:P77
1:0111

7:P70
1:23
2:2


MODE 2
SCAN RATE 0.0000


MODE 3

MODE 10
1:32
2:64


MODE 12
1:0
2:0000
```

APPENDIX D : Instrument Documentation

The appendix describes the instrument calibrations calculations undertaken to ensure accurate data was gathered during the electronic experimental program. It presents the procedures used to calibrate data from the pore water pressure transducers used during the centrifuge modelling procedure, the linear voltage displacement transducers, and the proving ring used during the drained direct shear box testing.

D.1. Porewater Pressure Transducer

The Druck PDCR81 miniature pore pressure probes were calibrated after each centrifuge test series in order to convert the millivolt output voltage (mV) for each probe into the correct unit of KiloPascal pressure (kPa). The probes were calibrated at 1g conditions by recording the probe output voltage from different depths inside a column of water (see fig. D.1.1). The derived linear formula $y = \xi x + b$, where x was the output voltage and ξ the calibration factor determined for each probe transducer was used to derive the porewater pressure data (kPa) from the voltage output (mV). Calibration was undertaken upon the centrifuge gondola to maintain complete unity with modelling conditions through incremental probe movement within the water column (see table D.1.1). Sensor calibration enabled the identification of specific PDCR81 probes that responded poorly to change in water pressure; this was found to be particularly useful during the interpretation of post-series porewater pressure data. A total of thirteen calibration tests were performed upon six pore pressure transducers-these results were recorded and an example of one set of calibrated output is summarised below:

Table D.1.1. Output voltage (mV) for each Druck pore pressure transducer at different water depths (cm). Calibration data recorded post-series NS/12D.

Depth (cm)	PWP #1	PWP #3	PWP #4	PWP #5	PWP #6	PWP #7
0	-0.895	4.145	-13.838	0.88	-1.11	11.843
10	-1.37	3.257	-13.399	0.008	-1.819	11.251
20	-2.893	2.385	-12.998	-0.888	-2.555	10.735
30	-4.05	1.506	-12.553	-1.827	-3.375	10.303
40	-4.965	0.634	-12.14	-2.76	-4.162	9.779
0	-0.102	4.137	-14.178	0.92	-1.007	11.603
10	-2.182	3.291	-13.772	-0.008	-1.793	11.14

Depth (cm)	PWP #1	PWP #3	PWP #4	PWP #5	PWP #6	PWP #7
20	-2.4	2.436	-13.053	-0.92	-2.58	10.7
30	-3.223	1.54	-12.681	-1.878	-3.384	10.202
40	-3.6	0.609	-12.232	-2.776	-4.145	9.753

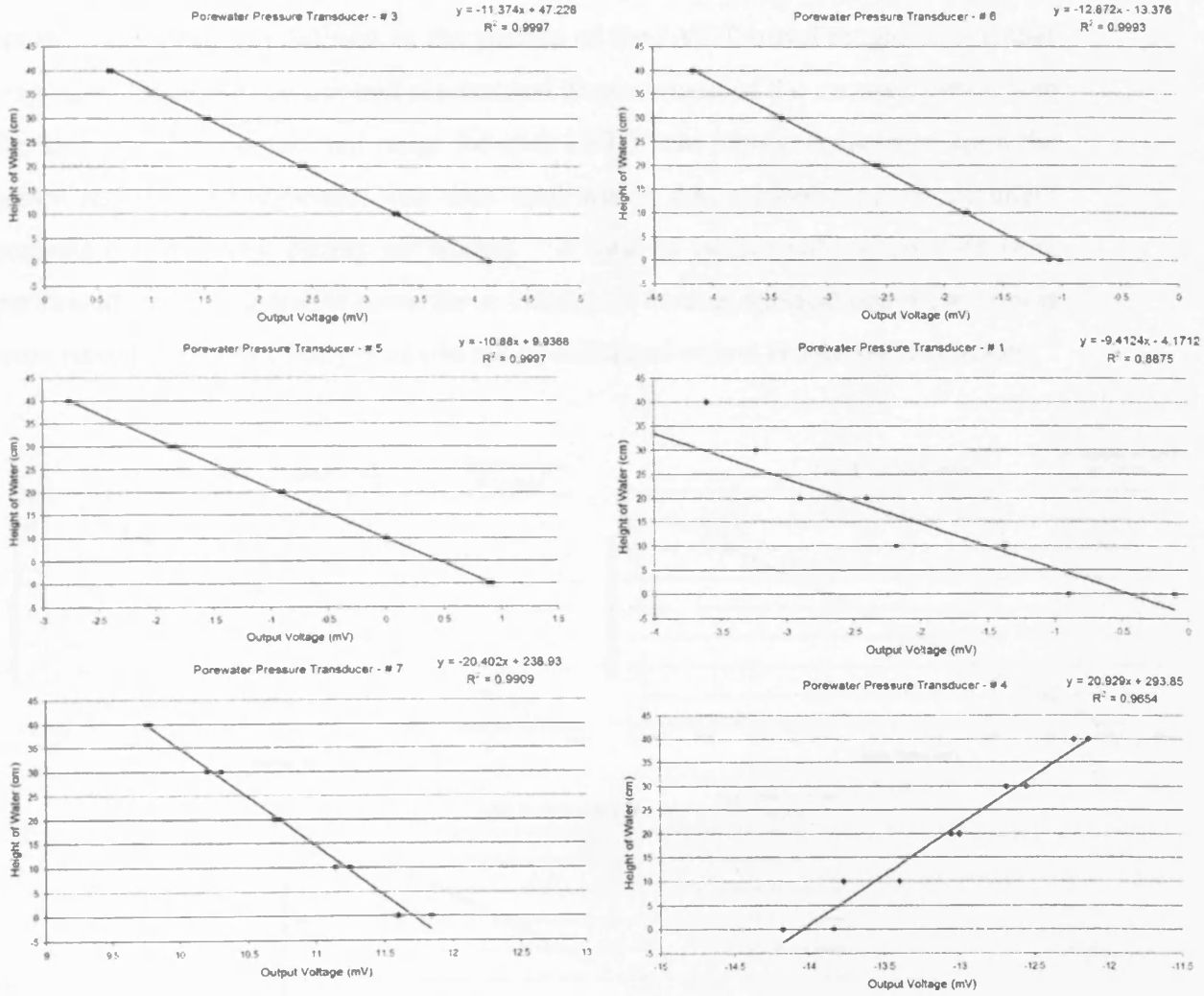

Figure D.1.1. Calibrated data for the complete suite of six porewater pressure transducers used during series 12D/NS.

D.2. Shear box and Frost Susceptibility Cell - LVDT

Linear voltage displacement transducers (LVDTs) were used to record horizontal and vertical displacement within the shear box (see section 4.5). Prior to experimental usage the transducers were calibrated to determine their operational range for undertaking accurate measurement. A calibration device enabled absolute LVDT displacement to be defined at micron scale against a fixed datum. An accurately applied amount of incremental displacement was placed upon the LVDT

whilst recording resulting changes to voltage output (mV) (see table D.2.1). The derived linear formula $y = \xi\ x + b$, where x was the output voltage and ξ the calibration factor determined for each probe transducer was used to derive the distance displacement (mm) from the voltage output (mV). The operational range for the transducer was defined as the portion of the LVDT travel magnetic coil that responded linearly to an applied mechanical displacement of the encased piston (see fig. D.2.1). The operational range for each LVDT was physically marked upon the piston sheath; the instrument was then used within that marked range to maintain accurate measurement during all testing. A total of twelve calibration tests were performed upon five transducers for a variety of testing applications-these results were recorded and an example of one set of calibrated output is summarised below:

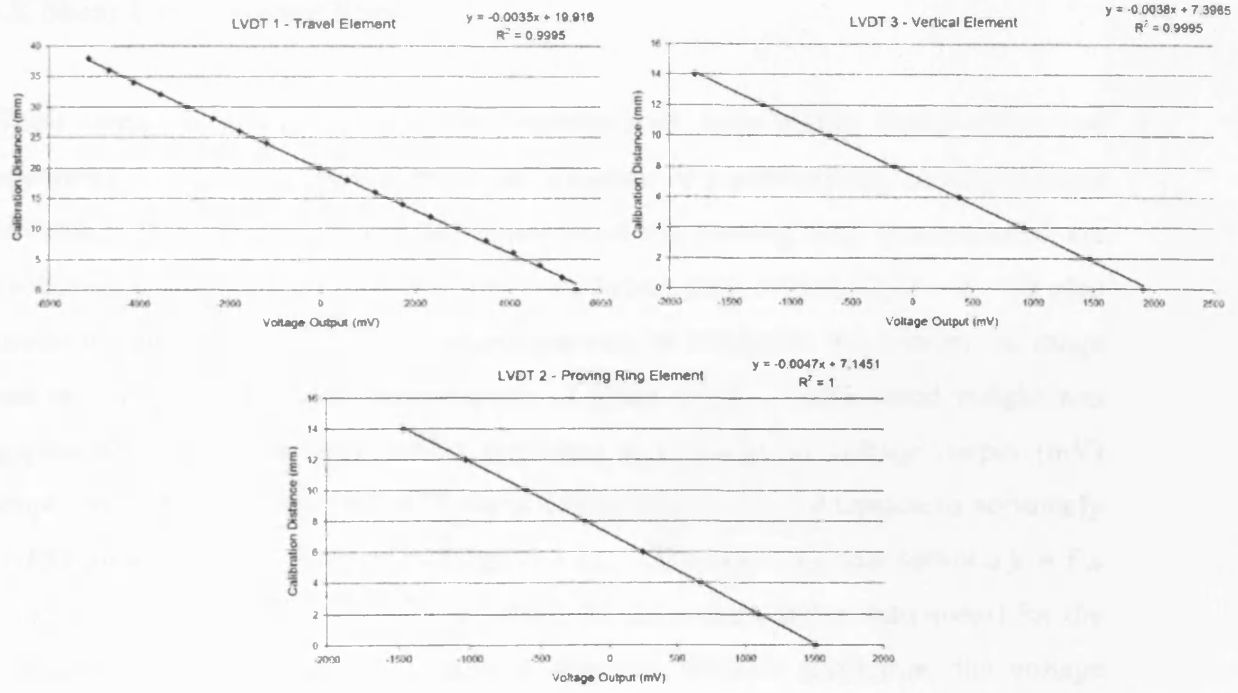

Figure D.2.1. Calibrated data for three LVDTs used during direct shear box testing series one and two (see appendix table A.2.2).

Table D.2.1. Output voltage (mV) for LVDTs subjected to increasing horizontal displacements (mm). Calibration data recorded before shear box series one and two.

Distance (mm)	LVDT 1 (Travel)	LVDT 2 (Proving Ring)	LVDT 3 (Vertical)
0	5444.344	1913.4575	1507.728
2	5137.779	1468.1015	1094.8625
4	4662.24	921.0365	667.062
6	4088.315	386.9535	246.5355
8	3487.919	-143.6215	-174.995

Distance (mm)	LVDT 1 (Travel)	LVDT 2 (Proving Ring)	LVDT 3 (Vertical)
10	2892.435	-679.762	-599.6895
12	2306.607	-1227.7375	-1031.0245
14	1722.276	-1789.251	-1464.15
16	1141.359	Nd	Nd
18	561.273	Nd	Nd
20	-17.49	Nd	Nd
24	-1178.899	Nd	Nd
26	-1760.482	Nd	Nd
28	-2341.067	Nd	Nd
30	-2920.653	Nd	Nd
32	-3507.064	Nd	Nd
34	-4094.474	Nd	Nd
36	-4654.832	Nd	Nd
38	-5110.81	Nd	Nd

Nd = No Data; LVDT reached maximum travel distance.

D.3. Shear box - Proving Ring

Shear stress was measured for the experimental soils within direct shear box apparatus. The apparatus used the deformation of a proving ring to record shear stresses within the soil unit. Deformation of the proving ring was recorded via calibrated linear voltage displacement transducers (see section D.2). It was also necessary to regularly calibrate the proving ring to determine the operational range and encourage an accurate measurement of shear stress. Incremental weight was applied to the proving ring whilst recording any change to voltage output (mV) within the centrally housed LVDT using both compression and tension to accurately reflect proving ring deflection (see fig. D.4.1). The derived linear formula $y = \xi x + b$, where x was the output voltage and ξ the calibration factor determined for the proving ring was used to derive the deformation distance (μm) from the voltage output (mV). The mV output was also transferred into shear stress (kPa) with respect to proving ring deformation recording in-situ soil stress. Deformation measurements were taken during two stages of unloading and loading to ensure accurate calibration of the proving ring unit (see tables D.3.1 & D.3.2). A total of three calibration tests were performed upon the same proving ring within the shear box testing program-these results were recorded and an example of one set of calibrated output is summarised below:

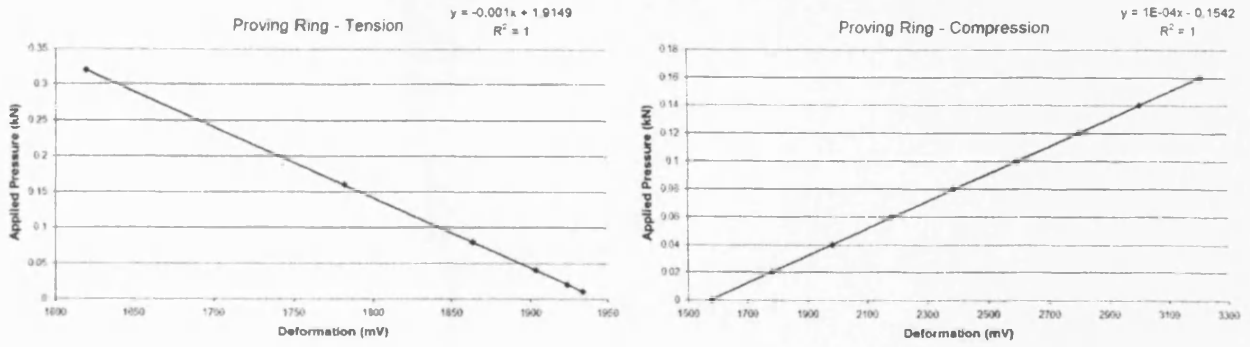

Figure D.3.1. Calibrated data for proving ring used during direct shear box series three (see table B.2.2).

Table D.3.1. Output voltage (mV) showing proving ring deformation under increasing compressive load (kN). Calibration data recorded before shear box series three.

Applied Load (KN)	Loading (Stage 1)	Unloading (Stage 1)	Loading (Stage 2)	Unloading (Stage 2)
0	1576.32	1578.1	1579.12	1578.38
0.02	1782.91	1772.76	1784.24	1783.41
0.04	1985.06	1977.45	1985.98	1980.78
0.06	2178.39	2181.06	2185.22	2184.43
0.08	2383.82	2386.7	2391.06	2392.52
0.1	2593.68	2590.1	2596.09	2598.92
0.12	2799.32	2796.93	2802.65	2801.23
0.14	3004.57	3000.97	3007.88	3007.29
0.16	3210.94	3204.7	3216.27	3211.36

Table D.3.2. Output voltage (mV) showing proving ring deformation under incrementally applied tension (kN). Calibration data recorded before shear box series three.

Applied Load (KN)	Loading (Stage 1)	Unloading (Stage 1)	Loading (Stage 2)	Unloading (Stage 2)
0.01	1933.78	1933.36	1933.66	1933.61
0.02	1923.72	1923.72	1923.38	1923.3
0.04	1903.09	1903.17	1903.34	1903.42
0.08	1863.78	1863.36	1863.16	1863.49
0.16	1781.56	1781.52	1781.72	1781.55
0.32	1618.34	1618.82	1619.71	1619.13